December 2020

Searching for new physics at colliders and from precision measurements

Yong Du
University of Massachusetts Amherst

SEARCHING FOR NEW PHYSICS AT COLLIDERS AND FROM PRECISION MEASUREMENTS

A Dissertation Presented

by

YONG DU

Submitted to the Graduate School of the
University of Massachusetts Amherst in partial fulfillment
of the requirements for the degree of

DOCTOR OF PHILOSOPHY

September 2020

Department of Physics

SEARCHING FOR NEW PHYSICS AT COLLIDERS AND FROM PRECISION MEASUREMENTS

A Dissertation Presented

by

YONG DU

Approved as to style and content by:

Michael J. Ramsey-Musolf, Chair

Daniela Calzetti, Member

Verena Martinez Outschoorn, Member

Lorenzo Sorbo, Member

Narayanan Menon, Department Chair
Department of Physics

DEDICATION

To my parents, and my sister.

ACKNOWLEDGMENTS

Along the way of finishing my PhD degree at the University of Massachusetts-Amherst, I am grateful to many, especially during this pandemic.

I would like to first thank the University of Massachusetts-Amherst for being diverse, equal and inclusive. The environment the University of Massachusetts-Amherst has been providing always makes me feel welcomed, accepted and respected.

I also thank my advisor Prof. Michael Ramsey-Musolf for his persistent guidance in the past five years. I appreciate the special hours during our regular group meetings when he taught us how to manage time, write research papers and prepare for scientific talks that have helped a lot during my PhD career at the University of Massachusetts-Amherst. It is also an unforgettable experience to have several Chinese conversation at the beginning of our group meetings, especially as an international student at Amherst. I would also like to thank my committee Prof. Daniela Calzetti, Prof. Verena Martinez Outschoorn and Prof. Lorenzo Sorbo, for their comments on my thesis and prompt help whenever I am in need of them. I want to express my gratitude to Prof. Jennie Traschen for her suggestion at the early stage of my PhD career and her encouragement during my tough time. I also thank Jane Knapp, she is so thoughtful and considerate to international students that without her kind and patient help, I could not have been able to adapt to the life at Amherst so quickly. Thank Carlo Dallapiccola, Katie Bryant and Sarah Rastallis for their great and nice help for preparing the paperwork that eventually allowed my wife and I to find our warm and happy home at the North Village, a great community that we love a lot, after our wedding so we never have to live apart.

Thank you my collaborators Satoru Inoue, Aaron Dunbrack, Jiang-Hao Yu, Ayres Frietas, Hiren Patel, Cheng-Wei Chiang, Giovanna Cottin, Kaori Fuyuto, Hao-Lin Li and Fei Huang for the collaboration, working with them on physics has been a great pleasure. Especially, I am indebted to Jiang-Hao Yu, Hiren Patel and Kaori Fuyuto for their encouragement and days of conservation during the very difficult time of my PhD career, the flame you ignited had warmed up me in the cold winter, my gratitude to you is inexpressible.

Thank you, my friends Satoru Inoue, Ling-Fei Wang, Chien-Yeah Seng, Huai-Ke Guo, Yang Lei, you might not know how you have encouraged me through my whole PhD career. Thank you Meng Xin, the friendship you share with me has been warming up my heart during these five years, it is also so lovely to be a neighbor with your family in the North Village community. I wish your lovely daughter Yi Xin healthy and strong. And, thank you Sebastian Urrutia Quiroga, your friendship makes the last few weeks of my time at Amherst memorable.

Thank you my family members, Chung-Jung Hsu, Chih-Lun Hsu, Lily Su, Mei-Zhe Wang, Wan-Ting Xie, Pei-Jian Wang, Shui-Yao Huang, Hao Cai, Jun-Xiao Ma, Yi-Ke Wang, Yan Zhang, Zheng Shao, Zoey, Selina, Amy, Johnny, Sara, Lu Ji, Fang Liu, Jiajia, Yuanyuan, Wen-Juan Yao, Xin-Jun Gao and many others for preparing and celebrating my wedding. Especially, thank you Chung-Jung and Chih-Lun, my gratitude to you are deeper than the sea, and higher than the sky. Thank you for your warm invitation when you learned my father's absence during my childhood. The love I received from you has reshaped me inside.

Thank you dad. I would never blame you for your absence and you have always been providing the best I need. You are the superhero of mom, your daughter, and your son. You, and mom, built our warm home out of nothing with four hands, I never expected anything more than that. Thank you mom, you sacrificed yourself too much for the family, and you expected nothing. You are the best mom among the

best moms in the world. And, thank you my sister, for your support since I was in high school. I can not imagine how you managed to support my flight ticket and my first few months' life expense in the US when your monthly wage was less than $400. You are not only a great sister, but also a great mother. I wish Susu grow happily in your company.

Thank you Kate for marrying me and flying with me to the US while I have nothing and you could have succeeded in many fields if you had chosen to stay in China. I love you.

ABSTRACT

SEARCHING FOR NEW PHYSICS AT COLLIDERS AND FROM PRECISION MEASUREMENTS

SEPTEMBER 2020

YONG DU

B.S., ZHENGZHOU UNIVERSITY

Ph.D., UNIVERSITY OF MASSACHUSETTS AMHERST

Directed by: Professor Michael J. Ramsey-Musolf

Beyond the great triumph of the Standard Model of particle physics, several fundamental questions remain unknown with the framework of the Standard Model. Among them are the non-zero neutrino masses, the dark matter and the baryon asymmetry of the Universe. Answers to these questions require new physics beyond the Standard Model and searching for the new physics beyond the SM has been a major task for modern particle physicists. The signal of this new physics can be searched through colliders, low- and high-energy precision measurements, as well as precision cosmological observation. Here I present my work in searching for the new physics through colliders and precision measurements that addresses the neutrino mass, the dark matter and the baryon asymmetry problems.

TABLE OF CONTENTS

LIST OF TABLES

Table **Page**

LIST OF FIGURES

Figure **Page**

INTRODUCTION

In the 1960s, the Standard Model (SM) of particle physics was constructed by Sheldon Glashow, Steven Weinberg and Abdus Salam [37–39] through an application of the Yang-Mills theory [40] and the incorporation of the Higgs mechanism [41–43]. The SM has been very successful in the explanation of the phenomenologies we observe since then, including the discovery of the W and the Z bosons in 1983 at CERN [44–47] and the top quark in 1995 at Fermilab [48, 49]. Scientists had been seeking for the last piece of the SM, the Higgs boson which is responsible for masses, for decades until its discovery in 2012 at the Large Hadron Collider (LHC) [50, 51].

Though SM has been very successful in explaining almost every aspect of particle physics, there are still several challenging but fundamental questions that SM does not provide any answers, these including

1. *The strong CP problem*: What is the neutron electric dipole moment and why does quantum chromodynamics (QCD) seem to conserve the Charge conjugation-Parity (CP) symmetry?

2. *The hierarchy problem*: What prevents observables, like the mass of the SM Higgs boson, at the electroweak scale from receiving quantum corrections at the Planck scale? Why are the electroweak and the Planck scales so different?

3. *Neutrinos*:: What are the absolute neutrino masses? What is (are) the mass generating mechanism(s) for neutrinos? Why are there three generations of neutrinos? Is there any CP violation from the neutrinos?

4. *Dark matter*: What is the nature of dark matter? How does dark matter interact with normal matter besides gravitation?

5. *Baryon asymmetry of the Universe*: What is responsible for the observed baryon asymmetry of the Universe?

6. *Charge quantization*: Why charge is quantized in unit of e? Why is fractional charge absent in nature? Does magnetic monopole exist?

7. *Quantum gravity*: Can quantum mechanics and general relativity be unified consistently? Is spacetime fundamentally discrete or continuous? Do gravitons exist and what is its particle nature?

Addressing all these problems in this thesis will be impossible, instead, in what follows, we focus on the neutrino mass, the baryon asymmetry and the dark matter problems.

0.1 Neutrino masses

Neutrino oscillation was first predicted by Bruno Pontecorvo in 1957 [52,53], which was later realized to be also capable of explaining the solar neutrino problem [54]. The oscillation would imply non-zero neutrino masses and was later observed by the Super-Kamiokande (Super-K) experiment in 1998 from atmospheric neutrino oscillation [55], the Sudbury Neutrino Observatory (SNO) experiment in 2001 from solar neutrino oscillation [56] and the Kamioka Liquid Scintillator Antineutrino Detector (KamLAND) experiment in 2002 from reactor neutrino oscillation [57]. Since then, the fact that neutrinos have non-zero masses has been accepted.

However, the SM is constructed based on the $\mathrm{SU(3)_c} \otimes \mathrm{SU(2)_L} \otimes \mathrm{U(1)_Y}$ gauge group, meaning that all terms in the Lagrangian have to obey this symmetry including neutrinos. In the SM, as we will discuss more in detail in Chapter 1, right-handed neutrinos are absent in the SM. As a result of the SM gauge group and the particle

contents of the SM, neutrinos are massless particles in the SM. In principle, one can introduce the right-handed partner of neutrinos and obtain neutrinos masses from the Higgs mechanism as we will discuss in Chapter 1, but the smallness of neutrinos masses would require the Yukawa couplings to be at most of $\mathcal{O}(10^{-13})$ and the question would then then becomes as why we have such a tiny coupling in the Lagrangian. On the other hand, neutrinos could in principle also receive masses from higher dimensional operators or loop corrections, which we will discuss more in Chapter 2. However, the mass term from these operators or loop corrections will violate the total lepton number by two units and is thus forbidden in the SM. Therefore, to explain non-vanishing neutrino masses, new physics beyond the SM is needed.

There are many beyond SM scenarios proposed to explain the tininess of neutrino masses and among them, perhaps the most widely considered ones are the seesaw mechanisms, where the tiny neutrino masses are obtained from the ratios of physical scales. At tree-level, only three types of seesaw mechanisms exist, known as the types-I, -II, and -III [58–75] seesaw models. However, due to the scales, which will become clearer in Chapter 2, involved for these three tree-level seesaw mechanisms, it turns out that the type-II seesaw mechanism is the only one accessible at colliders. Therefore, in this thesis, we will only focus on the type-II seesaw scenario for the explanation of neutrino masses. On one hand, the type-II seesaw mechanism introduces a complex triplet that transforms as $(1, 3, 2)$ under the SM gauge group, thus the triplet particles can be searched for at current and future colliders. Collider phenomenologies of the triplet will be discussed in detail in Chapter 6. On the other hand, due to interactions between the triplet and the SM Higgs doublet, the SM Higgs potential will be distorted such that the model would also be a potential candidate to explain the baryon asymmetry of the Universe through electroweak baryogenesis. This viable parameter space of the complex triplet model that can explain this asymmetry remains a research problem, and is beyond the scope of this thesis. In

what follows, we review the baryon asymmetry problem and the mechanisms that can explain this asymmetry.

0.2 Baryon Asymmetry of the Universe (BAU)

BAU has been precisely measured by the Planck satellite to be $n_B/s = (8.66 \pm 0.04) \times 10^{-11}$, which is also consistent with constraints from the Big Bang Nucleosynthesis (BBN) [29]. To generate this asymmetry, in 1967, Sakharov [76] found that three criteria, now known as the Sakharov conditions, need to be satisfied in the early Universe: (1) baryon number violation; (2) C and CP violation (CPV); (3) out of thermal equilibrium (or CPT violation). As will become clear in Chapter 3, each condition is indispensable to successfully generate the asymmetry in the early Universe and remain an observable asymmetry today.

Based on these three Sakharov conditions, many baryogenesis mechanisms have been proposed and studied in the past, such as baryogenesis in grand unified theories (GUTBG), Affleck-Dine baryogenesis (ADBG), leptogenesis, electroweak baryogenesis (EWBG) [12,13,77–87] etc. Among them, electroweak baryogenesis (EWBG) has attracted significant attention mainly for two reasons: (1) SM itself already has all the ingredients satisfying all the Sakharov conditions through EWBG; (2) When new physics is introduced to explain BAU through EWBG, the scale of new physics is at the weak scale such that the new physics could be discovered or refuted at current and future colliders.

However, despite the fact that SM already has all the ingredients in principle to realize the three Sakharov conditions, to successfully generate the asymmetry we observe today through the EWBG, it requires a strong first order electroweak phase transition (SFOEWPT) as well as a large CPV that is comparable to the order of the measured baryon asymmetry. However, as we will see in Chapter 3, both these two requirements are not satisfied in the SM – In fact, the dimensionless measure of

CPV in the SM that will be discussed in Chapter 3 is of $\mathcal{O}(10^{-20})$, which is about 10 orders of magnitude smaller than the observed baryon asymmetry. Furthermore, the SFOEWPT is also absent in the SM with the Higgs mass $m_h = 125\,\text{GeV}$ [1], which actually corresponds to a smooth crossover in the phase plot instead of a phase transition [88–93]. Therefore, to explain the BAU through EWBG, new physics is needed in the Higgs portal of SM to generate a SFOEWPT.

In this thesis, two models related to EWBG are studied in detail in Chapter 6 and Chapter 7 respectively. To be specific, we study the complex triplet model in Chapter 6 and the real triplet model in Chapter 7. Each model extends the Higgs sector of the SM by a new scalar that distorts the shape of the SM Higgs potential at high temperature such that the SFOEWPT is made possible. However, as mentioned above, for the complex triplet model in Chapter 6, we only focus on its collider phenomenologies and its ability to explain the BAU remains unexplored at the time when this thesis is writing. On the other hand, for the real triplet model studied in Chapter 7, we focus on the scenario where it provides a viable dark matter candidate in order to address the "dark matter" problem listed above, while we point it out that it has already been studied in Ref. [94–97] with respect to the BAU problem through EWBG. Before discussing more about dark matter in the real triplet model, we briefly review the dark matter problem next.

0.3 Dark matter (DM)

The first accepted evidence of the existence of DM was from the Swiss astrophysicist Fritz Zwicky in 1933 by studying the Coma Cluster [98, 99]. Upon the application of the virial theorem, he concluded that the cluster contained about 400 times more mass than what was visually observable, and he called the unseen matter the "dunkle Materie", meaning "dark matter". Later in the 1960s and 1970s, Vera Rubin *et al* provided a stronger evidence for the existence of DM through measuring

rotation curves of edge-on spiral galaxies [100], and they concluded that dark matter is about six times much than the visible matter. The idea of DM was broadly accepted since then with more evidence observed afterwards including gravitational lensing [101–103], Cosmic Microwave Background (CMB) anisotropy [29, 104–106], Baryon Acoustic Oscillation (BAO) [107, 108] and the Bullet Cluster [109].

Based on observation, the following features of DM are obtained: (1) DM is electrically neutral or its electrical charge is tiny to ensure that DM was not tightly coupled to the photon-electron-positron plasma in the early Universe; (2) The lifetime of DM should be comparable to or greater than the age of the Universe in order to explain the current DM relic density we observe; (3) For particle DM, it shall interact feebly with our matter world as DM seemingly only has gravitational interaction from current experiments. Looking into the SM, the only possible candidates are the neutrinos. However, as has been precisely measured by the Planck satellite [29], the neutrino energy density is $0.00144 \lesssim \Omega_\nu \lesssim 0.00287$, which is too few to account for the DM energy density $\Omega_{\rm DM} \simeq 0.267$ in our Universe. Another reason to reject the idea of pure neutrino DM is from the fact that the neutrinos are too hot to allow formation of small-scale structures that are essential for the born of late-time stars, galaxies and clusters of galaxies, in the early Universe. Therefore, physics beyond the SM (BSM) is needed in order to explain the measured DM relic density.

Many scenarios have been proposed and intensively studied to understand the particle nature of DM over a broad mass range as summarized in Figure 1, these include primordial black holes as DM [110–114], axions [115–117], sterile neutrinos [118], asymmetric DM [119–121], hidden sector DM – for a review, see Refs. [7, 122], self-interacting DM [123], Feebly Interacting Massive Particles (FIMP) [124–126], Weakly Interacting Massive Particle (WIMP) [127] etc. Among these interesting scenarios, WIMP DM has gained its popularity from two aspects: (1) To obtain the correct DM relic abundance, WIMP DM self-interaction cross section turns out to

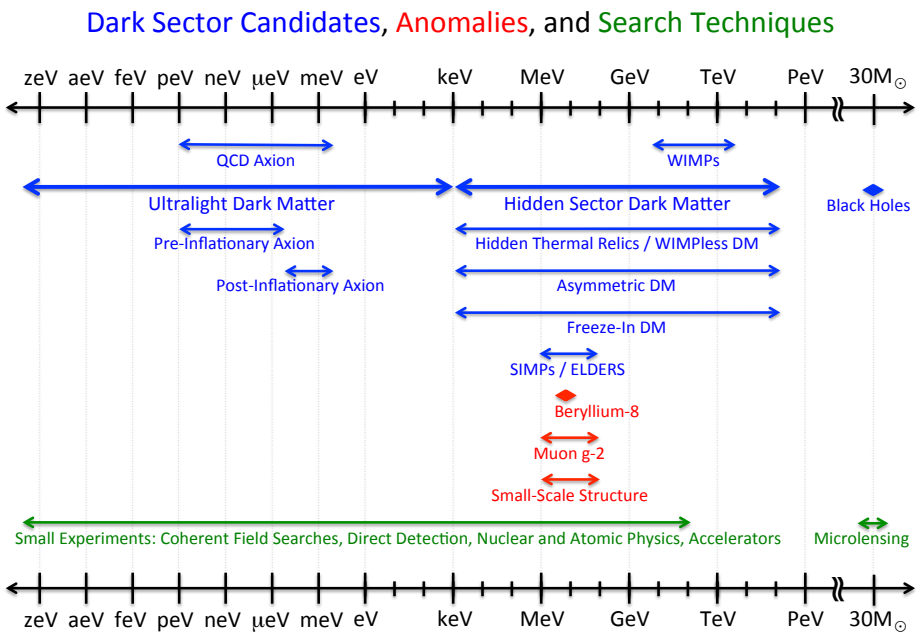

Figure 1: Mass range of different dark matter candidates and the corresponding searching strategies. Plot adopted from [7].

be what one would expect for particles at the weak scale. This is also known as the "WIMP miracle" that will be discussed in more detail in Chapter 4; (2) Since its mass is at the weak scale, WIMP dark matter can thus be discovered or refuted with current technologies. Due to these features, WIMP DM has been intensively studied at colliders, deep underground experiments and telescopes as we will discuss in more detail in Chapter 4.

Unfortunately, we have not yet seen any definitive signal from dark matter yet. For the recent excess from the XENON1T experiment [128], since the origin for that excess signal is still not clear, we will only briefly review this excess in Chapter 4. We will then present our recent work on WIMP dark matter in the real triplet model in Chapter 7 from a dedicated study on its collider phenomenologies and constraints from dark matter detection.

Understanding each of these three questions discussed above will eventually lead to the discovery of new physics beyond the SM paradigm and deepen our knowledge

of nature. In practice, people have been trying to search for new physics from various aspects that can be categorized into three frontiers: (1) The energy frontier; (2) The intensity frontier, and (3) the cosmic frontier.

0.4 Energy frontier

"Energy frontier" refers to experiments which take advantage of high-energy colliders to search for new particles directly. As mentioned earlier above, after the discovery of the Higgs boson at the LHC in 2012 [50, 51], the modern theory of particle physics has been completed. However, SM shall not be taken as the end of the story as it does not even predict the parameters in the Higgs potential, nor does it provide any solutions to the problems listed above. To push forward in this direction, the proposed High-Luminosity LHC (HL-LHC) [129] after the Long Shutdown 2 (LS2) and the High-Energy LHC (HE-LHC) [130] will start precision measurements of the Higgs boson and also provide opportunities to look for new physics at the TeV scale. Compelling opportunities have also been proposed and studied at a 100 TeV future circular colliders (FCC) in Europe [131–133], Super Proton Proton Collider (SppC) in China [134] as well as high-energy lepton colliders such as the Circular Electron Positron Collider (CEPC) in China [135,136], the International Linear Collider (ILC) in Japan [137–141] and the Compact Linear Collider (CLIC) in Europe [142–144]. For reviews and recent updates from the European Strategy Group, see for example, Refs. [145–147].

0.5 Intensity frontier

"Intensity frontier", or "precision frontier", refers to precision experiments measuring SM observables and looking for any deviations from SM prediction to search for any signals from BSM physics. This procedure can generally be divided into two directions: (1) Precision measurements at high-energy colliders such as aforementioned

FCC, CEPC, ILC and CLIC, which, as proposed, will be able to measure SM observables at percentage level to compare with SM prediction; (2) Precision measurements of SM observables from low energy experiments such as muon anomalous magnetic moment [148–150], weak mixing angle [16, 151–154] discussed in Chapter 5 and unitarity of the Cabibbo-Kobayashi-Maskawa (CKM) matrix [1] discussed in Chapter 1. As we will see in Chapter 5, low energy precision measurements could even be sensitive to BSM physics at the TeV or tens of TeV scale, making it complementary with high-energy searches; (3) rare and/or forbidden processes such as electric dipole moment (EDM) of leptons and nucleons that are sensitive to CPV, (neutrinoless) double beta decay that determines the Dirac or Majorana nature of neutrinos as will be discussed in more detail in Chapter 2, charged lepton flavor violation processes that are direct signals of new physics etc. For a review, see for example, Ref. [155].

0.6 Cosmic frontier

According to the latest Planck data [29], the Universe is composed of 26.7% of DM, 68.5% of dark energy and 4.8% of ordinary matter, where DM and dark energy are essential for structure formation and the expansion of our Universe. "Cosmic frontier" refers to experiments designed to understand the nature of DM and dark energy by using our Universe as the source. For DM detection, there are three ways that have been intensively studied: (1) DM direct detection by studying the recoiling energy of the ordinary matter object after being scattered from a DM particle such as the DARWIN [156], the LUX [30], the PandaX-II [31] and the XENON1T [32] experiments; (2) indirect detection of DM signals from DM annihilation into SM particles including cosmic gamma rays and cosmic neutrinos such as the Fermi-LAT [157, 158] and the PAMELA [159, 160] experiments, and (3) collider searches of DM through a dedicated analysis on the missing transverse energy by using, for example,

data from ATLAS and CMS [161–167]. A detailed discussion for DM direct and indirect detection as well as collider searches will be presented in Chapter 4.

It is worth pointing out that the three frontiers discussed above are complementary to each other for our understanding of the same fundamental questions in physics. A combined analysis of different experiments performed in these frontiers will eventually benefit our understanding on fundamental topics including the neutrino masses, the DM and the BAU problems we mentioned earlier.

The remaining of this thesis is organized as follows: In Chapter 1, we review the SM and discuss precision measurements on some of the parameters related to our discussion in the following chapters. In Chapter 2, we review the neutrino mass problem and three seesaw mechanisms that can naturally generate non-zero neutrino masses. We then discuss current status of neutrino mass measurements. To answer the BAU problem, in Chapter 3, we discuss how to explain the asymmetry through EWBG and review how SM fails to explain BAU through EWBG. The dark matter problem is discussed in Chapter 4, constraints from colliders searches, direct and indirect detection are also discussed. Then in Chapter 5, we discuss current status and future prospects on precision measurements of the weak mixing angle defined in Chapter 1. In Chapter 6, we study a specific model, i.e. the complex triplet Higgs model, at future colliders. The model address the neutrino mass problem through a type-II seesaw mechanism and could also explain the baryon asymmetry through EWBG. Chapter 7 is devoted to the dark matter problem within a real triplet model, which can also explain the BAU through EWBG. In Chapter 8, we present our work on two-loop electroweak corrections to the weak mixing angle defined in Chapter 1 and find that the corrections are beyond the precision goal of the most precise MOLLER project in the next decade as reviewed in Chapter 5. We then conclude.

CHAPTER 1

THE STANDARD MODEL

1.1 Introduction

The SM has been very successful in explaining almost every aspect of nature, a glimpse of its triumph can be found in Figure 1.1, where the timeline of the key particle discovery is shown. Despite the large number of particles, the different mass scales and different interacting strength strength among different particles, it turns out that the SM can be described by a simple theory under the $\mathrm{SU(3)_c} \otimes \mathrm{SU(2)_L} \otimes \mathrm{U(1)_Y}$ gauge group.

In this chapter, based on the $\mathrm{SU(3)_c} \otimes \mathrm{SU(2)_L} \otimes \mathrm{U(1)_Y}$ gauge group, we review the setup of the SM Lagrangian, discuss the role played by the Higgs mechanism to generate masses and mixing as well as CPV in the quark sector. Based on that, we then discuss precision measurements as well as global fitting of the SM parameters.

1.2 Lagrangian of the Standard Model

We start with introducing all the particle contents of the SM.

1.2.1 Gauge fields

As discussed above, the SM is constructed based on the gauge group $\mathrm{SU(3)_c} \otimes \mathrm{SU(2)_L} \otimes \mathrm{U(1)_Y}$, where c, L and Y indicate the color, the handness and the hypercharge respectively. Under this gauge group, one can introduce the following gauge fields that transform under the corresponding gauge group:

$$SU(3)_c \leftrightarrow G^i_\mu, \quad \text{with } i = 1, \ldots, 8 \tag{1.1}$$

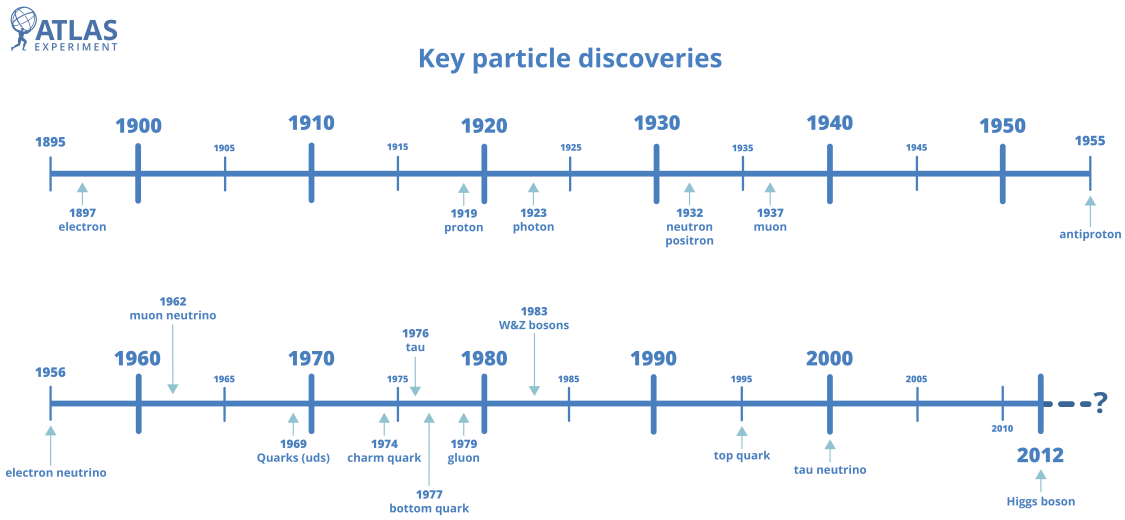

Figure 1.1: Timeline of key particle discoveries. Plot adopted from ATLAS, CERN made by Emma Ward [8].

$$SU(2)_L \leftrightarrow W_\mu^j, \qquad \text{with } j = 1, 2, 3 \tag{1.2}$$

$$U(1)_Y \leftrightarrow B_\mu, \tag{1.3}$$

where the index $i = 1, \ldots, 8$ in Eq. (1.1) represents the eight gluons in the $\mathrm{SU(3)_c}$ color group and the index $j = 1, 2, 3$ the three gauge bosons in the $\mathrm{SU(2)_L}$ gauge group.

1.2.2 Fermionic fields

At the same time, three generations of left-handed doublets and right-handed singlets are introduced in the leptonic and quark sectors respectively, which can be symbolically written as, in the flavor space,

$$L_j = \begin{pmatrix} \nu_\ell \\ \ell^- \end{pmatrix}_L, \quad Q'_1 = \begin{pmatrix} u' \\ d' \end{pmatrix}_L, \quad Q'_2 = \begin{pmatrix} c' \\ s' \end{pmatrix}_L, \quad Q'_3 = \begin{pmatrix} t' \\ b' \end{pmatrix}_L, \tag{1.4}$$

$$\ell^-_{R,j}, \quad U'_{R,j}, \quad D'_{R,j}, \text{ with } (\ell, U', D') = \begin{cases} (e, u', d'), \ j = 1, \\ (\mu, c', s'), \ j = 2, \\ (\tau, t', b'), \ j = 3. \end{cases} \tag{1.5}$$

1.2.3 Scalar fields

In the minimal case, the standard model only contains one scalar field, which is assumed to be singlet under $\mathrm{SU(3)_c}$, complex doublet under $\mathrm{SU(2)_L}$ and with hypercharge $Y_\Phi = 1$. This scalar filed is also known as the Higgs field. In the $SU(2)_L$ representation, its components can be written as

$$\Phi = \begin{pmatrix} \phi^\pm \\ \phi^0 \end{pmatrix}. \tag{1.6}$$

1.2.4 The Lagrangian of the Standard Model

With all the components above, the only gauge invariant, Lorentz invariant and renormalizable Lagrangian one can construct can be written as

$$\mathcal{L}_{\mathrm{SM}} = \mathcal{L}_{\mathrm{gauge}} + \mathcal{L}_{\mathrm{scalar}} + \mathcal{L}_{\mathrm{Dirac}} + \mathcal{L}_{\mathrm{Yukawa}}, \tag{1.7}$$

$$\mathcal{L}_{\mathrm{gauge}} = -\frac{1}{4} G^i_{\mu\nu} G_i^{\mu\nu} - \frac{1}{4} W^j_{\mu\nu} W_j^{\mu\nu} - \frac{1}{4} B_{\mu\nu} B^{\mu\nu}, \tag{1.8}$$

$$\mathcal{L}_{\mathrm{scalar}} = (D_\mu \Phi)^\dagger (D^\mu \Phi) + \mu^2 \Phi^\dagger \Phi - \lambda (\Phi^\dagger \Phi)^2, \tag{1.9}$$

$$\begin{aligned} \mathcal{L}_{\mathrm{Dirac}} =& \bar{L}_j (i D_\mu \gamma^\mu) L_j + \bar{\ell}_{R,j} (i D_\mu \gamma^\mu) \ell_{R,j} + \bar{Q'}_j (i D_\mu \gamma^\mu) Q'_j \\ &+ \bar{U'}_{R,j} (i D_\mu \gamma^\mu) U'_{R,j} + \bar{D'}_{R,u} (i D_\mu \gamma^\mu) D'_{R,j}, \end{aligned} \tag{1.10}$$

$$\mathcal{L}_{\mathrm{Yukawa}} = y_\ell^{ab} \bar{L}_a \Phi \ell_{R,b} + y_U^{ab} \bar{Q'}_a \tilde{\Phi} U'_{R,b} + y_D^{ab} \bar{Q'}_a \Phi D'_{R,b} + h.c., \tag{1.11}$$

$$\mathcal{L}_\theta = \bar{\theta} \frac{g_s^2}{32\pi^2} \epsilon^{\mu\nu\alpha\beta} F^i_{\mu\nu} F^i_{\alpha\beta}, \tag{1.12}$$

with subscripts and superscripts $i = 1, \ldots, 8$ and $a, b, j = 1, 2, 3$ above, "*h.c.*" abbreviated for "Hermitian conjugate" and $\bar{\theta}$ the strong CP phase. The covariant derivatives

Field	ℓ_L^-	$\ell_{R,j}^-$	$\nu_{\ell,L}$	U_L	D_L	U_R	D_R	ϕ^+	ϕ^0
T_3	$-\frac{1}{2}$	0	$\frac{1}{2}$	$\frac{1}{2}$	$-\frac{1}{2}$	0	0	$\frac{1}{2}$	$-\frac{1}{2}$
Y	-1	-2	-1	$\frac{1}{3}$	$\frac{1}{3}$	$\frac{4}{3}$	$-\frac{2}{3}$	1	1
$Q = T_3 + Y/2$	-1	-1	0	$\frac{2}{3}$	$-\frac{1}{3}$	$\frac{2}{3}$	$-\frac{1}{3}$	1	0

Table 1.1: Values of the third component of isospin T_3^f, hypercharge Y_f and electric charge Q_f assignment for particle f ($f = L_j, Q'_j, \ell^-_{R,j}, U'_{R,j}, D'_{R,j}, \Phi$) in the Standard Model.

	G_μ	W_μ	B_μ	Q'_j	$U'_{R,j}$	$D'_{R,j}$	L_j	$\ell^-_{R,j}$	Φ
$\mathrm{SU}(3)_c$	8	**1**	**1**	3	3	3	**1**	**1**	**1**
$\mathrm{SU}(2)_L$	**1**	3	**1**	2	**1**	**1**	2	**1**	2

Table 1.2: Quantum numbers of elementary fields in the Standard Model.

D_μ in eqs. (1.8) to (1.10) are defined as follows to ensure gauge invariance

$$D_\mu f = \left(\partial_\mu - ig_s\frac{\lambda_a}{2}G^a_\mu - ig_2\frac{\tau_a}{2}W^a_\mu - ig_1\frac{Y_f}{2}B_\mu\right) f, \quad \text{with } f = L_j, Q'_j, \ell_{R,j}, U'_{R,j}, D'_{R,j}, \Phi \tag{1.13}$$

with λ^a ($a = 1, \cdots, 8$) the Gell-Mann matrices for the $\mathrm{SU(3)_c}$ group, τ^a ($a = 1, 2, 3$) the Pauli matrices, Y_f ($f = L_j, Q'_j, \ell_{R,j}, U'_{R,j}, D'_{R,j}, \Phi$) the hypercharges of field f defined in the second row of Table 1.1. It is worthy pointing out that singlet representations in bold **1**'s in Table 1.2 would imply the absence of the corresponding gauge field(s) in the definition of covariant derivatives.

1.3 The Higgs mechanism

All gauge fields and fermions turn out to be massless upon expansion of Eq. (1.7). However, experimentally, the photon is the only massless fundamental particle we

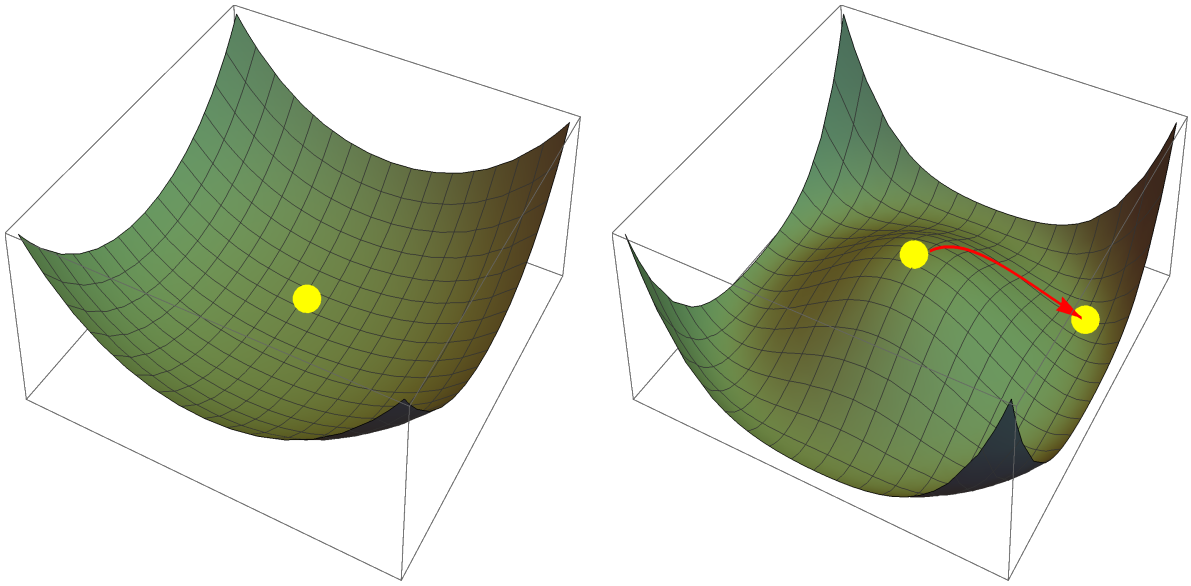

Figure 1.2: Plots of the Higgs potential before (left) and after (right) electroweak spontaneous symmetry breaking, where the z axis the Higgs potential $V(\Phi)$ and the x, y axes are ImΦ and ReΦ respectively.

observe experimentally in nature[i]. To circumvent this obvious contradiction, the Higgs mechanism[ii] is invented, which we will discuss below.

To see how the Higgs mechanism works, one can first look at the Higgs potential embedded in Eq. (1.9), which reads

$$V(\Phi) = -\mu^2 \Phi^\dagger \Phi + \lambda (\Phi^\dagger \Phi)^2. \tag{1.14}$$

To ensure stability of $V(\Phi)$ at large Φ, $\lambda > 0$ is required. Now depending sign(μ^2), the shape of the Higgs potential $V(\Phi)$ can be either in the form of the left plot when $\mu^2 < 0$ or the right one when $\mu^2 > 0$ in Figure 1.2, where the x, y axes are ImΦ and ReΦ respectively. Note that in the former case, the Higgs particle is already at

[i]Gluons are also massless particles, but since they carry colors, they are confined within hadrons and not observed directly experimentally.

[ii]It is also called as the Brout-Englert-Higgs mechanism, or Englert-Brout-Higgs-Guralnik-Hagen-Kibble mechanism, Anderson-Higgs mechanism, Anderson-Higgs-Kibble mechanism, Higgs-Kibble mechanism and ABEGHHK'tH mechanism.

the minimum of its potential at the origin, resulting in massless gauge bosons and fermions. On the other hand, if $\mu^2 > 0$, then the origin will be a local maximum of the Higgs potential as indicated by the right plot in Figure 1.2. Due to the instability, the Higgs particle, indicated by the yellow dot, will roll down the hill to its absolute minimum as suggested by the red arrow. Note that in the complex plane, the number of minimum of Φ is infinity, reflecting the fact the Higgs field is invariant under the $\mathrm{U(1)_Y}$ gauge group. However, when the Higgs particle rolls down to its absolute minimum, a random direction will be picked up by the Higgs particle. This process is called the spontaneous symmetry breaking: The minima of the Higgs field spontaneously break the $\mathrm{SU(2)_L} \otimes \mathrm{U(1)_Y}$ gauge group down to a residual $\mathrm{U(1)_{EM}}$ subgroup.

As aforementioned, if the Higgs were in the non-broken phase, all the gauge bosons and fermions will be massless. Next, we will discuss explicitly how spontaneous symmetry breaking naturally explains the masses of the SU(2) gauge bosons and the fermions.

1.3.1 Masses of gauge bosons and the weak mixing angle

In the broken phase, the Higgs field around its minimum denoted by v_Φ can be written as

$$\Phi = \begin{pmatrix} \phi^+ \\ \frac{1}{\sqrt{2}}(h + v_\Phi + i\chi) \end{pmatrix}. \tag{1.15}$$

Expanding Eq. (1.9) around this minimum, one has

$$\begin{aligned} \mathcal{L}_{\text{scalar}} =& (D_\mu \Phi)^\dagger (D^\mu \Phi) + \mu^2 \Phi^\dagger \Phi - \lambda (\Phi^\dagger \Phi)^2 \\ \supset& m_{W^\pm}^2 W_\mu^+ W^{-,\mu} + \frac{1}{2} m_Z^2 Z_\mu Z^\mu - \frac{1}{2} m_h^2 h^2, \end{aligned} \tag{1.16}$$

where only the mass terms are kept in the last line above and

$$m_h = \sqrt{2}\mu = \sqrt{2\lambda}v_\Phi, \tag{1.17}$$

$$m_{W^\pm} = \frac{g_2 v_\Phi}{2}, \tag{1.18}$$

$$m_Z = \frac{\sqrt{g_1^2 + g_2^2}v_\Phi}{2}, \tag{1.19}$$

$$m_\gamma = 0, \tag{1.20}$$

$$W_\mu^\pm = \frac{1}{\sqrt{2}}(W_\mu^1 \mp iW_\mu^2), \tag{1.21}$$

$$Z_\mu = \frac{1}{\sqrt{g_1^2 + g_2^2}}(g_2 W_\mu^3 - g_1 B_\mu), \tag{1.22}$$

$$A_\mu = \frac{1}{\sqrt{g_1^2 + g_2^2}}(g_1 W_\mu^3 + g_2 B_\mu), \tag{1.23}$$

with the U(1) gauge field A_μ remains massless and identified as the photon field. Another useful byproduct from the expansion above is that, the electric charge is recognized to be

$$e = \frac{g_1 g_2}{\sqrt{g_1^2 + g_2^2}}. \tag{1.24}$$

The last point we want to make in the subsection is that, written Eq. (1.22) and Eq. (1.23) in matrix form, we have

$$\begin{pmatrix} Z_\mu \\ A_\mu \end{pmatrix} = \begin{pmatrix} \frac{g_2}{\sqrt{g_1^2+g_2^2}} & -\frac{g_1}{\sqrt{g_1^2+g_2^2}} \\ \frac{g_1}{\sqrt{g_1^2+g_2^2}} & \frac{g_2}{\sqrt{g_1^2+g_2^2}} \end{pmatrix} \begin{pmatrix} W_\mu^3 \\ B_\mu \end{pmatrix} \tag{1.25}$$

$$\equiv \begin{pmatrix} \cos\theta_W & -\sin\theta_W \\ \sin\theta_W & \cos\theta_W \end{pmatrix} \begin{pmatrix} W_\mu^3 \\ B_\mu \end{pmatrix}, \tag{1.26}$$

with

$$\cos\theta_W \equiv \frac{g_2}{\sqrt{g_1^2 + g_2^2}}, \quad \sin\theta_W \equiv \frac{g_1}{\sqrt{g_1^2 + g_2^2}}, \quad e = g_2 \sin\theta_W = g_1 \cos\theta_W. \tag{1.27}$$

The mixing angle θ_W is called the weak mixing angle, or the Weinberg angle. From Eq. (1.18), Eq. (1.19) and Eq. (1.27), one finds a relation that defines the weak mixing angle in terms of physical observables:

$$\cos\theta_W = \frac{m_W}{m_Z}, \text{ or equivalently, } \sin^2\theta_W = 1 - \frac{m_W^2}{m_Z^2}. \tag{1.28}$$

The mixing angle is scheme dependent and historically, it has played a key role in developing and testing of the SM. Due to its importance, we will discuss more about it in Chapter 5.

1.3.2 Masses of fermions

Similarly, plugging Eq. (1.15) into Eq. (1.12) and keeping only the mass terms, one finds

$$\begin{aligned}\mathcal{L}_{\text{Yukawa}} =& y_\ell^{ab}\bar{L}_a\Phi\ell_{R,b} + y_U^{ab}\overline{Q'}_a\tilde{\Phi}U'_{R,b} + y_D^{ab}\overline{Q'}_a\Phi D'_{R,b} + \text{h.c.} \\ \supset& \frac{y_\ell^{ab}v_\Phi}{\sqrt{2}}\overline{\ell_L^a}\ell_R^b + \frac{y_U^{ab}v_\Phi}{\sqrt{2}}\overline{U'_{L,a}}U'_{R,b} + \frac{y_D^{ab}v_\Phi}{\sqrt{2}}\overline{D'_{L,a}}D'_{R,b},\end{aligned} \tag{1.29}$$

and the mass matrices are

$$m_{\nu_\ell} = 0, \quad m_\ell^{ab} = \frac{y_\ell^{ab}v_\Phi}{\sqrt{2}}, \quad M_U^{ab} = \frac{y_U^{ab}v_\Phi}{\sqrt{2}}, \quad M_D^{ab} = \frac{y_D^{ab}v_\Phi}{\sqrt{2}}. \tag{1.30}$$

Note that neutrinos are strictly massless in the Standard Model due to the absence of right-handed neutrinos in the SM and the requirement of gauge invariance. However, as discussed in the introduction, neutrinos are firmly established as massive from neutrino oscillation [55–57]. To explain neutrino masses, one could in principle also introduce right-handed singlet neutrinos $\nu_{\ell,R}$ into the SM such that a mass term

for neutrinos can be obtained as a result of the Higgs mechanism and can be written as

$$m_{\nu_\ell}^{ab} = \frac{y_{\nu_\ell}^{ab} v_\Phi}{\sqrt{2}} \overline{\nu_{\ell,L}^a} \nu_{\ell,R}^b. \tag{1.31}$$

However, from constraints on neutrino masses as discussed in detail in Chapter 2, one finds the neutrino Yukawa couplings is at most of $\mathcal{O}(10^{-13})$ and the question then becomes as why we have such a tiny coupling in the Lagrangian. We will discuss more about this issue later in Chapter 2.

1.4 Cabibbo-Kobayashi-Maskawa (CKM) matrix and CP violation (CPV)

In last subsection, we discussed that after electroweak spontaneous breaking, the mass terms of the quarks are given by

$$\mathcal{L}_{\text{Yukawa,mass}}^{\text{h-quark}} = M_U^{ab} \bar{U'}_{L,a} U'_{R,b} + M_D^{ab} \bar{D'}_{L,a} D'_{R,b} + \text{h.c..}, \tag{1.32}$$

where $M_{U(D)}^{ab} = y_{U(D)}^{ab} v/\sqrt{2}$ are the mass matrices for up- and down-type quarks. These generic complex mass matrices $M_{U(D)}^{ab}$ can be readily diagonalized by biunitary transformations as follows: Note that $M_{U(D)} M_{U(D)}^\dagger$ are Hermitian and thus have real eigenvalues as guaranteed by the finite-dimensional spectral theorem, one can diagonalize them by unitary matrices V_{UL} and V_{DL} respectively in the following way

$$M_U M_U^\dagger = V_{UL} m_u^2 V_{UL}^\dagger, \quad M_D M_D^\dagger = V_{DL} m_d^2 V_{DL}^\dagger, \text{ with } m_{u,d} \in \mathbb{R}, \tag{1.33}$$

then the mass matrices $M_{U(D)}$ can be decomposed using singular value decomposition

$$M_U = V_{UL} m_u U_{UR}^\dagger \quad M_D = V_{DL} m_d D_{DR}^\dagger, \tag{1.34}$$

$$\text{with } V_{UL}V_{UL}^\dagger = V_{DL}V_{DL}^\dagger = U_{UR}U_{UR}^\dagger = D_{DR}D_{DR}^\dagger = \mathbf{1}, \tag{1.35}$$

and the quark mass eigenstates are identified as

$$U_L = V_{UL}^\dagger U_L', \quad U_R = U_{UR}^\dagger U_R', \quad D_L = V_{DL}^\dagger D_L', \quad D_R = D_{DR}^\dagger D_R'. \tag{1.36}$$

Now plugging these relations into Eq. (1.10), one obtains, keeping only the weak charged current,

$$\mathcal{L}_{\rm CC}^q = -\frac{g_2}{\sqrt{2}}\bar{U}_{L,a}\gamma^\mu \left(V_{\rm CKM}\right)_{ab} D_{L,b}W_\mu^+ + \text{h.c.}, \tag{1.37}$$

where $V_{\rm CKM} = V_{UL}^\dagger V_{DL}$ is the CKM matrix with its components being

$$V_{\rm CKM} = \begin{pmatrix} V_{ud} & V_{us} & V_{ub} \\ V_{cd} & V_{cs} & V_{cb} \\ V_{td} & V_{ts} & V_{tb} \end{pmatrix}. \tag{1.38}$$

Note that since V_{UL} and V_{DL} are each unitary, $V_{\rm CKM}$ is also unitary, i.e.

$$V_{\rm CKM}V_{\rm CKM}^\dagger = \mathbf{1}, \tag{1.39}$$

or, in its component form, we have

$$\sum_k \left|\left(V_{\rm CKM}\right)_{ik}\right|^2 = \sum_i \left|\left(V_{\rm CKM}\right)_{ik}\right|^2 = 1, \tag{1.40}$$

$$\sum_k \left(V_{\rm CKM}\right)_{ik}\left(V_{\rm CKM}\right)_{jk}^* = 0, \tag{1.41}$$

There are several points worthy of stressing about the CKM matrix:

- Note that Eq. (1.40) indicates that the sum of all couplings of any of the up-type quarks to all the down-type quarks is the same for all generations, which is also known as "weak universality". On the other hand, Eq. (1.41) is known as the "unitarity triangle", which has been used to test SM and also a probe of new physics beyond the SM. We will discuss more about these triangles in section 1.4.4.

- The CKM matrix induces flavor-changing transitions in the charged sector at tree level, while there are no flavor-changing transitions in the neutral sector at tree level.

- To count the number of independent parameters in the CKM matrix, one can consider a general unitary $n \times n$ matrix, where n is the number of generations of quarks. A general unitary $n \times n$ matrix can be characterized by n^2 independent parameters. However, not all the parameters are physical observables as the Lagrangian will remain invariant under the following transformation:

$$U_{L,R} \to e^{i\phi_U} U_{L,R}, \quad D_{L,R} \to e^{i\phi_D} D_{L,R}, V_{\rm CKM} \to e^{i(\phi_U - \phi_D)} V_{\rm CKM}, \tag{1.42}$$

  which reduces the number of parameters by $(2n-1)$ and thus the CKM matrix for n quark generations is described by $(n-1)^2$ parameters: $n(n-1)/2$ parameters are angle-like and $(n-1)(n-2)/2$ parameters are phases. Therefore, in the SM with $n = 3$, the CKM matrix is parameterized by 3 mixing-angles and 1 phase. Though we have reduced the number of parameters down to 4, there are still various equivalent ways to parameterize the CKM matrix, and the choice of one instead of the others usually leads to natural relationship between the CKM parameters and physical observables for a specific situation. In what follows, we will discuss two of the parameterization usually used in literatures: the "standard" and the Wolfenstein parameterization.

1.4.1 Standard parameterization of the CKM matrix

The "standard" parameterization of the CKM matrix is advocated by the Particle Data Group, which introduces three Euler angles $(\theta_{12}, \theta_{23}, \theta_{13})$ and one CP-violating Kobayashi-Maskawa phase δ [168]:

$$V_{\rm CKM} = \begin{pmatrix} 1 & 0 & 0 \\ 0 & c_{23} & s_{23} \\ 0 & -s_{23} & c_{23} \end{pmatrix} \begin{pmatrix} c_{13} & 0 & s_{13}e^{-i\delta} \\ 0 & 1 & 0 \\ -s_{13}e^{i\delta} & 0 & c_{13} \end{pmatrix} \begin{pmatrix} c_{12} & s_{12} & 0 \\ -s_{12} & c_{12} & 0 \\ 0 & 0 & 1 \end{pmatrix} \tag{1.43}$$

$$= \begin{pmatrix} c_{12}c_{13} & s_{12}c_{13} & s_{13}e^{-i\delta} \\ -s_{12}c_{23} - c_{12}s_{23}s_{13}e^{i\delta} & c_{12}c_{23} - s_{12}s_{23}s_{13}e^{i\delta} & s_{23}c_{13} \\ s_{12}s_{23} - c_{12}c_{23}s_{13}e^{i\delta} & -c_{12}s_{23} - s_{12}c_{23}s_{13}e^{i\delta} & c_{23}c_{13} \end{pmatrix}, \tag{1.44}$$

where $s_{ij} = \sin\theta_{ij}$ and $c_{ij} = \cos\theta_{ij}$. Because CP conjugate processes correspond to interaction terms in the Lagrangian related by Hermitian conjugation, non-vanishing of the phase δ and thus the complex nature of the CKM matrix, may induce differences between rates of CP conjugate processes, leading to CPV. This point can also be seen in the Wolfenstein parameterization, which we will discuss in the next subsection.

1.4.2 Wolfenstein parameterization of the CKM matrix

Experimentally, it is known that $s_{13} \ll s_{23} \ll s_{12} \ll 1$, it is thus convenient to explicit this hierarchy using the Wolfenstein parameterization and define [169]

$$s_{12} = \lambda = \frac{|V_{us}|}{\sqrt{|V_{ud}|^2 + |V_{us}|^2}}, \quad s_{23} = A\lambda^2 = \lambda \left|\frac{V_{cb}}{V_{us}}\right|, \tag{1.45}$$

$$s_{13}e^{i\delta} = V_{ub}^* = \frac{A\lambda^3(\bar{\rho} + i\bar{\eta})\sqrt{1 - A^2\lambda^4}}{\sqrt{1-\lambda^2}[1 - A^2\lambda^4(\bar{\rho} + i\bar{\eta})]}^{\rm iii}, \tag{1.46}$$

from which, one can solve to find that

[iii] An alternative convention also exists in the literatures, which defines $\rho + i\eta = \frac{V_{ub}^*}{V_{us}V_{cb}^*} = \frac{(\bar{\rho}+i\bar{\eta})\sqrt{1-A^2\lambda^4}}{\sqrt{1-\lambda^2}[1-A^2\lambda^4(\bar{\rho}+i\bar{\eta})]}$.

$$\bar{\rho} + i\bar{\eta} = -\frac{V_{ud}V_{ub}^*}{V_{cd}V_{cb}^*}, \tag{1.47}$$

which ensures that it is phase convention independent and the CKM matrix written in terms of $\lambda, A, \bar{\rho}$ and $\bar{\eta}$ is unitary to all orders in λ.

Expanding the CKM matrix in small λ, one has, up to $\mathcal{O}(\lambda^6)$,

$$V_{\text{CKM}} = \begin{pmatrix} 1 - \frac{1}{2}\lambda^2 - \frac{1}{8}\lambda^4 & \lambda & A\lambda^3(\bar{\rho} - i\bar{\eta}) \\ -\lambda + \frac{1}{2}A^2\lambda^5[1 - 2(\bar{\rho} + i\bar{\eta})] & 1 - \frac{1}{2}\lambda^2 - \frac{1}{8}\lambda^4\left(1 + 4A^2\right) & A\lambda^2 \\ A\lambda^3[1 - (\bar{\rho} + i\bar{\eta})] & -A\lambda^2 + \frac{1}{2}A\lambda^4[1 - 2(\bar{\rho} + i\bar{\eta})] & 1 - \frac{1}{2}A^2\lambda^4 \end{pmatrix} \tag{1.48}$$

As one can see, the CKM matrix is complex due to non-vanishing $\bar{\eta}$, thus CPV is allowed if and only if $\bar{\eta} \neq 0$.

Given the many choices we have to parameterize the CKM matrix, Cecilia Jarlskog proposed a convention-independent parameter, now called the Jarlskog invariant, to measure CPV in 1985. Due to its convention independency, we will review the Jarlskog invariant in the next subsection, and then we will discuss how it is used to measure CPV.

1.4.3 The Jarlskog invariant

To eliminate the arbitrariness in choosing the variable that measures CPV in the CKM matrix, the Jarlskog invariant, which was proposed by Cecilia Jarlskog in 1985 [170], can be used. In what follows, I will briefly discuss her formalism in defining this invariant.

Note that in the SM, it is always possible to rotate to the Hermitian basis for the quark mass matrices such that $M_{U(D)} = M_{U(D)}^\dagger$. In this case, to diagonalize the mass

matrices, we only need to introduce two unitary matrices such that $V_{\rm CKM} = V_U^\dagger V_D$ with $M_{U(D)} = V_{U(D)} m_{u(d)} V_{U(D)}^\dagger$ and $m_{u(d)}$ diagonal. More explicitly,

$$m_u = \mathrm{diag}(m_u, m_c, m_t), \quad m_d = \mathrm{diag}(m_d, m_s, m_b). \tag{1.49}$$

Now consider a Hermitian traceless matrix C defined through the commutator of the two Hermitian quark mass matrices,

$$[M_U, M_D] = iC. \tag{1.50}$$

From above relations, it is straightforward to find

$$\begin{aligned} C =& -i[M_U, M_D] \\ =& -iV_U^\dagger [m_u, V_{\rm CKM} m_d V_{\rm CKM}^\dagger] V_U. \end{aligned} \tag{1.51}$$

Then after applying the Cayley-Hamilton theorem for the 3×3 matrix, one finds

$$\begin{aligned} \det(C) =& \frac{1}{6}\left[(\mathrm{tr}(C))^3 - 3\mathrm{tr}(C)\mathrm{tr}(C^2) + 2\mathrm{tr}(C^3)\right] \\ =& \frac{1}{3}\mathrm{tr}(C^3) \\ =& i\mathrm{tr}\left(M_U^2 M_D^2 M_U M_D - M_D^2 M_U^2 M_D M_U\right) \\ =& i\mathrm{tr}\left[2i\mathrm{Im}\left(M_U^2 M_D^2 M_U M_D\right)\right] \\ =& -2\mathrm{Im}\left[\mathrm{tr}\left(m_u^2 V_{\rm CKM} m_d^2 V_{\rm CKM}^\dagger m_u V_{\rm CKM} m_d V_{\rm CKM}^\dagger\right)\right] \\ =& -2\left\{\mathrm{Im}\left[(V_{\rm CKM})_{i\alpha}(V_{\rm CKM})_{j\beta}(V_{\rm CKM})_{i\beta}^*(V_{\rm CKM})_{j\alpha}^*\right]\right\}\left[\left(m_u^2\right)_i \left(m_d^2\right)_\alpha (m_u)_j (m_d)_\beta\right] \\ =& -2\left(\sum_{\gamma,k} J\epsilon_{\alpha\beta\gamma}\epsilon_{ijk}\right)\left[\left(m_u^2\right)_i \left(m_d^2\right)_\alpha (m_u)_j (m_d)_\beta\right], \end{aligned} \tag{1.52}$$

where we have used Einstein summation convention wherever possible and the traceless property of C in the second step, the cyclic permutation invariance of trace in

the third step and the Hermitian property of $M_{U,D}$ in the fourth step. The variable J in the last step defines the Jarlskog invariant, which can be expressed as, by focusing on the minor $(V_{\rm CKM})_{3,3}$ of the $V_{\rm CKM}$ matrix for example,

$$\det(C) = -2(m_t - m_c)(m_t - m_u)(m_c - m_u)(m_b - m_s)(m_b - m_d)(m_s - m_d)J, \tag{1.53}$$

$$J = \mathrm{Im}\left(V_{ud}V_{cs}V_{us}^*V_{cd}^*\right). \tag{1.54}$$

Since there are in total of nine minors of the CKM matrix, there are nine formulas that define the Jarlskog invariant that are all equivalent up to an overall sign due to unitarity of the CKM matrix. Expressing the Jarlskog invariant by variables from the two parameterization of the in the CKM matrix above, one finds

$$J = \begin{cases} c_{12}c_{23}c_{13}^2 s_{12}s_{23}s_{13}\sin\delta, & \text{Standard parameterization} \\ \lambda^6 A^2 \bar{\eta}, & \text{Wolfenstein parameterization} \end{cases} \tag{1.55}$$

Note that the Jarlskog invariant is directly proportional to the Kobayashi-Maskawa phase δ in the standard parameterization or the imaginary part $\bar{\eta}$ of the CKM matrix in the Wolfenstein parameterization, therefore, vanishing of the Jarlskog invariant immediately implies the conservation of CP in the quark sector.

Note that results above depend on the assumption that the mass matrices are Hermitian. In a more general situation where the mass matrices are not Hermitian, one needs to replace the definition in Eq. (1.50) by

$$[M_U M_U^\dagger, M_D M_D^\dagger] = iC', \tag{1.56}$$

and following the same procudure, one obtains

$$\det(C') = -6(m_t^2 - m_c^2)(m_t^2 - m_u^2)(m_c^2 - m_u^2)(m_b^2 - m_s^2)(m_b^2 - m_d^2)(m_s^2 - m_d^2)J. \tag{1.57}$$

The only difference compared with previous formalism is to replace the previous mass difference in Eq. (1.54) by the mass squared difference. Note that here the determinant of C' has a dimension of 12, the corresponding dimensionless measure of CPV could be obtained at $T = 100\,\mathrm{GeV}$ [12], the scale at which the sphaleron process that will be discussed in Chapter 3 becomes effective, leading to

$$\frac{\det(C')}{T^{12}} = \frac{\det(C')}{(100\,\mathrm{GeV})^{12}} \approx 10^{-20}. \tag{1.58}$$

It is due to the tininess of this ratio that people argue that CPV in SM is not enough to account for the baryon asymmetry we observe today. We will have more discussion on the baryon asymmetry in Chapter 3.

1.4.4 The Unitarity triangles

To understand the Jarlskog invariant more intuitively, it turns out there is an elegant geometrical interpretation for it called the "unitarity triangles", which are directly related to the unitarity of the CKM matrix. To be more specific, in total, the unitarity of the CKM matrix gives twelve equations with six of them for diagonal terms:

$$V_{ud}V_{ud}^* + V_{us}V_{us}^* + V_{ub}V_{ub}^* = 1, \tag{1.59}$$

$$V_{cd}V_{cd}^* + V_{cs}V_{cs}^* + V_{cb}V_{cb}^* = 1, \tag{1.60}$$

$$V_{td}V_{td}^* + V_{ts}V_{ts}^* + V_{tb}V_{tb}^* = 1, \tag{1.61}$$

$$V_{ud}V_{ud}^* + V_{cd}V_{cd}^* + V_{td}V_{td}^* = 1, \tag{1.62}$$

$$V_{us}V_{us}^* + V_{cs}V_{cs}^* + V_{ts}V_{ts}^* = 1, \tag{1.63}$$

$$V_{ub}V_{ub}^* + V_{cb}V_{cb}^* + V_{tb}V_{tb}^* = 1, \tag{1.64}$$

and six of them off-diagonal:

$$V_{ud}V_{us}^* + V_{cd}V_{cs}^* + V_{td}V_{ts}^* = 0 \tag{1.65}$$

$$V_{ud}V_{ub}^* + V_{cd}V_{cb}^* + V_{td}V_{tb}^* = 0 \tag{1.66}$$

$$V_{us}V_{ub}^* + V_{cs}V_{cb}^* + V_{ts}V_{tb}^* = 0 \tag{1.67}$$

$$V_{ud}V_{cd}^* + V_{us}V_{cs}^* + V_{ub}V_{cb}^* = 0 \tag{1.68}$$

$$V_{ud}V_{td}^* + V_{us}V_{ts}^* + V_{ub}V_{tb}^* = 0 \tag{1.69}$$

$$V_{cd}V_{tb}^* + V_{cs}V_{ts}^* + V_{cb}V_{tb}^* = 0. \tag{1.70}$$

It is these six off-diagonal equations that each represents a triangle, the so-called "unitarity triangle", in the complex plane. As we will show shortly, each of these six triangles has the same area that is half of the Jarlskog invariant, i.e.

$$\text{Area} = \frac{|J|}{2}. \tag{1.71}$$

To see why the above relation holds, one can consider Eq. (1.65-1.70). Note that in the Wolfenstein parameterization we have $\lambda \ll 1$, such that only the following two of the six unitarity triangles are not squashed [9]:

$$\underbrace{V_{ud}V_{ub}^*}_{\mathcal{O}(\lambda^3)} + \underbrace{V_{cd}V_{cb}^*}_{\mathcal{O}(\lambda^3)} + \underbrace{V_{td}V_{tb}^*}_{\mathcal{O}(\lambda^3)} = 0, \qquad \underbrace{V_{ud}V_{td}^*}_{\mathcal{O}(\lambda^3)} + \underbrace{V_{us}V_{ts}^*}_{\mathcal{O}(\lambda^3)} + \underbrace{V_{ub}V_{tb}^*}_{\mathcal{O}(\lambda^3)} = 0. \tag{1.72}$$

Using the Wolfenstein parameterization, it is easy to check that each side of these two triangles is of $\mathcal{O}(\lambda^3)$ and the corresponding diagrams in the complex plane are shown in Figure 1.3. Furthermore, it is a straightforward calculation to find that for each of these triangles, the area of the triangle is half of the Jarlskog invariant:

$$\text{Area} = \frac{1}{2}|V_{cd}V_{cb}^*||V_{ud}V_{ub}^* \sin\gamma| = \frac{1}{2}\left|V_{ud}V_{cd}V_{ub}^*V_{cb}^* \sin\left[\arg\left(-\frac{V_{ud}V_{ub}^*}{V_{cd}V_{cb}^*}\right)\right]\right| = \frac{|J|}{2}. \tag{1.73}$$

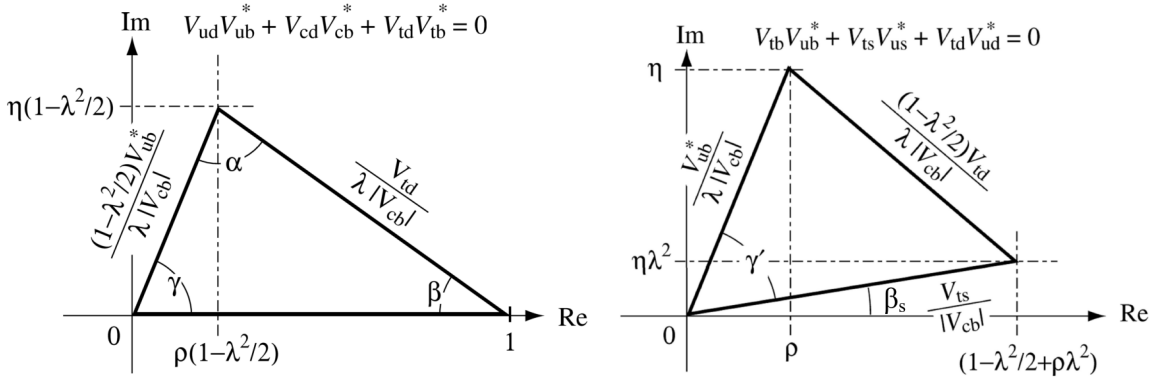

Figure 1.3: Representation of the two scaled unitarity triangles in the complex plane from Eq. (1.72). The three sides are rescaled by $V_{cd}V_{cb}^*$ and $V_{us}V_{cb}^*$ respectively. The three sides are given by Eq. (1.74). Plots adopted from Ref. [9].

In practice, it is conventional to rescale the first triangle in Eq. (1.72) by $V_{cd}V_{cb}^*$ and write its side length as, in the Wolfenstein parameterization,

$$R_u \equiv \left|\frac{V_{ud}V_{ub}^*}{V_{cd}V_{cb}^*}\right| = \sqrt{\bar{\rho}^2+\bar{\eta}^2}, \quad R_u \equiv \left|\frac{V_{cd}V_{cb}^*}{V_{cd}V_{cb}^*}\right| = 1, \quad R_t \equiv \left|\frac{V_{td}V_{tb}^*}{V_{cd}V_{cb}^*}\right| = \sqrt{(1-\bar{\rho})^2+\bar{\eta}^2}. \tag{1.74}$$

The parameters $\bar{\rho}$ and $\bar{\eta}$ are the coordinates of the triangle apex in the complex plane, while the other two apexes are at $(0,0)$ and $(1,0)$ respectively. The three interior angles of the triangle are, in the Wolfenstein parameterization,

$$\alpha \equiv \arg\left(-\frac{V_{td}V_{tb}^*}{V_{ud}V_{ub}^*}\right) = \arg\left(-\frac{1-\bar{\rho}-i\bar{\eta}}{\bar{\rho}+i\bar{\eta}}\right), \tag{1.75}$$

$$\beta \equiv \arg\left(-\frac{V_{cd}V_{cb}^*}{V_{td}V_{tb}^*}\right) = \arg\left(\frac{1}{1-\bar{\rho}-i\bar{\eta}}\right), \tag{1.76}$$

$$\gamma \equiv \arg\left(-\frac{V_{ud}V_{ub}^*}{V_{cd}V_{cb}^*}\right) = \arg\left(\bar{\rho}+i\bar{\eta}\right), \tag{1.77}$$

and by definition, they satisfy

$$\alpha+\beta+\gamma = \arg(-1) = \pi \bmod 2\pi. \tag{1.78}$$

Determination of each element of the CKM matrix is of fundamental importance in particle physics: Through precision measurements of the CKM matrix elements, one would be able to precisely determine CPV of the CKM matrix as well as a rigorous test of the unitarity of the CKM matrix. Note that CPV in the CKM matrix is the only CP violating source in the SM, its determination will be directly to the BAU problem mentioned in Introduction. On the other hand, its determination will also benefit our search for new physics if it turns out CPV effect in the CKM matrix is too small to explain the BAU problem. We will discuss more about this point in Chapter 3, and in what follows, we briefly review how to measure the CKM matrix elements.

1.4.5 Determination of the moduli of the CKM matrix elements

To determine the moduli of the CKM matrix elements, we mainly follow the discussion in [1].

1.4.5.1 $|V_{ud}|$

Since $|V_{ud}|$ involves only the first-generation of quarks, it is determined with the best precision. There are three different methods used for its determination: from super-allowed Fermi transition, from free-neutron lifetime and from pion decay $\pi^+ \to \pi^0 e^+ \nu_e$. Since the first method leads to the most precise determination of $|V_{ud}|$, we will only discuss it below. The super-allowed Fermi Transitions corresponds to beta decays between two $J^P = 0^+$ nuclides in the same isospin multiplet, where only vector current is involved. The $|V_{ud}|$ moduli is determined by [171, 172]

$$\begin{aligned} |V_{ud}|^2 =& \frac{\pi^3 \ln 2}{G_F^2 m_e^5 f t (1+\Delta_{\text{outer}})(1+\Delta_{\text{inner}})} = \frac{2984.432(3)\, s}{f t (1+\Delta_{\text{outer}})(1+\Delta_{\text{inner}})} \\ \equiv& \frac{2984.432(3)\, s}{F t (1+\Delta_{\text{inner}})} \end{aligned} \tag{1.79}$$

where t is the lifetime of the decaying nucleus, f the Coulomb correction factor, $\Delta_{\text{outer(inner)}}$ is the nuclear-dependent (universal) radiative corrections, and $Ft \equiv ft(1+\Delta_{\text{outer}})$ is nucleus-independent and obtained from the experimentally measured ft value by absorbing all nuclear-dependent corrections. The most precise value of Ft is $Ft = 3072.27(72)\,s$, obtained from the 14 best measured half-lives. The best value of Δ_{inner} is from Marciano and Sirlin [173], which gives $\Delta_{\text{inner}} = 0.02361(38)$, yielding a value of [1]

$$|V_{ud}| = 0.97420 \pm 0.00021. \tag{1.80}$$

The error is dominated by theoretical uncertainties from nuclear Coulomb distortions and radiative corrections.

1.4.5.2 $|V_{us}|$

$|V_{us}|$ is obtained from semi-leptonic decays of strange particles. Consider K_{e3} as an example, the hadronic matrix element, based on the Lorentz structure, can be written as

$$\langle \pi^+(p') \left| J_\mu \right| \overline{K^0}(p) \rangle = f_+(q^2)(p'+p)_\mu + f_-(q^2) q_\mu, \tag{1.81}$$

with $q_\mu = (p'-p)_\mu$ and $f_\pm(q^2)$ the hadronic form factors. Since $f_-(q^2)$ gives a contribution to the decay rate proportional to m_e^2, it can be neglected and one then has

$$\frac{d\Gamma(\overline{K^0} \to \pi^+ e^- \overline{\nu}_e)}{dx_\pi} = \frac{G_F^2 m_K^5}{192\pi^3} \left|V_{us}\right|^2 \left|f_+(q^2)\right|^2 \left(x_\pi^2 - \frac{4m_\pi^2}{m_K^2}\right)^{\frac{3}{2}}, \tag{1.82}$$

where $x_\pi \equiv 2E_\pi/m_K$, and E_π is the energy of pion in the final state. Upon fitting to the Dalitz-plot distribution using a model for $f_+(q^2)$ based on a K^*-pole approximation,

$$f_+(q^2) = \frac{f_+(0)}{1 - q^2/m_{K^*}^2} \tag{1.83}$$

and a calculation of $f_+(0)$ from the quark model or using lattice QCD, one can then extract $|V_{us}|$.

The average of $K_L^0 \to \pi e\nu$, $K_L^0 \to \pi\mu\nu$, $K^\pm \to \pi^0 e^\pm \nu$, $K^\pm \to \pi\mu^\pm\nu$ and $K_S^0 \to \pi e\nu$ leads to [1, 174]

$$|V_{us}|\, f_+(0) = 0.2165 \pm 0.0004. \tag{1.84}$$

The form factor average $f_+(0) = 0.9704 \pm 0.0032$ [175] is obtained from three-flavor lattice QCD calculations, leading to [1]

$$|V_{us}| = 0.2231 \pm 0.0008. \tag{1.85}$$

The calculation of the ratio of the kaon and pion decay constants also enables one to extract $|V_{us}/V_{ud}|$ from $K \to \mu\nu(\gamma)$ and $\pi \to \mu\nu(\gamma)$, where (γ) indicates that radiative decays are included. The KLOE measurement of the $K \to \mu\nu(\gamma)$ branching ratio combined with the lattice QCD result, $f_K/f_\pi = 1.1933 \pm 0.0029$ [175], leads to

$$|V_{us}| = 0.2253 \pm 0.0007, \tag{1.86}$$

where the accuracy is limited by the knowledge of the ratio of the decay constants. The average of above measurements lead to

$$|V_{us}| = 0.2243 \pm 0.0005. \tag{1.87}$$

1.4.5.3 $|V_{cd}|$

$|V_{cd}|$ can be extracted from semileptonic charm decays with the knowledge of the form factors. The normalization of the $D \to \pi\ell\nu$ and $D \to K\ell\nu$ form factors, as well as the dependence on the invariant mass of the letpon pair, have been predicted from lattice QCD calculations [175], while theoretical constraints are calculated analytically. Using three-flavor lattice QCD calculations for $D \to \pi\ell\nu$, $f_+^{D\pi}(0) = 0.666 \pm 0.029$ [175], and the average of measurements from BABAR, BESIII, CLEO-c and Belle of $D \to \pi\ell\nu$ [176–180], one obtains

$$|V_{cd}| = 0.2140 \pm 0.0029 \pm 0.0093, \tag{1.88}$$

with the first uncertainty experimental and the second one theoretical of the form factor.

$|V_{cd}|$ can also be determined from the leptonic decay of $D^+ \to \mu^+\nu$, which has been improved recently by BESIII [181]. Averaged with CLEO [182] and the $N_f = 2{+}1{+}1$ lattice result, $f_D = 212.15 \pm 1.45\,\text{MeV}$ [175], leads to

$$|V_{cd}| = 0.2164 \pm 0.0050 \pm 0.0014. \tag{1.89}$$

Another method to determine $|V_{cd}|$ is through neutrino scattering data, used by CDHS [183], CCFR [184, 185] and CHARM II [186]. Using the averaged value of $\mathcal{B}_\mu = 0.087 \pm 0.005$ from CDHS, CCFR, CHARM II and CHORUS [187] where $\mathcal{B}_\mu$ is the average semileptonic branching ratio of charm mesons, one obtains

$$|V_{cd}| = 0.230 \pm 0.011. \tag{1.90}$$

Then averaging over the three determinations above, one finds

$$|V_{cd}| = 0.218 \pm 0.004. \tag{1.91}$$

1.4.5.4 $|V_{cs}|$

$|V_{cs}|$ can be determined from semileptonic D or leptonic D_s decays using lattice QCD calculations of the form factor in D decay and of the decay constant in D_s decay. Using the lattice QCD result of $f_{D_s} = (248.83 \pm 1.27)\,\text{MeV}$ [175] and the average branching ratio $\mathcal{B}(D_s^+ \to \mu^+\nu) = (5.54 \pm 0.23) \times 10^{-3}$ from Belle, CLEO-c, BABAR, and BESIII; or the average of $\mathcal{B}(D_s^+ \to \tau^+\nu) = (5.51 \pm 0.24) \times 10^{-2}$ from CLEO-c, BABAR, Belle and BESIII [188–193], one can determine an averaged $|V_{cs}|$ from them and finds,

$$|V_{cs}| = 1.006 \pm 0.019, \tag{1.92}$$

with the error dominated by experimental uncertainty.

On the other hand, in semileptonic D decays, lattice QCD calculation of the $D \to K\ell\nu$ form factor with $f_+^{DK}(0) = 0.747 \pm 0.019$ [175] and the average of CLEO-c [179], Belle [180], BABAR [194] and recent BESIII [178] measurements of $D \to K\ell\nu$ decays, one obtains

$$|V_{cs}| = 0.967 \pm 0.025, \tag{1.93}$$

where the dominant error is from theoretical calculation of the form factor.

Averaging over the two determinations, one finds

$$|V_{cs}| = 0.997 \pm 0.017. \tag{1.94}$$

1.4.5.5 $|V_{cb}|$

$|V_{cb}|$ can be determined from exclusive and inclusive semileptonic decays of B mesons to charm. For the inclusive case, the theoretical basis is the operator product expansion [195, 196] that allows calculation of the decay rate and various spectra as

expansions in α_s and inverse powers of the heavy quark mass. Inclusive measurements have been performed using B mesons from Z decay at LEP and e^+e^- machines operated at the $\Upsilon(4S)$, leading to an average of [1]

$$|V_{cb}| = (42.2 \pm 0.8) \times 10^{-3}. \tag{1.95}$$

Exclusive measurements are based on semileptonic decays of B to D and D^*, where $|V_{cb}|$ is extracted in the $m_{b,c} \gg \Lambda_{QCD}$ limit where all form factors are given by a single Isgur-Wise functin [197, 198]. The current result is [1]

$$|V_{cb}| = (41.9 \pm 2.0) \times 10^{-3}. \tag{1.96}$$

The combination of above two results gives

$$|V_{cb}| = (42.2 \pm 0.8) \times 10^{-3}. \tag{1.97}$$

1.4.5.6 $|V_{ub}|$

$|V_{ub}|$ determination from inclusive $B \to X_u \ell \bar{\nu}$ is complicated due to large $B \to X_c \ell \bar{\nu}$ backgrounds. In most regions of phase space where the charm background is kinematically forbidden, the hadronic physics enters via the so-called unknown non-perturbative shape functions. Another approach is to make the measurements more inclusive by extending deeper into the $B \to X_c \ell \bar{\nu}$ region and reduce the theoretical uncertainties. The average given in Ref. [1] from inclusive decay is

$$|V_{ub}| = (4.49 \pm 0.16^{+0.16}_{-0.17} \pm 0.17) \times 10^{-3}, \tag{1.98}$$

with the first error experimental and the second one from model dependence quoted by individual measurements and the last one is an additional error estimated from [1].

Exclusive determination of $|V_{ub}|$ requires the knowledge of the form factors. The signal-to-background ratios are offset by smaller yields experimentally, and the $B \to \pi\ell\bar{\nu}$ branching ratio is known to 5% with the form factors there determined from lattice QCD calculations for high $q^2 > 16\,\text{or}\,18\,\text{GeV}^2$ region [199, 200]. A fit to experimental partial rates and lattice QCD result versus q^2 yields [176]

$$|V_{ub}| = (3.70 \pm 0.10 \pm 0.12) \times 10^{-3}. \tag{1.99}$$

On the other hand, light-cone QCD sum rules are used for $q^2 < 12\,\text{GeV}^2$ [201], yielding [1, 176]

$$|V_{ub}| = (3.67 \pm 0.09 \pm 0.12) \times 10^{-3}. \tag{1.100}$$

1.4.5.7 $|V_{td}|$ and $|V_{ts}|$

$|V_{td}|$ and $|V_{ts}|$ are not likely to be precisely measurable in tree-level processes involving top quarks, and one has to rely on determination from $B - \overline{B}$ oscillations mediated by box diagrams with top quarks or loop mediated rare K and B decays. Theoretical uncertainties in hadronic effects limit the accuracy of current determinations, but they can be reduced by taking the ratios of processes that are equal in the flavor SU(3) limit to determine $|V_{td}/V_{ts}|$.

The mixing of two B^0 mesons was first observed by ARGUS [202], and the mass splitting is precisely measured to be $\Delta m_d = (0.5064 \pm 0.0019)/\text{ps}$ [1]. In the B_s^0 system, Δm_s was first measured significantly by CDF [203] and the world average dominated by LHCb [204] gives $\Delta m_s = (17.757 \pm 0.021)/\text{ps}$ [1]. Neglecting suppressions of $|V_{tb}| - 1$ and using the lattice QCD results $f_{B_d}\sqrt{\hat{B}_{B_d}} = (219 \pm 14)\,\text{MeV}$ and $f_{B_s}\sqrt{\hat{B}_{B_s}} = (270 \pm 16)\,\text{MeV}$ [175], one obtains

$$|V_{td}| = (8.1 \pm 0.5) \times 10^{-3}, \quad |V_{ts}| = (39.4 \pm 2.3) \times 10^{-3}, \tag{1.101}$$

where the uncertainties are dominated by lattice QCD.

1.4.5.8 $|V_{tb}|$

Determination of $|V_{tb}|$ can be achieved from top decays using the ratio of branching fractions

$$\mathcal{R} = \frac{\mathcal{B}(t \to Wb)}{\mathcal{B}(t \to Wq)} = \frac{|V_{tb}|^2}{\sum_q |V_{tq}|^2} = |V_{tb}|^2 , \tag{1.102}$$

where the unitarity property of the CKM matrix is applies to obtain the last step. The CDF [205] and DØ [206] measurements from Run II of the Tevatron give $|V_{tb}| > 0.78$ and $0.90 < |V_{tb}| < 0.99$ respectively at 95% CL, and CMS [207] at 8 TeV gives $|V_{tb}| > 0.975$ at 95% CL.

Direct determination of $|V_{tb}|$ is possible from the single top production cross section, which does not depend on the unitarity assumption of the CKM matrix. The combined cross section of DØand CDF is $(3.30^{+0.52}_{-0.40})$ [208], leading to

$$|V_{tb}| = 1.02^{+0.06}_{-0.05}. \tag{1.103}$$

ATLAS and CMS at the LHC have measured single top production cross section in t-channel, Wt-channel, and s-channel at 7 TeV, 8 TeV and 13 TeV, leading to an average of [1]

$$|V_{tb}| = 1.019 \pm 0.028. \tag{1.104}$$

The average of the Tevatron and the LHC gives [1]

$$|V_{tb}| = 1.019 \pm 0.025. \tag{1.105}$$

1.4.6 Phases of CKM elements

As shown in Figure 1.3 and discussed above, CPV is directly related to the phases of the CKM elements, thus their determination is of fundamental importance. We will discuss determination of these phases below by following the discussion in Ref. [1].

1.4.6.1 ϵ and ϵ'

The standard parameter ϵ is defined as [171]

$$\begin{aligned}\epsilon \equiv & \frac{\langle \pi\pi \left|T\right| K_L\rangle\langle 0 \left|T\right| K_S\rangle - \langle 0 \left|T\right| K_L\rangle\langle \pi\pi \left|T\right| K_S\rangle}{\sqrt{2}\langle 0 \left|T\right| K_S\rangle^2} \\ \approx & \frac{i}{\sqrt{2}} e^{i(\delta_2-\delta_0)} \frac{\mathrm{Im}(A_2 A_0^*)}{\left|A_0\right|^2}.\end{aligned} \tag{1.106}$$

Experimentally, the ratio

$$\frac{\epsilon'}{\epsilon} \approx \frac{\eta_{+-} - \eta_{00}}{2\eta_{+-} + \eta_{00}}, \tag{1.107}$$

with $\eta_{ij} = \langle \pi^i\pi^j \left|\mathcal{H}\right| K_L\rangle / \langle \pi^i\pi^j \left|\mathcal{H}\right| K_S\rangle$ that each violates CP is more useful. Since $|\eta_{+-}| \approx |\eta_{00}| \approx |\epsilon| = (2.280 \pm 0.013) \times 10^{-3}$ [171] is small, one has

$$\frac{\epsilon'}{\epsilon} \approx \frac{1}{3}\left(1 - \frac{\eta_{00}}{\eta_{+-}}\right). \tag{1.108}$$

Experimentally, one measures $|\eta_{00}/\eta_{+-}|$, thus only $\mathrm{Re}(\epsilon'/\epsilon)$ can be obtained:

$$\mathrm{Re}\left(\frac{\epsilon'}{\epsilon}\right) \approx \frac{1}{6}\left(1 - \left|\frac{\eta_{00}}{\eta_{+-}}\right|\right). \tag{1.109}$$

The current value of $\mathrm{Re}(\epsilon'/\epsilon)$ is [1]

$$\mathrm{Re}\left(\frac{\epsilon'}{\epsilon}\right) = (1.67 \pm 0.23) \times 10^{-3}, \tag{1.110}$$

and its nonzero value demonstrates the existence of CPV.

CPV in B-meson decays also provide direct information on the angles α, β and γ defined in eq. (1.75-1.77). These overconstraining measurements can improve the determination of the CKM matrix elements and will also reveal effects of new physics. We discuss their determination below.

1.4.6.2 β

The time-dependence CP asymmetry of $B^0$and $\overline{B}^0$ decays with a common final state f is defined as [1, 209]

$$\mathcal{A}_f = \frac{\Gamma\left(\bar{B}^0(t) \to f\right) - \Gamma\left(B^0(t) \to f\right)}{\Gamma\left(\bar{B}^0(t) \to f\right) + \Gamma\left(B^0(t) \to f\right)} = S_f \sin\left(\Delta m_d t\right) - C_f \cos\left(\Delta m_d t\right), \quad (1.111)$$

with

$$S_f = \frac{2\,\mathrm{Im}\,\lambda_f}{1 + |\lambda_f|^2}, \quad C_f = \frac{1 - |\lambda_f|^2}{1 + |\lambda_f|^2}, \quad \lambda_f = \frac{q}{p}\frac{\bar{A}_f}{A_f}. \quad (1.112)$$

Theoretically, the $b \to c\bar{c}s$ decays to CP eigenstates are the cleanest example to measure β. The $b \to sq\bar{q}$ penguin amplitudes have dominantly the same weak phase as the $b \to c\bar{c}s$ tree amplitude. The e^+e^- asymmetric-energy B-factory experiments, BABAR [210] and Belle [211] provide precise measurements. The world average including LHCb and other measurements leads to [176]

$$\sin 2\beta = 0.691 \pm 0.017. \quad (1.113)$$

The four-fold ambiguity in β can be resolved by a global fit as we will discuss below. Experimentally, the two-fold ambiguity $\beta \to \pi/2 - \beta$ is resolved by a time-dependent angular analysis of $B^0 \to J/\psi K^{*0}$ [212, 213] or a time-dependent Dalitz plot analysis of $B^0 \to \overline{D}^0 h^0$ with $h^0 = \pi^0, \eta, \omega$ and $\overline{D}^0 \to K^0_S\pi^+\pi^-$ jointly performed by Belle and BABAR, and the $\pi/2 - \beta$ ambiguity is excluded with 7.3σ CL [214].

1.4.6.3 α

Note that α is the phase between $V_{tb}^* V_{td}$ and $V_{ub}^* V_{ud}$, only time-dependent CP asymmetries in $b \to u\bar{u}d$ decay dominated modes can be used to directly measure α. Currently, α has been measured in $B \to \pi\pi$, $\rho\pi$ and $\rho\rho$ decay modes.

Due to the sizable contribution of $b \to d$ penguin amplitudes in $B \to \pi\pi$ decays as established from data, the time-dependent $B^0 \to \pi^+\pi^0$ actually measures

$$S_{\pi^+\pi^-} = \sqrt{1 - C^2_{\pi^+\pi^-}} \sin(2\alpha + 2\Delta\alpha), \tag{1.114}$$

with $2\Delta\alpha$ the phase difference between $e^{2i\gamma}\overline{A}_{\pi^+\pi^-}$ and $A_{\pi^+\pi^-}$. The value of $\Delta\alpha$ and hence α can be extracted using the isospin relation among the amplitudes of $B^0 \to \pi^+\pi^-$, $B^0 \to \pi^0\pi^0$ and $B^+ \to \pi^+\pi^0$ decays. However, the isospin analysis with the experimental data $S_{\pi^+\pi^-} = -0.68 \pm 0.04$, $C_{\pi^+\pi^-} = -0.27 \pm 0.04$, and $C_{\pi^0\pi^0} = -0.33 \pm 0.22$ from BABAR, Belle and LHCb leads to 16 mirror solutions for $0 \leq \alpha \leq 2\pi$, as a result of this as well as uncertainties from experiments, one find, at 68% CL [176]:

$$-13.5^\circ < \alpha < 15.7^\circ, \quad 74.3^\circ < \alpha < 105.6^\circ, \quad 118.5^\circ < \alpha < 151.5^\circ. \tag{1.115}$$

The $B^0 \to \rho^+\rho^-$ is in general a mixture of CP-even and CP-odd components, making the extraction of α complicated. However, the longitudinal polarization fractions in $B^+ \to \rho^+\rho^0$ and $B^0 \to \rho^+\rho^-$ decays are measured to be close to one [215–218], implying the fact that the final states are almost purely CP-even. Using the world average for the isospin analysis combined with the time-dependent CP asymmetry, one finds [176], using the branching fractions $\mathcal{B}(B^0 \to \rho^0\rho^0)$, $\mathcal{B}(B^0 \to \rho^+\rho^-)$, $\mathcal{B}(B^+ \to \rho^+\rho^0)$

$$\alpha = (90.9^{+5.6}_{-5.5})^\circ, \quad \text{or,} \quad \alpha = (179.1^{+5.5}_{-5.6})^\circ, \tag{1.116}$$

with mirror solutions at $3\pi/2 - \alpha$.

Another decay channel one can make use of is $B \to \rho\pi$. The final state in $B^0 \to \rho^+\pi^-$ decay is not a CP eigenstate, but this decay mode proceeds via the same quark-level diagrams as $B^0 \to \pi^+\pi^-$ and both B^0 and $\overline{B}^0$ can decay to $\rho^+\pi^-$. Since the final state of $B^0 \to \rho^0\pi^0$ is a CP eigenstate, mixing-induced CPCV can occur in B^0 and $\overline{B}^0$ with $\rho^\pm\pi^\mp$ and $\rho^0\pi^0$ final states. Then the time-dependent Dalitz plot analysis of $B^0 \to \pi^+\pi^-\pi^0$ decays permits the extraction of α with a single discrete ambiguity, i.e. $\alpha \to \pi + \alpha$. The combination of Belle and BABAR gives

$$\alpha = (54.1^{+7.7}_{-10.3}), \quad \text{and} \quad \alpha = (141.8^{+4.8}_{-5.4}) \ [219], \tag{1.117}$$

and

$$\alpha = (53.4^{+8.0}_{-11.0}), \quad \text{and} \quad \alpha = (143.4^{+3.9}_{-4.8}) \ [1,176]. \tag{1.118}$$

Combining the results above, α is constrained to be $[1,176]$

$$\alpha = (84.5^{+5.9}_{-5.2}). \tag{1.119}$$

1.4.6.4 γ

The definition of γ in Eq. (1.77) does not depend on any CKM matrix elements that involve the top quark, thus γ can be determined from B decays at tree level, which also implies the fact that the measurements of γ are unlikely to be affected by any new physics.

To extract γ, the interference between $B^- \to D^0K^-(b \to c\bar{u}s)$ and $B^- \to \overline{D}^0K^-(b \to u\bar{c}s)$ is studied in both D^0 and $\overline{D}^0$ decays [209]. However, in practi-

cal, a complication arises due to the fact that the precision depends sensitively on the ratio r_B of the interfering amplitudes, where

$$r_B = \left| \frac{\mathcal{M}(B^- \to \overline{D}^0 K^-)}{\mathcal{M}(B^- \to D^0 K^-)} \right|. \tag{1.120}$$

To alleviate the smallness of r_B and to make the two amplitudes comparable, the GLW method [220, 221] considers D decaying to CP eigenstates; the ADS method [222, 223] instead considers final states where Cabibbo-allowed $\overline{D}^0$ and doubly-Cabibbo-suppressed D^0 decay interference. Measurements have been performed at the B factories, CDF and LHCb, the GLW method currently gives a loose constraint on γ:

$$\begin{aligned} 15.3^\circ < \gamma < 28.9^\circ, \quad 70.2^\circ < \gamma < 87.6^\circ, \\ 92.4^\circ < \gamma < 109.8^\circ, \quad 151.1^\circ < \gamma < 164.7^\circ \end{aligned} \tag{1.121}$$

at 68% CL; while the ADS method gives

$$\gamma = (73^{+12}_{-18})^\circ \ [1, 176]. \tag{1.122}$$

On the other hand, since both D^0 and $\overline{D}^0$ have large three-body decay branching ratios, it is realized that the analysis can be optimized by studying the Dalitz plot dependence of the interferences [224, 225]. The best present determination of γ is obtained from this method. Through the combination of Belle [226], BABAR [227] and LHCb [228] data, one finds

$$\gamma = (67.3^{+8.0}_{-7.9})^\circ \ [1, 176]. \tag{1.123}$$

Combining the GLW, ADS and the Dalitz analysis, γ is constrained to be

$$\gamma = (73.5^{+4.2}_{-5.1})^\circ \ [1, 176]. \tag{1.124}$$

1.4.7 Global fit of the CKM matrix

The CKM matrix elements can be most precisely determined using a global fit to all available measurements and imposing the SM constraints, i.e. three-generation unitarity. There are several approaches to combining the experimental data, such as CKMfitter [219, 229] and UTfit [230, 231] which use frequentist statistics and the Bayesian approach respectively and others [232–235], and they provide similar results.

Using CKMfitter and UTfit, the fitted Wolfenstein parameters are

$$\begin{aligned} \lambda &= 0.22453 \pm 0.00044, \quad A = 0.836 \pm 0.015, \\ \bar{\rho} &= 0.122^{+0.018}_{-0.017}, \quad \bar{\eta} = 0.355^{+0.012}_{-0.011} \qquad \text{(CKMfitter)} \end{aligned} \tag{1.125}$$

$$\begin{aligned} \lambda &= 0.22465 \pm 0.00039, \quad A = 0.832 \pm 0.009, \\ \bar{\rho} &= 0.139 \pm 0.016, \quad \bar{\eta} = 0.346 \pm 0.010 \qquad \text{(UTfit)}, \end{aligned} \tag{1.126}$$

and the fitted results for the CKM matrix are

$$V_{\text{CKM}} = \begin{pmatrix} 0.97446 \pm 0.00010 & 0.22452 \pm 0.00044 & 0.00365 \pm 0.00012 \\ 0.22438 \pm 0.00044 & 0.97359^{+0.00010}_{-0.00011} & 0.04214 \pm 0.00076 \\ 0.00896^{+0.00024}_{-0.00023} & 0.04133 \pm 0.00074 & 0.999105 \pm 0.000032 \end{pmatrix}, \tag{1.127}$$

leading to the Jarlskog invariant being

$$J = (3.18 \pm 0.15) \times 10^{-5}. \tag{1.128}$$

For completeness, we also include the plot of the global fit from [1] in Figure 1.4.

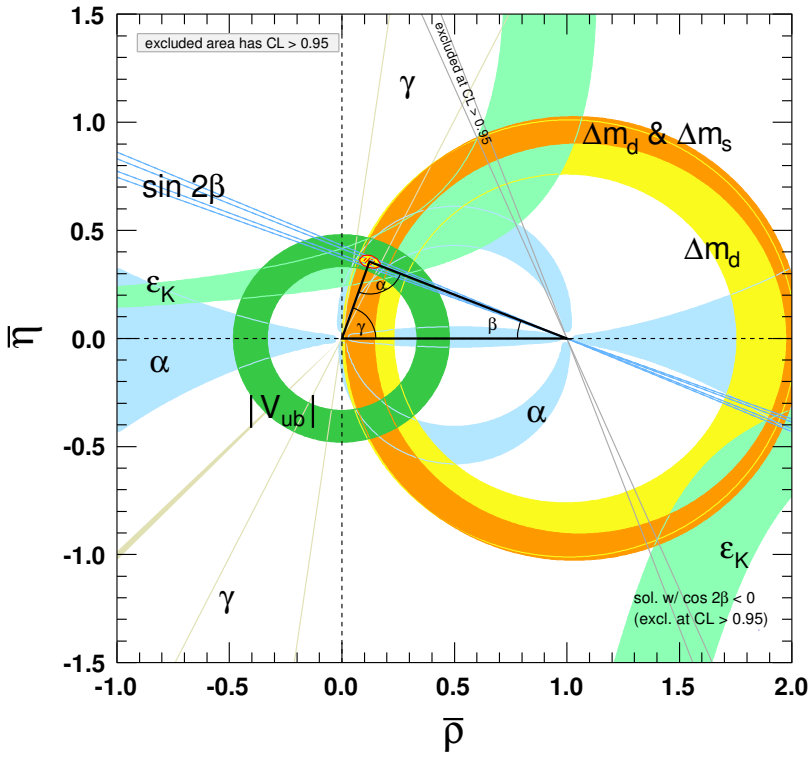

Figure 1.4: Constraints on the $(\overline{\rho}, \overline{\eta})$ plane from global fit discussed in the main text. Plots adopted from Ref. [1].

1.5 The ρ parameter and the oblique parameter S, T, U

The ρ parameter is defined as

$$\rho \equiv \frac{m_W^2}{m_Z^2 \cos^2 \theta_W}, \tag{1.129}$$

from Eq. (1.28), obviously $\rho = 1$ at tree level. The tree level value of the ρ parameter is actually guaranteed by the so-called custodial SU(2) symmetry of the SM: The Higgs potential is invariant under the SO(4) group, after spontaneous symmetry breaking when the Higgs doublet gets a non-vanishing vev, the SO(4) symmetry is broken down to SO(3). It is this residual symmetry that is called the custodial symmetry. However, since the Yukawa couplings do not respect this symmetry, contributions from them would modify the ρ parameter, the corrections is usually written in terms of Π functions for W and Z bosons:

$$\Delta\rho = \rho - 1 = \frac{\Pi_{WW}(0)}{m_W^2} - \frac{\Pi_{ZZ}(0)}{m_Z^2}, \tag{1.130}$$

where only the dominant contribution from the top quark loop is included here since top Yukawa is the largest. However, from considerations on new physics, $\Delta\rho$ is usually absorbed in the definition of the ρ parameter, which can be achieved in the $\overline{\text{MS}}$ scheme as will be discussed in more detail in Chapter 8. In this way, any significant deviation of the ρ parameter from unity will be a hint of new physics.

In the same spirit of looking for any new physics from any deviations in the ρ parameter, it turns out useful to use the so-called oblique parameters S, T and U which were originally proposed by Peskin and Takeuchi [10] and whose sensitivity to new physics were studied in Ref. [236–242]. The oblique parameters are defined as

$$S \equiv \frac{4c_W^2 s_W^2}{\alpha_{\text{EM}}} \left[\frac{\Pi_{ZZ}^{\text{NP}}(m_Z^2) - \Pi_{ZZ}^{\text{NP}}(0)}{m_Z^2} - \frac{c_W^2 - s_W^2}{c_W s_W} \frac{\Pi_{Z\gamma}^{\text{NP}}(m_Z^2)}{m_Z^2} - \frac{\Pi_{\gamma\gamma}^{\text{NP}}(m_Z^2)}{m_Z^2} \right] \tag{1.131}$$

$$T \equiv \frac{1}{\alpha_{\rm EM}} \left(\frac{\Pi^{\rm NP}_{WW}(0)}{m_W^2} - \frac{\Pi^{\rm NP}_{ZZ}(0)}{m_Z^2} \right) = \frac{\rho - 1}{\alpha_{\rm EM}} \tag{1.132}$$

$$U \equiv \frac{4 s_W^2}{\alpha_{\rm EM}} \left[\frac{\Pi^{\rm NP}_{WW}\left(m_W^2\right) - \Pi^{\rm NP}_{WW}(0)}{m_W^2} - \frac{c_W}{s_W} \frac{\Pi^{\rm NP}_{Z\gamma}\left(m_Z^2\right)}{m_Z^2} - \frac{\Pi^{\rm NP}_{\gamma\gamma}\left(m_Z^2\right)}{m_Z^2} \right] - S, \tag{1.133}$$

where $\alpha_{\rm EM} \equiv e^2/(4\pi)$ is the fine structure constant, "NP" is the abbreviation of "New Physics", $c_W \equiv \cos\theta_W$ and $s_W \equiv \sin\theta_W$. By definition, one has

$$S = T = U = 0, \tag{1.134}$$

and the latest experimental constraints on them are [1]

$$S = 0.02 \pm 0.10, \quad T = 0.07 \pm 0.12, \quad U = 0.00 \pm 0.09, \tag{1.135}$$

which agree very well with SM predictions.

In practice, since the U parameter is suppressed by $v_\Phi^2/M_{\rm NP}^2$ [243] compared with S and T, global analysis is usually carried out by fixing $U = 0$, resulting in a better global fit for S and T:

$$S = 0.02 \pm 0.07, \quad T = 0.06 \pm 0.06, \tag{1.136}$$

and the current allowed region for S and T is shown in Figure 1.5.

Due to the stringent constraints on the ρ and the oblique parameters, new physics will generically be constrained from precision measurements on these observables. In Chapter 6 and Chapter 7, we will discuss constrain on the type-II complex triplet model and the real triplet model respectively from precision measurement on the ρ parameter.

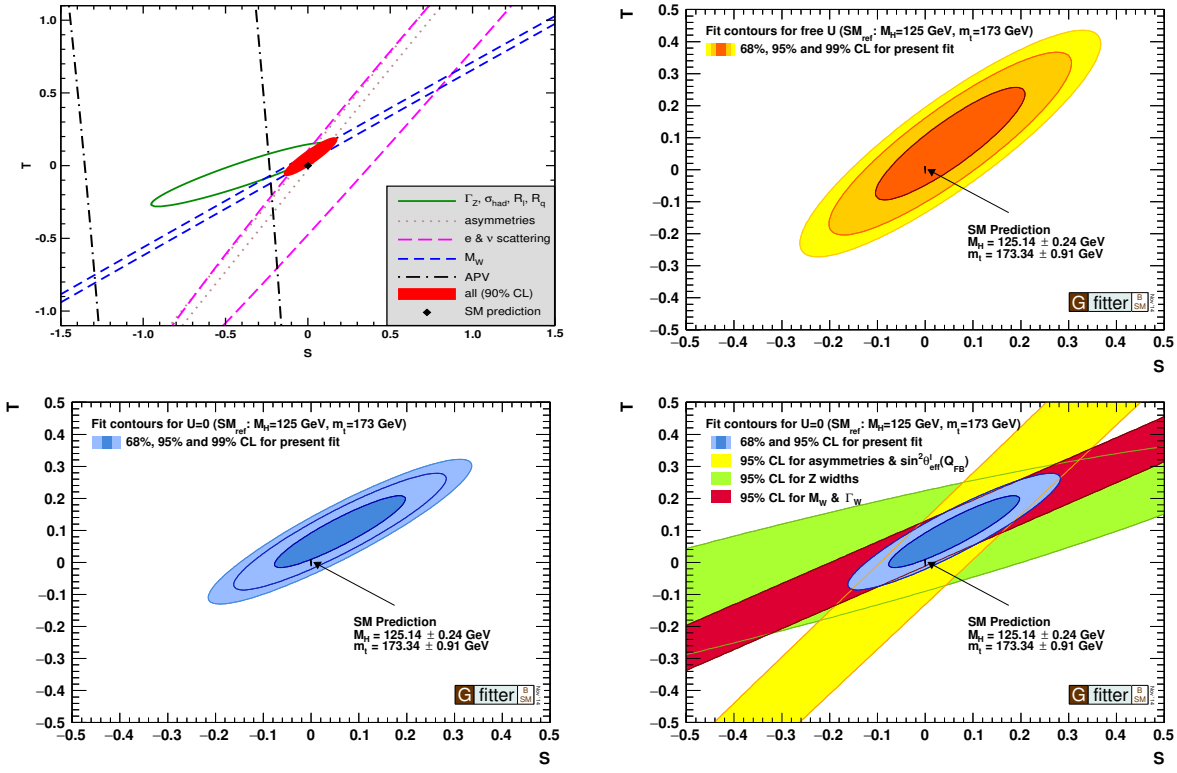

Figure 1.5: Upper left: Global fit of the S and T parameters with $U = 0$, $\alpha_s = 0.1187$. Upper right: Global fit of the S and T parameters with free U and $\alpha_s(m_Z^2) = 0.1192 \pm 0.0033$. Lower left: Global fit of the S and T parameters with $U = 0$ and $\alpha_s(m_Z^2) = 0.1192 \pm 0.0033$. Lower right: Global fit of the S and T parameters with $U = 0$, $\alpha_s(m_Z^2) = 0.1192 \pm 0.0033$ and the inclusion of the asymmetry measurements, partial widths of Z, m_W and Γ_W. Plots adopted from Refs. [1, 10].

CHAPTER 2

NEUTRINOS

2.1 Introduction

The concept of massive neutrinos has been broadly accepted since the observation of neutrino oscillations from the Super-K experiment in 1998 [55], the SNO experiment in 2001 [56] and the KamLAND experiment in 2002 [57]. Theoretically, the mixing between neutrinos of different flavor as a result of neutrino oscillation can be described by the so-called PMNS matrix that was originally introduced by Ziro Maki, Masami Nakagawa and Shoichi Sakata in 1962 [244] in order to explain the neutrino oscillation predicted by Bruno Pontecorvo in 1958 [245]. However, from the most general renormalizable Lagrangian one can write down based on the particle contents of SM and the gauge group under which the SM transforms, neutrinos are predicted strictly as massless as discussed in Chapter 1.

To circumvent the contradiction between SM prediction and the observation of neutrino oscillation, there are many beyond SM scenarios proposed to explain neutrino masses. In this chapter, we will only focus on the type-I, -II and -III seesaw mechanisms [58–75] since they are the only three mechanisms that are responsible for neutrino mass generation at tree level.

The seesaw mechanisms predict neutrinos to be of Majorana type, while in the SM, neutrinos are of Dirac type. Therefore, testing the Dirac or the Majorana nature of neutrinos is another fundamental task on neutrinos. As we will see shortly, in terms of the PMNS matrix, Dirac and Majorana neutrinos are only different by the phases in the matrix. To be more specific, the Majorana neutrinos own two more

phases than the Dirac neutrinos. However, oscillation experiments are only sensitive to the Dirac phase of the PMNS matrix, such that the oscillation behavior between Dirac and Majorana neutrinos are exactly the same.

Recall that, different from Dirac neutrinos, Majorana neutrinos are their own antiparticles and lepton number is violated by two units from neutrinoless double beta decay. Therefore, if neutrinos are Majorana particles, neutrino-less double beta decay could be observed experimentally. This unique feature has been utilized for decades in the neutrino community to determine the Dirac or Majorana nature of neutrinos, which will also be discussed in this chapter given its importance.

Another point related to our discussion in this thesis is that the type-II seesaw mechanism is the only one accessible at colliders among the three tree-level seesaw mechanisms, the reason will become clear shortly below. To explain neutrino masses through the type-II seesaw mechanism, a complex triplet is introduced, which mixes with the SM Higgs doublet. Due to the mixing, the triplet can be produced and explored at current and future colliders. We will discuss in detail about its collider phenomenologies in Chapter 6. Furthermore, interactions between the triplet and the SM Higgs doublet can also distort the shape of the Higgs potential such that the model could also be a potential candidate to explain the BAU problem through EWBG. Before going to any details, in what follows, we review the properties of neutrinos in this chapter.

2.2 Dirac versus Majorona

2.2.1 Dirac neutrinos

For explanation, let us consider free fermion fields and start with the Dirac case. The Dirac equation can be written as

$$\mathcal{L}_{\text{Dirac}} \supset \bar{\psi}(i\partial\!\!\!/ - m_D)\psi, \tag{2.1}$$

where ψ is the four-component conventional Dirac spinor and m_D corresponds to the Dirac mass term which can be written as

$$\mathcal{L}_{\text{Dirac}}^{\text{mass}} = \bar{\psi} m_D \psi = \bar{\psi}_L m_D \psi_R + \bar{\psi}_R m_D \psi_L, \tag{2.2}$$

with $\bar{\psi}_{L,R} = \frac{1 \pm \gamma_5}{2} \psi \equiv P_{L,R} \psi$ and γ_5 defined through the Dirac matrices as follows

$$\gamma_5 = i \gamma_0 \gamma_1 \gamma_2 \gamma_3. \tag{2.3}$$

Note that, on one hand, since $\bar{\psi}\psi$ is Hermitian, m_D is real. On the other hand, a non-vanishing m_D would require the existence of both the left-handed ψ_L and the right-handed Dirac spinor ψ_R. However, as discussed in Chapter 1, only left-handed neutrinos exist in the SM, thus neutrinos are massless in the SM.

2.2.2 Majorana neurinos

The Majorana mass terms, first introduced by Ettore Majorana in 1937 [246], can be obtained by constructing Lorentz scalars from both the Dirac spinor ψ and its charge conjugation ψ^c. The most general mass terms we can write down are

$$\mathcal{L}_{\text{Majorana}} \supset \frac{1}{2} (\bar{\psi} m_M \psi^c + \overline{\psi^c} m_M^* \psi) = \frac{1}{2} \bar{\psi} m_M \psi^c + h.c., \tag{2.4}$$

where $\psi^c \equiv C \psi C^{-1} = C \bar{\psi}^T$ is the charge conjugation of ψ and C the charge-conjugation operator. Similarly, $\psi^c_{L,R} \equiv C \overline{\psi_{L,R}}^T$. The factor of $1/2$ is to ensure that it corresponds to the conventional mass in the equation of motion of ψ and/or ψ^c. One representation of the charge-conjugation operator can be

$$C = i \gamma_2 \gamma_0. \tag{2.5}$$

Follow above conventions, one can claim that $\psi^c_{L(R)}$ is a right-handed (left-handed) field. We use ψ^c_R as an example to show this point below:

$$P_L\psi^c_R = P_L C\overline{\psi_R}^T = C(\overline{\psi_R}P_L)^T = C\overline{\psi_R}^T = \nu^c_R. \tag{2.6}$$

$$P_R\psi^c_R = P_L C\overline{\psi_R}^T = C(\overline{\psi_R}P_R)^T = 0. \tag{2.7}$$

Then one can write the mass terms in Eq. (2.4) symbolically as

$$\mathcal{L}_{\text{Majorana}} \supset \frac{1}{2}m_L(\overline{\psi_L}\psi^c_L + \overline{\psi^c_L}\psi_L) + \frac{1}{2}m_R(\overline{\psi_R}\psi^c_R + \overline{\psi^c_R}\psi_R), \tag{2.8}$$

where $m_{L,R}$ are both real and the Majorana masses.

2.2.3 An extension: The Dirac-Majorana case

The most general mass terms can be obtained through the combination of the Dirac and the Majorana cases discussed above, which can be written as

$$\mathcal{L}_{\text{Dirac+Majorana}} \supset \overline{\psi_L}m_D\psi_R + \frac{1}{2}(\overline{\psi^c_L}m_L\psi_L + \overline{\psi_R}m_R\psi^c_R) + h.c.\,. \tag{2.9}$$

Another possible term is $\overline{\psi^c_L}m_d\psi^c_R$, which however can be reduced to the first term above through the following identidy

$$\overline{\psi^c_L}m_d\psi^c_R = -\psi^T_L C^{-1}m_d C\gamma^T_0\psi^*_R = (\overline{\psi_R}m_d\psi_L)^T = \overline{\psi_R}m_{d'}\psi_L. \tag{2.10}$$

In general, all these matrices $m_{D,d,d',L,R}$ are $n\times n$ complex matrix with n the number of flavors and can be diagonalized by biunitary transformation as we discussed above while introducing the CKM matrix. We will not discuss the details again here to repeat.

2.3 Pontecorvo-Maki-Nakagawa-Sakata (PMNS) metrix and CP violation

As discussed above, to give neutrino masses, new physics beyond the SM is needed. Though we have not discussed any mechanism responsible for neutrino masses, let us for now discuss two scenarios, i.e. Dirac neutrinos and Majorana neutrinos, in which neutrino flavor eigenstates mix with neutrino mass eigenstates through the PMNS matrix. The discussion is similar to but not the same as what we discussed on the CKM matrix for quarks. We start by writing the mixing matrix as follows

$$\begin{pmatrix} \nu_e \\ \nu_\mu \\ \nu_\tau \end{pmatrix}_L = U_{\rm PMNS} \begin{pmatrix} \nu_1 \\ \nu_2 \\ \nu_3 \end{pmatrix}_L = \begin{pmatrix} U_{e1} & U_{e2} & U_{e3} \\ U_{\mu 1} & U_{\mu 2} & U_{\mu 3} \\ U_{\tau 1} & U_{\tau 2} & U_{\tau 3} \end{pmatrix} \begin{pmatrix} \nu_1 \\ \nu_2 \\ \nu_3 \end{pmatrix}_L , \tag{2.11}$$

or, in the component form,

$$\nu_{\alpha L} = (U_{\rm PMNS})_{\alpha i} \nu_{iL}, \tag{2.12}$$

where Einstein summation convention is used, the subscript L stands for left-handedness of the SM neutrinos, $\alpha = e, \mu, \tau$ are the flavor indices and $i = 1, 2, 3$ are the mass indices. We will consistently use Greek labels to represent the flavor indices and Roman labels for mass indices below. Just as for the CKM matrix, the PMNS matrix also satisfies the unitarity condition:

$$U_{\rm PMNS} U^\dagger_{\rm PMNS} = U^\dagger_{\rm PMNS} U_{\rm PMNS} = \mathbf{1}, \tag{2.13}$$

written in components,

$$(U_{\rm PMNS})_{\alpha i} (U_{\rm PMNS})^*_{\beta i} = \delta_{\alpha\beta}, \quad (U_{\rm PMNS})^*_{\alpha i} (U_{\rm PMNS})_{\alpha j} = \delta_{ij}, \tag{2.14}$$

As a result of this flavor mixing, neutrinos in the weak charged current in the leptonic sector will not be in their mass eigenstates but a coherent superposition of them:

$$\mathcal{L}^{\ell}_{\rm CC} = \frac{g_2}{\sqrt{2}} W^-_\mu \bar{\ell}_{\alpha L} \gamma^\mu \nu_{\alpha L} + h.c. = \frac{g_2}{\sqrt{2}} W^-_\mu \bar{\ell}_{\alpha L} \gamma^\mu (U_{\rm PMNS})_{\alpha i} \nu_{iL} + h.c.. \tag{2.15}$$

If neutrinos are Dirac, then the mass terms for leptons and neutrinos are

$$\mathcal{L}^{\rm mass}_{\rm Dirac} = -m_\ell \bar{\ell}_R \ell_L - m_\nu \bar{\nu}_R \nu_L + h.c.. \tag{2.16}$$

Based on the same argument as in the quark case, one can absorb five of the six phases in the fields by redefining

$$\ell_\alpha \to e^{i\phi_\alpha} \ell_\alpha, \quad \nu_i \to e^{i\phi_i} \nu_i, \tag{2.17}$$

while keeping the charged current and the mass Lagrangian above invariant as long as the PMNS matrix transforms accordingly as

$$(U_{\rm PMNS})_{\alpha i} \to e^{i(\phi_\alpha - \phi_i)} (U_{\rm PMNS})_{\alpha i}. \tag{2.18}$$

Therefore, in the end, to parameterize the PMNS matrix for Dirac neutrinos, we only need three mixing angles and one phase that corresponds to CPV in the leptonic sector.

On the other hand, if neutrinos are Majorana, we will then have the following mass terms[i]

$$\mathcal{L}^{\rm mass}_{\rm Majorana} = -m_\ell \bar{\ell}_R \ell_L - \frac{1}{2} m_\nu \bar{\nu}^c_L \nu_L + h.c.. \tag{2.19}$$

[i]Here for interpretation, we only keep the left-handed neutrinos. Including the full mass terms with the right-handed neutrinos, however, will not modify the argument below.

Since

$$C\gamma_\mu C^{-1} = -\gamma_\mu^T, \tag{2.20}$$

where T is the transposition transformation, one can now only absorb three of the phases of the charged leptons out of the total six phases in the PMNS matrix through

$$\ell_\alpha \to e^{i\phi_\alpha}\ell_\alpha \tag{2.21}$$

while simultaneously

$$(U_{\rm PMNS})_{\alpha i} \to e^{i\phi_\alpha}(U_{\rm PMNS})_{\alpha i}. \tag{2.22}$$

Thus, in the end, comparing with the Dirac neutrino case, Majorana neutrinos has two more phases in the PMNS matrix.

2.3.1 Standard parameterization of the PMNS matrix

Based on argument above, the PMNS matrix can be parameterized as

$$U_{\rm PMNS} = \begin{pmatrix} 1 & 0 & 0 \\ 0 & c_{23} & s_{23} \\ 0 & -s_{23} & c_{23} \end{pmatrix} \begin{pmatrix} c_{13} & 0 & s_{13}e^{-i\delta} \\ 0 & 1 & 0 \\ -s_{13}e^{i\delta} & 0 & c_{13} \end{pmatrix} \begin{pmatrix} c_{12} & s_{12} & 0 \\ -s_{12} & c_{12} & 0 \\ 0 & 0 & 1 \end{pmatrix} P \tag{2.23}$$

$$= \begin{pmatrix} c_{12}c_{13} & s_{12}c_{13} & s_{13}e^{-i\delta} \\ -s_{12}c_{23} - c_{12}s_{23}s_{13}e^{i\delta} & c_{12}c_{23} - s_{12}s_{23}s_{13}e^{i\delta} & s_{23}c_{13} \\ s_{12}s_{23} - c_{12}c_{23}s_{13}e^{i\delta} & -c_{12}s_{23} - s_{12}c_{23}s_{13}e^{i\delta} & c_{23}c_{13} \end{pmatrix} P, \tag{2.24}$$

where P is the matrix that accounts for the difference between Dirac and Majorana neutrinos, $c_{ij} = \cos\theta_{ij}$, $s_{ij} = \sin\theta_{ij}$ and δ is the so-called "Dirac-type phase". To be more explicit on P,

$$P_{\text{Dirac}} = \mathbf{1}, \tag{2.25}$$

$$P_{\text{Majorana}} = \begin{pmatrix} e^{i\alpha_1} & 0 & 0 \\ 0 & e^{i\alpha_2} & 0 \\ 0 & 0 & 1 \end{pmatrix}, \begin{pmatrix} 1 & 0 & 0 \\ 0 & e^{i\alpha_2} & 0 \\ 0 & 0 & e^{i(\alpha_1+\delta_m)} \end{pmatrix}, \begin{pmatrix} e^{i\rho} & 0 & 0 \\ 0 & 1 & 0 \\ 0 & 0 & e^{i\sigma} \end{pmatrix}. \tag{2.26}$$

For the Majorana case, we show here three kinds of parameterization of the P matrix that appear in literatures, wherein the phases are the so-called "Majorana-type phases".

For Dirac neutrinos, we have other very similar parameterization for the PMNS matrix, six unitarity triangles from orthogonality of the CKM matrix etc as in the case of the quark mixing CKM matrix. To illustrate the difference between quarks and neutrinos, we focus on Majorana neutrinos in the next subsection.

2.3.2 Unitarity triangles for Majorana neutrinos

As discussed above, the unitarity triangles will be very similar to the CKM matrix for Dirac neutrinos, i.e. six equivalent triangles with different orientation due to rephasing transformation of the Dirac neutrino fields. As a consequence, the orientation of the triangles has no physical meaning. However, the area of these triangles does have a physical meaning – Its area measures the amount CPV and can be represented by the so-called Jarlskog invariant J discussed in last chapter.

For Majorana neutrinos, however, two extra phases appear in the P matrix defined above. In light of this, one can define the following six triangles by multiplying two columns and two rows of U_{PMNS} respectively:

$$U_{e1}U_{e2}^{*}+U_{\mu1}U_{\mu2}^{*}+U_{\tau1}U_{\tau2}^{*}=0, \tag{2.27}$$

$$U_{e1}U_{e3}^{*}+U_{\mu1}U_{\mu3}^{*}+U_{\tau1}U_{\tau3}^{*}=0, \tag{2.28}$$

$$U_{e2}U_{e3}^{*}+U_{\mu2}U_{\mu3}^{*}+U_{\tau2}U_{\tau3}^{*}=0, \tag{2.29}$$

$$U_{e1}U_{\mu1}^{*}+U_{e2}U_{\mu2}^{*}+U_{e3}U_{\mu3}^{*}=0, \tag{2.30}$$

$$U_{e1}U_{\tau1}^{*}+U_{e2}U_{\tau2}^{*}+U_{e3}U_{\tau3}^{*}=0, \tag{2.31}$$

$$U_{\mu1}U_{\tau1}^{*}+U_{\mu2}U_{\tau2}^{*}+U_{\mu3}U_{\tau3}^{*}=0. \tag{2.32}$$

The first three of these triangles are called "Dirac triangles" since they rotate in the complex plane under rephasing transformation just as in the quark case. Correspondingly, they share a common area just as in the quark case

$$\text{Area}=\frac{|J_{\text{Dirac}}|}{2}, \quad \text{with } J_{\text{Dirac}}=\text{Im}(U_{\alpha i}U_{\beta j}U_{\alpha j}^{*}U_{\beta i}^{*}), \tag{2.33}$$

where $\alpha,\beta=e,\mu,\tau$ and $i,j=1,2,3$ and summation on repeated indices is not implied here.

Different from the quark and/or the Dirac neutrino cases, vanishing area of the Dirac triangles does not necessarily imply CP conservation since the minimal CP violating quantities $\text{Im}(U_{\alpha i}U_{\beta i}^{*})$ can still be non-vanishing. Instead, vanishing of J_{Dirac} only implies vanishing of the Dirac-type phase δ in the PMNS matrix, while the Majorana-type phases can still violate CP. This is why we often say that Dirac triangles only provide a necessary but not a sufficient condition for CP conservation.

The last three triangles, which do not rotate in the complex plane under rephasing transformation, are often called the "Majorana triangles". They, in contrast with the Dirac triangles, provide the necessary and sufficient conditions for CP conservation as was first studied by Aguilar-Saavedra and Branco in 2000 [247]. The conditions are:

1. The area of all Majorana triangles vanishes.

2. In the complex plane, all Majorana triangles shall orientate along the direction of the real or the imaginary axis.

The first condition implies that the Majorana triangles collapse into lines along the real or the imaginary axis in the complex plane and thus a vanishing Dirac phase. Now if the collapsed line or lines are parallel to the real axis, one has $\mathrm{Im}U_{\alpha i}U^*_{\beta i} = 0$ for any (α, β, i), thus CP is conserved. On the other hand, if the line or lines are parallel to the imaginary axis, one can always rotate the corresponding mass eigenstates ν_i and ν_j to the real axis by multiplying the i- and j-th rows by $\pm i$. Thus CP is again conserved.

Another way to look at this point is by introducing the Dirac-type phases and the Majorana-type phases. It turns out the Dirac-type phases can be expressed as a linear combination of the Majorana-type phases such that vanishing of the former obviously does not imply the vanishing of the latter. We put the details in Appendix B.1 for reference.

2.4 Neutrinos masses

Now we come back to the neutrino mass issue. Given the gauge group and the particle content of SM, on one hand, neutrinos are predicted as massless as a result of a minimal renormalizable theory; on the other hand, the renormalizable theory, i.e. the SM in this case, one can write down from that also obeys the following accidental global symmetry

$$U^{\mathrm{Global}}_{\mathrm{SM}} = U(1)_B \otimes U(1)_e \otimes U(1)_\mu \otimes U(1)_\tau, \tag{2.34}$$

where $U(1)_B$ is the baryon number symmetry and $U(1)_{e,\mu,\tau}$ are the three lepton flavor symmetries. Since this accidental global symmetry is respected by the SM, neutrinos are precisely massless in the SM, meaning that neutrino masses cannot receive any

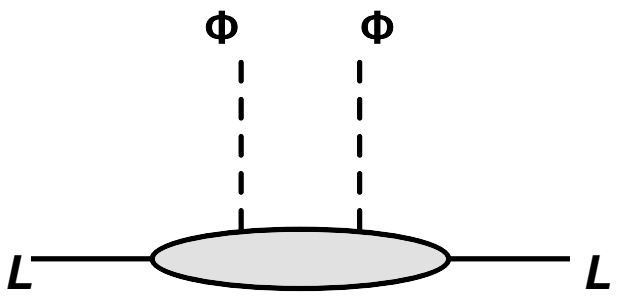

Figure 2.1: Feynman diagram for the dimension-5 Weinberg operator in Eq. (2.35), where L is the left-handed lepton doublet and Φ the Higgs doublet. The grey blob corresponds to the heavy new physics at scale Λ that has been integrated out.

loop corrections or non-perturbative corrections. As a consequence, there is no lepton mixing or CPV in the lepton sector of SM.

However, we now know that this is not the case since neutrino oscillation has been observed and the PMNS matrix that describes the mixing of the leptons has been measured with a high precision as will be discussed shortly below. Furthermore, in Chapter 3, we will discuss how this accidental symmetry is broken at high temperature when we discuss EWBG. Giving up the accidental lepton number conservation, neutrinos mass explanation with the SM fields only was first proposed by Steven Weinberg in 1979 [248]. In his famous paper, Weinberg proposed a dimension-5 operator, the now known "Weinberg operator", to explain the tiny neutrino masses. The operator can be written as [248]

$$\mathcal{L}^{(5)}_{\rm SM} = \frac{c_{\alpha\beta}}{\Lambda}(\overline{L^c_\alpha}\tilde{\Phi}^*)(\tilde{\Phi}^\dagger L_\beta) + h.c., \tag{2.35}$$

where the superscript "$^{(5)}$" represents the dimension of the operator, (α, β) the lepton flavor indices, $\tilde{\Phi} = i\sigma^2\Phi^*$ and Φ the Higgs doublet field, T the transposition transformation, c the charge conjugation, $c_{\alpha\beta}$ the Wilson coefficients and $\Lambda \gg v_\Phi$ the scale where new physics lives. It turns out there is only one dimension-5 operator one can construct from the SM particle content, that is why we use the "=" sign above. The

Feynman diagram corresponding to this operator is shown in Figure 2.1, where the gray blob represents the vertex of new physics that has been integrated out.

Now after electroweak spontaneous symmetry breaking when the Higgs doublet Φ obtains a non-zero vev, neutrino masses can be generated in the following form from the Weinberg operator:

$$\mathcal{L}^{(5)}_{\rm SM} = \frac{c_{\alpha\beta} v_\Phi^2}{\Lambda} (\overline{\nu^c_{L,\alpha}} \nu_{L,\beta}) + h.c.\,. \tag{2.36}$$

Obviously, the neutrinos here are of Majorana type, and furthermore, the lepton number is violated by two units:

$$\overline{\nu^c_{L,\alpha}} \nu_{L,\beta} \xrightarrow[\text{transformation}]{\text{Under } U(1)_L} \overline{\nu'^c_{L,\alpha}} \nu'_{L,\beta} = e^{i(2Q_L)\varphi} \overline{\nu^c_{L,\alpha}} \nu_{L,\beta}, \quad \text{with } \nu'_{L,\beta} = e^{iQ_L\varphi} \nu_{L,\beta}. \tag{2.37}$$

The absolute neutrino masses are unknown yet and now we only know the sum of neutrino masses satisfy $\sum_j m_j \lesssim 0.12\,\text{eV}$ [249]. Sum of neutrino masses will also be reviewed in more detail below. Now to estimate the scale of new physics Λ, one can plug $m_\nu = 0.1\,\text{eV}$ into Eq. (2.36) and find,

$$\Lambda \simeq 6.06 \times 10^{14} \times \left(\frac{c_{\alpha\beta}}{1}\right)\,\text{GeV}, \tag{2.38}$$

i.e. way above the weak scale and several orders of magnitude below the Planck scale. Therefore, as long as the Wilson coefficients $c_{\alpha\beta}$ is of $\mathcal{O}(1)$, the new physics will be at a too high scale to be explored at, for example, colliders. However, as we will see shortly, in some cases, for example, the type-II seesaw mechanism, the scale of new physics can be at the same order as weak scale or at the TeV scale such that it is accessible at colliders.

Now looking back at Figure 2.1, the natural question one can ask is what is the new physics that is responsible for neutrino masses? Or, what can the gray blob be?

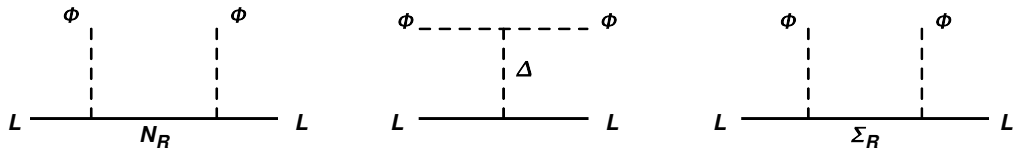

Figure 2.2: Feynman diagram for the type-I (left), type-II (middle) and type-III (right) seesaw mechanisms, where L is the left-handed lepton doublet, Φ the Higgs doublet, N_R the right-handed SU(2) singlet, Δ the $\mathrm{SU(2)_L}$ complex triplet and Σ_R the $\mathrm{SU(2)_L}$ triplet fermion. We generically assume that the masses $M_{N_R,\Delta,\Sigma_R} \gg v_\Phi$ such that at the weak scale one obtains the Weinberg operator in Eq. (2.35) after integrating out these heavy degrees of freedoms with $\Lambda \sim M_{N_R,\Delta,\Sigma_R}$.

It turns out that there are only three ways to generate the dimension-5 operator above at tree level, known as type-I, type-II and type-III seesaw mechanisms [58–75], with an $\mathrm{SU(2)_L}$ singlet fermion, a complex triplet and a triplet fermion respectively. We show the corresponding Feynman diagrams in Figure 2.2 respectively and will briefly review each of these three mechanisms in the next three subsections.

2.4.1 Type-I seesaw mechanism

The type-I seesaw mechanism is obtained by extending the SM with a singlet heavy right-handed Majorana neutrino N_R. Based on these assumptions, we can write down the Lagrangian as

$$\mathcal{L}_{\mathrm{type-I}} = \mathcal{L}_{\mathrm{SM}} + \mathcal{L}_{N_R}, \tag{2.39}$$

where the Lagrangian for N_R is

$$\mathcal{L}_{N_R} = i\overline{N_R}\not{\partial}N_R + \overline{L}\tilde{\Phi}Y_N N_R + \overline{N_R}Y_N^\dagger\tilde{\Phi}^\dagger L + \frac{1}{2}\overline{N_R}M_N N_R^c + \frac{1}{2}\overline{N_R^c}M_N^\dagger N_R, \tag{2.40}$$

where the lepton flavor indices for L and N_R have been suppressed above, and it should be understood that y_N and M_N are 3×3 complex matrices in general.

As just discussed above, the masses of N_R are much larger than the weak scale, i.e. $M_N \gg v_\Phi$, so one can integrate out N_R, for example Ref. [0210271], and obtain the following dimension-5 operator for SM neutrinos

$$\mathcal{L}^{(5)}_{\text{type}-\text{I}} \supset (\overline{L^c_\alpha}\tilde{\Phi}^*)\left(Y^*_N \frac{1}{2M_N} Y^\dagger_N\right)(\tilde{\Phi}^\dagger L_\beta) + h.c.\,. \tag{2.41}$$

Then after electroweak spontaneous symmetry breaking when the Higgs develops a vev, the neutrino masses can be expressed as

$$m_\nu = Y^*_N \frac{v^2_\Phi}{4M_N} Y^\dagger_N. \tag{2.42}$$

Taking $m_\nu = 0.01\,\text{eV}$ and $v_\Phi = 246\,\text{GeV}$, the scale for new physics in type-I seesaw is around

$$M_N \sim 1.5 \times 10^{15} \times \left(\frac{Y^*_N}{1}\right)\left(\frac{Y^\dagger_N}{1}\right)\,\text{GeV}. \tag{2.43}$$

Note that when the Yukawa couplings Y_N are of $\mathcal{O}(1)$, the right-handed neutrino is about $10^{15}\,\text{GeV}$, which is way above the reachability of current or future experiments.

2.4.2 Type-II seesaw mechanism

The second seesaw mechanism is the type-II one, where one introduces an SU(2)_L triplet with hypercharge $Y_\Delta = 2$. In its SU(2)_L representation, the complex triplet can be written as

$$\Delta = \begin{pmatrix} \frac{\Delta^+}{\sqrt{2}} & \Delta^{++} \\ \Delta^0 & -\frac{\Delta^+}{\sqrt{2}} \end{pmatrix}, \tag{2.44}$$

where the superscripts of Δ indicate the number of electric charges $Q = T_3 + \frac{Y_\Delta}{2}$ the triplet components carries. We will save our detailed discussion on the complex

triplet model to Chapter 6 and only focus on Lagrangian terms that are responsible for neutrino mass generation below:

$$\mathcal{L}_{\text{type-II}}^{\text{m}_\nu-\text{related}} = \mathcal{L}_{\text{SM}} + \mathcal{L}_{\Delta}, \tag{2.45}$$

with

$$\mathcal{L}_{\Delta} \supset \overline{L^c} Y_{\Delta\nu} i\tau_2 \Delta L + \mu \Phi^T i\tau_2 \Delta^\dagger \Phi + h.c., \tag{2.46}$$

where $Y_{\Delta\nu}$ is the Yukawa coupling which is in general a 3 complex matrix, Φ the Higgs doublet again, $\tau_2 = \sigma^2/2$ with σ^2 the second Pauli matrix and μ is a dimension-one parameter. Again, we have suppressed neutrino flavor indices above.

Similarly, after integrating out the heavy components of Δ, a dimension-5 operator responsible for neutrino mass generation can be obtained:

$$\mathcal{L}_{\text{type-II}}^{(5)} \supset (\overline{L_\alpha^c} \tilde{\Phi}^*) \left(2Y_{\Delta\nu} \frac{\mu}{M_\Delta^2} \right) (\tilde{\Phi}^\dagger L_\beta) + h.c.\,. \tag{2.47}$$

Then after electroweak spontaneous symmetry breaking, the neutrino masses can be written as

$$m_\nu = Y_{\Delta\nu} \frac{\mu \cdot v_\Phi^2}{M_\Delta^2}. \tag{2.48}$$

Plug in the numbers, we obtain

$$M_\Delta \sim 8 \times 10^7 \times \sqrt{\left(\frac{Y_{\Delta\nu}}{1} \right) \times \left(\frac{\mu}{\text{GeV}} \right)}\, \text{GeV}. \tag{2.49}$$

As will become clear in Chapter 6 where a complex triplet Higgs is introduced, the neutrino masses can also be expressed as $m_\nu = Y_{\Delta\nu} v_\Delta$ with v_Δ the vev of the complex

triplet Higgs field. Then v_Δ at the GeV scale would correspond to $Y_{\Delta\nu}$ of $\mathcal{O}(10^{-10})$ for $m_\nu \sim 0.1\,\text{eV}$. Eq.(2.49) would then imply $M_\Delta \sim \mathcal{O}(100)\,\text{GeV}$ for $\mu \sim \mathcal{O}(1)\,\text{GeV}$, making the complex triplet in the type-II seesaw promising to be tested at current and future colliders. In Chapter 6, we present our detailed study on this scenario.

2.4.3 Type-III seesaw mechanism

One obtains the type-III seesaw model by extending the SM with an additional SU(2)_L fermionic triplet $\vec{\Sigma} = (\Sigma^1, \Sigma^2, \Sigma^3)$ with its hypercharge $Y_{\vec{\Sigma}} = 0$. Its Majorana mass term can be written as [250]

$$\mathcal{L} = i\overline{\vec{\Sigma}_R}\not{D}\vec{\Sigma}_R - \left[\frac{1}{2}\overline{\vec{\Sigma}_R}M_\Sigma\vec{\Sigma}_R^c + \overline{\vec{\Sigma}_R}Y_{\Sigma\nu}\left(\tilde{\Phi}^\dagger\vec{\tau}L\right) + h.c.\right], \tag{2.50}$$

with M_Σ the mass of the fermionic triplet and $M_\Sigma \gg v_\Phi$, $\vec{\tau} = \vec{\sigma}/2$ and $\vec{\sigma}$ the Pauli matrices and $Y_{\Sigma\nu}$ the Yukawa coupling of $\vec{\Sigma}$.

After integrating out the heavy fermionic triplet, one obtains the following dimension-five operator

$$\mathcal{L}^{(5)}_{\text{type}-\text{III}} \supset (\overline{L^c_\alpha}\tilde{\Phi}^*)\left(2Y^T_{\Sigma\nu}\frac{1}{M_\Sigma}Y_{\Sigma\nu}\right)(\tilde{\Phi}^\dagger L_\beta) + h.c.\,, \tag{2.51}$$

and the neutrino masses from this mechanism after electroweak spontaneous symmetry breaking is

$$m_\nu = Y^T_{\Sigma\nu}\frac{v^2_\Phi}{M_\Sigma}Y_{\Sigma\nu}. \tag{2.52}$$

Plug in the representative numbers, we find

$$M_\Sigma \sim 6\times 10^{15}\times\left(\frac{Y^T_{\Sigma\nu}}{1}\right)\times\left(\frac{Y_{\Sigma\nu}}{1}\right)\,\text{GeV}. \tag{2.53}$$

Similar to the type-I seesaw scenario, the mass scale of the fermionic triplet makes it difficult to be tested at current and/or future colliders.

2.5 Neutrino mass hierarchies and PMNS matrix measurements

The neutrino masses are, however, not measured directly yet. In practice, neutrino oscillations are used as a method to measure the mass, or more precisely the mass squared difference among different flavor of neutrinos since neutrino oscillations are only sensitive to the mass squared difference. In this section, we will summarize the current status of the measurements of neutrino masses from oscillation experiments.

For neutrino oscillation experiments, since the Majorana phases in the PMNS matrix will not play a role [251, 252] as will become clear shortly below, in practice, one can use Eq. (2.24) and Eq. (2.25) for the oscillation-related calculations. Since the oscillation is a result of the mixing, we review the standard calculation below.

Due to the mixing from the PMNS matrix, the time evolution of neutrino mass eigenstate $|\nu_j\rangle$ can be calculated as follows. Suppose a neutrino of flavor α is produced at t_i, due to the PMNS mixing, we can write it as a superposition of the mass eigenstates as follows:

$$|\nu_j(t_i)\rangle = \sum_i (U_{\rm PMNS})^*_{\alpha i} |\nu_i(\vec{p})\rangle \ , \tag{2.54}$$

where $\vec{p}$ is the three-momenta of the neutrinos in the mass eigenstates. Since the mass eigenstates are eigenstates of the free Hamiltonian $\mathcal{H}$, one can write

$$\hat{\mathcal{H}} |\nu_i(\vec{p})\rangle = E_i(\vec{p}) |\nu_i(\vec{p})\rangle \ , \quad \text{with} \ \ E_i(\vec{p}) = \vec{p}^2 + m_i^2. \tag{2.55}$$

At a later time t_f, the initial state evolves to

$$|\nu_j(t_f)\rangle = e^{-i\hat{\mathcal{H}}(t_f - t_i)} |\nu_j(t_i)\rangle = \sum_i (U_{\rm PMNS})^*_{\alpha i} e^{-iE_i(\vec{p})(t_f - t_i)} |\nu_j(\vec{p})\rangle \ , \tag{2.56}$$

and the probability for a neutrino in flavor β at t_f can be obtained as

$$P(\nu_\alpha \to \nu_\beta) = |\langle \nu_\beta | \nu_\alpha \rangle|^2 = \left| \sum_i (U_{\rm PMNS})_{\beta i} (U_{\rm PMNS})^*_{\alpha i} e^{-iE_i(\vec{p})(t_f - t_i)} \right|^2 . \tag{2.57}$$

For ultra-relativistic neutrinos, we can approximate neutrino energy with $E_i(\vec{p}) \approx m_i^2/(2|\vec{p}|) + \mathcal{O}(m_i^4)$, leading to

$$P(\nu_\alpha \to \nu_\beta) = \sum_{i,j} (U_{\rm PMNS})^*_{\alpha i} (U_{\rm PMNS})_{\beta i} (U_{\rm PMNS})_{\alpha j} (U_{\rm PMNS})^*_{\beta j} e^{-\frac{i\Delta m^2_{ji} L}{2|\vec{p}|}}, \tag{2.58}$$

with $\Delta m_{ij} \equiv m_i^2 - m_j^2$ the mass square difference of neutrinos and $L \simeq t_f - t_i$ the total distance the neutrino travels during this time period. Using the unitarity of the PMNS matrix and defining $U_{\alpha\beta ij} \equiv (U_{\rm PMNS})_{\alpha i} (U_{\rm PMNS})_{\beta j} (U_{\rm PMNS})^*_{\alpha j} (U_{\rm PMNS})^*_{\beta i}$, one finally has

$$P(\bar{\nu}_\alpha \to \bar{\nu}_\beta) = \delta_{\alpha\beta} - 4 \sum_{j>i} {\rm Re}\left[U_{\alpha\beta ij}\right] \sin^2\left(\frac{\Delta m^2_{ij} L}{4E_\nu}\right) \mp 2 \sum_{j>i} {\rm Im}\left[U_{\alpha\beta ij}\right] \sin\left(\frac{\Delta m^2_{ij} L}{2E_\nu}\right), \tag{2.59}$$

where the "+" ("−") sign corresponds to neutrinos (antineutrinos) and $|\vec{p}| \simeq E_\nu$ has been applied. From the expression above, non-vanishing mass squared differences are essential for neutrino oscillations between different flavors. Note that, from our definition of $U_{\alpha\beta ij}$, the Majorana phases will cancel and not enter our calculation of the oscillation probability, that is why we can ignore the Majorana phases for our calculation.

It is worthy pointing out that derivation above only holds in the case where neutrinos propagate in vacuum. If neutrinos, however, propagate in some dense medium as is the case for solar neutrinos, then the matter effect needs to be included [253]. A discussion on the matter effect is beyond the scope of this thesis, and we refer to Ref. [253] for more discussion.

Experiment	Dominant	Important
Solar Experiments	θ_{12}	$\Delta m^2_{21}, \theta_{13}$
Reactor LBL (KamLAND)	Δm^2_{21}	θ_{12}, θ_{13}
Reactor MBL (Daya-Bay, Reno, D-Chooz)	$\theta_{13}, \left\|\Delta m^2_{31,32}\right\|$	
Atmospheric Experiments (SK, IC-DC)		$\theta_{23}, \left\|\Delta m^2_{31,32}\right\|, \theta_{13}, \delta$
Accel LBL $\nu_\mu, \bar{\nu}_\mu$, Disapp (K2K, MINOS, T2K, NOνA)	$\left\|\Delta m^2_{31,32}\right\|, \theta_{23}$	
Accel LBL $\nu_e, \bar{\nu}_e$ App (MINOS, T2K, NOνA)	δ	θ_{13}, θ_{23}

Table 2.1: Experiments contribute to the determination of oscillation parameters. Table adopted from Ref. [1].

Due to the nature of neutrinos oscillation, it is not possible to determine the absolute values of neutrino masses since the oscillation probability only depends on the mass squared differences. Due to this degeneracy, there are two conventions commonly referred to as the Normal Ordering (NO) with $m_1 < m_2 < m_3$ and the Inverted Ordering (IO) with $m_3 < m_1 < m_2$ in literatures. Experimental, it is observed that, in the SM, the mass differences satisfy $\Delta m^2_{21} \ll |\Delta m^2_{31}| \simeq |\Delta m^2_{32}|$. Note that as a result of this condition, Δm^2_{21} will always be the smallest mass splitting, $\Delta m^2_{31} = \Delta m^2_{32} + \Delta m^2_{21}$ is the largest mass splitting in NO and Δm^2_{32} is always the largest mass splitting in IO up to a sign.

To measure the mass squared difference, many oscillation experiments have been under active operation which are summarize them in Table 2.1. Due to the different focus of each experiment, a global analysis of the data from all these experiments is needed and has been performed by several groups. The results are shown in Table 2.2, from which one can conclude that

1. Due to the difference on $\sin^2\theta_{13}$ between Ref. [2] and other global fit, inclusion of the Super-Kamiokande in Table 2.2 is done by the PDG group through adding the χ^2 tabulated χ^2 map provided by Super-Kamiokande [1].

2. The best fit is for the NO and IO is disfavored by 2σ from long-baseline accelerator and short-baseline reactor data. The IO is disfavored by 3σ when data from Ref. [2] is included.

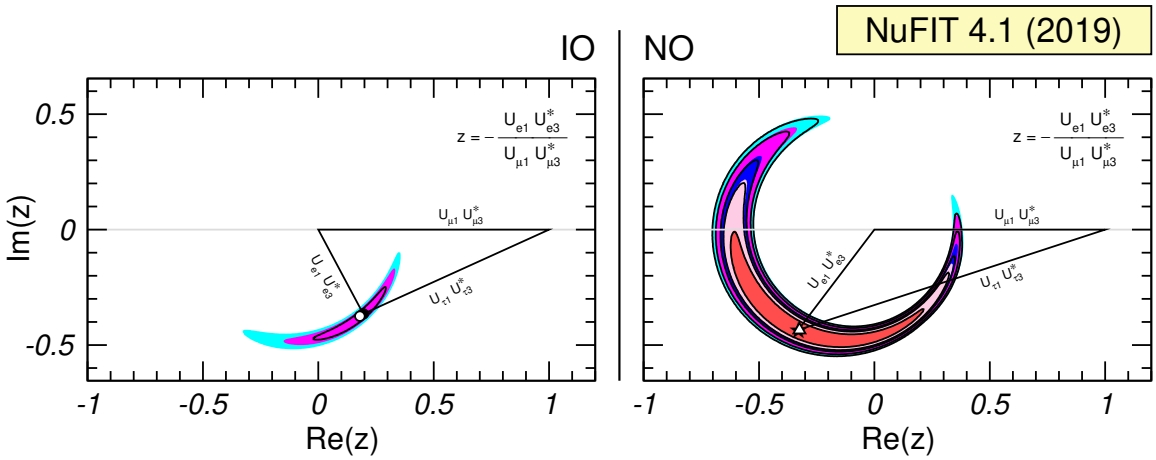

Figure 2.3: Leptonic unitarity triangle from the first row and third column of the PMNS matrix. Result is obtained from the `NuFIT` group. Plot adopted from [11].

3. θ_{23} in the second octant is preferred with a statistical significance below 3σ currently.

4. The best fit of the Dirac CP phase in the PMNS matrix is $\delta \sim 120^\circ$ in NO, implying CP conservation, i.e. $\delta = 180^\circ$ is still allowed at a 1-2σ CL. On the other hand, CP conservation is excluded at 3σ CL in IO. Using the global fitting results in Table 2.2, the Jarlskog invariant defined in Eq. (2.33) can be calculated. Defining further, in the standard parameterization,

$$J_{\rm Dirac} = {\rm Im}(U_{\alpha i} U_{\beta j} U^*_{\alpha j} U^*_{\beta i}) \equiv J^{\rm max}_{\rm CP} \sin\delta, \tag{2.60}$$

one find

$$J^{\rm max}_{\rm CP} = 0.3359 \pm 0.0006 (\pm 0.0019) \ \ [11, 254], \tag{2.61}$$

at 1σ (3σ) for both NO and IO, implying a non-zero best fit value for δ with

$$J^{\rm best}_{\rm CP} = -0.019 \ \ [1]. \tag{2.62}$$

5. From the global fitting results in Table 2.2, the scaled unitarity triangles corresponding to Eq. (2.28) discussed in section 2.3.2 are shown in Figure 2.3, where the left and right plots correspond to the IO and the NO respectively. Allowed regions for the third vertex below the $\mathrm{Im}(z)$ axis are shown at 1σ, 2σ and 3σ CL. Colored regions (black contour curves) are obtained without (with) the inclusion of the tabulated SM-ATM χ^2 data. Again, as can be seen from the left plot, CP conservation is excluded at 3σ for the IO.

6. the neutrino mass spectrum can be further classified depending on the value of the lightest neutrino mass:

   - Normal hierarchical spectrum (NH) with $m_1 \ll m_2 < m_3$. Then from Table 2.2, one finds

   $$m_2 \simeq \sqrt{\Delta m^2_{21}} \simeq 8.6 \times 10^{-3}\,\mathrm{eV}, \quad m_3 \simeq \sqrt{\Delta m^2_{32} + \Delta m^2_{21}} \simeq 0.0506\,\mathrm{eV}. \tag{2.63}$$

   - Inverted hierarchical spectrum (IH) with $m_3 \ll m_1 < m_2$. Then from Table 2.2, one finds

   $$m_1 \simeq \sqrt{|\Delta m^2_{32} + \Delta m^2_{21}|} \simeq 0.0497\,\mathrm{eV}, \quad m_2 \simeq \sqrt{|\Delta m^2_{32}|} \simeq 0.0504\,\mathrm{eV}. \tag{2.64}$$

   - Quasidegenerate spectrum (QD) with $m_1 \simeq m_2 \simeq m_3 \simeq m_0 \gg \sqrt{\left|\Delta m^2_{31(32)}\right|}$, with

   $$m_0 \geq 0.10\,\mathrm{eV}. \tag{2.65}$$

All existing constraints are consistent with the NH, IH and QD mass spectra discussed in the last bullet above. To find the absolute scale of neutrino masses,

	w/o SK-ATM [11]		w/ SK-ATM [11]		w/ SK-ATM [254]		w/ SK-ATM [255]	
NO	best fitting ordering		best fitting ordering		best fitting ordering		best fitting ordering	
Param.	$\pm 1\sigma$	3σ range	$\pm 1\sigma$	3σ range	$\pm 1\sigma$	3σ range	$\pm 1\sigma$	3σ range
$\frac{\sin^2\theta_{12}}{10}$	$3.10^{+0.13}_{-0.12}$	$2.75 \to 3.50$	$3.10^{+0.13}_{-0.12}$	$2.75 \to 3.50$	$3.04^{+0.14}_{-0.13}$	$2.65 \to 3.46$	$3.20^{+0.20}_{-0.16}$	$2.73 \to 3.79$
$\frac{\sin^2\theta_{12}}{10}$	$5.58^{+0.20}_{-0.33}$	$4.27 \to 6.09$	$5.63^{+0.18}_{-0.24}$	$4.33 \to 6.09$	$5.51^{+0.19}_{-0.80}$	$4.30 \to 6.02$	$5.47^{+0.20}_{-0.30}$	$4.45 \to 5.99$
$\frac{\sin^2\theta_{12}}{10^2}$	$2.241^{+0.066}_{-0.065}$	$2.046 \to 2.440$	$2.237^{+0.066}_{-0.065}$	$2.044 \to 2.435$	$2.14^{+0.09}_{-0.07}$	$1.90 \to 2.39$	$2.160^{+0.083}_{-0.069}$	$1.96 \to 2.41$
$\delta[^\circ]$	222^{+38}_{-28}	$141 \to 370$	221^{+39}_{-28}	$144 \to 357$	238^{+41}_{-33}	$149 \to 358$	218^{+38}_{-27}	$157 \to 349$
$\frac{\Delta m^2_{21}}{[10^{-5}\ \mathrm{eV}^2]}$	$7.39^{+0.21}_{-0.20}$	$6.79 \to 8.01$	$7.39^{+0.21}_{-0.20}$	$6.79 \to 8.01$	$7.34^{+0.17}_{-0.14}$	$6.92 \to 7.91$	$7.55^{+0.20}_{-0.16}$	$7.05 \to 8.24$
$\frac{\Delta m^2_{32}}{[10^{-3}\ \mathrm{eV}^2]}$	$2.449^{+0.032}_{-0.030}$	$2.358 \to 2.544$	$2.454^{+0.029}_{-0.031}$	$2.362 \to 2.544$	$2.419^{+0.035}_{-0.032}$	$2.319 \to 2.521$	2.424 ± 0.03	$2.334 \to 2.524$
IO	$\Delta\chi^2 = 6.2$		$\Delta\chi^2 = 10.4$		$\Delta\chi^2 = 9.5$		$\Delta\chi^2 = 11.7$	
$\frac{\sin^2\theta_{12}}{10}$	$3.10^{+0.13}_{-0.12}$	$2.75 \to 3.50$	$3.10^{+0.13}_{-0.12}$	$2.75 \to 3.50$	$3.03^{+0.14}_{-0.13}$	$2.64 \to 3.45$	$3.20^{+0.20}_{-0.16}$	$2.73 \to 3.79$
$\frac{\sin^2\theta_{12}}{10}$	$5.63^{+0.19}_{-0.26}$	$4.30 \to 6.12$	$5.65^{+0.17}_{-0.22}$	$4.36 \to 6.10$	$5.57^{+0.17}_{-0.24}$	$4.44 \to 6.03$	$5.51^{+0.18}_{-0.30}$	$4.53 \to 5.98$
$\frac{\sin^2\theta_{12}}{10^2}$	$2.261^{+0.067}_{-0.064}$	$2.066 \to 2.461$	$2.259^{+0.065}_{-0.065}$	$2.064 \to 2.457$	$2.18^{+0.08}_{-0.07}$	$1.95 \to 2.43$	$2.220^{+0.074}_{-0.076}$	$1.99 \to 2.44$
$\delta[^\circ]$	285^{+24}_{-26}	$205 \to 354$	282^{+23}_{-25}	$205 \to 348$	247^{+26}_{-27}	$193 \to 346$	281^{+23}_{-27}	$202 \to 349$
$\frac{\Delta m^2_{21}}{[10^{-5}\ \mathrm{eV}^2]}$	$7.39^{+0.21}_{-0.20}$	$6.79 \to 8.01$	$7.39^{+0.21}_{-0.20}$	$6.79 \to 8.01$	$7.34^{+0.17}_{-0.14}$	$6.92 \to 7.91$	$7.55^{+0.20}_{-0.16}$	$7.05 \to 8.24$
$\frac{\Delta m^2_{32}}{[10^{-3}\ \mathrm{eV}^2]}$	$-2.509^{+0.032}_{-0.032}$	$-2.603 \to -2.416$	$-2.510^{+0.030}_{-0.031}$	$-2.601 \to -2.419$	$-2.478^{+0.035}_{-0.033}$	$-2.577 \to -2.375$	$-2.50\pm^{+0.04}_{-0.03}$	$-2.59 \to -2.39$

Table 2.2: Global fitting to the PMNS matrix form oscillation experiments in the 3ν paradigm The SK-ATM columns represent the inclusion or exclusion of the atmospheric neutrinos from Super-Kamiokande in Ref. [2]. Table adapted from Ref. [1].

historically, the spectrum of electrons near the end point in ^{3}H β-decay, i.e. $^3H \to ^3He + e^- + \overline{\nu}_e$, was used [256–260]. Currently, the most stringent upper bounds on $m_{\overline{\nu}_e}$ is obtained in the Troitzk experiment [257, 260], giving

$$m_{\overline{\nu}_e} < 2.05\,\text{eV} \quad \text{at } 95\% \text{ CL.} \tag{2.66}$$

Similar result was obtained at Mainz [258],

$$m_{\overline{\nu}_e} < 2.3\,\text{eV} \quad \text{at } 95\% \text{ CL.} \tag{2.67}$$

In the near future, the KATRIN experiment [259] would be able to reach the $m_{\overline{\nu}_e} \simeq 0.20\,\text{eV}$ regime, making it possible to probe the region of the QD spectrum.

2.5.1 Sum of neutrino masses: $\sum_j m_j$

On the other hand, the neutrino masses can also be constrained from cosmological and astrophysical data. To see how this works, we first review the theoretical background below.

In the early Universe, neutrinos, photons, electrons and positrons are in thermal equilibrium with a common temperature. However, as the Universe expands and cools down, neutrinos will decouple from the rest of the plasma when the temperature of the Universe is around $T_{\text{dec}} \sim 2\,\text{MeV}$. Historically, the neutrinos were considered to decouple from the rest of the plasma instantaneously, resulting a number of $N_{\text{eff}} = 3$ in the SM, where N_{eff} is the effective number of neutrino species. However, it was soon realized that since T_{dec} is very close to electron mass, residual out-of-equilibrium electron-positron annihilating into neutrinos could heat up the neutrinos, and neutrino oscillation prior to the decoupling could also alter N_{eff}. A tremendous work has been done on this topic, but it is beyond the brief review here for this thesis. We refer to Ref. [1] and references therein for the reviews.

In either case, the neutrino energy density can be formulated as

$$\frac{\rho_\nu}{\rho_\gamma} = \frac{7}{8} N_{\rm eff} \left(\frac{4}{11}\right)^{\frac{4}{3}}, \tag{2.68}$$

where $N_{\rm eff} = 3$ would correspond to the instantaneous decoupling case and any deviation of $N_{\rm eff}$ from 3 would correspond to effects from non-instantaneous decoupling discussed above, and the most recent analysis from Ref. [261] gives $N_{\rm eff} = 3.045$.

The current temperature of the neutrinos T_ν^0 is found to be $T_\nu^0 \simeq 1.7 \times 10^{-4}\,{\rm eV}$ [1], which is smaller than at least two of the neutrino masses from the mass squared difference discussion above. Assuming all neutrinos being non-relativistic, the total neutrino energy density can be written as

$$\rho_\nu \simeq \sum_j m_j n_j = \left(\sum_j m_j\right) n_\nu, \tag{2.69}$$

where we have used the fact that all three flavor neutrinos have the same number density denoted as n_ν to arrive at the last step. We comment that it is possible that the lightest neutrino could still remain relativistic today such that the above formula would be slightly incorrect. But since the total energy density is always dominated by non-relativistic neutrinos, the error from using the above formula shall be negligible.

In units of the critical density $\rho_{\rm crit}^0$ today, the total neutrino energy density today is

$$\Omega_\nu \equiv \frac{\rho_\nu^0}{\rho_{\rm crit}^0} = \frac{\left(\sum_j m_j\right)}{\rho_{\rm crit}^0} \times \left(\frac{n_\nu^0}{n_\gamma^0}\right) \times n_\gamma^0, \tag{2.70}$$

where the superscript "0" always indicates the current value of the corresponding variable. Since n_γ^0 is known precisely from the measurement of the CMB temperature

and n_ν^0/n_γ^0 can be obtained from precision neutrino decoupling studies, the above relation can finally be written as

$$\Omega_\nu = \frac{1}{93.14h^2} \times \left(\frac{\sum_j m_j}{\text{eV}} \right), \tag{2.71}$$

where h is the Hubble constant in units of $100\,\text{km}/(\text{s Mpc})$. Therefore, through precision measurements on the Ω_ν parameter, constraints on the sum of neutrino masses can be obtained.

Experimentally, constraints on Ω_ν can be obtained from measuring the matter density, and much stronger constraints can be obtained from a combined analysis of CMB, the amplitude of density fluctuations on smaller scales, BAO and the Hubble parameter. For example, with the CMB data from the WMAP and the Planck experiments, the sum of neutrino masses is constrained to be [262]

$$\sum_j m_j \lesssim (0.3 - 1.3)\,\text{eV} \quad \text{at } 95\%\ \text{CL.} \tag{2.72}$$

This constraint is improved by using the CMB temperature power spectrum anisotropies, polarization, gravitational lensing effects, low l CMB polarization spectrum data and assuming three light massive neutrinos and the ΛCDM model, which gives [263, 264]

$$\sum_j m_j \lesssim (0.340 - 0.715)\,\text{eV} \quad \text{at } 95\%\ \text{CL.} \tag{2.73}$$

Adding data from the BAO, the result is further improved to [264]

$$\sum_j m_j \lesssim 0.170\,\text{eV} \quad \text{at } 95\%\ \text{CL.} \tag{2.74}$$

2.6 Nature of massive neutrinos from neutrinoless double beta decay ($0\nu\beta\beta$)

Neutrino oscillations are not dependent on the Majorana phases as discussed above, as a consequence, the Dirac or Majorana nature of massive neutrinos can not be determined from oscillation experiments [251, 252]. However, determining the Dirac or Majorana nature of massive neutrinos is of fundamental importance, and the reason will become clear in the following discussion.

Extensive studies have now shown that $0\nu\beta\beta$ is perhaps the most sensitive probe to the Majorana nature of massive neutrinos [265–268]. Observation of $0\nu\beta\beta$ and the measurement of the corresponding half-life with sufficient accuracy would lead to a rich harvest: (1) proof of lepton number violation, (2) the type of neutrino mass spectrum [269], (3) Majorana phases in the PMNS matrix [270–272], (4) and the absolute scale of neutrino masses [267–270, 273–285].

The measured quantity in $0\nu\beta\beta$ is the effective Majorana mass denoted by $< m >$ here. Assuming that there are only three massive neutrinos of Majorana type and $0\nu\beta\beta$ are only generated by the (V-A) type charge current weak interactions, the $0\nu\beta\beta$ decay amplitude can be written as [268, 286]

$$A(0\nu\beta\beta) \cong G_F^2 < m > M(A, Z), \tag{2.75}$$

where $M(A, Z)$ is the corresponding nuclear matrix element that does not depend on the neutrino mixing parameters and

$$\begin{aligned} | < m > | &= \left| m_1 U_{\mathrm{e}1}^2 + m_2 U_{\mathrm{e}2}^2 + m_3 U_{\mathrm{e}3}^2 \right| \\ &= \left| \left(m_1 c_{12}^2 + m_2 s_{12}^2 e^{i\alpha_2} \right) c_{13}^2 + m_3 s_{13}^2 e^{i(\alpha_3 - 2\delta)} \right|, \end{aligned} \tag{2.76}$$

where $\alpha_{2,3}$ and δ_m are the Majorana phases defined by the second matrix in Eq. (2.26).

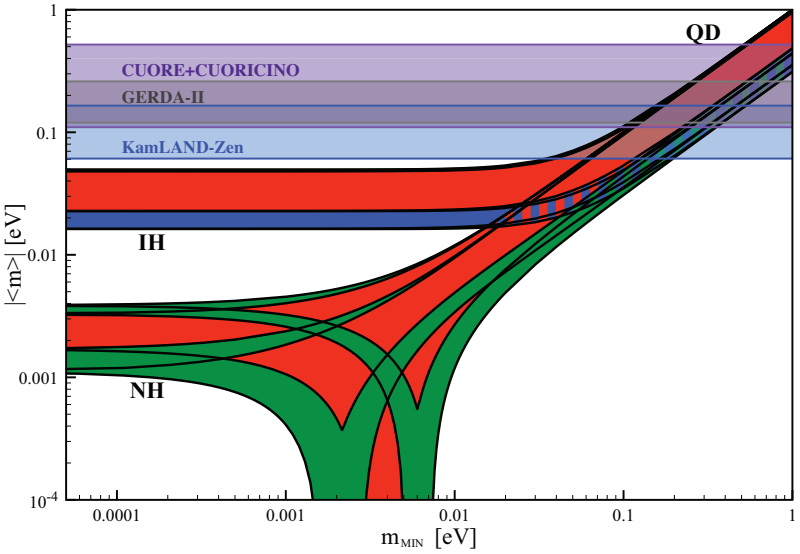

Figure 2.4: Majorana neutrino mass versus the lightest neutrino mass upon assumptions discussed in the main text. Plot adopted from [1].

Note that $m_{1,2,3}$ can be written in terms of Δm^2_{jk} and, e.g. $\min(m_j)$, $< m >$ is actually a function of the lightest neutrino mass $\min(m_j)$ and can be expressed as, assuming CP conservation [267–270, 273–285],

$$| < m > | \cong \left| \sqrt{\Delta m^2_{21}} s^2_{12} c^2_{13} + \sqrt{\Delta m^2_{31}} s^2_{13} e^{i(\alpha_3 - \alpha_2 - 2\delta_m)} \right|, \quad \text{NH} \tag{2.77}$$

$$| < m > | \cong \tilde{m} \left(1 - \sin^2 2\theta_{12} \sin^2 \frac{\alpha_2}{2} \right)^{\frac{1}{2}}, \quad \text{IH(IO) and QD}, \tag{2.78}$$

with $\tilde{m} \equiv \sqrt{\Delta m^2_{23} + m^2_3}$ and $\tilde{m} \equiv m_0$ for IH (IO) and QD spectrum respectively. Then using the 3σ ranges of the allowed values of the neutrino parameters in Table 2.2, the effective Majorana mass as a function of the lightest neutrino mass is plotted in Figure 2.4, where the current best constraints on $< m >$ are from KamLAND-Zen [287] and GERDA-II [288] from $0\nu\beta\beta$ searches using ^{136}Xe and ^{76}Ge respectively. The region for each experiment is a reflection of the estimated uncertainties in the relevant nuclear matrix elements, whose calculation can be found in the review paper [268]. The black lines in Figure 2.4 correspond to different pairs of CP conserving values

of α_2 and $(\alpha_3 - 2\delta_m)$: $(0,0)\,(0,\pi),(\pi,0)$ and (π,π) respectively. The red regions correspond to at least one of α_2 and $(\alpha_3 - 2\delta_m)$ having a CPV value, the blue and green regions correspond to α_2 and $(\alpha_3 - 2\delta_m)$ possessing CP conserving values.

A number of experiments are proposed to explore the $| < m > | \sim (0.01 - 0.05)\,\text{eV}$ regime. For reviews of currently running and future planned $0\nu\beta\beta$ experiments, see Refs. [267, 268, 273] for example. With the sensitivity to $| < m > |$ at $\mathcal{O}(0.01\,\text{eV})$, the experiments would be able to cover the whole range of the parameter space predicted by IO neutrino mass spectrum, and we would also be able to rule out both the IH and the QD spectrum for massive Majorana neutrinos. In the meantime, if neutrino oscillation experiments result in a negative $\Delta m^2_{31(32)}$, one would conclude that the massive neutrinos are either Dirac fermions, or they are Majorana particles that interfere destructively with additional contributions to reduce the amplitude of $0\nu\beta\beta$ decay. On the other hand, if $\Delta m^2_{31(32)} > 0$ is obtained from oscillation experiments, the upper limit $< m >< 0.01\,\text{eV}$ would be compatible with massive Majorana neutrinos possessing NH mass spectrum, or NO spectrum with partial hierarchy and the quest for $< m >$ would remain open [289].

CHAPTER 3

ELECTROWEAK BARYOGENESIS IN THE STANDARD MODEL

3.1 Introduction

From the Planck satellite, the baryon asymmetry, defined below, can be precisely measured. The current value for that asymmetry is $n_B/s = (8.66 \pm 0.04) \times 10^{-11}$ [29]. To explain this non-zero number, three Sakharov conditions [76] need to be satisfied in the early Universe: (1) baryon number violation, (2) C and CPV, and (3) out of thermal equilibrium, or CPT violation.

Based on these conditions, many scenarios have been proposed to explain the baryon asymmetry such as GUTBG, ADBG, leptogenesis, EWBG etc [12, 13, 77–87] mentioned in Introduction. Among them, EWBG has attracted significant attention since on one hand, SM itself already has all the ingredients satisfying the Sakharov conditions through EWBG; on the other hand, EWBG requires new physics to be at the weak scale, making EWBG testable at colliders. However, as we will see in this chapter, the SM fails to generate the observed baryon asymmetry for two reasons: (1) CPV in the SM is too weak, and (2) the SFOEWPT as required by the last Sakharov condition is absent in the SM.

In the following, we first review how the BAU is measured, then we discuss the three Sakharov conditions required to explain this asymmetry. We then discuss why the SM fails to generate the observed asymmetry successfully through EWBG.

3.2 The Baryon asymmetry

The baryon asymmetry Y_B is defined as

$$Y_B \equiv \frac{n_B}{s} = \frac{n_b - n_{\bar{b}}}{s}, \tag{3.1}$$

where $n_{b(\bar{b})}$ is the number density of baryons (anti-baryons) and s is the entropy density. Realizing the fact that $n_\gamma = \zeta_3 g_\gamma T_\gamma^3/\pi^2$ with g_γ the intrinsic degrees of freedom of photons and T_γ the photon temperature that can be precisely measured from CMB, the asymmetry can then be related to n_γ through

$$Y_B = \frac{\eta_B n_\gamma}{s}, \quad \text{with } \eta_B \equiv \frac{n_B}{n_\gamma}, \tag{3.2}$$

where η_B is the baryon-to-photon ratio, which historically was determined through BBN since the abundance of light elements such as ^{3}He, ^{4}He, D, ^{6}Li and ^{7}Li is very sensitive to η_B. On the other hand, η_B is also related to another observable, called the baryon number density $\Omega_B h^2$ by [290]

$$273.66\Omega_{\rm B}h^2 \equiv 10^{10}\eta_B\,(1.0 - 0.0071186Y_p)\left(\frac{\rm G_N}{6.673\times10^{-8}\rm cgs}\right)\left(\frac{T_{\gamma,0}}{2.725\rm K}\right)^3, \tag{3.3}$$

where h is the Hubble constant defined in units of $100\,\mathrm{km/(s\ Mpc)}$, G_N is the gravitational constant, Y_p is the primordial post-BBN mass fraction of baryons in the form of ^{4}He and $T_{\gamma,0}$ is the current temperature of the CMB. Using the most recent data from Planck [29], one obtains

$$Y_B = (8.66 \pm 0.04) \times 10^{-11}, \tag{3.4}$$

implying that the numbers of baryons is slightly larger than that of anti-baryons. Though very tiny, the precise and non-vanishing number however does indicate the

existence of this baryon asymmetry in our Universe, and the question we need to answer is why this asymmetry in our Universe given that our Universe started with the Big Bang without any baryon asymmetry.

In the past days, people also argued that the Universe could also start with the initial condition where the baryon asymmetry did exist at the Big Bang. However, if it were true, inflation after the Big Bang would washout this asymmetry at the end of the inflating epoch. Another postulation is based on the argument that the Universe is baryon-antibaryon symmetric on the large scale, while asymmetry appears at smaller scales. However, this proposal is also refuted since it would lead to an excess of gamma-rays from matter-antimatter annihilation and this kind of excess is not observed yet. Moreover, further study also finds that this scenario would predict less mass inside the Milky Way [291, 292].

In 1967, A. Sakharov [76] came up with three conditions that needs to be realized to generate the asymmetry observed today, which are now called the three Sakharov conditions that will be discussed below.

3.3 The Sakharov conditions

The three Sakharov criteria are, respectively: (1) baryon number violation; (2) C and CP violation (CPV); and (3) out of thermal equilibrium (or CPT violation).

Condition (1) is obvious since it is how baryon number asymmetry can be generated. If baryon number is not violated, any processes in the final state will have exactly the same amount of baryon number as in the initial state, as a result, the net change of baryon number is vanishing and thus no baryon asymmetry could be generated.

However, baryon number violation alone is still not enough. To see that, one can consider a generic decay process that is assumed to violate the baryon number and denoted as $X \to Y + Z$. Suppose now the charge conjugate C is conserved, it

would imply the charged conjugated process $\overline{X} \to \overline{Y} + \overline{Z}$ happens at the same rate as $X \to Y + Z$, meaning

$$\Gamma(X \to Y + Z) = \Gamma(\overline{X} \to \overline{Y} + \overline{Z}). \tag{3.5}$$

Then the net change of the baryon-antibaryon number, which can be expressed as

$$\Delta n_B \propto \Gamma(X \to Y + Z) - \Gamma(\overline{X} \to \overline{Y} + \overline{Z}), \tag{3.6}$$

would vanish and thus no baryon asymmetry could be generated. On the other hand, baryon number violation together with C violation would still not work, and the reason is as follows. When one considers a scenario where a scalar S decays into two left- and right-handed fermions respectively, i.e.

$$S \to f_L f_L, \quad S \to f_R f_R, \tag{3.7}$$

though C violation implies

$$\Gamma(S \to f_{L(R)} f_{L(R)}) \neq \Gamma(\overline{S} \to \overline{f}_{L(R)} \overline{f}_{L(R)}), \tag{3.8}$$

CP conservation however would imply that

$$\Gamma(S \to f_{L(R)} f_{L(R)}) = \Gamma(\overline{S} \to \overline{f}_{R(L)} \overline{f}_{R(L)}), \tag{3.9}$$

which leads to

$$\Gamma(S \to f_L f_L) + \Gamma(S \to f_R f_R) = \Gamma(\overline{S} \to \overline{f}_L \overline{f}_L) + \Gamma(\overline{S} \to \overline{f}_R \overline{f}_R), \tag{3.10}$$

and the net change of baryon-antibaryon number again vanishes.

The last condition besides baryon number violation, C and CP violation, turns out to be out of equilibrium. If the Universe were in thermal equilibrium during its evolution, then any process will happen at the same rate as the inverted one. In this way, any baryon asymmetry generated will be washed out from its inverse process.

Therefore, based on our discussion above, the three Sakharov conditions are necessary for a successful generation of the baryon-antibaryon asymmetry. Based on these three criteria, many scenarios have been proposed to explain the baryon asymmetry and the ability of SM of explaining this asymmetry through EWBG was also studied in the past. However, due to the reasons that will become clear in the next section, SM has now been excluded as the candidate to generate the observed baryon asymmetry through EWBG.

3.4 The Standard Model electroweak baryogenesis

In EWBG, the asymmetry can be produced during electroweak phase transition (EWPT), where the energy scale could be within the reachability of current technologies such as current and future colliders, and it has motivated significant efforts on phenomenologies of many beyond SM models. As will be discussed later, the type-II seesaw complex triplet Higgs model and the real triplet model are two of them, and their phenomenologies will be discussed in detail in Chapter 6 and Chapter 7. But before that, we will first review the how EWBG could be realized in the SM and why SM fails to explain the observed baryon asymmetry through EWBG.

3.4.1 Baryon number violation in the Standard Model

In the SM, the baryon number is violated through the so-called sphaleron process, which actually violates $B + L$ characterized by the transition between degenerated vacua. This process, however, is suppressed at zero temperature, which explains why we have not yet observed any baryon number violating processes directly so far. The-

oretically, the conservation of baryon number is promised by the accidental symmetry we discussed in Chapter 1. However, in 1976, 't Hooft [293] showed that $B + L$ is violated non-perturbatively, whose effect is negligibly small at low temperature but greatly enhanced at high temperature [294].

To be more specific, the baryon number is violated by the triangle anomaly that spoils the conservation of left-handed baryon and lepton currents, leading to

$$\partial_\mu J_B^\mu = i\frac{N_f}{32\pi^2}\left(g_1^2\epsilon_{\alpha\beta\rho\sigma}B^{\alpha\beta}B^{\rho\delta} - g_2^2\epsilon_{\alpha\beta\rho\sigma}W_a^{\alpha\beta}W_a^{\rho\delta}\right), \tag{3.11}$$

$$\partial_\mu J_L^\mu = i\frac{N_f}{32\pi^2}\left(g_1^2\epsilon_{\alpha\beta\rho\sigma}B^{\alpha\beta}B^{\rho\delta} - g_2^2\epsilon_{\alpha\beta\rho\sigma}W_a^{\alpha\beta}W_a^{\rho\delta}\right), \tag{3.12}$$

which immediately imply

$$\partial_\mu(J_B^\mu - J_L^\mu) = 0, \quad \partial_\mu(J_B^\mu + J_L^\mu) \neq 0, \tag{3.13}$$

with the latter called the $U(1)_{\mathrm{B+L}}$ anomaly. Note that even though $B + L$ is violated at quantum level, $B - L$ is conserved exactly. Since in total nine left-handed SU(2) quark doublets and three left-handed leptons are involved in the SM, this sphaleron process would violate baryon and lepton numbers by three, i.e.

$$\Delta B = \Delta L = \pm 3. \tag{3.14}$$

To relate this baryon number violation with the vacuum structure of the SU(N) gauge theories, we mainly follow the discussion in Ref. [12] and define the Chern-Simons number as

$$N_{\mathrm{CS}} = \int d^3x K^0, \tag{3.15}$$

with the current defined as

$$K^{\mu} = \frac{g^2}{32\pi^2}\epsilon^{\mu\nu\alpha\beta}\left(F^a_{\nu\alpha}A^{\alpha}_{\beta} - \frac{g}{3}\epsilon_{abc}A^a_{\nu}A^b_{\alpha}A^c_{\beta}\right) \tag{3.16}$$

and satisfy

$$\partial_{\mu}K^{\mu} = \frac{g^2}{32\pi^2}\epsilon^{\alpha\beta\rho\sigma}F^a_{\alpha\beta}F^{a,\rho\sigma}, \tag{3.17}$$

where g, $F^a_{\mu\nu}$ and ϵ_{abc} are the coupling strength, the gauge fields and the structure constants of the gauge group, and for $N = 2$, we would have $F^a_{\mu\nu} = W^a_{\mu\nu}$.

Note that from Eq. (3.11), the baryon number change within some period can be calculated

$$\begin{aligned} N_B(t_f) - N_B(t_i) &= \int_{t_i}^{t_f} dt \int d^3x \partial_t J^0_B \\ &= \int_{t_i}^{t_f} \int d^3x \left[\vec{\nabla}\cdot\vec{J}_B + N_f\frac{g^2}{32\pi^2}\epsilon\alpha\beta\rho\sigma W_{\alpha\beta}W_{\rho\sigma}\right], \end{aligned} \tag{3.18}$$

note that the first term in the bracket in the second line mush vanish to conserve the current, which leads to,

$$\Delta N_B = N_f\left[N_{\rm CS}(t_f) - N_{\rm CS}(t_i)\right] = N_f\omega, \tag{3.19}$$

where ω is an integer called the winding number. Note that since the sphaleron process violates the baryon number, one can then relate the sphaleron process to the change of the Chern-Simons number, or the transition between degenerated vacua. This is shown in Figure 3.1, where the x axis is $N_{\rm CS}$ and the y axis is the sphaleron energy.

At low energy, the sphalerons are at the minimum of the configurations, and the tunneling rate is suppressed [293] with the tunneling amplitude being proportional to

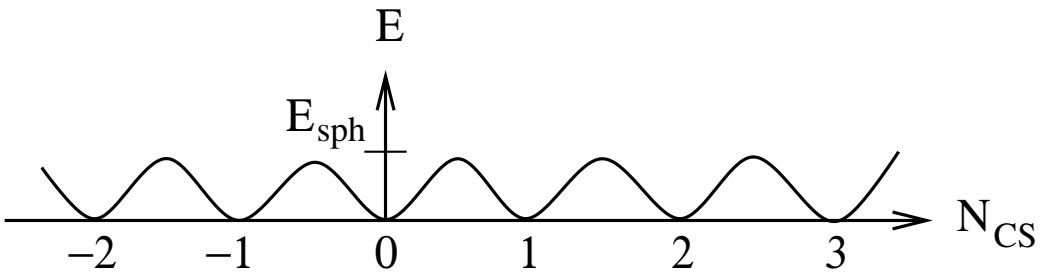

Figure 3.1: Energy of the SU(2) gauge field configurations as a function of the Chern-Simons number $N_{\rm CS}$. Plot adopted from [12]

$\mathcal{A} \sim e^{-8\pi^2/g^2} \sim 10^{-173}$. However, at high temperature, the tunneling rate is enhanced due to the thermal energy that enable the excitations, called the instantons, to hop over the barrier, which corresponds to a transition of the instantons between the degenerated vacua. The transition then results in a change in $N_{\rm CS}$, and thus a baryon number change according to Eq. (3.19).

3.4.2 C and CP violation in the Standard Model

Note that SM is a chiral theory, thus charge conjugate C is maximally violated, which is a result of the fact that the electroweak sector of SM is a linear combination of both axial and vector currents, and the former is invariant under C while the latter changes sign. On the other hand, though the SM does not predict the existence of the PMNS matrix and thus no CPV in the lepton sector, CPV however does exist in the quark sector from the CKM matrix discussed in Chapter 1. From Eq. (1.58), we conclude that CPV in the CKM matrix is of $\mathcal{O}(10^{-20})$, too small to account for the baryon asymmetry observed that is of $\mathcal{O}(10^{-10})$. However, the question on the robustness of the estimation from Eq. (1.58) has been in the air for a long time since from Eq. (1.54) that is defined originally from Jarlskog, the ratio one would obtain is indeed of $\mathcal{O}(10^{-10})$, which is at the same order as the baryon asymmetry. Though it is argued that the sign of fermion masses bears no physical meaning and any physical quantity should depend on mass squared, this argument however has no mathematical

foundation. A more specific criticism on Eq. (1.58) was given in Ref. [295], wherein the authors argued that the formalism could not be applied to the $K\overline{K}$ mixing system coming from the box diagram shown below. The authors pointed out that in such a system the relevant scale was much smaller than 100 GeV, and the actual scale should be the mass of the kaon. In this case, The idea that $\det(C)/T^{12}$ would be true only when all the mass ratiois could be treated as perturbatively small, which however is not the case for the top quark. Regardless of what was discussed above and the possibility that one could some mechanisms to make it work, most researchers in this field agree that new CPV sources are needed in order to explain the baryon asymmetry observed.

3.4.3 Out of thermal equilibrium

To satisfy the out of thermal equilibrium condition, the SM needs to undergo a first-order electroweak phase transition (FOEWPT), which is characterized by the Higgs vev. The initial condition for EWBG in the SM is assumed to be a hot and radiation-dominated Universe with no net baryon-antibaryon asymmetry and the full $\mathrm{SU(2)_L} \otimes \mathrm{U(1)_Y}$ symmetry respected [296,297]. Therefore, the Higgs vev is vanishing at high temperature. However, as the Universe expands and cools down to a temperature below the weak scale, i.e. $T \lesssim \mathcal{O}(100\,\mathrm{GeV})$, the Higgs field suddenly develops a non-zero vev v_c at a critical temperature T_c. As the Universe cools further down, the Higgs rests at the minimum of the potential until $v_c(T_0) = 246\,\mathrm{GeV}$ with T_0 the current temperature. The FOEWPT is identified from the discontinuity of the Higgs field as a function of the temperature.

However, a successful EWBG requires the FOEWPT to be strong to avoid the baryon number generated through the sphaleron process being washed out. This can be illustrated using the bubble nucleation of the broken phase within the surrounding

plasma in the unbroken or symmetric phase. For illustration, we follow the argument in Ref. [13] and adopt the plots therein for illustration.

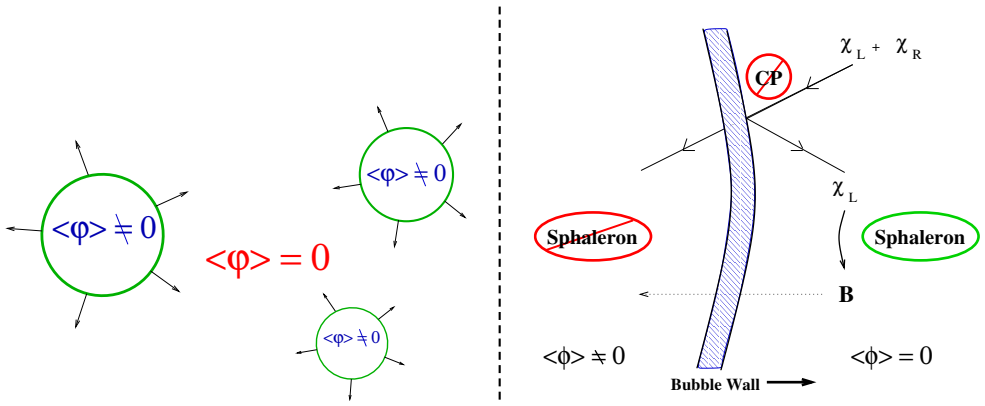

Figure 3.2: Illustration of bubble nucleation and the sphaleron process. To clear some possible confusion, ϕ and φ in the plots both stand for the Higgs field denoted as Φ in the main text. Plots adopted from [13].

The left plot in Figure 3.2 represents the bubble nucleation process, where inside the bubbles, the Higgs has a non-vanishing vev; while outside the bubbles, the Higgs does not develop any vev and thus still respects the $\mathrm{SU(2)_L} \otimes \mathrm{U(1)_Y}$ symmetry. Upon production, the bubbles will expand due to pressure difference. Expansion and collision of bubbles will result in larger bubbles and in the end the whole Universe falls in the broken phase. Obviously, this process corresponds to the phase transition discussed above.

On the other hand, the right plot in Figure 3.2 can help to understand how baryon asymmetry is generated and how the three Sakharov conditions are satisfied. To be specific, when particles scatter from the bubble wall and the theory is C and CP violated as it is in the SM, asymmetries in particle numbers will be generated. These asymmetries will then be converted to asymmetries in the baryon-antibaryon number densities through the sphaleron process. Then as the bubbles expand, the baryon asymmetry will reside in the bubbles and could give the correct baryon asymmetry we observe today. Note that the sphaleron process violates the baryon number. However,

one also notes that the sphaleron process happens both inside and outside the bubbles, which implies that any baryon asymmetry generated outside the bubbles will be washed out unless there is some mechanism to prevent the inverse process. That mechanism is the strong first-order EWPT (SFOEWPT) we mentioned above, which guarantees that the sphaleron process is exponentially suppressed inside the bubbles.

Note that the three Sakharov conditions are explicitly satisfied from our discussion above and one concludes that the SM of particle physics has all the ingredients needed to explain the baryon asymmetry we observe today. However, the discovery of the Higgs particle in 2012 with a mass of $m_h = 125\,\text{GeV}$ makes the SM alone not able to explain this asymmetry. The reason is simple: The SFOEWPT is absent in the SM. It turns out that, from lattice study, to give a SFOEWPT, the mass of the Higgs boson can not exceed $70\,\text{GeV}$ [298, 299]. More strictly, a Higgs boson with mass $m_h = 125\,\text{Gev}$ only corresponds to a smooth crossover on the phase transition plot [88–93].

3.5 Epilog

To explain the baryon asymmetry we observe in our Universe, the three Sakharov conditions need to be satisfied. The SM of particle physics has all the ingredients to realize the Sakharov conditions through EWBG: Baryon number violation from the sphaleron process, C violation from the chiral Lagrangian of the SM and CP violation from the CKM matrix in the quark sector, and out of equilibrium condition from a possible first-order electroweak phase transition. However, SM alone can not explain the baryon asymmetry we observe today, because the CPV effect in the CKM matrix is too small to generate enough baryon number asymmetry in the early Universe, and besides that, the SFOEWPT needed to prevent the washout of the baryon asymmetry is also absent in the SM since the mass of the Higgs boson is $125\,\text{GeV}$, corresponding to a crossover.

In light of that, we conclude that, to explain the baryon asymmetry through EWBG, new CPV sources are needed besides that presented in the SM, and new mechanisms are needed to provide a SFOEWPT. In Chapter 6 and Chapter 7, we will discuss two possible models that can potentially change the shape of the SM Higgs potential at high temperature, thus allowing a possible SFOEWPT to render an explanation of the observed baryon asymmetry.

CHAPTER 4

WIMP DARK MATTER

4.1 Introduction

Since the first evidence of dark matter from Fritz Zwicky in 1933 [98,99] from the observation of the Coma Cluster, much more evidence has been observed including the rotation curves from Vera Rubin *et al* in the 1960s and 1970s [100], gravitational lensing [101–103], CMB anisotropy [29,104–106], BAO [107,108], Bullet Cluster [109] etc. On the other hand, to understand the particle nature of dark matter, many more experiments have been ongoing including deep underground experiments such as LUX [30], PandaX-II [31], XENON1T [32] etc, collider searches such as experiments at the LHC [300–305] and the BaBar [306], as well as aerial experiments such as Fermi-LAT [307], AMS-02 [308,309], PAMELA [310] etc.

However, despite many decades of effort, the nature of dark matter still remains mysterious. Theoretically, the mass scale of dark matter span overs a huge range, from $\mathcal{O}(10^{-22}\,\mathrm{eV})$ to $\mathcal{O}(30M_\odot)$ with $M_\odot$ the mass of the Sun [7]. Discussion that covers the whole range is impossible in this thesis and instead, we only focus on the WIMP window, where the dark matter mass varies from a few GeV to about ten TeV. The WIMP dark matter scenario is interesting from two aspects: (1) To explain the current dark matter relic abundance, WIMP dark matter self-interaction cross section turns out to be what one would expect for particles at the weak scale, which is also known as the "WIMP miracle"; (2) WIMP dark matter is at the weak scale, therefore it can be tested at colliders as well as terrestrial and aerial experiments.

In what follows, we first review setup of the Boltzmann equation for WIMP dark matter, then we summarize constraints on this scenario from various experiments.

4.2 A pedagogical review of the Boltzmann equation

During the evolution of the Universe, the thermodynamic system is not always in a thermal equilibrium state as otherwise the stars or galaxies we observe today will not exist. To properly study the thermodynamics of such a system of the expanding Universe, one can make use of the Boltzmann equation that was first devised by Ludwig Boltzmann in 1872. The equation is named after him in remembrance. The Boltzmann equation generically reads

$$\hat{L}[f_\psi] = \hat{C}[f_\psi], \tag{4.1}$$

where $\hat{L}$ is the Liouville operator and $\hat{C}$ the collision operator. f_ψ is the probability density function or more generically the phase space distribution (PSD) of particle ψ that we assume to be eventually decouple from the the rest of the system for the rest of the discussion below.

In the non-relativistic limit, the PSD f is a function of $f(\vec{p}(t), \vec{x}(t))$ with $\vec{x}$ the canonical coordinates and $\vec{p}$ the corresponding conjugate momenta in the Euclidean space. The Euclidean Liouville operator can then be written as

$$\hat{L}_{\rm E} = \frac{d}{dt} + \frac{d\vec{v}}{dt} \cdot \vec{\nabla}_v + \frac{d\vec{x}}{dt} \cdot \vec{\nabla}_x = \frac{d}{dt} + \frac{\vec{F}}{m} \cdot \vec{\nabla}_v + \frac{\vec{p}}{m} \cdot \vec{\nabla}_x. \tag{4.2}$$

Relativistically, the PSD f is generalized as a function of the contravariant variables p^μ and x^μ, i.e. $f(p^\mu, x^\mu)$, and the corresponding covariant relativistic generalization of the Liouville operator is written as

$$\hat{L} = p^\alpha \frac{\partial}{\partial x^\alpha} - \Gamma^\alpha_{\beta\gamma} p^\beta p^\gamma \frac{\partial}{\partial p^\alpha}, \tag{4.3}$$

where $\Gamma^{\alpha}_{\beta\gamma}$ is the second kind Christoffel symbol and is defined through to the generic metric g as

$$\Gamma^{\alpha}_{\beta\gamma} = \frac{1}{2} g^{\alpha\xi} \left(\frac{\partial g_{\xi\beta}}{\partial x^{\gamma}} + \frac{\partial g_{\xi\gamma}}{\partial x^{\beta}} - \frac{\partial g_{\beta\gamma}}{\partial x^{\xi}} \right), \tag{4.4}$$

obviously, the Christoffel symbol of the second kind is symmetric with respect to the lower two indices, i.e.,

$$\Gamma^{\alpha}_{\beta\gamma} = \Gamma^{\alpha}_{\gamma\beta}. \tag{4.5}$$

Assuming the Universe is homogeneous and isotropic, the metric, also known as the Friedmann-Robsetson-Walker (FRW) metric, can be convinently written in the following form in the spatially spherical coordinates:

$$g = \mathrm{diag}\left(-1, \frac{a^2(t)}{1 - kr^2}, a^2(t) r^2, a^2(t) r^2 \sin^2\theta \right), \tag{4.6}$$

where diag stands for a diagonal matrix, $a(t)$ is the "scale factor", t the proper time and k the curvature constant. Here we use the most-positive convention as different from the convention used in quantum field theory.

On the other hand, for a homogeneous and isotropic Universe, the PSD $f(p^{\mu}, x^{\mu})$ will only depend on the magnitude of the momentum $p \equiv |\vec{p}|$, or equivalently the energy E, and the proper time t: $f(E, t)$. Therefore, under the homogeneous and isotropic assumption and applying the corresponding geodesic equation, the left hand side of Eq. (4.1) is simplified to

$$\hat{L}[f] = E \frac{\partial f}{\partial t} - H p^2 \frac{\partial f}{\partial E}, \quad \text{with } H \equiv \frac{1}{a} \frac{da}{dt}, \tag{4.7}$$

where H is known as the Hubble rate that measures how fast the Universe is expanding. The Boltzmann equation can then be written as

$$E\frac{\partial f}{\partial t} - Hp^2\frac{\partial f}{\partial E} = \hat{C}[f]. \tag{4.8}$$

Dividing both sides by E and integrating over the momentum space, one finds

$$\frac{dn}{dt} + 3Hn = \frac{g^{\rm dof}}{(2\pi)^3}\int \hat{C}[f]\frac{d^3p}{E}, \tag{4.9}$$

where $g^{\rm dof}$ is the number of degrees of freedom and n the total number density for the particle under consideration, the latter of which is explicitly defined as

$$n = \frac{g^{\rm dof}}{(2\pi)^3}\int d^3p f(E,t). \tag{4.10}$$

Note that in Eq. (4.9), the second term on the left-hand side correctly accounts for Hubble dilution due to the expansion of the Universe. In addition, we have

$$\frac{dn}{dt} + 3Hn = \frac{1}{a^3}\frac{d}{dt}(a^3 n), \tag{4.11}$$

which implies the total number of particles in the comoving volume is conserved when the collision term vanishes.

For a generic process $\psi + a + b + \cdots \to i + j + \cdots$, the collision term on the right-hand side of Eq. (4.9) is defined as

$$\begin{aligned}
&\frac{g_\psi^{\rm dof}}{(2\pi)^3}\int \hat{C}[f_\psi]\frac{d^3p_\psi}{E_\psi} \\
&= \int d\Pi_\psi d\Pi_a d\Pi_b \cdots d\Pi_i d\Pi_j \cdots \\
&\quad \times (2\pi)^4\delta^{(4)}(p_\psi + p_a + p_b + \cdots - p_i - p_j - \cdots)
\end{aligned}$$

$$\times \Big[|\mathcal{M}|^2_{i+j+\cdots\to\psi+a+b+\cdots} f_i f_j \cdots (1 \pm f_\psi)(1 \pm f_a)(1 \pm f_b) \cdots$$
$$- |\mathcal{M}|^2_{\psi+a+b+\cdots\to i+j+\cdots} f_\psi f_a f_b \cdots (1 \pm f_i)(1 \pm f_j) \cdots \Big], \quad \text{with } f_x \equiv f(E_x, t), \tag{4.12}$$

such that the Boltzmann equation can finally be written as

$$\begin{aligned}
\frac{dn_\psi}{dt} + 3Hn_\psi =& \frac{g_\psi^{\rm dof}}{(2\pi)^3} \int \hat{C}[f_\psi] \frac{d^3p_\psi}{E_\psi} \\
=& \int d\Pi_\psi d\Pi_a d\Pi_b \cdots d\Pi_i d\Pi_j \cdots \\
& \times (2\pi)^4 \delta^{(4)}(p_\psi + p_a + p_b + \cdots - p_i - p_j - \cdots) \\
& \times \Big[|\mathcal{M}|^2_{i+j+\cdots\to\psi+a+b+\cdots} f_i f_j \cdots (1 \pm f_\psi)(1 \pm f_a)(1 \pm f_b) \cdots \\
& - |\mathcal{M}|^2_{\psi+a+b+\cdots\to i+j+\cdots} f_\psi f_a f_b \cdots (1 \pm f_i)(1 \pm f_j) \cdots \Big],
\end{aligned} \tag{4.13}$$

which is understood as follows:

- The first line corresponds to an integration over the phase space for all the particles involved, where $d\Pi_i \equiv \frac{g_i}{(2\pi)^3} \frac{d^3p_i}{2E_i}$. The phase space integration becomes nontrivial and complicated as the number of particles involved gets larger and larger.

- The second line impose the four-momentum conservation.

- The third line corresponds to the production of ψ that increases the number of ψ and the last line corresponds to the annihilation process which decreases the number of ψ, the fact of which is indicated by the sign in front of each line.

- The $(1 \pm f_i)$ factors account for spin-statistics for species i, where the "+" sign leads to a Bose-Einstein enhancement for a bosonic i and the "-" sign corresponds to a Fermi-Dirac suppression for fermionic i. These factors reflect the fact the it is easier (harder) for a boson (fermion) to transit into a state that already contains a boson (fermion).

Further calculation of the Boltzmann equation, i.e. Eq. (4.13), generically depends on the specific process under consideration. However, in certain scenario, Eq. (4.13) can be further simplified based on approximations that we will discuss below.

4.2.1 Approximations to further simplify the Boltzmann equation

4.2.1.1 CP or T conservation

In nature, the CP symmetry is respected by gravitational, electromagnetic and strong interactions, while C and P are violated in the strongest possible way by the weak interactions. However, as discussed in Chapter 1, CP is only feebly violated by weak interactions in neutral kaon decays first observed in 1964 [311] and recently in B meson decays [226, 312–316]. Since WIMP dark matter decouples from the rest of the plasma way before QCD phase transition, CPV in weak interactions is not related to our discussion and therefore CP conservation is well justified.

With CP conservation, the following relation between the production and the annihilation invariant amplitudes in Eq. (4.13) is implied

$$\begin{aligned} &|\mathcal{M}|^2_{i+j+\cdots\to\psi+a+b+\cdots} f_i f_j \cdots (1 \pm f_\psi)(1 \pm f_a)(1 \pm f_b)\cdots \\ =&|\mathcal{M}|^2_{\psi+a+b+\cdots\to i+j+\cdots} f_\psi f_a f_b \cdots (1 \pm f_i)(1 \pm f_j)\cdots . \end{aligned} \tag{4.14}$$

4.2.1.2 Thermal equilibrium

In the early Universe, we assume all particles stay in thermal equilibrium with a common temperature $T(t)$ which is a function of time due to the expansion. This assumption is also well justified as long as one agrees that our Universe started from the Big Bang. However, for WIMP dark matter, if one assumes it stays in thermal equilibrium with the rest of the plasma during the full evolution of our Universe, its relic density today will be negligible small. Therefore, we assume that the dark matter particle, denoted as ψ above, eventually decouples from the rest of the thermal bath at some time T_f as a result of insufficient interaction rate due to the expansion

of the Universe. Based on above argument, at early time, the PSDs of all particles are in forms of Fermi-Dirac and/or Bose-Einstein:

$$f_i = \frac{1}{e^{(E_i-\mu_i)/T} \pm 1}, \tag{4.15}$$

where E_i and μ_i are the energy and chemical potential respectively, and T is the equilibrium temperature of system. While after T_f, the PSD of our dark matter particle ψ can no longer be described by the thermal distribution, instead, it is solved from the Boltzmann equation.

4.2.1.3 Negligible effects from spin-statistics

We further assume Bose-Einstein enhancement and/or Fermi-Dirac suppression factors can be ignored. This approximation can be realized as long as $e^{(E_i-\mu_i)/T_i} \gg 1$, where E_i and μ_i are the energy and chemical potential of particle i respectively. This assumption becomes exact when the particle i become non-relativistic, i.e. $(m_i-\mu_i) \gg T_i$. As we will see later, WIMP dark matter indeed becomes non-relativistic after decoupling. Under this approximation, $(1 \pm f) \simeq 1$.

4.2.1.4 Vanishing chemical potential

This approximation is well justified as long as the object under consideration is non-generate gas, meaning $|\mu| \ll T$ [317, 318]. On the other hand, since photons have vanishing chemical potential and the number densities of baryons and leptons are much smaller than that of the photon, the chemical potential of all species can be set to zero as a good approximation as long as the reactions under consideration conserve both lepton and baryon numbers. Though this is not the case due to the observed baryon asymmetry, as long as baryogenesis is not involved, our approximation above remains good and valid. Therefore, in what follows, we assume that, for all particles, their chemical potential $\mu = 0$.

Based on approximations above, the collision term finally simplifies to

$$
\begin{aligned}
&\frac{g_\psi^{\rm dof}}{(2\pi)^3}\int \hat{C}[f_\psi]\frac{d^3p_\psi}{E_\psi} \\
&=\int d\Pi_\psi d\Pi_a d\Pi_b\cdots d\Pi_i d\Pi_j\cdots\times(2\pi)^4\delta^{(4)}(p_\psi+p_a+p_b+\cdots-p_i-p_j-\cdots) \\
&\quad\times|\mathcal{M}|^2_{\psi+a+b+\cdots\to i+j+\cdots}\left(f_if_j\cdots-f_\psi f_af_b\cdots\right) \\
&=\int d\Pi_\psi d\Pi_a d\Pi_b\cdots d\Pi_i d\Pi_j\cdots\times(2\pi)^4\delta^{(4)}(p_\psi+p_a+p_b+\cdots-p_i-p_j-\cdots) \\
&\quad\times|\mathcal{M}|^2_{\psi+a+b+\cdots\to i+j+\cdots}\left(e^{-(E_i+E_j+\cdots)/T}-f_\psi e^{-(E_a+E_b+\cdots)/T}\right) \\
&=\int d\Pi_\psi d\Pi_a d\Pi_b\cdots d\Pi_i d\Pi_j\cdots\times(2\pi)^4\delta^{(4)}(p_\psi+p_a+p_b+\cdots-p_i-p_j-\cdots) \\
&\quad\times|\mathcal{M}|^2_{\psi+a+b+\cdots\to i+j+\cdots}\,e^{-(E_a+E_b+\cdots)/T}\left(e^{-E_\psi/T}-f_\psi\right) \qquad (4.16)
\end{aligned}
$$

where the detailed balance condition is used to obtain the last step. Finally, the Boltzmann equation can be written as

$$
\begin{aligned}
\frac{dn}{dt}+3Hn=&\int d\Pi_\psi d\Pi_a d\Pi_b\cdots d\Pi_i d\Pi_j\cdots\times(2\pi)^4\delta^{(4)}(p_\psi+p_a+p_b+\cdots-p_i-p_j-\cdots) \\
&\times|\mathcal{M}|^2_{\psi+a+b+\cdots\to i+j+\cdots}\,e^{-(E_a+E_b+\cdots)/T}\left(e^{-E_\psi/T}-f_\psi\right). \qquad (4.17)
\end{aligned}
$$

Clearly, if particle ψ stays in thermal equilibrium with the other particles in the plasma, the last term in the Boltzmann equation above will cancel such that

$$
\frac{dn_\psi}{dt}+3Hn_\psi=\frac{1}{a^3}\frac{d}{dt}(a^3n_\psi)=0, \qquad (4.18)
$$

i.e., the total number density for particle ψ in the comoving volume will stay unchanged as expected. In this case, if we finish the integral of Eq. (4.10), we will find

$$
n_\psi\approx g_\psi\left(\frac{m_\psi T^2}{2\pi}\right)^{\frac{3}{2}}e^{-\frac{m_\psi}{T}}, \qquad (4.19)
$$

implying that the number density of ψ today $n_\psi(T_0)$, with T_0 the temperature today and $T_0 \ll m_\psi$ in general, will be negligibly small today due to the Boltzmann suppression factor. Therefore, massive dark matter particles[i] cannot stay in thermal equilibrium with the SM plasma during the whole evolution of the Universe, they must decouple from the thermal bath at some point to explain the dark matter relic abundance we observe today.

4.3 WIMP dark matter

In last subsection, we conclude that if a massive particle ψ stays in thermal equilibrium with the SM thermal bath, its number density today will be negligibly small and thus can not account for the dark matter we observe today. To explain the the dark matter relic density, as discussed in the Introduction chapter, WIMP has attracted significant attention in the past due to the scale where WIMP lives. Furthermore, at early time, WIMP was also motivated to solve the hierarchy problem listed in the Introduction chapter. Therefore, we will discuss more about WIMP dark matter in this section.

4.3.1 The Boltzmann equation for WIMP dark matter in the 2→2 process

As an example, we consider dark matter annihilation into two SM particles: $\chi(p_1)\chi(p_2) \to \phi(k_1)\phi(k_2)$, where χ is the dark matter particle and ϕ represents SM particles. From the Boltzmann equation, we have

$$\frac{dn}{dt} + 3Hn = \int d\Pi_{\chi_1} d\Pi_{\chi_2} d\Pi_{\phi_1} d\Pi_{\phi_2} (2\pi)^4 \delta^{(4)}(p_1 + p_2 - k_1 - k_2) \times |\mathcal{M}|^2_{\chi(p_1)\chi(p_2)\to\phi(k_1)\phi(k_2)} \left[e^{-(E_{p_1}+E_{p_2})/T} - f_{\chi_1} f_{\chi_2}\right]$$

[i]Since the mass of dark matter spans over a large range [319, 320], if dark matter under consideration is instead very light, then our argument will not be valid any more. However, for light dark matter particles, our derivation of Eq. (4.17) would also need to be revised. That is however beyond the scope of this thesis.

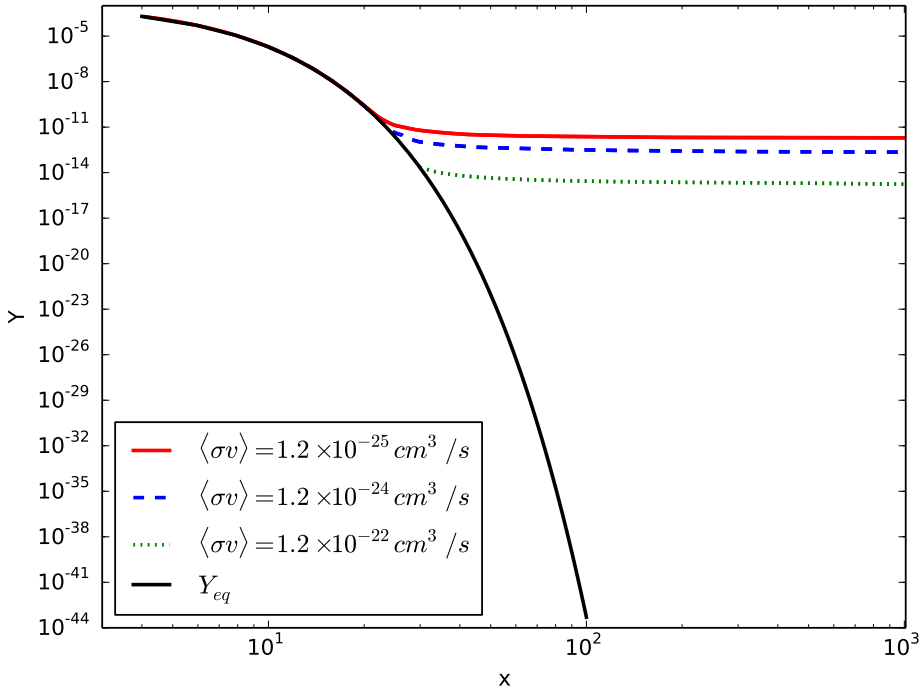

Figure 4.1: An illustration of the solution of the Boltzmann equation in Eq. (4.26) with the dark matter mass fixed at $m_\chi = 100\,\mathrm{GeV}$.

$$\equiv \langle \sigma_{\chi(p_1)\chi(p_2)\to\phi(k_1)\phi(k_2)} v_{\text{Møller}} \rangle \left[\left(n_\chi^{\text{eq}}\right)^2 - n_\chi^2 \right], \tag{4.20}$$

where n_χ^{eq} is the number density of χ when it is in thermal equilibrium with the SM plasma, $v_{\text{Møller}}$ is the Møller velocity and $\sigma_{\chi(p_1)\chi(p_2)\to\phi(k_1)\phi(k_2)}$ is the annihilation cross section. Their expressions are given by

$$n_\chi \approx g_\chi \left(\frac{m_\chi T^2}{2\pi}\right)^{\frac{3}{2}} e^{-\frac{m_\chi}{T}}, \tag{4.21}$$

$$v_{\text{Møller}} = \frac{\sqrt{(p_1 \cdot p_2)^2 - m_\chi^4}}{E_1 E_2}, \tag{4.22}$$

$$\langle \sigma_{\chi(p_1)\chi(p_2)\to\phi(k_1)\phi(k_2)} v_{\text{Møller}} \rangle = \frac{\int \sigma v_{\text{Møller}} dn_1^{\text{eq}} dn_2^{\text{eq}}}{\int dn_1^{\text{eq}} dn_2^{\text{eq}}}. \tag{4.23}$$

It turns out useful to introduce a dimensionless parameter, usually called the yield of the particle under consideration, defined as

$$Y \equiv \frac{n}{s}, \quad s = g_{*s}\frac{2\pi^2}{45}T^3, \tag{4.24}$$

where n, s and g_{*s} are the number density of the particle under consideration, the total entropy density of the Universe and the effective degrees of freedom for the entropy respectively, and express it as a function of another dimensionless parameter $x = m_\chi/T$ with m_χ the mass of dark matter and T the temperature of the thermal bath. In terms of the yield Y and x, the Boltzmann equation can be written as

$$\frac{dY}{dx} = -\frac{1}{3H}\frac{ds}{dx}\langle\sigma_{\chi(p_1)\chi(p_2)\to\phi(k_1)\phi(k_2)}v_{\text{Møller}}\rangle\left[\left(Y_\chi^{\text{eq}}\right)^2 - Y_\chi^2\right]. \tag{4.25}$$

Following the now standard parameterization of the energy density and the entropy density, we can finally express the evolution of Y as

$$\frac{dY}{dx} = -\left(\frac{45G}{\pi}\right)^{-\frac{1}{2}}\frac{m_\chi g_*^{\frac{1}{2}}}{x^2}\langle\sigma_{\chi(p_1)\chi(p_2)\to\phi(k_1)\phi(k_2)}v_{\text{Møller}}\rangle\left[\left(Y_\chi^{\text{eq}}\right)^2 - Y_\chi^2\right], \tag{4.26}$$

where G is the gravitational constant and g_* the number of degrees of freedom of the Universe. A dedicated study of g_* was performed in Ref. [321, 322]. For illustration, we choose $m_\chi = 100\,\text{GeV}$ and show the solution to Eq. (4.26) in Figure 4.1. The black curve corresponds to the situation where the dark matter particles stay in thermal equilibrium with the SM plasma, and the colorful curves correspond to solutions with different dark matter annihilation cross sections. The point where the colorful curves detaches from the black curve is when the dark matter particles decouple from the rest of the plasma. This process is usually called the decoupling process or the freeze-out of dark matter. It is obvious that, from the plot, the yield of dark matter is considerable compared with when the freeze-out of dark matter is absent.

Though Figure 4.1 is only illustrative, it reflects several common features of WIMP dark matter:

(1) If dark matter particles stay in thermal equilibrium with the SM plasma, its relic abundance today will be negligibly small as implied by the black curve. This point is also consistent with our theoretical prediction in Eq. (4.19).

(2) The typical decoupling temperature or the freeze-out temperature T_f of WIMP dark matter is around $T_f \simeq m_{\rm DM}/20$, with $m_{\rm DM}$ the mass of dark matter, implying the fact that WIMP dark matter is typically non-relativistic after freezing out. Since $m_{\rm DM}$ is usually at the GeV scale, $T_f \sim \mathcal{O}(1)\,\text{GeV} \sim \mathcal{O}(10^{13})\,\text{K}$.

(3) The decoupling condition can be approximated by $H \gtrsim \langle\sigma_{\chi\chi\to\phi\phi} v_{\text{Møller}}\rangle n_\chi$, therefore a faster annihilation rate of dark matter into SM particles in the early Universe would imply a later decoupling of the dark matter particles from the plasma. This fact is also reflected by the colorful curves in the plot.

(4) After decoupling, the equilibrium yield of dark matter $Y_\chi^{\rm eq}$ becomes negligible due to the Boltzmann suppression factor $e^{-m_{\rm DM}/T}$, while the actual yield of dark matter Y_χ stays constant.

Historically, features above leads to the conclusion of the "WIMP miracle", which we will discuss in detail in next subsection.

4.3.2 The WIMP miracle

In light of bullet (4) above, one can omit the $Y_\chi^{\rm eq}$ term in Eq. (4.26) and obtain the current yield of dark matter:

$$\frac{1}{Y_0} \approx \frac{1}{Y_f} + \left(\frac{45G}{\pi}\right)^{\frac{1}{2}} \int_{T_0}^{T_f} g_*^{\frac{1}{2}} \langle\sigma_{\chi(p_1)\chi(p_2)\to\phi(k_1)\phi(k_2)} v_{\text{Møller}}\rangle dT, \tag{4.27}$$

with T_0 and T_f the current and the freeze-out temperature respectively, and Y_0 and Y_f the current and the freeze-out yield of dark matter respectively. Knowing Y_0, one can compute the dark matter relic abundance today through

$$\Omega_{\rm DM}h^2 = \frac{\rho_0}{\rho_c}h^2 = \frac{8\pi G s_0 Y_0 m_{\rm DM}}{3\times 10^4}, \tag{4.28}$$

where ρ_0, ρ_c, s_0 and h are the current total energy density, the critical energy density, the total entropy density and the Hubble constant in units of $100\text{km}/(\text{s}\cdot\text{Mpc})$ respectively.

To estimate dark matter annihilation rate in the early Universe, we assume that:

1. Dark matter annihilation rate $\langle\sigma_{\chi\chi\to\phi\phi}v_{\rm Møller}\rangle$ roughly stays as a constant. This will be well justified as long as the scale of dark matter is above the weak scale such that, similarly to the Fermi theory, $\langle\sigma_{\chi\chi\to\phi\phi}v_{\rm Møller}\rangle$ can be approximated as

$$\langle\sigma_{\chi\chi\to\phi\phi}v_{\rm Møller}\rangle \sim \frac{g^2 g_{\rm dark}^2}{m_{\rm DM^2}} \tag{4.29}$$

   from dimension analysis, where g and g_χ are dark matter-SM particle and dark matter-dark matter interacting strength respectively.

2. The yield at the freeze-out temperature Y_f can be ignored. As discussed by Gondolo and Gelmini in 1991 [321], to achieve a very good approximation of Y_0, inclusion of Y_f is essential. However, as they also point out, the ignorance of Y_f is only of $\mathcal{O}(0.01)$ to Y_0. Thus omitting Y_f is safe for our estimation of $\langle\sigma_{\chi\chi\to\phi\phi}v_{\rm Møller}\rangle$ from Y_0.

With the two justified assumptions above, one obtains

$$\langle\sigma_{\chi\chi\to\phi\phi}v_{\rm Møller}\rangle \simeq \frac{16\pi^{\frac{5}{2}}}{3\times 10^4}\times\frac{g_{*s}}{\sqrt{45\pi g_*}}\times\frac{m_{\rm DM}}{T_f - T_0}\times\frac{G^{\frac{3}{2}}T_0^3}{\Omega h^2}$$

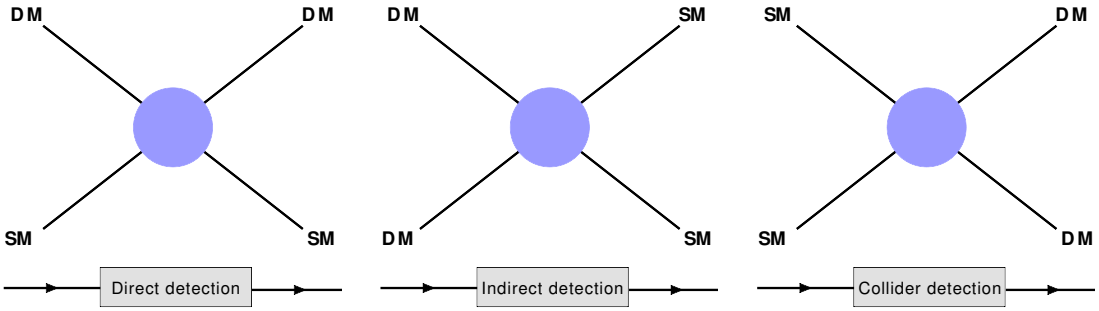

Figure 4.2: Direct, indirect and collider searches of WIMP dark matter, where the arrow at the bottom of each Feynman diagram represents the direction of time.

$$\simeq \frac{32\pi^{\frac{5}{2}}}{3\times 10^3}\times\frac{g_{*s}}{\sqrt{45\pi g_*}}\times\frac{G^{\frac{3}{2}}T_0^3}{\Omega h^2}. \tag{4.30}$$

To arrive at the last line, we apply the typical freeze-out temperature $T_f \simeq m_{\rm DM}/20$ and use the fact that $T_f \gg T_0$ based on our argument above. Plug in $T_0 = 2.7255\,\mathrm{K}$ [29, 323] and $\Omega h^2 = 0.1198$ [29], one finds

$$\langle\sigma_{\chi\chi\to\phi\phi}v_{\text{Møller}}\rangle \simeq 4.238\times10^{-26}\,\frac{\mathrm{cm}^3}{\mathrm{s}} \sim \left(\frac{g}{0.01}\right)^2\left(\frac{g_\chi}{1}\right)^2\left(\frac{100\,\mathrm{GeV}}{m_{\rm DM}}\right)^2, \tag{4.31}$$

implying that dark matter with masses at the weak scale and coupling with SM particles at the weak gauge coupling order can naturally explain the current dark matter relic abundance we observe today. This coincidence was historically called the "WIMP miracle".

Due to the scale of WIMP dark matter particles, they can be detected with nowadays techniques and have motivated broad searches which are usually cataloged as direct detection, indirect detection and collider searches of WIMP dark matter as depicted in Figure 4.2.

In what follows, we will briefly summarize the current constraints on and future prospects of WIMP dark matter searches in these three directions. We follow closely the discussion in Ref. [3] for theoretical background introduction and take current constraints on WIMP dark matter from [1].

4.4 Direct detection: Current constraints and future prospects

Dark matter direct detection corresponds to processes indicated by the left plot in Figure 4.2 and the measured quantity is the dark matter-nucleon scattering rate.[ii] In direct-detection, the scattering rate is dependent on the local density of dark matter, which was first estimated by J.H. Jeans in 1922 in the vicinity of our solar system. The current estimation of the local dark matter density is $\rho \simeq (0.39 \pm 0.03) \cdot (1.2 \pm 0.2) \cdot (1 \pm \delta_{\rm triax})\,{\rm GeV/cm^3}$ [1], where the first term on the right hand side gives the average dark matter density at a point one solar distance away from the center of our galaxy, the second term accounts for the baryons in the galactic disk that leads to an increase of local dark matter density and the last term corrects for possible deviations from a purely spherical dark matter halo with $\delta_{\rm triax} \leq 0.2$ according to Ref. [324].

The direct-detection rate also depends on the local dark matter velocity distribution $f(\vec{v})$, which is usually assumed to be a Gaussian distribution and written as

$$f(v){\rm d}v = \frac{v{\rm d}v}{v_e v_0 \sqrt{\pi}} \left\{ \exp\left[-\frac{(v-v_e)^2}{v_0^2} \right] - \exp\left[-\frac{(v+v_e)^2}{v_0^2} \right] \right\}, \tag{4.32}$$

where v_e is the velocity of the Earth around the Sun and $v_0 = 220{\rm km/s}$ is the orbit velocity of the Sun around the galactic center. The distribution is truncated at $v_{\rm esc.} = 533^{+54}_{-41}\,{\rm km/s}$, corresponding to the local escape velocity of dark matter from the Milky Way. The dark matter flux $F_{\rm DM}$ can then be approximated as

$$F_{\rm DM} = nv = \frac{\rho v}{m_{\rm DM}} \simeq \frac{10^5}{{\rm cm^2 s}} \tag{4.33}$$

for a non-relativistic dark matter particle with $m_{\rm DM} = 100\,{\rm GeV}$.

[ii] For direct, indirect detection and collider searches discussed below, we only focus on the discussion for the $2 \to 2$ processes only here.

Then the recoil energy induced by a dark matter particle with mass $m_{\rm DM}$ on a nucleus of mass m_N can be expresses as

$$E_R = \frac{q^2}{2m_N} = \frac{\mu^2 v^2}{m_N}(1-\cos\theta^*), \tag{4.34}$$

with q the momentum transfer, $\mu = m_{\rm DM}m_N/(m_{\rm DM}+m_N)$ the reduced mass and v the mean dark matter velocity relative to the target and θ^* the scattering angle in the center-of-mass frame. For detectors composed of different target nuclei, the total recoil energy spectrum can be obtained by summing the differential rates for all target nuclei weighted by their number per unit mass of detector N_N:

$$\frac{{\rm d}R}{{\rm d}E_R} = \sum_N N_N \frac{\rho}{m_X}\int_{v_{\rm min}}^{v_{\rm esc}} \frac{{\rm d}\sigma_N}{{\rm d}E_R} v f(\mathbf{v}) {\rm d}^3 v. \tag{4.35}$$

The individual nuclear recoil rates depend on the number density of the dark matter particle $\rho/m_{\rm DM}$ and the differential scattering cross section is

$$\frac{{\rm d}\sigma_N}{dE_R} = \frac{m_N}{2\mu^2 v\sqrt{v^2-2\delta/\mu}}\sigma_N\left(E_R\right), \tag{4.36}$$

where δ is the increment of the dark matter rest mass and $\delta = 0$ in the elastic case. The integration is truncated with a minimal velocity being

$$v_{\rm min} = \frac{m_N E_R^{\rm min}/\mu + \delta}{\sqrt{2m_N E_R^{\rm min}}}, \tag{4.37}$$

which depends on the minimal detectable recoil energy experimentally. If inelastic scattering is allowed, the minimal and maximal recoil energy can be expressed as

$$E_R^{\rm min,max} = \frac{\mu^2}{m_N}\left[v^2 - \frac{\delta}{\mu} \mp v\left(v^2 - 2\frac{\delta}{\mu}\right)^{1/2}\right]. \tag{4.38}$$

Experimentally, the recoil energy spectrum is convolved with an energy-resolution function and multiplied with an energy-dependent counting efficiency or cut acceptance. The fractional recoil energy that is experimentally visible is incorporated in a so-called "Q-factor" with $Q(E_R) = E_{\rm vis}/E_R$, determined from γ-ray using ^{50}Co or ^{137}Cs, and neutron using AmBe or ^{252}Cf calibration sources for background and signal events respectively.

Depending on the quantum statistics of dark matter, the scattering cross section σ_N can be dependent or independent on the spin of dark matter, resulting to the so-called spin-dependent and spin-independent cross sections respectively that we will discuss separately below.

4.4.1 Spin-independent case

Spin-independent (SI) cross sections result from scalar or vector couplings between dark matter and the nucleons, which can be expressed as

$$\sigma_N^{\rm SI}(E_R) = \left[Z + (A-Z)\,(f_n/f_p)\right]^2 \frac{\mu^2}{\mu_p^2}\sigma_p F_{\rm SI}^2(E_R)\,, \tag{4.39}$$

with Z and A the proton and total nucleon numbers of the target nucleus N, $f_{p(n)}$ the dark matter couplings, μ_p the reduced mass, and σ_p the total cross section per nucleon. $F_{\rm SI}(E_R)$ is the spin-independent nuclear form factor, i.e. the Fourier transform of the nucleon density in the nucleus, which is often assumed to be similar for protons and neutrons having the Helm form [325]

$$F_{\rm SI}^2(E_R) = \left(\frac{3j_1(qr_0)}{qr_0}\right)^2 e^{-s^2q^2}, \tag{4.40}$$

where j_1 is the spherical Bessel function of the first kind, $q = \sqrt{2m_N E_R}$, $r_0 \simeq \sqrt{(1.2\,{\rm fm}A^{1/3})^2 - 5s^2}$ is the effective nuclear radius and $s \sim 1\,{\rm fm}$ is the nuclear skin thickness.

Note that for iso-spin conserving couplings, i..e $f_n = f_p$, the cross section is enhanced by a factor of A^2 over the proton cross section, indicating that the whole nucleus interacts coherently provided that the inverse momentum transfer is smaller than the size of the nucleus.

For a scalar dark matter scattering off nuclei via a scalar mediator ϕ with mass m_ϕ and dimensionless couplings λ_x, λ_p and λ_n to dark matter, protons and neutrons respectively, the differential cross section can be written as

$$\frac{\mathrm{d}\sigma_N^{\mathrm{SI}}}{\mathrm{d}E_R} \simeq \frac{m_N}{\left(q^2+m_\phi^2\right)^2} \frac{\lambda_x^2\left[Z\lambda_p F_p\left(E_R\right)+(A-Z)\lambda_n F_n\left(E_R\right)\right]^2}{2\pi v\left(v^2-2\delta/\mu\right)^{1/2}}. \tag{4.41}$$

Since $E_R^{\max}-E_R^{\min}=2\mu^2 v(v^2-2\delta/\mu)^{1/2}/m_N$, the total SI cross section becomes

$$\sigma_N^{\mathrm{SI}}\left(E_R\right) \simeq \frac{\lambda_X^2\lambda_p^2\mu^2A^2}{\left(2m_N E_R+m_\phi^2\right)^2} F_{\mathrm{SI}}^2\left(E_R\right). \tag{4.42}$$

Note the overall enhancing factor A^2 in the numerator. Due to this feature, results from different detector targets can be compared directly by looking at the SI cross cross per nucleon and the result is shown in Figure 4.3.

Note that in Figure 4.3, the dark cyan regions correspond to results from the DAMA/LIBRA experiment with 14 annual cycles and a total exposure for over 20 years. The experiment makes use the idea of annual modulation of dark matter originally proposed in Refs. [326, 327], where the modulation is a simple result of the rotation of the Earth around the Sun as depicted in Figure 4.4: When the Earth and the Sun move in the same direction, the relative velocity is the sum of their velocities, resulting in a larger flux of dark matter with the maximum being around June; while when they move in opposite direction, the relative velocity is the subtraction of them, resulting in a smaller flux of dark matter with the minimal being around December.

Using the NaI(Tl) target, the DAMA/LIBRA annual modulation result from phase1 and phase 2 is consistent with a dark matter signal in the (2-6) keV energy

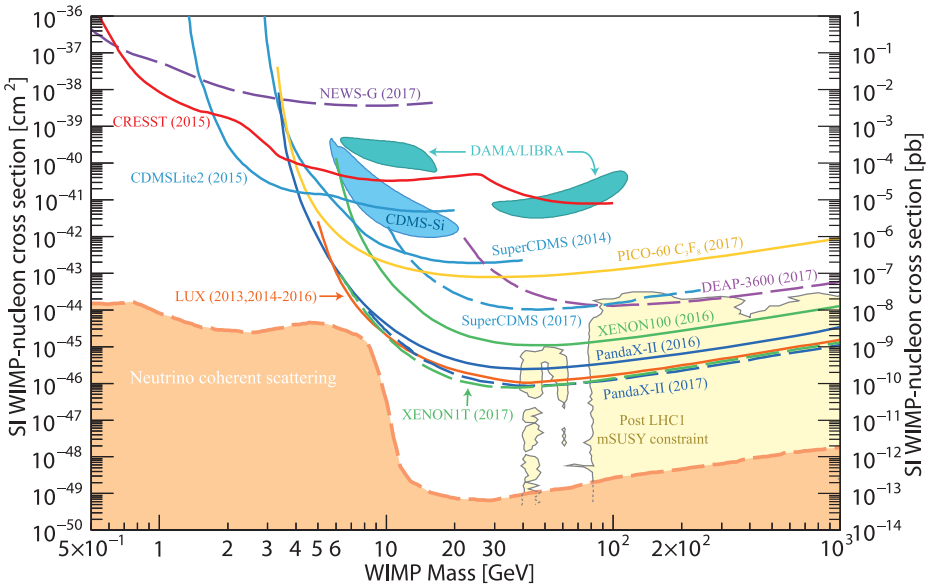

Figure 4.3: Constraints on SI dark matter-nucleon cross section versus WIMP dark matter mass from various experiments and is normalized to a single nucleon. Also shown in the plot is a scan of the parameter space of four typical SUSY models, CMSSM, NUHM1, NUHM2, pMSSM10 with black contours, which we will not discuss here as it is beyond the scope of this thesis. Plot adopted from [1].

range with the amplitude being (0.0112±0.0012) counts/kg/keV/day and the phase being (145±5) days and a period of (0.999±0.001) years [328]. The signal is observed at more than 5σ level. The other labeled "CDMS-Si" enclosed region comes from the CDMS-Si experiment, where three unexplained low-energy events were observed in the Si-detector data sample. However, the events were no longer seen after detector upgrading to CRESST-II [329, 330].

Other direct detection experiments with different target materials and better sensitivity such as LUX [30], PandaX-II [31], XENON1T [32] etc are developed to rigorously test the WIMP scenario and their results are shown in Figure 4.3. All these experiments claim a contradiction against the claim of discovery from DAMA/LIBRA. The debate is still ongoing and projects using exactly the same target material as the DAMA/LIBRA group are under way in order to settle down this issue, those include the COSINUS [331], the SABRE [332], the ANAIS-112 [333], the PICO-

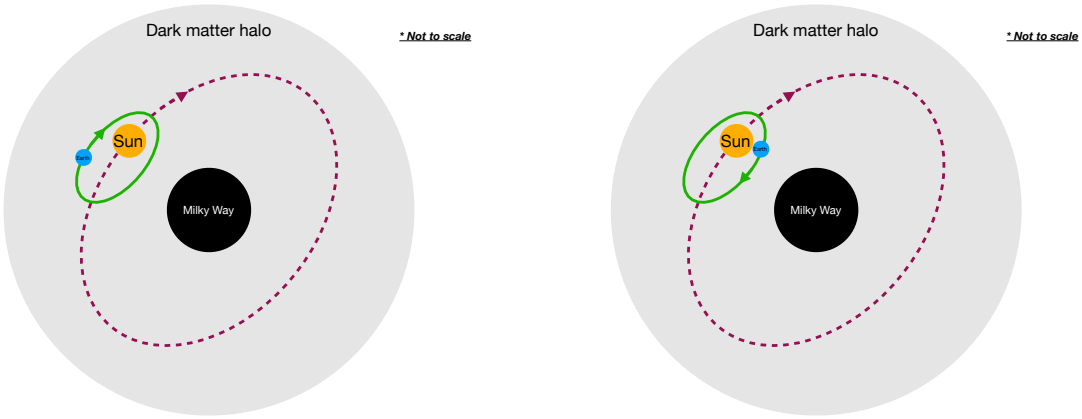

Figure 4.4: Illustrative figures of annual modulation in dark matter direct detection, where, in each plot, the grey sphere corresponds to the dark matter halo, the black dot represents the Milky Way, the yellow dot represents the Sun and the blue dot represents the Earth. The dashed purple curve indicated the trajectory of the Sun while the solid green curve is that of the Earth. The figures are not plotted to scale.

LON [334], the DM-Ice [335], the KIMS [336] and the COSINE-100 [337] experiments. In the past few years, some of them have reached the needed maturity to test the DAMA/LIBRA result, and DM-Ice, KIMS and ANAIS have been taking data. Among them, DM-Ice have recently published their results based on a 3.6 year run with 18 kg operated within the Ice Cube neutrino Telescope at a threshold of 4 keV, and no modulation was observed [335].

Despite the tension between DAMA/LIBRA and other experiments, from Figure 4.3, one can see that the WIMP dark matter scenario has almost been explored to the neutrino floor, where neutrino-nucleon scattering will become significant to mimic dark matter signals. On the other hand, regardless of the null result in searching for WIMP dark matter except the controversial result from DAMA/LIBRA, it is still worthy of exploring WIMP scenario down to the neutrino floor [338] to benefit our understanding of dark matter, which will be the goal for future precision measurements such as DARWIN [339], XENONnT, DEAP-50T and DarkSide-20k [1].

4.4.1.1 Review of the recent XENON1T excess and its current status

Recently, the XENON collaboration reported an excess of electron recoil events at XENON1T [128] below 7 keV oven known backgrounds. Though the energy range is not related to the dark matter scale we discussed here, since it is a potential signal of dark matter, we include a brief review of this result here.

As discussed above, the XENON1T experiment is primarily designed to detect WIMP dark matter particles through employment of a liquid-xenon time projection chamber. Due to its unprecedentedly low background rate, large target mass and low energy threshold, it is also sensitive to other dark matter candidates and other new physics beyond dark matter. Using the data obtained from February 2017 to February 2018 with an exposure of 0.65 tonne-years, the XENON collaboration find an excess above a known background. The excess can be explained by the solar axion model with a 3.5σ significance, or by the neutrino magnetic moment signal at 3.2σ significance, or by β decay of ^{3}H at 3.2σ significance. For the former two cases, the excess is however in strong tension with stellar constraints [340–344], while the tritium β decay explanation can neither be confirmed nor excluded with current knowledge.

Nevertheless, the XENON1T result discussed above has already triggered many discussions, such as the suggestion of crosscheck by searching for planetary dependence of the excess in Ref. [345], possible mismodeling of electron recoil data [346], missing backgrounds [347]. A reanalysis of XENON1T excess data is also done recently using NEST [348] and a confirmation of XENON1T excess is obtained though the significance is reduced to 1-2σ. An EFT approach and possible UV completion are explored in Ref. [349]. Further/refined analysis on neutrino magnetic moments [350,351], tritium [352] as well as solar axions and/or axions and/or axion-like particles are also investigated [353–364]. Other possible explanations of the excess include solar emission of dark photons [365], Co-SIMP thermal production of dark

matter [366], dark matter or dark-matter-like particles with a fast component of velocity [367, 368], dark photon dark matter [369], Migal ionization [370], low-mass luminous dark matter [371], sun-heated MeV-scale dark matter [372], decaying warm dark matter [373], exothermic dark matter [374], hidden photon dark matter production through gravitation [375], thermal dark matter production from freeze-out [376], electromagnetic signals of inelastic dark matter scattering [377], mirror dark matter [378], in-medium effects [379], a light Z' from the two Higgs doublet model [380], dark matter Z' from $U(1)_X$ [381], Higgs portal and relaxion model [382], pseudo-Dirac dark matter [383], pseudo-scalar produced in the Sun [384], semi-annihilating Z_3 dark matter [385], self-interacting dark matter [386], freeze-in inelastic dark matter [387], Z_2 dark matter in a dark sector [388], transition neutrino magnetic moment [389, 390], weak gravity conjecture [391], undulating dark matter [392], feebly interacting warm dark matter from $U(1)_{B-L}$ [393], dark matter acceleration towards the Earth due to long range forces from ordinary matter [394], dark matter from a secluded sector coupled to SM through energy-momentum tensors [395], boosted dark matter [**?**, 396–399], dark photon from keV dark fermion annihilation [400], new solar neutrino interactions mediated by a light scalar or a light vector [401], solar neutrinos [402], new/non-standard neutrino interactions mediated by a light vector-mediator and/or a light scalar [403–406], a dark sector containing two dark matter particles with a (2-3) keV mass splitting that interacts with SM particles from the exchange of a massive dark photon [407], atmospheric dark matter from inelastic collision of cosmic rays with the atmosphere [408], dark matter annihilations into a pair of on-shell mediators that subsequently decay into scalars which can interact with electrons [409], weakly-coupled boson, axion or dark photon production from dark matter annihilations [410], dark matter-SM interactions through higher dimensional Rayleigh operators [411] etc. On the other hand, collider constraints on dark matter interpretation of the excess [412] as well as implication of the excess on various new

physics [413–416] such as stellar cooling, muon anomalous magnetic moments etc have also been investigated.

Currently XENONnT is under installation, and it would be more than exciting to confirm this excess in the near future. Theoretical investigation is still ongoing, which will definitely deepen our understanding on the excess prior to any updated result in the near future.

4.4.2 Spin-dependent case

On the other hand, if axial vector coupling exist between dark matter and nucleons, the resulting cross sections will be spin-dependent (SD) and can be written as

$$\sigma_N^{\mathrm{SD}}\left(E_R\right) = 32\mu^2 G_F^2 \left(\frac{J_N+1}{J_N}\right)\left(\langle S_p\rangle\, a_p + \langle S_n\rangle\, a_n\right)^2 F_{\mathrm{SD}}^2\left(E_R\right), \tag{4.43}$$

where J_N is the nuclear spin, $a_{p,n}$ are the dark matter couplings to protons and neutrons, $F_{\mathrm{SD}}(E_R)$ is the spin-dependent nuclear form factor and $\langle S_{p,n}\rangle$ are the expectation values of the proton and neutron spin in the target nucleus [417–420]. Since all these factors are of $\mathcal{O}(1)$ and the absence of enhancing factor A^2, SD cross sections are in general smaller than SI cross sections. Correspondingly, the exclusion limit in the SD case will be weaker than that in the SI case.

Different from the SI case, in order to compare results from different targets, a common practice is to compare the cross section for the interaction with a single proton or neutron assuming no coupling to the other type of nucleon. Traditionally, $\langle S_{p,n}\rangle$ are calculated within the shell model [417–419], while recent calculations based on chiral effective field theory yield much better agreement between calculated and measured Xe spectra. Constraints for the SD case is shown in Figure 4.5.

The upper plot of Figure 4.5 corresponds to dark matter-neutron scattering, and the current best constraints from XENON100, PandaX-II and LUX, and among them,

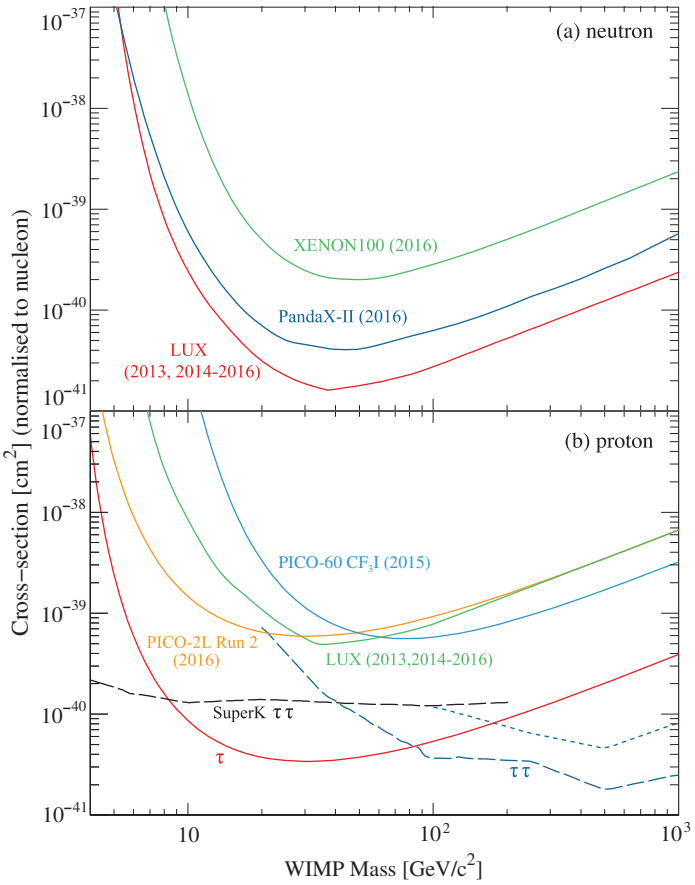

Figure 4.5: Constraints on SD dark matter-nucleon cross section versus WIMP dark matter mass from various experiments and is normalized to a single neutron (proton) in the upper (lower) plot. Plot adopted from [1].

LUX gives the most stringent constraint from a combination analysis of LUX 2013 and 2014-2016 data. The lower plot of Figure 4.5 corresponds to dark matter-proton scattering, and the current best constraints come from PICO-60 CF_3I 2015 data, PICO-2L Run2 data, and LUX 2013 and2014-2016 data as indicated by the light blue, the orange and the green curves respectively. As discussed above, since SD cross section is in general smaller than SI cross section due to the absence of the A^2 enhancing factor, the corresponding constraints on SD cross sections are weaker than that on SI cross sections.

4.5 Indirect detection: Current constraints and future prospects

Indirect detection corresponds to the middle plot in Figure 4.2, where a pair of dark matter particles in the dark matter halo around us annihilates into a pair of SM particles, resulting in a flux rise of γ-rays, neutrinos, antiprotons and positrons especially in regions with large local dark matter density. Assuming Majorana type dark matter particles,[iii], the annihilation yield of a dark matter particle pair X can be written as

$$\Phi_i(\mathbf{n}, E) = \langle \sigma_{X\bar{X}} v \rangle \frac{dN_i}{dE} \frac{1}{8\pi m_X^2} \int_{\text{los}} dl \rho_X^2[\mathbf{r}(l, \mathbf{n})], \tag{4.44}$$

where the index i denotes the secondary particle observed, l refers to the path length along the line of sight (los) in direction $\mathbf{n}$, dN_i/dE is the multiplicity spectrum of secondary particle i, m_X the mass of dark matter and $\rho_X^2[\mathbf{r}(l, \mathbf{n})]$ is the dark matter density along the los.

$\langle \sigma_{X\bar{X}} v \rangle$ is the annihilation cross section averaged over dark matter velocity distribution, which is usually assumed to be the same as that relevant for the freeze-out case. This, however, becomes invalid when the WIMP annihilation cross section has a strong velocity dependence as is the case when s-wave annihilations are suppresses. The reason is that freeze-out happens at $T_f \simeq m_X/20$ implying $v \simeq 0.4c$, exceeding the typical WIMP velocity in the Milky Way which is $v \simeq 300\,\text{km/s}$.

On the other hand, to separate dark matter profile dependence in the flux defined above, a dimensionless factor J is introduced [421]

$$J(\mathbf{n}) = \frac{1}{8.5\text{kpc}} \left(\frac{1}{0.3\text{GeVcm}^{-3}} \right)^2 \int_{\text{1.0.s.}} dl \rho_X^2[\mathbf{r}(l, \mathbf{n})], \tag{4.45}$$

[iii] If not, an additional factor of 1/2 shall be added

where $\rho_X \simeq 0.3\,\mathrm{GeV/cm^3}$ is used to make J dimensionless. From the definition, $\overline{J}(\mathbf{n}, \Delta\Omega)$ can be defined as the average of J over a circular region of solid angle $\Delta\Omega$. The flux from the region $\Delta\Omega$ can then be defined as

$$\Phi_i(\Delta\Omega, E) \simeq C\frac{dN_i}{dE}\left(\frac{\frac{1}{c}\langle\sigma_{X\bar{X}}v\rangle}{\mathrm{pb}}\right)\left(\frac{1\mathrm{TeV}}{m_X}\right)^2\overline{J}(\Delta\Omega)\Delta\Omega \tag{4.46}$$

with $C = 2.75 \times 10^{-12}/(\mathrm{cm}^2 \cdot \mathrm{s})$.

The enhancement of annihilation rates due to small-scale structure in the form of dark matter clumps is often included by the boosting factor defined as

$$B \simeq \frac{\langle\rho^2\rangle}{\langle\rho\rangle^2}, \tag{4.47}$$

measuring the annihilation yield relative to that from a smooth dark matter distribution. Another enhancement, called the Sommerfeld enhancement [422], can arise if dark matter interactions involve a light force mediator. The Sommerfeld enhancement may then lead to an increase in the annihilation cross section in galaxies and clusters while the thermal history of freeze-out intact [423]. In addition to the Sommerfeld enhancement, the internal bremsstrahlung can also enhance the annihilation cross section when, for example, the s-wave cross sections are suppressed by symmetries or helicity effects.

In terms of indirect detection with photons, a strong TeV source was discovered by the H.E.S.S. Cherenkov telescope [424, 425] from the central region of our galaxy, and the Fermi-LAT data also revealed a new extended source of GeV photons near the galactic center above and below the galactic plane, the so-called Fermi bubbles [307] as well as several dozen point sources of GeV photons in the inner kpc of our galaxy [307] that are consistent with several WIMP interpretations [426, 427]. However, the fitted "excess" depend significantly on the details of the fit, thus a claim of the observation of a dark matter signal can not be made yet. Due to the large

astrophysical background near the galactic center, the best bound on WIMP annihilations with photons in the final state comes from a combined analysis of Fermi-LAT observations of dwarf galaxies [428], which excludes hadronic or $\tau^+\tau^-$ annihilations of WIMP for $m_X \lesssim 100\,\mathrm{GeV}$ based on the s-wave annihilation assumption.

For positron and electron flux excesses, the best measurements at energies of tens to hundreds GeV come from AMS-02 [308, 309] and PAMELA [310]. Measurements of the total electron+positron energy spectrum by ATIC [429], Fermi-LAT [430] and H.E.S.S. [431] between 100 and 2000 GeV also exceed the prediction of purely secondary spectrum, but the dispersion of the magnitude of these excesses is still large. WIMP annihilation can in principle explain the excess, however, the cross section required for a thermal WIMP will be too large and stringent constraints will apply. In contrast, viable astrophysical explanations have been suggested to explain these excesses, such as pulsars [432, 433] and explosion of nearby supernova at about two million years ago [434].

For WIMP annihilations into antiproton, the best constraints come from the PAMELA satellite and the AMS-02 experiment [160, 435], which cover the kinetic energy region between 60 MeV and 350 GeV, which is in good agreement with secondary production and propagation models. The data also exclude WIMP models trying to explain the "$e^\pm$ excesses" discussed above through annihilation into $W^\pm$ or Z pairs.

From all indirect detection experiments, the best upper limit for low WIMP masses comes from Super-Kamiokande [1]. The limit is obtained by considering WIMP annihilation into $b\bar{b}$ and $\tau^+\tau^-$ pairs, and the result is shown in the lower plot of Figure 4.5. Note that the upper bounds are more than two orders of magnitude below the cross section required to explain the DAMA/LIRBA signal through SD scattering on protons. On the other hand, for heavier WIMPs, the best bounds are obtained from IceCube/DeepCore data, which supersede the Suuper-Kamiokande limits when

Name	D1	D2	D3	D4	D5	D6
Operator	$\overline{X}X\overline{q}q$	$\overline{X}\gamma_5 X\overline{q}q$	$\overline{X}X\overline{q}\gamma_5 q$	$\overline{X}\gamma_5 X\overline{q}\gamma_5 q$	$\overline{X}\gamma^\mu X\overline{q}\gamma_\mu q$	$\overline{X}\gamma^\mu\gamma_5 X\overline{q}\gamma_\mu q$
Coefficient	m_q/M_*^3	im_q/M_*^3	im_q/M_*^3	m_q/M_*^3	$1/M_*^2$	$1/M_*^2$
Name	D7	D8	D9	D10	D11	D12
Operator	$\overline{X}\gamma^\mu X\overline{q}\gamma_\mu\gamma_5 q$	$\overline{X}\gamma^\mu\gamma_5 X\overline{q}\gamma_\mu\gamma_5 q$	$\overline{X}\sigma^{\mu\nu}X\overline{q}\sigma^{\mu\nu}q$	$\overline{X}\sigma_{\mu\nu}\gamma_5 X\overline{q}\sigma^{\mu\nu}q$	$\overline{X}XG_{\mu\nu}G^{\mu\nu}$	$\overline{X}\gamma^5 XG_{\mu\nu}G^{\mu\nu}$
Coefficient	$1/M_*^2$	$1/M_*^2$	$1/M_*^2$	i/M_*^2	$\alpha_s/(4M_*^3)$	$i\alpha_s/(4M_*^3)$
Name	D13	D14	C1	C2	C3	C4
Operator	$\overline{X}XG_{\mu\nu}\tilde{G}^{\mu\nu}$	$\overline{X}\gamma^5 XG_{\mu\nu}\tilde{G}^{\mu\nu}$	$X^\dagger X\overline{q}q$	$X^\dagger X\overline{q}\gamma_5 q$	$X^\dagger\partial_\mu X\overline{q}\gamma^\mu q$	$X^\dagger\partial_\mu X\overline{q}\gamma^\mu\gamma_5 q$
Coefficient	$i\alpha_s/(4M_*^3)$	$\alpha_s/(4M_*^3)$	m_q/M_*^2	im_q/M_*^2	$1/M_*^2$	$1/M_*^2$
Name	C5	C6	R1	R2	R3	R4
Operator	$X^\dagger XG_{\mu\nu}G^{\mu\nu}$	$X^\dagger XG_{\mu\nu}\tilde{G}^{\mu\nu}$	$X^2\overline{q}q$	$X^2\overline{q}\gamma_5 q$	$X^2G_{\mu\nu}G^{\mu\nu}$	$X^2G_{\mu\nu}\tilde{G}^{\mu\nu}$
Coefficient	$\alpha_s/(4M_*^2)$	$i\alpha_s/(4M_*^2)$	$m_q/(2M_*^2)$	$im_q/(2M_*^2)$	$\alpha_s/(8M_*^2)$	$i\alpha_s/(8M_*^2)$

Table 4.1: Operators containing two dark matter particles X and two SM quarks q and gluons g. Operator with names starting with D, C and R apply to Dirac fermions, complex scalars and real scalars respectively. Table adapted from Ref. [3].

the dark matter mass is above 40 (100) GeV and annihilates into a $\tau^+\tau^-$ ($b\bar{b}$) pair, these bounds are also shown in the lower plot of Figure 4.5.

4.6 Collider searches: Current constraints and future prospects

Collider searches of dark matter correspond to the last plot in Figure 4.2, where a pair of SM particles collides to produce a pair of dark matter particles. Similar to neutrinos, dark matter particles escape detection at colliders due to their lack of electromagnetic interactions and their non-baryonic nature. As a consequence, they can only be observed through the missing transverse energy at colliders, which is then determined from the recoiling observed objects such as jets, heavy quarks, photons and leptons.

Depending on the models, dark matter could also be searched for through direct production at colliders if the production involves at least one visible particle in so-called mono-object events. The object can be either a jet, a photon, an electroweak gauge boson or even a Higgs boson. This mono-object can be generated either through initial state radiation or through radiation from an intermediate particle, and the dark matter signal would then appear directly as an excess in the tail of the transverse energy distribution. Discussion in this direction would depend on a specification of the model, which is out of the interest of this theses. In what follows, we will only focus

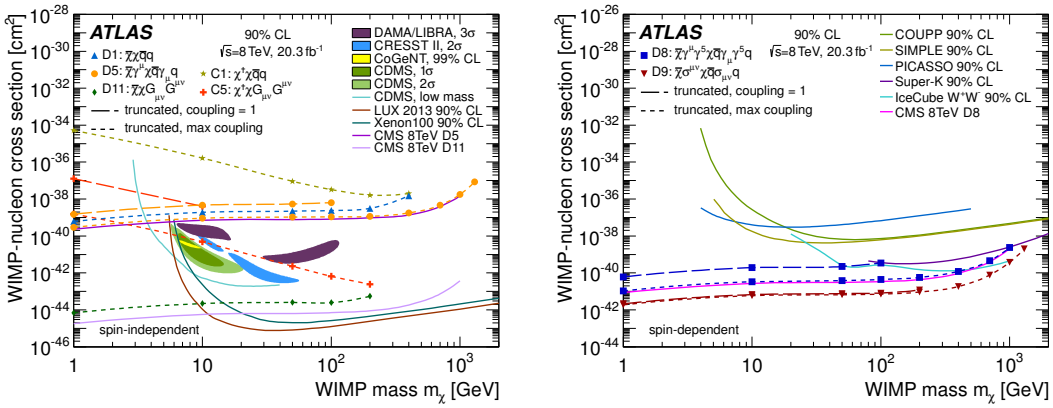

Figure 4.6: Comparison among constraints from dark matter searches at colliders and from direct and indirect detection. on SD dark matter-nucleon cross section versus WIMP dark matter mass from various experiments and is normalized to a single neutron (proton) in the upper (lower) plot. Plot adopted from [3].

on constraints on WIMP dark matter from collider searches in a model-independent way.

Suppose dark matter particles are much heavier than the center of mass energy at the LHC, then the model-independent way to search for dark matter at the LHC can be achieved using the effective field theory (EFT) approach, where the couplings between dark matter and SM particles are parameterized by a set of non-renormalizable, higher-dimensional operators. Those operators containing two dark matter particles can be categorized as shown in Table 4.1 [436].

In Table 4.1, M_* is the scale where dark matter particles live and is assumed to satisfy $M_* \gg v_\Phi$ with $v_\Phi = 246\,\text{GeV}$ the typical weak scale. In contrast to many dark matter models, the EFT approach only depends on a few parameters: the heavy scale M_* and the mass of dark matter m_X. On the other hand, another advantage of the EFT approach is that it makes it possible to compare LHC results with those from dark matter direct and indirect detection due to the crossing symmetry of the underlying Feynman diagrams [437], with the underlying point being that if the mediator is light, the EFT approach shall be modified.

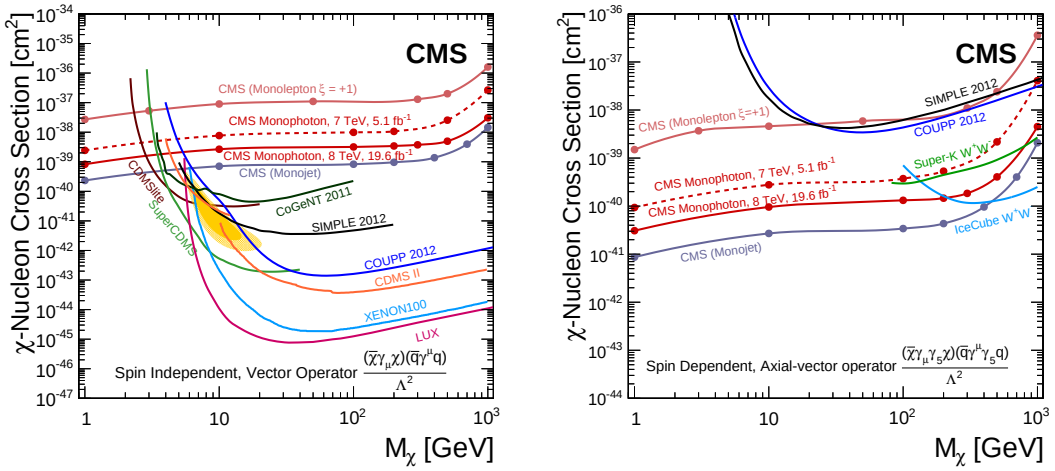

Figure 4.7: Comparison among constraints from dark matter searches at colliders and from direct and indirect detection. on SD dark matter-nucleon cross section versus WIMP dark matter mass from various experiments and is normalized to a single neutron (proton) in the upper (lower) plot. Plot adopted from [3].

Based on the EFT approach, an overview of the mono-jet results is shown in Figure 4.6 by focusing on the D1, D5, D11, C1 and C5 operators for the SI case, and D8 and D9 operators for the SD case. Note the competitive or even stronger constraints from colliders compared with direct detection results especially for light dark matter masses for both SI and SD cases. The collider results are obtained from Refs. [300, 301] and the plot is adopted from Ref. [3] obtained in 2015. Latest results have also been obtained by the ATLAS [163, 438, 439] and the CMS [164, 440–450] groups recently, however, transferring the collider constraints therein to obtain an updated version of Figure 4.6 is out of the scope of this thesis.

The mono-photon analyses of ATLAS [302] and CMS [303] are somewhat less competitive than the mono-jet analyses as shown in Figure 4.7, and similar conclusion holds for mono-lepton analyses. Since mono-lepton channel may involve different couplings of dark matter to quarks, the interference effects have been parameterized in the couplings with an additional factor $\xi = \pm 1$ in Figure 4.7. Note again the standout of collider results compared with direct detection at low dark matter masses.

In the future, measurements of correlations of visible particles such as the azimuthal angle between two jets may permit more discriminate cuts particularly between the signal and the irreducible background from invisible Z decays to two neutrinos [304]. With search strategies adapted to the new pile-up and detector conditions, the LHC experiments are expected to surpass the previous limits cited above. Within one year of data taking, the LHC shall reach the scale with $M_* \gtrsim 2\,\mathrm{TeV}$ at $\sqrt{s} = 14\,\mathrm{TeV}$ and $\mathcal{L} = 100\mathrm{fb}^{-1}$ [305].

CHAPTER 5

LOW-ENERGY PROBE OF ELECTROWEAK NEUTRAL CURRENT

5.1 Introduction

In the late 1970's, Prescott *et al* [451, 452] showed that parity is violated by the weak neutral current through measuring the the left-right asymmetry by scattering longitudinally polarized electrons from deuterium and hydrogen. The momentum transfer Q^2 in that experiment is $Q^2 = 1.6\,\mathrm{GeV}^2$, corresponding to an asymmetry around $-9.5 \times 10^{-5} Q^2$. Furthermore, by varying the fraction of electron energy change y, which is defined as $y \equiv (E_0 - E')/E_0$ with E_0 and E' the energy of the incident and the scattered electron respectively, within the range $0.15 \leq y \leq 0.36$, the weak mixing angle was determined to be

$$\sin^2 \theta_W = 0.224 \pm 0.020. \tag{5.1}$$

Through dependence of the asymmetry on the fraction y, the experiment was able to rule out several models that were invented to explain the negative results of the early atom parity violation APV experiments and singled out the electroweak unification theory by Glashow, Salam and Weinberg [37–39], resulting the award of Nobel prize.

Since then, the parity asymmetry from the electroweak neutral current, or the weak mixing angle that can be extractee from the asymmetry, has been measured with a higher and higher precision from various experiments, including precision measurements at colliders such as experiments at Tevatron, LEP, SLD and the LHC, and

low energy precision experiments such as neutrino-nucleon scattering, Qweak, SLAC-E158 etc. Currently, the most precise determination on the weak mixing angle comes from the LEP and the SLD [453–456] experiments at the Z pole, but their results differ by 3σ, leading to very different physics using one or the other [457]. In the near future, the asymmetry will be measured with an even higher precision to, on one hand, hopefully resolve this issue at HL-LHC, and on the other hand, to explore new physics at the TeV scale or above as we will discuss in this chapter.

In terms of new physics, the hint can be obtained by looking at any deviations of experimental result from SM prediction. To that end, one needs to first find the SM prediction at the same level of or even better than the precision from experiments. In light of this, we will first review SM prediction of the weak mixing angle in this chapter, and then we will review current results and future prospects on measurements/determination of the weak mixing angle from various experiments. After that, we will then discuss how the low energy probe of the weak mixing angle is sensitive to new physics.

5.2 Renormalization schemes of $\sin^2\theta_W$

In Chapter 1, we define the tree-level weak mixing angle in Eq. (1.28) as

$$\sin^2\theta_W = 1 - \frac{m_W^2}{m_Z^2}. \tag{1.28}$$

However, its value will depend on the renormalization scheme one chooses and for different choices of schemes, $\sin^2\theta_W$ can differ. In following subsections, I will briefly review these schemes.

5.2.1 The on-shell scheme

The on-shell scheme [458–461] is a promotion of the tree-level definition in Eq. (1.28) to all orders in perturbation theory. Note the correlation between m_Z, m_W and

$\sin^2\theta_W$, at tree level, the $W^\pm$ boson mass can be written as

$$m_W^2 = \frac{\pi\alpha_{\rm EM}}{\sqrt{2}G_\mu \sin^2\theta_W}, \tag{5.2}$$

where $\alpha_{\rm EM}$ is the fine structure constant precisely measured from Thomson scattering, G_μ is the Fermi constant precisely known from the muon lifetime. However, this simple tree-level relation will be modified due to the presence of radiative corrections. To obtain the quantum effects in the correlation between m_W, m_Z and $\sin^2\theta_W$, Marciano and Sirlin proposed the "on-shell" scheme, which resulted in the famous relation

$$m_W^2 = \frac{\pi\alpha_{\rm EM}}{\sqrt{2}G_\mu} \cdot \frac{1}{\sin^2\theta_W(1-\Delta r)}, \tag{5.3}$$

where Δr absorbs all higher-order corrections. In this scheme, the definition of the weak mixing angle remains the form expressed in Eq. (1.28) above and it shall be understood as a definition in terms of the $\mathrm{SU(2)_L}$ gauge boson masses. As a result, the definition will be valid to all orders in perturbation theory.

Currently, the value of Δr is $\Delta r = 0.03672 \mp 0.00017 \pm 0.00008$, where the first uncertainty comes from the uncertainty of m_t and the second one from $\alpha_{\rm EM}(m_Z)$. Due to the dominant uncertainty from the top quark mass, this scheme would introduce large spurious contributions at higher orders. In addition, in the presence of new physics that modifies gauge boson masses, the definition above would become even less convenient. In light of that, the modified minimal subtraction ($\overline{\rm MS}$) scheme has also been introduces as will be discuss below.

5.2.2 The $\overline{\rm MS}$ scheme

In this scheme, the mixing angle is defined through the gauge couplings as [462–465]

$$\sin^2\hat{\theta}_W(\mu) = \frac{\hat{g}_1^2(\mu)}{\hat{g}_1^2(\mu)+\hat{g}_2^2(\mu)}, \tag{5.4}$$

where the " ˆ " indicates the usual notation used in literatures for the $\overline{\rm MS}$ scheme. In this scheme, the weak mixing angle depends on the 't Hooft scale μ conventionally chosen to be at $\mu = m_Z$ for many electroweak processes. Comparing with the on-shell scheme, the $\sin^2\hat{\theta}_W(m_Z)$ is less sensitive to m_t and most type of new physics. At the same time, the counterparts of Eq. (5.3) are also introduced, written as

$$\sin^2\hat{\theta}_W = \frac{\pi\alpha_{\rm EM}}{\sqrt{2}G_\mu}\cdot\frac{1}{m_W^2(1-\Delta\hat{r}_W)}, \quad \sin^2\hat{\theta}_W\cos^2\hat{\theta}_W = \frac{\pi\alpha_{\rm EM}}{\sqrt{2}G_\mu}\cdot\frac{1}{m_Z^2(1-\Delta\hat{r})}. \quad (5.5)$$

The $\overline{\rm MS}$ scheme also benefits in the aspect that it appropriately incorporates the effects from large m_t at $\mathcal{O}((\delta\bar{\rho})^2)$ with $\delta\bar{\rho} = 3\alpha_{\rm EM}m_t^2/(16\pi\sin^2\theta_W m_W^2)$, solving the mismatch between the use of Eq. (5.3) and the insertion of Δr from one-loop calculation [463, 465].[i]

5.2.3 The effective mixing angle $\sin^2\theta_f^{\rm eff}$

An alternative definition of the weak mixing is a flavor-dependent "effective" weak mixing angle first employed by the LEP workers [466] and is defined through the ratio of vector and axial vector couplings of the weak neutral current at Z pole. The coupling of $Zf\bar{f}$ can be written as [5, 456]

$$v_f^Z = T_f - 2Q_f\sin^2\theta_f^{\rm eff}, \quad (5.6)$$

where Q_f and T_f are the fermion charge and its third isospin component respectively. At higher orders, the gauge boson self-energy and $Z\bar{f}f$ vertex corrections are absorbed

[i]Decoupling and/or non-decoupling of the finite $\alpha_{\rm EM}\ln(m_t/m_Z)$ terms will lead to variant definitions of $\sin^2\hat{\theta}_W$, we will not discuss these cases here and one can refer to Refs. [462, 464, 465] for more discussion.

into a scheme dependent form factors called ρ_f and κ_f, corresponding to corrections to overall coupling strengths and the weak mixing angle respectively. At tree level,

$$\rho_f = 1, \quad \kappa_f = 1. \tag{5.7}$$

At loop level, the κ_f form factor is defined by

$$\sin^2\theta_f^{\rm eff}(q^2) \equiv \kappa_f(q^2,\mu)\sin^2\hat{\theta}_W(\mu), \tag{5.8}$$

where q^2 is the momentum transfer and one choice of the 't Hooft scale is $\mu = m_Z$ given that $\sin^2\hat{\theta}_W(m_Z)$ has been measured to a very high precision from LEP and SLD [453–456]. And, at m_Z, there is a simple relation between $\sin^2\theta_f^{\rm eff}$ and $\sin^2\hat{\theta}_W$ first derived in Ref. [467] and was later improved by Marciano to be [468]

$$\sin^2\hat{\theta}_W - \sin^2\theta_\ell^{\rm eff} \simeq 0.0002. \tag{5.9}$$

$\sin^2\theta_f^{\rm eff}$ remains a useful definition as long as contributions from electroweak boxes are negligible. As pointed by authors in Ref. [5] decades ago, this ignorance may no longer remain valid especially given the fact that we are now entering the precision era of particle physics. Based on this consideration, the authors in Refs. [4, 5] have considered the running of the mixing angle in the $\overline{\rm MS}$ scheme and a better precision has been achieved, leading to

$$\sin^2\hat{\theta}_W - \sin^2\theta_\ell^{\rm eff} \simeq 0.00718 \pm 0.0002. \tag{5.10}$$

We will discuss the running of the mixing angle in next section by reviewing first that of $\sin^2\theta_f^{\rm eff}$, and then that in the $\overline{\rm MS}$ scheme. As we will see, the latter indeed improves the precision of theoretical prediction.

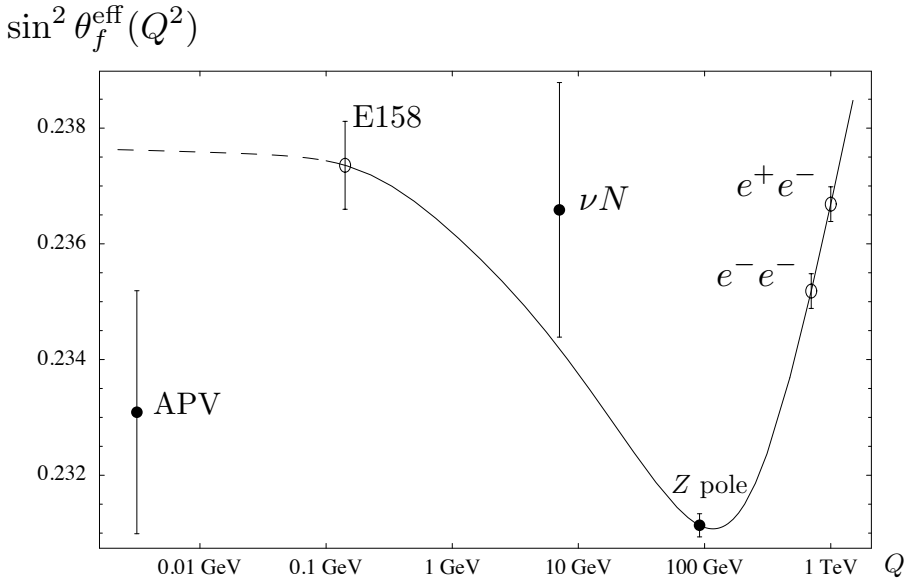

Figure 5.1: Running of $\sin^2\theta_f^{\rm eff}(Q^2)$ as a function of Q. The solid curve is the RGE running of $\sin^2\theta_f^{\rm eff}(Q^2)$ from Eq. (5.11) and the dots represent measurements or prospects from different experiments. Plot adapted from Ref. [14].

5.3 Running of $\sin\theta_W$

As mentioned at the end of last section, this section will be devoted to the review of the running of $\sin^2\theta_f^{\rm eff}$ and the running of $\sin^2\theta_W$ in the $\overline{\rm MS}$ scheme.

5.3.1 Running of $\sin^2\theta_f^{\rm eff}(Q^2)$

Based on our discussion in subsection 5.2.3, the 't Hooft scale for the effective mixing angle is usually fixed at m_Z such that the effective mixing angle is now only a function of $q^2 \equiv -Q^2$:

$$\begin{aligned}\sin^2\theta_f^{\rm eff}(Q^2) \equiv& \kappa_f(Q^2, m_Z)\sin^2\hat{\theta}_W(m_Z)\\ =& \left[\kappa_F(Q^2)+\kappa_B(Q^2)\right]\sin^2\hat{\theta}_W(m_Z),\end{aligned} \tag{5.11}$$

where κ_f now corresponds to one-loop fermionic (κ_F) and bosonic (κ_B) corrections evaluated at m_Z, which has already been evaluated by Czarnecki and Marciano [14] given below

$$\kappa_F\left(Q^2\right) = 1 - \frac{\alpha_{\rm EM}}{2\pi \sin^2\theta_W}\left\{\frac{1}{3}\sum_f \left(T_{3f}Q_f - 2\sin^2\theta_W Q_f^2\right) \times \left[\ln\left(\frac{m_f^2}{m_Z^2}\right) - \frac{5}{3} + 4z_f + (1-2z_f)\,p_f \ln\left(\frac{p_f+1}{p_f-1}\right)\right]\right\}, \tag{5.12}$$

$$\text{with } z_f \equiv \frac{m_f^2}{Q^2}, \quad p_f \equiv \sqrt{1+4z_f} \tag{5.13}$$

and

$$\kappa_B\left(Q^2\right) = 1 - \frac{\alpha_{\rm EM}}{2\pi \sin^2\theta_W}\left\{-\frac{42\cos^2\theta_W + 1}{12}\ln\cos^2\theta_W + \frac{1}{18} - \left[\frac{p}{2}\ln\left(\frac{p+1}{p-1}\right) - 1\right]\left[(7-4z)\cos^2\theta_W + \frac{1}{6}(1+4z)\right] - z\left[\frac{3}{4} - z + \left(z - \frac{3}{2}\right)p\ln\left(\frac{p+1}{p-1}\right) + z(2-z)\ln^2\left(\frac{p+1}{p-1}\right)\right]\right\}, \tag{5.14}$$

$$\text{with } z \equiv \frac{m_W^2}{Q^2}, \quad p \equiv \sqrt{1+4z}. \tag{5.15}$$

The running of $\sin^2\theta_f^{\rm eff}(Q^2)$ is then shown in Figure 5.1, which is adapted from Ref. [14]. Together with the running of $\sin^2\theta_f^{\rm eff}(Q^2)$ as shown by the solid curve, current experimental results and future prospects at the time when Ref. 5.1 came out are also plotted in the original paper, these are indicated by the dots. Note that solid dots are experimental results and empty dots corresponds future prospects at that time. We have and will have more high and/or low energy precision measurements from different experiments nowadays and in the future while the author is writing this thesis. We will discuss more about those experiments in section 5.4.

5.3.2 Running of $\sin^2\hat{\theta}_W(Q^2)$

Due to the reasons discussed in section 5.2, the authors in Ref. [5] consider the RGE running of $\sin^2\hat{\theta}_W(Q^2)$ in the $\overline{\rm MS}$ scheme at both $\mathcal{O}[\alpha_{\rm EM}^n \ln^n(\mu_0/\mu)]$ and $\mathcal{O}[\alpha_{\rm EM}^{n+1} \ln^n(\mu_0/\mu)]$, $\mathcal{O}[\alpha_{\rm EM}\alpha_s^n \ln^n(\mu_0/\mu)]$, $\mathcal{O}[\alpha_{\rm EM}\alpha_s^{n+1} \ln^n(\mu_0/\mu)]$ and $\mathcal{O}[\alpha_{\rm EM}\alpha_s^{n+2} \ln^n(\mu_0/\mu)]$ to reduce theoretical uncertainties. Recently, the authors also update their result by including higher order corrections from the singlet contributions to the RGE evolution at four and five loop order as well as updating their treatment on hadronic corrections by using experimental data through the application of the dispersion integral [4]. I will briefly review their work below.

In the $\overline{\rm MS}$ scheme, the RGE for the mixing angle and the fine structure constant can be written as [4, 5]

$$\mu^2\frac{d\hat{\alpha}_{\rm EM}}{d\mu^2} = \frac{\hat{\alpha}_{\rm EM}^2}{\pi}\left[\frac{1}{24}\sum_i K_i\gamma_i Q_i^2 + \sigma\left(\sum_q Q_q\right)^2\right], \tag{5.16}$$

$$\mu^2\frac{d\hat{v}_f}{d\mu^2} = \frac{\hat{\alpha}_{\rm EM}Q_f}{24\pi}\left[\sum_i K_i\gamma_i\hat{v}_i Q_i + 12\sigma\left(\sum_q Q_q\right)\left(\sum_q \hat{v}_q\right)\right], \tag{5.17}$$

where $\hat{v}_f \equiv T_f - 2Q_f\sin^2\hat{\theta}_W$ and

$$\begin{aligned} K_i &= N_i^c\left\{1 + \frac{3}{4}Q_i^2\frac{\hat{\alpha}_{\rm EM}}{\pi} + \frac{\hat{\alpha}_s}{\pi} + \frac{\hat{\alpha}_s^2}{\pi^2}\left[\frac{125}{48} - \frac{11}{72}n_q\right]\right. \\ &+ \frac{\hat{\alpha}_s^3}{\pi^3}\left[\frac{10487}{1728} + \frac{55}{18}\zeta_3 - n_q\left(\frac{707}{864} + \frac{55}{54}\zeta_3\right) - \frac{77}{3888}n_q^2\right] \\ &+ \frac{\hat{\alpha}_s^4}{4\pi^4}\left[\frac{2665349}{41472} + \frac{182335}{864}\zeta_3 - \frac{605}{16}\zeta_4 - \frac{31375}{288}\zeta_5\right. \\ &- n_q\left(\frac{11785}{648} + \frac{58625}{864}\zeta_3 - \frac{715}{48}\zeta_4 - \frac{13325}{432}\zeta_5\right) \\ &\left.\left. - n_q^2\left(\frac{4729}{31104} - \frac{3163}{1296}\zeta_3 + \frac{55}{72}\zeta_4\right) + n_q^3\left(\frac{107}{15552} + \frac{1}{108}\zeta_3\right)\right]\right\}, \end{aligned} \tag{5.18}$$

$$\sigma = \frac{\hat{\alpha}_s^3}{\pi^3}\left[\frac{55}{216} - \frac{5}{9}\zeta_3\right] + \frac{\hat{\alpha}_s^4}{\pi^4}\left[\frac{11065}{3456} - \frac{34775}{3456}\zeta_3 + \frac{55}{32}\zeta_4 + \frac{3875}{864}\zeta_5\right.$$

boson	γ_i	fermion	γ_i
real scalar	1	chiral fermion	4
complex scalar	2	Majorana fermion	4
massless gauge boson	-22	Dirac fermion	8

Table 5.1: RGE contributions of different particle types. Table adopted from Ref. [4].

$$- \quad n_q \left(\frac{275}{1728} - \frac{205}{576}\zeta_3 + \frac{5}{48}\zeta_4 + \frac{25}{144}\zeta_5 \right) \Bigg] , \tag{5.19}$$

where n_q is the number of active quarks and N_i^c is the color factor. $N_i^c = 3$ for quarks, $N_i^c = 1$ and $\hat{\alpha}_s = 0$ for leptons. $K_i = 1$ for bosons. γ_i's are constants shown in Table 5.1.

Solving the RGE for the weak mixing angle in the $\overline{\text{MS}}$ scheme, one obtains

$$\begin{aligned} \hat{s}^2(\mu) =& \hat{s}^2(\mu_0) \frac{\hat{\alpha}_{\text{EM}}(\mu)}{\hat{\alpha}_{\text{EM}}(\mu_0)} + \lambda_1 \left[1 - \frac{\hat{\alpha}(\mu)}{\hat{\alpha}(\mu_0)} \right] + \\ & \frac{\hat{\alpha}_{\text{EM}}(\mu)}{\pi} \left[\frac{\lambda_2}{3} \ln \frac{\mu^2}{\mu_0^2} + \frac{3\lambda_3}{4} \ln \frac{\hat{\alpha}_{\text{EM}}(\mu)}{\hat{\alpha}_{\text{EM}}(\mu_0)} + \tilde{\sigma}(\mu_0) - \tilde{\sigma}(\mu) \right] , \end{aligned} \tag{5.20}$$

with

$$\tilde{\sigma}(\mu) = \frac{\lambda_4}{33 - 2n_q} \frac{5}{36} \left[(11 - 24\zeta_3) \frac{\hat{\alpha}_s^2(\mu)}{\pi^2} + b \frac{\hat{\alpha}_s^3(\mu)}{\pi^3} \right] , \tag{5.21}$$

$$\begin{aligned} b \equiv & \frac{2213}{24} - \frac{6955}{24}\zeta_3 + \frac{99}{2}\zeta_4 + \frac{775}{6}\zeta_5 - n_q \left(\frac{55}{12} - \frac{41}{4}\zeta_3 + 3\zeta_4 + 5\zeta_5 \right) \\ & - \frac{(153 - 19n_q)(11 - 24\zeta_3)}{99 - 6n_q} , \end{aligned} \tag{5.22}$$

where $\tilde{\sigma}(\mu)$ corresponds to contributions to the RGE evolution of the weak mixing angle from quark-antiquark annihilation diagrams at four- and five-loop order that are suppressed in perturbative QCD but give rise to violation of the OZI-rule in the non-perturbative regime. The values of λ_i are summarized in Table 5.2.

Energy range	λ_1	λ_2	λ_3	λ_4
$\bar{m}_t \leq \mu$	$\frac{9}{20}$	$\frac{289}{80}$	$\frac{14}{55}$	$\frac{9}{20}$
$M_W \leq \mu < \bar{m}_t$	$\frac{21}{44}$	$\frac{625}{176}$	$\frac{6}{11}$	$\frac{3}{22}$
$\bar{m}_b \leq \mu < M_W$	$\frac{21}{44}$	$\frac{15}{22}$	$\frac{51}{440}$	$\frac{3}{22}$
$m_\tau \leq \mu < \bar{m}_b$	$\frac{9}{20}$	$\frac{3}{5}$	$\frac{2}{19}$	$\frac{1}{5}$
$\bar{m}_c \leq \mu < m_\tau$	$\frac{9}{20}$	$\frac{2}{5}$	$\frac{7}{80}$	$\frac{1}{5}$
$\bar{m}_s \leq \mu < \bar{m}_c$	$\frac{1}{2}$	$\frac{1}{2}$	$\frac{5}{36}$	0
$\bar{m}_d \leq \mu < \bar{m}_s$	$\frac{9}{20}$	$\frac{2}{5}$	$\frac{13}{110}$	$\frac{1}{20}$
$\bar{m}_u \leq \mu < \bar{m}_d$	$\frac{3}{8}$	$\frac{1}{4}$	$\frac{3}{40}$	0
$m_\mu \leq \mu < \bar{m}_u$	$\frac{1}{4}$	0	0	0
$m_e \leq \mu < m_\mu$	$\frac{1}{4}$	0	0	0
$\mu < m_e$	0	0	0	0

Table 5.2: λ_i's entering the higher order RGE for the weak mixing angle in Eq. (5.20). $\bar{m}_q$'s in the table correspond to the threshold quark masses for quarks defined in a way such that $\hat{\alpha}^+_{\rm EM}(\bar{m}_q) = \hat{\alpha}^-_{\rm EM}(\bar{m}_q)$, where $+$ and $-$ correspond to the effective theories wherein the fermion q is included and excluded respectively. For a detailed discussion on this point, see Ref. [5]. Table adopted from Ref. [5].

Due to the change of λ_i at each threshold, as long as all matching scales μ at which the active particle decouples are known, Eq. (5.20) and the solution to the four-loop QCD β-function [469, 470] together would represent a complete solution. We refer to Refs. [4, 5, 471–473] for a detailed discussion on the matching conditions, Refs. [4, 5, 474–476] for the implementation of experimental input to treat appropriately the non-perturbative effects on $\hat{\alpha}_{\rm EM}$ from QCD using the dispersion integral, Refs. [4, 5, 477] for the discussion on singlet contributions to $\hat{\alpha}_s$ and Refs. [4, 5] for the discussion on flavor separation and threshold masses used for the matching.

The final solution of the running of the weak mixing angle is shown in Figure 5.2, where the blue solid line represents the scale dependence of the weak mixing angle, whose uncertainty is indicated by the thickness of the solid curve. The red dots correspond to the scales where the indicated particles are integrated out. The slope of the weak mixing angle changes sign at $\mu = m_W$, which is a result of overcompensation

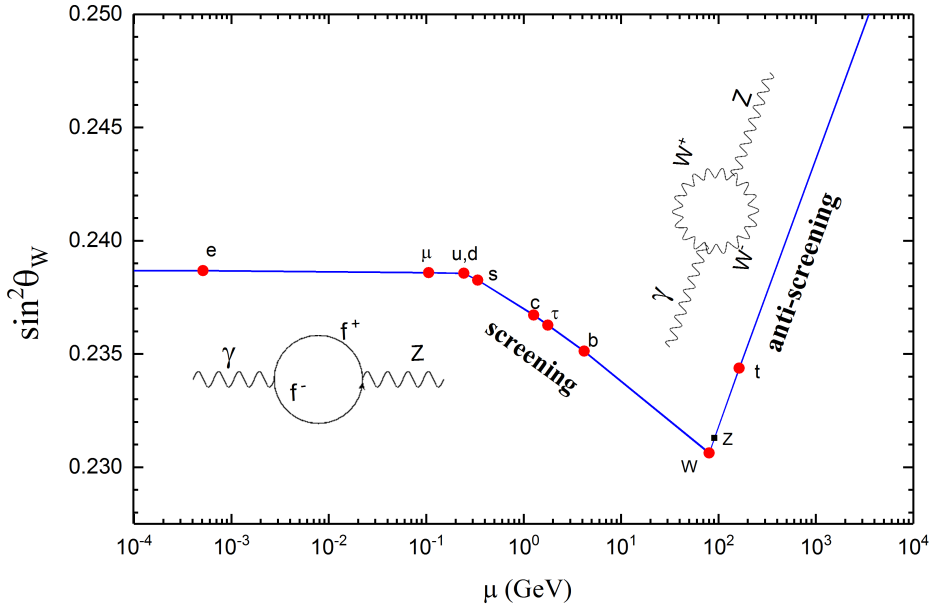

Figure 5.2: Scale dependence of the weak mixing angle in the $\overline{\text{MS}}$ renormalization scheme, where the dots correspond to the scales at which a particle is integrated out. The thickness of the line represents the total uncertainty. Plots adopted from Ref. [4].

of the fermionic screening effects from the bosonic anti-screening effects. At m_W and m_f there are discontinuities arising from the matching conditions which ensure the various effective field theories within a given loop order are describing the same physics. For completeness, we also include theoretical sources of uncertainties and their magnitude in Table 5.3.

5.4 Precision measurements of $\sin^2\theta_W$

In this section, I will discuss precision measurements on the weak mixing angle from current experiments as well as prospects from future programs.

source	$\delta \sin^2 \hat{\theta}_W(0) \times 10^5$
$\Delta\hat{\alpha}^{(3)}(2\text{ GeV})$	1.2
flavor separation	1.0
isospin breaking	0.7
singlet contribution	0.3
PQCD	0.6
Total	1.8

Table 5.3: Theoretical uncertainties in the weak mixing angle at the low energy scale. Table adopted from Ref. [4].

5.4.1 Results from current experiments

First, we will review experimental results from current experiments. The overall status from this aspect is summarized in Figure 5.3 from PDG [1], the details of each experiments is discussed individually below.

5.4.1.1 Atomic Parity Violation (APV)

In 1956 Lee and Yang [478] predicted parity violation, its discovery was observed in nuclear β decay from Wu [479] in 1957, followed by the Nobel Prize in physics awarded to Lee and Yang in 1957. Soon after that, effects of parity violation in atoms, especially in heavy atoms where the parity violation effects can be amplified, were calculated and conclusions were drawn that experimental observation of parity violation could be achieved in heavy atoms such as Cs. The first parity violating signal was observed in 1978 from Bi, followed by a measurement of Tl in 1979 and 1981, which were before the direct observations of $W^{\pm}$ and Z at CERN in 1983.

Since the scale where APV happens is around $1/m_Z$, the interaction can be described by a contact interaction with the following Hamiltonian [468]

$$H_{\text{APV}} = \frac{G_{\text{F}}}{\sqrt{2}} \sum_q \left(C_q^{(1)} \bar{e}\gamma_\mu\gamma_5 e \bar{q}\gamma^\mu q + C_q^{(2)} \bar{e}\gamma_\mu e \bar{q}\gamma^\mu\gamma_5 q \right), \tag{5.23}$$

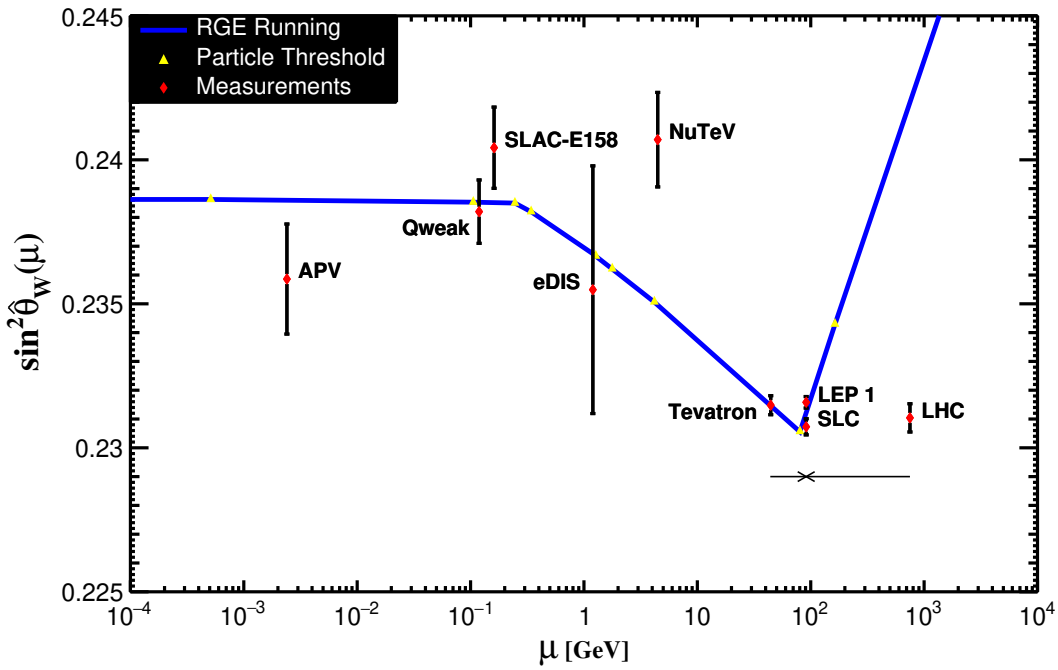

Figure 5.3: Scale dependence of the weak mixing angle in the $\overline{\text{MS}}$ renormalization scheme, where the solid curve corresponds to the running of $\sin^2\hat{\theta}_W$ from Ref. [4] shown in Figure 5.2, yellow triangles on the curve correspond to the thresholds discussed in last section and the red dots indicate experimental results that are discussed in detail in the main text. LHC and Tevatron results are measurements at Z pole same as SLC and LEP 1 results, they are shown horizontally for clarity. Plots adopted from Ref. [1].

where G_F is the Fermi constant and $q = \{u, d, s, \cdots\}$ are quarks. $C_q^{(1)}$ are electron axial-vector currents to the quark-vector currents and $C_q^{(2)}$ are couplings of the electron-vector currents to quark axial-vector currents. Their expressions are

$$C_p^{(1)} = 2C_u^{(1)} + C_d^{(1)}, \quad C_n^{(1)} = C_u^{(1)} + 2C_d^{(1)}, \tag{5.24}$$

where

$$C_p^{(1)} = \frac{1}{2}(1 - 4\sin^2\theta_W), \quad C_n^{(1)} = -\frac{1}{2}, \quad C_p^{(2)} = -C_n^{(2)} = g_A C_p^{(1)}, \tag{5.25}$$

where $g_A \approx 1.26$ is the scale factor accounting for the partially conserved axial-vector current.

The weak charge for a generic atom with proton number Z and nucleon number N is defined as

$$Q_W \equiv 2ZC_p^{(1)} + 2NC_n^{(1)}. \tag{5.26}$$

Note that since $\sin^2\theta_W \approx 1/4$, $Q_W \approx -N$ at "tree level". Radiative corrections to Q_W can be computed, which are typically of $\mathcal{O}(1\%)$. Upon the extraction of Q_W from experimental results and the comparison with its theoretical prediction in the SM, any difference between them would imply new physics beyond the SM.

Now the question is: How to extract Q_W in order to find any hint to new physics? The methods for extracting Q_W from APV are divided into two: The "optical rotation" technique [480] and the Stark interference technique [481]. In the former case, the technique is based on the interference between APV and the allowed magnetic dipole transition amplitudes. Due to parity violation, atoms with left- and right-circularly polarized light will interact differently, leading to a rotation of the polarization vector of linearly polarized light when it passes through an atomic vapor. The rotation angle, which can be measured experimentally, is proportional to the ratio of APV and the magnetic dipole transition amplitude. Historically, this technique has been applied for the first direct measurement of APV in ^{209}Bi in 1978 and was also used for atom ^{209}Pb and ^{205}Tl. The latter technique was used in Cs, Tl and Yb APV experiments, leading to the most accurate result to date from ^{133}Cs. Therefore, we will discuss parity violation measurements in Cs using the Stark interference technique in more detail next.

Cs is an alkali-mental atom with 55 electrons and has only one valence electron outside a tightly bound Xe-like core. Its ground state is [Xe]$6s\ ^2S_{1/2}$, or simply denoted as $6S_{1/2}$ in some literatures. The optical transition between the ground state

$6S_{1/2}$ and an excited state of the same parity $7S_{1/2}$ is forbidden by the parity selection rule, while the weak interaction leads to an admixture of $P_{1/2}$ and $S_{1/2}$, leading to a small electric dipole transition amplitude $E_{\rm APV}$. However, $E_{\rm APV}$ can be amplified by the Stark interference through the application of an external electric field, which induces an additional admixture of P states. Through changing the direction of the external electric field, the excitation rate can be modulated and the APV amplitude $E_{\rm APV}$ can thus be isolated. Through this technique, as long as $E_{\rm APV}$ is known, the weak charge Q_W can be extracted from

$$E_{\rm APV} = k_{\rm APV} Q_W, \tag{5.27}$$

where $k_{\rm APV}$ is the so-called atomic-structure factor.

Experimentally, the measured quantity is $R_{\rm Stark} \equiv {\rm Im}(E_{\rm APV})/\beta$, where β is the vector transition polarizability and ${\rm Im}(E_{\rm APV})$ is the nuclear-spin-independent part of the transition amplitude. The most accurate measurement on $R_{\rm Stark}$ is obtained from a series measurements from the JILA group, achieving an accuracy of 0.35% on $R_{\rm Stark}$. Reaching an equal or better theoretical accuracy for $k_{\rm APV}$ is challenging, and efforts on reducing the theoretical uncertainty of $k_{\rm APV}$ span over two decades [482]. Current uncertainty on $k_{\rm APV}$ is 0.5% from the work of Dzuba *et al* [153], still larger than that in experiments. To be specific, using this method, Dzuba *et al* obtain [153]

$$\delta Q_W(^{133}{\rm Cs}) = 0.65(43) \approx -4Z\delta(\sin^2\theta_W) \Longrightarrow \sin^2\theta_W = 0.2356(20). \tag{5.28}$$

Translating their result from Cs onto the running of the weak mixing angle, the result is shown in Figure 5.3, indicated by the APV data on the left, which corresponds to a low-energy momentum transfer at $Q = 2.4\,{\rm MeV}$.

5.4.1.2 The Qweak experiment

Instead, the Qweak experiment is a precision measurement of the weak charge of the proton, Q_W^p, compared with the APV discussed above. Q_W^p is defined through the Wilson coefficients in the low-energy effective Lagrangian of SM [483]

$$\mathcal{L}_{\rm SM}^{\rm PV} = -\frac{G_F}{\sqrt{2}}\bar{e}\gamma_\mu\gamma_5 e\sum_q C_q^{(1)}\bar{q}\gamma^\mu q, \tag{5.29}$$

and

$$Q_W^p = -2(2C_u^{(1)} + C_d^{(1)}), \tag{5.30}$$

representing the sum of the weak vector couplings of Z boson to the constituent u and d quarks of the proton.

Experimentally, contributions from Z exchange can be separated using the unique parity violating signature of weak interactions as shown in Figure 5.4, and the interference between γ and Z mediated interactions leads to a parity violating asymmetry A_{ep}. The asymmetry A_{ep} can then be measured by an incident longitudinally polarized electron on an unpolarized proton target, resulting in the measured quantity

$$A_{ep} = \frac{\sigma_+ - \sigma_-}{\sigma_+ + \sigma_-}, \tag{5.31}$$

where $\pm$ correspond to the helicity of the incoming electron. Expressing A_{ep} in terms of the momentum transfer Q^2, one has the definition for the reduced asymmetry:

$$\frac{A_{ep}}{A_0} = Q_W^p + Q^2 B(Q^2,\theta), \tag{5.32}$$

where $A_0 = -G_F Q^2/(4\sqrt{2}\pi\alpha_{\rm EM})$, $B(Q^2,\theta)$ is the extended structure of proton defined in terms of electromagnetic, strange and axial form factors, and θ is the polar

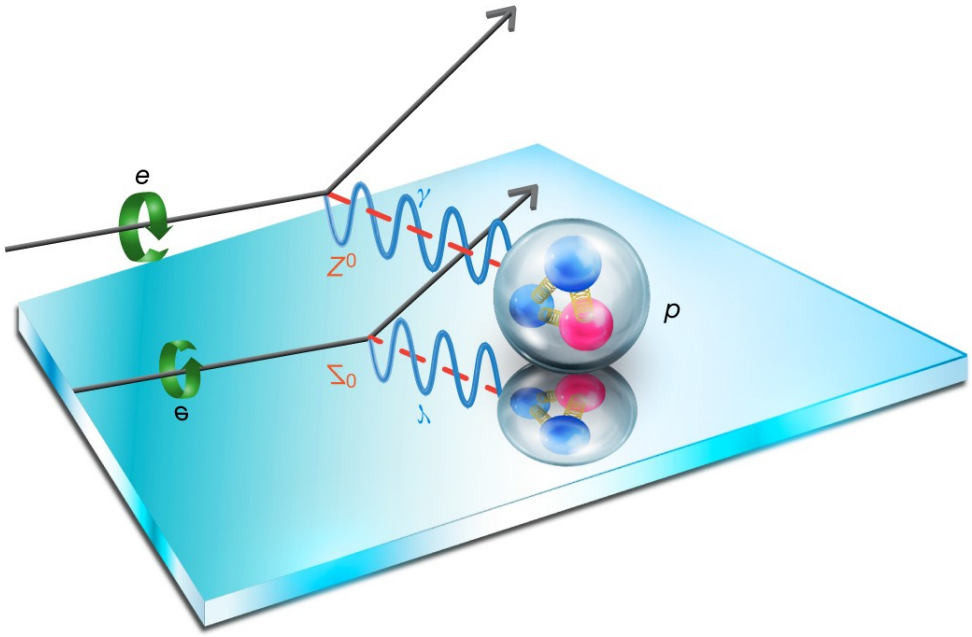

Figure 5.4: Parity-violating scattering of electron from proton. As shown in the plot, incoming electron with helicity +1 scatters away from the mirror, which represents the P transformation. The image in the mirror is an incoming electron with -1 helicity, and it scatters out of the mirror instead of into it as a result of parity violation. Plot adopted from Ref. [15].

scattering angle of the electron in the lab frame with respect to the beam axis. The Qweak experiment only selects events at $\theta = 5.8^\circ$ and 11.6° respectively.

The measured A_{ep} from Qweak is

$$A_{ep} = -226.5 \pm 7.3\,(\text{stat}) \pm 5.8\,(\text{syst})\,\text{ppb}, \tag{5.33}$$

with the total uncertainty being (9.3) ppb, corresponding to a new level of precision for parity-violating electron scattering (PVES) from a nucleus. Using the experimental value of A_{ep}, the Qweak experiment leads to a result for $\sin^2\hat{\theta}_W$ at $Q = 0.158\,\text{GeV}$

$$\sin^2\hat{\theta}_W = 0.23818 \pm 0.0011, \tag{5.34}$$

consistent with SM prediction. The experimental result is shown in Figure 5.3 with label Qweak.

5.4.1.3 The eDIS experiment

The electron-deuteron deep inelastic scattering (eDIS) experiment [451, 452], instead of using atoms, uses the deuteron as the target, corresponding to the process

$$e(\text{polarized}) \ + \ d(\text{unpolarized}) \rightarrow e' + X, \tag{5.35}$$

where X represents particles we do not care about for this experiment. The beam energy is 19.4 GeV with an averaged polarization being 0.37 and the energy of the scattered electron ranges from 10.2 GeV to 16.3 GeV. The parity violation effect in this process is a result from the interference between the weak neutral current and the electromagnetic current, leading to an asymmetry, called the left-right asymmetry, defined as

$$A_{\text{PV(eDIS)}} \equiv \frac{\sigma_R - \sigma_L}{\sigma_R + \sigma_L}, \tag{5.36}$$

with $\sigma_{L(R)}$ the inelastic scattering cross section for a left (right)-handed incident electron. The general form of $A_{\text{PV(eDIS)}}$ can be written as

$$\frac{A_{\text{PV(eDIS)}}}{Q^2} = a_1 + a_2 \times \frac{1-(1-y)^2}{1+(1-y)^2}, \tag{5.37}$$

where $y \equiv (E_0 - E')/E_0$ with E_0 and E' the energy of the incident and the scattered electrons respectively and Q is the momentum transfer. In general, $a_{1,2}$ may depend on kinematic parameters except for an isoscalar target such as deuterium where they become constants and are related to the weak mixing angle. $a_{1,2}$ can be determined by varying the values of y. The values of y for this experiment lie within the range $0.15 \leq y \leq 0.36$. Upon the determination of $a_{1,2}$, as a result, one is also able to determine $\sin^2\theta_W$.

From the measured asymmetry $A_{\mathrm{PV(eDIS)}}$ with Q^2 varied between $1\,\mathrm{GeV}^2$ and $1.9\,\mathrm{GeV}^2$, they determined

$$a_1 = (-9.7 \pm 2.6) \times 10^{-5}, \quad a_2 = (4.9 \pm 8.1) \times 10^{-5}, \tag{5.38}$$

leading to

$$\sin^2 \theta_W = 0.224 \pm 0.020, \tag{5.39}$$

where the error comes from a linear combination of two sources: a fitting error of 0.012 and a systematic uncertainty of the beam polarization of 0.008. The result is quite consistent with the prediction of the SM, and the experimental result is also plotted in Figure 5.3.

5.4.1.4 The PVDIS experiment

The second result from parity-violating deep inelastic scattering (PVDIS) was obtained recently in 2014 [484], about 40 years after the eDIS though PVES played a key role in testing and the picking out the SM from other models as the one for particle physics in the past. In 40 years after eDIS, PVDIS was the only experiment measuring the asymmetry. The difference between eDIS and PVDIS is that: eDIS, as well as Qweak and APV obtained a precision measurement on $C_q^{(1)}$ corresponding to four-fermion contact interacting strength with axial electron currents and vector quark currents, while PVDIS is more sensitive to the vector electron current and axial quark currents $C_q^{(2)}$ due to the energy range difference between these two categories. The PVIDS focused on regions with large Bjorken x where hadron structure barely affect the asymmetry and the QCD effects can be isolated by the kinematic dependence. In this regime, the asymmetry can be written as

$$A_{\mathrm{PV(PVDIS)}} = \frac{\sigma_R - \sigma_L}{\sigma_R + \sigma_L}$$

$$= \frac{G_F Q^2}{4\sqrt{2}\pi\alpha_{\rm EM}} \left[a_1(x,Q^2) Y_1(x,y,Q^2) + a_3(x,Q^2) Y_3(x,y,Q^2) \right], \qquad (5.40)$$

where $y = (E - E')/E$ with E and E' the energy of the incoming and outgoing electrons respectively, x the Bjorken scaling variable and

$$a_1 = \frac{6}{5}(2C_u^{(1)} - C_d^{(1)}), \quad a_3 = \frac{6}{5}(2C_u^{(2)} - C_d^{(2)}). \qquad (5.41)$$

Experimentally, one could extract a_1 and a_3 by varying Y_1 and Y_3, however, a precision determination of a_3 is difficult because its smallness. To be specific, $a_1 = -0.719$, and $a_3 = -0.095$ as predicted in the SM. This difficulty was overcome by the use of a custom electronic nd data acquisition system, and with a total of about 170 billion scattered electrons, the symmetry was measured to be

$$(A_{\rm PV(PVDIS)})_{\rm exp1} = [-91.1 \pm 3.1({\rm stat}) \pm 3.0({\rm sys})] \times 10^{-6} \qquad (5.42)$$

with $E = 6.067\,{\rm GeV}$, $\langle x \rangle = 0.241$, $Y_1 = 1.0$, $Y_3 = 0.44$ and $\langle Q^2 \rangle = 1.085\,{\rm GeV}^2$. Another measurement gave

$$(A_{\rm PV(PVDIS)})_{\rm exp2} = [-160.8 \pm 6.4({\rm stat}) \pm 3.1({\rm sys})] \times 10^{-6} \qquad (5.43)$$

with $E = 6.067\,{\rm GeV}$, $\langle x \rangle = 0.295$, $Y_1 = 1.0$, $Y_3 = 0.69$ and $\langle Q^2 \rangle = 1.901\,{\rm GeV}^2$. In both cases, x and Q^2 are averaged over the spectrometer acceptance and the asymmetry is to be compared with SM prediction, which is

$$(A_{\rm PV(PVDIS)})_{\rm SM} = -87.7 \times 10^{-6}, \qquad (5.44)$$

with an uncertainty of 0.7×10^{-6}, dominantly coming from the uncertainty in PDF and parameterizations of how partons that form the nucleon carry the nucleon's energy.

To extract a_1 and a_3, the MSTW2008 leading-order PDF parameterization of the asymmetry was applied and one found, corresponding to the two experiments,

$$(A_{\mathrm{PV(PVDIS)}})_{\mathrm{SM1}} = (1.156 \times 10^{-4})[(2C_u^{(1)} - C_d^{(1)}) + 0.348(2C_u^{(2)} - C_d^{(2)})], \quad (5.45)$$

$$(A_{\mathrm{PV(PVDIS)}})_{\mathrm{SM2}} = (2.022 \times 10^{-4})[(2C_u^{(1)} - C_d^{(1)}) + 0.594(2C_u^{(2)} - C_d^{(2)})], \quad (5.46)$$

resulting a value of

$$(2C_u^{(2)} - C_d^{(2)})\,|_{Q^2=0} = -0.145 \pm 0.066(\mathrm{exp}) \pm 0.011(\mathrm{PDF}) \pm 0.012(\mathrm{HT}), \quad (5.47)$$

by using the values of $C_{u,d}^{(1)}$ from APV(Cs). Here, the "HT" uncertainty comes from the so-called higher-twist effects from interactions among quarks inside the target. Note that the result above is consistent with SM prediction, which gives

$$(2C_u^{(2)} - C_d^{(2)})\,|^{\mathrm{SM}}_{Q^2=0} = -0.0950 \pm 0.0004, \quad (5.48)$$

Interpreting the result in terms of the weak mixing angle evolved at Z pole in the $\overline{\mathrm{MS}}$ scheme is

$$\sin^2\hat{\theta}_W = 0.2299 \pm 0.0043, \quad (5.49)$$

consistent with SM prediction but the uncertainty is much larger than other high-energy results at the Z pole, thus this result is not shown in Figure 5.3.

5.4.1.5 The SLAC-E158 experiment

Another low energy precision measurement of the weak neutral current is the SLAC-E158 experiment, which, like the Qweak experiment, also goes into the PVES category. Instead of *ep* scattering, the SLAC-E158 experiment employs longitudinally

polarized electrons scatter off unpolarized electrons, resulting in a parity-violating asymmetry $A_{\rm PV}$ from the interference of the electromagnetic and the weak amplitudes. The asymmetry is generically defined as

$$A_{\rm PV(E158)} \equiv \frac{\sigma_R - \sigma_L}{\sigma_R + \sigma_L}, \tag{5.50}$$

where L, R correspond to the handness of incoming electrons and $\sigma_{L(R)}$ are the cross sections for incident left (right)-handed electrons. At tree level [485],

$$A_{\rm PV(E158)} = \frac{G_\mu Q^2}{\sqrt{2}\pi\alpha_{\rm EM}} \frac{1-y}{1+y^4+(1-y)^4} \left(1 - 4\sin^2\theta_W\right), \tag{5.51}$$

where G_μ is the Fermi constant determined from muon lifetime, Q^2 is the momentum transfer and $y = Q^2/s$ with s the Mandelstam variable. Since $\sin^2\theta_W \approx 1/4$ at tree level, the asymmetry is sensitive to the weak mixing angle. Compared with experiments discussed above and will be discussed below, the Møller scattering also benefit from the fact that it is a pure leptonic reaction with little theoretical uncertainty. We summarize how the experiment works below.

The high-intensity longitudinally polarized electron beam is delivered in $\sim 270\,$ns pulses at the rate of $120\,$Hz, it then passes through a $1.57\,$m long cylindrical cell filled with liquid hydrogen. The scattered electrons are then selected by the magnetic spectrometer within $4.4 < \theta_{\rm lab} < 7.5\,$mrad over the full azimuthal range, while the primary beam and forward angle photons pass unimpededly to the beam dump. Then sixty meters downstream of the target, the scattered electrons, or the Møller electrons, in the range of 13-24 GeV form an azimuthally symmetric ring and are spatially separated from electrons scattered from target protons, which corresponds to *ep* scattering. The charged particle flux is then finally seized by the primary copper/fused silica fiber sandwich calorimeter with both radial and azimuthal segmentation. Among them, four radial rings are uniformly covered azimuthally by 10,

20, 20 and 10 photomultipliers with the inner three rings, usually referred to as the Inner, Middle and Outer Møller rings, predominantly sensitive to Møller scattered electrons, while with the Outermost ring to the bulk of the *ep* scattering flux. The asymmetry is then measured by extracting the fractional difference in the integrated calorimeter response for incident right- and left-handed electrons and after run I, II and III, the combined result from SLAC-E158 is

$$A_{\mathrm{PV(E158)}} = -131 \pm 14\,(\mathrm{stat}) \pm 10\,(\mathrm{stat})\,\mathrm{ppb}, \tag{5.52}$$

corresponding to,

$$\sin^2\theta_W^{\mathrm{eff}} = 0.2397 \pm 0.0010\,(\mathrm{stat}) \pm 0.0008\,(\mathrm{syst}) \tag{5.53}$$

at $Q^2 = 0.026\,\mathrm{GeV}^2$. Translated to the $\overline{\mathrm{MS}}$ scheme, the result is shown in Figure 5.3 indicated by SLAC-E158.

5.4.1.6 The NuTeV experiment

The NuTeV experiment provides another precision measurement of the weak mixing angle at $Q \approx 4.47\,\mathrm{GeV}$ [154], which extracts the value of $\sin^2\theta_W$ from neutrino-nucleon scattering. At the momentum transfer, the Lagrangian for weak neutral current ν-q scattering can be written as [154]

$$\mathcal{L} = -\frac{G_F\rho_0}{\sqrt{2}}\left[\bar{\nu}\gamma^\mu\left(1-\gamma^5\right)\nu\right] \times \left[\epsilon_L^q\bar{q}\gamma_\mu\left(1-\gamma^5\right)q + \epsilon_R^q\bar{q}\gamma_\mu\left(1+\gamma^5\right)q\right], \tag{5.54}$$

where $\rho_0 = 1$ in the SM and any deviations from that would indicate non-standard sources of $\mathrm{SU(2)_L}$ breaking, $\epsilon_{L,R}^q$ are the chiral quark couplings that have the following values

$$\epsilon_L^q = \begin{cases} T_3^{\mathrm{weak}}, & \text{for weak charged current} \\ T_3^{\mathrm{weak}} - Q_q\sin^2\theta_W, & \text{for weak neutral current} \end{cases}, \tag{5.55}$$

$$\epsilon_R^q = \begin{cases} 0, & \text{for weak charged current} \\ -Q_q \sin^2\theta_W, & \text{for weak neutral current} \end{cases}, \tag{5.56}$$

where Q_q is the electric charge of quarks in units of e.

At the NuTeV experiment, the measured quantity is the ratio of neutral current to charged current cross sections for either ν or $\overline{\nu}$ scattering from isoscalar targets of u and d quarks, which can be written as [486]

$$R^{\nu(\overline{\nu})} \equiv \frac{\sigma\left(\overset{(-)}{\nu} N \to \overset{(-)}{\nu} X\right)}{\sigma\left(\overset{(-)}{\nu} N \to \ell^{-(+)} X\right)} = (g_L^2 + r^{(-1)} g_R^2), \tag{5.57}$$

$$r \equiv \frac{\sigma(\overline{\nu} N \to \ell^+ X)}{\sigma(\nu N \to \ell^- X)} \sim \frac{1}{2}, \tag{5.58}$$

with

$$g_{L,R}^2 = (\epsilon_{L,R}^u)^2 + (\epsilon_{L,R}^d)^2. \tag{5.59}$$

Corrections to $R^{\nu(\overline{\nu})}$ can be obtained from the presence of heavy sea quarks, production of heavy quarks in the target, higher order terms in $\sigma\left(\overset{(-)}{\nu} N \to \overset{(-)}{\nu} X\right)$ and $\sigma\left(\overset{(-)}{\nu} N \to \ell^{-(+)} X\right)$ and isovector component of light quarks in the target. Especially, when a final-state c quark is produced from a d or s quark in the nucleon, large uncertainties arise from mass suppression of the c quark. This uncertainty has limited the precision of measurements of $\sin^2\theta_W$ in the neutrino-nucleon scattering experiments.

One solution to reduce the aforementioned uncertainty from c quark production is suggested by Paschos and Wolfenstein [487] using the following observabale

$$R^- \equiv \frac{\sigma\left(\nu_\mu N \to \nu_\mu X\right) - \sigma\left(\bar{\nu}_\mu N \to \bar{\nu}_\mu X\right)}{\sigma\left(\nu_\mu N \to \mu^- X\right) - \sigma\left(\bar{\nu}_\mu N \to \mu^+ X\right)} \tag{5.60}$$

$$= \frac{R^{\nu} - rR^{\bar{\nu}}}{1-r} = \left(g_L^2 - g_R^2\right). \tag{5.61}$$

However, R^- is more difficult to measure than $R^{\nu(\overline{\nu})}$. The main reason is that the final state from the neutral current scattering of ν and $\overline{\nu}$ can not be distinguished without knowing the initial state neutrino *a priori*. Therefore, the NuTeV experiment adopted $R^{\nu(\overline{\nu})}$ as the measured quantity to extract the value of $\sin^2\theta_W$. For that purpose, one needs to separate the events into charged current and neutral current ones. This can be done by utilizing the fact that muon neutrino charged current events typically come with a charged muon in the final state that can be recognized by the scintillation counters, while neutral current events usually do not have any final state muons. Using this difference, the NuTeV group find

$$R^{\nu}_{\text{exp}} = 0.3916 \pm 0.0007, \quad R^{\bar{\nu}}_{\text{exp}} = 0.4050 \pm 0.0016, \tag{5.62}$$

from which the value of $\sin^2\theta_W$ can be extracted. Fixing $\rho_0 = 1$, they find, in the on-shell scheme,

$$\sin^2\theta_W = 0.2227 \pm 0.0004. \tag{5.63}$$

Fitting ρ_0 and $\sin^2\theta_W$ simultaneously, they find

$$\rho_0 = 0.9983 \pm 0.0040, \quad \sin^2\theta_W = 0.2265 \pm 0.0031. \tag{5.64}$$

Recall that $Q \approx 4.47\,\text{GeV}$, result of $\sin^2\theta_W$ from NuTeV is shown in Figure 5.3 after translating to the $\overline{\text{MS}}$ scheme.

5.4.1.7 The LEP experiment

Different from low-energy measurements above, the LEP experiment and the SLC experiment, which we will discuss next, are both high-energy experiments performed at the Z pole. Here in this subsubsection, we focus on the LEP experiment first.

Due to parity violation, fermion-antifermion pair in the final state from Z decay will possess different polarizations. At the LEP, the detectors are only sensitive to the polarizations of τ leptons in final state, making them capable of measuring an asymmetry from the weak neutral current. The asymmetry, which we will define below, depends on the vector and axial vector couplings of the weak neutral current. In the SM, the couplings are directly related to the effective weak mixing angle we discussed in section 5.3.1. Therefore, utilizing this will-be-defined asymmetry from $Z \to \tau\bar{\tau}$ below, we can achieve a precision measurement on the weak mixing angle.

The polarization of τ from the decay of Z is defined as [488]

$$P_\tau \equiv P_{\tau^-} \equiv \frac{\sigma_+ - \sigma_-}{\sigma_+ + \sigma_-} = -P_{\tau^+}, \tag{5.65}$$

where $\sigma_{+(-)}$ is the production cross-section of τ^- leptons with positive (negative) helicity and $P_{\tau^{-(+)}}$ represents the polarization of $\tau^{-(+)}$. Upon the assumption that the incoming electrons from the source beam at LEP are unpolarized, the lowest order differential cross sections for $\sigma_{+(-)}$ can be expresses as [488]

$$\frac{1}{\sigma_{\text{total}}}\frac{d\sigma_+}{d\cos\theta_{\tau^-}} = \frac{3}{16}\left[(1+\langle P_\tau\rangle)\left(1+\cos^2\theta_{\tau^-}\right) + \frac{8}{3}\left(\mathrm{A_{FB}} + \mathrm{A_{pol}^{FB}}\right)\cos\theta_{\tau^-}\right], \tag{5.66}$$

$$\frac{1}{\sigma_{\text{total}}}\frac{d\sigma_-}{d\cos\theta_{\tau^-}} = \frac{3}{16}\left[(1-\langle P_\tau\rangle)\left(1+\cos^2\theta_{\tau^-}\right) + \frac{8}{3}\left(\mathrm{A_{FB}} - \mathrm{A_{pol}^{FB}}\right)\cos\theta_{\tau^-}\right], \tag{5.67}$$

where θ_{τ^-} is the angle between the incoming e^- and the outgoing τ^-, $\sigma_{\text{total}} = (\sigma_+ + \sigma_-)_{-1<\cos\theta_{\tau^-}<1}$ and $\langle P_\tau\rangle$ is averaged polarization of τ defined as [488]

$$\langle P_\tau\rangle \equiv \frac{(\sigma_+)_{-1<\cos\theta_{\tau^-}<1} - (\sigma_-)_{-1<\cos\theta_{\tau^-}<1}}{\sigma_{\text{total}}}. \tag{5.68}$$

The forward-backward asymmetry $A_{\rm FB}$ of the τ pair is defined as [488]

$$A_{\rm FB} \equiv \frac{(\sigma)_{\cos\theta_{\tau^-}>0} - (\sigma)_{\cos\theta_{\tau^-}<0}}{\sigma_{\rm total}}, \tag{5.69}$$

and the forward-backward τ polarization asymmetry is defined as [488]

$$A_{\rm pol}^{\rm FB} \equiv \frac{(\sigma_+ - \sigma_-)_{\cos\theta_{\tau^-}>0} - (\sigma_+ - \sigma_-)_{\cos\theta_{\tau^-}<0}}{\sigma_{\rm total}}. \tag{5.70}$$

Putting together, Eq. (5.66) and Eq. (5.67) imply [488]

$$P_\tau(\cos\theta_{\tau^-}) = \frac{\langle P_\tau\rangle(1+\cos^2\theta_{\tau^-}) + \frac{8}{3}A_{\rm pol}^{\rm FB}\cos\theta_{\tau^-}}{(1+\cos^2\theta_{\tau^-}) + \frac{8}{3}A_{\rm FB}\cos\theta_{\tau^-}}. \tag{5.71}$$

The observables $\langle P_\tau\rangle$, $A_{\rm pol}^{\rm FB}$ and $A_{\rm FB}$ defined above can be extracted from data, whose values include contributions from Z and γ exchange, $\gamma - Z$ mixing as well as photonic radiative corrections. At LEP where $\sqrt{s}$ is near m_Z, the pure Z exchange process dominates the polarization due to the resonance. When only the pure Z exchange is taken into account,[ii] remarkably simple results can be obtained:

$$\langle P_\tau\rangle = -\mathcal{A}_\tau, \quad A_{\rm pol}^{\rm FB} = -\frac{3}{4}\mathcal{A}_e, \tag{5.72}$$

with the asymmetry parameters defined as [488]

$$\mathcal{A}_\ell \equiv \frac{2g_{V\ell}/g_{A\ell}}{1+(g_{V\ell}/g_{A\ell})^2}, \tag{5.73}$$

where $g_{V\ell}$ and $g_{A\ell}$ are the effective vector and the axial vector couplings of $Zf\bar{f}$ as discussed in more detail in Ref. [489]. In the context of SM,

$$g_{V\ell}/g_{A\ell} = 1 - 4\sin^2\theta_{\rm eff}^{\rm lept}, \tag{5.74}$$

[ii] For a more general discussion, see Ref. [489] for example.

and that is why we claim above that we can extract the effective weak mixing angle from $\langle P_\tau \rangle$, $A_{\rm pol}^{\rm FB}$ and $A_{\rm FB}$ at LEP.

Using the data obtained with the OPAL detector at LEP I and based on a simultaneous analysis of $\tau \to e\nu_e\nu_\tau$, $\tau \to \mu\nu_\mu\nu_\tau$, $\tau \to \pi\nu_\tau$, $\tau \to \rho\nu_\tau$ and $\tau \to 3\pi^\pm\nu_\tau$, the fitted result for $g_{V\ell}$ and $g_{A\ell}$ are [456]

$$g_{V\ell} = -0.0358 \pm 0.0014, \quad g_{A\ell} = -0.50089 \pm 0.00045, \tag{5.75}$$

reasulting in, at $Q = m_Z$,

$$\sin^2\theta_{\rm eff}^{\rm lept.} = 0.23211 \pm 0.00068, \tag{5.76}$$

in agreement with SM prediction and representing one of the most precise measurements to date.

5.4.1.8 The SLD experiment

The SLD experiment [453–455] at the SLAC Linear Collider (SLC) is another high-energy experiment at the Z pole. Different from SLAC-E158 and the LEP experiments, the SLD experiment obtained the left-right asymmetry in two ways: (1) from Bhabha scattering $e^+e^- \to e^+e^-$ and (2) from the hadronic and $\tau^+\tau^-$ decay of Z. We will discuss them separately below. The measured left-right asymmetry is a result of parity violation from the Z boson exchange, defined as

$$A_{\rm PV(SLC)} = \frac{\sigma_L - \sigma_R}{\sigma_L + \sigma_R}, \tag{5.77}$$

with $\sigma_{L(R)}$ the production cross section of e^+e^- from Z decay with left (right)-handed incident electrons. At leading order in SM, the asymmetry is predicted to be

$$A_{\rm PV(SLC)} = \frac{2(1 - 4\sin^2\theta_{\rm eff}^{\rm lept})}{1 + (1 - 4\sin^2\theta_{\rm eff}^{\rm lept})^2}, \tag{5.78}$$

again, we see that since $\sin^2\theta_{\rm eff}^{\rm lept} \approx 1/4$, the asymmetry $A_{\rm PV(SLC)}$ is very sensitive to the value of $\sin^2\theta_{\rm eff}^{\rm lept}$.

To measure the asymmetry at SLC, the analysis was done in two ways: (1) In the Bhabha case, the experiment utilizes the calorimetry systems of the SLD detector, where small angle coverage in the 28-65 mrad range from the beam line is provided by the finely-segmented silicon-didode/tungsten-radiator luminosity calorimeters (LUM). The LUM measurement in this small angle range also provides a check of the smallness of $A_{\rm PV(SLC)}$. Events at larger angles, > 200 mrad, from the beamline are measured with the liquid argon calorimeter (LAC), covering 98% of the solid angle with projective tower segmentation. The systematic uncertainties due to detector misalignment in the LUM is minimized by employing the "gross-precise" method, while events in the LAC are selected making use of the distinct topology of the e^+e^- final state with the efficiency and contamination from $e^+e^- \to \gamma\gamma$ and $e^+e^- \to \tau^+\tau^-$ calculated from Monte Carlo simulations. From the combined 1992 and 1993 date, the effective mixing angle is measured to be

$$\sin^2\theta_{\rm eff}^{\rm lept} = 0.2245 \pm 0.0049({\rm stat}) \pm 0.0010({\rm syst}). \tag{5.79}$$

(2) In the hadronic and $\tau^+\tau^-$ decay of Z case, as indicated by its name, $A_{\rm PV(SLC)}$ is measured by counting hadronic and $\tau^+\tau^-$ decay of Z for each of the two longitudinal polarization states of the electron beam. The measurement requires knowledge of the absolute beam polarization, but not that of the absolute luminosity, detector acceptance or efficiency, which, in the Bhabha case, are however required. Using a sample of 49,392 Z decays, the effective mixing angle is determined to be

$$\sin^2\theta_{\rm eff}^{\rm lept} = 0.2292 \pm 0.0009({\rm stat}) \pm 0.0004({\rm syst}), \tag{5.80}$$

representing another most precise measurement of the mixing angle at the Z pole besides that at LEP.

5.4.1.9 The Tevatron experiment

Drell-Yan lepton pairs are produced through $\bar{p}p \to \ell^+\ell^-$ mediated by γ/Z at the Fermilab Tevatron proton-antiproton collider, where X represents any other inclusive products from the collision. The forward-backward asymmetry, defined below, in the polar-angle distribution of ℓ^- as a function versus the invariant mass of the $\ell^+\ell^-$ pair turns out to be sensitive to the effective leptonic weak mixing angle $\sin^2\theta_{\rm eff}^{\rm lept}$ in the Collins-Soper frame [490]. To see how it works, we can look at the Drell-Yan production of lepton pairs at the Born level, i.e.

$$q\bar{q} \to \gamma^* \to \ell^+\ell^-, \quad q\bar{q} \to Z \to \ell^+\ell^-, \tag{5.81}$$

where γ^* represents an off-shell photon. The interaction vertex $Z\bar{q}q$ contains both vector and axial vector parts, which, at Born-level, can be written as

$$g_V^f = T_3^f - 2Q_f \sin^2\theta_W, \quad g_A^f = T_3^f. \tag{5.82}$$

The dependence of the forward-backward asymmetry on the effective weak mixing angle becomes clear when working in the Collins-Soper frame, wherein the polar angle ϑ is defined as

$$\cos\vartheta = \frac{l_+^- l_-^+ - l_-^- l_+^+}{M\sqrt{M^2 + p_T^2}}, \tag{5.83}$$

where $l_\pm = (E \pm p_z)$ with the superscripts $\pm$ of l indicating the electric charge of the charged lepton, E, p_T and p_z are the energy, the transverse momentum and the momentum component along the lab axis of the negatively charged lepton respectively,

and M is the invariant mass of the lepton pair in the final state. On the other hand, the azimuthal angle φ in this frame is given by

$$\tan\varphi = \frac{\sqrt{M^2 + p_T^2}}{M} \times \frac{\vec{\Delta}\cdot\hat{R}_T}{\vec{\Delta}\cdot\hat{p}_T}, \tag{5.84}$$

where $\hat{R}_T$ is the unit vector along $\vec{p}_p \times \vec{p}$ with $\vec{p}_p$ and $\vec{p}$ the spatial momentum of proton and the lepton-pair respectively, and $\hat{p}_T$ is the unit vector along the transverse momentum of the lepton pair.

The general angular distribution of the lepton pair can then be expressed as [491, 492]

$$\begin{aligned}\frac{dN}{d\Omega} \propto \left(1+\cos^2\vartheta\right) + A_0\frac{1}{2}\left(1-3\cos^2\vartheta\right) + A_1\sin 2\vartheta\cos\varphi + \\ A_2\frac{1}{2}\sin^2\vartheta\cos 2\varphi + A_3\sin\vartheta\cos\varphi + A_4\cos\vartheta + \\ A_5\sin^2\vartheta\sin 2\varphi + A_6\sin 2\vartheta\sin\varphi + A_7\sin\vartheta\sin\varphi,\end{aligned} \tag{5.85}$$

with $A_{0-3,5-7}$ functions of kinematic variables that all approach zero when the transverse momentum of the lepton pari approaches zero. A_4, on the other hand, does not behave similarly, instead, it is responsible for the generation of the forward-backward asymmetry in $\cos\vartheta$. Its violation of the parity comes from two sources: The interference between the Z vector and axial vector amplitudes and the interference between the photon vector and the Z axial vector amplitudes. At born level, one has [493]

$$A_4\cos\vartheta = T_3^\ell(1-4|Q_\ell|\sin^2\theta_W)T_3^q(1-4|Q_q|\sin^2\theta_W), \tag{5.86}$$

implying the possibility to extract the weak mixing angle from the asymmetry.

More specifically, the aforementioned forward-backward asymmetry is defined as

$$A_{\rm fb}(M) = \frac{\sigma_f(M)-\sigma_b(M)}{\sigma_f(M)+\sigma_b(M)} = \frac{3}{8}A_4(M), \tag{5.87}$$

with $\sigma_{f(b)}$ the Drell-Yan production cross section for the forward (backward) orientation of the lepton pair with $\cos\vartheta \geq 0$ ($\cos\vartheta < 0$).

After a combined analysis of the CDF and the D0 measurements, the Tevatron experiment gives [493]

$$\sin^2\theta_{\rm eff}^{\rm lept} = 0.23148 \pm 0.00033, \tag{5.88}$$

with the leading uncertainty coming from statistics and the sub-leading uncertainty from parton distribution function (PDF). Using the `ZFITTER` package [494], the corresponding weak mixing angle in the on-shell scheme is

$$\sin^2\theta_W = 0.22324 \pm 0.00033. \tag{5.89}$$

5.4.1.10 The LHC experiment

The forward-backward asymmetry discussed in section 5.4.1.9 is also measured by the LHCb [495], the ATLAS [496] and the CMS [497, 498] collaboration at the LHC with $\sqrt{s}_{\rm LHCb} = 7\,{\rm TeV}$ and $8\,{\rm TeV}$, $\mathcal{L}_{\rm LHCb} = 1{\rm fb}^{-1}$ and $2{\rm fb}^{-1}$, $\sqrt{s}_{\rm ATLAS} = 7\,{\rm TeV}$, $\mathcal{L}_{\rm ATLAS} = 4.8{\rm fb}^{-1}$, and $\sqrt{s}_{\rm CMS} = 8\,{\rm TeV}$, $\mathcal{L}_{\rm ATLAS} = 18.8{\rm fb}^{-1}$ and $19.6{\rm fb}^{-1}$ respectively. After a careful analysis with millions of events, they obtain[iii]

$$(\sin^2\theta_{\rm eff}^{\rm lept})_{\rm LHCb} = 0.23142 \pm 0.00073({\rm stat}) \pm 0.00052({\rm syst}) \pm 0.00056({\rm theo}), \tag{5.90}$$

$$(\sin^2\theta_{\rm eff}^{\rm lept})_{\rm ATLAS} = 0.2308 \pm 0.0005({\rm stat}) \pm 0.0006({\rm syst}) \pm 0.0009({\rm PDF}), \tag{5.91}$$

$$\begin{aligned}(\sin^2\theta_{\rm eff}^{\rm lept})_{\rm CMS} = 0.23101 &\pm 0.00036({\rm stat}) \pm 0.00018({\rm syst}) \\ &\pm 0.00016({\rm theo}) \pm 0.00031({\rm PDF}),\end{aligned} \tag{5.92}$$

[iii] Here we only cite the published numbers. For ATLAS, the preliminary result they recently obtain is $(\sin^2\theta_{\rm eff}^{\rm lept})_{\rm ATLAS-preliminary} = 0.23140 \pm 0.00021({\rm stat}) \pm 0.00016({\rm syst}) \pm 0.00024({\rm PDF})$ [499], which is much improved compared with the latest published result in the main text, and the preliminary result of the comparison among LEP, SLD, Tevatron, LHCb, CMS and ATLAS on the measurement of the weak mixing angle can also be found in figure 11 of Ref. [499].

where "stat", "syst", "theo" and "PDF" represent uncertainties from statistics, systematics, theory and PDF respectively. The ATLAS group incorporates theoretical uncertainties into the systematic uncertainties, while the LHCb group incorporates PDF uncertainties into theoretical uncertainties. PDF uncertainties remain the dominant source for the uncertainties included in the analysis for each group and needs to be reduced in future experiments.

5.4.2 Prospects from future experiments

From our discuss in last subsection, one can note that currently the world's leading results come from the LEP and the SLC experiments. However, the SLC result differs from LEP result 3σ [16], and adopting either the SLC result or the LEP result could result in very different physics beyond the SM [457]. The difference still remains an issue to be understood. In the near future, several low-energy and high-energy experiments are ongoing, aiming to provide more independent precision measurements on the weak mixing angle and possibly also to provide some hint for new physics. In the next subsection, we will briefly review the these experiments. Note that not all the proposals discussed below have a main goal at providing a better measurement on the weak mixing angle, however, here we will only focus on the discussion related to precision measurement of the weak mixing angle. For their other scientific goals, we refer to the original paper from each proposal. On the other hand, some future projects such as weak mixing angle measurements at future colliders are still under development/proposal, for these projects, we will mainly discuss theoretical study or proposed determination of the weak mixing angle.

5.4.2.1 The MOLLER project

The MOLLER experiment, abbreviated for Measurement Of a Lepton Lepton Electroweak Reaction, is a proposal low-energy experiment at the Jefferson Laboratory, aiming at improving the the SLAC-E158 result discussed above by a factor a

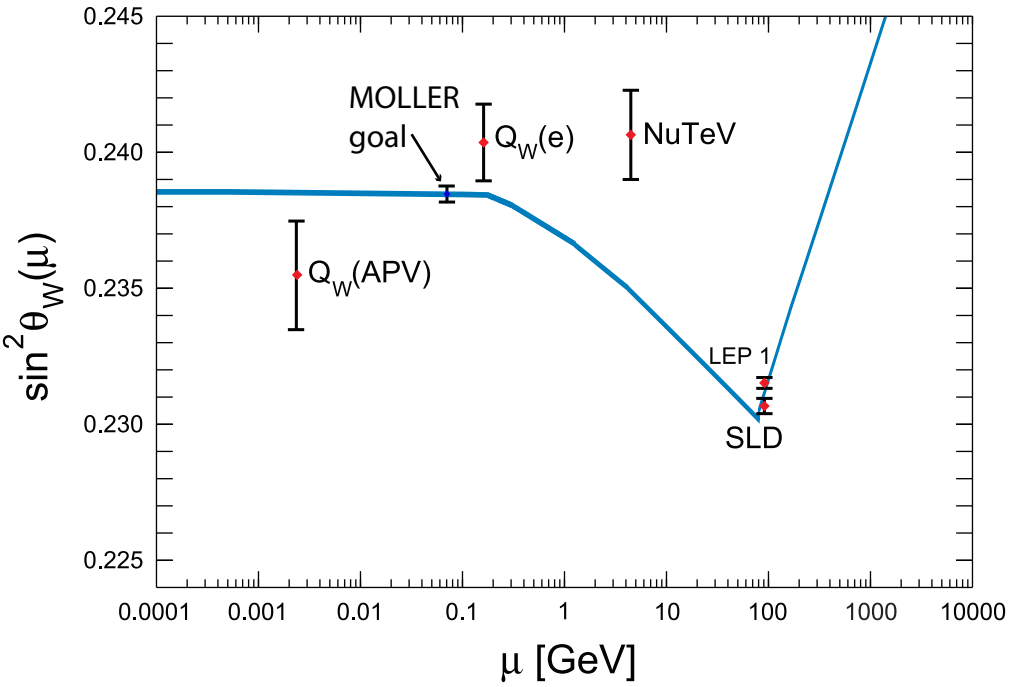

Figure 5.5: Precision comparison for the determination of the weak mixing angle. Plot adopted from Ref. [16].

five [16]. The improved result will correspond to the most precise measurement of the weak mixing angle at low or high energy experiments in the next decade, making it also a sensitive probe of new physics at the $(O)(10-100)$ TeV scale though the scale is model dependent.

To achieve that goal, the MOLLER experiment aims at measuring the left-right asymmetry from Møller scattering employing the upgraded 11 GeV beam in Hall A at the Jefferson Laboratory. The 11 GeV electron beam is longitudinally polarized before scattering off the 1.5 m liquid hydrogen target. The Møller electrons, i.e. beam electrons scattering off target electrons, in the full azimuthal range and the polar angle range within 5mrad $< \theta <$ 17 mrad are separated from the background before being brought into the Møller ring. The Møller ring would then be seized by a system of quartz detectors, resulting in Cherenkov light that would provide a relative measure of the scattered flux.

Developing of the techniques to produce ultra-stable polarized electron beam and systematic control at the parts per billion (ppb) level and calibration techniques to control normalization errors like the electron beam polarization at the percent level have been continuously improved since the proposal. For a detailed discussion, see for example [16].

The goal of MOLLER is to measure $A_{\mathrm{PV(Møller)}}$ to an overall fractional accuracy of 2.4%, corresponding to a determination of the weak mixing angle of

$$\delta(\sin^2\theta_W) = \pm 0.00028, \tag{5.93}$$

at the same level of precision with the LEP and the SLC experiments. Comparison between Møller and other precision experiments discussed above is included in Figure 5.5 for completion.

5.4.2.2 The Mainz MESA P2 project

Similar to Qweak, the MESA P2 project also use *ep* scattering and aims at measuring parity-violating asymmetry that can result in a determination of the weak mixing angle at a precision level of 0.13% [17]. The asymmetry from the scattering is defined through the cross sections:

$$A_{\mathrm{PV(P2)}} = \frac{\sigma_L - \sigma_R}{\sigma_L + \sigma_R}, \tag{5.94}$$

with $\sigma_{L(R)}$ the cross section from a left (right)-handed incident electron. In terms of the weak charge of proton, the asymmetry can be expressed as [17]

$$A_{\mathrm{PV(P2)}} = \frac{G_F Q^2}{4\sqrt{2}\pi\alpha_{\mathrm{EM}}}(Q_W^p + F(Q^2)), \tag{5.95}$$

with $F(Q^2)$ usually written as $F(Q^2) = Q^2 B(Q^2)$ like in Eq. (5.32). Q_W^p is the proton weak charge, defined as the limit of the asymmetry in vanishing momentum transfer,

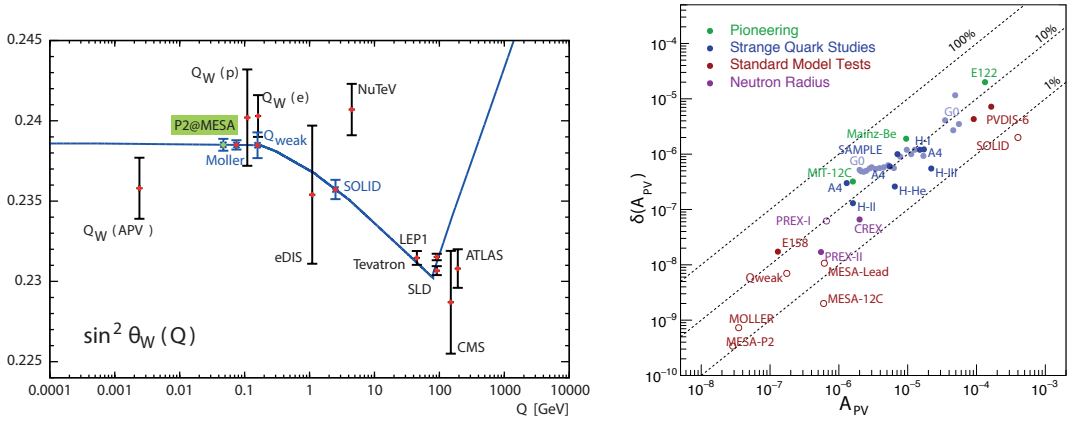

Figure 5.6: Comparison between MESA P2 and other experiments for the measurement of the weak mixing angle (left) and the uncertainty of the parity-violating asymmetry (right). Plots adopted from Ref. [17, 18].

normalized in a way such that Eq. (5.95) holds, i.e. $F(0) = 0$. Neglecting radiative corrections, the tree-level expression for the weak charge of proton is very simple

$$Q_W^p = 1 - 4\sin^2\theta_W, \tag{5.96}$$

using the Gaussian error propagation and $\sin^2\theta_W \approx 0.23$ for estimation, one finds,

$$\frac{\delta(\sin^2\theta_W)}{\sin^2\theta_W} = \frac{1-4\sin^2\theta_W}{4\sin^2\theta_W}\cdot\frac{\delta Q_W^p}{Q_W^p} \approx 0.09\cdot\frac{\delta Q_W^p}{Q_W^p}, \tag{5.97}$$

implying that a precision measurement of the proton weak charge can lead to approximately a factor of 10 improvement on the determination of the weak mixing angle.

To achieve a precision measurement of the proton weak charge, several techniques have been developed or under developing for the P2 experiment: The Mainz Energy-Recovery Superconducting Accelerator (MESA) is being built to meet the stability requirement for P2; An invasive double Mott polarimeter at the electron source and a Hydro-Møller polarimeter will be simultaneously applied to improve the beam polarization at a level better than 0.5%; A closed recirculating cryogenic liquid hydrogen

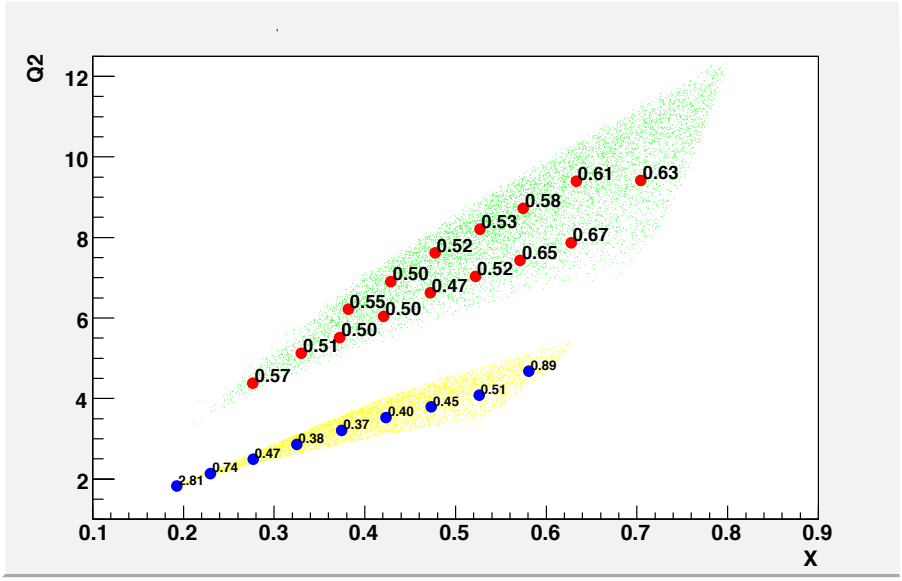

Figure 5.7: Projected uncertainties for $A_{\mathrm{PV(SoLID)}}$ in percent as a function of Q^2 and x. The green and yellow dots are from 11 GeV and 6.6 GeV beam respectively. Plots adopted from Ref. [19].

target loop will be built to provide a high luminosity liquid hydrogen for the measurement of the very small asymmetry with a very high precision; and a large superconducting solenoid will be designed and used for the P2 spectrometer to improve statistics and suppress backgrounds from Møller scattering and/or bremsstrahlung.

The prospect of the MESA P2 experiment together with its comparison with other experiments are shown in Figure 5.6.

5.4.2.3 Weak mixing angle at SoLID

The SoLID, abbreviated for Solenoidal Large Intensity Device, is a proposed experiment at the Jefferson Lab, aiming to improve the precision compared with that at PVDIS discussed in last section in order to obtain a better determined $C_{u,d}^{(2)}$ and thus a value for $\sin^2\hat{\theta}_W$ with higher precision. Due to the importance of $C_{u,d}^{(2)}$ in the determination of the weak mixing angle, the goal of SoLID is to achieve a similar precision level of $C_{u,d}^{(2)}$ compared with $C_{u,d}^{(1)}$ from other PVES experiments discussed in last section.

	Experiment	Theory error	Main sources
$\sin^2\theta^{\ell}_{\text{eff}}$	0.23153 ± 0.00016	4.5×10^{-5}	$\alpha^3_{\text{EM}}, \alpha^2_{\text{EM}}\alpha_s$

Table 5.4: Current value for the effective leptonic mixing angle, its theoretical error and its main error sources.

	Measurement error			Intrinsic theory	
	ILC	CEPC	FCC-ee	Current	Future
$\sin^2\theta^{\ell}_{\text{eff}}(\times 10^6)$	1	2.3	0.6	4.5	1.5

Table 5.5: Prospects of precision measurements on the weak mixing angle from future colliders including ILC, CEPC and FCC-ee, together with estimated theoretical errors in the last two columns.

The SoLID project is still under development, however, as stated in the conceptual design [19, 500, 501], the apparatus is able to measure $A_{\text{PV(SoLID)}}$ for about 20 kinetic points shown in Figure 5.7 with the Bjorken scale $x > 0.4$ and the momentum transfer $1 \lesssim Q^2 \lesssim 12\,\text{GeV}^2$ with a statistical precision of about 0.5%, resulting in roughly an order of magnitude improvement on the uncertainty of the asymmetry as can be see from the right panel of Figure 5.6.

5.4.2.4 Weak mixing angle at future high-energy colliders

Due to the fact that colliders that will be discussed in this subsection are not operating yet, what we will present here is a summary of their prospects on measuring the weak mixing angle from theoretical estimation. For a recent review, see Ref. [502].

In terms of the effective leptonic mixing angle, the current status is given in Table 5.4 from [503]. In the future, proposed e^+e^- colliders such as the GigaZ option of the ILC [504], the FCC-ee [505, 506] and the CEPC [135] colliders will operate at a level that will lead to a more precise determination of the mixing angle, the projected values are, respectively, shown in Table 5.5.

As is obvious from Table 5.5, current theoretical calculation for the SM predictions will become insufficient in the future, and it turns out at least a major part of the

three-loop and the partial four-loop corrections should be computed to reduce the uncertainties. In recent years, many efforts have been put on the study on FCC-ee, whose the uncertainties for $A_{\rm fb}^{\mu\mu}$ are 3×10^{-6} and $2-5 \times 10^{-6}$ for statistical and systematic respectively. For the FCC-ee Tera-Z, the estimated uncertainties for $\delta(\sin^2\theta_{\rm eff}^{\ell})$ are 6×10^{-6} and 7×10^{-6} on the experimental and the theoretical sides respectively [507], where the theoretical uncertainties in the last two columns of Table 5.5 are obtained from a rough estimate on electroweak 3-loop and the dominant 4-loop electroweak-QCD corrections [131, 503, 507–509].

5.4.2.5 Weak mixing angle at DUNE

The Deep Underground Neutrino Experiment (DUNE) [510] is a long-baseline neutrino experiment with a neutrino beam and a near detector at Fermilab and a far detector at the Sanford Underground Research Facility, which is 1300 km away from Fermilab. Especially, the DUNE experiment will exploit the high-intensity, broad-band Long-Baseline Neutrino Facility (LBNF) neutrino beam and the long baseline to make a comprehensive precision measurements, including the neutrino mass hierarchy.

Due to the high beam intensity at DUNE and the relatively small uncertainties in the neutrino-electron cross section compared with that in neutrino-nucleus scattering from nuclear and non-perturbative effects, it has been recently studied to use DUNE as a probe to precisely measure the weak mixing angle [20]. Challenges, however, do exist: (1) The cross section for neutrino-electron scattering is about three orders of magnitude smaller than that for neutrino-nucleus scattering, resulting in a smaller statistics; (2) Neutrinos at DUNE are from the inflight decay of charged mesons, first-principles calculations of the meson production rate and kinematics are not possible and one needs to rely on phenomenological models and experimental data, resulting in neutrino flux and energy distribution uncertainties.

To reduce some of the uncertainties in the flux and cross sections, the DUNE-PRISM near detector is designed. The near detector is capable of moving in the direction perpendicular to the neutrino beam axis. Since the ratios of on-axis and off-axis fluxes can be described by meson-decay kinematics only, the uncertainties in the neutrino-electron scattering spectrum can be reduced at different off-axis positions, thus a precise measurement of the weak mixing angle is made possible. The weak mixing angle is related to the neutrino-electron scattering cross section as

$$\begin{aligned}\frac{d\sigma}{dE_R} &= \frac{2G_F^2 m_e}{\pi}\left\{g_1^2 + g_2^2\left(1-\frac{E_R}{E_{\nu_\alpha}}\right)^2 - g_1 g_2 \frac{m_e E_R}{E_{\nu_\alpha}^2}\right\} \\ &\simeq 1.72\times 10^{-41}\left\{g_1^2 + g_2^2\left(1-\frac{E_R}{E_{\nu_\alpha}}\right)^2\right\}\frac{\mathrm{cm}^2}{\mathrm{GeV}},\end{aligned} \tag{5.98}$$

where m_e is the electron mass, E_R is the recoil energy of the electron and $\alpha = e, \mu, \tau$ stands for the neutrino flavor. The couplings $g_{1,2}$ depend on the flavor of neutrinos, which is summarized below:

ν_α	g_1	g_1(SM)	g_2	g_2(SM)
ν_e	$1+(g_V+g_A)/2$	$1/2+\sin^2\theta_W$	$(g_V-g_A)/2$	$\sin^2\theta_W$
$\nu_{\mu,\tau}$	$(g_V+g_A)/2$	$-1/2+\sin^2\theta_W$	$(g_V-g_A)/2$	$\sin^2\theta_W$
$\bar{\nu}_e$	$(g_V-g_A)/2$	$\sin^2\theta_W$	$1+(g_V+g_A)/2$	$1/2+\sin^2\theta_W$
$\bar{\nu}_{\mu,\tau}$	$(g_V-g_A)/2$	$\sin^2\theta_W$	$(g_V+g_A)/2$	$-1/2+\sin^2\theta_W$

Table 5.6: Expression for $g_{1,2}$ in terms of vector and axial vector couplings and their values in the SM.

Due to kinematics and the energy profile of DUNE neutrino flux, $0.2 \lesssim E_R \lesssim 10\,\mathrm{GeV}$, corresponding to $10 \lesssim Q^2 \lesssim 100\,\mathrm{MeV}^2$. In this range, the weak mixing angle is insensitive to the running scale as can be seen from Figure 5.2.

To accumulate events, the authors assume a 75 ton fiducial mass liquid argon time projection chamber and a 1.2 MW proton beam with years of data taking equally di-

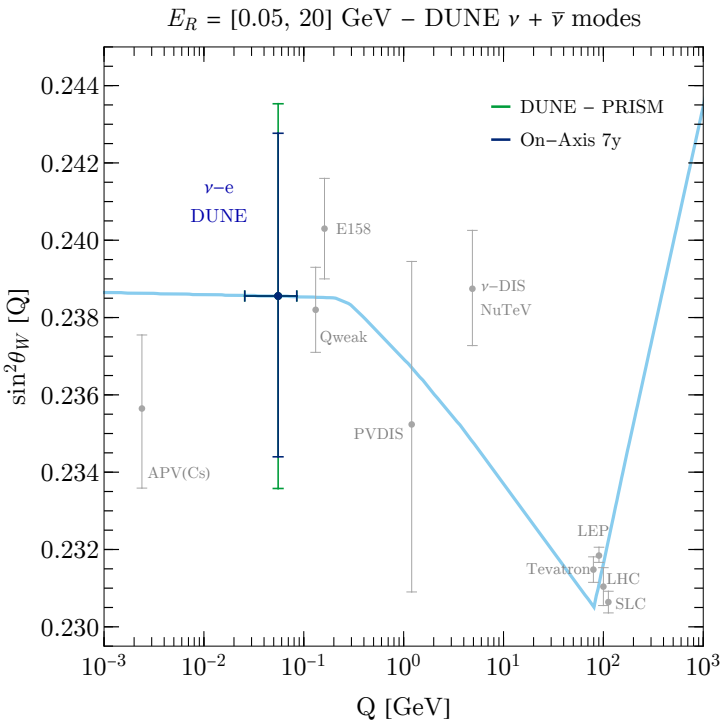

Figure 5.8: DUNE sensitivity to the determination of the weak mixing angle. The dark blue data point is the fitting result from DUNE on-axis and the green data is for DUNE-PRISM. The horizontal error bars correspond to the range of Q^2 discussed in the main text. Plots adopted from Ref. [20].

vided between neutrino and antineutrino modes. To account for the energy-dependent neutrino-flux uncertainties and the correlations between the fluxes at different off-axis angles, they use the covariance matrix spanning all DUNE-PRISM positions and neutrino flavors. The backgrounds are simulated with the NuWro event generator [511]. Translating their results into a measurement of the weak mixing angle, their result is shown in Figure 5.8.

5.4.2.6 Weak mixing angle from Coherent Elastic Neutrino Nucleus Scattering (CENNS) experiments

The first observation of the CENNS events by the COHERENT Collaboration [512] and future experiments like GEMMA [513] that is expected to improve the precision of the former, provide new opportunities to precisely measure the weak

mixing angle. Recent work has focus on the case of the TEXONO [514] and the NONUS [515] experiments, which is later reanalyzed in [6], which also includes future prospects of the CONNIE [516,517], the MINER [518] and the RED100 [519] research programs.

The dependence on the weak mixing angle in the CENNS experiments can be seen explicitly from the coherent scattering cross section

$$\left(\frac{d\sigma}{dT}\right)_{\rm SM}^{\rm coh} = \frac{G_F^2 M}{2\pi}\left[1 - \frac{MT}{E_\nu^2} + \left(1 - \frac{T}{E_\nu}\right)^2\right]\left[Z g_V^p F_Z\left(Q^2\right) + N g_V^n F_N\left(Q^2\right)\right]^2, \tag{5.99}$$

where M is the mass of the nucleus, E_ν the neutrino energy, T the nucleus recoil energy, Q^2 the momentum transfer, $F_{Z,N}(Q^2)$ are the nuclear form factors, and $g_V^{n,p}$ the neutral current vector couplings given by [520]

$$g_V^p = \rho_{\nu N}^{NC}\left(\frac{1}{2} - 2\hat{\kappa}_{\nu N}\sin^2\theta_W\right) + 2\lambda^{uL} + 2\lambda^{uR} + \lambda^{dL} + \lambda^{dR}, \tag{5.100}$$

$$g_V^n = -\frac{1}{2}\rho_{\nu N}^{NC} + \lambda^{uL} + \lambda^{uR} + 2\lambda^{dL} + 2\lambda^{dR}, \tag{5.101}$$

with radiative corrections included and $\rho_{\nu N}^{NC} = 1.0082, \sin^2\theta_W = 0.23129, \hat{\kappa}_{\nu N} = 0.9972, \lambda^{uL} = -0.0031, \lambda^{dL} = -0.0025, \lambda^{dR} = 2\lambda^{uR} = 7.5 \times 10^{-5}$. Note that the explicit dependence of the cross section on the weak mixing angle.

Upon the χ^2 analysis by assuming the experiments mentioned above (1) are capable of a 100% efficiency, (2) are capable of a 50% efficiency and (3) are with current systematic uncertainty from the theoretical antineutrino flux and with a statistical error corresponding to a 100% efficiency, they obtain sensitivity for each experiment summarized in the table below: Finally, the prospects of CENNS experiments are also shown in the running of the weak mixing angle plot for comparison.

experiment	50 % $\delta_{\sin^2\theta_W}$	eff. %	100 % $\delta_{\sin^2\theta_W}$	eff. %	including $\delta_{\sin^2\theta_W}$	systematics %
TEXONO	0.0015	0.6	0.0011	0.5	0.0028	1.2
RED100	0.0004	0.2	0.0003	0.1	0.0031	1.3
MINER	0.0010	0.4	0.0007	0.3	0.003	1.3
CONNIE	0.0023	1.0	0.0017	0.7	0.003	1.3
CONUS	0.0003	0.1	0.0002	0.1	0.0023	1.0

Table 5.7: Expected sensitivity to the weak mixing angle for each experiment quoted with 1σ expected sensitivity in the case of a 50 % (100%) efficiency of the experiment and for the case where the systematic error equals the current reactor spectrum uncertainty. Table adapted from [6].

5.4.2.7 Weak mixing angle at the Super Charm-Tau factories

Precision measurements at flavor factories such as low-energy electron-positron colliders CESR(-c), BEPC, BEPC II, PEP-II and KEKB, have produced a rich harvest of fundamental physics and the new generation of experiments, the super flavor factories, are upcoming, especially, the Super B-factory SuperKEKB has already being taken data, and two Super Charm-Tau (SCT) factories are also under consideration. [521, 522]. Both the two SCT factories are planning to measure the left-right asymmetry from longitudinally polarized incident electrons. The asymmetry is a result of the parity-violating interaction of the Z boson with leptons leading to degeneracy of $e^+e^- \to J/\psi$ cross section from the interference between $e^+e^- \to \gamma^* \to \bar{c}c$ and $e^+e^- \to Z \to \bar{c}c$. The asymmetry

$$A_{\mathrm{LR(SCT)}} = \frac{\sigma_R - \sigma_L}{\sigma_R + \sigma_L}, \tag{5.102}$$

with $\sigma_{L(R)}$ the J/ψ production cross section from left (right)-handed incident electrons. At tree-level, SM prediction of the asymmetry can be written as [523]

$$A_{\mathrm{LR(SCT)}} = \frac{3 - 8\sin^2\theta^c_{\mathrm{eff}}}{16\sin^2\theta^c_{\mathrm{eff}}(1 - \sin^2\theta^c_{\mathrm{eff}})} \times \left(\frac{m_{J/\psi}}{m_Z}\right)^2 \approx 4.7 \times 10^{-4}, \tag{5.103}$$

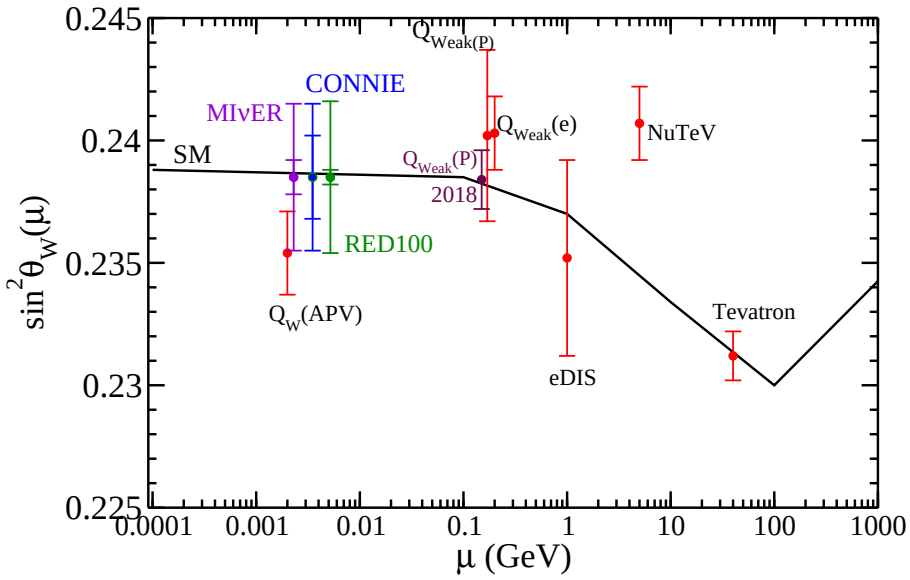

Figure 5.9: Expected sensitivity of CENNS experiments to the weak mixing angle in the $\overline{\text{MS}}$ scheme, where $Q_{W(e)}$ represents the SLAC-E158 result and $Q_{Weak(P)}$ represents the Qweak result. Plots adopted from Ref. [6].

where $m_{J/\psi} = 3096.9\,\text{MeV}$, $m_Z = 91.19\,\text{GeV}$ and $\sin^2\theta^c_{\text{eff}} \approx 0.23$ are used to obtain the numerical number in the last step. Experimentally, the asymmetry would also be affected by the polarization of the incident electron beam $\mathcal{P}_e$, and it turns out that relative uncertainties of about 1% on $A^{\text{exp}}_{\text{LR(SCT)}} \equiv A_{\text{LR(SCT)}}\mathcal{P}_e$ and $\mathcal{P}_e$ is needed to obtain a precise measurement on the weak mixing angle [522], wherein the authors claim that the expected statistical precision of the weak mixing angle is $\delta(\sin^2\theta^c_{\text{eff}})/\sin^2\theta^c_{\text{eff}} \approx 0.3\%$, which would approach the current most precise measurements from LEP and SLC discussed above.

5.4.2.8 Global analysis from low-energy neutrino experiments

For completeness, we also include the recent global analysis studied in Ref. [21], where the global analysis is done to all available neutrino-electron scattering data from reactor antineutrino experiments. Their combined result from reactor and accelerator data for the weak mixing angle is $\sin^2\theta_W = 0.254\pm0.024$, the precision level is far from

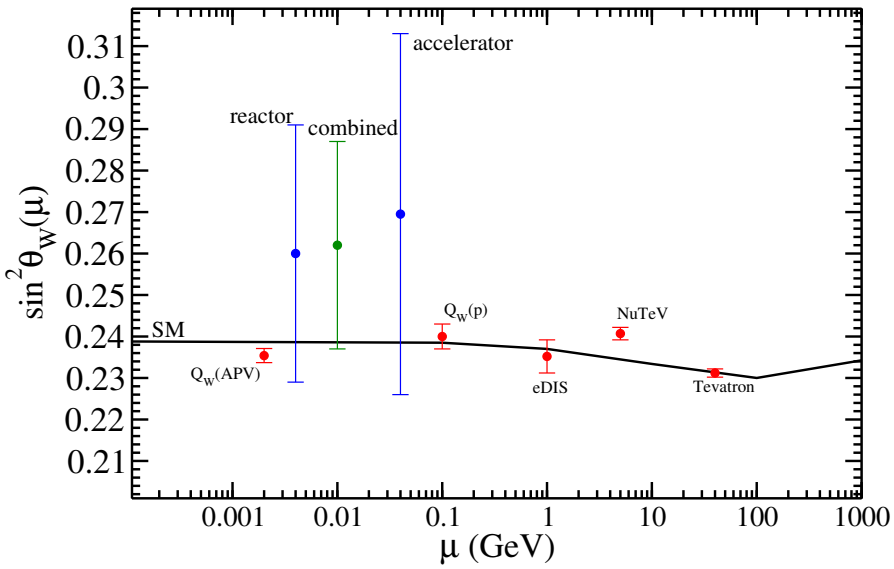

Figure 5.10: Global fitting of the weak mixing angle in the $\overline{\text{MS}}$ scheme from low-energy neutrino experiments. Plot adopted from Ref. [21].

that compared with experiments we discussed above. Nevertheless, their result on the running plot of the weak mixing angle in the $\overline{\text{MS}}$ scheme is shown in Figure 5.10.

5.5 Sensitivity to new physics from low-energy precision measurements on $\sin^2\theta_W$

With more and more precise measurements on the weak mixing angle coming out in the near future, the natural question one can ask is: How will these precision measurements be sensitive to new physics? To answer this question, various efforts have been spent on this topic [502, 524–528]. In this section, we summarize the sensitivity to new physics from low-energy precision measurements on the weak mixing angle by looking at the parity-violating observables. We follow the discussion in Ref. [524].

For each parity-violating observables discussed in last section, the quantity of interest is the weak charge Q_W, either the weak charge of the nucleus $Q_W^{\text{N,P}}$ or the

weak charge of the electron Q_W^e. In general, they can be written formally as

$$Q_W = Q_W^0 + \Delta Q_W, \tag{5.104}$$

where Q_W^0 is the prediction from the SM and ΔQ_W indicates any possible contributions from new physics. Suppose no new light degrees of freedom below the weak scale and that any possible new physics scale Λ is much higher than the weak scale, the dynamics of this kind of new physics can then be parameterized by the following contact interaction:

$$\mathcal{L}^{\mathrm{PV}} = \mathcal{L}_{\mathrm{SM}}^{\mathrm{PV}} + \mathcal{L}_{\mathrm{NP}}^{\mathrm{PV}}, \tag{5.105}$$

with

$$\mathcal{L}_{\mathrm{SM}}^{\mathrm{PV}} = \frac{G_F}{2\sqrt{2}} g_A^e \bar{e}\gamma_\mu\gamma_5 e \sum_f g_V^f \bar{f}\gamma^\mu f, \tag{5.106}$$

$$\mathcal{L}_{\mathrm{NP}}^{\mathrm{PV}} = \frac{4\pi\kappa^2}{\Lambda^2} \bar{e}\gamma_\mu\gamma_5 e \sum_f h_V^f \bar{f}\gamma^\mu f, \tag{5.107}$$

where $g_V^f = 2T_3^f - 4Q_f \sin^2\theta_W$ and $g_A^f = -2T_3^f$. h_V^f characterizes the interaction between the electron axial vector current and the vector current of fermion f induced from any new physics. κ sets the coupling strength that roughly takes $\kappa^2 \sim 1$ for strongly interacting and $\kappa^2 \sim \alpha_{\mathrm{EM}}$ for weakly interacting theories. Note that contributions to ΔQ_W from new scalar-pseudoscalar or tensor-pseudotensor interactions are not included. Interactions between the electron vector current and the axial vector current of f are not included either since they do not contribute to Q_W.

The Lagrangian above then leads to corrections to the weak charge in the following form

$$\Delta Q_W^P = \zeta \left(2h_V^u + h_V^d\right), \tag{5.108}$$

$$\Delta Q_W^N = \zeta \left(h_V^u + 2h_V^d \right), \tag{5.109}$$

$$\Delta Q_W^e = \zeta h_V^e, \tag{5.110}$$

with

$$\zeta = \frac{8\sqrt{2}\pi\kappa^2}{\Lambda^2 G_F}. \tag{5.111}$$

Assuming g_V^f and h_V^f entering Q_W and ΔQ_W are of the same order of magnitude, the fractional correction induced by the new physics can be written as

$$\frac{\Delta Q_W}{Q_W^0} = \frac{8\sqrt{2}\pi\kappa^2}{\Lambda^2 G_F}, \tag{5.112}$$

resulting a lower bound on the mass scale of the new physics of

$$\Lambda \geqslant \left[\frac{8\sqrt{2}\pi\kappa^2}{0.01 G_F} \right]^{1/2} \approx 20\kappa \,\mathrm{TeV}, \tag{5.113}$$

upon the assumption that a one percent or better level of the determination of Q_W can be achieved. This level of precision determination is indeed at the precision level that can be reached by the most precise MOLLER and the MESA P2 projects in the next decade. Given the energy scale at which the MOLLER and the MESA P2 projects will be operating, their complementary role in searching for new physics is impressive compared with that from high-energy collider searches.

There are also discussion on reachability of new physics from future low-energy and high-energy experiments and constraints on the scale of new physics from some well-known models such as the Z' model, the leptoquark model etc. See Refs. [16, 19, 484, 500, 501, 528–544] for example.

5.6 Motivation for NNLO calculations of $\sin\theta_W$

From our discussion, the MOLLER is the one with the best precision goal among the other proposed low energy precision measurements on the weak mixing angle. An EFT study has found that the MOLLER project could be sensitive to new physics at the TeV or even tens of TeV scale. However, before we can claim any hint of new physics, SM prediction for the measured quantity shall at least match the experimental precision goal. To that end, previous studies have concluded a full two-loop corrections to the weak mixing angle need to be calculated [545–550]. In Chapter 8, we will present our work on this part, which represents the first complete calculation of a gauge invariant and dominant subset of the full two-loop corrections to the weak mixing angle from SM.

CHAPTER 6

TYPE-II SEESAW SCALAR TRIPLET MODEL AT A FUTURE 100 TEV pp COLLIDER

6.1 Introduction

As discussed in Chapter 2, the origin of neutrino masses is a key open problem in particle physics, and at tree level, only three mechanisms known as types I, II, and III models [58–72, 74, 75, 551] are responsible for neutrino masses. From eqs. (2.43), (2.49) and (2.53), one can see that the type-II seesaw mechanism [63, 65–68, 75] is the only one reachable at current and near future colliders. In light of this, we consider the complex triplet Higgs model (CTHM) within the type-II seesaw framework in this chapter.

In this model, the neutrino mass m_ν is governed by the product of Yukawa couplings h_ν and the vacuum expectation value (vev) v_Δ of the neutral component of a complex triplet Δ that transforms as (1,3,2) under the SM gauge groups. Constraints from electroweak precision tests require that v_Δ be no larger than a few GeV, though it could be considerably smaller. Consequently, the Yukawa couplings h_ν may be as large as $\mathcal{O}(1)$.

On the other hand, the introduced complex triplet Δ may enhance the stability of the SM Higgs potential through interactions between Δ and the Higgs doublet Φ as has been noted in Refs. [552–555]. In addition, Δ-Φ interactions may also allow for a SFOEWPT, thereby providing the needed conditions for generation of the

cosmic baryon asymmetry through EWBG discussed in Chapter 3.[i] In both cases, knowledge of the Higgs portal couplings λ_4 and λ_5 (defined below) is essential. This study represents our first effort to provide a roadmap for discovery of the Δ and determination of its scalar sector couplings, building on the results of earlier studies that focus on the collider phenomenology of the Δ at LEP and the LHC as well as its impact contributions on the SM Higgs di-photon decay rate [553, 556–634].

Searches for the complex triplet scalars – including doubly charged $H^{\pm\pm}$, singly charged $H^{\pm}$, and neutral Higgs particles H and A – have been carried out at the LHC. A smoking gun signature for the CTHM has conventionally been the presence of the $H^{\pm\pm}$ decaying into a same-sign di-lepton final state and has been intensively investigated by the ATLAS and CMS collaboration [22, 23, 635–641]. For other channels related to CTHM discovery, there are also many studies have been done at the LHC, see Appendix A.1 for a detailed summary. In what follows, we explore the potential for both discovery of the Δ and determination of its scalar sector couplings at a prospective future 100 TeV proton-proton collider, such as the Super Proton Proton Collider (SppC) under consideration in China and the CERN Future Circular Collider (FCC-hh). Given the higher center of mass energy and prospective integrated luminosity, a 100 TeV pp collider will provide coverage for a considerably larger portion of model parameter space than is feasible with the Large Hadron Collider (LHC). In this context, there exist two distinct mass spectra for the Δ (governed by the model parameters), as discussed in detail in section 6.3.1. In this chapter, we will only focus on the "normal mass hierarchy" where $m_h \leq m_{H/A} \approx m_\Delta \leq m_{H^\pm} \leq m_{H^{\pm\pm}}$ with m_Δ the mass scale of the model.

[i] However, we will not discuss EWBG from the CTHM in this chapter, and using the CTHM to explain the BAU via EWBG remains unexplored at the time this thesis is written.

6.2 The Complex Triplet Higgs Model (CTHM)

We start by setting up the CTHM as well as various model constraints in this section. The model key features is also discussed in section 6.2.3, and the Type-II seesaw mechanism is briefly reviewed in the CTHM along with our discussion on current constraints on the neutrino masses.

6.2.1 The CTHM

The type-II seesaw model contains the SM Higgs doublet Φ with hypercharge $Y_\Phi = 1$ and the complex triplet Higgs field Δ with hypercharge $Y_\Delta = 2$ [65] written in a matrix form [62, 63, 66, 67]

$$\Phi = \begin{bmatrix} \varphi^+ \\ \frac{1}{\sqrt{2}}(\varphi + v_\Phi + i\chi) \end{bmatrix}, \quad \Delta = \begin{bmatrix} \frac{\Delta^+}{\sqrt{2}} & H^{++} \\ \frac{1}{\sqrt{2}}(\delta + v_\Delta + i\eta) & -\frac{\Delta^+}{\sqrt{2}} \end{bmatrix}, \tag{6.1}$$

where v_Φ denotes the doublet vev satisfying $\sqrt{v_\Phi^2 + v_\Delta^2} \equiv v \approx 246\,\text{GeV}$, which is the scale of electroweak spontaneous symmetry breaking (EWSB). From the quantum charges of Φ and Δ, the kinetic Lagrangian can be written as

$$\mathcal{L}_{\text{kin}} = (D_\mu \Phi)^\dagger (D^\mu \Phi) + \text{Tr}[(\text{D}_\mu \Delta)^\dagger (\text{D}^\mu \Delta)], \tag{6.2}$$

with the covariant derivatives defined as

$$D_\mu \Phi = \left(\partial_\mu + i\frac{g_2}{2}\tau^a W_\mu^a + i\frac{g_1 Y_\Phi}{2} B_\mu \right) \Phi, \tag{6.3}$$

$$D_\mu \Delta = \partial_\mu \Delta + i\frac{g_2}{2}[\tau^a W_\mu^a, \Delta] + i\frac{g_1 Y_\Delta}{2} B_\mu \Delta. \tag{6.4}$$

The most general CTHM potential can be written as

$$V(\Phi, \Delta) = -m^2 \Phi^\dagger \Phi + M^2 \text{Tr}(\Delta^\dagger \Delta) + \left[\mu \Phi^{\text{T}} \text{i}\tau_2 \Delta^\dagger \Phi + \text{h.c.}\right] + \lambda_1 (\Phi^\dagger \Phi)^2$$

$$+\lambda_2\left[\mathrm{Tr}(\Delta^\dagger\Delta)\right]^2+\lambda_3\mathrm{Tr}[\Delta^\dagger\Delta\Delta^\dagger\Delta]+\lambda_4(\Phi^\dagger\Phi)\mathrm{Tr}(\Delta^\dagger\Delta)+\lambda_5\Phi^\dagger\Delta\Delta^\dagger\Phi, \tag{6.5}$$

where m and M are the mass parameters and λ_i (i=1,..., 5) are the dimensionless quartic scalar couplings, which are all real due to hermiticity of the Lagrangian. The μ parameter can in general be complex and thus a possible source of CPV. But as discussed in Ref. [642, 643], the CPV phase from μ is in fact unphysical and can always be absorbed by a redefinition of the triplet field.

After EWSB, the minimization conditions

$$\frac{\partial V}{\partial \Phi_j}=0, \qquad \frac{\partial V}{\partial \Delta_j}=0 \tag{6.6}$$

imply that

$$m^2 = \lambda_1 v_\Phi^2+\frac{\lambda_{45}v_\Delta^2}{2}-\sqrt{2}\mu v_\Delta, \tag{6.7}$$

$$M^2 = \frac{\mu v_\Phi^2}{\sqrt{2}v_\Delta}-\lambda_{23}v_\Delta^2-\frac{\lambda_{45}v_\Phi^2}{2}, \tag{6.8}$$

with

$$\lambda_{ij}\equiv\lambda_i+\lambda_j. \tag{6.9}$$

Not all scalars are in their mass eigenstates after EWSB, and to diagonalize the corresponding mass matrices, we introduce the following rotating matrices:

$$\begin{pmatrix}\varphi\\ \delta\end{pmatrix} = \begin{pmatrix}\cos\alpha & -\sin\alpha\\ \sin\alpha & \cos\alpha\end{pmatrix}\begin{pmatrix}h\\ H\end{pmatrix}, \tag{6.10}$$

$$\begin{pmatrix}\varphi^\pm\\ \Delta^\pm\end{pmatrix} = \begin{pmatrix}\cos\beta_\pm & -\sin\beta_\pm\\ \sin\beta_\pm & \cos\beta_\pm\end{pmatrix}\begin{pmatrix}G^\pm\\ H^\pm\end{pmatrix}, \tag{6.11}$$

$$\begin{pmatrix} \chi \\ \eta \end{pmatrix} = \begin{pmatrix} \cos\beta_0 & -\sin\beta_0 \\ \sin\beta_0 & \cos\beta_0 \end{pmatrix} \begin{pmatrix} G^0 \\ A \end{pmatrix}, \tag{6.12}$$

with the mixing angles given by

$$\cos\beta_\pm = \frac{v_\Phi}{\sqrt{v_\Phi^2+2v_\Delta^2}}, \quad \sin\beta_\pm = \frac{\sqrt{2}v_\Delta}{\sqrt{v_\Phi^2+2v_\Delta^2}}, \quad \tan\beta_\pm = \frac{\sqrt{2}v_\Delta}{v_\Phi}, \tag{6.13}$$

$$\cos\beta_0 = \frac{v_\Phi}{\sqrt{v_\Phi^2+4v_\Delta^2}}, \quad \sin\beta_0 = \frac{2v_\Delta}{\sqrt{v_\Phi^2+4v_\Delta^2}}, \quad \tan\beta_0 = \frac{2v_\Delta}{v_\Phi}, \tag{6.14}$$

$$\tan 2\alpha = \frac{v_\Delta}{v_\Phi} \cdot \frac{2v_\Phi\lambda_{45} - \frac{2\sqrt{2}\mu v_\Phi}{v_\Delta}}{2v_\Phi\lambda_1 - \frac{v_\Phi\mu}{\sqrt{2}v_\Delta} - \frac{2v_\Delta^2\lambda_{23}}{v_\Phi}}. \tag{6.15}$$

Here G^0 and $G^\pm$ are the would-be Goldstone bosons that become the longitudinal components of the Z and $W^\pm$. Among the remaining scalars, A is the pseudoscalar; h is the CP-even Higgs, which is recognized as the SM Higgs particle; H is the other CP-even Higgs particle with a heavier mass compared with h; and $H^\pm$ and $H^{\pm\pm}$ are the singly- and doubly-charged Higgs particles respectively.

After the rotation, the mass eigenvalues in terms of the parameters in the potential, vevs, and mixing angles are given by:

$$m_{H^{\pm\pm}}^2 = m_\Delta^2 - v_\Delta^2\lambda_3 - \frac{\lambda_5}{2}v_\Phi^2, \tag{6.16}$$

$$m_{H^\pm}^2 = \left(m_\Delta^2 - \frac{\lambda_5}{4}v_\Phi^2\right)\left(1+\frac{2v_\Delta^2}{v_\Phi^2}\right), \tag{6.17}$$

$$m_A^2 = m_\Delta^2\left(1+\frac{4v_\Delta^2}{v_\Phi^2}\right), \tag{6.18}$$

$$m_h^2 = 2v_\Phi^2\lambda_1\cos^2\alpha + \left(m_\Delta^2+2\lambda_{23}v_\Delta^2\right)\sin^2\alpha + \left(\lambda_{45}v_\Phi v_\Delta - \frac{2v_\Delta}{v_\Phi}m_\Delta^2\right)\sin 2\alpha, \tag{6.19}$$

$$m_H^2 = 2v_\Phi^2\lambda_1\sin^2\alpha + \left(m_\Delta^2+2\lambda_{23}v_\Delta^2\right)\cos^2\alpha - \left(\lambda_{45}v_\Phi v_\Delta - \frac{2v_\Delta}{v_\Phi}m_\Delta^2\right)\sin 2\alpha, \tag{6.20}$$

where

$$m_\Delta^2 \equiv \frac{v_\Phi^2\mu}{\sqrt{2}v_\Delta}. \tag{6.21}$$

On the other hand, the potential parameters can be expressed in terms of the mass eigenvalues:

$$\mu = \frac{\sqrt{2}v_\Delta^2}{v_\Phi^2} m_\Delta^2 = \frac{\sqrt{2}v_\Delta}{v_\Phi^2 + 4v_\Delta^2} m_A^2, \tag{6.22}$$

$$\lambda_1 = \frac{1}{2v_\Phi^2}(m_h^2 \cos^2\alpha + m_H^2 \sin^2\alpha), \tag{6.23}$$

$$\lambda_2 = \frac{1}{2v_\Delta^2}\left[2m_{H^{\pm\pm}}^2 + v_\Phi^2\left(\frac{m_A^2}{v_\Phi^2 + 4v_\Delta^2} - \frac{4m_{H^\pm}^2}{v_\Phi^2 + 2v_\Delta^2}\right) + m_H^2 \cos^2\alpha + m_h^2 \sin^2\alpha\right], \tag{6.24}$$

$$\lambda_3 = \frac{v_\Phi^2}{v_\Delta^2}\left(\frac{2m_{H^\pm}^2}{v_\Phi^2 + 2v_\Delta^2} - \frac{m_{H^{\pm\pm}}^2}{v_\Phi^2} - \frac{m_A^2}{v_\Phi^2 + 4v_\Delta^2}\right), \tag{6.25}$$

$$\lambda_4 = \frac{4m_{H^\pm}^2}{v_\Phi^2 + 2v_\Delta^2} - \frac{2m_A^2}{v_\Phi^2 + 4v_\Delta^2} + \frac{m_h^2 - m_H^2}{2v_\Phi v_\Delta}\sin 2\alpha, \tag{6.26}$$

$$\lambda_5 = 4\left(\frac{m_A^2}{v_\Phi^2 + 4v_\Delta^2} - \frac{m_{H^\pm}^2}{v_\Phi^2 + 2v_\Delta^2}\right). \tag{6.27}$$

6.2.2 Theoretical constraints on the CTHM

6.2.2.1 Constraint on v_Δ from the ρ parameter

Due to the interacting terms in the kinetic Lagrangian in Eq. (6.4), the electroweak gauge boson masses will receive contributions from both Φ and Δ after the EWSB. At tree level, one finds

$$m_W^2 = \frac{g^2}{4}(v_\Phi^2 + 2v_\Delta^2), \quad m_Z^2 = \frac{g^2}{4\cos^2\theta_W}(v_\Phi^2 + 4v_\Delta^2), \tag{6.28}$$

$$\Rightarrow \rho \overset{\text{CTHM}}{=\!=\!=} \frac{1 + \frac{2v_\Delta^2}{v_\Phi^2}}{1 + \frac{4v_\Delta^2}{v_\Phi^2}}. \tag{6.29}$$

From our discussion on the ρ parameter in Chapter 1, the stringent constraints on ρ lead to

$$0 \leq v_\Delta \lesssim 3.0 \text{ GeV} \tag{6.30}$$

and thus $v_\Delta \ll v_\Phi$.

6.2.2.2 Constraint from stability, perturbative unitarity, and perturbativity

Constraints from vacuum stability, perturbative unitarity, and perturbativity have been studied in [552–555, 642, 644–652] and are summarized below in our notation:

- Vacuum stability (VS):[ii]

$$\lambda_1 \geq 0 \ \& \ \lambda_2 + \text{Min}\left\{\lambda_3, \frac{\lambda_3}{2}\right\} \geq 0 \ \& \\ \lambda_4 + \text{Min}\left\{0, \lambda_5\right\} + 2\text{Min}\left\{\sqrt{\lambda_1\lambda_{23}}, \sqrt{\lambda_1(\lambda_2 + \frac{\lambda_3}{2})}\right\} \geq 0. \tag{6.31}$$

- Perturbative unitarity (PU):

$$|\lambda_{45}| \leq \kappa\pi \ \& \ |\lambda_4| \leq \kappa\pi \ \& \ |2\lambda_4 + 3\lambda_5| \leq 2\kappa\pi \ \& \ 2|\lambda_1| \leq \kappa\pi \ \& \ 2|\lambda_2| \leq \kappa\pi \ \& \\ 2|\lambda_{23}| \leq \kappa\pi \ \& \ |\lambda_4 - \frac{\lambda_5}{2}| \leq \kappa\pi \ \& \ |2\lambda_2 - \lambda_3| \leq \kappa\pi \ \& \\ |\lambda_{12} + 2\lambda_3 \pm \sqrt{(\lambda_1 - \lambda_2 - 2\lambda_3)^2 + \lambda_5^2}| \leq \kappa\pi \ \& \\ |3\lambda_{13} + 4\lambda_2 \pm \sqrt{(3\lambda_1 - 4\lambda_2 - 3\lambda_3)^2 + \frac{3}{2}(2\lambda_4 + \lambda_5)^2}| \leq \kappa\pi, \tag{6.32}$$

  where $\kappa = 8$ or 16 depending on one's choice on the partial wave amplitude of an elastic scalar scattering from the consideration of S-matrix unitarity. For detailed discussion, see Ref. [642].

- Perturbativity: Keeping only the top Yukawa coupling, gauge interactions, and scalar potential couplings, the one-loop RGEs rewritten in our notation are[iii]

$$(4\pi)^2 \frac{dg_i}{dt} = b_i g_i^3 \text{ with } b_i = \left(\frac{47}{10}, -\frac{5}{2}, -7\right), \tag{6.33}$$

[ii] Here and below, "&" means the logical conjunction "and".

[iii] Two-loop RGEs for the Higgs portal parameters have been studied in Ref. [552].

$$(4\pi)^2 \frac{dy_t}{dt} = y_t \left[\frac{9}{2}y_t^2 - \left(\frac{17}{20}g_1^2 + \frac{9}{4}g_2^2 + 8g_3^2\right)\right], \tag{6.34}$$

$$(4\pi)^2 \frac{d\lambda_1}{dt} = \frac{27}{200}g_1^4 + \frac{9}{20}g_1^2 g_2^2 + \frac{9}{8}g_2^4 - \left(\frac{9}{5}g_1^2 + 9g_2^2\right)\lambda_1 + 24\lambda_1^2 + 3\lambda_4^2 + 3\lambda_4\lambda_5 + \frac{5}{4}{\lambda_5}^2 + 12\lambda_1 y_t^2 - 6y_t^4, \tag{6.35}$$

$$(4\pi)^2 \frac{d\lambda_2}{dt} = \frac{54}{25}g_1^4 - \frac{36}{5}g_1^2 g_2^2 + 15g_2^4 - \left(\frac{36}{5}g_1^2 + 24g_2^2\right)\lambda_2 + 2\lambda_4^2 + 2\lambda_4\lambda_5 + 28\lambda_2^2 + 24\lambda_2\lambda_3 + 6{\lambda_3}^2, \tag{6.36}$$

$$(4\pi)^2 \frac{d\lambda_3}{dt} = \frac{72}{5}g_1^2 g_2^2 - 6g_2^4 + {\lambda_5}^2 - \left(\frac{36}{5}g_1^2 + 24g_2^2\right)\lambda_3 + 24\lambda_2\lambda_3 + 18{\lambda_3}^2, \tag{6.37}$$

$$(4\pi)^2 \frac{d\lambda_4}{dt} = \frac{27}{25}g_1^4 - \frac{18}{5}g_1^2 g_2^2 + 6g_2^4 - \left(\frac{9}{2}g_1^2 + \frac{33}{2}g_2^2\right)\lambda_4 + 12\lambda_1\lambda_4 + 4\lambda_1\lambda_5 + 4\lambda_4^2 + 16\lambda_2\lambda_4 + 12\lambda_3\lambda_4 + {\lambda_5}^2 + 6\lambda_2\lambda_5 + 2\lambda_3\lambda_5 + 6\lambda_4 y_t^2, \tag{6.38}$$

$$(4\pi)^2 \frac{d\lambda_5}{dt} = \frac{36}{5}g_1^2 g_2^2 - \left(\frac{9}{2}g_1^2 + \frac{33}{2}g_2^2\right)\lambda_5 + 4\lambda_1\lambda_5 + 8\lambda_4\lambda_5 + 4{\lambda_5}^2 + 4\lambda_2\lambda_5 + 8\lambda_3\lambda_5 + 6\lambda_5 y_t^2. \tag{6.39}$$

with $t \equiv \ln(\mu/m_t)$. For perturbativity, we require a similar approximate condition on the quartic Higgs couplings as in Ref. [653], which is based on the work of Ref. [654] i.e.,

$$\lambda_i(\mu) \lesssim \lambda_{\rm FP}/3, \quad \forall\ m_Z \leq \mu \leq \Lambda, \tag{6.40}$$

where $\lambda_{\rm FP} \simeq 12$ in the renormalization of Ref. [655] and Λ is the cutoff scale of the theory.

Figure 6.1 presents the constraints from VS (green region) and PU (orange region) at tree-level. The black dot corresponds to our benchmark point discussed in section 6.6.1, i.e.,

$$\lambda_2 = 0.2\,, \quad \lambda_3 = \lambda_4 = 0\,, \quad \lambda_5 = -0.1\,. \tag{6.41}$$

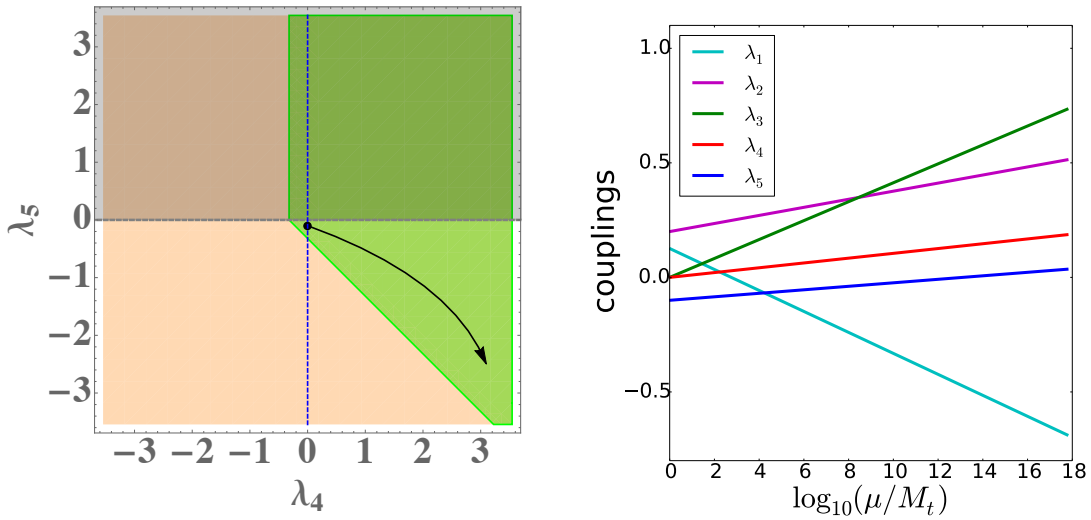

Figure 6.1: Left panel: Tree-level vacuum stability (green region) and perturbative unitarity (orange region) constraints on the λ_4-λ_5 plane with $\lambda_2 = 0.2$ and $\lambda_3 = 0$. Right panel: One-loop running of the Higgs quartic couplings at $\lambda_2 = 0.2$, $\lambda_3 = 0$, $\lambda_4 = 0$ and $\lambda_5 = -0.1$ with $M_t = 173.1\,\text{GeV}$ being our input scale. The black arrow in the left figure corresponds to regions in which vacuum stability is stable up to a higher scale.

After solving the above mentioned RGEs, one finds that that VS and perturbativity up to the Planck scale impose stringent constraints on λ_i's [552]. For our benchmark point as input at the scale $\mu = m_t$, the resulting running couplings are shown in Figure 6.1. From the right panel of Figure 6.1, it is clear that the CTHM stays perturbative even at the Planck scale. We also find that the potential develops a second minimum at $\mathcal{O}(10^5\text{-}10^6\,\text{GeV})$. The presence of this second minimum implies that the SM vacuum may become either unstable or metastable above this scale. In principle, stability could be preserved to higher scales with the presence of additional contributions to the RGEs associated with particles heavier than this threshold. A detailed investigation of the possible U.V. embedding of the CTHM goes beyond the scope of the present study. We observe, however, that the stability region for our benchmark point lies well above the range of triplet scalar masses that we consider below. Moreover, one may also increase the scale at which the potential may develop

a second minimum by increasing λ_4 while preserving perturbativity, which is indicated by the black arrow in the left panel of Figure 6.1. We will discuss this point further in section 6.5.4.

6.2.3 Key features of the CTHM

Since $v_\Delta \ll v_\Phi$, all the mixing angles defined in eq. (6.13-6.15) are small from v_Δ suppression and the expressions for the masses given in Eq. (6.16-6.20) can then be simplified to

$$m_h^2 \simeq 2v_\Phi^2\lambda_1 \simeq 2v^2\lambda_1, \quad m_H \simeq m_\Delta \simeq m_A, \quad m_{H^\pm}^2 \simeq m_\Delta^2 - \frac{\lambda_5}{4}v_\Phi^2, \quad m_{H^{\pm\pm}}^2 \simeq m_\Delta^2 - \frac{\lambda_5}{2}v_\Phi^2. \tag{6.42}$$

Note that m_Δ basically sets the overall mass scale of Δ and λ_1 is determined by m_h and v. Moreover, in the large m_Δ limit, the mass splitting is

$$\Delta m = |m_{H^{\pm\pm}} - m_{H^\pm}| \approx |m_{H^\pm} - m_{H,A}| \approx \frac{|\lambda_5|v_\Phi^2}{8m_\Delta} \approx \frac{|\lambda_5|v^2}{8m_\Delta}, \tag{6.43}$$

and only depends on λ_5, m_Δ, and v. Thus, by measuring the masses of any two triplet scalars of differing charges, one could determine both m_Δ and the Higgs portal coupling λ_5. A practical corollary is in the large m_Δ limit, once one of the triplet Higgs particles is discovered, the relatively small mass splitting (compared to m_Δ) would provide guidance as to the mass region for discovery of the other triplet Higgs scalars.

6.2.4 Neutrino masses from a type-II seesaw mechanism

In the CTHM, the neutrino masses generation has already been discussed in Chapter 2. Using the convention [62, 63, 66, 67]

$$\mathcal{L}_Y = (h_\nu)_{ij}\overline{L^{ic}}i\tau_2\Delta L^j + \text{h.c.}, \tag{6.44}$$

the Majorana neutrino masses can be written as[iv]

$$(m_\nu)_{ij} = \sqrt{2}(h_\nu)_{ij} v_\Delta. \tag{6.45}$$

Given experimental constraints on neutrino masses discussed in Chapter 2, we choose $m_\nu = 0.01\,\text{eV}$ for each of the three light neutrinos throughout the paper. In principle, one can choose a larger (smaller) value for the neutrino masses while still satisfying the experimental constraints. Larger (smaller) neutrino masses will correspond to a larger (smaller) h_ν for fixed v_Δ, which will in turn affect the same-sign di-lepton decay BRs of $H^{\pm\pm}$. The BRs will then affect the parameter space relevant for model discovery. We will discuss effects from smaller/larger m_ν in section 6.5.4.

6.3 Model parameter determination

6.3.1 Mass spectrum and determination of λ_1 and λ_5

In section 6.2.3, we find that, in the small mixing angles limit,

$$m_h^2 \simeq 2v_\Phi^2\lambda_1, \quad m_H \simeq m_\Delta \simeq m_A, \quad m_{H^\pm}^2 \simeq m_\Delta^2 - \frac{\lambda_5}{4}v_\Phi^2, \quad m_{H^{\pm\pm}}^2 \simeq m_\Delta^2 - \frac{\lambda_5}{2}v_\Phi^2, \tag{6.42}$$

implying that: (a) When $\lambda_5 \leq 0$, $m_h < m_H \simeq m_A \leq m_{H^\pm} \leq m_{H^{\pm\pm}}$, we call this the Normal Mass Hierarchy (NMH); (b) while when $\lambda_5 \geq 0$, $m_{H^{\pm\pm}} \leq m_{H^\pm} \leq m_A \simeq m_H$ and $m_h < m_H$, we call this the Reversed Mass Hierarchy (RMH). For the NMH, SM h is the lightest particle and $H^{\pm\pm}$ is the heaviest one, the order of the mass spectra is unique. While for the RMH, A or equivalently H is the heaviest particle, but the

[iv] In principle, one could assign a lepton number of -2 to Δ so that the overall Lagrangian conserves lepton number before EWSB. The third term in $V(\Phi, \Delta)$ would then explicitly break lepton number conservation. The coefficient of the the dimension five lepton number violating mass term $\bar{L^C} H^T H L$ is then proportional to μ/M^2.

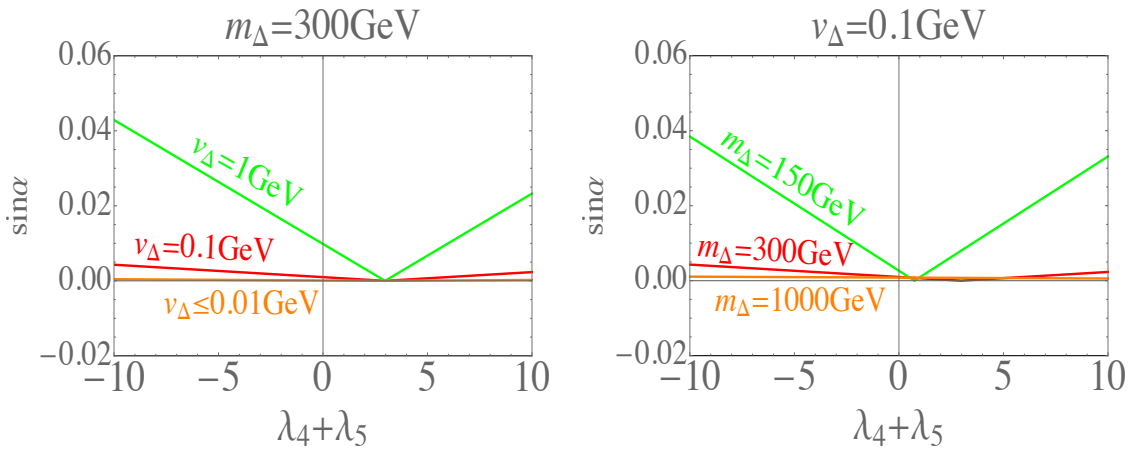

Figure 6.2: The dependence of $\sin\alpha$ on λ_{23} is negligible due to the smallness of v_Δ, and $\lambda_1 \approx m_h^2/(2v^2) \approx 0.129$, such that $\sin\alpha$ is approximately a function of λ_{45}, m_Δ and v_Δ. On the left (right) panel we fix $m_\Delta = 300\,\text{GeV}$ ($v_\Delta = 0.1\,\text{GeV}$) and plot $\sin\alpha$ with respect to λ_{45} with different v_Δ's (m_Δ's). One observes that $\sin\alpha$ becomes sufficiently small for increasing m_Δ and/or decreasing v_Δ.

mass order between h and ($H^\pm$, $H^{\pm\pm}$) is unclear and will generally depend on our model input.

On the other hand, from $m_h^2 \simeq 2v^2\lambda_1$, we conclude that $\lambda_1 \approx \frac{m_h^2}{2v^2} \approx 0.129$. While to determine λ_5, one can use the mass splitting $\Delta m \approx \frac{|\lambda_5|v^2}{8m_\Delta}$ as defined in Eq. (6.43) upon discovery.

6.3.2 Measurement of the mixing angle $\sin\alpha$ for determination of λ_4

To determine λ_4, we note that

$$\alpha \approx \begin{cases} \frac{1}{2}\arctan\left(\frac{v_\Delta}{v_\Phi}\cdot\frac{2v_\Phi^2\lambda_{45}-4m_\Delta^2}{m_h^2-m_\Delta^2}\right), & \text{if } \frac{2v_\Phi^2\lambda_{45}-4m_\Delta^2}{m_h^2-m_\Delta^2} \geq 0 \\ \pi+\frac{1}{2}\arctan\left(\frac{v_\Delta}{v_\Phi}\cdot\frac{2v_\Phi^2\lambda_{45}-4m_\Delta^2}{m_h^2-m_\Delta^2}\right), & \text{if } \frac{2v_\Phi^2\lambda_{45}-4m_\Delta^2}{m_h^2-m_\Delta^2} < 0 \end{cases}, \tag{6.46}$$

which implies $\sin\alpha$ is in general a two-to-one function as graphically reflected in Figure 6.2. Note that $\sin\alpha$ decreases with increasing m_Δ and/or decreasing v_Δ.

On the other hand, the variation feature of $\sin\alpha$ with λ_{45} can be used to determine λ_{45} through various gauge boson-Higgs couplings. We focus on gauge boson-Higgs

Vertex	Coupling
hAZ	$-\frac{g}{2\cos\theta_W}(\cos\alpha\sin\beta_0 - 2\sin\alpha\cos\beta_0)$
HZZ	$\frac{2iem_Z}{\sin 2\theta_W}(2\sin\beta_0\cos\alpha - \cos\beta_0\sin\alpha)$
HW^+W^-	$igm_Z\cos\theta_W(\sin\beta_0\cos\alpha - \cos\beta_0\sin\alpha)$
hH^-W^+	$\frac{ig}{2}(\sin\beta_\pm\cos\alpha - \sqrt{2}\cos\beta_\pm\sin\alpha)$

Table 6.1: Three-point vertices related to the determination of $\lambda_{4,5}$. λ_5 is determined through mass splitting, λ_4 is determined through the mixing angle $\sin\alpha$, which is sensitive to λ_{45}.

vertices as electroweak production of the triplet Higgs particles is the dominant production mechanism in the CTHM. After a careful investigation of all the triple vertices listed in Appendix A.4, we find that only four of the gauge boson-Higgs couplings, as listed in Table 6.1, are linearly dependent on $\sin\alpha$.[v] These couplings will eventually affect the decay BRs of the BSM particles. Thus, after their discovery, one could determine λ_5 from the mass splitting and λ_4 from the triplet Higgs decay BRs.[vi]

6.3.3 λ_2 and λ_3 determination

λ_2 and λ_3 are in general very difficult or even impossible to measure as they are always suppressed by either v_Δ^2 or v_Δ. On the other hand, since λ_2 and λ_3 are irrelevant to electroweak phase transition, we will not pay too much attention to their determination here.

---

[v] Some of the non gauge boson-Higgs type vertices are also $\sin\alpha$ linearly dependent as can be seen from the $hH^{++}H^{--}$ vertex in Appendix A.4, but the corresponding production cross section is smaller compared with the dominant electroweak production.

[vi] Here we remind the reader that the Higgs portal parameters $\lambda_{4,5}$ are of particular interest as they may allow a SFOEWPT to explain the baryon asymmetry of the universe (BAU). In this paper, however, we will not discuss the effects on phase transition or baryogenesis from the CTHM but rather leave it for future work.

6.3.4 Choice of input model parameters

Recall that, in section 6.2.2.1, the ρ parameter requires $v_\Delta \ll v_\Phi$ or v. The ratio of the Higgs masses and v_Δ will thus lead to very large $\lambda_{2,3}$ from Eq. (6.24-6.25) if we choose the masses as our input. Then to preserve perturbativity of the CTHM, one will have to "fine-tune" the Higgs masses to obtain reasonable values for $\lambda_{2,3}$. To avoid this "fine tuning", we choose $\lambda_{2,3}$ to be the model input in our theoretical study. Similarly, as discussed in section 6.3.1 and section 6.3.2, (a) Since we know the Higgs mass exactly, we choose m_h instead of λ_1 as our model input; (b) we choose m_Δ and λ_5 as our model input as they determine the mass spectrum; (c) $\sin\alpha$ is negligible at small v_Δ, thus to avoid "fine tuning" λ_4, we choose λ_4 instead of $\sin\alpha$ as our model input. Another reason for choosing λ_4 as our model input is that it frequently appears in pair with λ_5 such that one can infer λ_4 from the combination once λ_5 is known. At the same time, relevant quantities may depend separately on λ_4 and λ_5, e.g., $H^\pm$ decay BRs. To summarize, our model input parameters are $\{\alpha_{E.M.}, G_F, m_Z, m_h, m_\Delta, v_\Delta, \lambda_2, \lambda_3, \lambda_4, \lambda_5, m_\nu\}$.

6.4 Production and Decay Rates of the Scalars in the CTHM

Since the mass ordering of the RMH will in general depend on our model input, for simplicity, we will only discuss the NMH here. While we stress that, in the RMH, though the decay patterns, the decay BRs and thus our Figure 6.7 and Figure 6.11 will change, the same channels studied in this paper can still be used for model discovery and Higgs portal parameter determination.

6.4.1 Production cross section of the Higgs particles in the CTHM

Due to suppression from small v_Δ, single production of the triplet Higgs particles will not be considered. For double scalar production, a pair of triplet scalars can be produced through electroweak Drell-Yan processes or gluon fusion. As in the

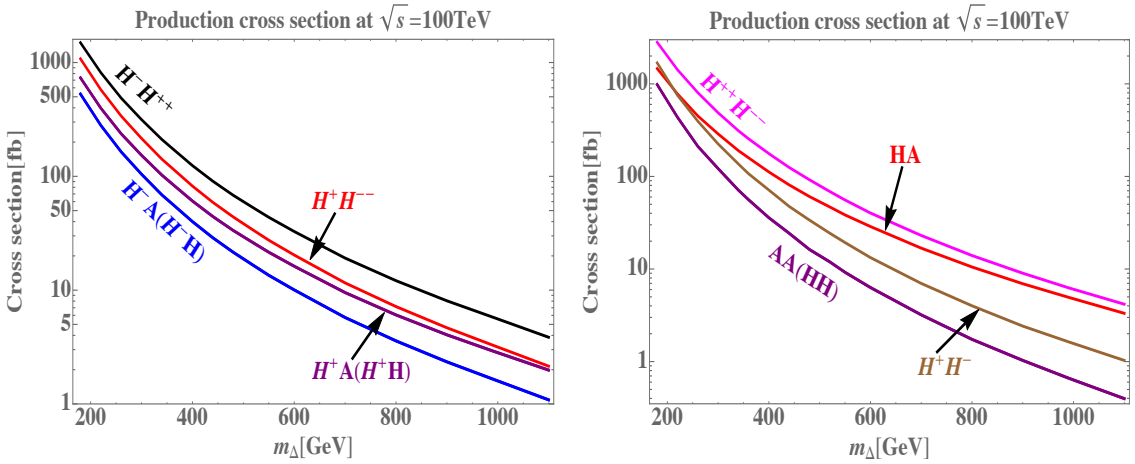

Figure 6.3: Production cross section as a function of m_Δ at $\sqrt{s} = 100\,\text{TeV}$ with $v_\Delta = 10^{-3}\,\text{GeV}$. We set $\lambda_2 = 0.2$, $\lambda_3 = 0$, $\lambda_4 = 0$ and $\lambda_5 = -0.1$, which correspond to the black dot in the left panel of Figure 6.1 in order to be consistent with the NMH framework and to satisfy the model constraints discussed in section 6.2.2.2. The left panel is for associated Higgs production channels while the right one is for pair production except the HA channel. Since the production cross section of HA is very close to H^-H^{++}, we include it in the right panel to make the plots more readable.

single Higgs production case, however, double scalar Higgs particle production via an intermediate H or A, which is produced through gluon fusion, is again highly suppressed by small v_Δ. No such suppression occurs for electroweak pair production. Consequently, we focus on the latter.

To study quantitively the production cross sections of the triplet Higgs particles, we first use `Mathematica` and `FeynRules` 2.3.13 [656, 657] to generate the Universal FeynRules Output (UFO) model file [658] of the CTHM, then we use `MadGraph` 2.3.3 [659] to implement the CTHM UFO file to obtain the production cross sections at $\sqrt{s} = 14\,\text{TeV}$ and $\sqrt{s} = 100\,\text{TeV}$. However, we find that for the channels we are going to study in this paper, the number of events at $\sqrt{s} = 14\,\text{TeV}$ and $\mathcal{L} = 3\,\text{ab}^{-1}$ is too few even without considering the corresponding backgrounds, so we only list the cross section result at $\sqrt{s} = 100\,\text{TeV}$ here.

The pair production cross sections depend on the couplings of the electroweak gauge bosons to the scalars and on the scalar masses. In what follows, we cast these dependences in terms of our independent parameters. Note that λ_1 is basically fixed by v and m_h, while the effects of $\lambda_{2,3}$ are suppressed by small v_Δ. In short, the production cross sections will be largely insensitive to $\lambda_{2,3}$ but will depend significantly on $\lambda_{4,5}$. To be consistent with the NMH, which requires a negative λ_5, and to satisfy the constraints discussed in section 6.2.2, we choose $\lambda_2 = 0.2$, $\lambda_3 = 0$, $\lambda_4 = 0$ and $\lambda_5 = -0.1$. As an example, we fix $v_\Delta = 10^{-3}\,\text{GeV}$ and obtain the production cross sections given in Figure 6.3, from which we see that pair production of $H^{++}H^{--}$ has the largest production cross section followed by $H^{++}H^{-}$. On the other hand, $H^{+}H^{--}$ will always be produced simultaneously with $H^{-}H^{++}$. We therefore expect an enhancement of the cross section from the combination of $H^{-}H^{++}$ and $H^{+}H^{--}$ channels.

The hierarchy of the various production cross sections is briefly explained below: (a) Besides a factor of four enhancement from the electric charge of $H^{\pm\pm}$, $H^{++}H^{--}$ pair has a larger cross section than $H^{+}H^{-}$ because it is constructively produced through s-channel γ and Z exchange. In contrast, the $H^{+}H^{-}$ pair production is suppressed due to destructive interference [570]. Note that even though $m_{H^{\pm\pm}} > m_{H^{\pm}}$, the mass splitting is not large due to our choice of λ_5; therefore, the lighter $H^{\pm}$ mass does not compensate for the aforementioned factors. (b) $H^{++}H^{-}$ has a larger cross section than $H^{--}H^{+}$ because the former is dominantly produced through a W^{+} while the latter is through a W^{-}. (c) HH and AA channels, or $H^{\pm}A$ and $H^{\pm}H$ channels, have the same production cross sections due to mass degeneracy of H and A. (d) $H^{\pm}A/H^{\pm}H$ has a smaller cross section than HH/AA, and HA has a smaller cross section than $H^{++}H^{--}/H^{++}H^{-}$, because of the couplings. (e) In the NMH, $m_{H^{\pm}} > m_{H/A}$, but the couplings involved for $H^{+}H^{-}$ is larger than those for $H^{+}A/H^{+}H$, the phase space and the couplings will compete such that at small m_Δ,

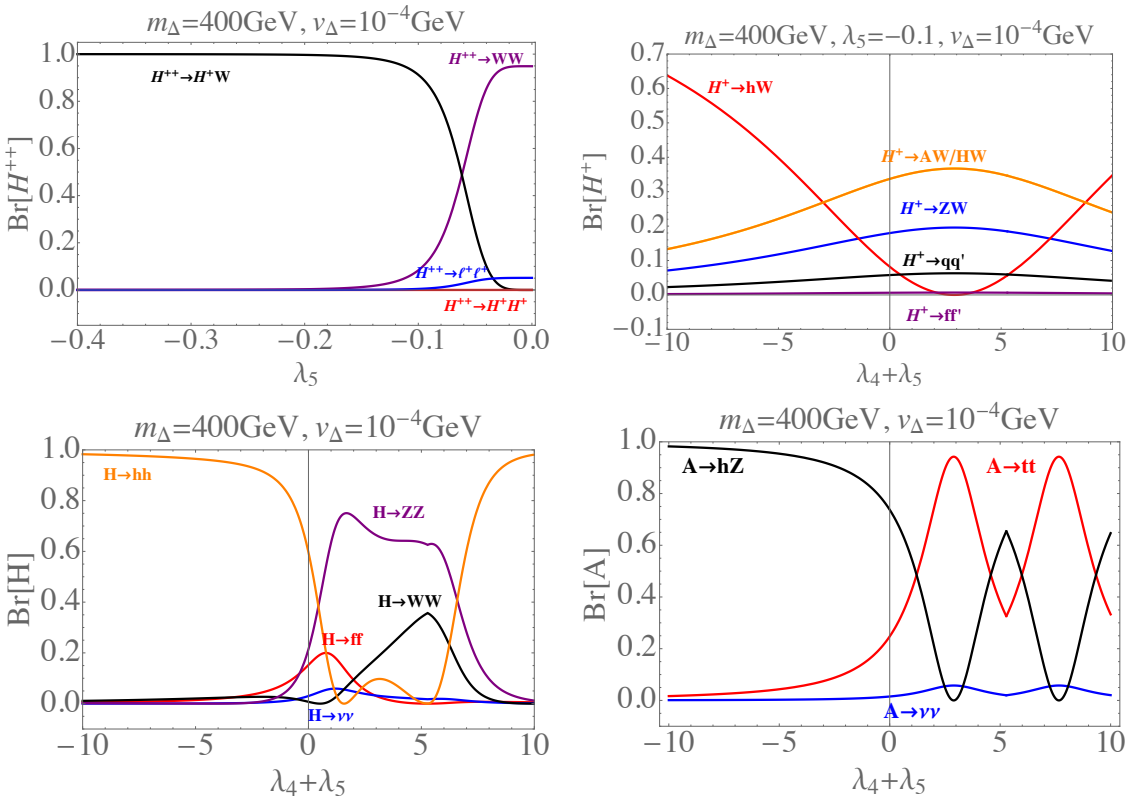

Figure 6.4: Decay BRs for H, A, $H^{\pm\pm}$ and $H^{\pm}$ as a function of λ_4 and λ_5 for representative values of $m_\Delta = 400\,\text{GeV}$ and $v_\Delta = 10^{-4}\,\text{GeV}$. For a detailed discussion on the decay features, one can refer to the main text in section 6.4.2.

H^+H^- has larger cross section while at large m_Δ, H^+A/H^+H has a larger cross section. This is also true for HA and H^+H^- channels.

In order to study the collider signatures of the triplet Higgs particles, it is natural to focus on $H^{\pm\pm}H^{\mp\mp}$ and $H^{\pm\pm}H^{\mp}$ channels since they have the largest production cross sections compared with other channels. To determine the final states, we will study their dominant decay channels in next sub-section.

6.4.2 Decay rates of the scalar Higgs particles in the CTHM

To further determine the dominant decay modes of the triplet Higgs particles in the CTHM for collider simulation, we calculate their decay rates by taking $h_\nu = \mathbf{1}_{3\times3}$

for simplicity. All our decay formulas agree with those in Appendix A of Ref. [585] if one also takes the unit matrix limit there.

In order to illustrate the potential parameter-dependence of various decay channels, we show in Figure 6.4 the BRs for the charged and neutral triplet states as functions of the relevant combinations of λ_4 and λ_5 for representative values of $m_\Delta = 400\,\text{GeV}$ and $v_\Delta = 10^{-4}\,\text{GeV}$.

In this study, we will focus on the NMH with $\lambda_5 < 0$. From the top left panel of Figure 6.4, we observe that the $H^{\pm\pm}$ BRs to $H^\pm W^\pm$ and $W^\pm W^\pm$ depend strongly on this parameter in the vicinity of our benchmark point value: $\lambda_5 = -0.1$. From the top right plot, we also observe that the BR($H^\pm \to hW^\pm$) also depends strongly on $\lambda_4 + \lambda_5$. Even though in the vicinity of our benchmark point with $\lambda_4 + \lambda_5 = -0.1$ the $hW^\pm$ mode is subdominant, the corresponding BR depends more strongly on $\lambda_4 + \lambda_5$ than do the other modes. Consequently, we will focus on this channel for the decay of the singly-charged scalar. The bottom two panels give the neutral scalar BRs. Though we will not utilize this information in the present study, we include them here for completeness and for future reference.

It is also useful to determine how the $H^{\pm\pm}$ BRs vary with m_Δ and v_Δ. To that end, in Figure 6.5, we show the regions of parameter space where the BR to various final states is greater than 40% for $H^{\pm\pm}$. In the left panel of Figure 6.5, we consider the (v_Δ, λ_5) plane for fixed m_Δ, while the right panel gives the (m_Δ, λ_5) plane for fixed v_Δ. Note that $H^{\pm\pm}$ decay BRs are independent on λ_4 and for the NMH, one has $\lambda_5 < 0$.

From Figure 6.5, we observe that for $H^{\pm\pm}$, the dominant decay channels are $H^{\pm\pm} \to \ell^\pm \ell^\pm$ ($W^\pm W^\pm$) at small (large) v_Δ when $m_\Delta = 400\,\text{GeV}$. For intermediate values of the triplet vev, e.g. $v_\Delta = 10^{-4}\,\text{GeV}$, those two channels dominate when $\lambda_5 \geq -0.2$. Besides the large BRs in the corresponding regions of v_Δ, additional advantages for these channels are: (1) Clean final states: Leptons in the final states are

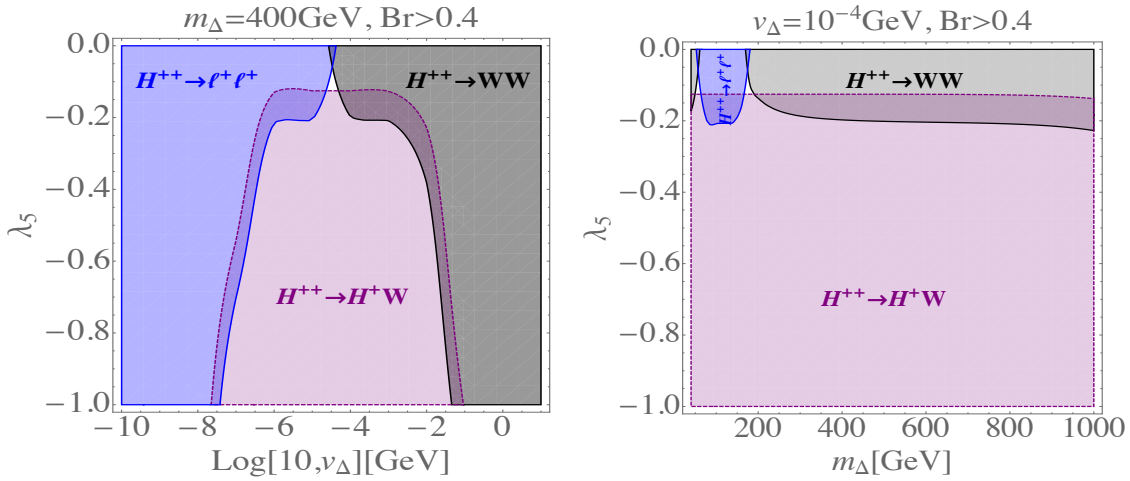

Figure 6.5: Decay region plots for $H^{\pm\pm}$ with BR$\geq$ 40%. Left panel is with m_Δ = 400 GeV and right panel is with $v_\Delta = 10^{-4}$ GeV. Purple region is the $H^\pm W^\pm$ channel, black is the same-sign di-W boson channel and blue is the same-sign di-lepton channel. λ_5 is in the negative region to be consistent with the NMH framework.

relatively easy to identify and analyze experimentally; (2) Absence of cascade decay: The $H^\pm W^\pm$ decay mode will introduce extra decay chains, making the final state more complicated. We emphasize, however, that even though the same-sign di-W boson (di-lepton) channel dominates for large (small) v_Δ, one may still probe the intermediate v_Δ region using the $\ell^\pm\ell^\pm$ and $W^\pm W^\pm$ channels. Although these channels have relatively small BRs in this v_Δ region, we find that by combining thesechannels with information from other triplet Higgses, one could still explore this region without resorting to the $H^{\pm\pm} \to W^\pm H^\pm$ channel. This feature will become more apparent in our main discovery reach plot Figure 6.7 and attendant discussion.

We also note in passing that at small v_Δ, same-sign di-lepton channel dominates and actually has a 100% decay BR. For those regions where the same-sign di-lepton channel has a 100% decay BR, experimental constraints are strong. We will discuss this point in detail in section 6.5.4.

In Figure 6.6, we show the regions of parameter space where the $H^\pm$ decay BR to various final states is greater than 40%. Since the BR functions for $H^\pm$ depend on

v_Δ, m_Δ, λ_4 and λ_5 individually, the decay region plots for $H^\pm$ are more complicated than those for the doubly charged scalars. We thus plot the dominant decay channels in different planes: In the first row of Figure 6.6, we consider the (v_Δ, m_Δ) plane with varying λ_{45}, while in the second (third) row, we consider the (v_Δ, $\lambda_{5(4)}$) plane with fixed $\lambda_{4(5)}$ and v_Δ. Recall that from Table 6.1, only the $H^\pm \to hW^\pm$ channel is related to the determination of λ_4 through the mixing angle $\sin\alpha$ as discussed in section 6.3.2. We observe that $\lambda_{45} < 0$ generally leads to a large BR for the $H^\pm \to hW^\pm$ channel, though there also exist some regions giving a large BR($H^\pm \to hW^\pm$) for $\lambda_{45} > 0$.

With the foregoing observations in mind, we will next study the following channels for model discovery: $pp \to H^{++}H^{--}$ and $pp \to H^{\pm\pm}H^\mp$ with $H^{\pm\pm} \to \ell^\pm\ell^\pm$ ($W^\pm W^\pm$) and $H^\mp \to hW^\mp$.

6.4.3 Present experimental constraints

Present experimental constraints on the charged Higgs particles we study here already exclude some portions of the CTHM parameter space especially from studies on the $pp \to H^{++}H^{--} \to \ell^+\ell^-\ell'^-\ell'^-$ ($\ell = e, \mu$) process. Thus, before moving to the detailed collider study of some specific channels, we review the current direct LHC experimental constraints. A detailed summary can be found in Appendix A.1, with the most stringent ones given below:

1. For $H^{\pm\pm}$: By assuming a 100% di-lepton decay BR, the lower limit on $m_{H^{\pm\pm}}$ is constrained to be 870 GeV [22] for a $\mu^\pm\mu^\pm$ final state. In Ref. [637], an upper limit on the cross section with the $\ell^\pm\ell^\pm$ ($\ell = e, \mu$) final state is set to be between 1.7 fb and 67 fb. While by assuming $H^{\pm\pm}$ is long-lived,[vii] $m_{H^{\pm\pm}} \in [50, 600]$ GeV is excluded [640].

[vii] As explained in the footnote of Ref. [640], "long-lived" means a particle that does not decay within the full depth of the ATLAS detector.

2. For $H^{\pm}$: $\sigma(pp \to H^{\pm}t[b]) \times \mathrm{BR}(H^{\pm} \to \tau\nu) < 1.9\,\mathrm{fb}$-$15\,\mathrm{fb}$ for $m_H^{\pm} \in (200, 2000)\,\mathrm{GeV}$ [660], while for a VBF produced $H^{\pm}$, $\sigma(pp \to H^{\pm} + X) \times \mathrm{BR}(H^{\pm} \to W^{\pm}Z) <$ $36\,\mathrm{fb}$-$573\,\mathrm{fb}$ for $m_H^{\pm} \in (200, 2000)\,\mathrm{GeV}$ [661]. Here, a larger mass corresponds to a smaller upper bound on the product of the production cross section and the BR. A similar meaning is implied in the following.

3. For H and A: In Ref. [662], the upper limit on $\sigma(pp \to S' \to SZ) \times \mathrm{BR}(S \to b\bar{b}(\tau^+\tau^-)) \times \mathrm{BR}(Z \to \ell^+\ell^-)$ (S', S are H or A with $m_{S'} > m_S$) is constrained to be $5\,\mathrm{fb}$-$10\,\mathrm{fb}$ for $\ell^+\ell^-\tau^+\tau^-$ final state with $m_{H/A} \in (500, 1000)\,\mathrm{GeV}$ and $m_{A/H} \in (90, 400)$ GeV; while for $\ell^+\ell^-b\bar{b}$ final state, the upper limit is $1\,\mathrm{fb}$-$100\,\mathrm{fb}$ with $m_H \in [300, 100000]$ GeV. For the degenerate case, i.e., $m_A = m_H$, which is true in our case, the parameter space remains unexplored.

For the charged Higgs particles, we will recast constraints from the charged Higgs particles to the parameter space of the CTHM in section 6.5.4, in which we show the part of the parameter space that is already ruled out by current experimental constraints for the benchmark point we choose.

6.5 Model discovery

As discussed in last section, $H^{++}H^{--}$ has the largest production cross section and will be the dominant discovery channel for the triplet model; $H^{\pm}H^{\mp\mp}$ has the second largest production cross section and is directly related to the determination of $\lambda_{4,5}$. In addition, since the same-sign di-lepton decay channel of the $H^{\pm\pm}$ particle is dominant only at small v_Δ from left panel of Figure 6.5 and the $H^{\pm} \to hW^{\pm}$ decay channel dominates at large v_Δ from first row of Figure 6.6, we expect these two channels to be complementary to each other to cover most of the model parameter space. Therefore, in this section, we will study in detail the discovery of the triplet

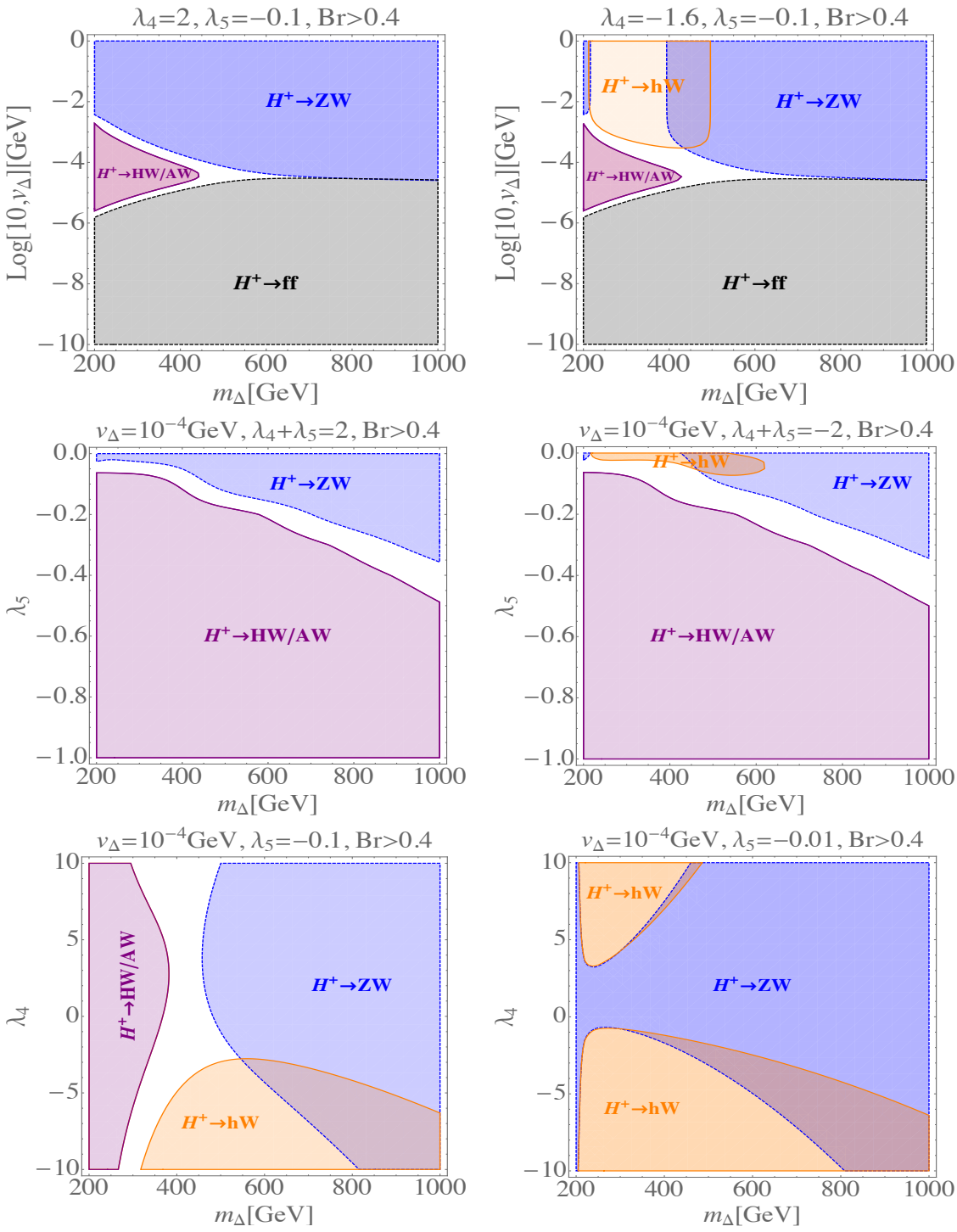

Figure 6.6: Decay region plots for $H^{\pm}$ with BR $\geq 40\%$. Purple region is for HW and AW, blue for ZW, orange for hW and black for the lepton final state. The first row is with the same λ_5 but opposite-sign λ_4; the second row is with the same v_Δ but opposite-sign λ_{45} and the third row is with the same v_Δ but different λ_5. From those plots we conclude that $H^{\pm} \to hW^{\pm}$ channel prefers $\lambda_{45} < 0$ in general. For $\lambda_5 = -0.01$, $H^{\pm} \to hW^{\pm}$ also gains a large branching ratio when λ_4 goes from negative to positive as can be seen from the last graph.

model through these two channels, i.e., $pp \to H^{++}H^{--}$ and $pp \to H^{\pm\pm}H^{\mp}$ with $H^{\pm\pm} \to \ell^{\pm}\ell^{\pm}/W^{\pm}W^{\pm}$ and $H^{\pm} \to hW^{\pm}$.

6.5.1 Discovery for small v_{Δ}: $pp \to H^{++}H^{--} \to \ell^{+}\ell^{+}\ell'^{-}\ell'^{-}$

The dominant discovery channel for the triplet model is $H^{++}H^{--}$ and the cleanest discovery process is $pp \to H^{++}H^{--} \to \ell^{+}\ell^{+}\ell'^{-}\ell'^{-}$. Several theoretical and experimental phenomenological studies of its LHC signatures have been performed [22, 23, 561, 566, 572, 578, 622–629, 635–641]. Recent related theoretical studies relevant to higher energy colliders include: (1) at a lepton collider with $\sqrt{s} = 380\,\text{GeV}$ and 3 TeV, the production and decays of $H^{\pm\pm}$ were studied by Agrawal et al. [630]; (2) the $H^{++}H^{--}$ pair production cross section at the future 100 TeV pp collider was studied by Cai et al. [631]; (3) the $H^{++}H^{--} \to \tau^{\pm}\ell^{\pm}\ell^{\mp}\ell^{\mp}/\ell^{+}\tau^{+}\ell^{-}\tau^{-}$ processes were studied by Li [632] at the high-luminosity and high-energy LHC as well as the future 100 TeV circular pp collider (FCC); (4) the multi-lepton final state of $H^{++}H^{--}$ at 13 TeV LHC and FCC was studied by Mitra et al. [567] in the RMH by fixing $\lambda_1 = 0.13$ and $\lambda_2 = \lambda_3 = \lambda_4 = 1$. To the best of our knowledge, in the NMH this channel at the FCC has not yet been studied.

In what follows, we discuss our collider simulation for this channel with a mass range from 40 GeV to 5000 GeV. The simulation is done by using `MadGraph` 2.3.3 [659] and the aforementioned pre-generated CTHM UFO file to generate events, and then each generated event undergoes parton shower and hadronization through `Pythia-pgs` 2.4.4 [663] before arriving at the detector. The detector response is simulated by `Delphes` 3.3.0 [664], where the 100 TeV FCC `Delphes` card [665] is used at this step. To analyze the data collected by `Delphes`, we use `ROOT` 6.06.02 [666].

The dominant backgrounds for this channel are $ZW^{\pm}W^{\mp}$ and ZZ as we are performing an exclusive analysis. In total, we generate 1,000,000 events for both the signal and the two backgrounds, and our preselection cuts for the signal and the

$\not{E}_T$: Missing transverse energy; HT: Scalar sum of transverse momentum
$m_{H^{++}}$: Positively doubly-charged Higgs mass, $m_{H^{--}}$: Negatively doubly-charged Higgs mass
$p_{T,\ell^+}^{\text{leading}}$, $p_{T,\ell^+}^{\text{sub-leading}}$: Transverse momentum of ℓ^+ with leading and sub-leading p_T
$p_{T,\ell^-}^{\text{leading}}$, $p_{T,\ell^-}^{\text{sub-leading}}$: Transverse momentum of ℓ^- with leading and sub-leading p_T
$\Delta\phi_{\ell^+\ell^+}$, $\Delta R_{\ell^+\ell^+}$: $\Delta\phi$ and ΔR of the two positively charged leptons
$\Delta\phi_{\ell^-\ell^-}$, $\Delta R_{\ell^-\ell^-}$: $\Delta\phi$ and ΔR of the two negatively charged leptons
$m_{Z,1}$, $m_{Z,2}$: Two minimal combinations of the four leptons with same flavor and opposite charges

Table 6.2: A list of BDT variables for the $pp \to H^{\pm\pm}H^{\mp\mp} \to \ell^+\ell^+\ell'^-\ell'^-$ signal and its backgrounds.

backgrounds are: (1) transverse momentum $p_T > 20\,\text{GeV}$ for all final state particles; (2) absolute pseudorapidity $|\eta| < 2.5$ for all final state particles. Since the Boosted Decision Trees (BDT) [667] can maximize the cut efficiency and thus have better performance than a cut-based analysis [668], we will utilize this feature of BDT to train and test all the events that have passed the preselection cuts. We list the variables used during BDT training and test in Table 6.2.

6.5.2 Discovery for large v_Δ: $pp \to H^{++}H^{--} \to W^+W^+W^-W^- \to \ell^+\ell^+\ell'^-\ell'^-\not{E}_T$

From the BR discussion in section 6.4.2, we observe that the $H^{++}H^{--} \to \ell^+\ell^+\ell'^-\ell'^-$ channel can only cover the small v_Δ region, and we expect the large v_Δ region to be covered by the $pp \to H^{++}H^{--} \to W^+W^+W^-W^-$ channel. In this paper, we only focus on the $W^\pm \to \ell^\pm\nu_\ell$ mode for all the four W bosons. In this case, the $4W$ channel has exactly the same backgrounds as the $H^{++}H^{--} \to \ell^+\ell^+\ell'^-\ell'^-$ channel considered in last sub-section.

Repeating the same procedures as for the $H^{++}H^{--} \to \ell^+\ell^+\ell'^-\ell'^-$ channel, we generate 1,000,000 events for our signal and use the background data generated in last sub-section. We also use the same BDT training and test variables as those listed in Table 6.2 to analyze this channel.

Signal	$pp \to H^{\mp}H^{\pm\pm} \to hW^{\mp}\ell^{\pm}\ell^{\pm} \to b\bar{b}\ell'^{\mp}\ell^{\pm}\ell^{\pm}\not{E}_T$ (for intermediate v_Δ)
	$pp \to H^{\mp}H^{\pm\pm} \to hW^{\mp}W^{\pm}W^{\pm} \to b\bar{b}\ell'^{\mp}\ell^{\pm}\ell^{\pm}\not{E}_T$ (for large v_Δ)
Background	$pp \to hZW^{\pm} \to b\bar{b}\ell^{+}\ell^{-}\ell'^{\pm}\not{E}_T$
	$pp \to hZZ \to b\bar{b}\ell^{+}\ell^{-}\ell'^{+}\ell'^{-}$
	$pp \to ZW^{\pm}jj \to \ell^{+}\ell^{-}\ell'^{\pm}jj\not{E}_T$
	$pp \to t\bar{t}Z \to W^{+}bW^{-}b\ell^{+}\ell^{-} \to bb\ell'^{+}\ell''^{-}\ell^{+}\ell^{-}\not{E}_T$
	$pp \to ZW^{\pm}b\bar{b} \to b\bar{b}\ell^{+}\ell^{-}\ell'^{\pm}\not{E}_T$
	$pp \to W^{+}W^{-}bbj \to bb\ell^{+}\ell'^{-}j\not{E}_T$
	$pp \to t\bar{t}W^{\pm} \to W^{+}bW^{-}b\ell^{\pm}\not{E}_T \to bb\ell'^{+}\ell''^{-}\ell^{\pm}\not{E}_T$
	$pp \to t\bar{t}j \to W^{+}bW^{-}bj \to bb\ell'^{+}\ell''^{-}j\not{E}_T$

Table 6.3: Signals for intermediate and large v_Δ are listed in the first two rows. The two signals share the same backgrounds, which are listed in the following eight rows.

6.5.3 Discovery for intermediate and large v_Δ: $pp \to H^{\pm\pm}H^{\mp} \to \ell^{\pm}\ell^{\pm}hW^{\mp} \to \ell^{\pm}\ell^{\pm}b\bar{b}\ell^{\mp}\not{E}_T$ and $pp \to H^{\pm\pm}H^{\mp} \to W^{\pm}W^{\pm}hW^{\mp} \to \ell^{\pm}\ell^{\pm}b\bar{b}\ell^{\mp}\not{E}_T$

While the $H^{++}H^{--} \to \ell^{+}\ell^{+}\ell'^{-}\ell'^{-}$ ($pp \to H^{++}H^{--} \to W^{+}W^{+}W^{-}W^{-} \to \ell^{+}\ell^{+}\ell'^{-}\ell'^{-}\not{E}_T$) only covers the small (large) v_Δ region, the $H^{\pm}H^{\mp\mp}$ can provide complementary discovery potential for the large and intermediate v_Δ region. To obtain information about $\lambda_{4,5}$, we require $H^{\pm}$ to decay into a $hW^{\pm}$ final state, while $H^{\mp\mp}$ can decay into either an $\ell^{\mp}\ell^{\mp}$ or a $W^{\mp}W^{\mp}$ final state. These two processes yield the same final state particles and, thus, share the same backgrounds. The backgrounds we consider for these two processes are: $hZW^{\pm}; t\bar{t}j$ and $W^{\pm}W^{\mp}b\bar{b}j$ with the light jet j misidentified as a lepton with a fake rate of 0.01% [665]; $t\bar{t}W^{\pm}$, $t\bar{t}Z$ and ZZh with one lepton missing; $ZW^{\pm}jj$ with the two light jets misidentified as two b quarks with a fake rate of 10% for c misidentified as b and a 0.01% fake rate for other light quarks [665]; and $ZW^{\pm}b\bar{b}$. The signals and the backgrounds are summarized below in Table 6.3.

As for the $H^{++}H^{--}$ process, we use the same tools to generate events, the same preselection cuts to analyze the events. For the BDT training and test, the training variables we use for these two processes and the backgrounds are listed in Table 6.4. In addition, for the $t\bar{t}j$, $W^{\pm}W^{\mp}b\bar{b}j$ and $ZW^{\pm}jj$ backgrounds, we also add the following cuts at the generator level: (1) $p_T^{j,b} \geq 10\,\text{GeV}$; (2) $|\eta^{j,b}| \leq 5$; (3)$\Delta R^{jj,bb,bj} \geq 0.05$. With

$\not{E}_T$: Missing transverse energy; HT: Scalar sum of transverse momentum
$m_{H^{\pm\pm}}$: Doubly-charged Higgs mass
m_h, m_Z: SM Higgs and Z boson mass; $m_{W,T}$: transverse mass of $W^{\mp}$ boson
$\Delta\phi_{b\bar{b}}$, $\Delta R_{b\bar{b}}$: $\Delta\phi$ and ΔR of two b quarks; $\Delta\phi_{\ell^\pm\ell^\pm}$, $\Delta R_{\ell^\pm\ell^\pm}$: $\Delta\phi$ and ΔR of two same-sign leptons
$p_{T,b}^{\text{leading}}$, $p_{T,b}^{\text{sub-leading}}$: leading and sub-leading transverse momentum of the b quark
η_b^{leading}, $\eta_b^{\text{sub-leading}}$: pseudo-rapidity of the b quark with leading and sub-leading p_T respectively
$p_{T,\ell^{\text{same}}}^{\text{leading}}$, $p_{T,\ell^{\text{same}}}^{\text{sub-leading}}$: leading and sub-leading transverse momentum of the same-sign leptons
$\eta_\ell^{\text{leading}}$, $\eta_\ell^{\text{sub-leading}}$: pseudo-rapidity of the same-sign leptons with leading and sub-leading p_T respectively
$\eta_{\ell^{\text{oppo.}}}$, $p_{T,\ell^{\text{oppo.}}}$: pseudo-rapidity and transverse momentum of the opposite-sign lepton

Table 6.4: A list of BDT variables for $W^\pm W^\pm h W^\mp$, $\ell^\pm\ell^\pm h W^\mp$ channels and their backgrounds. Since these two signals share the same backgrounds, we use the same BDT variables for both channels.

these requirements, in total, we generate 50,000,000 events for signal $\ell^\pm\ell^\pm h W^\mp$ and 1,000,000 events for signal $W^\pm W^\pm h W^\mp$; 4,579,172 events for $W^\pm W^\mp b\bar{b}j$; 5,000,000 events for ZZh and $ZhW^\pm$; 29,000,000 events for $t\bar{t}Z$; 30,000,000 events for $t\bar{t}W^\pm$ and $t\bar{t}j$; 15,000,000 events for $ZW^\pm jj$ and $ZW^\pm bb$.

6.5.4 Discovery potential at the 100 TeV collider

The significance is defined as $\frac{S}{\sqrt{S+B}}$ throughout the paper, with $S = \sigma_s \cdot \mathcal{L}$ and $B = \sigma_{\text{bkg}}^{\text{tot}} \cdot \mathcal{L}$ the total signal and background event number at the collider, where σ_s and $\sigma_{\text{bkg}}^{\text{tot}}$ are the final signal and final total background cross section respectively, and $\mathcal{L}$ is the integrated luminosity, which we choose to be $30\,\text{ab}^{-1}$ [669, 670] throughout the paper. By requiring the signal significance to be greater or equal to 5, the BDT based result for the discovery channels is given in Figure 6.7. Several features of these results merit emphasizing:

- We see that at small v_Δ where the neutrino masses are naturally generated through the type-II seesaw mechanism, the CTHM can be discovered over a very wide mass range from tens of GeV to several TeV through the $pp \to H^{++}H^{--} \to \ell^+\ell^+\ell'^-\ell'^-$ channel. We also recast the current LHC constraints for this channel at 8 TeV and 13 TeV, which is done by rescaling the production cross sections and the BRs in Refs. [22, 23]. We find that the current LHC

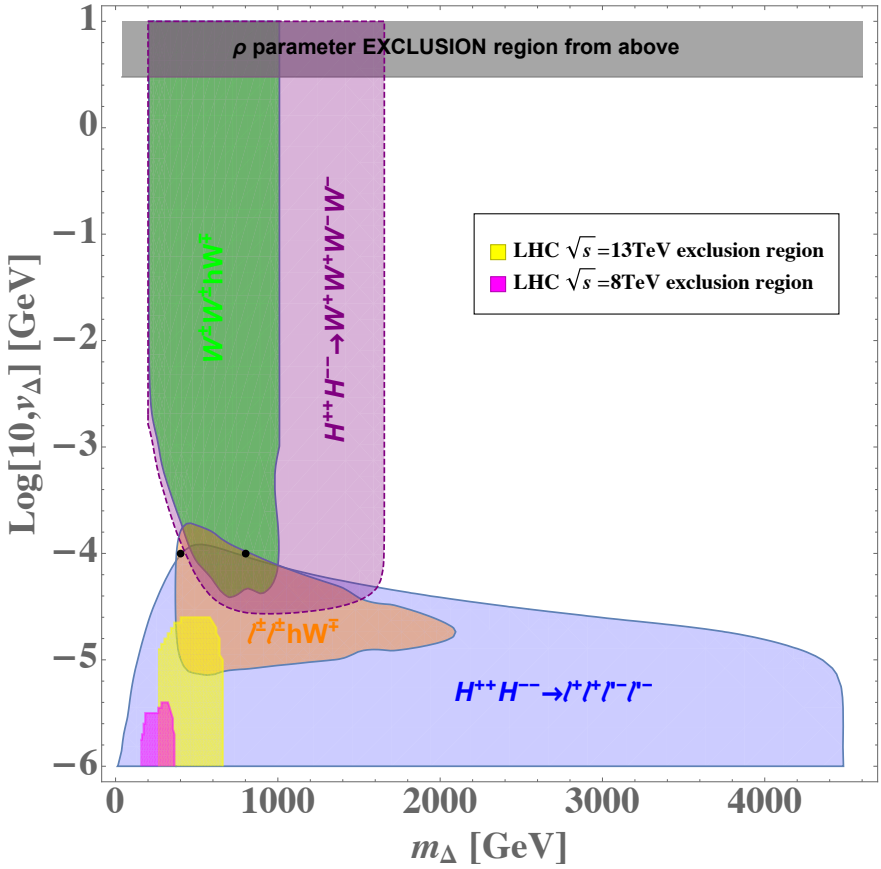

Figure 6.7: Regions of significance $\geq 5\sigma$ in the $m_\Delta - v_\Delta$ plane with $m_{\nu_\ell} = 0.01\,\text{eV}$ ($\ell = e, \mu, \tau$), $\lambda_4 = 0$, $\lambda_5 = -0.1$ and integrated luminosity of $30\,\text{ab}^{-1}$: The blue region corresponds to discovery using the $pp \to H^{++}H^{--} \to \ell^+\ell^+\ell'^-\ell'^-$ channel; the brown region is for the $H^{\pm\pm}H^{\mp} \to \ell^\pm\ell^\pm\, hW^\mp$ channel ; the green region gives discovery using the $H^{\pm\pm}H^{\mp} \to W^\pm W^\pm\, hW^\mp$ mode. The yellow and magenta regions indicate the current LHC exclusion limits at $\sqrt{s} = 13$ TeV [22] and $\sqrt{s} = 8$ TeV [23], respectively. LEP constraints [24,25] are automatically satisfied since our benchmark point corresponds to $m_{H^{\pm\pm}} \gtrsim 54.78\,\text{GeV}$. See the main text for a detail discussion. The black dots show two benchmark values of m_Δ used for Higgs portal coupling determination (see section 6.6).

constraints only exclude the relatively small m_Δ and small v_Δ region of the CTHM parameter space for our benchmark point, which therefore motivates a future collider study as we have done above.

- For the benchmark point we use,

$$m_{H^{\pm\pm}} = m_\Delta^2 + 3001\,(\mathrm{GeV}^2) \Rightarrow m_{H^{\pm\pm}} \gtrsim 54.78\,\mathrm{GeV}, \tag{6.47}$$

such that LEP constraints [24, 25] are automatically satisfied. Note that our Figure 6.7 is plotted as a function of m_Δ such that $m_\Delta = 0$ corresponds a minimal mass of $m_{H^{\pm\pm}} \simeq 54.78\,\mathrm{GeV}$.

- For the large v_Δ region, the $pp \to H^{\pm\pm}H^{\mp} \to W^{\pm}W^{\pm}hW^{\mp}$ channel allows discovery of the CTHM up to about 1 TeV. The LHC constraints for this channel are currently absent, and the corresponding parameter space will be covered by the future 100 TeV collider. In addition, for intermediate v_Δ's, the overlap among $W^{\pm}W^{\pm}hW^{\mp}$, $\ell^{\pm}\ell^{\pm}hW^{\mp}$ and $H^{++}H^{--}$ channels can also allow us to roughly determine $m_\Delta \in [400, 1000]\,\mathrm{GeV}$ and $v_\Delta \in [10^{-4.4}, 10^{-3.9}]\,\mathrm{GeV}$ if all these three channels are observed with significance 5 or more. The redundancy among these models would provide an important cross check that the signals are due to the CTHM.

- For large v_Δ and large m_Δ region where the $H^{\pm\pm} \to W^{\pm}W^{\pm}$ channel dominates as can be seen from left panel of Figure 6.5, one would expect the $H^{++}H^{--} \to W^+W^+W^-W^- \to \ell^+\ell^+\ell'^-\ell'^-\not{E}_T$ channel to cover much of that parameter space. Although our present analysis is not optimized to extend beyond $m_\Delta \sim$ 1.6 TeV for this channel, one might expect use of other W decay modes (and a correspondingly different BDT training) to allow extension to higher masses. As an example, we note that the authors in Ref. [620] have studied the channel

$pp \to H^{++}(\to W^+\ell\nu_\ell)H^{--}(\to W^- jj)$ and concluded that $H^{\pm\pm}$ could be discovered at the 14 TeV LHC with $\mathcal{L} = 10\text{-}30\,\text{fb}^{-1}$. It is worth exploring whether use of this channel (or others) may also afford greater coverage for $m_\Delta \gtrsim 1.6$ TeV.

- One may also consider using the $H^{\pm\pm}H^{\mp\mp} \to W^\pm W^\pm \ell^\mp \ell^\mp$ channel to cover part of the parameter space. We note, however, that since the same-sign di-W and the same-sign di-lepton decay channels are dominant only at large and small v_Δ respectively (as can be seen from the left panel of Figure 6.5), we thus expect these channels to have enough significance only at $v_\Delta \sim (10^{-5}, 10^{-4})\,\text{GeV}$. The same region is already well covered by the $\ell^\pm\ell^\pm hW^\mp$ and $H^{++}H^{--} \to \ell^\pm\ell^\pm\ell'^\mp\ell'^\mp$ channels.

- The $H^{++}H^{--}$ channel covers a very wide range over m_Δ at small v_Δ and the $W^\pm W^\pm\, hW^\mp$ channel disappears around $m_\Delta = 1$ TeV. The reason for the "long tail" of the $H^{++}H^{--}$ channel can be understood from the blue region in Figure 6.8 (a), from which we see that the BR($\text{H}^{\pm\pm} \to \ell^\pm\ell^\pm$) decreases slowly with increasing m_Δ for $v_\Delta \lesssim 10^{-4}\,\text{GeV}$, leading to a very slowly decreasing significance. In contrast, for the $W^\pm W^\pm\, hW^\mp$ channel, the significance drops dramatically at $m_\Delta \approx 1$ TeV because of phase space suppression for heavier particles and decay BR suppression at smaller v_Δ's as can be seen from Figure 6.8(b).

- We remind the reader that we choose $m_\nu = 0.01\,\text{eV}$ for all the three light neutrinos generation throughout the paper. Since a larger (smaller) m_ν will correspond to a larger (smaller) Yukawa coupling and thus a larger (smaller) same-sign di-lepton decay BR of $H^{\pm\pm}$, we therefore expect the same-sign di-lepton decay regions in Figure 6.7 will shift upward (downward) for larger (smaller) m_ν's.

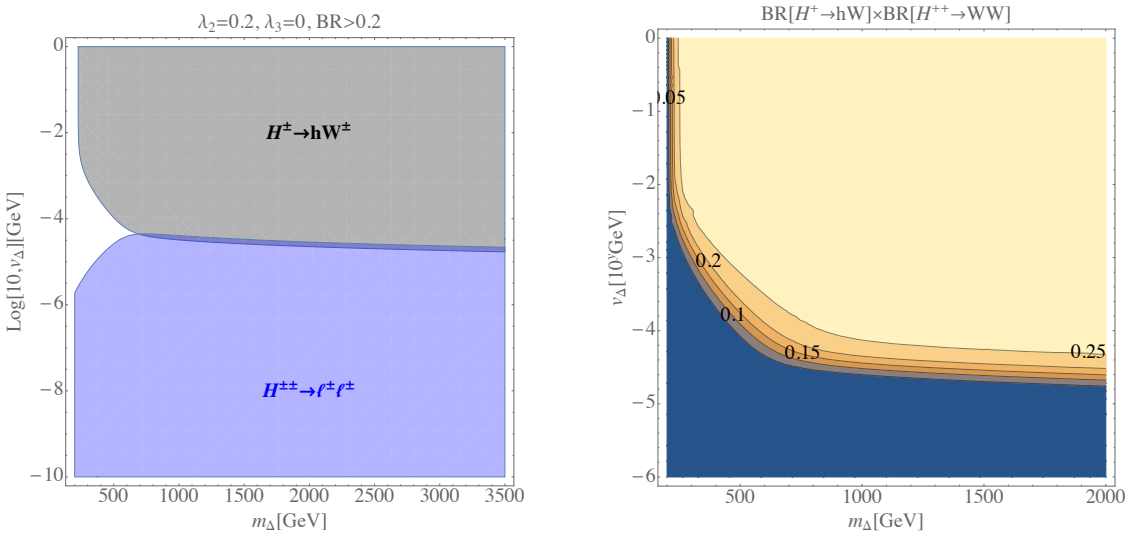

(a) (b)

Figure 6.8: Decay BRs for $\lambda_4 = 0$, $\lambda_5 = -0.1$ and $m_\nu = 0.01\,\text{eV}$. Figure (a): Decay BR$\geq 20\%$ regions for $H^\pm \to hW^\pm$ and $H^{\pm\pm} \to \ell^\pm\ell^\pm$ channels. The slowly decreasing BR($\text{H}^{\pm\pm} \to \ell^\pm\ell^\pm$) with increasing m_Δ explains the "long-tail" of the significance plot for $H^{++}H^{--} \to \ell^+\ell^+\ell'^-\ell'^-$ in Figure 6.7. Figure (b): The solid lines indicate constant contours for BR($\text{H}^\pm \to \text{hW}^\pm$) $\times$ BR($\text{H}^{\mp\mp} \to \text{W}^\mp\text{W}^\mp$). Product of the BRs is suppressed for small v_Δ's, which explains feature of the $W^\pm W^\pm\, hW^\mp$ channel in Figure 6.7 in the small v_Δ region.

- Finally, for our benchmark point, vacuum stability is not guaranteed at the Planck scale as discussed in section 6.2.2.2. In Ref. [552], it was shown that vacuum stability up to the Planck scale actually prefers positive λ_4's as indicated by the black arrow in the left panel of Figure 6.1. This difference is not, in general, problematic, as the stability region for our benchmark point amply covers the triplet mass range considered here. One could anticipate additional degrees of freedom modifying the behavior of the potential at larger scale, so as to ensure stability to the Planck scale. Nevertheless, it is interesting to ask how the reach indicated in Figure 6.7 would evolve as we move along the black arrow in Figure 6.1 corresponding to higher stability scales. We expect the discovery regions including the $H^\pm \to hW^\pm$ channel in Figure 6.7 to shrink for $0 \lesssim \lambda_4 \lesssim 3$ as the $H^\pm \to hW^\pm$ decay BR decreases for λ_4's in this region as can be seen

directly from the upper right panel of Figure 6.4. For $\lambda_4 \gtrsim 6$, one would expect the discovery regions including the $H^\pm \to hW^\pm$ chain to expand even though one needs to re-consider all the model constraints discussed in section 6.2.2. For these larger values of the λ_4, however, we would expect to reach the limit of perturbativity well below the stability scale.

6.6 Triplet Higgs potential determination and simulation

From our result in the previous section, for $m_\Delta \lesssim 4500\,\text{GeV}$, the $H^{++}H^{--} \to \ell^+\ell^+\ell'^-\ell'^-$, $W^\pm W^\pm hW^\mp$ and $\ell^\pm\ell^\pm hW^\mp$ channels can cover a significant portion of the parameter space of the CTHM except the region where $m_\Delta \gtrsim 1\,\text{TeV}$ and $v_\Delta \gtrsim 10^{-4}\,\text{GeV}$. We expect some of the latter region to be covered by the $H^{++}H^{--} \to W^+W^+W^-W^-$ channel as discussed in last section. Therefore, the discovery potential for the CTHM at a 100 TeV pp collider is considerable. Assuming discovery of the doubly- and singly-charged scalars, we can fix λ_5 straightforwardly through the mass splitting as discussed in section 6.3.1. However, to determine the important Higgs portal parameter λ_4, additional information will be needed. For v_Δ larger than $\sim 10^{-5}$ GeV, the BR for $H^\pm \to hW^\pm$ is particularly useful as discussed in section 6.3.2.[viii]

To investigate this possibility, we adopt the following strategy. First, we will carry out a detailed simulation for a choice of $\lambda_4 + \lambda_5$ in the region where the BR($H^\pm \to hW^\pm$) is strongly-dependent on $\lambda_4 + \lambda_5$, according to the top right panel of Figure 6.4. We will carry out this study for a choice of the λ_j consistent with the stability and perturbativity considerations discussed above and for two different choices of the overall triplet mass scale, m_Δ. Second, we will scan over the values of λ_4 and m_Δ for fixed λ_5, thereby varying the production cross section and BR from the values

[viii] Note that, according to Figure 6.7 for v_Δ below $\sim 10^{-5}$GeV, the $\ell^\pm\ell^\pm hW^\mp$ and the $W^\pm W^\pm hW^\mp$ channels will not be observable. In this region, one would need to explore other possible channels in order to determine $\lambda_{4,5}$.

corresponding to our benchmark points. In doing so, we will rescale the significance of the signal accordingly. Third, we will repeat this analysis for different representative choices of v_Δ to indicate how the varying $H^{\pm\pm}$ BR affects the λ_4-sensitivity. Finally, we will compare the sensitivity with that of the observation of the rate for the SM Higgs boson to decay to a di-photon pair, as loop corrections from charged triplet scalars will affect the corresponding rate as functions of the Higgs portal couplings and m_Δ. The results are plotted in Figure 6.11, where we show the corresponding regions of 5σ sensitivity to the model parameters.

In what follows, we provide a more detailed discussion of the collider simulation and analysis than we provided for the results in Figure 6.7, given that we focus on the $H^\pm \to hW^\pm$ channel for coupling determination.

6.6.1 Benchmark points

As discussed in section 6.4.2, the $H^{++}H^{--} \to \ell^+\ell^+\ell'^-\ell'^-$ channel is powerful for the triplet model discovery at small v_Δ, but it can not determine λ_4 as it is λ_4-independent. In contrast, $H^\mp H^{\pm\pm} \to hW^\mp\ell^\pm\ell^\pm / hW^\mp W^\pm W^\pm$ are promising for the determination of λ_4 at intermediate and large v_Δ. In order to determine their collider signatures, we choose two representative benchmark points, taking into account vacuum stability, perturbative unitarity, perturbativity, neutrino masses and our result in Figure 6.7: $m_\Delta = 800\,\text{GeV}$ ($m_\Delta = 400\,\text{GeV}$), $v_\Delta = 10^{-4}\,\text{GeV}$, $m_h = 125\,\text{GeV}$, $m_Z = 91.1876\,\text{GeV}$, $m_\nu = 0.01\,\text{eV}$, $\lambda_2 = 0.2$, $\lambda_3 = 0$, $\lambda_4 = 0$, $\lambda_5 = -0.1$ for the $W^\pm W^\pm hW^\mp$ ($\ell^\pm\ell^\pm hW^\mp$) channel, which is a representative point of the large (small) m_Δ region. Note that although these benchmark parameter choices have $\lambda_4 = 0$, the sum $\lambda_4 + \lambda_5$ differs from zero and lies in a region where $\text{BR}(H^\pm \to hW^\pm)$ varies significantly with this combination of couplings. The choice of two the two different mass scales corresponds to the edges of various overlapping discovery regions, as indicated by the two black points in Figure 6.7.

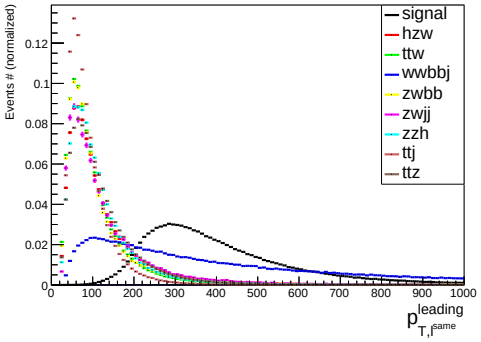

(a) same-sign lepton leading p_T

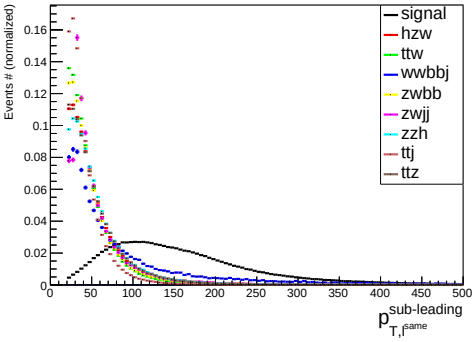

(b) same-sign lepton sub-leading p_T

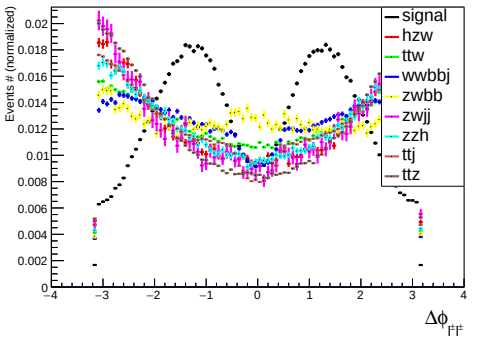

(c) same-sign lepton $\Delta\phi$

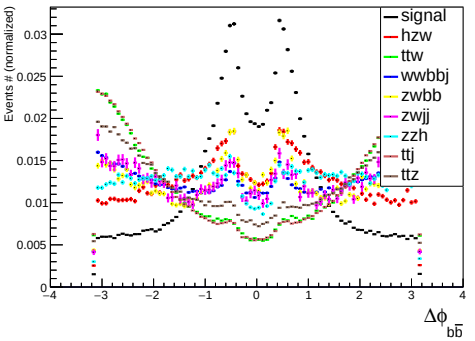

(d) $\Delta\phi$ of two b quarks

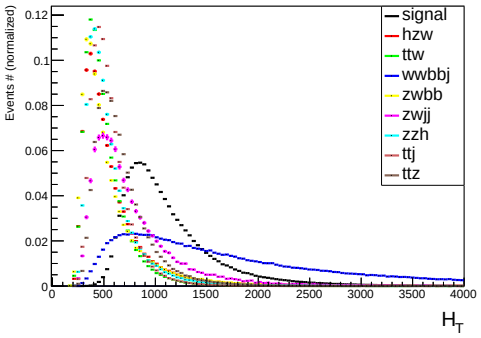

(e) H_T

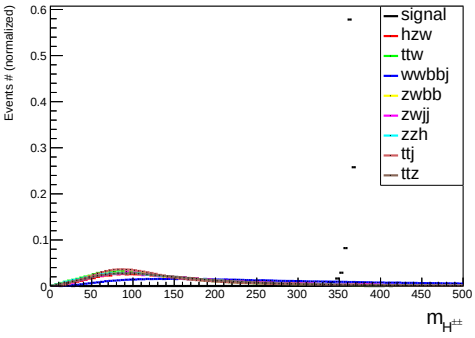

(f) Doubly-Charged Higgs invariant mass

Figure 6.9: Representative reconstructed variables for the $\ell^\pm\ell^\pm hW^\mp$ channel after the basic cuts. We use the word "signal" to represent the $pp \to H^{\pm\pm}H^\mp \to \ell^\pm\ell^\pm hW^\mp$ channel in all histograms above.

proc	original cs	-	bc	hc1	hc1-2	hc1-3	hc1-4	hc1-5	hc1-6
		eff.	2.94	5.78	5.84	14.86	95.95	45.07	6.25
hzw	0.6817	cs	0.02	1.1584E-3	6.7652E-5	1.0053E-5	9.6460E-6	4.3474E-6	2.7268E-7
		eff.	3.47	5.03	3.99	53.16	99.46	30.98	0
zzh	0.1107	cs	3.8413E-3	1.9322E-4	7.7094E-6	4.0983E-6	4.0762E-6	1.2628E-6	0
		eff.	0.25	5.04	3.34	48.39	100	46.67	14.29
zwjj	46.165	cs	0.1133	5.7091E-3	1.9082E-4	9.233E-5	9.233E-5	4.3087E-5	6.1553E-6
		eff.	3.98	4.73	1.85	43.25	81.88	17.09	0
ttz	135.7	cs	5.4044	0.2556	4.7167E-3	2.0402E-3	1.6705E-3	2.8544E-4	0
		eff.	0.83	1.95	2.32	25	100	14.29	0
zwbb	42.66	cs	0.3521	6.8711E-3	1.5926E-4	3.9816E-5	3.9816E-5	5.688E-6	0
		eff.	8.42	8.92	12.69	30.61	93.34	49.56	9.55
wwbbj	2.293	cs	0.1932	1.7223E-2	2.1858E-3	6.6900E-4	6.2442E-4	3.0946E-4	2.9544E-5
		eff.	2.74	19.40	1.18	39.94	81.03	27.33	12.57
ttw	68.7	cs	1.8824	0.3652	4.3235E-3	1.7267E-3	1.3992E-3	3.8243E-4	4.809E-5
		eff.	6.89	16.16	0.44	51.58	82.13	27.44	8.28
ttj	257	cs	17.7094	2.8610	1.2456E-2	6.425E-3	5.2771E-3	1.4478E-3	1.1993E-4
$\sigma_{\mathbf{bkg}}^{\mathbf{tot}}$	507.1454	-	25.6786	3.5130	2.4107E-2	1.1007E-2	9.1171E-3	2.4795E-3	2.0399E-4
		eff.	16.15	62.03	58.30	87.20	96.94	78.43	98.50
signal	0.0148	cs	0.0024	1.4862E-3	8.6373E-4	7.5321E-4	7.3012E-4	5.7264E-4	7.3848E-4
signi.	0.1138	-	0.0820	0.1373	0.9467	1.2030	1.2744	1.7953	4.1664

Table 6.5: Cut flow table for $pp \to H^{\pm\pm}H^{\mp} \to \ell^{\pm}\ell^{\pm}hW^{\mp}$ under basic cuts (bc) and hard cuts (hc) with integrated luminosity of $30\,\mathrm{ab}^{-1}$. Here and in Table 6.9, we use the same abbreviations: "proc." for "processes"; "E" for "base 10 exponential function"; "cs" for "cross section" with unit fb; "eff." for "efficiency" in percent; "signi." for "significance" and "hci-j" means "applying hard cuts i, $\cdots$, j".

6.6.2 Simulation: $pp \to H^{\mp}H^{\pm\pm} \to hW^{\mp}\ell^{\pm}\ell^{\pm} \to b\bar{b}\ell^{\mp}\ell^{\pm}\ell^{\pm}\not{E}_T$ for intermediate v_Δ

In this section we will first generate data for $pp \to H^{\mp}H^{\pm\pm} \to hW^{\mp}\ell^{\pm}\ell^{\pm} \to b\bar{b}\ell^{\mp}\ell^{\pm}\ell^{\pm}\not{E}_T$ using `MadGraph`, and then analyze the data by both a cut-based analysis and using the BDT method. In the former, we choose a set of "hard cuts" by first comparing various signal and background distributions and endeavoring to optimize by hand the choice for greatest signal significance. As an alternative, we employ the BDT. As we show below, the BDT method generally provides a better signal efficiency and significance.

$m_Z \geq 82\,\text{GeV}$ or $m_Z \leq 98\,\text{GeV}$, $80\,\text{GeV} \leq m_h \leq 130\,\text{GeV}$
$p_{T,b}^{\text{leading}} \geq 80\,\text{GeV}$, $p_{T,\ell^{\text{oppo.}}} \geq 40\,\text{GeV}$, $p_{T,\ell^{\text{same}}}^{\text{leading}} \geq 200\,\text{GeV}$, $p_{T,\ell^{\text{same}}}^{\text{sub-leading}} \geq 70\,\text{GeV}$, $H_T \geq 700\,\text{GeV}$
$0 \leq m_{WT} \leq 90\,\text{GeV}$
$-2 \leq \Delta\phi_{b\bar{b}} \leq 2$, $0 \leq \Delta R_{b\bar{b}} \leq 2$
$-1.8 \leq \Delta\phi_{\ell^\pm\ell^\pm} \leq 1.8$, $0.6 \leq \Delta R_{\ell^\pm\ell^\pm} \leq 2.8$
$340\,\text{GeV} \leq m_{H^{\pm\pm}} \leq 390\,\text{GeV}$

Table 6.6: A list of hard cuts for the $pp \to H^{\pm\pm}H^{\mp} \to \ell^\pm\ell^\pm hW^\mp$ channel.

	BDT	**Cut based**
signal efficiency	0.839	0.308
signal significance	6.8922	4.1664
final signal cross section (fb)	1.2417×10^{-2}	7.3848×10^{-4}
event number at detector	60	22

Table 6.7: Comparison between BDT and cut-flow based results at $\mathcal{L} = 30\,\text{ab}^{-1}$ for $pp \to H^{\pm\pm}H^{\mp} \to \ell^\pm\ell^\pm hW^\mp$.

6.6.2.1 Cut based analysis: basic cuts

While analyzing the data by ROOT 6.06.02, we require all the final state particles have transverse momentum $p_T > 20\,\text{GeV}$ and pseudorapidity $|\eta| < 2.5$; we also require exactly three leptons in the final state[ix] and exactly two jets in the final state[x] for the signal and the $t\bar{t}W^\pm$, $t\bar{t}Z$, $hZW^\pm$, $ZW^\pm b\bar{b}$ and hZZ backgrounds. For the $t\bar{t}j$ and $W^+W^-b\bar{b}j$ backgrounds, we require there are exactly two leptons and three jets[xi] in the final state. For the $ZW^\pm jj$ background, when the light jet is a c quark, we use a fake rate of 10%; and when the light jets are other light quarks, we use a fake rate of 0.01% [665].

[ix] With two of them are of same charge and of same flavor, and the third one with an opposite charge only.

[x] With at least one of them being a b quark.

[xi] With at least one and at most two of the three jets are b quarks. The light jet with the smallest p_T among these three jets is taken to be a lepton with a 0.01% fake rate [665].

After the basic cuts, the result of reconstructed variables is given in Figure 6.9, and the cut efficiency is given in Table 6.5. By comparing the signal and the background distributions in Figure 6.9, we find that $\Delta\phi$ and ΔR between the two b quarks, scalar sum of the transverse momentum H_T, same-sign lepton leading and sub-leading p_T, same-sign lepton $\Delta\phi$ and ΔR, m_h, $m_{H^{\pm\pm}}$ and W boson transverse mass m_{WT} have distinct features between our signal and the backgrounds, which can be exploited to reduce the backgrounds. These variables are the hard cuts we apply next.

6.6.2.2 Cut based analysis: hard cuts

To improve the significance of the signal, we apply the following hard cuts in the same order as they are listed in Table 6.6. After applying them, the cut efficiency for each hard cut and significance of our signal are presented in Table 6.5. From the table, it is seen that the backgrounds are efficiently reduced and our signal has a final cross section about 7.3848×10^{-4} fb, with the significance being around 4; and the estimated event number for the signal after the basic cuts and the hard cuts is around 22 at the FCC with $\mathcal{L} = 30\text{ab}^{-1}$.

6.6.2.3 BDT based analysis result

To improve the cut efficiency, we also carry out a BDT based analysis as for analyzing model discovery at the 100 TeV collider in section 6.5. The result is shown in parallel with the cut-based result in Table 6.7 for comparison, and we find that the BDT method improves the signal significance by about a factor of 2 through optimizing the cut efficiency; in addition, the signal efficiency as well as the signal cross section are also improved by about a factor of 3.

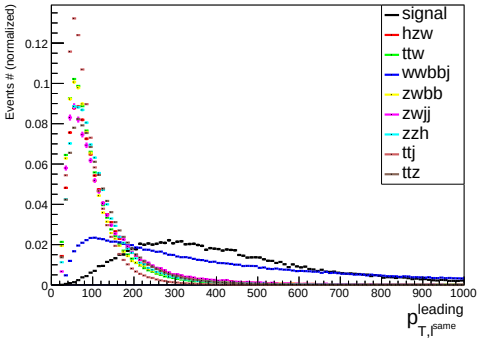

(a) same-sign lepton leading p_T

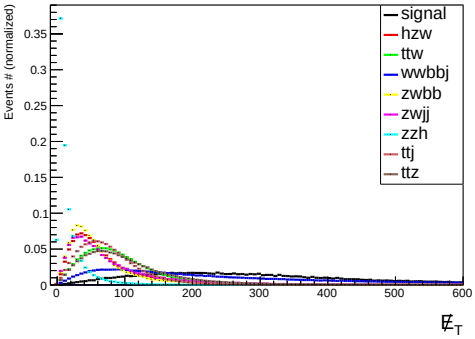

(b) Missing E_T

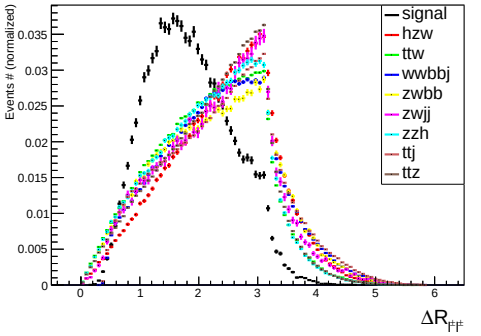

(c) same-sign lepton ΔR

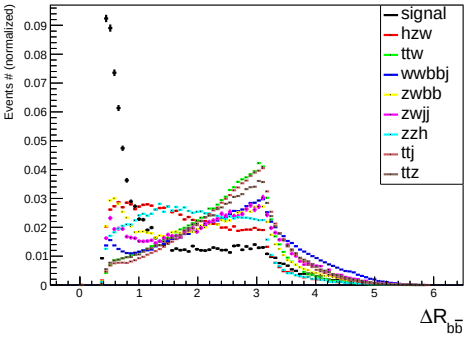

(d) ΔR of two b quarks

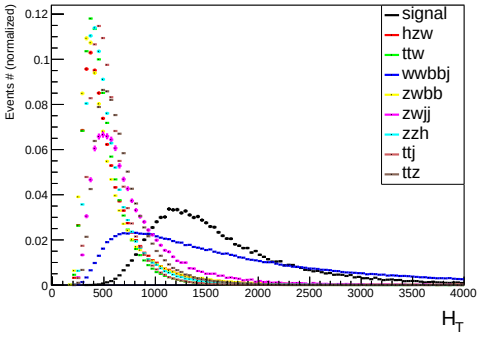

(e) H_T

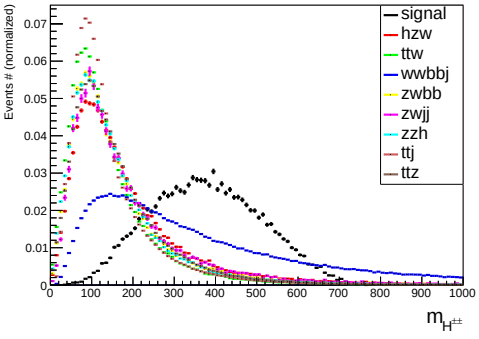

(f) Doubly-charged Higgs invariant mass

Figure 6.10: Reconstructed variables for the $W^{\pm}W^{\pm}hW^{\mp}$ channel under basic cuts. We use the word "signal" to represent the $pp \to H^{\pm\pm}H^{\mp} \to W^{\pm}W^{\pm}hW^{\mp}$ channel in all histograms above.

$m_Z \geq 80\,\text{GeV}$ or $m_Z \leq 100\,\text{GeV}$, $80\,\text{GeV} \leq m_h \leq 140\,\text{GeV}$
$p_{T,b}^{\text{leading}} \geq 80\,\text{GeV}$, $p_{T,\ell^{\text{oppo.}}} \geq 40\,\text{GeV}$, $p_{T,\ell^{\text{same}}}^{\text{leading}} \geq 80\,\text{GeV}$, $p_{T,\ell^{\text{same}}}^{\text{sub-leading}} \geq 50\,\text{GeV}$, $800\,\text{GeV} \leq H_T \leq 2200\,\text{GeV}$
$-1.4 \leq \Delta\phi_{b\bar{b}} \leq 1.4$, $0 \leq \Delta R_{b\bar{b}} \leq 2$
$-2 \leq \Delta\phi_{\ell^\pm\ell^\pm} \leq 2$, $0 \leq \Delta R_{\ell^\pm\ell^\pm} \leq 2.8$
$200\,\text{GeV} \leq m_{H^{\pm\pm}} \leq 800\,\text{GeV}$

Table 6.8: A list of hard cuts for the $pp \to H^{\pm\pm}H^{\mp} \to W^{\pm}W^{\pm}hW^{\mp}$ channel.

6.6.3 Simulation: $H^{\mp}H^{\pm\pm} \to hW^{\mp}W^{\pm}W^{\pm} \to b\bar{b}\ell^{\mp}\ell^{\pm}\ell^{\pm}\not{E}_T$ process for intermediate and large v_Δ

The $H^{\mp}H^{\pm\pm} \to hW^{\mp}\ell^{\pm}\ell^{\pm}$ channel is helpful for the determination of λ_4 only at intermediate v_Δ, for large v_Δ's, the $H^{\mp}H^{\pm\pm} \to hW^{\mp}W^{\pm}W^{\pm}$ channel can be used. Since it shares the same backgrounds as the $H^{\mp}H^{\pm\pm} \to hW^{\mp}\ell^{\pm}\ell^{\pm}$ channel in last sub-section, we generate 1,000,000 events for this signal and use the background data generated for the $H^{\mp}H^{\pm\pm} \to hW^{\mp}\ell^{\pm}\ell^{\pm}$ channel to study its collider phenomenologies. We still perform an exclusive analysis, and by using the same basic cuts as for the $\ell^{\pm}\ell^{\pm}hW^{\mp}$ channel, we obtain the reconstructed variables under basic cuts for the $W^{\pm}W^{\pm}hW^{\mp}$ channel shown in Figure 6.10. Note that $\Delta\Phi$ and ΔR between the two b quarks and the two same-sign leptons, leading p_T of the same-sign leptons, SM h, the doubly-charged Higgs and Z boson masses and the transverse W boson mass are the hard cuts that can be applied to further separate the signal from the backgrounds. Those hard cuts are applied in the same order as they are listed in Table 6.8.

Results after applying the hard cuts are given in Table 6.9. And for comparison, the BDT based analysis is presented in parallel in Table 6.10, we see that BDT based analysis still gives a larger significance, which is about three times larger compared with cut-based result.

6.6.4 Determination of λ_4 upon discovery at the future 100 TeV collider

As we have been addressing throughout the paper, the $H^{\mp}H^{\pm\pm} \to hW^{\mp}\ell^{\pm}\ell^{\pm}$ and the $H^{\mp}H^{\pm\pm} \to hW^{\mp}W^{\pm}W^{\pm}$ channels are important for the determination of

proc.	original cs	-	bc	hc1	hc1-2	hc1-3	hc1-4	hc1-5
		eff.	2.94	4.37	10.35	97.29	39.72	52.92
hzw	0.6817	cs	0.02	8.741E-4	9.0474E-5	8.8025E-5	3.4965E-5	1.8503E-5
		eff.	3.47	3.80	7.02	93.30	51.62	54.71
zzh	0.1107	cs	3.8413E-3	1.4586E-4	1.0246E-5	9.5603E-6	4.9351E-6	2.6999E-6
		eff.	0.25	5.40	9.20	89.62	61.59	55.45
zwjj	46.165	cs	0.1133	6.1201E-3	5.6308E-4	5.0462E-4	3.1077E-4	1.7231E-4
		eff.	3.98	5.08	4.62	63.02	36.59	41.05
ttz	135.7	cs	5.4044	0.2748	1.2704E-2	8.0062E-3	2.9292E-3	1.2026E-3
		eff.	0.83	1.66	3.90	82.5	74.24	44.90
zwbb	42.66	cs	0.3521	5.8326E-3	2.2750E-4	1.8769E-4	1.3935E-4	6.2563E-5
		eff.	8.42	10.72	24.12	83.77	52.14	65.83
wwbbj	2.293	cs	0.1932	2.0719E-2	4.9978E-3	4.1865E-3	2.1826E-3	1.4369E-3
		eff.	2.74	22.76	1.94	59.90	42.10	53.38
ttw	68.7	cs	1.8824	0.4139	8.3198E-3	4.9832E-3	2.0977E-3	1.1198E-3
		eff.	6.89	18.54	1.26	65.57	45.23	34.56
ttj	257	cs	17.7094	3.2826	4.1454E-2	2.7182E-2	1.2293E-2	4.2491E-3
$\sigma_{\mathbf{bkg}}^{\mathbf{tot}}$	507.1454	-	25.6786	4.0050	6.8367E-2	4.5148E-2	1.9993E-2	8.2645E-3
		eff.	5.68	51.03	79.46	100	70.07	94.24
signal	0.0971	cs	5.5079E-3	2.8104E-3	2.2331E-3	2.1615E-3	1.5146E-3	1.4273E-3
sig.	0.7467	-	0.1883	0.2433	1.4564	1.7220	1.7896	2.5123

Table 6.9: Cut flow table for $H^{\mp}H^{\pm\pm} \to hW^{\mp}W^{\pm}W^{\pm}$ under basic cuts (bc) and hard cuts (hc) with integrated luminosity of $30\,\mathrm{ab}^{-1}$. Here we use the same abbreviations as in Table 6.5.

λ_4, but our study above is done at only one benchmark point for both $H^{\mp}H^{\pm\pm} \to hW^{\mp}\ell^{\pm}\ell^{\pm}$ and $H^{\mp}H^{\pm\pm} \to hW^{\mp}W^{\pm}W^{\pm}$. To see how our result is sensitive to λ_4, we fix $\lambda_5 = -0.1$ and perform a scan in the λ_4-m_Δ plane.[xii] Doing so, it is straightforward to rescale the signal and, thereby, obtain the variation in signal significance. The corresponding results are given in Figure 6.11 (a), (b), (c) with $v_\Delta = 10^{-1}\,\mathrm{GeV}$, $v_\Delta = 10^{-4}\,\mathrm{GeV}$ and $v_\Delta = 10^{-5}\,\mathrm{GeV}$ respectively. There, we indicate the regions giving larger than 5σ significance for the two channels considered here.

In Figure 6.11(a), i.e., at large $v_\Delta = 10^{-1}\,\mathrm{GeV}$, only the $W^{\pm}W^{\pm}hW^{\mp}$ channel is useful, whereas the significance for $\ell^{\pm}\ell^{\pm}hW^{\mp}$ is less than 5 in the entire parameter space. The reason is that the rate for $H^{\pm\pm} \to \ell^{\pm}\ell^{\pm}$ is highly suppressed at large v_Δ

[xii] Note that $\lambda_{2,3}$ are suppressed by v_Δ, so their values do not matter here.

	BDT	Cut based
signal efficiency	0.6009	0.2591
signal significance	6.8507	2.5123
final signal cross section (fb)	3.3097×10^{-3}	1.4273×10^{-3}
event number at detector	99	42

Table 6.10: Comparison between BDT and cut-flow based results at $\mathcal{L} = 30\,\text{ab}^{-1}$ for $pp \to H^{\pm\pm}H^{\mp} \to W^{\pm}W^{\pm}hW^{\mp}$.

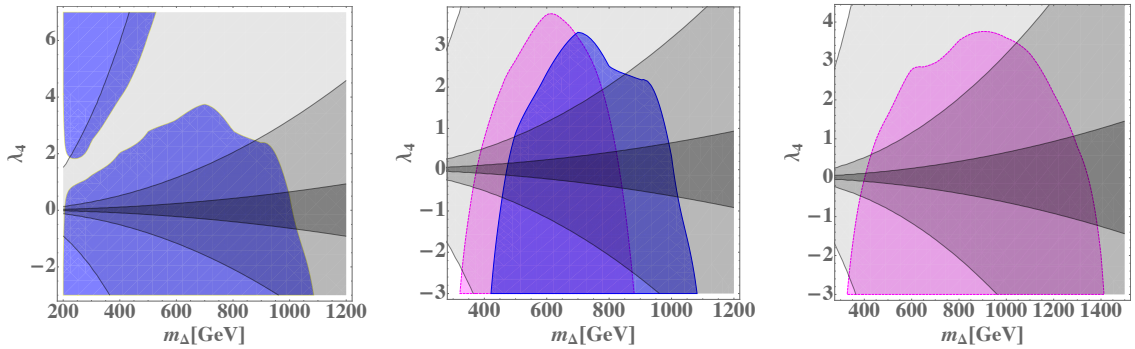

(a) $v_\Delta = 10^{-1}\,\text{GeV}$ (b) $v_\Delta = 10^{-4}\,\text{GeV}$ (c) $v_\Delta = 10^{-5}\,\text{GeV}$

Figure 6.11: Blue is significance ≥ 5 region for the $hW^{\mp}W^{\pm}W^{\pm}$ channel and magenta is that for the $hW^{\mp}\ell^{\pm}\ell^{\pm}$ channel. The outermost very light black region is the combined constraint on $R_{h\gamma\gamma}$ from ATLAS and CMS at 7 TeV and 8 TeV; the intermediate light black region is the planned FCC-ee constraint and the innermost black region is the planned FCC-ee+FCC-hh constraint on $R_{h\gamma\gamma}$.

as can be seen from left panel of Figure 6.5. For $W^{\pm}W^{\pm}hW^{\mp}$, the appearance of the region at the upper-left corner is due to an increase of the decay BR for $H^{\pm} \to hW^{\pm}$ when λ_4 goes from negative to positive as can be seen from the upper right panel of Figure 6.4. Therefore, at large v_Δ, the $W^{\pm}W^{\pm}hW^{\mp}$ channel is more helpful for the determination of λ_4 at the FCC.

From Figure 6.11(b), i.e., corresponding to intermediate $v_\Delta = 10^{-4}\,\text{GeV}$, both $W^{\pm}W^{\pm}hW^{\mp}$ and $\ell^{\pm}\ell^{\pm}hW^{\mp}$ can help to determine λ_4. The $W^{\pm}W^{\pm}hW^{\mp}$ channel covers a larger region at a higher mass scale while the $\ell^{\pm}\ell^{\pm}hW^{\mp}$ channel provides more coverage at a lower mass scale. The overlap between these two channels makes

them useful as a cross check if the triplet scale is around $m_\Delta \in [400, 900]\,\text{GeV}$. For $m_\Delta \in [900, 1100]\,\text{GeV}$, the $W^\pm W^\pm h W^\mp$ channel can be used to determine λ_4; and for $m_\Delta \in [300, 400]\,\text{GeV}$, we can use the $\ell^\pm \ell^\pm h W^\mp$ channel.

And from Figure 6.11(c), i.e., at small $v_\Delta = 10^{-5}\,\text{GeV}$, only the $\ell^\pm \ell^\pm h W^\mp$ channel can be used to determine λ_4 since the $H^{\pm\pm} \to W^\pm W^\pm$ channel is highly suppressed as can be seen from the left panel of Figure 6.5. Comparing this result with those at $v_\Delta = 10^{-1}\,\text{GeV}$ and $v_\Delta = 10^{-4}\,\text{GeV}$, we see that at $v_\Delta = 10^{-5}\,\text{GeV}$, the $\ell^\pm \ell^\pm h W^\mp$ channel covers the largest mass region up to about 1.4 TeV.

It is now interesting to consider the possible complementarity between these direct probes of the Higgs portal coupling and mass with indirect tests. As has been studied in Refs. [584,671], the doubly-charged Higgs particle of the CTHM can give a sizable contribution to the $h \to \gamma\gamma$ decay rate especially for negative λ_4 and λ_{45} due to a constructive interference [554]. We therefore expect the $h \to \gamma\gamma$ decay rate to provide an indirect determination of λ_4 by excluding some of the parameter space on the λ_4-m_Δ plane. In this context, we consider the ratio $R_{h\gamma\gamma}$ given

$$R_{h\gamma\gamma} = \frac{\Gamma^{\text{NP}}(h \to \gamma\gamma) + \Gamma^{\text{SM}}(h \to \gamma\gamma)}{\Gamma^{\text{SM}}(h \to \gamma\gamma)}, \tag{6.48}$$

with Γ^{NP} and Γ^{SM} the new physics (NP) and pure SM contribution to the decay rate of $h \to \gamma\gamma$ respectively. From Eq. (6.48) we see that, if nature is completely described by SM, then this ratio will exactly be one; and any value that deviates from one might be a source of new physics. For the quark loop contributions, we retain only the dominant t quark for the fermion loop contribution to $R_{h\gamma\gamma}$. The current LHC and the proposed FCC constraints on this ratio is indicated in the λ_4-m_Δ plane in Figure 6.11 (a), (b), (c),[xiii] where the lightest black region is the combined constraint

[xiii] The values we use for $R_{h\gamma\gamma}$ are: For the LHC, we use the current experimental value $1.16^{+0.20}_{-0.18}$ [578,672]; For the FCC-ee collider, we use the proposed values, i.e.; 1 ± 0.05, and 1 ± 0.01 for FCC-hh collider [673].

on $R_{h\gamma\gamma}$ from ATLAS and CMS at 7 TeV and 8 TeV; the intermediate black region is the planned FCC-ee constraint and the darkest black region shows the combined planned FCC-ee+FCC-hh constraint on $R_{h\gamma\gamma}$.

From Figure 6.11 (a), we see that the current LHC constraint on $R_{h\gamma\gamma}$ is almost ruled out the small m_Δ and large λ_4 region, but in other regions, the current LHC constraints on the λ_4-m_Δ plane are relatively weak. This situation, however, will be changed considerably by the future 100 TeV collider as can be seen from the darker black region in Figure 6.11 (a), (b), (c).

Thus, combination of the direct and indirect probes of the CTHM would be advantageous in the determination of λ_4. If future precision measurements of the $h \to \gamma\gamma$ decay rate agree with the SM expectations, a substantial portion of the λ_4-m_Δ parameter space will be excluded, thereby assisting in the determination of λ_4. In the remaining regions of parameter space, λ_4 could eventually be determined by $H^\mp H^{\pm\pm} \to \ell^\pm \ell^\pm h W^\mp$ and $H^\mp H^{\pm\pm} \to W^\pm W^\pm h W^\mp$ based on our study above. It is also possible that future experiments at the LHC, FCC-ee, or FCC-hh see a deviation of $R_{h\gamma\gamma}$ from the SM prediction. In this case, if λ_5 is determined from mass splitting (-0.1 in our case), we might also also conclude that: (1) If the deviation is detected through the $hW^\mp W^\pm W^\pm$ ($hW^\mp \ell^\pm \ell^\pm$) channel, the triplet will have a large (small) vev with $|\lambda_4| \sim 1$; (2) if the deviation is observed from both $hW^\mp W^\pm W^\pm$ and $hW^\mp \ell^\pm \ell^\pm$ channels, an intermediate triplet vev can be inferred with $|\lambda_4| \sim 1$.

6.7 Discussion and summary

In this chapter, we have investigated the model discovery and Higgs portal parameter determination of the Complex Triplet Higgs Model at a prospective 100 TeV pp collider. The triplet with Y=2 has long been known as a key ingredient in generating non-zero neutrino masses through the type-II seesaw mechanism. The triplet interacts with the SM through its electroweak gauge interactions, its coupling to the leptons

in the type-II see saw interaction, and to the Higgs doublet via the Higgs portal parameters λ_4 and λ_5. The latter modify the scalar potential and may enable a strong first order electroweak phase transition, as needed for electroweak baryogenesis.

The CTHM parameter space is constrained by current experiments at the LHC in the region where the triplet is light ($\lesssim 600\,\text{GeV}$) and its vev, v_Δ, is small ($\lesssim 10^{-4.6}\,\text{GeV}$). In this paper, we have analyzed the reach of a prospective 100 TeV pp collider by working in the Normal Mass Hierarchy (NMH) framework, wherein the doubly-charged Higgs particle $H^{\pm\pm}$ is the heaviest. Based on our study, we conclude that a large part of the CTHM parameter space will be covered by the 100 TeV collider in the future as shown in our Figure 6.7. More specifically, we find that :

1. The $H^{++}H^{--}$ and $H^{\pm\pm}H^{\mp}$ channels have the largest and the second largest cross section respectively, making them the dominant discovery channels of the CTHM. Importantly, the $H^{++}H^{--} \to \ell^+\ell^+\ell'^-\ell'^-$ channel is recognized as the smoking-gun signature of the CTHM, which can be used to discover the triplet up to a mass $\sim$4.5 TeV when $v_\Delta \lesssim 10^{-4}\,\text{GeV}$. In addition, for $v_\Delta \gtrsim 10^{-4}\,\text{GeV}$, the triplet model can be discovered by the $H^{\pm\pm}H^{\mp} \to \ell^\pm\ell^\pm hW^\mp/W^\pm W^\pm hW^\mp$ channel when the triplet mass is below $\sim$1 TeV.

2. For $v_\Delta \gtrsim 10^{-4}\,\text{GeV}$, the triplet can also be discovered through the $H^{++}H^{--} \to W^+W^+W^-W^- \to \ell^+\ell^+\ell'^-\ell'^-\not{E}_T$ channel when the triplet mass is below $\sim$1.7 TeV. In arriving at this conclusion, we use the same BDT training and test variables as for the $H^{++}H^{--} \to \ell^+\ell^+\ell'^-\ell'^-$ channel. However, if one were to choose a different set of BDT training and test variables to optimize the cut efficiency, or if one were to study different final states like in Ref. [620], one might anticipate that the quartic-W channel will also cover the upper right white corner in Figure 6.7, such that the whole parameter space can be explored at the future 100 TeV collider.

3. Upon discovery, Higgs portal parameter λ_5 can be determined straightforwardly from the mass splitting $\Delta m \approx \frac{|\lambda_5|v^2}{8m_\Delta}$ defined in Eq. (6.43).

While the triplet can be discovered over a wide range and λ_5 can be calculated straightforwardly from the mass splitting upon discovery, determination of the other Higgs portal parameter λ_4 is more complicated even after discovery. Fortunately, we can obtain λ_4 through precise measurements of the decay branching ratios. We find that only four decay vertices are helpful and summarize them in Table 6.1. At the same time, to further narrow down the parameter space, precise measurements on the $h \to \gamma\gamma$ decay rate can help indirectly to the determination of λ_4 by excluding some of the parameter space, as shown in our Figure 6.11.

In this work, we only focus on the charged triplet Higgs particles in the NMH framework. However, the neutral triplet Higgs particles can also be used for model discovery and the Higgs portal parameter determination at the 100 TeV collider. Looking ahead to future studies of the neutral states, we comment that:

1. In the NMH framework, the HA channel has the third largest cross section. We present the decay patterns of H and A in Figure A.1 and Figure A.2 respectively in Appendix A.3. Recall from Table 6.1 that $A \to hZ$ is relevant for λ_4 determination, we find that the $pp \to HA \to hh\,hZ \to \gamma\gamma b\bar{b}b\bar{b}\ell^+\ell^-$ channel only has $\mathcal{O}(100)$ events at the future collider with $\sqrt{s} = 100\,\text{TeV}$ and $\mathcal{L} = 30\,\text{ab}^{-1}$ even without considering the backgrounds. Again, the event number can be improved by studying different final states or different decays chain including vertices in Table 6.1.

2. For λ_4 determination, the $H^\pm \to hW^\pm$ channel has a larger branching ratio for $\lambda_{45} < 0$. In comparison, $H \to ZZ$ has a larger branching ratio $\lambda_{45} > 0$, which makes the vacuum stable to a higher scale compared with the benchmark point we use in this work. On the other hand, $H \to W^+W^-/A \to hZ$ channel

dominates for both positive and negative λ_{45} as can be seen from the right panel of Figure A.1 and Figure A.2. Therefore, theoretically, the HA channel also provides a way to for model discovery and $\lambda_{4,5}$ determination at the 100 TeV collider.

CHAPTER 7

REAL SCALAR TRIPLET DARK MATTER

7.1 Introduction

Deciphering the identity of dark matter (DM) is one of the primary ambitions in particle physics as discussed in Chapter 4. Among many of those interesting proposals, we consider here a viable WIMP candidate from the neutral component of an electroweak multiplet that is singlet under $\mathrm{SU}(3)_C$. A comprehensive study of all possible electroweak multiplets has been done in [674], and the related phenomenology has been studied in a multitude of works [33, 675–700]. Among these scenarios is the real $SU(2)_L$ triplet scalar (Σ) with a vanishing hypercharge ($Y = 0$) to avoid the stringent constraints from dark matter detection discussed in Chapter 4. This model – the ΣSM– corresponds to the simplest extension of the SM scalar sector involving particles carrying electroweak charge, and imposing a Z_2 symmetry enables the neutral component (Σ^0) of Σ to be stable and our dark matter candidate. Previous works have shown that the correct thermal relic abundance is obtained if the mass of the neutral component is around 2.5 TeV. For this mass regime, the corresponding search at the LHC is challenging.

However, though $\Sigma^\pm$ and Σ^0 are degenerate at tree level, one-loop radiative corrections generate a small mass splitting between them being $\Delta m \sim 166\,\mathrm{MeV}$ [674], which gets further modified by a few MeV if two-loop corrections are also included [701]. In this case, the charged scalar becomes long-lived with a decay length of $O(1)$ cm such that a disappearing track in detectors could be observed. The disappearing feature comes from the following fact: The main decay mode of $\Sigma^\pm$ is $\Sigma^\pm \to \Sigma^0\pi^\pm$ with the

branching ratio being around 97%, since the mass splitting is very close to the rest mass of pion in the final state, the pion will be too soft to be observed at detectors, resulting a disappearing track from the decay of $\Sigma^{\pm}$. The disappearing track signature has comprehensively been discussed to search for compressed dark sectors [702], neutralino DM at the LHC [26] and future hadron collider [702–705].

In this chapter, we explore the discovery reach for the triplet scalar DM with a disappearing charged track (DCT) signature at the LHC and a prospective future 100 TeV pp collider. We pay particular attention to the triplet interaction with the SM Higgs doublet. Previous studies [28, 674] have neglected the corresponding Higgs portal coupling, whose presence may modify both the DM and collider analyses in the following ways: 1) annihilation cross sections of the DM, 2) the DM-nucleon spin-independent elastic cross section, and 3) production cross sections of the charged scalars. Our analysis not only updates the possibility of the DM candidate in the ΣSM taking into account the nonzero Higgs portal coupling, but also investigates the reach of a DCT search at the 13 TeV LHC and provides a rough estimate at a future 100 TeV hadron collider. To start, we discuss the setup of this model in the next section.

7.2 The Real Triplet Model (ΣSM)

The scalar sector Lagrangian for the ΣSM is given by

$$\mathcal{L} = (D_\mu H)^\dagger (D^\mu H) + (D_\mu \Sigma)^\dagger (D^\mu \Sigma) - V(H, \Sigma), \tag{7.1}$$

where the $SU(2)$ doublet Higgs H and triplet scalar Σ are cast into the form

$$H = \begin{pmatrix} G^+ \\ \frac{1}{\sqrt{2}}(v + h + iG^0) \end{pmatrix}, \qquad \Sigma = \frac{1}{2}\begin{pmatrix} \Sigma^0 & \sqrt{2}\Sigma^+ \\ \sqrt{2}\Sigma^- & -\Sigma^0 \end{pmatrix}, \tag{7.2}$$

with the Higgs vacuum expectation value (VEV) $v \simeq 246$ GeV. The covariant derivative acting on Σ is defined by $D_\mu \Sigma = \partial_\mu \Sigma + i g_2 [W_\mu, \Sigma]$ with the product of the $SU(2)$ gauge boson and Pauli matrices $W_\mu = W_\mu^a \tau^a / 2$ (the corresponding expression for $D_\mu H$ is standard). The scalar potential is given by

$$V(H, \Sigma) = -\mu^2 H^\dagger H + \lambda_0 \left(H^\dagger H\right)^2 - \frac{1}{2}\mu_\Sigma^2 F + \frac{b_4}{4} F^2 + \frac{a_2}{2} H^\dagger H F, \tag{7.3}$$

where $F = (\Sigma^0)^2 + 2\Sigma^+\Sigma^-$. In the above potential, a Z_2 discrete symmetry is imposed, under which Σ transforms with a Z_2-odd parity while all the others are Z_2-even. As a result, the scalar trilinear term $H^\dagger \Sigma H$ is forbidden. At tree level, the scalar masses are given by

$$m_h^2 = 2\lambda_0 v^2, \tag{7.4}$$

$$m_{\Sigma^0}^2 = m_{\Sigma^\pm}^2 = -\mu_\Sigma^2 + \frac{a_2 v^2}{2} \equiv m_0^2. \tag{7.5}$$

The degeneracy between $\Sigma^\pm$ and Σ^0 is broken by including the electroweak radiative corrections [674]:

$$\Delta m = m_{\Sigma^\pm} - m_{\Sigma^0} = \frac{\alpha_2 m_0}{4\pi} \left[f\left(\frac{m_W}{m_0}\right) - c_W^2 f\left(\frac{m_Z}{m_0}\right) \right], \tag{7.6}$$

where $\alpha_2 = g_2^2 / (4\pi)$, $m_{W(Z)}$ is the $W(Z)$ boson mass, $c_W = \cos\theta_W$ is the cosine of the weak mixing angle, and k is a UV regulator. The loop functions are

$$f(r) = -\frac{r}{4} \left[2r^3 \log r - kr + \left(r^2 - 4\right)^{\frac{3}{2}} \ln A(r) \right], \tag{7.7}$$

where

$$A(r) = \frac{1}{2} \left(r^2 - 2 - r\sqrt{r^2 - 2} \right). \tag{7.8}$$

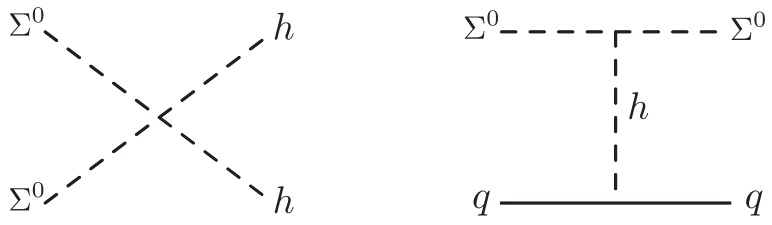

Figure 7.1: Examples of contributions from the Higgs portal coupling to the DM annihilation (left) and spin-independent (right) cross section. The variable q represents the SM quarks.

In the case of $m_0 \gg m_W$, the above expression can be simplified, leading to $\Delta m = (166 \pm 1)\,\mathrm{MeV}$. This mass splitting ensures the decay channel $\Sigma^\pm \to \Sigma^0\pi^\pm$ is kinematically allowed, and the corresponding rate is

$$\Gamma\left(\Sigma^\pm \to \Sigma^0\pi^0\right) = \frac{2G_F^2}{\pi} f_\pi^2 V_{ud}^2 \left(\Delta m\right)^3 \sqrt{1 - \frac{m_\pi^2}{\left(\Delta m\right)^2}}, \tag{7.9}$$

where the other quantities in this expression are the Fermi constant G_F, pion decay constant f_π (= 131 MeV), the CKM matrix V_{ud} and pion mass m_π.[i] This decay mode accounts for 97% of the branching ratio, and the remaining modes are $\Sigma^\pm \to \Sigma^0\mu^\pm\nu_\mu$ and $\Sigma^\pm \to \Sigma^0 e^\pm \nu_e$. And, it follows that the charged scalar has a relatively long lifetime $\tau_{\Sigma^\pm} \sim 0.17$ ns.

7.2.1 Phenomenological aspects

Here, we briefly comment on the following two main points:

- DM candidate : Σ^0

  To provide a dark matter candidate in the ΣSM, the triplet VEV $\langle\Sigma\rangle = 0$ is needed in addition to the Z_2 symmetry. Otherwise, the Higgs portal interaction in the potential would introduce mixing between the SM Higgs and Σ^0,

[i] The expression corresponds to the leading term of an expansion with respect to $\Delta m/m_{\Sigma^\pm}$, in which dependence on $m_{\Sigma^\pm}$ is canceled out and only the mass difference remains.

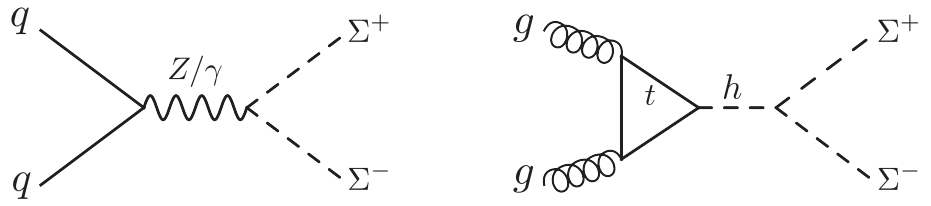

Figure 7.2: Examples of production mechanisms of the charged scalars : the DY (left) and ggF (right) processes.

allowing Σ^0 to decay. Under these conditions, Σ^0 becomes our dark matter candidate and previous studies showed that the mass of this DM candidate must be around 2.5 TeV [28,674] if Σ^0 saturates the dark matter relic density. However, the results were obtained by neglecting the Higgs portal coupling a_2. Consequently, diagrams in Fig. 7.1 were not considered. However, in a recent study of electroweak multiplet dark matter for higher dimensional representations of $\mathrm{SU}(2)_L$, it was shown that inclusion of the non-vanishing Higgs portal coupling can substantially alter the relationship between the relic density and dark matter mass [683]. Therefore, inclusion of non-vanishing a_2 will be considered here.

- Disappearing track search : $\Sigma^\pm \to \Sigma^0 \pi^\pm$

  The small mass splitting between $\Sigma^\pm$ and Σ^0 leads to a smoking gun signature of the disappearing charged track (DCT), which has been searched for at the LHC [26, 706]. The previous study in [33] analyzed disappearing track events in the electroweak Drell-Yann (DY) process (left diagram of Fig. 7.2) with a single initial state radiation. The authors concluded that one could expect to see several hundreds of track events in 100 fb^{-1} at the LHC. However, for the DM mass range considered in that work, Σ^0 can explain only a portion of the present relic density. In the presence of the Higgs portal coupling, an additional production mechanism, gluon-gluon fusion process (ggF) in the right diagram of Fig. 7.2, can increase the number of disappearing track events. In what

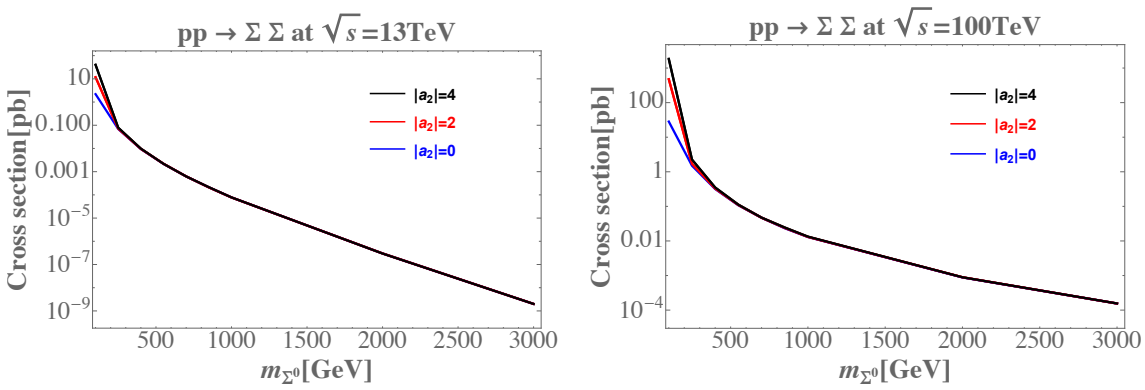

Figure 7.3: Pair production cross sections of triplet particles $\Sigma = \Sigma^{\pm,0}$ at 13 TeV and 100 TeV pp colliders as a function of m_{Σ^0} with representative values of a_2.

follows, by including the ggF process, we analyze the reach with disappearing track searches, including a mass range for m_{Σ^0} consistent with the observed relic density.

7.3 Collider phenomenology with disappearing track searches

ATLAS can currently reconstruct tracks as short as $\mathcal{O}(10)$ cm, providing the opportunity to search for long-lived particle with lifetimes of $\mathcal{O}(0.2)$ ns [26].[ii]. We, therefore, study the discovery potential of the ΣSM at the LHC by recasting the ATLAS search for disappearing tracks reported in Ref. [26]. We also provide optimistic projections for the High-Luminosity LHC (HL-LHC) and a rough extrapolation of the reach to a hypothetical 100 TeV collider. We adopt a benchmark set of parameters yielding $c\tau = 68.42, 55.36, 46.11$ mm throughout our study, consistent with $\Delta m = 160, 166, 172$ MeV, respectively[iii].

[ii]For a state-of-art review on long-lived particle searches at the LHC, see Ref. [707]

[iii]Our choice of mass splittings is motivated through considering two-loop corrections to the mass splitting. See, for instance, Ref. [701].

Fig. 7.3 shows the pair production cross-sections for $pp \to \Sigma\Sigma$, with $\Sigma = \Sigma^{\pm,0}$, at both 13 TeV and 100 TeV colliders calculated with `MadGraph2.6.1` [659].[iv] Note that the cross sections have some a_2 dependence only when $m_{\Sigma^0} \lesssim 300\,\text{GeV}$ and that $m_\Sigma \lesssim 90\,\text{GeV}$ has already been excluded by LEP [711].[v] The a_2 dependence in Fig. 7.3 can be understood as follows:

- For the $\Sigma^\pm\Sigma^0$ final state, it is uniquely produced through $qq' \to W^{\pm *} \to \Sigma^\pm\Sigma^0$, and there is no a_2 dependence.

- For the $\Sigma^+\Sigma^-$ ($\Sigma^0\Sigma^0$) final state, the production channels are $gg/q\bar{q} \to h^*/\gamma^*, Z^* \to \Sigma^+\Sigma^-$ ($gg/q\bar{q} \to h^* \to \Sigma^0\Sigma^0$), where the a_2 dependence arises from the $h\Sigma^+\Sigma^-$ ($h\Sigma^0\Sigma^0$) vertex. However, when the triplet becomes heavy such that the square of the parton center of mass energy $\hat{s} > 4m_t^2$, where m_t is the top quark mass, the ggh form factor decreases dramatically such that the Drell-Yan processes dominate. In this regime, we thus lose the a_2 dependence.

We point out that the pair production cross sections given in Fig. 7.3 are all calculated at the leading order (LO) with `MadGraph2.6.1`. As discussed in Ref. [713], next-to-leading-order (NLO) QCD corrections could enhance the cross section by a factor of about 2 for the ggF process. Therefore, our production cross section above for the $\Sigma^{\pm(0)}\Sigma^{\mp(0)}$ processes for $|a_2| \sim \mathcal{O}(1)$ or larger is an underestimate when the triplet is light. When the triplet is heavy, which is relevant for our DM study as detailed below, since the ggF process will be suppressed as discussed above, the most relevant NLO QCD corrections are those applicable to the electroweak Drell-Yan process. As summarized in Ref. [708], the corresponding K-factor is about 1.18 for the LHC with $\sqrt{s} = 13\,\text{TeV}$, which corresponds to mild corrections to our LO results.

[iv] We compute cross sections at the LO at both 13 TeV and 100 TeV. The NLO effects are very modest, with a $K-$factor of 1.18 at the 13 TeV LHC. See, e.g. the discussion in Ref. [708–710].

[v] LEP places a combined lower limit on chargino mass, for example, at 92.4 GeV [712].

Thus, we do not expect the NLO QCD corrections to have a substantial impact on our analysis of the LHC sensitivity. On the other hand, since the corresponding K-factor for a future 100 TeV collider does not exist, we will not include the corresponding corrections in our analysis of the higher energy pp Drell-Yan process.

In what follows, we present the recast details of the ATLAS search for disappearing tracks in Ref. [26].

7.3.1 Validation of the ATLAS 13 TeV disappearing track search

The ATLAS 13 TeV search in Ref. [26] looks for long-lived charginos based on a DCT signature. To make sure the calibration of our simulations is reliable before its application to the ΣSM, we first validate the ATLAS result for their electroweak anomaly-mediated supersymmetry breaking (AMSB) benchmark model. Events are generated with `MadGraph2.6.1` [659] and showered with `Pythia8` [714]. Our detector simulation is based on a custom made code which replicates the ATLAS 13 TeV search.

The ATLAS search selects events with large missing transverse momentum ($\not{p}_T$), and the signal topology targeted is characterized to have a high-p_T jet to ensure large $\not{p}_T$. A candidate event is required to have at least one "pixel tracklet", which is a short track with only pixel hits (i.e with no associated hits in the the strip semiconductor tracker or SCT). Furthermore, the candidate pixel tracklets are required to have $p_T > 100\,\text{GeV}$. In Ref. [26], the authors interpreted the result in the context of AMSB for both electroweak and strong production of charginos. We use the efficiency maps directly on Monte Carlo truth information (i.e., generator-level chargino decay position, η and p_T), as we can not simulate the tracklet's quality requirements and disappearance condition.

Backgrounds for disappearing tracks can arise from charged particles scattered by the material and fake tracks. The ATLAS search in [26] provides a functional form for the p_T distribution of fake tracklets, which can be used to estimate the fake

tracklet background. We do not perform any background estimation in this article given the complexity of the estimation. Instead, we compare with the ATLAS model independent upper limit on the cross section in Sec. 7.3.2 for the 13 TeV case. For the 100 TeV case, we use the results in Ref. [704], and show our result in Sec. 7.3.3. Earlier projections from disappearing track searches from a compressed dark sector at 100 TeV were carried out in [702].

Our reconstruction proceeds as follows. At the generator level, $\not{p}_T$ is reconstructed as the vector sum of the p_T of neutrinos, neutralinos and charginos since the tracklet p_T is not used in the experimental reconstruction of missing transverse momenta. We reconstruct jets with `FastJet3.1.3` [715] with $R = 0.4$, and take as input all particles but muons, neutrinos, neutralinos and charginos with $c\tau > 10$ mm.

We use the benchmark SLHA files provided by the ATLAS collaboration and consider electroweak production of charginos via $pp \to \tilde{\chi}_1^{\pm}\tilde{\chi}_1^0 j$ and $pp \to \tilde{\chi}_1^{+}\tilde{\chi}_1^{-} j$ at 13 TeV in `MadGraph`. We store the chargino decay vertex by setting the `time_of_flight` variable in the run card, decay the chargino in `Pythia` and match our events with up to two extra partons using the MLM prescription [716].

The following analysis selection criteria are imposed:

- Trigger : $\not{p}_T > 140$ GeV
- Lepton veto : no electrons or muons
- Jet $p_T/\Delta\phi$: at least one jet with $p_T > 140$ GeV, and $\Delta\phi$ between the $\not{p}_T$ vector and each of the up to four hardest jets with $p_T > 50$ GeV to be bigger than 1.0

In what follows, we use "overall event level efficiency" to refer to the efficiency after these selection cuts. On top of these event selection requirements, we correct for

detector effects and resolutions by multiplying the overall event level efficiency with the event efficiency provided by ATLAS in Table 2 of [26].[vi]

Then we proceed to select tracklets and require the following:

- Tracklet selection : at least one tracklet (generator-level chargino) with :
  - $p_T > 20\,\text{GeV}$ and $0.1 < |\eta| < 1.9$
  - 122.5 mm < decay position < 295 mm
  - ΔR distance between the tracklet and each of the up to four highest$-p_T$ jets with $p_T > 50\,\text{GeV}$ to be bigger than 0.4
  - we apply the tracklet acceptance $\times$ efficiency map[vii] provided by ATLAS, which is based on the decay position and η. This is applied to selected tracklets passing the above selections.
- Tracklet p_T : Select tracklets with $p_T > 100\,\text{GeV}$.

In what follows, we use "overall tracklet efficiency" to refer to the efficiency after these tracklet selection cuts. We correct our overall tracklet efficiency by a factor of 0.57, as presented in the last column of Table 2 from Ref. [26], which takes into account the experimental efficiency for reconstructing a tracklet with $p_T > 100\,\text{GeV}$.

In Fig. 7.4, we show the ATLAS result and our result by following the cutflow of Table 1 in Ref. [26]. As can be seen from the plot, we reproduce the overall efficiency after all selection requirements are imposed. For $(m_{\tilde{\chi}_1^\pm}, c\tau_{\tilde{\chi}_1^\pm}) = (400\ \text{GeV}, 59.96\,\text{mm})$, the final efficiency for ATLAS is 0.38% and we obtain 0.43%.

[vi] Note that Table 2 is provided and meant to be used for reinterpretation purposes, so we consider the event efficiencies and tracklet probability or T_P in our validation, and later for our signal.

[vii] We use auxiliary figure 9 of [26] directly to account for the tracklet efficiency.

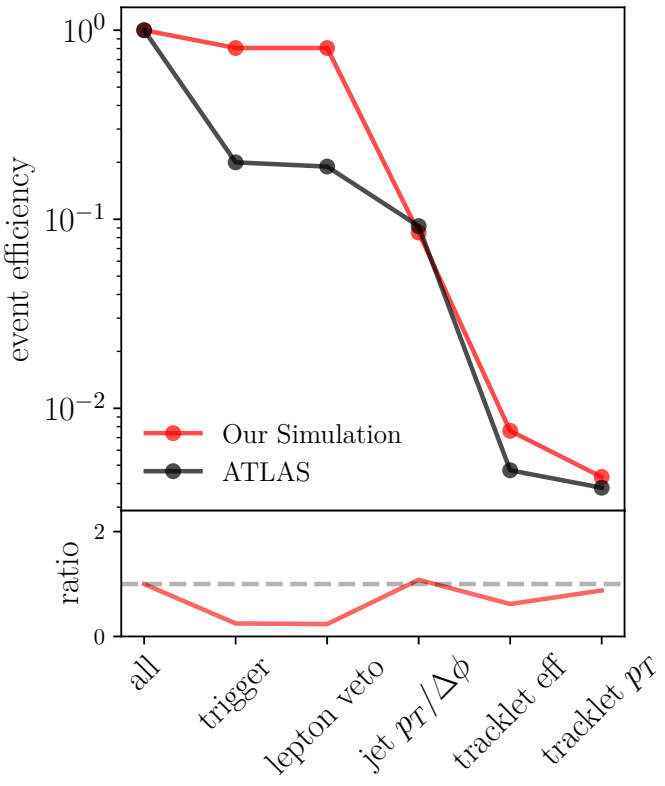

Figure 7.4: Validation of the ATLAS disappearing track search efficiency for a chargino produced electroweakly with $(m_{\tilde{\chi}_1^\pm}, c\tau_{\tilde{\chi}_1^\pm}) = (400\,\text{GeV}, 59.96\,\text{mm})$. The black curve corresponds to the ATLAS efficiency in Table 1 of Ref. [26] and the red curve corresponds to our simulation. The bottom rectangle shows the ratio of ATLAS's result to our estimate.

7.3.2 Sensitivity of the ΣSM at the LHC

For the ΣSM, we apply the same selection cuts as discussed in secton 7.3.1, but we now replace the chargino with the charged Σ. ATLAS presents a model-independent observed limit at 95% confidence level (CL) in table 4 of Ref. [26], $\sigma_{\text{obs95}} = 0.22$ fb for $\mathcal{L} = 36.1\ \text{fb}^{-1}$ and $\sqrt{s} = 13\,\text{TeV}$. We calculate our theoretical cross section $\sigma_{\text{theory}} \equiv \sigma \times \epsilon$ for each mass point and compare that with σ_{obs95}. If the ratio $\sigma_{\text{theory}}/\sigma_{\text{obs95}} > 1$, then we consider the point to be excluded. The result is presented in figure 7.5.

As the mass splitting decreases from 172 MeV to 160 MeV, the lifetime increases, making it more favorable for the reach of the ATLAS disappearing charged tracks

search. The efficiency of the recasted ATLAS analysis is higher for our 68.42 mm benchmark, raising to 0.4% from 0.33%. For higher luminosities, we obtain our exclusion limits based on the assumption as follows: Since $S \propto$ the total integrated luminosity $\mathcal{L}$, and $B \propto \mathcal{L}$, the sensitivity $\sqrt{S}/\sqrt{S+B}$ will scale as $\sqrt{\mathcal{L}}$. For the estimation, we also assume $\sigma_{\text{obs95}} \propto 1/\sqrt{\mathcal{L}}$ and show the extrapolated $\sqrt{s} = 13\,\text{TeV}$ results at the HL-LHC in figure 7.5. We emphasize that this is a very optimistic estimation of the sensitivity at the HL-LHC. In general, performing this kind of extrapolations is challenging for long-lived particle searches, particularly due to the difficulty in estimating instrumental backgrounds and uncertainties outside the experimental collaborations. A more conservative extrapolation procedure for disappearing charged track searches can be found in Ref. [717]. There the authors argued that, while the HL-LHC would be a much busier environment where backgrounds would not necessarily scale with luminosity, it was also likely that trigger upgrades/strategies could be improved, compensating the larger backgrounds and therefore providing a larger signal statistics.

From figure 7.5, we find that the 13 TeV LHC with $\mathcal{L} = 36\,\text{fb}^{-1}$ excludes a triplet lighter than $\sim 275\,\text{GeV}$ for ($\Delta m = 160\,\text{MeV}$, $c\tau = 68.42\,\text{mm}$), and lighter than $\sim 248\,\text{GeV}$ for ($\Delta m = 172\,\text{MeV}$, $c\tau = 46.11\,\text{mm}$). At $300\,\text{fb}^{-1}$ (3000fb^{-1}) a potential exclusion could reach $\sim 590\,\text{GeV}$ ($\sim 745\,\text{GeV}$) and $\sim 535\,\text{GeV}$ ($\sim 666\,\text{GeV}$) for ($\Delta m = 160\,\text{MeV}$, $c\tau = 68.42$ mm) and ($\Delta m = 172\,\text{MeV}$, $c\tau = 46.11$ mm), respectively.

7.3.3 Sensitivity of the ΣSM at a 100 TeV pp collider

To assess the prospective sensitivity of a future 100 TeV pp collider, we rescale the leading jet p_T and the $\not{p}_T$ cuts as suggested in [704] with the following selections:

- Trigger : $\not{p}_T > 1\,\text{TeV}$ or $\not{p}_T > 4\,\text{TeV}$ depending on the benchmark as discussed below.

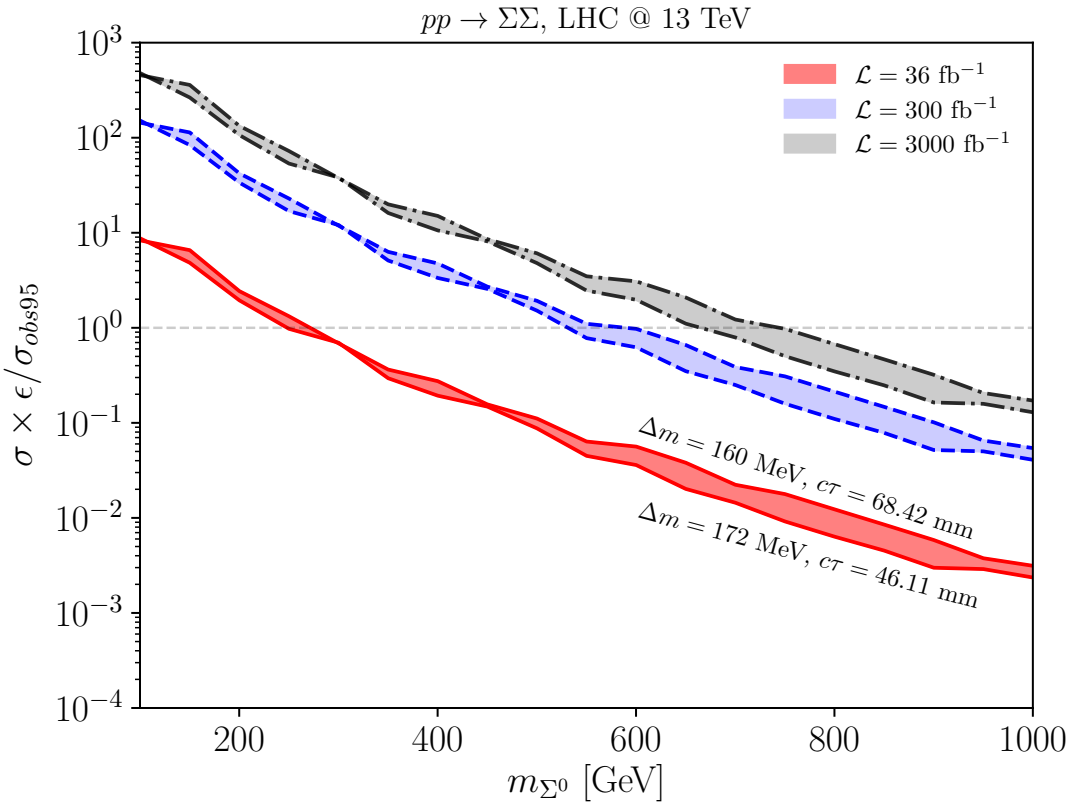

Figure 7.5: 95% CL limits at the 13 TeV LHC versus m_{Σ^0} and projected sensitivity with higher luminosities assuming that, optimistically, backgrounds would scale with luminosity. The lower lines in the three contours in the figure correspond to the ($\Delta m = 172$ MeV, $c\tau = 46.11$ mm) benchmark, while the upper lines are for ($\Delta m = 160$ MeV, $c\tau = 68.42$ mm).

- Lepton veto : no electrons or muons.
- Jet $p_T/\Delta\phi$: at least one jet with $p_T > 1$ TeV, and $\Delta\phi$ between the $\not{p}_T$ vector and each of the up to four hardest jets with $p_T > 50$ GeV to be bigger than 1.0.

The tracklet selection and tracklet p_T cut remain the same as in the 13 TeV case. The number of expected signal events at a 100 TeV pp collider with 30 ab^{-1} of luminosity are given in table 7.1, for two benchmarks. For the 1 (3) TeV benchmark point, the trigger threshold used is 1 (4) TeV.

Benchmark	σ [pb]	ϵ	S	B	$S/\sqrt{B}$
$m_{\Sigma^\pm} = 1.1\,\text{TeV}$, $\overline{\mu} = 200$	5.8×10^{-2}	3.17×10^{-4}	553	673	21.3
$m_{\Sigma^\pm} = 1.1\,\text{TeV}$, $\overline{\mu} = 500$	5.8×10^{-2}	3.17×10^{-4}	553	8214	6
$m_{\Sigma^\pm} = 3.1\,\text{TeV}$, $\overline{\mu} = 200$	9.4×10^{-4}	4.69×10^{-4}	13.3	1.9	9.6
$m_{\Sigma^\pm} = 3.1\,\text{TeV}$, $\overline{\mu} = 500$	9.4×10^{-4}	4.69×10^{-4}	13.3	27	2.6

Table 7.1: Cross section, overall event efficiency ϵ, number of expected signal (background) events S (B) with $\mathcal{L} = 30$ ab^{-1} and significance $S/\sqrt{B}$ at a 100 TeV pp collider for two benchmarks with $(m_{\Sigma^\pm}, c\tau_{\chi_1^\pm}) = (1.1\,\text{TeV}, 59.96\,\text{mm})$ and $(m_{\Sigma^\pm}, c\tau_{\Sigma^\pm}) = (3.1\,\text{TeV}, 59.96\,\text{mm})$, wherein the table $\bar{\mu}$ represents the average number of pp interactions per bunch crossing. See the text for details.

The authors in [704] carefully considered the effect that multiple pp collisions occurring simultaneously with a signal event (pileup) would have on the background. For each benchmark case, we adopt their fake tracklet background numbers considering the two different pileup scenarios described in [704]. We consider two values for $\overline{\mu}$ – the average number of pp interactions per bunch crossing – the authors studied: $\overline{\mu} = 200$ and $\overline{\mu} = 500$. Values of B in our Table 7.1 are taken directly from Table 3 and 4 of [704]. We then estimate the significance as $S/\sqrt{B}$. We conclude that a 100 TeV pp collider could discover $m_{\Sigma^0} = 1\,\text{TeV}$ and $m_{\Sigma^\pm} = 1.1\,\text{TeV}$ (significance larger than 5σ) for both pileup scenarios. While with controlled pileup scenario ($\overline{\mu} < 500$), the 100 TeV collider could discover real triplet scalars with masses up to $m_{\Sigma^0} = 3\,\text{TeV}$ and $m_{\Sigma^\pm} = 3.1\,\text{TeV}$. As we discuss below, this reach would cover the entire DM viability range for portal coupling having a magnitude $\sim \mathcal{O}(1)$ and below. We also stress that by optimizing the inner-tracker layout as done in Ref. [704], more optimal reach for the ΣSM could be attained.

7.4 Triplet dark matter and direct detection

In Sec. 7.3, we discussed ΣSM DM searches from the DCT signature at the LHC and a 100 TeV pp collider. We find that, as shown in Fig. 7.5, the 13 TeV LHC can only reach the $m_\Sigma \sim \mathcal{O}(100\,\text{GeV})$ parameter space. However, as has been previously

studied in Refs. [28, 674] in the case when $a_2 = 0$, m_{Σ^0} has to be about 2.5 TeV in order to account for the entire DM relic density. Such a TeV scale is beyond the reach of the LHC, while for a 100 TeV pp collider, the reach may extend to $m_{\Sigma^0} \sim 3$ TeV if pileup is under sufficient control. Recall that for both colliders, the impact of the Higgs portal interaction with coefficient a_2 is minimal, except for the very light mass regime that is already excluded by LEP bounds. It is interesting, however, to study the interplay between the collider reach and DM dynamics in the presence of a non-vanishing Higgs portal interaction. As already observed in Ref. [683] for higher dimensional electroweak multiplet DM, the impact of the portal coupling on DM dynamics and direct detection sensitivity can be substantial. With this observation in mind, in this section, by taking non-zero a_2 into account, we discuss the parameter space where the ΣSM can generate the measured DM relic density. We discuss constraints from DM direct detection at the end of this section.

7.4.1 Boltzmann equation with coannihilation

In Chapter 4, we reviewed the Boltzmann equation which can be written as[viii]

$$\frac{dY}{dx} = \frac{1}{3H}\frac{ds}{dx}\langle\sigma v_{\text{Møller}}\rangle_T (Y^2 - Y_{\text{eq}}^2). \tag{7.10}$$

However, since $\Sigma^\pm$ is only 166 MeV heavier than our DM candidate Σ^0, coannihilation – as first discussed in [718,719] – needs to be included. To do so, we follow the general procedure described in Ref. [720] and rewrite the Boltzmann equation as

$$\frac{dY}{dx} = \frac{1}{3H}\frac{ds}{dx}\langle\sigma_{\text{eff}} v_{\text{Møller}}\rangle_T (Y^2 - Y_{\text{eq}}^2), \tag{7.11}$$

where $\langle\sigma_{\text{eff}} v_{\text{Møller}}\rangle_T$ can be written in a compact form:

[viii] For reviews on this topic, see, for example, Refs. [317, 321].

$$\langle \sigma_{\rm eff} v_{\rm Møller} \rangle_T \equiv \frac{\displaystyle\int_0^\infty dp_{\rm eff} p_{\rm eff}^2 W_{\rm eff} K_1\left(\frac{\sqrt{\tilde{s}}}{T}\right)}{m_{\rm DM}^4 T \left[\displaystyle\sum_i \frac{g_i}{g_{\rm DM}} \frac{m_i^2}{m_{\rm DM}^2} K_2\left(\frac{m_i}{T}\right)\right]^2}, \tag{7.12}$$

and now with $Y \equiv \sum_i n_i/s$ with n_i the number density of species i which is either the DM particle or other particles that will eventually decay into the DM particle, $K_{1(2)}$ the Bessel function of the first (second) kind, $\tilde{s}$ the Mandelstam variable, g_i the number of degrees of freedom of species i, $m_{\rm DM}$ the mass of DM, $p_{\rm eff} = \sqrt{\tilde{s}/4 - m_{\rm DM}^2}$ and $W_{\rm eff} = \sum_{ij}(4p_{ij}^2/p_{\rm eff})(g_i g_i/g_{\rm DM}^2)\sqrt{\tilde{s}}\sigma_{ij}$, where $p_{ij} = \sqrt{(\tilde{s} - (m_i + m_j)^2)(\tilde{s} - (m_i - m_j)^2)}/(2\sqrt{\tilde{s}})$ and the indices i, j are the same as that in aforementioned n_i.

During the evolution of the universe, one can track the DM number density by solving Eq. (7.11). To get the current DM relic density, noting that $Y \gg Y_{\rm eq}$ after the freeze-out, one has

$$\frac{1}{Y_0} = \frac{1}{Y_f} + \int_{x_0}^{x_f} dx \frac{1}{3H}\frac{ds}{dx}\langle \sigma_{\rm eff} v_{\rm Møller} \rangle_T \,, \tag{7.13}$$

with $x_{f(0)} = m_{\rm DM}/T_{f(0)}$, $T_{f(0)}$ the freeze-out (current) temperature, Y_f the yield of DM at freeze-out and Y_0 the current yield of DM. Knowing Y_0, one can then compute the current dark matter relic density from

$$\Omega_{\rm DM} h^2 = \frac{\rho_0}{\rho_c} h^2 = \frac{8\pi G s_0 Y_0 m_{\rm DM}}{3 \times 10^4} \,, \tag{7.14}$$

with $\rho_c = 3H^2/(8\pi G)$ the critical density, G the gravitational constant and s_0 the current entropy density.

7.4.2 Triplet dark matter relic density

The annihilation and coannihilation processes discussed above are listed in Table 7.2. In Ref. [28], the authors obtained the ΣSM relic density for $a_2 = 0$. To

Annihilation	Coannihilation			
$*\Sigma^0\Sigma^0 \to W^\pm W^\mp$	$\Sigma^0\Sigma^\pm \to f f'$	$*\Sigma^\pm\Sigma^\mp \to f f$	$*\Sigma^\pm\Sigma^\mp \to h\gamma$	$\Sigma^\pm\Sigma^\mp \to \nu\bar{\nu}$
$*\Sigma^0\Sigma^0 \to ZZ$	$\Sigma^0\Sigma^\pm \to W^\pm Z$	$*\Sigma^\pm\Sigma^\mp \to W^\pm W^\mp$	$*\Sigma^\pm\Sigma^\mp \to hh$	$\Sigma^\pm\Sigma^\pm \to W^\pm W^\pm$
$*\Sigma^0\Sigma^0 \to hh$	$\Sigma^0\Sigma^\pm \to W^\pm\gamma$	$*\Sigma^\pm\Sigma^\mp \to ZZ$	$\Sigma^\pm\Sigma^\mp \to Z\gamma$	
$*\Sigma^0\Sigma^0 \to f\bar{f}$	$*\Sigma^0\Sigma^\pm \to W^\pm h$	$*\Sigma^\pm\Sigma^\mp \to Zh$	$\Sigma^\pm\Sigma^\mp \to \gamma\gamma$	

Table 7.2: Annihilation and coannihilation processes related to the DM relic density calculation, where $f = e, \mu, \tau, u, d, c, s, t, b$ and $\nu = \nu_e, \nu_\mu, \nu_\tau$. Processes starting with an asterisk (*) are a_2 dependent.

include the effect from non-vanishing a_2, we first use `LanHEP` [721] to generate the model file, then we implement the model file in `CalcHEP` [722] to calculate the annihilation and coannihilation cross sections. Then we use `Mathematica` and `Python` to solve the Boltzmann equation, Eq. (7.11).

7.4.2.1 Validation of code setup

Since results at $a_2 = 0$ are already known, we start by validating our private code with results in literatures and results obtained from other packages such as MicrOMEGAs [27]. Our result are shown in Figure 7.6, where the red and the green curves are plotted with data extracted from Ref. [28], corresponding to exclusion and inclusion of the Sommerfeld effect respectively; the black and the purple curves are obtained from MicrOMEGAs, corresponding to the exclusion of three-body decay and the inclusion of both three-body decay and coannihilations respectively; finally, the cyan curve is obtained from private code with the inclusion of coannihilations.

As can be seen from Figure 7.6, consistent result is obtained compared with other approaches for $a_2 = 0$, implying the correctness of our private code. As a next step, we generalize to the case with non-vanishing a_2 and study constraints from dark matter relic density on the model parameter space of ΣSM next.

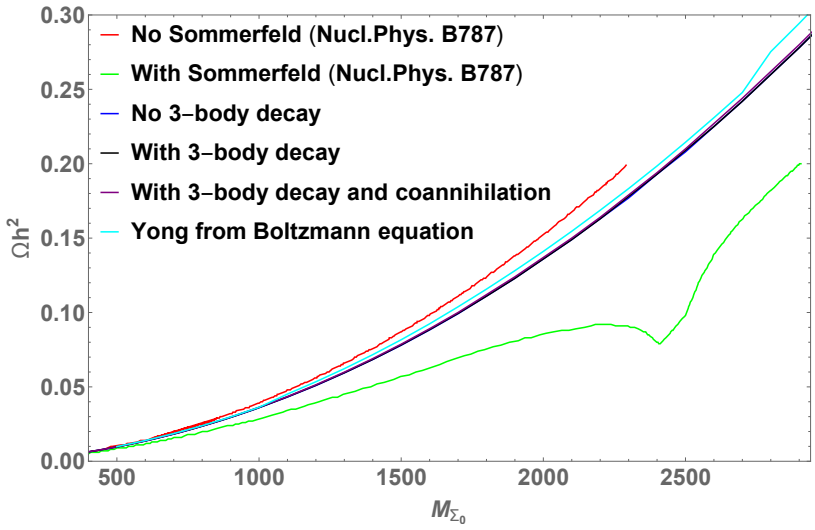

Figure 7.6: Comparison among results obtained from MicrOMEGAs [27], Ref. [28] and private code. The red and the green curves are extracted from Ref. [28], the black and the purple curves are from MicrOMEGAs, and the cyan curve is obtained from private code.

7.4.2.2 Final result for dark matter relic density

After generalizing our code to the case with $a_2 \neq 0$ and solving the Boltzmann equation, our results are shown in Fig. 7.7, where we indicate the fraction of the relic density given by the Σ^0 (colored bands) in the (m_{Σ^0}, a_2) plane – For a general a_2, we again get agreement with results obtained from using MicrOMEGAs [27]. Numbers in boxes on the curves correspond to the fraction of the relic density comprised by the Σ^0. The blue and the red vertical bands correspond to the collider exclusion limits we have obtained from the DCT signature as shown in figure 7.5. Note that since we assume $m_{\Sigma^0} > 2m_{\rm SM}$ so that the real triplet can decay into all possible SM final states, the exclusion limit from $\mathcal{L} = 36\,\text{fb}^{-1}$ in Fig. 7.5, which is $\sim 287\,\text{GeV}$, is not explicitly shown in Fig. 7.7. Black dashed and solid vertical lines in Fig. 7.7 are the discovery reach we obtain for a future 100 TeV pp collider in Table 7.1 under the optimistic pileup scenario.

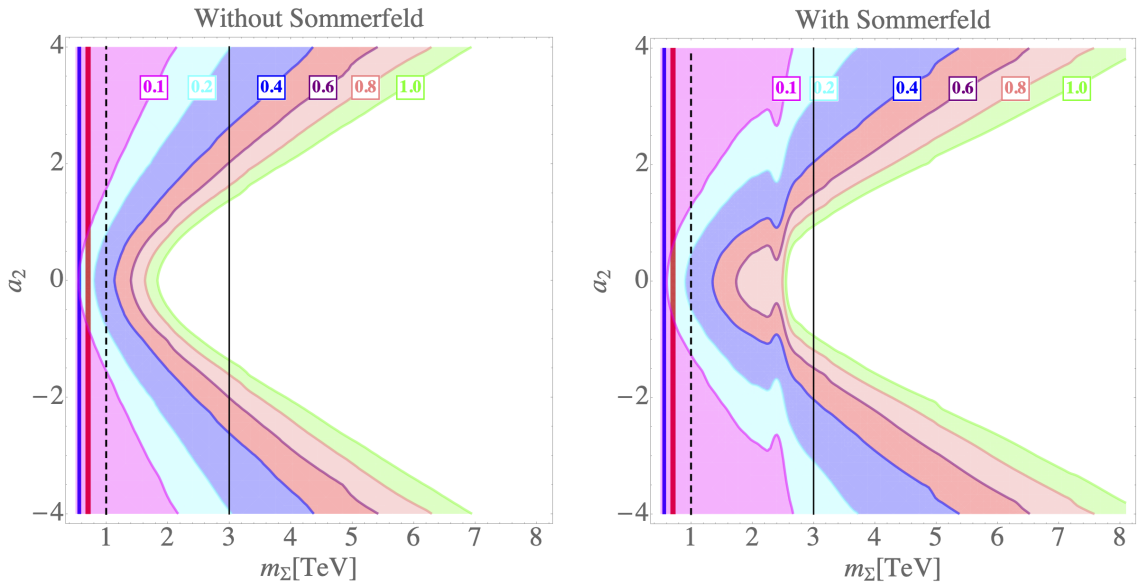

Figure 7.7: Left panel: The parameter space that can explain current DM relic density without including the Sommerfeld effect. Numbers in boxes on the curves correspond to the fractions of ΣSM contribution to the total DM relic density measured by Planck [29]. The blue (red) vertical band corresponds to the exclusion limit obtained from figure 7.5 for the LHC with $\mathcal{L} = 300\ (3000)\,\text{fb}^{-1}$, and the black dashed and solid lines correspond to the $\geq 5\sigma$ discovery benchmark points we obtain in table 7.1 for a future 100 TeV pp collider with $\mathcal{L} = 30\,\text{ab}^{-1}$. Right panel: Same as the left but with the Sommerfeld effect included.

From the left panel of Fig. 7.7, one might naïvely conclude that the LHC (HL-LHC) requires the triplet to contribute at least ∼10% (20%) of the total DM relic abundance from our study on the null DCT signature, as indicated by the red dashed (solid) vertical line. One would further conclude that if the triplet is the only component of DM, m_Σ is required to be $\gtrsim 2\,\text{TeV}$ ($m_\Sigma \simeq 2\,\text{TeV}$ when $a_2 \simeq 0$.), which is consistent with the previous studies [28, 674].

However, when Σ^0 is of $\mathcal{O}(\text{ TeV})$, SM particles can be effectively taken as massless and non-perturbative contributions to the cross sections, also known as the Sommerfeld effect, need to be included [723]. To do so, we first obtain the ratio of DM relic abundance between the two curves in the upper left panel of Figure 3 in Ref. [28]. We then rescale our thermal-averaged cross sections in Eq. (7.11) by the corresponding

factor for each m_Σ[ix], and show our results in the right panel of Fig. 7.7. The feature near $m_\sigma \sim 2.5$ TeV indicates the existence of a DM bound state due to the attraction between DM particles from the Sommerfeld effect.[x] Now due to the Sommerfeld enhancement of $\langle \sigma_{\rm eff} v_{\rm Møller} \rangle$, DM freezes out from the SM thermal bath at a later time and results in a smaller DM relic density. Therefore, for a fixed a_2, the DM particle has to be heavier to freeze out earlier in order to explain the observed DM relic density. On the other hand, if the DM mass is fixed, then the coupling between DM and SM doublet has to decrease to have a smaller cross section for the DM to decouple from the SM thermal bath earlier. Note that now both the LHC and the HL-LHC would require the triplet to contribute at least about 10% of the total DM relic abundance if no disappearing track signature is observed at 95% CL. For the ΣSM to saturate the DM relic density, one must have $m_\Sigma \gtrsim 2.5\,\text{TeV}$.

As discussed above, the Sommerfeld enhancement corresponding to the right plot of figure 7.7 is obtained from a rescaling using the data from Ref. [28]. The enhancement is maximized around 2 TeV where a bound state is formed. The enhancement on the annihilation cross sections near 2 TeV causes a later freeze-out of DM than when the enhancement is absent, as a result, a smaller relic density is obtained at the scale of the bound state formation.

To estimate the uncertainty of our rescaling, we first use the Hulthen potential approximation to calculate the Sommerfeld enhancement factor and find that there is indeed only one bound state near 2 TeV when $m_\Sigma \leq 8\,\text{TeV}$ as is the range we focus on in this work. However, when $m_\Sigma \geq 2\,\text{TeV}$, the enhancement factor, as well as the rescaling factor, decreases dramatically. As a result, corrections from the Sommerfeld effect also drops dramatically beyond 2 TeV. Therefore, to maximally

[ix]For $m_\Sigma \gtrsim 3\,\text{TeV}$, we make an extrapolation. And for each m_Σ, we use the same rescaling factor regardless of a_2.

[x]The dip always appears near $m_\Sigma \simeq 2.5\,\text{TeV}$ because we use the same factor obtained from Ref. [28] to rescale $\langle \sigma_{\rm eff} v_{\rm Møller} \rangle$.

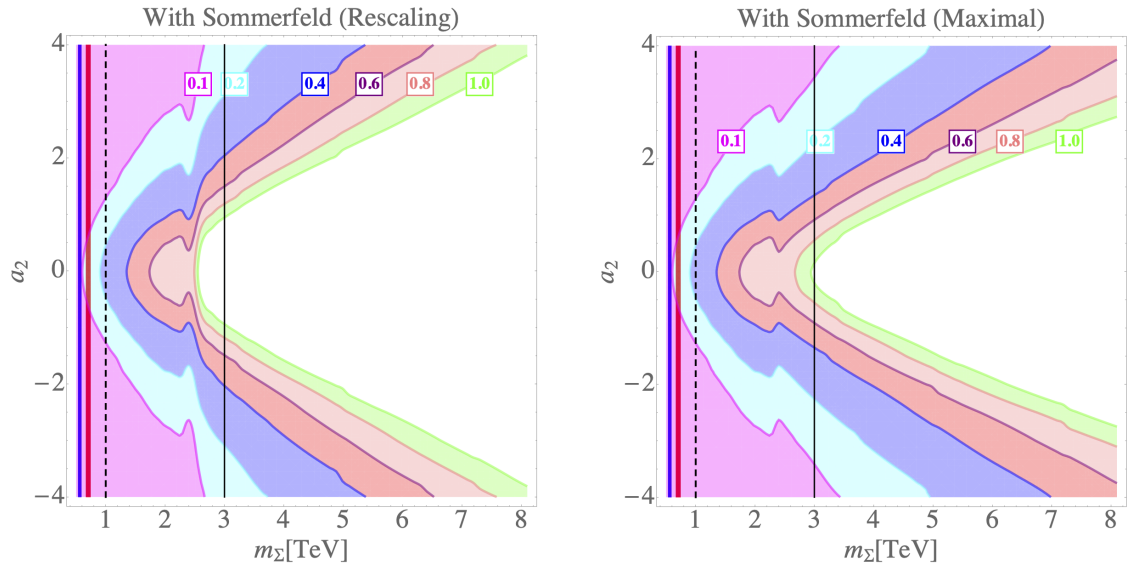

Figure 7.8: Left panel: The right plot of figure 7.7 obtained from rescaling. Right Panel: New treatment on the Sommerfeld effect as described in the main text.

estimate corrections to the right plot of figure 7.7, one can assume that the Sommerfeld factor remains at its maximum beyond 2 TeV to solve the Boltzmann equation again. We find that the correction to the right plot of figure 7.7 is maximized near $a_2 = 0$, and to saturate the DM relic density from the real triplet, one now has $m_\Sigma \simeq 3\,\text{TeV}$, which is about 500 GeV larger than our conclusion above as can be see from figure 7.8, where the left plot corresponds to the right panel of figure 7.7 obtained from the rescaling and the right plot of figure 7.8 corresponds to that obtained from the method described above. Note that the right plot of figure 7.8 also indicates that the dark matter relic density is now less sensitive to a_2 as can be seen from the slopes of each boundary. However, since the Sommerfeld factor actually decreases beyond 2 TeV, we expect the correction to the saturated mass is even smaller than 500 GeV, and an exact treatment of the Sommerfeld effect shall not modify our main result here too much.

The bound state effects have been studied only recently in limited scenarios [724–727], and contradictory conclusions on bound state effects have been drawn for a U(1) model in Ref. [724–726], where Ref. [725] concluded that bound state effects were not

important during thermal freeze-out of DM while Ref. [724,726] claimed the opposite. Bound state effects for WIMP DM were studied in Ref. [728–730] by including only late time annihilations and leaving out the freeze-out processes. An effective field theory (EFT) approach to the wino scenario was developed in Ref. [731–733], and the simplest setup with a dark sector charged under $\mathrm{SU}(2)_{\mathrm{L}}$ was recently considered in Ref. [734]. Using the framework developed in Ref. [724,726], the authors of Ref. [734] also claimed the importance of inclusion of the bound state effects especially near the unitarity bound. However, due to the controversiality discussed above and the mass scale we are concentrating on here, which is much smaller than the unitarity bound, the bound state effect will not be further studied in this work.

On the other hand, due to the mass scale of the real triplet dark matter, DM annihilation into energetic SM particles happening in the dark matter halo could result in observable signals that can be detected from DM indirect detection, though it usually exhibits large uncertainties. The constraints from DM indirect detection could be strong and rule out part of our model parameter space. Actually, in the minimal dark matter scenario where the only free parameter of the real triplet is m_Σ, DM relic density would require $m_\Sigma = 2.5\,\mathrm{TeV}$, which has already been ruled out from DM indirect detection [674, 688, 693]. However, as already stated in Appendix B of Ref. [688], in the non-minimal case as studied in this work, a portion of its parameter space could still survive from constraints from DM indirect detection. However, due to their non-triviality, the exact Sommerfeld effects, the bound state effects and DM indirect detection within the ΣSM will be studied in a future project.

7.4.3 Triplet dark matter direct detection

Given the mass scale discussed in this chapter for the real triplet, dark matter direct detection discussed in Chapter 4 will give the most stringent constraints. Furthermore, since we are considering a real triplet scalar, we anticipate that for

non-vanishing a_2, the SI cross section from dark matter scattering off nucleons will be severely constrained from deep underground experiments such as LUX [30], PandaX-II [31] and XENON1T [32].

Historically, the SI cross section was first studied by using the effective Lagrangian between DM and light quarks and gluons by Drees and Nojiri [735] and then followed by Refs. [127,683,736–740]. Here we adopt the formula in Ref. [683] for $m_\Sigma \gg m_W \gg m_q$ $(q = u, d, s)$ which takes into account contributions from the twist-two operator and write the SI cross section as

$$\begin{aligned} \sigma_{\rm SI} &= \frac{\mu^2}{4\pi}\frac{m_N^2}{M_\Sigma^2}\left(f_N\frac{a_2}{m_h^2}+\frac{3}{4}f_T f_N^{\rm PDF}\right)^2, \\ \text{where } f_T &= \frac{\alpha_2^2}{4m_W^2}\left\{\omega\ln\omega+4+\frac{(4-\omega)(2+\omega)\arctan 2b_\omega/\sqrt{\omega}}{b_\omega\sqrt{\omega}}\right\}, \end{aligned} \tag{7.15}$$

with $\mu = m_N m_\Sigma/(m_N + m_\Sigma)$ the reduced mass, $\omega = m_W^2/m_\Sigma^2$, m_N the nucleon mass, f_N the SI effective coupling with $f_N \simeq 0.287(0.084)$ for $N = p\,(n)$ [27], $f_N^{\rm PDF} = 0.526$ [741] the second moment of nucleon parton distribution function (PDF) and f_T the effective coupling of the twist-two operator in the effective Lagrangian.

Using Eq. (7.15) and recasting constraints from LUX, PandaX-II and XENON1T onto the a_2-m_Σ plane, we calculate the scaled SI cross section, which is defined as

$$\sigma_{\rm SI}^{\rm scaled} \equiv \frac{\sigma_{\rm SI}\Omega h^2}{(\Omega h^2)_{\rm Planck}} \quad \text{with } (\Omega h^2)_{\rm Planck} = 0.01198 \text{ [29]}, \tag{7.16}$$

and plot constraints from those experiments in Fig. 7.9. In both plots, the yellow region corresponds to the exclusion limit from LUX, the purple region is excluded from PandaX-II, the blue region is excluded from XENON1T, and the green region is the projected exclusion limit from XENON20T [32]. Several points are worth stressing:

- Among the considered underground experiments, XENON1T gives the most stringent constraint in the a_2-m_Σ parameter space. As can be seen from the

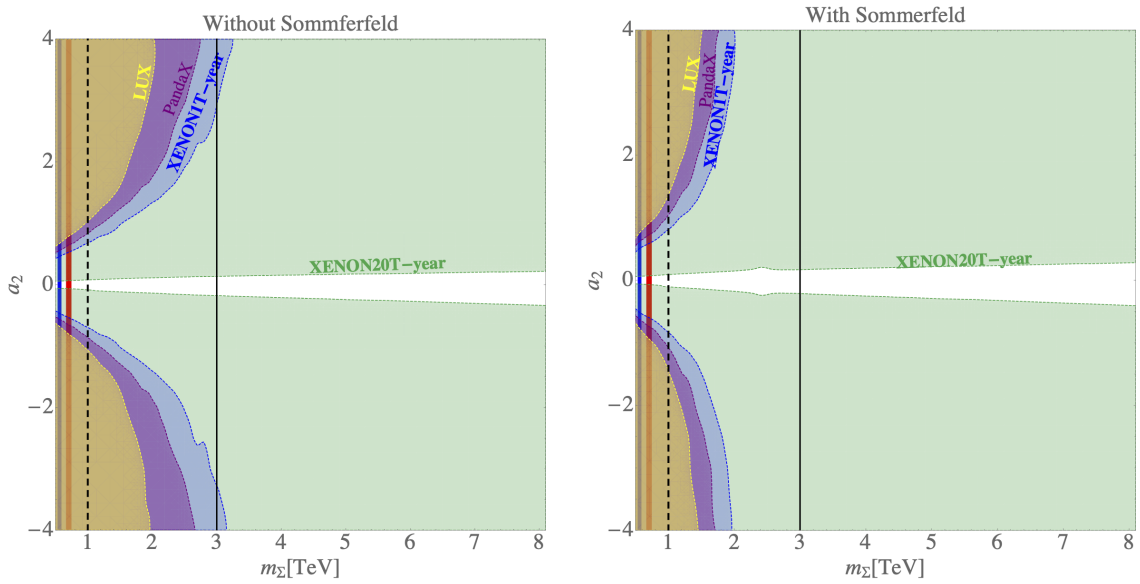

Figure 7.9: Scaled spin-independent cross section $\sigma_{\rm SI}^{\rm scaled}$ on the a_2-m_Σ plane. Left panel: Exclusion regions when the Sommerfeld effect is not included, where the yellow region is the constraint from LUX [30], purple from PandaX-II [31], blue from XENON1T [32] and green from the projected XENON20T. The vertical lines have the same meaning as in Fig. 7.7. Right panel: Same as the left but with the Sommerfeld effect included.

left (right) panel of Fig. 7.9, XENON1T excludes $m_\Sigma \lesssim 3.2$ (2) TeV for $|a_2| \simeq 4$ when the Sommerfeld effect is not (is) included. However, for $|a_2| \lesssim 0.25$, the triplet can be as light as $\mathcal{O}(100$ GeV), but cannot saturate the current DM relic density, as seen in Fig. 7.7.

- From Fig. 7.7 and Fig. 7.9, we conclude that, with or without including the Sommerfeld enhancement effect, current DM direct detection still permits the real triplet to be the sole DM candidate. Moreover, looking into the future, XENON20T will cover almost the entire parameter space of the ΣSM. Therefore, it is very promising for XENON20T to directly observe the signal of a real triplet DM.

- As can be seen from the right panel of Fig. 7.9, when the Sommerfeld effect is included, exclusion regions from deep underground experiments all shrink.

The reason is that, after including the Sommerfeld effect, the theoretical DM relic density Ωh^2 at the same point in the plane becomes smaller due to a later freeze-out, as also seen in Fig. 7.7. As a result, $\sigma_{\rm SI}^{\rm scaled}$ also becomes smaller and the corresponding parameter space is less constrained.

- In both plots of Fig. 7.9, the blue (red) vertical band corresponds to the exclusion limit we obtain in Fig. 7.5 for the LHC with $\mathcal{L} = 300$ (3000) fb^{-1} and the black dashed and solid lines correspond to the $\geq 5\sigma$ discovery benchmark points we have in Table 7.1 for a future 100 TeV pp collider with $\mathcal{L} = 30\,\text{ab}^{-1}$. As one may see, the LHC can only reach the low mass regime up to about 1 TeV, well below the mass required to saturate the relic density. However, a future 100 TeV pp collider will reach further into the TeV regime. In particular, in the white regions where XENON20T loses its sensitivity when $|a_2| \lesssim 0.1$, future hadron colliders will be the key for model discovery.

- Theoretical constraints on the triplet potential including bounded from below, unitarity and perturbativity have been studied in Ref. [742, 743] and recently reviewed in Ref. [97]. For the parameter space we consider here, perturbativity and perturbative unitarity are satisfied with a cutoff scale $\Lambda \gtrsim 10^6\,\text{GeV}$ ($\Lambda \simeq 10^6\,\text{GeV}$ for $a_2 \simeq 4$) as implied in the right panel of Figure 1 in Ref. [97]. Requiring perturbativity and perturbative unitarity up to a higher scale will result in a smaller upper bound on a_2 than what we choose in Fig. 7.9.

7.4.4 Comment on determination of a_2

Suppose the real triplet model is discovered at colliders through the DCT signature, then one natural question one can ask is how to determine the value a_2? Note that in Fig. 7.7 and/or Fig. 7.9, one can see that dark matter relic density is not sensitive to the sign of a_2, implying that using dark matter relic density, one can only determine the magnitude of a_2.

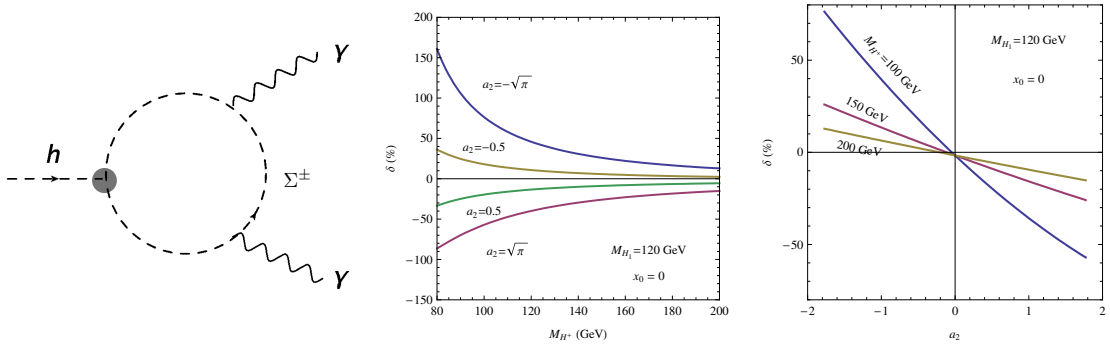

Figure 7.10: Left: Feynman diagram representing new contributions to the $h \to \gamma\gamma$ decay rate in the ΣSM. The gray blob represents the vertex with the a_2 dependence. Middle: Percent correction to $h \to \gamma\gamma$ decay rate versus triplet mass. Right: Percent correction to $h \to \gamma\gamma$ decay rate versus a_2. The last two plots are adopted from Ref. [33]

However, note that $h \to \gamma\gamma$ rate will be measured very precisely in the near future at the HL-LHC and the 100 TeV pp collider and the ΣSM will add new contributions to the decay rate as indicated by the left plot of Figure 7.10. The a_2 dependence of the decay rate enters through the $h\Sigma^+\Sigma^-$ vertex as indicated by the gray blob. Therefore, one can expect to determine the value, not just the magnitude, through a precision measurement on $h \to \gamma\gamma$ decay rate. At the LHC, the sensitivity of $h \to \gamma\gamma$ rate to a_2 was studied in Ref. [33] and the results are shown in the last two plots of Figure 7.10. In both the last two plots, the y axis represents the percent correction to the decay rate defined as

$$\delta = \frac{\Gamma^{\Sigma\mathrm{SM}}(h \to \gamma\gamma) - \Gamma^{\mathrm{SM}}(h \to \gamma\gamma)}{\Gamma^{\mathrm{SM}}(h \to \gamma\gamma)}. \tag{7.17}$$

Note that, from both the last two plots of Figure 7.10, the sign of a_2 determines that of δ, making it possible to determine the sign of a_2 from precision measurement of δ. For illustration, assume $|a_2|$ is measured from dark matter relic density. Now to determine the sign of a_2, if δ is negative, then one can conclude that a_2 is also negative. Thus a full determination of a_2 is possible through a combined analysis of

dark matter relic density and the $h \to \gamma\gamma$ decay rate. However, note that the last two plots in Figure 7.10 only studied the light scalar case below 200 GeV, which is way below the TeV scale that is needed to explain dark matter relic density. Thus, further studied is needed to draw any conclusions on the determination of a_2.

7.5 Closing remarks

We consider a simple extension of the SM with a real triplet Σ, which transforms as (1,3,0) under the SM gauge group. The charged triplet component, $\Sigma^{\pm}$, has a degenerate mass as the neutral component, Σ^0, at tree level, but receives electroweak radiative corrections to become 166 MeV heavier than Σ^0 at the one-loop level, and a further few MeV if two-loop corrections are also included. The neutral component Σ^0 becomes stable and a dark matter candidate if $\langle\Sigma\rangle = 0$ and an additional discrete Z_2 symmetry is imposed. Due to the small mass splitting between $\Sigma^{\pm}$ and Σ^0, $\Sigma^{\pm}$ becomes relatively long-lived, with the dominant decay channels being $\Sigma^{\pm} \to \pi^{\pm}\Sigma^0$. The pion in the final state is too soft to be reconstructed in colliders. Therefore, once $\Sigma^{\pm}$ is produced at colliders, a disappearing track, to which the LHC is currently sensitive, can be observed.

In this chapter, the disappearing track signature at the LHC and a hypothetical 100 TeV pp collider is studied. We reproduce the ATLAS disappearing track efficiency in Ref. [26], as shown in Fig. 7.4, and then apply the same setup to our model. Our simulation result for the ΣSM is shown in Fig. 7.5. We find that, using the disappearing track signature, the 13 TeV LHC excludes a real triplet lighter than248 (275) GeV, 535 (590) GeV and 666 (745) GeV for $\mathcal{L} = 36\,\text{fb}^{-1}$, $300\,\text{fb}^{-1}$, $3000\,\text{fb}^{-1}$ and $\Delta m = 160\,(172)$ MeV, respectively. We also extrapolate the disappearing track efficiency for a 100 TeV pp collider and study the reach at two benchmark points representative of FCC-pileup conditions, following the study by the authors in [704]. We find that, even though the LHC can only cover the $\mathcal{O}(100\,\text{GeV})$ regime of the

ΣSM, a 100 TeV pp collider will potentially be able to reach the TeV regime of the parameter space, provided that future pileup levels remain low, as shown in Table 7.1. We stress that this is a motivation for more detailed experimental studies at 100 TeV, as they can alter the potential of discovering the ΣSM significantly.

On the other hand, understanding the particle nature of DM has been a profound problem in modern particle physics. It has been known that to explain the current DM relic density measured by the Planck satellite, the triplet needs to be heavier than about 2.5 TeV, way above the scale that can be reached by the LHC. However, the triplet DM can interact with the SM particles via a Higgs portal coupling a_2 and the effects can be observed through DM direct detection from nucleon recoils. We investigate the constraints from LUX, PandaX-II, XENON1T and the projected XENON20T, and show our result in Fig. 7.9. We find that currently XENON1T gives the most stringent constraint on our model parameter space and, for example, has excluded a triplet lighter than $\sim$ 3 TeV for $|a_2| \simeq 4$. In the future, XENON20T will be able to cover almost the entire parameter space of the ΣSM model, except for $|a_2| \lesssim 0.1$, where the interaction between the DM and the nucleons becomes too weak for deep underground detectors to have any sensitivity. Fortunately, a 100 TeV pp collider could have the chance to explore this region in the future.

CHAPTER 8

PARITY-VIOLATING MØLLER SCATTERING AT NNLO

8.1 Introduction

In Chapter 5, we discussed the vital role precision measurements of electroweak processes played in the development and testing of the Standard Model of particle physics. With the discovery of the Higgs boson at the CERN Large Hadron Collider, the focus of precision tests now falls squarely on the search for signs of physics beyond the Standard Model (BSM). While a variety of open questions clearly point to the existence of BSM physics, it remains to be determined at what mass scale this physics lives and how it interacts with the known elementary particles of the SM.

A powerful probe in this context is parity-violating electron scattering (PVES). The relevant observable in PVES experiments is the asymmetry A_{LR} in the number of events when otherwise identical beams of longitudinally-polarized electrons of left (L) and right (R) helicities scatter from a fixed target

$$A_{LR} = \frac{d\sigma_L - d\sigma_R}{d\sigma_L + d\sigma_R}\,. \tag{8.1}$$

Historically, the measurement A_{LR} in deep-inelastic electron-deuteron scattering singled-out the Glashow-Weinberg-Salam theory [37–39] of the electroweak interaction from other alternatives and provided the first measurement of the all-important weak mixing angle, θ_W. Improved results were later obtained by a variety of PVES measurements at low energies, along with observations of parity violation in atomic Cesium and neutrino-nucleus deep-inelastic scattering. Parity-violating (PV) Møller scattering provides one of the theoretically cleanest such tests. The first measurement of this

asymmetry was made by the E158 Collaboration at SLAC in the mid-2000's [151], yielding a confirmation of the predicted running of $\sin^2\theta_W$ with 6σ significance.

A new, more precise measurement of the PV Møller asymmetry— dubbed MOLLER and approved to run at the Jefferson Lab [16,744]—aims to determine A_{LR} with 2.4% uncertainty. Assuming only SM contributions, the MOLLER experiment will yield a value of $\sin^2\theta_W$ with an uncertainty comparable to the earlier determinations in high energy e^+e^- annihilation. Within the Standard Model, this measurement can be interpreted as a precision test of the scale-dependence of $\sin^2\theta_W$ [4, 5, 745]. Its value at $\mu = m_Z$ can be obtained either from fits to high energy electroweak precision observables, while PVES experiments yield $\sin^2\theta_W$ at a low scale $\mu \ll m_Z$.

More significantly, MOLLER will provide a new probe for BSM physics that could reside at either high or low-mass scales. Examples include $1-10$ TeV doubly-charged scalar bosons that are implied by left-right symmetric models for the non-vanishing neutrino masses [746] and a light "dark" Z boson that, under certain conditions, may also account for the observed deviation of the muon anomalous magnetic moment from SM predictions [747–749]. In both examples, the PV Møller asymmetry provides a complementary probe to other tests at low- and high-energies.

The unique potential of the PV Møller scattering follows from two features: the purely leptonic character of the process and a fortuitous suppression of the leading-order (LO) asymmetry by $1-4\sin^2\theta_W$ ($\sin^2\theta_W$ is numerically close to 1/4). Specifically, the theoretical prediction for the PV Møller asymmetry can be written as [485]

$$A_{LR} = \frac{G_\mu Q^2}{\sqrt{2}\pi\alpha}\,\frac{1-y}{1+y^4+(1-y)^4}(1-4\sin^2\theta_W+\Delta Q_W^e) \tag{8.2}$$

where $y = Q^2/s$, and ΔQ_W^e accounts for radiative corrections.

Some terms (SM and possibly BSM) entering through ΔQ_W^e do not carry the factor $1-4\sin^2\theta_W$ and thus their relative impact is enhanced. Importantly, the NLO electroweak corrections, whose relative impact should be nominally $\mathcal{O}(\alpha)\sim 0.01$ are

roughly 40% in magnitude [750]. These corrections are dominated by contributions from closed-fermion loops that enter the running of $\sin^2\theta_W$. The WW and γZ boxes also produce sizeable corrections. Given this enhanced NLO sensitivity, it is important to determine the magnitude of NNLO SM corrections if one wishes to interpret correctly a 2.4% measurement of A_{LR} in terms of BSM physics. Partial results at the NNLO level have been presented in Refs. [547–549, 751]. Furthermore, second-order QED effects have been studied in the context of electron-proton scattering [752], which shares many features with electron-electron scattering.

In what follows, we report on a computation of all NNLO contributions involving closed fermion loops. This subset of the complete NNLO electroweak corrections is gauge-invariant and, thus, constitutes a well-defined contribution to the asymmetry. Since closed fermion loops dominate the NLO corrections and since they entail a sum over all colors and flavors of SM fermions, we expect them to generate the leading effect at NNLO. We find a resulting one percent correction to the LO asymmetry, again significantly larger than one might expect based on $\alpha/4\pi$ counting. As we discuss below, we expect the contributions from the remaining NNLO corrections to be smaller in magnitude. We thus anticipate the overall uncertainty in the SM prediction for A_{LR} lies below the planned experimental uncertainty.

8.2 Methods for two-loop integrals

We start by briefly introducing the methods of evaluating loop integrals. There are many analytical and numerical ways to calculate loop integrals, for reviews, see Ref. [34, 753–755] for example. In this section, we will only focus on some of these methods that are directly related to our calculation for the MOLLER project. For each of these methods, we will illustrate the idea by providing some examples.

8.2.1 Integration by parts (IBPs)

The idea of IBP is to solve the original integrals from a set of equations from differentiating the initial integrals with respect to the loop momenta. The set of equations can then be used to express the initial integrals in terms of a set of master integrals. These master integrals are in general much easier to calculate or already known analytically. To see how IPB works, we will next use two examples at one- and two-loop respectively to illustrate.

8.2.1.1 IBP at one-loop

Suppose we want to evaluate the following one-loop integral in $d = 4 - 2\epsilon$ dimensional spacetime:

$$I_1(n) = \int \frac{d^d k}{(k^2 - m^2)^n}. \tag{8.3}$$

The IBP identity can be obtained by differentiating with respect to the loop momentum k on both sides of the following identity:

$$0 = \int d^d k \frac{k_\mu}{(k^2 - m^2)^n} \tag{8.4}$$

one then has

$$\begin{aligned} 0 =& \int d^d k \frac{\partial}{\partial k_\mu} \frac{k_\mu}{(k^2 - m^2)^n} \\ =& (d - 2n) I_1(n) - 2nm^2 I_1(n+1), \end{aligned} \tag{8.5}$$

or,

$$I_1(n+1) = \frac{d - 2n}{2nm^2} I_1(n). \tag{8.6}$$

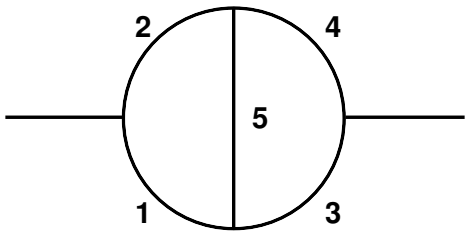

Figure 8.1: Feynman diagram corresponds to the two-loop Feynman integral we are interested in in Eq. (8.9).

Therefore, any integrals with $n > 1$ can be recursively solved from above equation and expressed by $I_1(1)$:

$$I_1(n) = \frac{(-1)^n \left(1 - \frac{d}{2}\right)_{n-1}}{(n-1)!(m^2)^{n-1}} I_1(1), \tag{8.7}$$

where $(x)_n \equiv \Gamma(x+n)/\Gamma(x)$ is the Pochhammer symbol defined as the ratio f two Gamma functions, and $I_1(1)$ is the master integral in this case that is known analytically:

$$I_1(1) = -i\pi^{\frac{d}{2}} \Gamma\left(1 - \frac{d}{2}\right) (m^2)^{\frac{d-2}{2}}. \tag{8.8}$$

Therefore, with the master integral known, the original integral can be obtained directly using the recursive formula. It is this same idea that is applied to more complicated integrals to reduce them into a set of master integrals. These master integrals are usually much easier to calculate. Thus, in short, with the help of IBPs, much more complicated can be reduced to a finite, and usually small, set of simpler master integrals that can be evaluated straightforwardly.

8.2.1.2 IBP at two-loop

Since most of our calculations are Feynman integrals at two-loop, we consider a simple example to illustrate the application of the IBP method below. Suppose the

two loop integral we are interested in is

$$I_2(q^2; n_1, n_2, n_3, n_4, n_5; d) = \int\int \frac{d^d k d^d l}{(k^2)^{n_1}[(k-q)^2]^{n_2}(l^2)^{n_3}[(l-q)^2]^{n_4}[(k-l)^2]^{n_5}}, \tag{8.9}$$

where q is the external momentum and for simplicity we assume all internal masses inside the loops are vanishing. When one of n_i becomes zero, the above integral effectively corresponds to a product of two one-loop integrals. This can be seen in a special case where $n_5 = 0$. For our discussion below, we consider the case with all $n_i > 0$. Then one of the IBP identity can be obtained through

$$0 = \int\int \frac{d^d k d^d l}{(l^2)^{n_3}[(l-q)^2]^{n_4}} \frac{\partial}{\partial k_\mu} \left(\frac{k_\mu - l_\mu}{(k^2)^{n_1}[(k-q)^2]^{n_2}[(k-l)^2]^{n_5}} \right). \tag{8.10}$$

Similarly as in the one-loop example, after solving this equation, one finds

$$\begin{aligned} I_2(q^2; n_1, n_2, n_3, n_4, n_5; d) =& \frac{1}{n_1 + n_2 + 2n_5 - d} \\ & \times \big[n_1 I_2(q^2; n_1 + 1, n_2, n_3 - 1, n_4, n_5; d) \\ & \quad - n_1 I_2(q^2; n_1 + 1, n_2, n_3, n_4, n_5 - 1; d) \\ & \quad + \{1 \leftrightarrow 2, 3 \leftrightarrow 4\} \big]. \end{aligned} \tag{8.11}$$

Note that in this IBP identity, the sum $n_3 + n_4 + n_5$ on the right hand side is reduced by one compare with that on the left, therefore, by successfully applying this IBP identity, the original integral can be reduced into integrals with at least one of the n_i's vanishing. As long as one of the n_i's is vanishing, the two-loop integral can be broken into a product a two one-loop integrals as discussed above. Since one-loop integrals are analytically known, one concludes that application of the IBP identities solves the original two-loop integral.

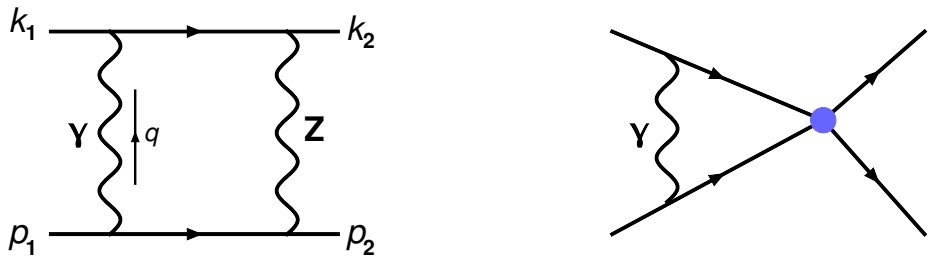

Figure 8.2: Left: Feynman diagram corresponds to the one-loop Feynman integral we are interested in in Eq. (8.12). Right: Effective Feynman diagram after EBRs, corresponding to the leading $\mathcal{O}(1/m_Z^2)$ term in Eq. (8.15).

In practice, derivation of the IBP identities can become very tedious and complicated, and computer algebra has been utilized to fulfill this task. Publicly available packages include `FIRE` [756], `LiteRed` [757], `AIR` [758], `Reduze` [759] and `TARCER` [760].

8.2.2 Expansion by regions (EBRs)

Another useful method to evaluate Feynman integrals is through EBRs, especially when the number of scales involved is large. The idea for EBRs is as follows: When evaluating the Feynman integrals involving different scales, the original integrals can be calculated by expanding the integrand around the small scales. Depending on the precision goal, the expansion is truncated accordingly. The advantage of this method is that, after the expansion, the number of scales inside the integrand is usually significantly reduced, and the resulting integrals can then be easily evaluated. To illustrate the idea, just as in the IBP case, we use two examples at one- and two-loop respectively to show how EBRs work.

8.2.2.1 EBRs at one-loop

Assume the one-loop integral we are interested in is the box diagram shown in Figure 8.2, the integral can be written as

$$I_3(k_1,p_1,k_2,p_2,m_Z)=\int\frac{d^dq}{q^2(q+k_1)^2(q-p_1)^2[(q+k_1-k_2)^2-m_Z^2]}, \tag{8.12}$$

where we have neglected the fermion masses in the integrand. Furthermore, suppose we are interested in the case where $p_{\text{ext}}^2 \ll m_Z^2$ where $p_{\text{ext}} = p_1, k_1, p_2, k_2$, then we can expand the above integral based on the magnitude q^2:

- When q^2 is of the same order as m_Z^2, i.e. $q^2 \sim m_Z^2 \sim M^2$, then expanding around $p_{\text{ext}} \sim 0$ and truncating at leading order, one finds

$$I_3^{q^2\sim m_Z^2}(k_1,p_1,k_2,p_2,m_Z)=\int\frac{d^dq}{(q^2)^3[q^2-m_Z^2]}+\mathcal{O}\left(\frac{p_{\text{ext}}^2}{M^2}\cdot\frac{1}{M^4}\right). \tag{8.13}$$

- On the other hand, if $q^2 \sim p_{\text{ext}}^2$, then one can expand the integrand around $m_Z \sim \infty$ and finds

$$I_3^{q^2\sim p_{\text{ext}}^2}(k_1,p_1,k_2,p_2,m_Z)=\int\frac{d^dq}{q^2(q+k_1)^2(q-p_1)^2(-m_Z^2)}+\mathcal{O}\left(\frac{1}{M^4}\right). \tag{8.14}$$

Therefore, if we are interested in result up to $\mathcal{O}(1/m_Z^2)$, the original integral can be approximated by

$$\begin{aligned} I_3(k_1,p_1,k_2,p_2,m_Z) =& I_3^{q^2\sim m_Z^2}(k_1,p_1,k_2,p_2,m_Z)+I_3^{q^2\sim p_{\text{ext}}^2}(k_1,p_1,k_2,p_2,m_Z) \\ =& \int\frac{d^dq}{q^2(q+k_1)^2(q-p_1)^2(-m_Z^2)}+\mathcal{O}\left(\frac{1}{M^4}\right), \end{aligned} \tag{8.15}$$

where the leading term, i.e. the first term on the right hand side of the last line above, corresponds to the right plot in Figure 8.2. Note that, the integral corresponds to this leading term is much more easier to evaluate than the original integral.

8.2.2.2 EBRs at two-loop

At two-loop, we still use the two-loop self-energy Feynman diagram shown in Figure 8.1 by assuming that $n_i = 1$ $(i = 1, \cdots, 5)$ and the only massive propagator is the one labelled with number 5 and the corresponding mass is assumed to be m. Then the corresponding integral can be written as

$$I_2(q^2, m) = \int\int \frac{d^d k d^d l}{(k^2)[(k-q)^2](l^2)[(l-q)^2][(k-l)^2 - m^2]}, \tag{8.16}$$

where q is the external momentum, k and l are the loop momenta.

Suppose we are interested in the case where $q^2 \ll m^2 \sim M^2$, then depending on the scales of the loop momenta k and l, the EBRs give:

- Region (1) with $k^2 \sim m^2$ and $l^2 \sim q^2$:

$$I_2^{(1)}(q^2, m) = \int\int \frac{d^d k d^d l}{(k^2)^2(l^2)[(l-q)^2][k^2 - m^2]} + \mathcal{O}\left(\frac{1}{M^4}\right), \tag{8.17}$$

- Region (2) with $k^2 \sim l^2 \sim m^2$:

$$I_2^{(2)}(q^2, m) = \int\int \frac{d^d k d^d l}{(k^2)^2(l^2)^2[(k-l)^2 - m^2]} + \mathcal{O}\left(\frac{1}{M^4}\right), \tag{8.18}$$

- Region (3) with $l^2 \sim m^2$ and $k^2 \sim q^2$:

$$I_2^{(3)}(q^2, m) = \int\int \frac{d^d k d^d l}{(k^2)[(k-q)^2](l^2)^2[l^2 - m^2]} + \mathcal{O}\left(\frac{1}{M^4}\right), \tag{8.19}$$

- Region (4) with $k^2 \sim l^2 \sim q^2$:

$$I_2^{(4)}(q^2, m) = \int\int \frac{d^d k d^d l}{(k^2)[(k-q)^2](l^2)[(l-q)^2](-m^2)} + \mathcal{O}\left(\frac{1}{M^4}\right), \tag{8.20}$$

- Region (5) with $k^2 \sim l^2 \sim m^2$ and $(k-l)^2 \sim q^2$:

$$\begin{aligned} I_2^{(5)}(q^2,m) &= \int\int \frac{d^dk d^dl}{(k^2)[(k-q)^2](l^2)[(l-q)^2][(k-l)^2-m^2]} \\ &= \int\int d^dk d^dl \frac{1}{[(k-l)+l]^2[(k-l)+(l-q)]^2[(l-k)+k]^2} \\ &\qquad \times \frac{1}{[(l-k)+(k-q)]^2[(k-l)^2-m^2]} \\ &= \int\int d^dk d^dl \frac{1}{(l^2)^2(k^2)^2(-m^2)} + \mathcal{O}\left(\frac{1}{M^8}\right). \end{aligned} \tag{8.21}$$

Here we comment on that, in each region above, we only keep the leading term after expanding each propagator with respect to the small scales in the corresponding region. However, in practice, one needs to expand each propagator in each region consistently by truncating at the order that meets the required precision goal. For that goal, one needs to check the expanding order of each term at each step of the expansion. Here, for the purpose of illustration, we do not consider this aspect since we do not specify the truncating order for this example. In the end, if we are only interested results up to $\mathcal{O}(1/M^2)$, then from above results, one finds the original integral can be expressed as

$$\begin{aligned} I_2(q^2,m) =& I_2^{(1)}(q^2,m) + I_2^{(2)}(q^2,m) + I_2^{(3)}(q^2,m) + I_2^{(4)}(q^2,m) + I_2^{(5)}(q^2,m) \\ =& \int\int d^dk d^dl \left\{ \frac{1}{(k^2)^2(l^2)[(l-q)^2][k^2-m^2]} + \frac{d^dk d^dl}{(k^2)^2(l^2)^2[(k-l)^2-m^2]} \right. \\ &+ \frac{d^dk d^dl}{(k^2)[(k-q)^2](l^2)^2[l^2-m^2]} \\ &\left. + \frac{d^dk d^dl}{(k^2)[(k-q)^2](l^2)[(l-q)^2](-m^2)} + \mathcal{O}\left(\frac{1}{M^4}\right) \right\}. \end{aligned} \tag{8.22}$$

Note that each integral in the curly bracket of Eq. (8.22) corresponds to a product of two one-loop integrals that are very straightforward to evaluate, for example, with the help of the IBP method discussed above. In one sentence, with the help of EBRs, the original complicated two-loop integral in this example is reduced to the product

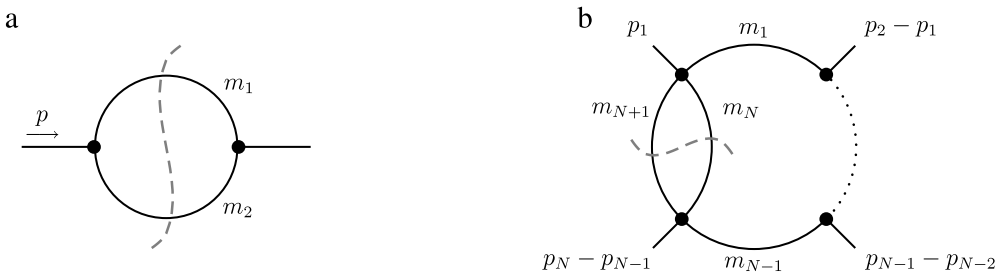

Figure 8.3: Plot (a) on the left: A one-loop scalar self-energy diagram with the cut contributing to its discontinuity; Plot (b) on the right: A generic two-loop scalar diagram with a self-energy subloop. Plot adopted from Ref. [34].

of two one-loop integrals, and these one-loop integrals are very straightforward to evaluate. This features one of the powerful advantage of the EBR method.

8.2.3 Dispersion relations

Dispersion relations are based on the analytical properties of the S-matrix elements and can be used to construct the whole integral from its imaginary part. The imaginary part, on the other hand, can be constructed from cuts through internal lines of the corresponding loop diagrams using the Cutkosky rules [761, 762]. In general, a dispersion relation can be written as [34]

$$I(q^2) = \frac{1}{2\pi i} \int_{s_0}^{\infty} \frac{\Delta I(s)}{s - q^2 - i\epsilon}, \tag{8.23}$$

where q^2 is a characteristic squared external momentum and

$$\Delta I(s) = \frac{1}{2i} \mathrm{Im} I(s) \tag{8.24}$$

is the imaginary part of the loop integral $I(s)$.

The core of this idea lies in the fact that the imaginary part of an integral is relatively easy to determine from the Cutkosky rules, and once the imaginary part is known, one can use Eq. (8.23) to obtain the full result of the integral. Another advantage of the dispersion integral is that it can be applied to a multi-loop integral or to some subloop. We will use an example to illustrate this point more clearly.

Consider a one-loop self-energy integral as indicated by the left plot in Figure 8.3, which is conventionally expressed by $B_0(p^2, m_1^2, m_2^2)$, where p is the external momentum and $m_{1,2}$ are the masses in the loop. As a function of p^2, the B_0 function has a discontinuity along the positive real axis when $p^2 > (m_1 + m_2)^2$. The discontinuity can be calculated by cutting the diagram along the dashed line in the left plot of Figure 8.3. In dimensional regularization, the results can be expressed by

$$\begin{aligned} B_0\left(p^2, m_1^2, m_2^2\right) =& \int_{(m_1+m_2)^2}^{\infty} \mathrm{d}s \frac{\Delta B_0\left(s, m_1^2, m_2^2\right)}{s - p^2 - i\varepsilon}, \\ \Delta B_0\left(s, m_1^2, m_2^2\right) =& \frac{\Gamma\left(\frac{d}{2} - 1\right)}{\Gamma(d-2)} \frac{\left[\lambda\left(s, m_1^2, m_2^2\right)\right]^{\frac{d-3}{2}}}{s^{\frac{d}{2}-1}}, \end{aligned} \tag{8.25}$$

with $\lambda(a, b, c) \equiv a^2 + b^2 + c^2 - 2(ab + ac - bc)$. Then, with this expression, the scalar two-loop integral as shown in the right plot of Figure 8.3 can be expressed as [763]

$$\begin{aligned} I_{2-\text{loop}}(p_i; m_i^2) = & - \int_{(m_N+m_{N+1})^2}^{\infty} ds \Delta B_0(s, m_N^2, m_{N+1}^2) \\ & \times \int \frac{d^d q}{i\pi^{\frac{d}{2}}} \frac{1}{q^2 - s} \frac{1}{(q + p_1)^2 - m_1^2} \cdots \frac{1}{(q + p_{N-1})^2 - m_{N-1}^2}. \end{aligned} \tag{8.26}$$

The integral in the second line corresponds to an N-point one-loop integral, whose analytical expression is well-known [764, 765].

The dispersion approach can also be extended to two-loop integrals with a self-energy subloop and a non-trivial tensor structure, which will be discussed in next section when we apply above-discussed methods to the MOLLER project.

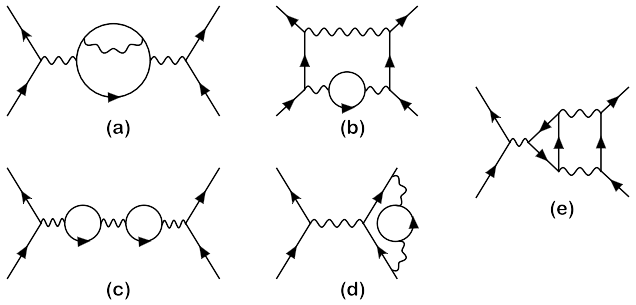

Figure 8.4: Examples of two-loop Feynman diagrams with at least one closed fermion loop.

8.3 Application to the MOLLER project at NNLO

We calculate the left-right asymmetry by expanding eq. (8.1) up to two-loop order. Non vanishing contributions to A_{LR} arise from the interference of a purely electromagnetic amplitude with the PV component of the weak neutral current amplitude arising from Z-exchange, with the electromagnetic contributions dominating the denominator in eq. (8.1). For these building blocks, the NNLO corrections to $d\sigma$ stem from two-loop matrix elements contracted with Born amplitudes, as well as the interference of two one-loop matrix elements. The two-loop matrix elements receive contributions from genuine two-loop self-energy, vertex and box diagrams, and from one-particle reducible two-loop diagrams (see Fig. 8.4 for examples).

When counting the numbers of fermion loops, we do so at the level of the final observable A_{LR}. This means that we include contributions from two-loop diagrams with at least one closed fermion loop, as well as products a one-loop diagram with fermion loop with another one-loop diagram. However, for consistency we exclude products of one-loop diagrams without closed fermion loops that could arise from interference terms obtained by expanding the denominator of Eq. (8.1) to two-loop order.

Logarithmically enhanced contributions from virtual photon loops cancel out in the ratio (8.1). While individual loop contributions exhibit IR divergences, cancella-

tion takes place once all terms that contribute to the ratio have been combined. We use a small photon mass m_γ and electron mass m_e to regulate the soft and collinear divergencies appearing at intermediate steps, respectively. The real photon radiation contributions require a separate treatment and depend on the kinematic acceptances specific to the experiment. We do not consider them here.

There are also ultraviolet (UV) divergences, for which we employ dimensional regularization. The UV divergencies are eliminated by appropriate renormalization conditions. We employ a renormalization scheme similar to Ref. [750], where the on-shell (OS) scheme is used for the electromagnetic coupling and the Z-boson, Higgs boson and fermion masses. For the weak mixing angle $\sin^2\theta_W$ we use the $\overline{\text{MS}}$ renormalization scheme to make contact with descriptions of $\sin^2\theta_W$ as a running parameter in the literature. Specifically, we use the $\overline{\text{MS}}$ scheme in the full SM, without any decoupled degrees of freedom, which ensures that $\sin^2\theta_W(\mu)_{\overline{\text{MS}}}$ is gauge invariant. By default, the scale choice $\mu = m_Z$ is used in the following. Expressions for the on-shell counterterms can be found in Ref. [766].

To guarantee the cancellation of UV divergencies, one must impose the relation $\sin^2\theta_W = 1 - m_W^2/m_Z^2$, where m_W and m_Z are the renormalized gauge boson masses in any given renormalization scheme (not necessarily the OS scheme). This implies that one cannot choose an independent renormalization condition for m_W, but instead the m_W counterterm is restricted to

$$\delta m_W^2 = (1 - s_W^2)\delta m_{Z,\text{OS}}^2 - m_Z^2 \delta s_{W,\overline{\text{MS}}}^2 \,, \tag{8.27}$$

where $s_W^2 \equiv \sin^2\theta_W(\mu)_{\overline{\text{MS}}}$. The renormalized mass, $m_{W,\text{ren}}$, defined in this fashion differs from the OS mass, $m_{W,\text{OS}}$, and an additional finite correction would be needed to relate the two. However, given that m_W is never used as an input or output in our calculation, this correction is never explicitly needed in our case.

When performing calculations in dimensional regularization, one has to be careful about the treatment of γ_5. In $d \neq 4$ dimensions, the anticommutation rule $\{\gamma^\mu, \gamma_5\}$ is incompatible with the trace identity $\mathrm{tr}\{\gamma^\alpha\gamma^\beta\gamma^\gamma\gamma^\delta\gamma_5\} = -4i\epsilon^{\alpha\beta\gamma\delta}$. Contributions from such traces arise from vertex diagrams with a triangle sub-loop, see Fig. 8.4 (e), and from box diagrams. However, in both of these cases, contributions stemming from ϵ-tensors are UV-finite (after including the sub-loop counterterms for the box graphs) and thus can be computed in 4 dimensions without ambiguity[i]. Also, we have confirmed that the triangle diagrams with photons and Z-bosons vanish in the limit of vanishing fermion masses, as required by anomaly cancellation condition.

Throughout the calculation, we exploit the hierarchy of scales $m_e^2 \ll Q^2 \ll m_{\mathrm{weak}}^2$, where $m_{\mathrm{weak}} \sim m_W, m_Z, m_H, m_t$. In practice, this means that the mass of the external electrons is set to zero everywhere except where it is needed to regularize collinear singularities. Furthermore, we perform a large-mass expansion for $m_{\mathrm{weak}}^2 \gg Q^2$, up to order m_{weak}^{-2}, which is the leading order needed for parity violating effects [485, 750]. This expansion is based on the method of regions [755, 769, 770], and in many cases it leads to products of one-loop integrals and two-loop vacuum integrals, which are analytically known [649, 764, 771, 772]. The only exception are vertex and box diagrams with a light-fermion loop inside a photon or photon-Z propagator (see Fig. 8.4 (b)). Here "light fermion" refers to any SM fermion except the top quark.

We evaluate these two-loop integrals using the numerical dispersion integral technique [763] (see also Refs. [773, 774]). Since only the transverse part of the sub-loop self-energy $\Sigma_{\mu\nu}(k^2)$ contributes, we decompose it as

$$\Sigma_{\mu\nu} = [g_{\mu\nu}k^2 - k_\mu k_\nu]\Pi_{\mathrm{T}}(k^2)\,, \tag{8.28}$$

$$\Pi_{\mathrm{T}}(k^2) = c_\epsilon + \frac{k^2}{\pi}\int_0^\infty d\sigma\, \frac{\mathrm{Im}\{\Pi_{\mathrm{T}}(\sigma)\}}{\sigma(\sigma - k^2 - i0)}\,. \tag{8.29}$$

[i] A similar argument holds for a set of useful identities for 4-fermion scattering matrix elements [767, 768].

The contribution of a fermion with mass m_f is given by

$$c_\epsilon = \frac{N_c g_1 g_2}{12\pi}\left(\frac{1}{\epsilon} + \ln\frac{\mu^2}{m_f^2}\right), \tag{8.30}$$

$$\begin{aligned}\mathrm{Im}\{\Pi_{\mathrm{T}}(\sigma)\} &= \frac{N_c g_1 g_2}{12\pi}\Big(1 + \frac{2m_f^2}{\sigma}\Big) \\ &\quad\times\sqrt{1-\frac{4m_f^2}{\sigma}}\;\Theta(\sigma-4m_f^2)\,,\end{aligned} \tag{8.31}$$

where $\epsilon = 2/(4-d)$, $\Theta(x)$ is the Heaviside step function, and $N_c = 1$ (3) for leptons (quarks). The couplings are $g_1 g_2 = e^2 Q_f^2$ and $g_1 g_2 = \frac{e^2 Q_f (2 s_W^2 Q_f - I_{3f})}{2 s_W c_W}$ for the photon and photon-Z self-energy, respectively. Inserting these expressions into the outer loop leads to integrals of the form

$$\begin{aligned}\int \frac{d^d k}{i\pi^{d/2}}\,&\frac{N(k)}{\prod_i[(k+p_i)^2 - m_i^2 + i0]} \\ &\times\left[c_\epsilon - \frac{1}{\pi}\int\frac{d\sigma}{\sigma}\,\mathrm{Im}\{\Pi_{\mathrm{T}}(\sigma)\}\frac{k^2}{k^2-\sigma+i0}\right].\end{aligned} \tag{8.32}$$

Here p_i are sets of external momenta, as they appear in a given vertex or box diagram, and $N(k)$ accounts for dot products $(k^2, k\cdot p_i)$ and $\not{k}$ in the numerator. The k-integral in Eq. (8.32) is a conventional one-loop integral, which can be performed analytically and reduced to basic scalar one-loop functions using the standard Passarino-Veltman method. The remaining σ integral, which is UV-finite, is easily evaluated numerically with high precision. It is interesting to note that the σ integrals involving $\log m_\gamma^2$ and $\log m_e^2$ may be performed analytically so that the cancellation of IR singularities in the full result can be checked algebraically.

These dispersion integrals are not well-defined for light quarks ($f = u, d, s$) in the inner loop, since the dominant contribution to the integral arises from region where $k^2 \sim m_f^2$, where hadronization effects become important. In fact, the same problem already occurs at the one-loop level for the self-energy contribution to the γ-Z self-energy in the t- and u-channel [750, 775], due to the fact that $Q^2 < \Lambda_{\mathrm{QCD}}^2$.

The non-perturbative hadronic corrections can be evaluated only approximately. One option is to use effective quark masses, such as the threshold masses derived in Refs. [4, 5]. An alternative possibility is to determine the dispersion integrals by directly inserting the required spectral functions derived from data that are provided e.g. in Ref. [776]. We opted not to follow this method since no uncertainty associated with the required flavor symmetry hypothesis is reported[ii]. Therefore in our calculation, we use the threshold quark masses in all places where mass-dependent terms remain after expanding in large $m^2_{\rm weak}$. However, for consistency, we exclude two-loop self-energy diagrams involving only quark and photon propagators in the loops, such as Fig. 8.4 (a) with a photon inside the loop, since QED effects are already subsumed in the non-perturbative hadron dynamics. In addition, following Ref. [750], we also set $Q^2 \to 0$ in the t- and u-channel self-energies, since the differences $\Pi^{\gamma\gamma}_{\rm T}(t) - \Pi^{\gamma\gamma}_{\rm T}(0)$ and $\Pi^{\gamma Z}_{\rm T}(t) - \Pi^{\gamma Z}_{\rm T}(0)$ are estimated to be negligibly small [750] (similar for t replaced by u). We leave a more detailed study of hadronic effects for future work.

As shown in Eq. (8.2), A_{LR} is commonly normalized in terms of the Fermi constant G_μ, which is related to SM parameters according to

$$\frac{G_\mu}{\sqrt{2}} = \frac{\pi\alpha}{2 s^2_W c^2_W m^2_Z}(1 + \Delta r), \tag{8.33}$$

where Δr includes radiative corrections. The required two-loop contributions to Δr with one or two closed fermion loops have been taken from Refs. [766, 777] (see also Ref. [778]).

The calculation has been carried out with extensive use of computer algebra tools. Diagrams and amplitudes were generated with FeynArts [779]. For the Lorentz and

[ii]However, one can verify that the running behavior of the weak coupling derived in Ref. [776] can be almost exactly reproduced by a suitable choice of effective quark masses. The difference between this choice of quark masses and those of Ref [4] leads to a shift of the two-loop corrections to A_{LR} that is one order of magnitude below the expected level of precision of MOLLER.

Dirac algebra, we employed PACKAGE-X [780] and cross-checked against private code written in MATHEMATICA. The large-mass expansion was implemented in-house in two independently developed MATHEMATICA programs. Two-loop integrals with non-trivial numerator structures have been reduced to simple scalar integrals using FIRE 5 [756] and using private code based on Ref. [781, 782]. For basic one-loop integrals and two-loop vacuum integrals, analytical formulae are available [649, 764, 771, 772]. We have numerically checked our implementation of the one-loop formulae against the COLLIER library [35]. The numerical dispersion integrals for two-loop vertex and box integrals have been implemented in C and MATHEMATICA.

Each building block of the final result has been computed in two independent setups within our collaboration and cross-checked against each other. We have confirmed cancellation of UV and IR divergencies in the full result by verifying that the coefficients of the $1/\epsilon$, $\log m_e^2$ and $\log m_\gamma^2$ terms vanish algebraically. Furthermore, as an intermediate step, we have reproduced the one-loop result of Ref. [750] and found exact agreement with the analytical formulae given there.

8.4 Results

To evaluate the numerical impact of the closed fermion-loop NNLO corrections to A_{LR}, we used the following input parameters:

$$\begin{aligned}
m_Z &= 91.1876\,\text{GeV}, & s_W^2 &= 0.2314,\\
m_H &= 125.1\,\text{GeV}, & m_t &= 173.0\,\text{GeV},\\
m_\tau &= 1.777\,\text{GeV}, & m_b &= 3.99\,\text{GeV},\\
m_\mu &= 105.7\,\text{MeV}, & m_c &= 1.185\,\text{GeV},\\
m_e &= 0.511\,\text{MeV}, & m_s &= 0.342^{+0.048}_{-0.053}\,\text{GeV},\\
& & m_{u,d} &= 0.246^{+0.054}_{-0.057}\,\text{GeV},\\
\Delta\alpha &= 0.02761_{\text{had.}} + 0.0314976_{\text{lep.}}, & & \qquad (8.34)
\end{aligned}$$

at the representative kinematic point

$$\sqrt{s} = 11\,\mathrm{MeV}, \qquad y = 0.4. \tag{8.35}$$

Here $\Delta\alpha$ accounts for the renormalization group running of the fine structure constant between scales $\mu = 0$ and $\mu = m_Z$, and enters our calculation through the OS charge renormalization. The first number reflects the hadronic contribution to $\Delta\alpha$, which is obtained from $e^+e^- \to$ hadrons data (see Refs. [776, 783, 784] for recent evaluations), while the second number is the perturbatively calculable leptonic contribution [785].

As explained above, the light fermion masses m_f, $f \neq t$ enter in loop integrals with a fermionic photon or γ-Z self-energy subloop. The values for the light quark masses are taken from Ref. [4]. There is a strong anti-correlation between the reported uncertainties of m_s and $m_{u,d}$. We will assume them to be 100% anti-correlated for the results which we present below.

With these inputs we obtain numerical results for the asymmetry (8.2) as shown in Table 8.1. The first row corresponds to the tree-level contribution, and the remaining rows $\Delta Q^e_{W(L,n_f)}$ are the radiative corrections with L loops and n_f closed fermion loops. No resummation of logarithms has been carried out. In particular, the electroweak logarithms, which conventionally define the running $\sin^2\theta_W$, are left explicitly in the one and two loop results. The last two rows $\Delta Q^e_{W(2,2)}$ and $\Delta Q^e_{W(2,1)}$ are obtained using our newly computed NNLO corrections to the asymmetry. The error intervals reflect the hadronic uncertainties due to the threshold quark masses in Eq. (8.34).

The precision goal for the MOLLER experiment corresponds to a measurement of the weak charge with an uncertainty of $\delta_{\mathrm{exp}} Q^e_W = 1.1 \times 10^{-3}$. The individual corrections from two and one closed fermion loops, $\Delta Q^e_{W(2,2)}$ and $\Delta Q^e_{W(2,1)}$ respectively, are each larger than the experimental target, thus highlighting the importance of accounting for the NNLO corrections. However, the sum of both contributions

Quantity	Contribution ($\times 10^{-3}$)
$1-4\sin^2\theta_W$	$+74.4$
$\Delta Q^e_{W(1,1)}$	-29.0
$\Delta Q^e_{W(1,0)}$	$+\ 3.1$
$\Delta Q^e_{W(2,2)}$	$-\ 2.12^{+0.014}_{-0.024}$
$\Delta Q^e_{W(2,1)}$	$+\ 1.65^{+0.010}_{-0.007}$
$\Delta Q^e_{W(2,0)}$	$\pm\ 0.18$ (estimate)

Table 8.1: Numerical estimates of the calculated contributions to the polarized Møller scattering asymmetry defined in (8.2) through NNLO using input values in (8.34) and (8.35). Subscripted indices on $\Delta Q^e_{W(L,n_f)}$ refer to the loop order L and number of closed loops n_f.

$$\Delta Q^e_{W(2,2)} + \Delta Q^e_{W(2,1)} = -0.47^{+0.007}_{-0.014} \times 10^{-3} \tag{8.36}$$

is significantly smaller due to a coincidental cancellation. Furthermore, anti-correlation between the hadronic uncertainties in the individual contributions leads to a reduced overall hadronic uncertainty.

The resulting hadronic uncertainty from quark loops is negligible compared to the experimental target precision. It is likely that the our estimate based on quark mass errors overestimates this uncertainty, since we cannot account for correlations between the quark masses and the K factors in Ref. [4][iii]. A more detailed analysis of these hadronic effects will be studied in the future, and in what follows, we provide an estimate of these hadronic uncertainties as depicted in detail below.

In our calculation above, the $Z\gamma$ and $\gamma\gamma$ vacuum polarization functions are treated perturbatively and effective quark masses are used for the numerical evaluation. This approximation shall be compared with the full non-perturbative QCD effects to obtain the uncertainties due to uncontrolled QCD corrections. In order to assess the uncertainty in our treatment of the vacuum polarization functions, we investigate

[iii] In fact, when estimating the leading hadronic effects by plugging these quark masses into the NLO correction, one finds an uncertainty that is a factor few larger than the detailed renormalization-group evaluation in Ref. [4].

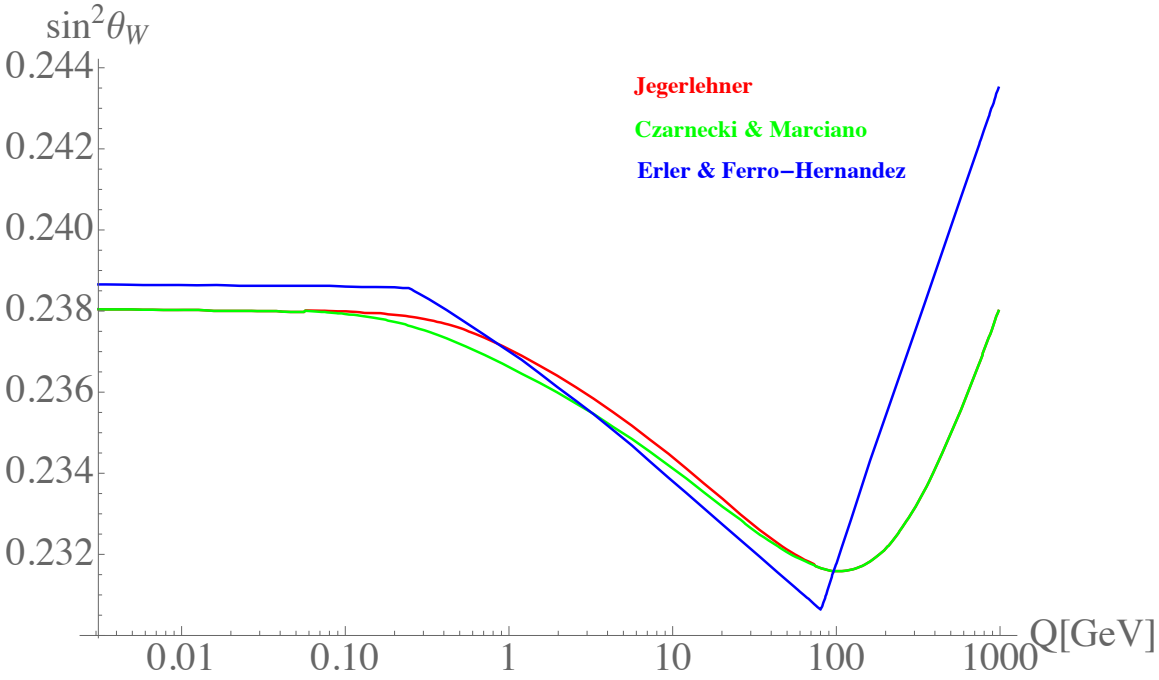

Figure 8.5: Comparison of the determination of the weak mixing angle, where the red curve is from Ref. [35], the green curve is from Ref. [36] and the blue curve is from Ref. [4]. See the main text for more discussion.

to what extent other methods would affect the prediction of the asymmetry at the two-loop level. To that end, we compared shifts in the value of $\sin^2\theta_W(0)$ by using effective quark masses used in Ref. [36], a dispersive treatment followed by Jegerlehner as reported in Ref. [35], and an NLO RGE analysis by Erler and Ferro-Hernandez in Ref. [4]. Their determinations are compared in Figure 8.5, where the red curve is from Ref. [35], the green curve is from Ref. [36] and the blue curve is from Ref. [4].

We find that there is reasonable agreement between the blue curve from Ref. [4] and the dispersion-derived curve from Jegerlehner in Ref. [35]. In particular, the difference between the two curves is bounded and well behaved in the non-perturbative region around a few GeV, which justifies the use of quark masses in diagrams of type (b) and (d) in Figure 8.4, where we integrate over Q^2. There is even better agreement between the results of Jegerlehner and Czarnecki+Marciano indicated by the green curve. Therefore, if we insert in our two-loop calculations the effective quark masses

from Marciano and Sirlin in Ref. [786], which were used for the green curve, we get a shift for our two-loop prediction by an amount

$$\delta(\Delta Q_{W(2,2)}) = -0.14 \times 10^{-3}$$
$$\delta(\Delta Q_{W(2,1)}) = +0.04 \times 10^{-3}$$
$$\delta(\Delta Q_{\text{total}}) = -0.10 \times 10^{-3}.$$

compared to the threshold quark masses taken from Erler and Ferro-Hernandez in Ref. [4]. The shift is one order of magnitude below the planned level of precision of MOLLER. Given the agreement in the behavior of $\sin^2\Theta_W$ between the effective quark masses from Marciano and Sirlin and the dispersive treatment by Jegerlehner, we expect that the difference of the latter to our result will also be well below the experimental target precision. One can use the shift $\Delta Q_{W,\text{total}}$ as a more conservative estimate of the hadronic uncertainties in our two-loop result.

On the other hand, the correction to ΔQ^e_W depends very mildly on y (i.e. on the scattering angle). Varying y in the experimentally relevant range $(0.25, 0.75)$ [16], we find that ΔQ^e_W changes by 0.04×10^{-3} for the NLO corrections, and by 0.01×10^{-3} for the NNLO corrections, both of which are negligible.

Finally, we attempt to estimate size of the currently missing NNLO corrections without closed fermion loops $\Delta Q^e_{W(2,0)}$ (called "bosonic" corrections in the following). For this purpose, we begin by comparing the relative size of the fermion-loop and bosonic correction at NLO. From Table 8.1, these are $\Delta Q^e_{W(1,1)} = -0.0290$ and $\Delta Q^e_{W(1,0)} = +0.0031$, respectively. Assuming a similar ratio between the corrections with one closed fermion loop and the bosonic corrections at NNLO, we obtain an estimate of 0.18×10^{-3} for the size of the latter. This would be safely below the experimental target precision.

8.5 Discussion and summary

To correctly interpret the proposed 2.4% measurement of the parity-violating asymmetry A_{LR} from the MOLLER experiment at the Jefferson Lab in terms of BSM physics, we calculate the NNLO SM contributions to A_{LR} using large-mass expansion and numerical integration of sub-loop dispersion relation. We summarize our results in Table 8.1. We find that individual corrections to ΔQ_W^e from one and two closed fermion loops are each larger than the experimental target precision. However, their sum is significantly smaller due to a cancellation. The dependence of ΔQ_W^e on the scattering angle is very mild in the experimentally relevant range and can be ignored for most practical purposes. Finally, we also consider the impact of the remaining bosonic NNLO correctionsas well as hadronic uncertainties arising from using effective quark masses instead of a full dispersive treatment for $Z\gamma$ and $\gamma\gamma$ vacuum polarization functions, and estimate them to be negligible compared to the MOLLER precision goal. However, it is desirable to confirm this with an explicit calculation in the future.

CONCLUSION

From the observation of amber electricity from the ancient Greeks, to the discovery of the Higgs particle in 2012 [50, 51] and the observation of gravitational waves in 2016 [787, 788], it is surprisingly amazing how far we human beings have been going in understanding the nature ranging from the microscopic scale of $\mathcal{O}(10^{-18}\,\mathrm{m})$ of the weak scale to the macroscopic scale of $\mathcal{O}(10^{26}\,\mathrm{m})$ of the size of our Universe. Despite the complicatedness, microscopically, the nature can be described by the SM of particle physics based on the gauge group of $\mathrm{SU(3)_c} \otimes \mathrm{SU(2)_L} \otimes \mathrm{U(1)_Y}$, and macroscopically, our Universe can be described by general relativity.

However, the successfulness and the shininess of the SM are shadowed by several profound questions discussed in the Introduction of this thesis, and three of them that we are particularly interested in are

1. The massive neutrino problem: In SM, neutrinos are massless as a result of the gauge group and the particle contents of SM, while experimentally, neutrino oscillation requires neutrinos to be light but with non-vanishing masses.

2. The dark matter problem: SM does not provide any candidates that can explain the dark matter we observe today.

3. The baryon asymmetry problem: The observed baryon asymmetry far exceeds what is being predicted by the SM.

Therefore, to answer each of these questions listed above, new physics beyond the SM is needed.

Understanding what the new physics could be has been a major task of particle physicists recently, and experiments from various aspects searching for new physics are under active operation or under construction. These experiments can be generically classified into three categories: (1) Energy frontier, (2) intensity frontier, and (3) cosmic frontier. This thesis is meant to provide one contribution to search for the potential new physics responsible for the problems listed above.

To that end, we first reviewed the SM in Chapter 1 and then discussed precision measurements on the model parameters from a combined analysis of the three frontiers. From the review, we clearly showed how the neutrinos remained massless as a result of the gauge symmetry and the particle contents of the SM, and also discussed the extent to which CP was violated in the SM from a detailed discussion on the CKM matrix.

We then reviewed the neutrino mass problem in Chapter 2 and showed why neutrino oscillations require non-vanishing neutrino masses. We concluded that SM could not be responsible for neutrino oscillations and then discussed the three only seesaw mechanisms that could account for neutrino masses at tree level, i.e. type-I, -II and -III seesaw mechanisms. On one hand, the neutrino mass matrix leads to the existence of the PMNS matrix that mixes neutrinos of different flavor and thus neutrino oscillation; on the other hand, the neutrino mass terms could result in neutrinos of Dirac and/or Majorana types. Note that the PMNS matrix can be precisely measured from oscillation experiments as reviewed in Chapter 2, however, oscillation experiments are not sensitive to the Majorana phases and the absolute masses of neutrinos, instead, they only depend on the Dirac phase and neutrino mass squared difference. Therefore, oscillation experiments can not tell Dirac neutrinos from Majorana neutrinos, and they can not determine the absolute scale of neutrino masses either. Since neutrino masses are of fundamental importance, we review current constraints on the masses from various experiments using cosmological and astrophysical data. For Ma-

jorana neutrinos, we discuss how $0\nu\beta\beta$ can be used to constrain the absolute Majorana neutrino masses.

In Chapter 3, we discussed how baryon asymmetry could be successfully generated through reviewing the three Sakharov conditions: (1) baryon number violation, (2) C and CP violation, and (3) out of equilibrium. Surprisingly, it was realized that the SM already had all the ingredients to explain the baryon asymmetry through EWBG. However, a careful study found that CP was only feebly violated in the SM as also discussed in Chapter 1, and the SFOEWPT required by the out of equilibrium condition was also absent in SM. Therefore, we concluded that SM could not account for the baryon asymmetry observed and new physics was needed to be responsible for the baryon asymmetry.

The dark matter problem was reviewed in Chapter 4. We focused on the WIMP dark matter scenario only in this thesis since typical WIMP lives at the weak scale. As a result, it could solve the hierarchy problem and can also be tested with current technologies. Experimental efforts on searching for dark matter, not just WIMP dark matter, are tremendous, we summarized those experimental constraints from collider searches, direct and indirect detection in Chapter 4.

To address the neutrino mass problem, the baryon asymmetry problem and the dark matter problem, we presented our work on the complex triplet and the real triplet model in Chapter 6 and Chapter 7 respectively. Both models could explain the baryon asymmetry through EWBG due to distortion of the SM Higgs potential by new interactions between the SM Higgs doublet and the triplet, making a SFOEWPT possible. More specifically, besides the baryon asymmetry problem, the complex triplet could also explain the neutrino mass problem within the type-II seesaw framework, while the real triplet could provide a WIMP dark matter candidate. For the complex triplet, we studied in detail the model discovery at future 100 TeV pp colliders as well as Higgs portal parameter determination that was closely related

to EWBG. We concluded that a significant portion of the parameter space of the complex triplet model could be covered by the future colliders, and the Higgs portal couplings could be constrained within the $[-1, 1]$ range through a combined analysis of precision measurements on the branching ratio of SM Higgs decaying into two photons. On the other hand, for the real triplet, since previous work had already studied its ability to explain baryon asymmetry, we only focused on its explanation to dark matter in Chapter 7. To be specific, we studied real triplet model discovery through the disappearing charge track signature at the LHC, HL-LHC as well as a future 100 TeV pp collider and also considered constraints from dark matter direct detection as discussed in Chapter 4. We found that the future XENON20T could cover almost the entire parameter space of the real triplet model.

In terms of precision measurements in the intensity frontier, we reviewed precision measurements of the weak mixing angle in Chapter 5 by first discussing SM prediction of the running of the weak mixing angle in different schemes. Then we reviewed measurements from various collider and low-energy experiments. Currently, the most precise measurements came from SLD and LEP at the Z pole, and they differ by about 3σ. Each value would imply very different physics and weak mixing angle determination with better precision is needed. In Chapter 5, we reviewed prospects of future experiments and concluded that the MOLLER project at the Jefferson Lab would be the one with the smallest uncertainty among the proposed low energy experiments in the next decade. To match its high precision goal, a full two-loop calculation within SM was needed in order to correctly interpret future experimental result from MOLLER. To that end, we presented our result in Chapter 8, representing the first result of a gauge invariant and dominant subset of the two-loop corrections to the weak mixing angle from SM.

This thesis represents only a tiny portion of the efforts of the whole community in searching for new physics. Though unfortunately we have not seen any definitive

signal of new physics yet, looking back in the 1900s, we might be in a similar situation where outburst of new physics is on the way. In searching for new physics, the passion of the author never ends, though it might be a long long journey.

APPENDIX A

TYPE-II SEESAW TRIPLET

A.1 Summary of current experimental constraints on the CTHM

All upper/lower limits below are at 95% confidence level unless otherwise specified.

A.1.1 Singly charged Higgs particle $H^{\pm}$

- For pp collision at $\sqrt{s} = 7\,\text{TeV}$, $\int \mathcal{L}dt = 4.5\,\text{fb}^{-1}$, corresponding to the m_h^{max} scenario of the Minimal Supersymmetric Standard Model (MSSM) [789], $90\,\text{GeV} < m_H^{\pm} < 150\,\text{GeV}$ is excluded by assuming $\text{BR}(H^+ \to \tau\nu) = 100\%$ [790], where BR stands for BR and same notation below.

- For pp collision at $\sqrt{s} = 7\,\text{TeV}$ $\int \mathcal{L}dt = 4.5\,\text{fb}^{-1}$ and $\text{BR}(H^+ \to \tau\nu) = 100\%$, they find $\text{BR}(t \to bH^+) < 1\%\text{-}5\%$ for $m_H^+ \in [90, 150]\,\text{GeV}$ [790]. Later in the same year after the discovery of the Higgs particle, they improve their result to be $\text{BR}(t \to bH^+) < 0.8\%\text{-}3.4\%$ for $m_H^+ \in [90, 160]\,\text{GeV}$ [791]. And assuming $\text{BR}(H^+ \to c\bar{s}) = 100\%$ instead, they find $\text{BR}(t \to bH^+) < 1\%\text{-}5\%$ for $m_H^+ \in [90, 150]\,\text{GeV}$ [792]. While for $\sqrt{s} = 8\,\text{TeV}$ $\int \mathcal{L}dt = 19.5\,\text{fb}^{-1}$, they find $\text{BR}(t \to H^+b) \times \text{BR}(H^{\pm} \to \tau^{\pm}\nu) < 0.23\%\text{-}1.3\%$ for $m_H^+ \in [80, 160]\,\text{GeV}$. They also conclude that $\sigma(pp \to tH^{\pm} + X) \times \text{BR}(H^+ \to \tau\nu) < 0.76\,\text{pb-}4.5\,\text{pb}$ for $m_H^+ \in [180, 1000]\,\text{GeV}$, which excludes the mass region $m_H^{\pm} \in [200, 250]\,\text{GeV}$ with large $\tan\beta$ in the context of MSSM [793].

- For pp collision at $\sqrt{s} = 8\,\text{TeV}$, $\int \mathcal{L}dt = 20.3\,\text{fb}^{-1}$ and a VBF produced $H^{\pm}$, $\sigma(pp \to H^{\pm} + X) \times \text{BR}(H^{\pm} \to W^{\pm}Z) < 31\,\text{fb-}1020\,\text{fb}$ for $m_H^{\pm} \in (200, 1000)\,\text{GeV}$ [794].

- For pp collision at $\sqrt{s} = 13\,\text{TeV}$ and $\int \mathcal{L}dt = 3.2\,\text{fb}^{-1}$, $\sigma(pp \to H^{\pm}t[b]) \times \text{BR}(H^{\pm} \to \tau\nu) < 1.9\,\text{fb-}15\,\text{fb}$ for $m_H^{\pm} \in (200, 2000)\,\text{GeV}$ [660].

- For pp collision at $\sqrt{s} = 13\,\text{TeV}$ and $\int \mathcal{L}dt = 3.2\,\text{fb}^{-1}$ and a VBF produced $H^{\pm}$, $\sigma(pp \to H^{\pm} + X) \times \text{BR}(H^{\pm} \to W^{\pm}Z) < 36\,\text{fb-}573\,\text{fb}$ for $m_H^{\pm} \in (200, 2000)\,\text{GeV}$ [661].

A.1.2 doubly charged Higgs particle $H^{\pm\pm}$:

- For pp collision at $\sqrt{s} = 7\,\text{TeV}$ and $\int \mathcal{L}dt = 1.6\,\text{fb}^{-1}$, $\sigma(H^{++}H^{--}) \times \text{BR}(H^{\pm\pm} \to \mu^{\pm}\mu^{\pm}) < 1.7\,\text{fb-}11\,\text{fb}$ for $m_H^{\pm\pm} \in [100, 400]\,\text{GeV}$. Interpreted in left-right symmetric models [795–798], $m_{H^{\pm\pm}}^L < 355\,\text{GeV}$ and $m_{H^{\pm\pm}}^R < 251\,\text{GeV}$ are excluded by assuming $\text{BR}(H^{\pm\pm} \to \mu^{\pm}\mu^{\pm}) = 100\%$. For $\text{BR}(H^{\pm\pm} \to \mu^{\pm}\mu^{\pm}) = 33\%$, $m_{H^{\pm\pm}}^L < 244\,\text{GeV}$ and $m_{H^{\pm\pm}}^R < 209\,\text{GeV}$ are excluded [635].

- For pp collision at $\sqrt{s} = 1.96\,\text{TeV}$ and $\int \mathcal{L}dt = 6.1\,\text{fb}^{-1}$, $m_{H^{\pm\pm}} < 190\text{-}245\,\text{GeV}$ (depending on the decay modes and the couplings) are excluded [636].

- For pp collision at $\sqrt{s} = 7\,\text{TeV}$ and $\int \mathcal{L}dt = 4.7\,\text{fb}^{-1}$, the cross section of a same-sign di-lepton pair in the fiducial region with $p_T^{e^{\pm}} > 20\,\text{GeV}$, $p_T^{\mu^{\pm}} > 25\,\text{GeV}$ and $|\eta| < 2.5$ is constrained to be between 1.7fb and 64fb [637].

- For pp collision at $\sqrt{s} = 7\,\text{TeV}$ and $\int \mathcal{L}dt = 4.7\,\text{fb}^{-1}$, assuming pair production of $H^{++}H^{--}$, $m_{H^{\pm\pm}} < 409\,\text{GeV}$, $m_{H^{\pm\pm}} < 375\,\text{GeV}$, $m_{H^{\pm\pm}} < 398\,\text{GeV}$ are excluded from $e^{\pm}e^{\pm}$, $e^{\pm}\mu^{\pm}$ and $\mu^{\pm}\mu^{\pm}$ final states respectively by assuming 100% BR for each final state [638].

- For pp collision at $\sqrt{s} = 8\,\text{TeV}$ and $\int \mathcal{L}dt = 20.3\,\text{fb}^{-1}$, by assuming $\text{BR}(H^{\pm\pm} \to e\tau/\mu\tau) = 100\%$, $m_{H^{\pm\pm}} < 400\,\text{GeV}$ is excluded [639].

- For pp collision at $\sqrt{s} = 8\,\text{TeV}$ and $\int \mathcal{L}dt = 20.3\,\text{fb}^{-1}$, by assuming $\text{BR}(H^{\pm\pm} \to e^{\pm}e^{\pm}/e^{\pm}\mu^{\pm}/\mu^{\pm}\mu^{\pm}) = 100\%$, $m_{H^{\pm\pm}}^L < 465\,\text{GeV} - 550\,\text{GeV}$ and $m_{H^{\pm\pm}}^R < 370\,\text{GeV}\text{-}435\,\text{GeV}$ are excluded [23].

- For pp collision at $\sqrt{s} = 8\,\text{TeV}$ and $\int \mathcal{L}dt = 20.3\,\text{fb}^{-1}$, for long-lived $H^{\pm\pm}$ pair produced through a Drell-Yan process (with only photon exchange included), $m_{H^{\pm\pm}} \in [50, 660]\,\text{GeV}$ is excluded [640].

- For pp collision at $\sqrt{s} = 13\,\text{TeV}$ and $\int \mathcal{L}dt = 35.9\,\text{fb}^{-1}$, for a VBF produced $H^{\pm\pm}$ particle, $s_H > 0.18$ and $s_H > 0.44$ are excluded for $m_{H^{\pm\pm}} = 200\,\text{GeV}$ and $m_{H^{\pm\pm}} = 1000\,\text{GeV}$ respectively in the GMM [641].

- For pp collision at $\sqrt{s} = 13\,\text{TeV}$ and $\int \mathcal{L}dt = 36.1\,\text{fb}^{-1}$, by assuming $\text{BR}(H^{\pm\pm} \to e^{\pm}e^{\pm}/e^{\pm}\mu^{\pm}/\mu^{\pm}\mu^{\pm}) = 100\%$, $m^{L}_{H^{\pm\pm}} < 770\,\text{GeV} - 870\,\text{GeV}$ are excluded [22].

A.1.3 Electric charge neutral particles:

- For pp collision at $\sqrt{s} = 8\,\text{TeV}$ and $\int \mathcal{L}dt = 19.5 - 20.3\,\text{fb}^{-1}$, $m_A = 140\,\text{GeV}$ and $\tan\beta > 5.4$ in the m_h^{max} scenario of the MSSM is excluded [799].

- For pp collision at $\sqrt{s} = 8\,\text{TeV}$ and $\int \mathcal{L}dt = 20.3\,\text{fb}^{-1}$, $\sigma(gg \to A) \times \text{BR}(A \to Zh) \times \text{BR}(h \to \tau\bar{\tau}(b\bar{b})) < 0.098\,\text{pb}$-$0.013\,\text{pb}$ (0.57fb-$0.014\,\text{pb}$) for $m_A \in [220, 1000]\,\text{GeV}$ [800]. Constraints on the 2HDM parameter space are also discussed therein.

- For pp collision at $\sqrt{s} = 8\,\text{TeV}$ and $\int \mathcal{L}dt = 19.7\,\text{fb}^{-1}$, $\sigma(pp \to A) \times \text{BR}(A \to hZ \to b\bar{b}\ell^{+}\ell^{-}) \in [3, 30]\,\text{fb}$ (with $\ell = e, \mu$) is excluded for $m_A \in [250, 600]\,\text{GeV}$ [801]. The result is used to reduce the parameter space of the 2HDM, see figure 5 therein.

- For pp collision at $\sqrt{s} = 8\,\text{TeV}$ and $\int \mathcal{L}dt = 20.3\,\text{fb}^{-1}$, $\sigma(pp \to H) \times \text{BR}(H \to ZZ) < 0.008\,\text{pb}$-$0.53\,\text{pb}(0.009\,\text{pb}$-$0.31\,\text{pb})$ for a gluon-fusion (VBF) produced H for $m_H \in [195, 950]\,\text{GeV}$ [802], which is also used to constrain the 2HDM parameter space.

- For pp collision at $\sqrt{s}$=8 TeV and $\int \mathcal{L}dt$=20.3 fb^{-1}, the strongest limits are in the narrow-width: $\sigma_H \times \text{BR}(H \to W^{+}W^{-})$¡830(240) fb for a gluon-fusion

(VBF) produced H at $m_H = 300\,\text{GeV}$. For $m_H = 1500\,\text{GeV}$, $\sigma_H \times \text{BR}(H \to W^+W^-)$¡22(6.6) fb [803].

- By studying $h \to (\gamma\gamma, ZZ^* \to 4\ell, WW^* \to \ell\nu\ell\nu, Z\gamma, b\bar{b}, \tau^+\tau^-, \mu^+\mu^-)$ based on pp collision data at $\sqrt{s} = 7\,\text{TeV}$ and $\int \mathcal{L}dt$=4.7 fb^{-1} and $\sqrt{s} = 8\,\text{TeV}$ and $\int \mathcal{L}dt = 20.3\,\text{fb}^{-1}$, the authors in Ref. [804] set constraints on the parameter space of Minimal Composite Higgs Models (MCHM), additional electroweak singlet models and 2HDM. Especially, $m_A > 370\,\text{GeV}$ is constrained in hMSSM.

- For pp collision at $\sqrt{s} = 8\,\text{TeV}$ and $\int \mathcal{L}dt = 19.7\,\text{fb}^{-1}$, in Ref. [805] $\sigma(ggH) \times \text{BR}(H \to hh \to b\bar{b}\tau^+\tau^-)$¡0.2fb-0.8fb for $m_H \in [260, 350]\,\text{GeV}$ and $\sigma(ggA) \times \text{BR}(A \to hZ \to \tau^+\tau^-\ell^+\ell^-)$¡20fb-40fb for $m_A \in [220, 350]\,\text{GeV}$. The results are also interpreted in the context of MSSM and type-II 2HDM.

- For pp collision at $\sqrt{s} = 8\,\text{TeV}$ and $\int \mathcal{L}dt = 19.8\,\text{fb}^{-1}$, the lower limit on $\sigma(pp \to S' \to SZ) \times \text{BR}(S \to b\bar{b}(\tau^+\tau^-)) \times \text{BR}(Z \to \ell^+\ell^-)$ (S', S are neutral Higgs bosons and $m_{S'} > m_S$.) is constrained to be 5fb for $\ell^+\ell^-\tau^+\tau^-$ final state, $m_{H/A} \in (500, 1000)\,\text{GeV}$, $m_{A/H} \in (90, 400)\,\text{GeV}$ and 1-100fb for $\ell^+\ell^-b\bar{b}$ final state, $m_A \in [300, 100000]\,\text{GeV}$ respectively. While for the degenerate case, i.e., $m_A = m_H$, the parameter space is unexplored. The result is also explained in the context of 2HDM [662].

- For pp collision at $\sqrt{s}$=8 TeV and $\int \mathcal{L}dt$=20.3 fb^{-1}, in the context of a type-II 2HDM, $m_A \lesssim 500\,\text{GeV}$, $m_H \lesssim 640\,\text{GeV}$, m_A=$m_H \lesssim 620\,\text{GeV}$ is excluded by considering only a pseudoscalar A, only a scalar H and the mass-degenerate scenario m_A=m_H respectively [806].

- For pp collision at $\sqrt{s} = 13\,\text{TeV}$ and $\int \mathcal{L}dt = 36.1\,\text{fb}^{-1}$, $\sigma(pp \to X \to W(Z)h) \times \text{BR}(W(Z) \to q\bar{q}^{(\prime)}) \times \text{BR}(h \to b\bar{b})$¡83fb-1.6fb(77fb-1.1fb) for $m_X \in [1.1, 3.8]\,\text{TeV}$ for a simplified model with a heavy vector triplet [807].

- For pp collision at $\sqrt{s}$=13 TeV and $\int \mathcal{L}dt$=36.1 fb^{-1}, the upper limit of $\sigma(pp \to X) \times \text{BR}(X \to ZV)$¡1.7fb-1.4fb(0.42fb-1fb) (V=W, Z, and X a heavy resonance) for $m_X \in [300, 3000]$ GeV with a X produced through a gluon-gluon-Fusion (VBF) process [808].

- For pp collision at $\sqrt{s} = 13$ TeV and $\int \mathcal{L}dt = 36.1$ fb^{-1}, heavy neutral Higgs and gauge bosons in the ditau final state is studied and result is interpreted in hMSSM scenario, which excludes $\tan\beta$¿1.0(42) for m_A=250(1500) GeV [809].

- For pp collision at $\sqrt{s} = 13$ TeV and $\int \mathcal{L}dt = 36.1$ fb^{-1}, a heavy resonances (Y) decaying into a SM h and another new particle X (X then decays into a light quark pair) is studied for $m_Y \in [1, 4]$ TeV and $m_X \in [50, 1000]$ GeV. $\sigma(pp \to Y \to Xh)$¡10^{-2} pb-10^{-3} pb in the mass ranges under consideration [810].

- For pp collision at $\sqrt{s} = 13$ TeV, $\int \mathcal{L}dt = 36.1$ fb^{-1}, upper limit for $\sigma(pp \to A \to hZ) \times \text{BR}(h \to b\bar{b})$ is set to be from 5.5×10^{-3} pb to 2.4×10^{-1} pb for gluon-fusion production and 3.4×10^{-3} pb to 7.3×10^{-1} pb for associated production with b-quarks with $m_A \in [220, 2000]$ GeV [811].

- For pp collision at $\sqrt{s} = 13$ TeV, $\int \mathcal{L}dt = 36.1$ fb^{-1}, upper limits for $\sigma \times \text{BR}(H \to bb)$ are 14−830 fb for gluon-gluon fusion and 26−570 for b-associated production with $m_H \in [130, 700]$ GeV and $m_A \in [230, 800]$ GeV [812].

- For pp collision at $\sqrt{s} = 13$ TeV, $\int \mathcal{L}dt = 35.9$ fb^{-1}, $pp \to X \to ZZ \to 4\ell/2\ell 2q/2\ell 2\nu$, where X is a heavy resonance, is studied in detail in Ref. [813] for $m_X \in [130, 3000]$ GeV. Limits on production cross section and the BR is set from their work.

- For pp collision at $\sqrt{s} = 13\,\text{TeV}$, $\int \mathcal{L}dt = 35.9\,\text{fb}^{-1}$, an upper limit is set on the $t\bar{t}h$ production cross section relative to the SM expectation of $\mu = \sigma/\sigma_{\text{SM}}$, the best fit value for which is $\mu = 0.72 \pm 0.24(\text{stat}) \pm 0.38(\text{syst})$ [814].

A.2 Decay rates of $h \to \gamma\gamma$

Here we briefly review the computation of the ratio $R_{h\gamma\gamma}$. The current combined value from ATLAS and CMS at $\sqrt{s} = 7\,\text{TeV}$ and $\sqrt{s} = 8\,\text{TeV}$ is $R_{h\gamma\gamma} = 1.16^{+0.20}_{-0.18}$ [578, 672], and in the CTHM, the singly- and doubly-charged Higgs particles will contribute to Γ^{BSM} through loop effects. There has been many literatures studying this contribution [554, 573, 578, 584, 671], and it was also shown that in the CTHM ([584, 671]), the doubly-charged Higgs particle will give a sizable contribution to the decay rate of $h \to \gamma\gamma$ especially for negative λ_4 and λ_{45} due to a constructive interference [554]. Since we choose negative λ_4 and λ_{45} in our cases, contributions to the rate from the CTHM can in turn be used to constrain the parameter space of the CTHM. To study this effect, we rewrite the result in Ref. [578, 815] by using our notation as follows:

$$\Gamma(h \to \gamma\gamma) = \frac{G_F \alpha^2 m_h^3}{128\sqrt{2}\pi^3} \left| \sum_f N_c Q_f^2 g_{hff} A_{1/2}^h(\tau_f) + g_{hW^+W^-} A_1^h(\tau_W) \right.$$
$$\left. + \frac{4m_W}{g m_h^2} g_{hH^\pm H^\mp} A_0^h(\tau_{H^\pm}) - \frac{16 m_W v_\Phi}{g m_h^2} g_{hH^{\pm\pm}H^{\mp\mp}} A_0^h(\tau_{H^{\pm\pm}}) \right|^2 , \qquad \text{(A.1)}$$

with α the fine structure constant, g the U(1) coupling, N_c^f the color factor (N_c^f=3 for quarks and 1 for leptons), Q_f the fermion electric charge, G_F the Fermi constant and $\tau_i = \frac{4m_i^2}{m_h^2} (i = f, W, H^\pm, H^{\pm\pm})$. $g_{hW^\pm W^\mp}$, $g_{hH^\pm H^\mp}$ and $g_{hH^{\pm\pm}H^{\mp\mp}}$[i] are the couplings given in Appendix A.4. And the loop functions A_i are defined as:

[i] Note that these couplings are function of $\lambda_{4,5}$ as can be seen from Appendix A.4.

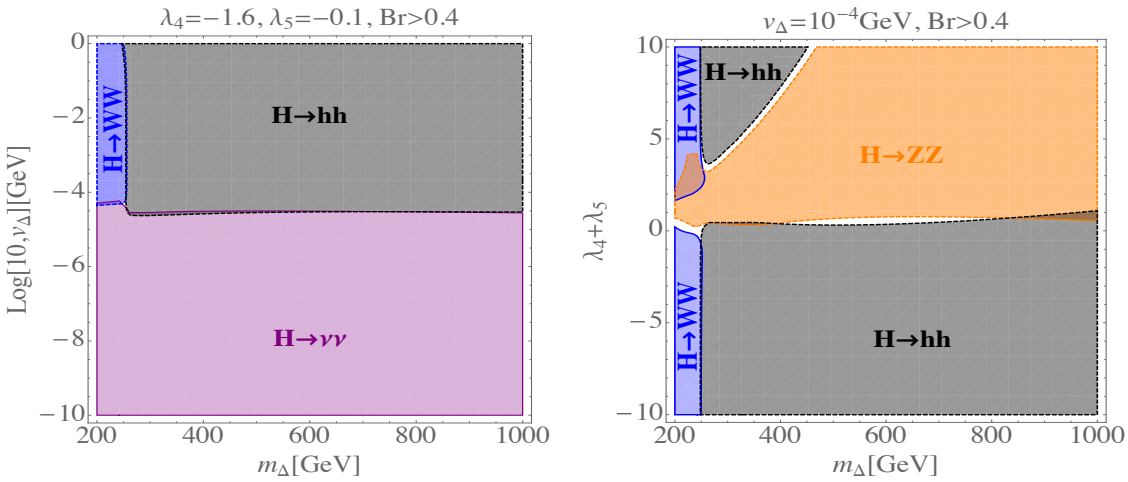

Figure A.1: Decay region plots for H with BR $\geq 40\%$. Black region for the di-Higgs channel, blue region for the di-W boson channel and purple region for the di-neutrino channel. From the left panel, di-neutrino/di-h channel dominates at small/large v_Δ respectively, and W-pair channel dominates at the large v_Δ and small m_Δ region. While from the right panel, we observe that di-h (di-Z boson) channel dominates for negative (positive) λ_{45}.

$$A_{1/2}(\tau_x) = -2\tau_x \{1 + (1-\tau_x)\mathcal{F}(\tau_x)\} \ , \tag{A.2}$$

$$A_1(\tau_x) = 2 + 3\tau_x + 3\tau_x(2-\tau_x)\mathcal{F}(\tau_x) \ , \tag{A.3}$$

$$A_0(\tau_x) = 1 - \tau_x \mathcal{F}(\tau_x) \ , \tag{A.4}$$

$$\mathcal{F}(\tau_x) = \begin{cases} \left[\sin^{-1}\left(\sqrt{\frac{1}{\tau_x}}\right)\right]^2 & \text{for} \quad \tau_x \geq 1, \\ -\frac{1}{4}\left[\ln\left(\frac{1+\sqrt{1-\tau_x}}{1-\sqrt{1-\tau_x}}\right) - i\pi\right]^2 & \text{for} \quad \tau_x < 1. \end{cases} \tag{A.5}$$

A.3 H and A decays

In this section, we give the dominant decay channels of the neutral Higgs bosons. Note that $H \to ZZ/WW$ and $A \to hZ$ are relevant for $\lambda_{4,5}$ determination, we see that $A \to hZ$ and $H \to WW$ can be used for both positive and negative λ_{45}, while $H \to ZZ$ only works for positive λ_{45}. This scenario is different for the fourth channel related to the determination of λ_{45}, i.e., $H^\pm \to hW^\pm$, which works only for negative λ_{45} .

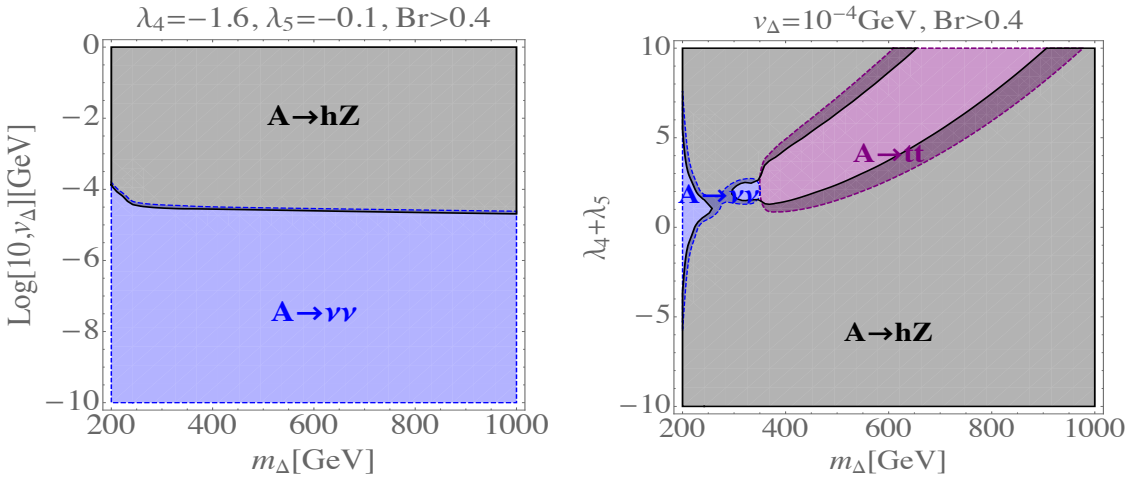

Figure A.2: Decay region plots for A with BR $\geq$ 40%. Black region for the hZ channel, purple region for the t quark pair channel and blue region for the di-neutrino region.

A.4 Feynman rules for the CTHM

We list the Feynman rules for the CTHM here.[ii]

[ii]Assuming all particles are incoming into the vertex, and to save ink, we use the following notations: $c_w \equiv \cos\theta_W, s_w \equiv \sin\theta_W, c_\alpha \equiv \cos\alpha, s_\alpha \equiv \sin\alpha, c_{\beta_{0,\pm}} \equiv \cos\beta_{0,\pm}, s_{\beta_{0,\pm}} \equiv \sin\beta_{0,\pm}, c_{2w} \equiv \cos(2\theta_W), s_{2w} \equiv \sin(2\theta_W), c_{2\alpha} \equiv \cos(2\alpha), s_{2\alpha} \equiv \sin(2\alpha), c_{2\beta_\pm} \equiv \cos(2\beta_\pm), s_{2\beta_\pm} \equiv \sin(2\beta_\pm), t_{\beta_0} \equiv \tan\beta_0$.

Interaction	Feynman Rule
$hW^{\mp}H^{\pm}$	$+\frac{ig}{2}(c_\alpha s_{\beta_\pm} - \sqrt{2}s_\alpha c_{\beta_\pm})(p_h - p_{H^\pm})^\mu$
$HW^{\mp}H^{\pm}$	$-\frac{ig}{2}(s_\alpha s_{\beta_\pm} + \sqrt{2}c_\alpha c_{\beta_\pm})(p_H - p_{H^\pm})^\mu$
$AW^{\mp}H^{\pm}$	$+\frac{g}{2}(s_{\beta_0} s_{\beta_\pm} + \sqrt{2}c_{\beta_0} c_{\beta_\pm})(p_A - p_{H^\pm})^\mu$
hAZ	$-\frac{g}{2c_w}(c_\alpha s_{\beta_0} - 2s_\alpha c_{\beta_0})(p_h - p_A)^\mu$
HAZ	$+\frac{g}{2c_w}(s_\alpha s_{\beta_0} + 2c_\alpha c_{\beta_0})(p_H - p_A)^\mu$
H^+H^-Z	$\frac{ig}{2c_w}(c_{2w}s^2_{\beta^\pm} - 2s^2_w c^2_{\beta^\pm})(p_{H^-} - p_{H^+})^\mu$
$H^+H^-\gamma$	$igs_w(p_{H^-} - p_{H^+})^\mu$
$H^{++}H^{--}Z$	$\frac{ig}{c_w}c_{2w}(p_{H^{--}} - p_{H^{++}})^\mu$
$H^{++}H^{--}\gamma$	$igs_w(p_{H^{--}} - p_{H^{++}})^\mu$
hZZ	$\frac{2iem_Z}{s_{2w}}(c_{\beta_0}c_\alpha + 2s_{\beta_0}s_\alpha)g_{\mu\nu}$
HZZ	$\frac{2iem_Z}{s_{2w}}(-c_{\beta_0}s_\alpha + 2s_{\beta_0}c_\alpha)g_{\mu\nu}$
hW^+W^-	$igm_Z c_w(c_{\beta_0}c_\alpha + s_{\beta_0}s_\alpha)g_{\mu\nu}$
HW^+W^-	$igm_Z c_w(-c_{\beta_0}s_\alpha + s_{\beta_0}c_\alpha)g_{\mu\nu}$
$H^{\pm\pm}W^{\mp}W^{\mp}$	$-\frac{i\sqrt{2}e^2 v_\Delta}{s^2_w}g_{\mu\nu}$
$ZW^{\pm}H^{\mp}$	$-\frac{ig^2 v_\Phi s_{\beta^\pm}}{2c_w}g_{\mu\nu}$
$H^{\pm\pm}H^{\mp}W^{\mp}$	$igc_{\beta^\pm}(p_{H^{\pm\pm}} - p_{H^\mp})^\mu$
$hH^{++}H^{--}$	$-iv_\Phi(\lambda_4 c_\alpha + \lambda_2 t_{\beta_0}s_\alpha)$
$HH^{++}H^{--}$	$-iv_\Phi(-\lambda_4 s_\alpha + \lambda_2 t_{\beta_0}c_\alpha)$
hH^+H^-	$-\frac{i}{4}\left\{(8\lambda_1 v_\Phi s^2_{\beta^\pm} + 4\lambda_4 v_\Phi c^2_{\beta^\pm} + 2\lambda_5 v_\Phi c_{2\beta^\pm} + 4\mu s_{2\beta^\pm})c_\alpha + (8\lambda_{23}v_\Delta c^2_{\beta^\pm} + 4\lambda_4 v_\Delta s^2_{\beta^\pm} - 4v_\Delta\lambda_5 c^2_{\beta^\pm})s_\alpha\right\}$
HH^+H^-	$-\frac{i}{4}\left\{-(8\lambda_1 v_\Phi s^2_{\beta^\pm} + 4\lambda_4 v_\Phi c^2_{\beta^\pm} + 2\lambda_5 v_\Phi c_{2\beta^\pm} + 4\mu s_{2\beta^\pm})s_\alpha + (8\lambda_{23}v_\Delta c^2_{\beta^\pm} + 4\lambda_4 v_\Delta s^2_{\beta^\pm} - 4v_\Delta\lambda_5 c^2_{\beta^\pm})c_\alpha\right\}$
Hhh	$-\frac{i}{2}\left\{-2\sqrt{2}\mu c_\alpha(1-3s^2_\alpha) - 2[6\lambda_1 c^2_\alpha + \lambda_{45}(1-3c^2_\alpha)]v_\Phi s_\alpha + 2[6\lambda_{23}s^2_\alpha + \lambda_{45}(1-3s^2_\alpha)]v_\Delta c_\alpha\right\}$
HAA	$-\frac{i}{2}\left\{-2\sqrt{2}\mu s_{\beta_0}(2s_\alpha c_{\beta_0} - c_\alpha s_{\beta_0}) - 2(2\lambda_1 s^2_{\beta_0} + \lambda_{45}c^2_{\beta_0})v_\Phi s_\alpha + 2(2\lambda_{23}c^2_{\beta_0} + \lambda_{45}s^2_{\beta_0})v_\Delta c_\alpha\right\}$
$H^{\pm\pm}H^{\mp}H^{\mp}$	$-\frac{i}{2}\left(-2\sqrt{2}\lambda_3 v_\Delta c^2_{\beta^\pm} + 2\lambda_5 v_\Phi s_{\beta^\pm}c_{\beta^\pm} + 4\mu s^2_{\beta^\pm}\right)$
hhh	$-6i\left[-\frac{s_\alpha c^2_\alpha \mu}{\sqrt{2}} + \frac{s_\alpha v_\Delta}{2}(\lambda_{45}c^2_\alpha + 2\lambda_{23}s^2_\alpha) + \frac{c_\alpha v_\Phi}{2}(2\lambda_1 c^2_\alpha + \lambda_{45}s^2_\alpha)\right]$
HHH	$-6i\left[-\frac{s^2_\alpha c_\alpha \mu}{\sqrt{2}} + \frac{c_\alpha v_\Delta}{2}(\lambda_{45}s^2_\alpha + 2\lambda_{23}c^2_\alpha) - \frac{s_\alpha v_\Phi}{2}(2\lambda_1 s^2_\alpha + \lambda_{45}c^2_\alpha)\right]$
hHH	$-\frac{i}{2}\left\{2\left[6\lambda_1 s^2_\alpha + \lambda_{45}(1-3s^2_\alpha)\right]v_\Phi c_\alpha + 2\left[6\lambda_{23}c^2_\alpha + \lambda_{45}(1-3c^2_\alpha)\right]v_\Delta s_\alpha - 2\sqrt{2}\mu s_\alpha(1-3c^2_\alpha)\right\}$
hAA	$-\frac{i}{2}\left[2\sqrt{2}\mu s_{\beta_0}(2c_\alpha c_{\beta_0} + s_\alpha s_{\beta_0}) + 2(2\lambda_1 s^2_{\beta_0} + \lambda_{45}c^2_{\beta_0})v_\Phi c_\alpha + 2(2\lambda_{23}c^2_{\beta_0} + \lambda_{45}s^2_{\beta_0})v_\Delta s_\alpha\right]$

APPENDIX B

MORE ON THE PHASES OF THE PMNS MATRIX

B.1 Dirac-type phases and Majorana-type phases in the leptonic sector of SM

In this appendix, we use the Dirac-type and the Majorana-type phases as an alternative to show the CPV from the Dirac triangles only necessarily implies CPV from the Majorana triangles. For this purpose, we follow closely the work done in Ref. [0809.2799].

The general Dirac-type and Majorana-type phases can be written as

$$\Phi_{\rm Dirac}(\alpha,\beta;i,j) = {\rm Im}(U_{\alpha i}U_{\beta j}U^*_{\alpha j}U^*_{\beta i}),\ \text{with } \alpha\neq\beta \text{ and } i\neq j. \tag{B.1}$$

$$\Phi_{\rm Majorana}(\alpha;i,j) = {\rm Im}(U_{\alpha i}U^*_{\alpha j}),\ \text{with } i\neq j. \tag{B.2}$$

Obviously, not all these phases are independent due to the rephasing transformation. For a 3×3 PMNS matrix, the independent number of Majorana-type and Dirac-type phases are six and four respectively. Without loss of generality, one can choose, for example

$$\Phi_{\rm Dirac}(e,\beta;1,j) = {\rm Im}(U_{\alpha i}U_{\beta j}U^*_{\alpha j}U^*_{\beta i}),\ \text{with } \beta=(\mu,\tau) \text{ and } j=(2,3). \tag{B.3}$$

$$\Phi_{\rm Majorana}(\alpha;1,j) = {\rm Im}(U_{\alpha i}U^*_{\alpha j}),\ \text{with } \alpha=(e,\mu,\tau) \text{ and } j=(2,3). \tag{B.4}$$

Then, it is readily to see that

$$\begin{aligned}\Phi_{\rm Dirac}(e,\beta;1,j) =& \Phi_{\rm Majorana}(e;1,j) - \Phi_{\rm Majorana}(\beta;1,j'),\\ &\text{where } \beta=(\mu,\tau), j\neq j' \text{ and } j,j'\neq 1.\end{aligned} \tag{B.5}$$

Therefore, when the Dirac-type phases $\Phi_{\rm Dirac}(\alpha,\beta;i,j)$ vanish, the Majorana-type phases $\Phi_{\rm Majorana}(\alpha;i,j)$ can still survive such that CP conservation is not respected in the lepton sector due to these Majorana phases.

BIBLIOGRAPHY

[1] **Particle Data Group** Collaboration, M. Tanabashi *et al.*, "Review of Particle Physics," *Phys. Rev.* **D98** no. 3, (2018) 030001.

[2] **Super-Kamiokande** Collaboration, K. Abe *et al.*, "Atmospheric neutrino oscillation analysis with external constraints in Super-Kamiokande I-IV," *Phys. Rev. D* **97** no. 7, (2018) 072001, arXiv:1710.09126 [hep-ex].

[3] M. Klasen, M. Pohl, and G. Sigl, "Indirect and direct search for dark matter," *Prog. Part. Nucl. Phys.* **85** (2015) 1–32, arXiv:1507.03800 [hep-ph].

[4] J. Erler and R. Ferro-Hernández, "Weak Mixing Angle in the Thomson Limit," *JHEP* **03** (2018) 196, arXiv:1712.09146 [hep-ph].

[5] J. Erler and M. J. Ramsey-Musolf, "The Weak mixing angle at low energies," *Phys. Rev. D* **72** (2005) 073003, arXiv:hep-ph/0409169.

[6] B. Cañas, E. Garcés, O. Miranda, and A. Parada, "Future perspectives for a weak mixing angle measurement in coherent elastic neutrino nucleus scattering experiments," *Phys. Lett. B* **784** (2018) 159–162, arXiv:1806.01310 [hep-ph].

[7] M. Battaglieri *et al.*, "US Cosmic Visions: New Ideas in Dark Matter 2017: Community Report," in *U.S. Cosmic Visions: New Ideas in Dark Matter*. 7, 2017. arXiv:1707.04591 [hep-ph].

[8] https://cds.cern.ch/record/2665175.

[9] S. Descotes-Genon and P. Koppenburg, "The CKM Parameters," *Ann. Rev. Nucl. Part. Sci.* **67** (2017) 97–127, arXiv:1702.08834 [hep-ex].

[10] M. E. Peskin and T. Takeuchi, "Estimation of oblique electroweak corrections," *Phys. Rev. D* **46** (1992) 381–409.

[11] I. Esteban *et al.*, "Nufit4.1 at nufit webpage,". http://www.nu-fit.org.

[12] J. M. Cline, "Baryogenesis," in *Les Houches Summer School - Session 86: Particle Physics and Cosmology: The Fabric of Spacetime Les Houches, France, July 31-August 25, 2006*. 2006. arXiv:hep-ph/0609145 [hep-ph].

[13] D. E. Morrissey and M. J. Ramsey-Musolf, "Electroweak baryogenesis," *New J. Phys.* **14** (2012) 125003, arXiv:1206.2942 [hep-ph].

[14] A. Czarnecki and W. J. Marciano, "Polarized Moller scattering asymmetries," *Int. J. Mod. Phys. A* **15** (2000) 2365–2376, arXiv:hep-ph/0003049.

[15] **Qweak** Collaboration, D. Androić *et al.*, "Precision measurement of the weak charge of the proton," *Nature* **557** no. 7704, (2018) 207–211, arXiv:1905.08283 [nucl-ex].

[16] **MOLLER** Collaboration, J. Benesch *et al.*, "The MOLLER Experiment: An Ultra-Precise Measurement of the Weak Mixing Angle Using Møller Scattering," arXiv:1411.4088 [nucl-ex].

[17] N. Berger *et al.*, "Measuring the weak mixing angle with the P2 experiment at MESA," *J. Univ. Sci. Tech. China* **46** no. 6, (2016) 481–487, arXiv:1511.03934 [physics.ins-det].

[18] D. Becker *et al.*, "The P2 experiment," arXiv:1802.04759 [nucl-ex].

[19] **SoLID** Collaboration, J. P. Chen, H. Gao, T. K. Hemmick, Z. E. Meziani, and P. A. Souder, "A White Paper on SoLID (Solenoidal Large Intensity Device)," arXiv:1409.7741 [nucl-ex].

[20] A. de Gouvea, P. A. Machado, Y. F. Perez-Gonzalez, and Z. Tabrizi, "Measuring the Weak Mixing Angle in the DUNE Near Detector Complex," arXiv:1912.06658 [hep-ph].

[21] B. Canas, E. Garces, O. Miranda, M. Tortola, and J. Valle, "The weak mixing angle from low energy neutrino measurements: a global update," *Phys. Lett. B* **761** (2016) 450–455, arXiv:1608.02671 [hep-ph].

[22] **ATLAS** Collaboration, M. Aaboud *et al.*, "Search for doubly charged Higgs boson production in multi-lepton final states with the ATLAS detector using proton–proton collisions at $\sqrt{s} = 13\,\text{TeV}$," *Eur. Phys. J.* **C78** no. 3, (2018) 199, arXiv:1710.09748 [hep-ex].

[23] **ATLAS** Collaboration, G. Aad *et al.*, "Search for anomalous production of prompt same-sign lepton pairs and pair-produced doubly charged Higgs bosons with $\sqrt{s} = 8$ TeV *pp* collisions using the ATLAS detector," *JHEP* **03** (2015) 041, arXiv:1412.0237 [hep-ex].

[24] **OPAL** Collaboration, P. D. Acton *et al.*, "A Search for doubly charged Higgs production in Z0 decays," *Phys. Lett.* **B295** (1992) 347–356.

[25] **OPAL** Collaboration, G. Abbiendi *et al.*, "Search for doubly charged Higgs bosons with the OPAL detector at LEP," *Phys. Lett.* **B526** (2002) 221–232, arXiv:hep-ex/0111059 [hep-ex].

[26] **ATLAS** Collaboration, M. Aaboud *et al.*, "Search for long-lived charginos based on a disappearing-track signature in pp collisions at $\sqrt{s} = 13$ TeV with the ATLAS detector," *JHEP* **06** (2018) 022, arXiv:1712.02118 [hep-ex].

[27] G. Belanger, F. Boudjema, A. Pukhov, and A. Semenov, "micrOMEGAs_3: A program for calculating dark matter observables," *Comput. Phys. Commun.* **185** (2014) 960–985, arXiv:1305.0237 [hep-ph].

[28] M. Cirelli, A. Strumia, and M. Tamburini, "Cosmology and Astrophysics of Minimal Dark Matter," *Nucl. Phys.* **B787** (2007) 152–175, arXiv:0706.4071 [hep-ph].

[29] **Planck** Collaboration, N. Aghanim *et al.*, "Planck 2018 results. VI. Cosmological parameters," arXiv:1807.06209 [astro-ph.CO].

[30] **LUX** Collaboration, D. S. Akerib *et al.*, "Results from a search for dark matter in the complete LUX exposure," *Phys. Rev. Lett.* **118** no. 2, (2017) 021303, arXiv:1608.07648 [astro-ph.CO].

[31] **PandaX-II** Collaboration, X. Cui *et al.*, "Dark Matter Results From 54-Ton-Day Exposure of PandaX-II Experiment," *Phys. Rev. Lett.* **119** no. 18, (2017) 181302, arXiv:1708.06917 [astro-ph.CO].

[32] **XENON** Collaboration, E. Aprile *et al.*, "Dark Matter Search Results from a One Ton-Year Exposure of XENON1T," *Phys. Rev. Lett.* **121** no. 11, (2018) 111302, arXiv:1805.12562 [astro-ph.CO].

[33] P. Fileviez Perez, H. H. Patel, M. Ramsey-Musolf, and K. Wang, "Triplet Scalars and Dark Matter at the LHC," *Phys. Rev.* **D79** (2009) 055024, arXiv:0811.3957 [hep-ph].

[34] A. Freitas, "Numerical multi-loop integrals and applications," *Prog. Part. Nucl. Phys.* **90** (2016) 201–240, arXiv:1604.00406 [hep-ph].

[35] A. Denner, S. Dittmaier, and L. Hofer, "Collier: a fortran-based Complex One-Loop LIbrary in Extended Regularizations," *Comput. Phys. Commun.* **212** (2017) 220–238, arXiv:1604.06792 [hep-ph].

[36] W. Marciano and A. Sirlin, "Precise SU(5) Predictions for sin**2-Theta(W), m(W) and m(Z)," *Phys. Rev. Lett.* **46** (1981) 163.

[37] S. L. Glashow, "Partial Symmetries of Weak Interactions," *Nucl. Phys.* **22** (1961) 579–588.

[38] S. Weinberg, "A Model of Leptons," *Phys. Rev. Lett.* **19** (1967) 1264–1266.

[39] A. Salam, "Weak and Electromagnetic Interactions," *Conf. Proc.* **C680519** (1968) 367–377.

[40] C.-N. Yang and R. L. Mills, "Conservation of Isotopic Spin and Isotopic Gauge Invariance," *Phys. Rev.* **96** (1954) 191–195. [,150(1954); ,150(1954); ,150(1954)].

[41] F. Englert and R. Brout, "Broken Symmetry and the Mass of Gauge Vector Mesons," *Phys. Rev. Lett.* **13** (1964) 321–323. [,157(1964)].

[42] P. W. Higgs, "Broken Symmetries and the Masses of Gauge Bosons," *Phys. Rev. Lett.* **13** (1964) 508–509. [,160(1964)].

[43] G. S. Guralnik, C. R. Hagen, and T. W. B. Kibble, "Global Conservation Laws and Massless Particles," *Phys. Rev. Lett.* **13** (1964) 585–587. [,162(1964)].

[44] **UA1** Collaboration, G. Arnison *et al.*, "Experimental Observation of Isolated Large Transverse Energy Electrons with Associated Missing Energy at s**(1/2) = 540-GeV," *Phys. Lett. B* **122** (1983) 103–116.

[45] **UA2** Collaboration, M. Banner *et al.*, "Observation of Single Isolated Electrons of High Transverse Momentum in Events with Missing Transverse Energy at the CERN anti-p p Collider," *Phys. Lett. B* **122** (1983) 476–485.

[46] **UA1** Collaboration, G. Arnison *et al.*, "Experimental Observation of Lepton Pairs of Invariant Mass Around 95-GeV/c**2 at the CERN SPS Collider," *Phys. Lett. B* **126** (1983) 398–410.

[47] **UA2** Collaboration, P. Bagnaia *et al.*, "Evidence for Z0 —¿ e+ e- at the CERN anti-p p Collider," *Phys. Lett. B* **129** (1983) 130–140.

[48] **CDF** Collaboration, F. Abe *et al.*, "Observation of top quark production in $\bar{p}p$ collisions," *Phys. Rev. Lett.* **74** (1995) 2626–2631, arXiv:hep-ex/9503002 [hep-ex].

[49] **D0** Collaboration, S. Abachi *et al.*, "Search for high mass top quark production in $p\bar{p}$ collisions at $\sqrt{s} = 1.8$ TeV," *Phys. Rev. Lett.* **74** (1995) 2422–2426, arXiv:hep-ex/9411001 [hep-ex].

[50] **ATLAS** Collaboration, G. Aad *et al.*, "Observation of a new particle in the search for the Standard Model Higgs boson with the ATLAS detector at the LHC," *Phys. Lett.* **B716** (2012) 1–29, arXiv:1207.7214 [hep-ex].

[51] **CMS** Collaboration, S. Chatrchyan *et al.*, "Observation of a New Boson at a Mass of 125 GeV with the CMS Experiment at the LHC," *Phys. Lett.* **B716** (2012) 30–61, arXiv:1207.7235 [hep-ex].

[52] B. Pontecorvo, "Mesonium and anti-mesonium," *Sov. Phys. JETP* **6** (1957) 429. [Zh. Eksp. Teor. Fiz.33,549(1957)].

[53] B. Pontecorvo, "Neutrino Experiments and the Problem of Conservation of Leptonic Charge," *Sov. Phys. JETP* **26** (1968) 984–988. [Zh. Eksp. Teor. Fiz.53,1717(1967)].

[54] J. N. Bahcall and R. Davis, "Solar Neutrinos - a Scientific Puzzle," *Science* **191** (1976) 264–267.

[55] **Super-Kamiokande** Collaboration, Y. Fukuda *et al.*, "Evidence for oscillation of atmospheric neutrinos," *Phys. Rev. Lett.* **81** (1998) 1562–1567, arXiv:hep-ex/9807003 [hep-ex].

[56] **SNO** Collaboration, Q. R. Ahmad *et al.*, "Measurement of the rate of $\nu_e + d \to p + p + e^-$ interactions produced by ^8B solar neutrinos at the Sudbury Neutrino Observatory," *Phys. Rev. Lett.* **87** (2001) 071301, arXiv:nucl-ex/0106015 [nucl-ex].

[57] **KamLAND** Collaboration, K. Eguchi *et al.*, "First results from KamLAND: Evidence for reactor anti-neutrino disappearance," *Phys. Rev. Lett.* **90** (2003) 021802, arXiv:hep-ex/0212021 [hep-ex].

[58] P. Minkowski, "$\mu \to e\gamma$ at a Rate of One Out of 10^9 Muon Decays?," *Phys. Lett.* **67B** (1977) 421–428.

[59] P. Ramond, "The Family Group in Grand Unified Theories," in *International Symposium on Fundamentals of Quantum Theory and Quantum Field Theory Palm Coast, Florida, February 25-March 2, 1979*, pp. 265–280. 1979. arXiv:hep-ph/9809459 [hep-ph].

[60] M. Gell-Mann, P. Ramond, and R. Slansky, "Complex Spinors and Unified Theories," *Conf. Proc.* **C790927** (1979) 315–321, arXiv:1306.4669 [hep-th].

[61] T. Yanagida, "HORIZONTAL SYMMETRY AND MASSES OF NEUTRINOS," *Conf. Proc.* **C7902131** (1979) 95–99.

[62] R. N. Mohapatra and G. Senjanovic, "Neutrino Mass and Spontaneous Parity Violation," *Phys. Rev. Lett.* **44** (1980) 912.

[63] J. Schechter and J. W. F. Valle, "Neutrino Masses in SU(2) x U(1) Theories," *Phys. Rev.* **D22** (1980) 2227.

[64] J. Schechter and J. W. F. Valle, "Neutrino Decay and Spontaneous Violation of Lepton Number," *Phys. Rev.* **D25** (1982) 774.

[65] W. Konetschny and W. Kummer, "Nonconservation of Total Lepton Number with Scalar Bosons," *Phys. Lett.* **70B** (1977) 433–435.

[66] T. P. Cheng and L.-F. Li, "Neutrino Masses, Mixings and Oscillations in SU(2) x U(1) Models of Electroweak Interactions," *Phys. Rev.* **D22** (1980) 2860.

[67] G. Lazarides, Q. Shafi, and C. Wetterich, "Proton Lifetime and Fermion Masses in an SO(10) Model," *Nucl. Phys.* **B181** (1981) 287–300.

[68] M. Magg and C. Wetterich, "Neutrino Mass Problem and Gauge Hierarchy," *Phys. Lett.* **94B** (1980) 61–64.

[69] R. Foot, H. Lew, X. G. He, and G. C. Joshi, "Seesaw Neutrino Masses Induced by a Triplet of Leptons," *Z. Phys.* **C44** (1989) 441.

[70] E. Witten, "New Issues in Manifolds of SU(3) Holonomy," *Nucl. Phys.* **B268** (1986) 79.

[71] R. N. Mohapatra, "Mechanism for Understanding Small Neutrino Mass in Superstring Theories," *Phys. Rev. Lett.* **56** (1986) 561–563.

[72] R. N. Mohapatra and J. W. F. Valle, "Neutrino Mass and Baryon Number Nonconservation in Superstring Models," *Phys. Rev.* **D34** (1986) 1642.

[73] J. W. F. Valle *NUCLEAR BETA DECAYS AND NEUTRINO: proceedings. Edited by T. Kotani, H. Ejiri, E. Takasugi, Singapore,* (1986) 542p.

[74] S. M. Barr, "A Different seesaw formula for neutrino masses," *Phys. Rev. Lett.* **92** (2004) 101601, arXiv:hep-ph/0309152 [hep-ph].

[75] R. N. Mohapatra and G. Senjanovic, "Neutrino Masses and Mixings in Gauge Models with Spontaneous Parity Violation," *Phys. Rev.* **D23** (1981) 165.

[76] A. D. Sakharov, "Violation of CP Invariance, C asymmetry, and baryon asymmetry of the universe," *Pisma Zh. Eksp. Teor. Fiz.* **5** (1967) 32–35. [JETP Lett.5,24(1967); Sov. Phys. Usp.34,no.5,392(1991); Usp. Fiz. Nauk161,no.5,61(1991)].

[77] E. W. Kolb and S. Wolfram, "Baryon Number Generation in the Early Universe," *Nucl. Phys.* **B172** (1980) 224. [Erratum: Nucl. Phys.B195,542(1982)].

[78] A. Riotto, "Theories of baryogenesis," in *Proceedings, Summer School in High-energy physics and cosmology: Trieste, Italy, June 29-July 17, 1998*, pp. 326–436. 1998. arXiv:hep-ph/9807454 [hep-ph].

[79] A. Riotto and M. Trodden, "Recent progress in baryogenesis," *Ann. Rev. Nucl. Part. Sci.* **49** (1999) 35–75, arXiv:hep-ph/9901362 [hep-ph].

[80] M. Dine and A. Kusenko, "The Origin of the matter - antimatter asymmetry," *Rev. Mod. Phys.* **76** (2003) 1, arXiv:hep-ph/0303065 [hep-ph].

[81] W. Buchmuller, P. Di Bari, and M. Plumacher, "Leptogenesis for pedestrians," *Annals Phys.* **315** (2005) 305–351, arXiv:hep-ph/0401240 [hep-ph].

[82] W. Buchmuller, R. D. Peccei, and T. Yanagida, "Leptogenesis as the origin of matter," *Ann. Rev. Nucl. Part. Sci.* **55** (2005) 311–355, arXiv:hep-ph/0502169 [hep-ph].

[83] A. G. Cohen, D. B. Kaplan, and A. E. Nelson, "Progress in electroweak baryogenesis," *Ann. Rev. Nucl. Part. Sci.* **43** (1993) 27–70, arXiv:hep-ph/9302210 [hep-ph].

[84] M. Trodden, "Electroweak baryogenesis," *Rev. Mod. Phys.* **71** (1999) 1463–1500, arXiv:hep-ph/9803479 [hep-ph].

[85] V. A. Kuzmin, V. A. Rubakov, and M. E. Shaposhnikov, "On the Anomalous Electroweak Baryon Number Nonconservation in the Early Universe," *Phys. Lett.* **155B** (1985) 36.

[86] M. E. Shaposhnikov, "Baryon Asymmetry of the Universe in Standard Electroweak Theory," *Nucl. Phys.* **B287** (1987) 757–775.

[87] M. E. Shaposhnikov, "Possible Appearance of the Baryon Asymmetry of the Universe in an Electroweak Theory," *JETP Lett.* **44** (1986) 465–468. [Pisma Zh. Eksp. Teor. Fiz.44,364(1986)].

[88] Y. Aoki, F. Csikor, Z. Fodor, and A. Ukawa, "The Endpoint of the first order phase transition of the SU(2) gauge Higgs model on a four-dimensional isotropic lattice," *Phys. Rev.* **D60** (1999) 013001, arXiv:hep-lat/9901021 [hep-lat].

[89] K. Rummukainen, M. Tsypin, K. Kajantie, M. Laine, and M. E. Shaposhnikov, "The Universality class of the electroweak theory," *Nucl. Phys.* **B532** (1998) 283–314, arXiv:hep-lat/9805013 [hep-lat].

[90] F. Csikor, Z. Fodor, and J. Heitger, "Endpoint of the hot electroweak phase transition," *Phys. Rev. Lett.* **82** (1999) 21–24, arXiv:hep-ph/9809291 [hep-ph].

[91] M. Laine and K. Rummukainen, "What's new with the electroweak phase transition?," *Nucl. Phys. Proc. Suppl.* **73** (1999) 180–185, arXiv:hep-lat/9809045 [hep-lat]. [,180(1998)].

[92] M. Gurtler, E.-M. Ilgenfritz, and A. Schiller, "Where the electroweak phase transition ends," *Phys. Rev.* **D56** (1997) 3888–3895, arXiv:hep-lat/9704013 [hep-lat].

[93] K. Kajantie, M. Laine, K. Rummukainen, and M. E. Shaposhnikov, "Generic rules for high temperature dimensional reduction and their application to the standard model," *Nucl. Phys.* **B458** (1996) 90–136, arXiv:hep-ph/9508379 [hep-ph].

[94] H. H. Patel and M. J. Ramsey-Musolf, "Stepping Into Electroweak Symmetry Breaking: Phase Transitions and Higgs Phenomenology," *Phys. Rev. D* **88** (2013) 035013, arXiv:1212.5652 [hep-ph].

[95] M. Chala, M. Ramos, and M. Spannowsky, "Gravitational wave and collider probes of a triplet Higgs sector with a low cutoff," *Eur. Phys. J. C* **79** no. 2, (2019) 156, arXiv:1812.01901 [hep-ph].

[96] L. Niemi, H. H. Patel, M. J. Ramsey-Musolf, T. V. Tenkanen, and D. J. Weir, "Electroweak phase transition in the real triplet extension of the SM: Dimensional reduction," *Phys. Rev. D* **100** no. 3, (2019) 035002, arXiv:1802.10500 [hep-ph].

[97] N. F. Bell, M. J. Dolan, L. S. Friedrich, M. J. Ramsey-Musolf, and R. R. Volkas, "Two-Step Electroweak Symmetry-Breaking: Theory Meets Experiment," *JHEP* **05** (2020) 050, arXiv:2001.05335 [hep-ph].

[98] F. Zwicky, "Die Rotverschiebung von extragalaktischen Nebeln," *Helv. Phys. Acta* **6** (1933) 110–127. [Gen. Rel. Grav.41,207(2009)].

[99] F. Zwicky, "On the Masses of Nebulae and of Clusters of Nebulae," *Astrophys. J.* **86** (1937) 217–246.

[100] V. C. Rubin and W. K. Ford, Jr., "Rotation of the Andromeda Nebula from a Spectroscopic Survey of Emission Regions," *Astrophys. J.* **159** (1970) 379–403.

[101] H. Hoekstra, H. Yee, and M. Gladders, "Current status of weak gravitational lensing," *New Astron. Rev.* **46** (2002) 767–781, arXiv:astro-ph/0205205 [astro-ph].

[102] R. B. Metcalf, L. A. Moustakas, A. J. Bunker, and I. R. Parry, "Spectroscopic gravitational lensing and limits on the dark matter substructure in Q2237+0305," *Astrophys. J.* **607** (2004) 43–59, arXiv:astro-ph/0309738 [astro-ph].

[103] L. A. Moustakas and R. B. Metcalf, "Detecting dark matter substructure spectroscopically in strong gravitational lenses," *Mon. Not. Roy. Astron. Soc.* **339** (2003) 607, arXiv:astro-ph/0206176 [astro-ph].

[104] **COBE** Collaboration, G. F. Smoot *et al.*, "Structure in the COBE differential microwave radiometer first year maps," *Astrophys. J.* **396** (1992) L1–L5.

[105] **Boomerang** Collaboration, P. de Bernardis *et al.*, "A Flat universe from high resolution maps of the cosmic microwave background radiation," *Nature* **404** (2000) 955–959, arXiv:astro-ph/0004404 [astro-ph].

[106] **WMAP** Collaboration, D. N. Spergel *et al.*, "First year Wilkinson Microwave Anisotropy Probe (WMAP) observations: Determination of cosmological parameters," *Astrophys. J. Suppl.* **148** (2003) 175–194, arXiv:astro-ph/0302209 [astro-ph].

[107] **WMAP** Collaboration, E. Komatsu *et al.*, "Five-Year Wilkinson Microwave Anisotropy Probe (WMAP) Observations: Cosmological Interpretation," *Astrophys. J. Suppl.* **180** (2009) 330–376, arXiv:0803.0547 [astro-ph].

[108] K. A. Olive, G. Steigman, and T. P. Walker, "Primordial nucleosynthesis: Theory and observations," *Phys. Rept.* **333** (2000) 389–407, arXiv:astro-ph/9905320 [astro-ph].

[109] D. Clowe, M. Bradac, A. H. Gonzalez, M. Markevitch, S. W. Randall, C. Jones, and D. Zaritsky, "A direct empirical proof of the existence of dark matter," *Astrophys. J.* **648** (2006) L109–L113, arXiv:astro-ph/0608407 [astro-ph].

[110] S. Hawking, "Gravitationally collapsed objects of very low mass," *Mon. Not. Roy. Astron. Soc.* **152** (1971) 75.

[111] B. J. Carr and S. Hawking, "Black holes in the early Universe," *Mon. Not. Roy. Astron. Soc.* **168** (1974) 399–415.

[112] G. F. Chapline, "Cosmological effects of primordial black holes," *Nature* **253** no. 5489, (1975) 251–252.

[113] P. Meszaros, "Primeval black holes and galaxy formation," *Astron. Astrophys.* **38** (1975) 5–13.

[114] B. J. Carr, "The Primordial black hole mass spectrum," *Astrophys. J.* **201** (1975) 1–19.

[115] R. Peccei and H. R. Quinn, "CP Conservation in the Presence of Instantons," *Phys. Rev. Lett.* **38** (1977) 1440–1443.

[116] S. Weinberg, "A New Light Boson?," *Phys. Rev. Lett.* **40** (1978) 223–226.

[117] F. Wilczek, "Problem of Strong P and T Invariance in the Presence of Instantons," *Phys. Rev. Lett.* **40** (1978) 279–282.

[118] S. Dodelson and L. M. Widrow, "Sterile-neutrinos as dark matter," *Phys. Rev. Lett.* **72** (1994) 17–20, arXiv:hep-ph/9303287.

[119] S. Nussinov, "TECHNOCOSMOLOGY: COULD A TECHNIBARYON EXCESS PROVIDE A 'NATURAL' MISSING MASS CANDIDATE?," *Phys. Lett. B* **165** (1985) 55–58.

[120] G. Gelmini, L. J. Hall, and M. Lin, "What Is the Cosmion?," *Nucl. Phys. B* **281** (1987) 726.

[121] K. M. Zurek, "Asymmetric Dark Matter: Theories, Signatures, and Constraints," *Phys. Rept.* **537** (2014) 91–121, arXiv:1308.0338 [hep-ph].

[122] J. Alexander *et al.*, "Dark Sectors 2016 Workshop: Community Report," 8, 2016. arXiv:1608.08632 [hep-ph].

[123] D. N. Spergel and P. J. Steinhardt, "Observational evidence for selfinteracting cold dark matter," *Phys. Rev. Lett.* **84** (2000) 3760–3763, arXiv:astro-ph/9909386.

[124] J. McDonald, "Thermally generated gauge singlet scalars as selfinteracting dark matter," *Phys. Rev. Lett.* **88** (2002) 091304, arXiv:hep-ph/0106249 [hep-ph].

[125] L. J. Hall, K. Jedamzik, J. March-Russell, and S. M. West, "Freeze-In Production of FIMP Dark Matter," *JHEP* **03** (2010) 080, arXiv:0911.1120 [hep-ph].

[126] N. Bernal, M. Heikinheimo, T. Tenkanen, K. Tuominen, and V. Vaskonen, "The Dawn of FIMP Dark Matter: A Review of Models and Constraints," *Int. J. Mod. Phys.* **A32** no. 27, (2017) 1730023, arXiv:1706.07442 [hep-ph].

[127] G. Jungman, M. Kamionkowski, and K. Griest, "Supersymmetric dark matter," *Phys. Rept.* **267** (1996) 195–373, arXiv:hep-ph/9506380 [hep-ph].

[128] **XENON** Collaboration, E. Aprile *et al.*, "Observation of Excess Electronic Recoil Events in XENON1T," arXiv:2006.09721 [hep-ex].

[129] G. Apollinari, I. Béjar Alonso, O. Brüning, M. Lamont, and L. Rossi, "High-Luminosity Large Hadron Collider (HL-LHC) : Preliminary Design Report,".

[130] **FCC** Collaboration, A. Abada *et al.*, "HE-LHC: The High-Energy Large Hadron Collider," *Eur. Phys. J. ST* **228** no. 5, (2019) 1109–1382.

[131] **FCC** Collaboration, A. Abada *et al.*, "FCC-ee: The Lepton Collider," *Eur. Phys. J. ST* **228** no. 2, (2019) 261–623.

[132] **FCC** Collaboration, A. Abada *et al.*, "FCC-hh: The Hadron Collider," *Eur. Phys. J. ST* **228** no. 4, (2019) 755–1107.

[133] **FCC** Collaboration, A. Abada *et al.*, "FCC Physics Opportunities," *Eur. Phys. J.* **C79** no. 6, (2019) 474.

[134] J. Tang *et al.*, "Concept for a Future Super Proton-Proton Collider," arXiv:1507.03224 [physics.acc-ph].

[135] M. Ahmad *et al.*, "CEPC-SPPC Preliminary Conceptual Design Report. 1. Physics and Detector,".

[136] **CEPC Study Group** Collaboration, M. Dong *et al.*, "CEPC Conceptual Design Report: Volume 2 - Physics & Detector," arXiv:1811.10545 [hep-ex].

[137] T. Behnke, J. E. Brau, B. Foster, J. Fuster, M. Harrison, J. M. Paterson, M. Peskin, M. Stanitzki, N. Walker, and H. Yamamoto, "The International Linear Collider Technical Design Report - Volume 1: Executive Summary," arXiv:1306.6327 [physics.acc-ph].

[138] H. Baer, T. Barklow, K. Fujii, Y. Gao, A. Hoang, S. Kanemura, J. List, H. E. Logan, A. Nomerotski, M. Perelstein, *et al.*, "The International Linear Collider Technical Design Report - Volume 2: Physics," arXiv:1306.6352 [hep-ph].

[139] C. Adolphsen, M. Barone, B. Barish, K. Buesser, P. Burrows, J. Carwardine, J. Clark, H. Mainaud Durand, G. Dugan, E. Elsen, *et al.*, "The International Linear Collider Technical Design Report - Volume 3.I: Accelerator & in the Technical Design Phase," arXiv:1306.6353 [physics.acc-ph].

[140] C. Adolphsen, M. Barone, B. Barish, K. Buesser, P. Burrows, J. Carwardine, J. Clark, H. Mainaud Durand, G. Dugan, E. Elsen, *et al.*, "The International Linear Collider Technical Design Report - Volume 3.II: Accelerator Baseline Design," arXiv:1306.6328 [physics.acc-ph].

[141] H. Abramowicz *et al.*, "The International Linear Collider Technical Design Report - Volume 4: Detectors," arXiv:1306.6329 [physics.ins-det].

[142] M. Aicheler, P. Burrows, M. Draper, T. Garvey, P. Lebrun, K. Peach, N. Phinney, H. Schmickler, D. Schulte, and N. Toge, "A Multi-TeV Linear Collider Based on CLIC Technology,".

[143] L. Linssen, A. Miyamoto, M. Stanitzki, and H. Weerts, "Physics and Detectors at CLIC: CLIC Conceptual Design Report," arXiv:1202.5940 [physics.ins-det].

[144] **CLIC Physics Working Group** Collaboration, E. Accomando *et al.*, "Physics at the CLIC multi-TeV linear collider," in *Proceedings, 11th International Conference on Hadron spectroscopy (Hadron 2005): Rio de Janeiro, Brazil, August 21-26, 2005*. 2004. arXiv:hep-ph/0412251 [hep-ph]. http://weblib.cern.ch/abstract?CERN-2004-005.

[145] **European Strategy for Particle Physics Preparatory Group** Collaboration, R. Aleksan *et al.*, "Physics Briefing Book: Input for the Strategy Group to draft the update of the European Strategy for Particle Physics,".

[146] R. K. Ellis *et al.*, "Physics Briefing Book: Input for the European Strategy for Particle Physics Update 2020," arXiv:1910.11775 [hep-ex].

[147] **European Strategy Group** Collaboration, *2020 Update of the European Strategy for Particle Physics*. CERN Council, Geneva, 2020.

[148] **Muon g-2** Collaboration, G. W. Bennett *et al.*, "Final Report of the Muon E821 Anomalous Magnetic Moment Measurement at BNL," *Phys. Rev.* **D73** (2006) 072003, arXiv:hep-ex/0602035 [hep-ex].

[149] **Fermilab E989** Collaboration, G. Venanzoni, "The New Muon g−2 experiment at Fermilab," *Nucl. Part. Phys. Proc.* **273-275** (2016) 584–588, arXiv:1411.2555 [physics.ins-det].

[150] **E34** Collaboration, M. Otani, "Status of the Muon g-2/EDM Experiment at J-PARC (E34)," *JPS Conf. Proc.* **8** (2015) 025008.

[151] **SLAC E158** Collaboration, P. L. Anthony *et al.*, "Precision measurement of the weak mixing angle in Moller scattering," *Phys. Rev. Lett.* **95** (2005) 081601, arXiv:hep-ex/0504049 [hep-ex].

[152] **CCFR** Collaboration, C. Arroyo *et al.*, "A Precise measurement of the weak mixing angle in neutrino nucleon scattering," *Phys. Rev. Lett.* **72** (1994) 3452–3455, arXiv:hep-ex/9405008 [hep-ex].

[153] V. A. Dzuba, J. C. Berengut, V. V. Flambaum, and B. Roberts, "Revisiting parity non-conservation in cesium," *Phys. Rev. Lett.* **109** (2012) 203003, arXiv:1207.5864 [hep-ph].

[154] **NuTeV** Collaboration, G. P. Zeller *et al.*, "A Precise Determination of Electroweak Parameters in Neutrino Nucleon Scattering," *Phys. Rev. Lett.* **88** (2002) 091802, arXiv:hep-ex/0110059 [hep-ex]. [Erratum: Phys. Rev. Lett.90,239902(2003)].

[155] *Fundamental Physics at the Intensity Frontier*. 5, 2012. arXiv:1205.2671 [hep-ex].

[156] **DARWIN** Collaboration, J. Aalbers *et al.*, "DARWIN: towards the ultimate dark matter detector," *JCAP* **1611** (2016) 017, arXiv:1606.07001 [astro-ph.IM].

[157] **Fermi-LAT** Collaboration, A. A. Abdo *et al.*, "The Spectrum of the Isotropic Diffuse Gamma-Ray Emission Derived From First-Year Fermi Large Area Telescope Data," *Phys. Rev. Lett.* **104** (2010) 101101, arXiv:1002.3603 [astro-ph.HE].

[158] **Fermi-LAT** Collaboration, M. Ackermann *et al.*, "Measurement of separate cosmic-ray electron and positron spectra with the Fermi Large Area Telescope," *Phys. Rev. Lett.* **108** (2012) 011103, arXiv:1109.0521 [astro-ph.HE].

[159] **PAMELA** Collaboration, O. Adriani *et al.*, "An anomalous positron abundance in cosmic rays with energies 1.5-100 GeV," *Nature* **458** (2009) 607–609, arXiv:0810.4995 [astro-ph].

[160] **PAMELA** Collaboration, O. Adriani *et al.*, "PAMELA results on the cosmic-ray antiproton flux from 60 MeV to 180 GeV in kinetic energy," *Phys. Rev. Lett.* **105** (2010) 121101, arXiv:1007.0821 [astro-ph.HE].

[161] **ATLAS** Collaboration, M. Aaboud *et al.*, "Search for new phenomena in dijet events using 37 fb^{-1} of pp collision data collected at $\sqrt{s}$ =13 TeV with the ATLAS detector," *Phys. Rev.* **D96** no. 5, (2017) 052004, arXiv:1703.09127 [hep-ex].

[162] **ATLAS** Collaboration, M. Aaboud *et al.*, "Search for new high-mass phenomena in the dilepton final state using 36 fb^{-1} of proton-proton collision data at $\sqrt{s} = 13$ TeV with the ATLAS detector," *JHEP* **10** (2017) 182, arXiv:1707.02424 [hep-ex].

[163] **ATLAS** Collaboration, M. Aaboud *et al.*, "Search for dark matter and other new phenomena in events with an energetic jet and large missing transverse momentum using the ATLAS detector," *JHEP* **01** (2018) 126, arXiv:1711.03301 [hep-ex].

[164] **CMS** Collaboration, A. M. Sirunyan *et al.*, "Search for new physics in final states with an energetic jet or a hadronically decaying W or Z boson and transverse momentum imbalance at $\sqrt{s} = 13$ TeV," *Phys. Rev.* **D97** no. 9, (2018) 092005, arXiv:1712.02345 [hep-ex].

[165] **CMS** Collaboration, A. M. Sirunyan *et al.*, "Search for new physics in events with a leptonically decaying Z boson and a large transverse momentum imbalance in proton–proton collisions at $\sqrt{s} = 13$ TeV," *Eur. Phys. J.* **C78** no. 4, (2018) 291, arXiv:1711.00431 [hep-ex].

[166] **CMS** Collaboration, A. M. Sirunyan *et al.*, "Search for dark matter produced in association with a Higgs boson decaying to a pair of bottom quarks in proton–proton collisions at $\sqrt{s} = 13$ TeV," *Eur. Phys. J.* **C79** no. 3, (2019) 280, arXiv:1811.06562 [hep-ex].

[167] **CMS** Collaboration, A. M. Sirunyan *et al.*, "Search for dark matter produced in association with a single top quark or a top quark pair in proton-proton collisions at $\sqrt{s} = 13$ TeV," *JHEP* **03** (2019) 141, arXiv:1901.01553 [hep-ex].

[168] L.-L. Chau and W.-Y. Keung, "Comments on the Parametrization of the Kobayashi-Maskawa Matrix," *Phys. Rev. Lett.* **53** (1984) 1802.

[169] L. Wolfenstein, "Parametrization of the Kobayashi-Maskawa Matrix," *Phys. Rev. Lett.* **51** (1983) 1945.

[170] C. Jarlskog, "Commutator of the Quark Mass Matrices in the Standard Electroweak Model and a Measure of Maximal CP Violation," *Phys. Rev. Lett.* **55** (1985) 1039.

[171] G. C. Branco, L. Lavoura, and J. P. Silva, *CP Violation*, vol. 103. 1999.

[172] C.-Y. Seng, M. Gorchtein, H. H. Patel, and M. J. Ramsey-Musolf, "Reduced Hadronic Uncertainty in the Determination of V_{ud}," *Phys. Rev. Lett.* **121** no. 24, (2018) 241804, arXiv:1807.10197 [hep-ph].

[173] W. J. Marciano and A. Sirlin, "Improved calculation of electroweak radiative corrections and the value of V(ud)," *Phys. Rev. Lett.* **96** (2006) 032002, arXiv:hep-ph/0510099.

[174] **FlaviaNet Working Group on Kaon Decays** Collaboration, M. Antonelli *et al.*, "An Evaluation of $|V_{us}|$ and precise tests of the Standard Model from world data on leptonic and semileptonic kaon decays," *Eur. Phys. J. C* **69** (2010) 399–424, arXiv:1005.2323 [hep-ph].

[175] S. Aoki *et al.*, "Review of lattice results concerning low-energy particle physics," *Eur. Phys. J. C* **77** no. 2, (2017) 112, arXiv:1607.00299 [hep-lat].

[176] **HFLAV** Collaboration, Y. Amhis *et al.*, "Averages of b-hadron, c-hadron, and τ-lepton properties as of summer 2016," *Eur. Phys. J. C* **77** no. 12, (2017) 895, arXiv:1612.07233 [hep-ex].

[177] **BaBar** Collaboration, J. Lees *et al.*, "Measurement of the $D^0 \to \pi^- e^+ \nu_e$ differential decay branching fraction as a function of q^2 and study of form factor parameterizations," *Phys. Rev. D* **91** no. 5, (2015) 052022, arXiv:1412.5502 [hep-ex].

[178] **BESIII** Collaboration, M. Ablikim *et al.*, "Study of Dynamics of $D^0 \to K^- e^+ \nu_e$ and $D^0 \to \pi^- e^+ \nu_e$ Decays," *Phys. Rev. D* **92** no. 7, (2015) 072012, arXiv:1508.07560 [hep-ex].

[179] **CLEO** Collaboration, D. Besson *et al.*, "Improved measurements of D meson semileptonic decays to pi and K mesons," *Phys. Rev. D* **80** (2009) 032005, arXiv:0906.2983 [hep-ex].

[180] **Belle** Collaboration, L. Widhalm *et al.*, "Measurement of D0 —¿ pi l nu (Kl nu) Form Factors and Absolute Branching Fractions," *Phys. Rev. Lett.* **97** (2006) 061804, arXiv:hep-ex/0604049.

[181] **BESIII** Collaboration, M. Ablikim *et al.*, "Precision measurements of $B(D^+ \to \mu^+ \nu_\mu)$, the pseudoscalar decay constant f_{D^+}, and the quark mixing matrix element $|V_{\rm cd}|$," *Phys. Rev. D* **89** no. 5, (2014) 051104, arXiv:1312.0374 [hep-ex].

[182] **CLEO** Collaboration, B. Eisenstein *et al.*, "Precision Measurement of B(D+ —¿ mu+ nu) and the Pseudoscalar Decay Constant f(D+)," *Phys. Rev. D* **78** (2008) 052003, arXiv:0806.2112 [hep-ex].

[183] H. Abramowicz *et al.*, "Experimental Study of Opposite Sign Dimuons Produced in Neutrino and anti-neutrinos Interactions," *Z. Phys. C* **15** (1982) 19.

[184] S. Rabinowitz *et al.*, "Measurement of the strange sea distribution using neutrino charm production," *Phys. Rev. Lett.* **70** (1993) 134–137.

[185] **CCFR** Collaboration, A. Bazarko *et al.*, "Determination of the strange quark content of the nucleon from a next-to-leading order QCD analysis of neutrino charm production," *Z. Phys. C* **65** (1995) 189–198, arXiv:hep-ex/9406007.

[186] **CHARM II** Collaboration, P. Vilain *et al.*, "Leading order QCD analysis of neutrino induced dimuon events," *Eur. Phys. J. C* **11** (1999) 19–34.

[187] **CHORUS** Collaboration, A. Kayis-Topaksu *et al.*, "Measurement of topological muonic branching ratios of charmed hadrons produced in neutrino-induced charged-current interactions," *Phys. Lett. B* **626** (2005) 24–34.

[188] **Belle** Collaboration, A. Zupanc *et al.*, "Measurements of branching fractions of leptonic and hadronic D_s^+ meson decays and extraction of the D_s^+ meson decay constant," *JHEP* **09** (2013) 139, arXiv:1307.6240 [hep-ex].

[189] **CLEO** Collaboration, J. Alexander *et al.*, "Measurement of $BD_s^+ \to \ell^+\nu$ and the Decay Constant fD_s^+ From 600 $/pb^{-1}$ of $e^\pm$ Annihilation Data Near 4170 MeV," *Phys. Rev. D* **79** (2009) 052001, arXiv:0901.1216 [hep-ex].

[190] **BaBar** Collaboration, P. del Amo Sanchez *et al.*, "Measurement of the Absolute Branching Fractions for $D_s^- \to \ell^- \bar{\nu}_\ell$ and Extraction of the Decay Constant f_{D_s}," *Phys. Rev. D* **82** (2010) 091103, arXiv:1008.4080 [hep-ex]. [Erratum: Phys.Rev.D 91, 019901 (2015)].

[191] **BESIII** Collaboration, M. Ablikim *et al.*, "Measurement of the $D_s^+ \to \ell^+\nu_\ell$ branching fractions and the decay constant $f_{D_s^+}$," *Phys. Rev. D* **94** no. 7, (2016) 072004, arXiv:1608.06732 [hep-ex].

[192] **CLEO** Collaboration, P. Naik *et al.*, "Measurement of the Pseudoscalar Decay Constant f(D(s)) Using D(s)+ —¿ tau+ nu, tau+ —¿ rho+ anti-nu Decays," *Phys. Rev. D* **80** (2009) 112004, arXiv:0910.3602 [hep-ex].

[193] **CLEO** Collaboration, P. Onyisi *et al.*, "Improved Measurement of Absolute Branching Fraction of D(s)+ —¿ tau+ nu(tau)," *Phys. Rev. D* **79** (2009) 052002, arXiv:0901.1147 [hep-ex].

[194] **BaBar** Collaboration, B. Aubert *et al.*, "Measurement of the hadronic form-factor in $D^0 \to K^- e^+ \nu_e$ 1," *Phys. Rev. D* **76** (2007) 052005, arXiv:0704.0020 [hep-ex].

[195] I. I. Bigi, M. A. Shifman, N. Uraltsev, and A. I. Vainshtein, "QCD predictions for lepton spectra in inclusive heavy flavor decays," *Phys. Rev. Lett.* **71** (1993) 496–499, arXiv:hep-ph/9304225.

[196] A. V. Manohar and M. B. Wise, "Inclusive semileptonic B and polarized Lambda(b) decays from QCD," *Phys. Rev. D* **49** (1994) 1310–1329, arXiv:hep-ph/9308246.

[197] N. Isgur and M. B. Wise, "WEAK TRANSITION FORM-FACTORS BETWEEN HEAVY MESONS," *Phys. Lett. B* **237** (1990) 527–530.

[198] N. Isgur and M. B. Wise, "Weak Decays of Heavy Mesons in the Static Quark Approximation," *Phys. Lett. B* **232** (1989) 113–117.

[199] E. Dalgic, A. Gray, M. Wingate, C. T. Davies, G. Lepage, and J. Shigemitsu, "B meson semileptonic form-factors from unquenched lattice QCD," *Phys. Rev. D* **73** (2006) 074502, arXiv:hep-lat/0601021. [Erratum: Phys.Rev.D 75, 119906 (2007)].

[200] **Fermilab Lattice, MILC** Collaboration, J. A. Bailey *et al.*, "$|V_{ub}|$ from $B \to \pi \ell \nu$ decays and (2+1)-flavor lattice QCD," *Phys. Rev. D* **92** no. 1, (2015) 014024, arXiv:1503.07839 [hep-lat].

[201] A. Khodjamirian, T. Mannel, N. Offen, and Y.-M. Wang, "$B \to \pi \ell \nu_l$ Width and $|V_{ub}|$ from QCD Light-Cone Sum Rules," *Phys. Rev. D* **83** (2011) 094031, arXiv:1103.2655 [hep-ph].

[202] **ARGUS** Collaboration, H. Albrecht *et al.*, "Observation of B0 - anti-B0 Mixing,".

[203] **CDF** Collaboration, A. Abulencia *et al.*, "Observation of $B_s^0 - \bar{B}_s^0$ Oscillations," *Phys. Rev. Lett.* **97** (2006) 242003, arXiv:hep-ex/0609040.

[204] **LHCb** Collaboration, R. Aaij *et al.*, "Precision measurement of the B_s^0-$\bar{B}_s^0$ oscillation frequency with the decay $B_s^0 \to D_s^- \pi^+$," *New J. Phys.* **15** (2013) 053021, arXiv:1304.4741 [hep-ex].

[205] **CDF** Collaboration, D. Acosta *et al.*, "Measurement of $B(t \to Wb)/B(t \to Wq)$ at the Collider Detector at Fermilab," *Phys. Rev. Lett.* **95** (2005) 102002, arXiv:hep-ex/0505091.

[206] **D0** Collaboration, V. Abazov *et al.*, "Precision measurement of the ratio B$(t \to Wb)$/B$(t \to Wq)$ and Extraction of V_{tb}," *Phys. Rev. Lett.* **107** (2011) 121802, arXiv:1106.5436 [hep-ex].

[207] **CMS** Collaboration, V. Khachatryan *et al.*, "Measurement of the ratio $\mathcal{B}(t \to Wb)/\mathcal{B}(t \to Wq)$ in pp collisions at $\sqrt{s} = 8$ TeV," *Phys. Lett. B* **736** (2014) 33–57, arXiv:1404.2292 [hep-ex].

[208] **CDF, D0** Collaboration, T. A. Aaltonen *et al.*, "Tevatron Combination of Single-Top-Quark Cross Sections and Determination of the Magnitude of the Cabibbo-Kobayashi-Maskawa Matrix Element $\mathbf{V_{tb}}$," *Phys. Rev. Lett.* **115** no. 15, (2015) 152003, arXiv:1503.05027 [hep-ex].

[209] A. B. Carter and A. Sanda, "CP Violation in B Meson Decays," *Phys. Rev. D* **23** (1981) 1567.

[210] **BaBar** Collaboration, B. Aubert *et al.*, "Measurement of Time-Dependent CP Asymmetry in B0 —¿ c anti-c K(*)0 Decays," *Phys. Rev. D* **79** (2009) 072009, arXiv:0902.1708 [hep-ex].

[211] **Belle** Collaboration, I. Adachi *et al.*, "Precise measurement of the CP violation parameter $\sin 2\phi_1$ in $B^0 \to (c\bar{c})K^0$ decays," *Phys. Rev. Lett.* **108** (2012) 171802, arXiv:1201.4643 [hep-ex].

[212] **BaBar** Collaboration, B. Aubert *et al.*, "Ambiguity-free measurement of $\cos(2\beta)$: Time-integrated and time-dependent angular analyses of $B \to J/\psi K\pi$," *Phys. Rev. D* **71** (2005) 032005, arXiv:hep-ex/0411016.

[213] **Belle** Collaboration, R. Itoh *et al.*, "Studies of CP violation in B —¿ J/psi K* decays," *Phys. Rev. Lett.* **95** (2005) 091601, arXiv:hep-ex/0504030.

[214] **BaBar, Belle** Collaboration, I. Adachi *et al.*, "Measurement of $\cos 2\beta$ in $B^0 \to D^{(*)}h^0$ with $D \to K^0_S\pi^+\pi^-$ decays by a combined time-dependent Dalitz plot analysis of BaBar and Belle data," *Phys. Rev. D* **98** no. 11, (2018) 112012, arXiv:1804.06153 [hep-ex].

[215] **Belle** Collaboration, J. Zhang *et al.*, "Observation of B+ —¿ rho+ rho0," *Phys. Rev. Lett.* **91** (2003) 221801, arXiv:hep-ex/0306007.

[216] **Belle** Collaboration, A. Somov *et al.*, "Measurement of the branching fraction, polarization, and CP asymmetry for B0 —¿ rho+ rho- decays, and determination of the CKM phase phi(2)," *Phys. Rev. Lett.* **96** (2006) 171801, arXiv:hep-ex/0601024.

[217] **BaBar** Collaboration, B. Aubert *et al.*, "Measurements of branching fraction, polarization, and charge asymmetry of $B^\pm \to \rho^\pm\rho^0$ and a search for $B^\pm \to \rho^\pm$ f0(980)," *Phys. Rev. Lett.* **97** (2006) 261801, arXiv:hep-ex/0607092.

[218] **BaBar** Collaboration, B. Aubert *et al.*, "A Study of B0 —¿ rho+ rho- Decays and Constraints on the CKM Angle alpha," *Phys. Rev. D* **76** (2007) 052007, arXiv:0705.2157 [hep-ex].

[219] A. Hocker, H. Lacker, S. Laplace, and F. Le Diberder, "A New approach to a global fit of the CKM matrix," *Eur. Phys. J. C* **21** (2001) 225–259, arXiv:hep-ph/0104062.

[220] M. Gronau and D. London, "How to determine all the angles of the unitarity triangle from B(d)0 —¿ D K(s) and B(s)0 —¿ D0," *Phys. Lett. B* **253** (1991) 483–488.

[221] M. Gronau and D. Wyler, "On determining a weak phase from CP asymmetries in charged B decays," *Phys. Lett. B* **265** (1991) 172–176.

[222] D. Atwood, I. Dunietz, and A. Soni, "Enhanced CP violation with B —¿ K D0 (anti-D0) modes and extraction of the CKM angle gamma," *Phys. Rev. Lett.* **78** (1997) 3257–3260, arXiv:hep-ph/9612433.

[223] D. Atwood, I. Dunietz, and A. Soni, "Improved methods for observing CP violation in B+- —¿ K D and measuring the CKM phase gamma," *Phys. Rev. D* **63** (2001) 036005, arXiv:hep-ph/0008090.

[224] **Belle** Collaboration, A. Poluektov *et al.*, "Measurement of phi(3) with Dalitz plot analysis of B+- —¿ D**(*) K+- decay," *Phys. Rev. D* **70** (2004) 072003, arXiv:hep-ex/0406067.

[225] A. Giri, Y. Grossman, A. Soffer, and J. Zupan, "Determining gamma using B+- —¿ DK+- with multibody D decays," *Phys. Rev. D* **68** (2003) 054018, arXiv:hep-ph/0303187.

[226] **Belle** Collaboration, A. Poluektov *et al.*, "Evidence for direct CP violation in the decay B-¿D(*)K, D-¿KsPi+Pi- and measurement of the CKM phase phi3," *Phys. Rev. D* **81** (2010) 112002, arXiv:1003.3360 [hep-ex].

[227] **BaBar** Collaboration, P. del Amo Sanchez *et al.*, "Evidence for direct CP violation in the measurement of the Cabibbo-Kobayashi-Maskawa angle gamma with B-+ —¿ D(*) K(*)-+ decays," *Phys. Rev. Lett.* **105** (2010) 121801, arXiv:1005.1096 [hep-ex].

[228] **LHCb** Collaboration, R. Aaij *et al.*, "Measurement of the CKM angle γ using $B^{\pm} \to DK^{\pm}$ with $D \to K^0_S\pi^+\pi^-, K^0_S K^+K^-$ decays," *JHEP* **10** (2014) 097, arXiv:1408.2748 [hep-ex].

[229] **CKMfitter Group** Collaboration, J. Charles, A. Hocker, H. Lacker, S. Laplace, F. Le Diberder, J. Malcles, J. Ocariz, M. Pivk, and L. Roos, "CP violation and the CKM matrix: Assessing the impact of the asymmetric B factories," *Eur. Phys. J. C* **41** no. 1, (2005) 1–131, arXiv:hep-ph/0406184.

[230] **UTfit** Collaboration, M. Bona *et al.*, "The 2004 UTfit collaboration report on the status of the unitarity triangle in the standard model," *JHEP* **07** (2005) 028, arXiv:hep-ph/0501199.

[231] **UTfit** Collaboration, M. Bona *et al.*, "Model-independent constraints on $\Delta F = 2$ operators and the scale of new physics," *JHEP* **03** (2008) 049, arXiv:0707.0636 [hep-ph].

[232] G. Dubois-Felsmann, D. Hitlin, F. Porter, and G. Eigen, "Sensitivity of CKM fits to theoretical uncertainties and their representation," in *21st International Symposium on Lepton and Photon Interactions at High Energies (LP 03)*. 8, 2003. arXiv:hep-ph/0308262.

[233] G. Eigen, G. Dubois-Felsmann, D. G. Hitlin, and F. C. Porter, "Global CKM Fits with the Scan Method," *Phys. Rev. D* **89** no. 3, (2014) 033004, arXiv:1301.5867 [hep-ex].

[234] **BaBar** Collaboration, D. Boutigny *et al.*, *The BABAR physics book: Physics at an asymmetric B factory*. 10, 1998.

[235] S. Plaszczynski and M.-H. Schune, "Overall determination of the CKM matrix," *PoS* **hf8** (1999) 019, arXiv:hep-ph/9911280.

[236] M. E. Peskin and T. Takeuchi, "A New constraint on a strongly interacting Higgs sector," *Phys. Rev. Lett.* **65** (1990) 964–967.

[237] M. Golden and L. Randall, "Radiative Corrections to Electroweak Parameters in Technicolor Theories," *Nucl. Phys. B* **361** (1991) 3–23.

[238] D. Kennedy and P. Langacker, "Precision electroweak experiments and heavy physics: An Update," *Phys. Rev. D* **44** (1991) 1591–1592.

[239] G. Altarelli and R. Barbieri, "Vacuum polarization effects of new physics on electroweak processes," *Phys. Lett. B* **253** (1991) 161–167.

[240] B. Holdom and J. Terning, "Large corrections to electroweak parameters in technicolor theories," *Phys. Lett. B* **247** (1990) 88–92.

[241] B. Lynn, M. E. Peskin, and R. Stuart, "RADIATIVE CORRECTIONS IN SU(2) x U(1): LEP / SLC," 7, 1985.

[242] K. Hagiwara, S. Matsumoto, D. Haidt, and C. Kim, "A Novel approach to confront electroweak data and theory," *Z. Phys. C* **64** (1994) 559–620, arXiv:hep-ph/9409380. [Erratum: Z.Phys.C 68, 352 (1995)].

[243] B. Grinstein and M. B. Wise, "Operator analysis for precision electroweak physics," *Phys. Lett. B* **265** (1991) 326–334.

[244] Z. Maki, M. Nakagawa, and S. Sakata, "Remarks on the unified model of elementary particles," *Prog. Theor. Phys.* **28** (1962) 870–880.

[245] B. Pontecorvo, "Inverse beta processes and nonconservation of lepton charge," *Sov. Phys. JETP* **7** (1958) 172–173.

[246] E. Majorana, "Teoria simmetrica dell'elettrone e del positrone," *Nuovo Cim.* **14** (1937) 171–184.

[247] J. Aguilar-Saavedra and G. Branco, "Unitarity triangles and geometrical description of CP violation with Majorana neutrinos," *Phys. Rev. D* **62** (2000) 096009, arXiv:hep-ph/0007025.

[248] S. Weinberg, "Baryon and Lepton Nonconserving Processes," *Phys. Rev. Lett.* **43** (1979) 1566–1570.

[249] S. Roy Choudhury and S. Choubey, "Updated Bounds on Sum of Neutrino Masses in Various Cosmological Scenarios," *JCAP* **09** (2018) 017, arXiv:1806.10832 [astro-ph.CO].

[250] A. Abada, C. Biggio, F. Bonnet, M. Gavela, and T. Hambye, "Low energy effects of neutrino masses," *JHEP* **12** (2007) 061, arXiv:0707.4058 [hep-ph].

[251] S. M. Bilenky, J. Hosek, and S. Petcov, "On Oscillations of Neutrinos with Dirac and Majorana Masses," *Phys. Lett. B* **94** (1980) 495–498.

[252] P. Langacker, S. Petcov, G. Steigman, and S. Toshev, "On the Mikheev-Smirnov-Wolfenstein (MSW) Mechanism of Amplification of Neutrino Oscillations in Matter," *Nucl. Phys. B* **282** (1987) 589–609.

[253] L. Wolfenstein, "Neutrino Oscillations in Matter," *Phys. Rev. D* **17** (1978) 2369–2374.

[254] F. Capozzi, E. Lisi, A. Marrone, and A. Palazzo, "Current unknowns in the three neutrino framework," *Prog. Part. Nucl. Phys.* **102** (2018) 48–72, arXiv:1804.09678 [hep-ph].

[255] P. de Salas, D. Forero, C. Ternes, M. Tortola, and J. Valle, "Status of neutrino oscillations 2018: 3σ hint for normal mass ordering and improved CP sensitivity," *Phys. Lett. B* **782** (2018) 633–640, arXiv:1708.01186 [hep-ph].

[256] E. Fermi, "An attempt of a theory of beta radiation. 1.," *Z. Phys.* **88** (1934) 161–177.

[257] V. Lobashev, "The search for the neutrino mass by direct method in the tritium beta-decay and perspectives of study it in the project KATRIN," *Nucl. Phys. A* **719** (2003) 153–160.

[258] C. Kraus *et al.*, "Final results from phase II of the Mainz neutrino mass search in tritium beta decay," *Eur. Phys. J. C* **40** (2005) 447–468, arXiv:hep-ex/0412056.

[259] K. Eitel, "Direct neutrino mass experiments," *Nucl. Phys. B Proc. Suppl.* **143** (2005) 197–204.

[260] **Troitsk** Collaboration, V. Aseev *et al.*, "An upper limit on electron antineutrino mass from Troitsk experiment," *Phys. Rev. D* **84** (2011) 112003, arXiv:1108.5034 [hep-ex].

[261] P. F. de Salas and S. Pastor, "Relic neutrino decoupling with flavour oscillations revisited," *JCAP* **07** (2016) 051, arXiv:1606.06986 [hep-ph].

[262] K. N. Abazajian and M. Kaplinghat, "Neutrino Physics from the Cosmic Microwave Background and Large-Scale Structure," *Ann. Rev. Nucl. Part. Sci.* **66** no. 1, (2016) 401–420.

[263] **Planck** Collaboration, P. Ade *et al.*, "Planck 2013 results. XVI. Cosmological parameters," *Astron. Astrophys.* **571** (2014) A16, arXiv:1303.5076 [astro-ph.CO].

[264] **Planck** Collaboration, P. Ade *et al.*, "Planck 2015 results. XIII. Cosmological parameters," *Astron. Astrophys.* **594** (2016) A13, arXiv:1502.01589 [astro-ph.CO].

[265] A. Morales and J. Morales, "The Neutrinoless double beta decay: The Case for germanium detectors," *Nucl. Phys. B Proc. Suppl.* **114** (2003) 141–157, arXiv:hep-ph/0211332.

[266] J. Gomez-Cadenas, J. Martin-Albo, M. Mezzetto, F. Monrabal, and M. Sorel, "The Search for neutrinoless double beta decay," *Riv. Nuovo Cim.* **35** no. 2, (2012) 29–98, arXiv:1109.5515 [hep-ex].

[267] S. Dell'Oro, S. Marcocci, M. Viel, and F. Vissani, "Neutrinoless double beta decay: 2015 review," *Adv. High Energy Phys.* **2016** (2016) 2162659, arXiv:1601.07512 [hep-ph].

[268] J. Vergados, H. Ejiri, and F. ˇ Simkovic, "Neutrinoless double beta decay and neutrino mass," *Int. J. Mod. Phys. E* **25** no. 11, (2016) 1630007, arXiv:1612.02924 [hep-ph].

[269] S. Pascoli and S. Petcov, "The SNO solar neutrino data, neutrinoless double beta decay and neutrino mass spectrum," *Phys. Lett. B* **544** (2002) 239–250, arXiv:hep-ph/0205022.

[270] S. M. Bilenky, C. Giunti, C. Kim, and S. Petcov, "Short baseline neutrino oscillations and neutrinoless (Beta Beta) decay in schemes with an inverted mass spectrum," *Phys. Rev. D* **54** (1996) 4432–4444, arXiv:hep-ph/9604364.

[271] S. M. Bilenky, S. Pascoli, and S. Petcov, "Majorana neutrinos, neutrino mass spectrum, CP violation and neutrinoless double beta decay. 1. The Three neutrino mixing case," *Phys. Rev. D* **64** (2001) 053010, arXiv:hep-ph/0102265.

[272] S. M. Bilenky, S. Pascoli, and S. Petcov, "Majorana neutrinos, neutrino mass spectrum, CP violation and neutrinoless double beta decay. 2. Mixing of four neutrinos," *Phys. Rev. D* **64** (2001) 113003, arXiv:hep-ph/0104218.

[273] **LEGEND** Collaboration, N. Abgrall *et al.*, "The Large Enriched Germanium Experiment for Neutrinoless Double Beta Decay (LEGEND)," *AIP Conf. Proc.* **1894** no. 1, (2017) 020027, arXiv:1709.01980 [physics.ins-det].

[274] F. Iachello, J. Kotila, and J. Barea, "Quenching of g_A and its impact in double beta decay," *PoS* **NEUTEL2015** (2015) 047.

[275] S. M. Bilenky, C. Giunti, W. Grimus, B. Kayser, and S. Petcov, "Constraints from neutrino oscillation experiments on the effective Majorana mass in neutrinoless double beta decay," *Phys. Lett. B* **465** (1999) 193–202, arXiv:hep-ph/9907234.

[276] F. Vissani, "Signal of neutrinoless double beta decay, neutrino spectrum and oscillation scenarios," *JHEP* **06** (1999) 022, arXiv:hep-ph/9906525.

[277] K. Matsuda, N. Takeda, T. Fukuyama, and H. Nishiura, "CP violations in lepton number violation processes and neutrino oscillations," *Phys. Rev. D* **62** (2000) 093001, arXiv:hep-ph/0003055.

[278] M. Czakon, J. Gluza, and M. Zralek, "Perspectives on finding the neutrino nature," arXiv:hep-ph/0003161.

[279] H. Klapdor-Kleingrothaus, H. Pas, and A. Smirnov, "Neutrino mass spectrum and neutrinoless double beta decay," *Phys. Rev. D* **63** (2001) 073005, arXiv:hep-ph/0003219.

[280] S. Pascoli, S. Petcov, and W. Rodejohann, "On the CP violation associated with Majorana neutrinos and neutrinoless double beta decay," *Phys. Lett. B* **549** (2002) 177–193, arXiv:hep-ph/0209059.

[281] S. Pascoli, S. Petcov, and W. Rodejohann, "On the neutrino mass spectrum and neutrinoless double beta decay," *Phys. Lett. B* **558** (2003) 141–156, arXiv:hep-ph/0212113.

[282] H. Murayama and C. Pena-Garay, "Neutrinoless double beta decay in light of SNO salt data," *Phys. Rev. D* **69** (2004) 031301, arXiv:hep-ph/0309114.

[283] S. Pascoli, S. Petcov, and T. Schwetz, "The Absolute neutrino mass scale, neutrino mass spectrum, majorana CP-violation and neutrinoless double-beta decay," *Nucl. Phys. B* **734** (2006) 24–49, arXiv:hep-ph/0505226.

[284] M. Lindner, A. Merle, and W. Rodejohann, "Improved limit on theta(13) and implications for neutrino masses in neutrino-less double beta decay and cosmology," *Phys. Rev. D* **73** (2006) 053005, arXiv:hep-ph/0512143.

[285] A. Faessler, G. Fogli, E. Lisi, V. Rodin, A. Rotunno, and F. Simkovic, "QRPA uncertainties and their correlations in the analysis of 0 nu beta beta decay," *Phys. Rev. D* **79** (2009) 053001, arXiv:0810.5733 [hep-ph].

[286] S. M. Bilenky and S. Petcov, "Massive Neutrinos and Neutrino Oscillations," *Rev. Mod. Phys.* **59** (1987) 671. [Erratum: Rev.Mod.Phys. 61, 169 (1989), Erratum: Rev.Mod.Phys. 60, 575–575 (1988)].

[287] **KamLAND-Zen** Collaboration, A. Gando *et al.*, "Search for Majorana Neutrinos near the Inverted Mass Hierarchy Region with KamLAND-Zen," *Phys. Rev. Lett.* **117** no. 8, (2016) 082503, arXiv:1605.02889 [hep-ex]. [Addendum: Phys.Rev.Lett. 117, 109903 (2016)].

[288] **GERDA** Collaboration, M. Agostini *et al.*, "Improved Limit on Neutrinoless Double-β Decay of ^{76}Ge from GERDA Phase II," *Phys. Rev. Lett.* **120** no. 13, (2018) 132503, arXiv:1803.11100 [nucl-ex].

[289] S. Pascoli and S. Petcov, "Majorana Neutrinos, Neutrino Mass Spectrum and the — ¡ m ¿ — ˜ $10-^3$ eV Frontier in Neutrinoless Double Beta Decay," *Phys. Rev. D* **77** (2008) 113003, arXiv:0711.4993 [hep-ph].

[290] R. H. Cyburt, "Primordial nucleosynthesis for the new cosmology: Determining uncertainties and examining concordance," *Phys. Rev. D* **70** (2004) 023505, arXiv:astro-ph/0401091.

[291] G. Steigman, "Observational tests of antimatter cosmologies," *Ann. Rev. Astron. Astrophys.* **14** (1976) 339–372.

[292] K. Funakubo, "CP violation and baryogenesis at the electroweak phase transition," *Prog. Theor. Phys.* **96** (1996) 475–520, arXiv:hep-ph/9608358.

[293] G. 't Hooft, "Symmetry Breaking Through Bell-Jackiw Anomalies," *Phys. Rev. Lett.* **37** (1976) 8–11.

[294] F. R. Klinkhamer and N. Manton, "A Saddle Point Solution in the Weinberg-Salam Theory," *Phys. Rev. D* **30** (1984) 2212.

[295] M. Gavela, P. Hernandez, J. Orloff, and O. Pene, "Standard model CP violation and baryon asymmetry," *Mod. Phys. Lett. A* **9** (1994) 795–810, arXiv:hep-ph/9312215.

[296] L. Dolan and R. Jackiw, "Symmetry Behavior at Finite Temperature," *Phys. Rev. D* **9** (1974) 3320–3341.

[297] D. Kirzhnits and A. D. Linde, "Macroscopic Consequences of the Weinberg Model," *Phys. Lett. B* **42** (1972) 471–474.

[298] A. Bochkarev and M. Shaposhnikov, "Electroweak Production of Baryon Asymmetry and Upper Bounds on the Higgs and Top Masses," *Mod. Phys. Lett. A* **2** (1987) 417.

[299] K. Kajantie, M. Laine, K. Rummukainen, and M. E. Shaposhnikov, "The Electroweak phase transition: A Nonperturbative analysis," *Nucl. Phys. B* **466** (1996) 189–258, arXiv:hep-lat/9510020.

[300] **ATLAS** Collaboration, G. Aad *et al.*, "Search for new phenomena in final states with an energetic jet and large missing transverse momentum in pp collisions at $\sqrt{s}$ =8 TeV with the ATLAS detector," *Eur. Phys. J. C* **75** no. 7, (2015) 299, arXiv:1502.01518 [hep-ex]. [Erratum: Eur.Phys.J.C 75, 408 (2015)].

[301] **CMS** Collaboration, V. Khachatryan *et al.*, "Search for dark matter, extra dimensions, and unparticles in monojet events in proton–proton collisions at $\sqrt{s} = 8$ TeV," *Eur. Phys. J. C* **75** no. 5, (2015) 235, arXiv:1408.3583 [hep-ex].

[302] **ATLAS** Collaboration, G. Aad *et al.*, "Search for new phenomena in events with a photon and missing transverse momentum in *pp* collisions at $\sqrt{s} = 8$ TeV with the ATLAS detector," *Phys. Rev. D* **91** no. 1, (2015) 012008, arXiv:1411.1559 [hep-ex]. [Erratum: Phys.Rev.D 92, 059903 (2015)].

[303] **CMS** Collaboration, V. Khachatryan *et al.*, "Search for new phenomena in monophoton final states in proton-proton collisions at $\sqrt{s} = 8$ TeV," *Phys. Lett. B* **755** (2016) 102–124, arXiv:1410.8812 [hep-ex].

[304] U. Haisch, "Dark matter at the LHC," in *50th Rencontres de Moriond on EW Interactions and Unified Theories*, pp. 431–436. 5, 2015. arXiv:1505.06629 [hep-ph].

[305] **ATLAS, CMS** Collaboration, C. Doglioni, "Dark matter searches at ATLAS and CMS: run 1 results and run 2 potential," in *50th Rencontres de Moriond on EW Interactions and Unified Theories*, pp. 437–444. 2015.

[306] **BaBar** Collaboration, J. Lees *et al.*, "Search for Invisible Decays of a Dark Photon Produced in e^+e^- Collisions at BaBar," *Phys. Rev. Lett.* **119** no. 13, (2017) 131804, arXiv:1702.03327 [hep-ex].

[307] **Fermi-LAT** Collaboration, M. Ackermann *et al.*, "The Fermi Galactic Center GeV Excess and Implications for Dark Matter," *Astrophys. J.* **840** no. 1, (2017) 43, arXiv:1704.03910 [astro-ph.HE].

[308] **AMS** Collaboration, L. Accardo *et al.*, "High Statistics Measurement of the Positron Fraction in Primary Cosmic Rays of 0.5–500 GeV with the Alpha Magnetic Spectrometer on the International Space Station," *Phys. Rev. Lett.* **113** (2014) 121101.

[309] **AMS** Collaboration, M. Aguilar *et al.*, "Electron and Positron Fluxes in Primary Cosmic Rays Measured with the Alpha Magnetic Spectrometer on the International Space Station," *Phys. Rev. Lett.* **113** (2014) 121102.

[310] **PAMELA** Collaboration, O. Adriani *et al.*, "Cosmic-Ray Positron Energy Spectrum Measured by PAMELA," *Phys. Rev. Lett.* **111** (2013) 081102, arXiv:1308.0133 [astro-ph.HE].

[311] J. Christenson, J. Cronin, V. Fitch, and R. Turlay, "Evidence for the 2π Decay of the K_2^0 Meson," *Phys. Rev. Lett.* **13** (1964) 138–140.

[312] **BaBar** Collaboration, B. Aubert *et al.*, "Observation of direct CP violation in $B^0 \to K^+\pi^-$ decays," *Phys. Rev. Lett.* **93** (2004) 131801, arXiv:hep-ex/0407057.

[313] **Belle** Collaboration, Y. Chao *et al.*, "Evidence for direct CP violation in B0 —¿ K+ pi- decays," *Phys. Rev. Lett.* **93** (2004) 191802, arXiv:hep-ex/0408100.

[314] **BaBar** Collaboration, P. del Amo Sanchez *et al.*, "Measurement of CP observables in $B^{+-} - > D_{CP}K^{+-}$ decays and constraints on the CKM angle γ," *Phys. Rev. D* **82** (2010) 072004, arXiv:1007.0504 [hep-ex].

[315] **LHCb** Collaboration, R. Aaij *et al.*, "Observation of CP violation in $B^\pm \to DK^\pm$ decays," *Phys. Lett. B* **712** (2012) 203–212, arXiv:1203.3662 [hep-ex]. [Erratum: Phys.Lett.B 713, 351 (2012)].

[316] **LHCb** Collaboration, R. Aaij *et al.*, "First observation of CP violation in the decays of B_s^0 mesons," *Phys. Rev. Lett.* **110** no. 22, (2013) 221601, arXiv:1304.6173 [hep-ex].

[317] E. W. Kolb and M. S. Turner, *The Early Universe*, vol. 69. 1990.

[318] H. Mo, F. van den Bosch, and S. White, *Galaxy Formation and Evolution*. 2010.

[319] S. Tremaine and J. Gunn, "Dynamical Role of Light Neutral Leptons in Cosmology," *Phys. Rev. Lett.* **42** (1979) 407–410.

[320] A. Boyarsky, O. Ruchayskiy, and D. Iakubovskyi, "A Lower bound on the mass of Dark Matter particles," *JCAP* **03** (2009) 005, arXiv:0808.3902 [hep-ph].

[321] P. Gondolo and G. Gelmini, "Cosmic abundances of stable particles: Improved analysis," *Nucl. Phys. B* **360** (1991) 145–179.

[322] L. Husdal, "On Effective Degrees of Freedom in the Early Universe," *Galaxies* **4** no. 4, (2016) 78, arXiv:1609.04979 [astro-ph.CO].

[323] D. Fixsen, "The Temperature of the Cosmic Microwave Background," *Astrophys. J.* **707** (2009) 916–920, arXiv:0911.1955 [astro-ph.CO].

[324] N. Bernal, J. E. Forero-Romero, R. Garani, and S. Palomares-Ruiz, "Systematic uncertainties from halo asphericity in dark matter searches," *JCAP* **09** (2014) 004, arXiv:1405.6240 [astro-ph.CO].

[325] R. H. Helm, "Inelastic and Elastic Scattering of 187-Mev Electrons from Selected Even-Even Nuclei," *Phys. Rev.* **104** (1956) 1466–1475.

[326] A. Drukier, K. Freese, and D. Spergel, "Detecting Cold Dark Matter Candidates," *Phys. Rev. D* **33** (1986) 3495–3508.

[327] K. Freese, J. A. Frieman, and A. Gould, "Signal Modulation in Cold Dark Matter Detection," *Phys. Rev. D* **37** (1988) 3388–3405.

[328] R. Bernabei *et al.*, "First model independent results from DAMA/LIBRA-phase2," *Nucl. Phys. Atom. Energy* **19** no. 4, (2018) 307–325, arXiv:1805.10486 [hep-ex].

[329] G. Angloher *et al.*, "Results from 730 kg days of the CRESST-II Dark Matter Search," *Eur. Phys. J. C* **72** (2012) 1971, arXiv:1109.0702 [astro-ph.CO].

[330] **CRESST-II** Collaboration, G. Angloher *et al.*, "Results on low mass WIMPs using an upgraded CRESST-II detector," *Eur. Phys. J. C* **74** no. 12, (2014) 3184, arXiv:1407.3146 [astro-ph.CO].

[331] G. Angloher *et al.*, "The COSINUS project - perspectives of a NaI scintillating calorimeter for dark matter search," *Eur. Phys. J. C* **76** no. 8, (2016) 441, arXiv:1603.02214 [physics.ins-det].

[332] **SABRE** Collaboration, M. Antonello *et al.*, "The SABRE project and the SABRE Proof-of-Principle," *Eur. Phys. J. C* **79** no. 4, (2019) 363, arXiv:1806.09340 [physics.ins-det].

[333] I. Coarasa *et al.*, "ANAIS-112 sensitivity in the search for dark matter annual modulation," *Eur. Phys. J. C* **79** no. 3, (2019) 233, arXiv:1812.02000 [astro-ph.IM].

[334] **PICO-LON** Collaboration, K. Fushimi *et al.*, "Dark matter search project PICO-LON," *J. Phys. Conf. Ser.* **718** no. 4, (2016) 042022, arXiv:1512.04645 [astro-ph.IM].

[335] **DM-Ice** Collaboration, E. Barbosa de Souza *et al.*, "First search for a dark matter annual modulation signal with NaI(Tl) in the Southern Hemisphere by DM-Ice17," *Phys. Rev. D* **95** no. 3, (2017) 032006, arXiv:1602.05939 [physics.ins-det].

[336] J. Park, P. Adhikari, G. Adhikari, S. Oh, N. Kim, Y. Kim, C. Ha, K. Park, H. Lee, and E. Jeon, "Performance of a prototype active veto system using liquid scintillator for a dark matter search experiment," *Nucl. Instrum. Meth. A* **851** (2017) 103–107, arXiv:1701.04514 [astro-ph.IM].

[337] G. Adhikari *et al.*, "Initial Performance of the COSINE-100 Experiment," *Eur. Phys. J. C* **78** no. 2, (2018) 107, arXiv:1710.05299 [physics.ins-det].

[338] G. Bertone and M. Tait, Tim, "A new era in the search for dark matter," *Nature* **562** no. 7725, (2018) 51–56, arXiv:1810.01668 [astro-ph.CO].

[339] **DARWIN Consortium** Collaboration, L. Baudis, "DARWIN: dark matter WIMP search with noble liquids," *J. Phys. Conf. Ser.* **375** (2012) 012028, arXiv:1201.2402 [astro-ph.IM].

[340] M. M. Miller Bertolami, B. E. Melendez, L. G. Althaus, and J. Isern, "Revisiting the axion bounds from the Galactic white dwarf luminosity function," *JCAP* **10** (2014) 069, arXiv:1406.7712 [hep-ph].

[341] A. Ayala, I. Domínguez, M. Giannotti, A. Mirizzi, and O. Straniero, "Revisiting the bound on axion-photon coupling from Globular Clusters," *Phys. Rev. Lett.* **113** no. 19, (2014) 191302, arXiv:1406.6053 [astro-ph.SR].

[342] N. Viaux, M. Catelan, P. B. Stetson, G. Raffelt, J. Redondo, A. A. R. Valcarce, and A. Weiss, "Neutrino and axion bounds from the globular cluster M5 (NGC 5904)," *Phys. Rev. Lett.* **111** (2013) 231301, arXiv:1311.1669 [astro-ph.SR].

[343] M. Giannotti, I. G. Irastorza, J. Redondo, A. Ringwald, and K. Saikawa, "Stellar Recipes for Axion Hunters," *JCAP* **10** (2017) 010, arXiv:1708.02111 [hep-ph].

[344] L. Di Luzio, M. Giannotti, E. Nardi, and L. Visinelli, "The landscape of QCD axion models," arXiv:2003.01100 [hep-ph].

[345] K. Zioutas, G. Cantatore, M. Karuza, A. Kryemadhi, M. Maroudas, and Y. Semertzidis, "Response-suggestion to The XENON1T excess: an overlooked dark matter signature?," arXiv:2006.16907 [hep-ph].

[346] C. Dessert, J. W. Foster, Y. Kahn, and B. R. Safdi, "Systematics in the XENON1T data: the 15-keV anti-axion," arXiv:2006.16220 [hep-ph].

[347] B. Bhattacherjee and R. Sengupta, "XENON1T Excess: Some Possible Backgrounds," arXiv:2006.16172 [hep-ph].

[348] M. Szydagis, C. Levy, G. Blockinger, A. Kamaha, N. Parveen, and G. Rischbieter, "Investigating the XENON1T Low-Energy Electronic Recoil Excess Using NEST," arXiv:2007.00528 [hep-ex].

[349] H.-J. He, Y.-C. Wang, and J. Zheng, "EFT Analysis of Inelastic Dark Matter for Xenon Electron Recoil Detection," arXiv:2007.04963 [hep-ph].

[350] K. Babu, S. Jana, and M. Lindner, "Large Neutrino Magnetic Moments in the Light of Recent Experiments," arXiv:2007.04291 [hep-ph].

[351] M. Chala and A. Titov, "One-loop running of dimension-six Higgs-neutrino operators and implications of a large neutrino dipole moment," arXiv:2006.14596 [hep-ph].

[352] A. E. Robinson, "XENON1T observes tritium," arXiv:2006.13278 [hep-ex].

[353] F. Takahashi, M. Yamada, and W. Yin, "XENON1T anomaly from anomaly-free ALP dark matter and its implications for stellar cooling anomaly," arXiv:2006.10035 [hep-ph].

[354] C. A. O'Hare, A. Caputo, A. J. Millar, and E. Vitagliano, "Axion helioscopes as solar magnetometers," arXiv:2006.10415 [astro-ph.CO].

[355] C. Gao, J. Liu, L.-T. Wang, X.-P. Wang, W. Xue, and Y.-M. Zhong, "Re-examining the Solar Axion Explanation for the XENON1T Excess," arXiv:2006.14598 [hep-ph].

[356] L. Di Luzio, M. Fedele, M. Giannotti, F. Mescia, and E. Nardi, "Solar axions cannot explain the XENON1T excess," arXiv:2006.12487 [hep-ph].

[357] J. B. Dent, B. Dutta, J. L. Newstead, and A. Thompson, "Inverse Primakoff Scattering as a Probe of Solar Axions at Liquid Xenon Direct Detection Experiments," arXiv:2006.15118 [hep-ph].

[358] J. Sun and X.-G. He, "Axion Couplings Revisited," arXiv:2006.16931 [hep-ph].

[359] D. Croon, S. D. McDermott, and J. Sakstein, "Missing in Axion: where are XENON1T's big black holes?," arXiv:2007.00650 [hep-ph].

[360] T. Li, "The KSVZ Axion and Pseudo-Nambu-Goldstone Boson Models for the XENON1T Excess," arXiv:2007.00874 [hep-ph].

[361] S. Inan and A. Kisselev, "Polarized light-by-light scattering at the CLIC induced by axion-like particles," arXiv:2007.01693 [hep-ph].

[362] Y. Giraldo, R. Martinez, E. Rojas, and J. C. Salazar, "Flavored axions and the flavor problem," arXiv:2007.05653 [hep-ph].

[363] P. Athron *et al.*, "Global fits of axion-like particles to XENON1T and astrophysical data," arXiv:2007.05517 [astro-ph.CO].

[364] F. Arias-Aragon, F. D'Eramo, R. Z. Ferreira, L. Merlo, and A. Notari, "Cosmic Imprints of XENON1T Axions," arXiv:2007.06579 [hep-ph].

[365] H. An, M. Pospelov, J. Pradler, and A. Ritz, "New limits on dark photons from solar emission and keV scale dark matter," arXiv:2006.13929 [hep-ph].

[366] J. Smirnov and J. F. Beacom, "Co-SIMP Miracle," arXiv:2002.04038 [hep-ph].

[367] K. Kannike, M. Raidal, H. Veermäe, A. Strumia, and D. Teresi, "Dark Matter and the XENON1T electron recoil excess," arXiv:2006.10735 [hep-ph].

[368] S. Chigusa, M. Endo, and K. Kohri, "Constraints on electron-scattering interpretation of XENON1T excess," arXiv:2007.01663 [hep-ph].

[369] G. Alonso-Álvarez, F. Ertas, J. Jaeckel, F. Kahlhoefer, and L. J. Thormaehlen, "Hidden Photon Dark Matter in the Light of XENON1T and Stellar Cooling," arXiv:2006.11243 [hep-ph].

[370] U. K. Dey, T. N. Maity, and T. S. Ray, "Prospects of Migdal Effect in the Explanation of XENON1T Electron Recoil Excess," arXiv:2006.12529 [hep-ph].

[371] N. F. Bell, J. B. Dent, B. Dutta, S. Ghosh, J. Kumar, and J. L. Newstead, "Explaining the XENON1T excess with Luminous Dark Matter," arXiv:2006.12461 [hep-ph].

[372] Y. Chen, J. Shu, X. Xue, G. Yuan, and Q. Yuan, "Sun Heated MeV-scale Dark Matter and the XENON1T Electron Recoil Excess," arXiv:2006.12447 [hep-ph].

[373] G. Choi, M. Suzuki, and T. T. Yanagida, "XENON1T Anomaly and its Implication for Decaying Warm Dark Matter," arXiv:2006.12348 [hep-ph].

[374] H. M. Lee, "Exothermic Dark Matter for XENON1T Excess," arXiv:2006.13183 [hep-ph].

[375] K. Nakayama and Y. Tang, "Gravitational Production of Hidden Photon Dark Matter in light of the XENON1T Excess," arXiv:2006.13159 [hep-ph].

[376] J. Bramante and N. Song, "Electric But Not Eclectic: Thermal Relic Dark Matter for the XENON1T Excess," arXiv:2006.14089 [hep-ph].

[377] M. Baryakhtar, A. Berlin, H. Liu, and N. Weiner, "Electromagnetic Signals of Inelastic Dark Matter Scattering," arXiv:2006.13918 [hep-ph].

[378] L. Zu, G.-W. Yuan, L. Feng, and Y.-Z. Fan, "Mirror Dark Matter and Electronic Recoil Events in XENON1T," arXiv:2006.14577 [hep-ph].

[379] G. B. Gelmini, V. Takhistov, and E. Vitagliano, "Scalar Direct Detection: In-Medium Effects," arXiv:2006.13909 [hep-ph].

[380] M. Lindner, Y. Mambrini, T. B. d. Melo, and F. S. Queiroz, "XENON1T Anomaly: A Light Z'," arXiv:2006.14590 [hep-ph].

[381] N. Okada, S. Okada, D. Raut, and Q. Shafi, "Dark Matter Z' and XENON1T Excess from $U(1)_X$ Extended Standard Model," arXiv:2007.02898 [hep-ph].

[382] R. Budnik, H. Kim, O. Matsedonskyi, G. Perez, and Y. Soreq, "Probing the relaxed relaxion and Higgs-portal with S1 & S2," arXiv:2006.14568 [hep-ph].

[383] W. Chao, Y. Gao, and M. j. Jin, "Pseudo-Dirac Dark Matter in XENON1T," arXiv:2006.16145 [hep-ph].

[384] C. Cai, H. H. Zhang, G. Cacciapaglia, M. Rosenlyst, and M. T. Frandsen, "XENON1T solar axion and the Higgs boson emerging from the dark," arXiv:2006.16267 [hep-ph].

[385] P. Ko and Y. Tang, "Semi-annihilating Z_3 Dark Matter for XENON1T Excess," arXiv:2006.15822 [hep-ph].

[386] A. Hryczuk and K. Jodł owski, "Self-interacting dark matter from late decays and the H_0 tension," arXiv:2006.16139 [hep-ph].

[387] H. An and D. Yang, "Direct detection of freeze-in inelastic dark matter," arXiv:2006.15672 [hep-ph].

[388] S. Baek, J. Kim, and P. Ko, "XENON1T excess in local Z_2 DM models with light dark sector," arXiv:2006.16876 [hep-ph].

[389] O. Miranda, D. Papoulias, M. Tórtola, and J. Valle, "XENON1T signal from transition neutrino magnetic moments," arXiv:2007.01765 [hep-ph].

[390] I. M. Shoemaker, Y.-D. Tsai, and J. Wyenberg, "An Active-to-Sterile Neutrino Transition Dipole Moment and the XENON1T Excess," arXiv:2007.05513 [hep-ph].

[391] K. Benakli, C. Branchina, and G. Lafforgue-Marmet, "U(1) mixing and the Weak Gravity Conjecture," arXiv:2007.02655 [hep-ph].

[392] J. Davighi, M. McCullough, and J. Tooby-Smith, "Undulating Dark Matter," arXiv:2007.03662 [hep-ph].

[393] G. Choi, T. T. Yanagida, and N. Yokozaki, "Feebly Interacting $U(1)_{\mathrm{B-L}}$ Gauge Boson Warm Dark Matter and XENON1T Anomaly," arXiv:2007.04278 [hep-ph].

[394] H. Davoudiasl, P. B. Denton, and J. Gehrlein, "An Attractive Scenario for Light Dark Matter Direct Detection," arXiv:2007.04989 [hep-ph].

[395] P. Anastasopoulos, K. Kaneta, Y. Mambrini, and M. Pierre, "Energy-Momentum portal to dark matter and emergent gravity," arXiv:2007.06534 [hep-ph].

[396] B. Fornal, P. Sandick, J. Shu, M. Su, and Y. Zhao, "Boosted Dark Matter Interpretation of the XENON1T Excess," arXiv:2006.11264 [hep-ph].

[397] Q.-H. Cao, R. Ding, and Q.-F. Xiang, "Exploring for sub-MeV Boosted Dark Matter from Xenon Electron Direct Detection," arXiv:2006.12767 [hep-ph].

[398] Y. Jho, J.-C. Park, S. C. Park, and P.-Y. Tseng, "Gauged Lepton Number and Cosmic-ray Boosted Dark Matter for the XENON1T Excess," arXiv:2006.13910 [hep-ph].

[399] L. Delle Rose, G. Hütsi, C. Marzo, and L. Marzola, "Impact of loop-induced processes on the boosted dark matter interpretation of the XENON1T excess," arXiv:2006.16078 [hep-ph].

[400] C.-W. Chiang and B.-Q. Lu, "Evidence of A Simple Dark Sector from XENON1T Anomaly," arXiv:2007.06401 [hep-ph].

[401] C. Boehm, D. G. Cerdeno, M. Fairbairn, P. A. Machado, and A. C. Vincent, "Light new physics in XENON1T," arXiv:2006.11250 [hep-ph].

[402] P. Coloma, P. Huber, and J. M. Link, "Telling Solar Neutrinos from Solar Axions When You Can't Shut Off the Sun," arXiv:2006.15767 [hep-ph].

[403] A. Bally, S. Jana, and A. Trautner, "Neutrino self-interactions and XENON1T electron recoil excess," arXiv:2006.11919 [hep-ph].

[404] D. Aristizabal Sierra, V. De Romeri, L. Flores, and D. Papoulias, "Light vector mediators facing XENON1T data," arXiv:2006.12457 [hep-ph].

[405] A. N. Khan, "Nonstandard Neutrino Interactions can explain the XENON1T spectral excess?," arXiv:2006.12887 [hep-ph].

[406] Y. Gao and T. Li, "Lepton Number Violating Electron Recoils at XENON1T by the $U(1)_{B-L}$ Model with Non-Standard Interactions," arXiv:2006.16192 [hep-ph].

[407] K. Harigaya, Y. Nakai, and M. Suzuki, "Inelastic Dark Matter Electron Scattering and the XENON1T Excess," arXiv:2006.11938 [hep-ph].

[408] L. Su, W. Wang, L. Wu, J. M. Yang, and B. Zhu, "Atmospheric Dark Matter from Inelastic Cosmic Ray Collision in Xenon1T," arXiv:2006.11837 [hep-ph].

[409] M. Du, J. Liang, Z. Liu, V. Q. Tran, and Y. Xue, "On-shell mediator dark matter models and the Xenon1T anomaly," arXiv:2006.11949 [hep-ph].

[410] J. Buch, M. A. Buen-Abad, J. Fan, and J. S. C. Leung, "Galactic Origin of Relativistic Bosons and XENON1T Excess," arXiv:2006.12488 [hep-ph].

[411] G. Paz, A. A. Petrov, M. Tammaro, and J. Zupan, "Shining dark matter in Xenon1T," arXiv:2006.12462 [hep-ph].

[412] R. Primulando, J. Julio, and P. Uttayarat, "Collider Constraints on a Dark Matter Interpretation of the XENON1T Excess," arXiv:2006.13161 [hep-ph].

[413] I. M. Bloch, A. Caputo, R. Essig, D. Redigolo, M. Sholapurkar, and T. Volansky, "Exploring New Physics with O(keV) Electron Recoils in Direct Detection Experiments," arXiv:2006.14521 [hep-ph].

[414] H. Alhazmi, D. Kim, K. Kong, G. Mohlabeng, J.-C. Park, and S. Shin, "Implications of the XENON1T Excess on the Dark Matter Interpretation," arXiv:2006.16252 [hep-ph].

[415] d. Amaral, Dorian Warren Praia, D. G. Cerdeno, P. Foldenauer, and E. Reid, "Solar neutrino probes of the muon anomalous magnetic moment in the gauged $U(1)_{L_\mu - L_\tau}$," arXiv:2006.11225 [hep-ph].

[416] W. DeRocco, P. W. Graham, and S. Rajendran, "Exploring the robustness of stellar cooling constraints on light particles," arXiv:2006.15112 [hep-ph].

[417] M. Ressell and D. Dean, "Spin dependent neutralino - nucleus scattering for A approximately 127 nuclei," *Phys. Rev. C* **56** (1997) 535–546, arXiv:hep-ph/9702290.

[418] V. Bednyakov and F. Simkovic, "Nuclear spin structure in dark matter search: The Zero momentum transfer limit," *Phys. Part. Nucl.* **36** (2005) 131–152, arXiv:hep-ph/0406218.

[419] P. Toivanen, M. Kortelainen, J. Suhonen, and J. Toivanen, "Large-scale shell-model calculations of elastic and inelastic scattering rates of lightest supersymmetric particles (LSP) on I-127, Xe-129, Xe-131, and Cs-133 nuclei," *Phys. Rev. C* **79** (2009) 044302.

[420] M. Cannoni, "Reanalysis of nuclear spin matrix elements for dark matter spin-dependent scattering," *Phys. Rev. D* **87** no. 7, (2013) 075014, arXiv:1211.6050 [astro-ph.CO].

[421] L. Bergstrom, P. Ullio, and J. H. Buckley, "Observability of gamma-rays from dark matter neutralino annihilations in the Milky Way halo," *Astropart. Phys.* **9** (1998) 137–162, arXiv:astro-ph/9712318.

[422] A. Sommerfeld *Annalen der Physik* **403** (1931) 257.

[423] N. Arkani-Hamed, D. P. Finkbeiner, T. R. Slatyer, and N. Weiner, "A Theory of Dark Matter," *Phys. Rev. D* **79** (2009) 015014, arXiv:0810.0713 [hep-ph].

[424] **H.E.S.S.** Collaboration, F. Aharonian, "Spectrum and variability of the Galactic Center VHE gamma-ray source HESS J1745-290," *Astron. Astrophys.* **503** (2009) 817, arXiv:0906.1247 [astro-ph.GA].

[425] **H.E.S.S.** Collaboration, F. Acero, "Localising the VHE gamma-ray source at the Galactic Centre," *Mon. Not. Roy. Astron. Soc.* **402** (2010) 1877–1882, arXiv:0911.1912 [astro-ph.GA].

[426] D. Hooper and L. Goodenough, "Dark Matter Annihilation in The Galactic Center As Seen by the Fermi Gamma Ray Space Telescope," *Phys. Lett. B* **697** (2011) 412–428, arXiv:1010.2752 [hep-ph].

[427] T. Daylan, D. P. Finkbeiner, D. Hooper, T. Linden, S. K. N. Portillo, N. L. Rodd, and T. R. Slatyer, "The characterization of the gamma-ray signal from the central Milky Way: A case for annihilating dark matter," *Phys. Dark Univ.* **12** (2016) 1–23, arXiv:1402.6703 [astro-ph.HE].

[428] **Fermi-LAT** Collaboration, M. Ackermann *et al.*, "Searching for Dark Matter Annihilation from Milky Way Dwarf Spheroidal Galaxies with Six Years of Fermi Large Area Telescope Data," *Phys. Rev. Lett.* **115** no. 23, (2015) 231301, arXiv:1503.02641 [astro-ph.HE].

[429] J. Chang *et al.*, "An excess of cosmic ray electrons at energies of 300-800 GeV," *Nature* **456** (2008) 362–365.

[430] **Fermi-LAT** Collaboration, S. Abdollahi *et al.*, "Cosmic-ray electron-positron spectrum from 7 GeV to 2 TeV with the Fermi Large Area Telescope," *Phys. Rev. D* **95** no. 8, (2017) 082007, arXiv:1704.07195 [astro-ph.HE].

[431] **H.E.S.S.** Collaboration, F. Aharonian *et al.*, "Probing the ATIC peak in the cosmic-ray electron spectrum with H.E.S.S," *Astron. Astrophys.* **508** (2009) 561, arXiv:0905.0105 [astro-ph.HE].

[432] M. Cirelli, "Indirect Searches for Dark Matter: a status review," *Pramana* **79** (2012) 1021–1043, arXiv:1202.1454 [hep-ph].

[433] S. Profumo, "Dissecting cosmic-ray electron-positron data with Occam's Razor: the role of known Pulsars," *Central Eur. J. Phys.* **10** (2011) 1–31, arXiv:0812.4457 [astro-ph].

[434] M. Kachelrieß, A. Neronov, and D. V. Semikoz, "Signatures of a two million year old supernova in the spectra of cosmic ray protons, antiprotons and positrons," *Phys. Rev. Lett.* **115** no. 18, (2015) 181103, arXiv:1504.06472 [astro-ph.HE].

[435] **AMS** Collaboration, M. Aguilar *et al.*, "Antiproton Flux, Antiproton-to-Proton Flux Ratio, and Properties of Elementary Particle Fluxes in Primary Cosmic Rays Measured with the Alpha Magnetic Spectrometer on the International Space Station," *Phys. Rev. Lett.* **117** no. 9, (2016) 091103.

[436] J. Goodman, M. Ibe, A. Rajaraman, W. Shepherd, T. M. Tait, and H.-B. Yu, "Constraints on Dark Matter from Colliders," *Phys. Rev. D* **82** (2010) 116010, arXiv:1008.1783 [hep-ph].

[437] P. J. Fox, R. Harnik, J. Kopp, and Y. Tsai, "Missing Energy Signatures of Dark Matter at the LHC," *Phys. Rev. D* **85** (2012) 056011, arXiv:1109.4398 [hep-ph].

[438] **ATLAS** Collaboration, "Search for dark matter and other new phenomena in events with an energetic jet and large missing transverse momentum using the ATLAS detector,".

[439] **ATLAS** Collaboration, M. Aaboud *et al.*, "Search for new phenomena in final states with an energetic jet and large missing transverse momentum in pp collisions at $\sqrt{s} = 13$ TeV using the ATLAS detector," *Phys. Rev. D* **94** no. 3, (2016) 032005, arXiv:1604.07773 [hep-ex].

[440] **CMS** Collaboration, "Search for new physics in final states with an energetic jet or a hadronically decaying W or Z boson using 35.9 fb^{-1} of data at $\sqrt{s} = 13$ TeV,".

[441] **CMS** Collaboration, A. M. Sirunyan *et al.*, "Search for dark matter produced with an energetic jet or a hadronically decaying W or Z boson at $\sqrt{s} = 13$ TeV," *JHEP* **07** (2017) 014, arXiv:1703.01651 [hep-ex].

[442] **CMS** Collaboration, "Search for dark matter in final states with an energetic jet, or a hadronically decaying W or Z boson using 12.9 fb^{-1} of data at $\sqrt{s} = 13$ TeV,".

[443] **CMS** Collaboration, A. M. Sirunyan *et al.*, "Search for dark matter and unparticles in events with a Z boson and missing transverse momentum in proton-proton collisions at $\sqrt{s} = 13$ TeV," *JHEP* **03** (2017) 061, arXiv:1701.02042 [hep-ex]. [Erratum: JHEP 09, 106 (2017)].

[444] **CMS** Collaboration, "Search for dark matter in Z + $E_{\mathrm{T}}^{\mathrm{miss}}$ events using 12.9 fb^{-1} of 2016 data,".

[445] **CMS** Collaboration, V. Khachatryan *et al.*, "Search for dark matter in proton-proton collisions at 8 TeV with missing transverse momentum and vector boson tagged jets," *JHEP* **12** (2016) 083, arXiv:1607.05764 [hep-ex]. [Erratum: JHEP 08, 035 (2017)].

[446] **CMS** Collaboration, V. Khachatryan *et al.*, "Search for Dark Matter and Supersymmetry with a Compressed Mass Spectrum in the Vector Boson Fusion Topology in Proton-Proton Collisions at $\sqrt{s} = 8$ TeV," *Phys. Rev. Lett.* **118** no. 2, (2017) 021802, arXiv:1605.09305 [hep-ex].

[447] **CMS** Collaboration, "Search for dark matter production in association with jets, or hadronically decaying W or Z boson at $\sqrt{s} = 13$ TeV,".

[448] **CMS** Collaboration, V. Khachatryan *et al.*, "Search for dark matter particles in proton-proton collisions at $\sqrt{s} = 8$ TeV using the razor variables," *JHEP* **12** (2016) 088, arXiv:1603.08914 [hep-ex].

[449] **CMS** Collaboration, V. Khachatryan *et al.*, "Search for dark matter and unparticles produced in association with a Z boson in proton-proton collisions at $\sqrt{s} = 8$ TeV," *Phys. Rev. D* **93** no. 5, (2016) 052011, arXiv:1511.09375 [hep-ex]. [Erratum: Phys.Rev.D 97, 099903 (2018)].

[450] **CMS** Collaboration, V. Khachatryan *et al.*, "Search for the production of dark matter in association with top-quark pairs in the single-lepton final state in proton-proton collisions at sqrt(s) = 8 TeV," *JHEP* **06** (2015) 121, arXiv:1504.03198 [hep-ex].

[451] C. Prescott *et al.*, "Parity Nonconservation in Inelastic Electron Scattering," *Phys. Lett. B* **77** (1978) 347–352.

[452] C. Prescott *et al.*, "Further Measurements of Parity Nonconservation in Inelastic electron Scattering," *Phys. Lett. B* **84** (1979) 524–528.

[453] **SLD** Collaboration, K. Abe *et al.*, "First measurement of the left-right cross-section asymmetry in Z boson production by e+ e- collisions," *Phys. Rev. Lett.* **70** (1993) 2515–2520.

[454] **SLD** Collaboration, K. Abe *et al.*, "Precise measurement of the left-right cross-section asymmetry in Z boson production by e+ e- collisions," *Phys. Rev. Lett.* **73** (1994) 25–29, arXiv:hep-ex/9404001.

[455] **SLD** Collaboration, K. Abe *et al.*, "Polarized Bhabha scattering a precision measurement of the electron neutral current couplings," *Phys. Rev. Lett.* **74** (1995) 2880–2884, arXiv:hep-ex/9410009.

[456] **ALEPH, DELPHI, L3, OPAL, SLD, LEP Electroweak Working Group, SLD Electroweak Group, SLD Heavy Flavour Group** Collaboration, S. Schael *et al.*, "Precision electroweak measurements on the Z resonance," *Phys. Rept.* **427** (2006) 257–454, arXiv:hep-ex/0509008 [hep-ex].

[457] W. Marciano, "The Weak Mixing Angle and "New Physics" (A Tale of Two Numbers)," *AIP Conf. Proc.* **870** no. 1, (2006) 236–239.

[458] A. Sirlin, "Radiative Corrections in the SU(2)-L x U(1) Theory: A Simple Renormalization Framework," *Phys. Rev. D* **22** (1980) 971–981.

[459] D. Kennedy, B. Lynn, C. Im, and R. Stuart, "Electroweak Cross-Sections and Asymmetries at the Z0," *Nucl. Phys. B* **321** (1989) 83–107.

[460] D. Bardin, M. S. Bilenky, G. Mitselmakher, T. Riemann, and M. Sachwitz, "A Realistic Approach to the Standard Z Peak," *Z. Phys. C* **44** (1989) 493.

[461] W. Hollik, "Radiative Corrections in the Standard Model and their Role for Precision Tests of the Electroweak Theory," *Fortsch. Phys.* **38** (1990) 165–260.

[462] W. J. Marciano and J. L. Rosner, "Atomic parity violation as a probe of new physics," *Phys. Rev. Lett.* **65** (1990) 2963–2966. [Erratum: Phys.Rev.Lett. 68, 898 (1992)].

[463] M. Consoli, W. Hollik, and F. Jegerlehner, "The Effect of the Top Quark on the M(W)-M(Z) Interdependence and Possible Decoupling of Heavy Fermions from Low-Energy Physics," *Phys. Lett. B* **227** (1989) 167–170.

[464] S. Fanchiotti, B. A. Kniehl, and A. Sirlin, "Incorporation of QCD effects in basic corrections of the electroweak theory," *Phys. Rev. D* **48** (1993) 307–331, arXiv:hep-ph/9212285.

[465] G. Degrassi, S. Fanchiotti, and A. Sirlin, "Relations Between the On-shell and Ms Frameworks and the M (W) - M (Z) Interdependence," *Nucl. Phys. B* **351** (1991) 49–69.

[466] M. Bohm *et al.*, "FORWARD - BACKWARD ASYMMETRIES," in *LEP Physics Workshop*, pp. 203–234. 9, 1989.

[467] P. Gambino and A. Sirlin, "Relation between sin**2 Theta-w (m(z)) and sin**2 Theta-effective (leptonic)," *Phys. Rev. D* **49** (1994) 1160–1162, arXiv:hep-ph/9309326.

[468] W. J. Marciano, *Radiative corrections to neutral current processes*, vol. 14, pp. 170–200. 1995.

[469] T. van Ritbergen, J. Vermaseren, and S. Larin, "The Four loop beta function in quantum chromodynamics," *Phys. Lett. B* **400** (1997) 379–384, arXiv:hep-ph/9701390.

[470] M. Czakon, "The Four-loop QCD beta-function and anomalous dimensions," *Nucl. Phys. B* **710** (2005) 485–498, arXiv:hep-ph/0411261.

[471] K. Chetyrkin, B. A. Kniehl, and M. Steinhauser, "Decoupling relations to O (alpha-s**3) and their connection to low-energy theorems," *Nucl. Phys. B* **510** (1998) 61–87, arXiv:hep-ph/9708255.

[472] K. Chetyrkin, J. H. Kuhn, and C. Sturm, "Four-loop moments of the heavy quark vacuum polarization function in perturbative QCD," *Eur. Phys. J. C* **48** (2006) 107–110, arXiv:hep-ph/0604234.

[473] B. A. Kniehl and A. V. Kotikov, "Heavy-quark QCD vacuum polarisation function: Analytical results at four loops," *Phys. Lett. B* **642** (2006) 68–71, arXiv:hep-ph/0607201.

[474] J. Erler, "Calculation of the QED coupling alpha (M(Z)) in the modified minimal subtraction scheme," *Phys. Rev. D* **59** (1999) 054008, arXiv:hep-ph/9803453.

[475] R. Alemany, M. Davier, and A. Hocker, "Improved determination of the hadronic contribution to the muon (g-2) and to alpha (M(z)) using new data from hadronic tau decays," *Eur. Phys. J. C* **2** (1998) 123–135, arXiv:hep-ph/9703220.

[476] S. Eidelman, F. Jegerlehner, A. Kataev, and O. Veretin, "Testing nonperturbative strong interaction effects via the Adler function," *Phys. Lett. B* **454** (1999) 369–380, arXiv:hep-ph/9812521.

[477] T. Blum, P. Boyle, T. Izubuchi, L. Jin, A. Jüttner, C. Lehner, K. Maltman, M. Marinkovic, A. Portelli, and M. Spraggs, "Calculation of the hadronic vacuum polarization disconnected contribution to the muon anomalous magnetic moment," *Phys. Rev. Lett.* **116** no. 23, (2016) 232002, arXiv:1512.09054 [hep-lat].

[478] T. Lee and C.-N. Yang, "Question of Parity Conservation in Weak Interactions," *Phys. Rev.* **104** (1956) 254–258.

[479] C. Wu, E. Ambler, R. Hayward, D. Hoppes, and R. Hudson, "Experimental Test of Parity Conservation in β Decay," *Phys. Rev.* **105** (1957) 1413–1414.

[480] L. Barko and M. Zolotarev, "Measurement of optical activity of bismuth vapor," *JETP Lett.* **28** (1978) 503.

[481] M. Bouchiat and C. Bouchiat, "Parity Violation Induced by Weak Neutral Currents in Atomic Physics. Part 2," *J. Phys. (France)* **36** (1975) 493–509.

[482] M. Safronova, D. Budker, D. DeMille, D. F. J. Kimball, A. Derevianko, and C. Clark, "Search for New Physics with Atoms and Molecules," *Rev. Mod. Phys.* **90** no. 2, (2018) 025008, arXiv:1710.01833 [physics.atom-ph].

[483] J. Erler, A. Kurylov, and M. J. Ramsey-Musolf, "The Weak charge of the proton and new physics," *Phys. Rev. D* **68** (2003) 016006, arXiv:hep-ph/0302149.

[484] **PVDIS** Collaboration, D. Wang *et al.*, "Measurement of parity violation in electron–quark scattering," *Nature* **506** no. 7486, (2014) 67–70.

[485] E. Derman and W. J. Marciano, "Parity Violating Asymmetries in Polarized Electron Scattering," *Annals Phys.* **121** (1979) 147.

[486] C. Llewellyn Smith, "On the Determination of sin**2-Theta-w in Semileptonic Neutrino Interactions," *Nucl. Phys. B* **228** (1983) 205–215.

[487] E. Paschos and L. Wolfenstein, "Tests for Neutral Currents in Neutrino Reactions," *Phys. Rev. D* **7** (1973) 91–95.

[488] **OPAL** Collaboration, G. Abbiendi *et al.*, "Precision neutral current asymmetry parameter measurements from the tau polarization at LEP," *Eur. Phys. J. C* **21** (2001) 1–21, arXiv:hep-ex/0103045.

[489] D. Y. Bardin, M. Grunewald, and G. Passarino, "Precision calculation project report," arXiv:hep-ph/9902452.

[490] J. C. Collins and D. E. Soper, "Angular Distribution of Dileptons in High-Energy Hadron Collisions," *Phys. Rev. D* **16** (1977) 2219.

[491] E. Mirkes, "Angular decay distribution of leptons from W bosons at NLO in hadronic collisions," *Nucl. Phys. B* **387** (1992) 3–85.

[492] E. Mirkes and J. Ohnemus, "W and Z polarization effects in hadronic collisions," *Phys. Rev. D* **50** (1994) 5692–5703, arXiv:hep-ph/9406381.

[493] **CDF, D0** Collaboration, T. A. Aaltonen *et al.*, "Tevatron Run II combination of the effective leptonic electroweak mixing angle," *Phys. Rev. D* **97** no. 11, (2018) 112007, arXiv:1801.06283 [hep-ex].

[494] A. Arbuzov, M. Awramik, M. Czakon, A. Freitas, M. Grunewald, K. Monig, S. Riemann, and T. Riemann, "ZFITTER: A Semi-analytical program for fermion pair production in e+ e- annihilation, from version 6.21 to version 6.42," *Comput. Phys. Commun.* **174** (2006) 728–758, arXiv:hep-ph/0507146.

[495] **LHCb** Collaboration, R. Aaij *et al.*, "Measurement of the forward-backward asymmetry in $Z/\gamma^* \to \mu^+\mu^-$ decays and determination of the effective weak mixing angle," *JHEP* **11** (2015) 190, arXiv:1509.07645 [hep-ex].

[496] **ATLAS** Collaboration, G. Aad *et al.*, "Measurement of the forward-backward asymmetry of electron and muon pair-production in pp collisions at $\sqrt{s} = 7$ TeV with the ATLAS detector," *JHEP* **09** (2015) 049, arXiv:1503.03709 [hep-ex].

[497] **CMS** Collaboration, "Measurement of the weak mixing angle with the forward-backward asymmetry of Drell-Yan events at 8 TeV,".

[498] **CMS** Collaboration, A. M. Sirunyan *et al.*, "Measurement of the weak mixing angle using the forward-backward asymmetry of Drell-Yan events in pp collisions at 8 TeV," *Eur. Phys. J. C* **78** no. 9, (2018) 701, arXiv:1806.00863 [hep-ex].

[499] **ATLAS** Collaboration, "Measurement of the effective leptonic weak mixing angle using electron and muon pairs from Z-boson decay in the ATLAS experiment at $\sqrt{s} = 8$ TeV,".

[500] P. Souder, "Parity-violating DIS at 12 GeV," in *3rd International Workshop on From Parity Violation to Hadronic Structure and More*, pp. 211–215. 2007.

[501] P. Souder, "Parity at high x," *AIP Conf. Proc.* **747** no. 1, (2005) 199–204.

[502] J. Erler and M. Schott, "Electroweak Precision Tests of the Standard Model after the Discovery of the Higgs Boson," *Prog. Part. Nucl. Phys.* **106** (2019) 68–119, arXiv:1902.05142 [hep-ph].

[503] I. Dubovyk, A. Freitas, J. Gluza, T. Riemann, and J. Usovitsch, "Electroweak Bosonic 2-loop Corrections to the Z-pole Precision Observables," *Acta Phys. Polon. B* **48** (2017) 2321.

[504] R. Hawkings and K. Monig, "Electroweak and CP violation physics at a linear collider Z factory," *Eur. Phys. J. direct* **1** no. 1, (1999) 8, arXiv:hep-ex/9910022.

[505] **TLEP Design Study Working Group** Collaboration, M. Bicer *et al.*, "First Look at the Physics Case of TLEP," *JHEP* **01** (2014) 164, arXiv:1308.6176 [hep-ex].

[506] D. d'Enterria, "Physics at the FCC-ee," in *17th Lomonosov Conference on Elementary Particle Physics*, pp. 182–191. 2017. arXiv:1602.05043 [hep-ex].

[507] A. Blondel *et al.*, "Standard model theory for the FCC-ee Tera-Z stage," in *Mini Workshop on Precision EW and QCD Calculations for the FCC Studies : Methods and Techniques*, vol. 3/2019 of *CERN Yellow Reports: Monographs*. CERN, Geneva, 9, 2018. arXiv:1809.01830 [hep-ph].

[508] A. Blondel, A. Freitas, J. Gluza, T. Riemann, S. Heinemeyer, S. Jadach, and P. Janot, "Theory Requirements and Possibilities for the FCC-ee and other Future High Energy and Precision Frontier Lepton Colliders," arXiv:1901.02648 [hep-ph].

[509] A. Freitas *et al.*, "Theoretical uncertainties for electroweak and Higgs-boson precision measurements at FCC-ee," arXiv:1906.05379 [hep-ph].

[510] **DUNE** Collaboration, R. Acciarri *et al.*, "Long-Baseline Neutrino Facility (LBNF) and Deep Underground Neutrino Experiment (DUNE): Conceptual Design Report, Volume 2: The Physics Program for DUNE at LBNF," arXiv:1512.06148 [physics.ins-det].

[511] T. Golan, C. Juszczak, and J. T. Sobczyk, "Final State Interactions Effects in Neutrino-Nucleus Interactions," *Phys. Rev. C* **86** (2012) 015505, arXiv:1202.4197 [nucl-th].

[512] **COHERENT** Collaboration, D. Akimov *et al.*, "Observation of Coherent Elastic Neutrino-Nucleus Scattering," *Science* **357** no. 6356, (2017) 1123–1126, arXiv:1708.01294 [nucl-ex].

[513] A. Beda, V. Brudanin, V. Egorov, D. Medvedev, V. Pogosov, E. Shevchik, M. Shirchenko, A. Starostin, and I. Zhitnikov, "Gemma experiment: The results of neutrino magnetic moment search," *Phys. Part. Nucl. Lett.* **10** (2013) 139–143.

[514] T. Kosmas, O. Miranda, D. Papoulias, M. Tortola, and J. Valle, "Sensitivities to neutrino electromagnetic properties at the TEXONO experiment," *Phys. Lett. B* **750** (2015) 459–465, arXiv:1506.08377 [hep-ph].

[515] M. Lindner, W. Rodejohann, and X.-J. Xu, "Coherent Neutrino-Nucleus Scattering and new Neutrino Interactions," *JHEP* **03** (2017) 097, arXiv:1612.04150 [hep-ph].

[516] **CONNIE** Collaboration, A. Aguilar-Arevalo *et al.*, "Results of the Engineering Run of the Coherent Neutrino Nucleus Interaction Experiment (CONNIE)," *JINST* **11** no. 07, (2016) P07024, arXiv:1604.01343 [physics.ins-det].

[517] **CONNIE** Collaboration, A. Aguilar-Arevalo *et al.*, "The CONNIE experiment," *J. Phys. Conf. Ser.* **761** no. 1, (2016) 012057, arXiv:1608.01565 [physics.ins-det].

[518] **MINER** Collaboration, G. Agnolet *et al.*, "Background Studies for the MINER Coherent Neutrino Scattering Reactor Experiment," *Nucl. Instrum. Meth. A* **853** (2017) 53–60, arXiv:1609.02066 [physics.ins-det].

[519] **RED** Collaboration, D. Akimov *et al.*, "Prospects for observation of neutrino-nuclear neutral current coherent scattering with two-phase Xenon emission detector," *JINST* **8** (2013) P10023, arXiv:1212.1938 [physics.ins-det].

[520] J. Barranco, O. Miranda, and T. Rashba, "Probing new physics with coherent neutrino scattering off nuclei," *JHEP* **12** (2005) 021, arXiv:hep-ph/0508299.

[521] **Charm-Tau Factory** Collaboration, A. Bondar *et al.*, "Project of a Super Charm-Tau factory at the Budker Institute of Nuclear Physics in Novosibirsk," *Yad. Fiz.* **76** no. 9, (2013) 1132–1145.

[522] A. Bondar, A. Grabovsky, A. Reznichenko, A. Rudenko, and V. Vorobyev, "Measurement of the weak mixing angle at a Super Charm-Tau factory with data-driven monitoring of the average electron beam polarization," *JHEP* **20** (2020) 076, arXiv:1912.09760 [hep-ph].

[523] Y. Skovpen and I. Khriplovich, "WEAK NEUTRAL CURRENTS OF NEW QUARKS IN e+ e- ANNIHILATION," *Sov. J. Nucl. Phys.* **30** (1979) 303.

[524] M. Ramsey-Musolf, "Low-energy parity violation and new physics," *Phys. Rev. C* **60** (1999) 015501, arXiv:hep-ph/9903264.

[525] M. Ramsey-Musolf and S. Su, "Low Energy Precision Test of Supersymmetry," *Phys. Rept.* **456** (2008) 1–88, arXiv:hep-ph/0612057.

[526] J. Erler and S. Su, "The Weak Neutral Current," *Prog. Part. Nucl. Phys.* **71** (2013) 119–149, arXiv:1303.5522 [hep-ph].

[527] W.-F. Chang, J. N. Ng, and J. M. Wu, "Non-Supersymmetric New Physics and Polarized Moller Scattering," *Phys. Rev. D* **79** (2009) 055016, arXiv:0901.0613 [hep-ph].

[528] K. Kumar, S. Mantry, W. Marciano, and P. Souder, "Low Energy Measurements of the Weak Mixing Angle," *Ann. Rev. Nucl. Part. Sci.* **63** (2013) 237–267, arXiv:1302.6263 [hep-ex].

[529] **ALEPH** Collaboration, S. Schael *et al.*, "Fermion pair production in e^+e^- collisions at 189-209-GeV and constraints on physics beyond the standard model," *Eur. Phys. J. C* **49** (2007) 411–437, arXiv:hep-ex/0609051.

[530] **ALEPH, DELPHI, L3, OPAL, LEP Electroweak** Collaboration, S. Schael *et al.*, "Electroweak Measurements in Electron-Positron Collisions at W-Boson-Pair Energies at LEP," *Phys. Rept.* **532** (2013) 119–244, arXiv:1302.3415 [hep-ex].

[531] **LEP, ALEPH, DELPHI, L3, LEP Electroweak Working Group, SLD Electroweak Group, SLD Heavy Flavour Group, OPAL** Collaboration, "A Combination of preliminary electroweak measurements and constraints on the standard model," arXiv:hep-ex/0412015.

[532] **ATLAS** Collaboration, G. Aad *et al.*, "Search for contact interactions and large extra dimensions in dilepton events from pp collisions at $\sqrt{s} = 7$ TeV with the ATLAS detector," *Phys. Rev. D* **87** no. 1, (2013) 015010, arXiv:1211.1150 [hep-ex].

[533] **H1** Collaboration, F. Aaron *et al.*, "Search for Contact Interactions in $e^{\pm}p$ Collisions at HERA," *Phys. Lett. B* **705** (2011) 52–58, arXiv:1107.2478 [hep-ex].

[534] **ZEUS** Collaboration, S. Chekanov *et al.*, "Search for contact interactions, large extra dimensions and finite quark radius in e p collisions at HERA," *Phys. Lett. B* **591** (2004) 23–41, arXiv:hep-ex/0401009.

[535] K. S. Kumar and P. Souder, "Strange quarks and parity violation," *Prog. Part. Nucl. Phys.* **45** (2000) S333–S395.

[536] R. D. Young, J. Roche, R. D. Carlini, and A. W. Thomas, "Extracting nucleon strange and anapole form factors from world data," *Phys. Rev. Lett.* **97** (2006) 102002, arXiv:nucl-ex/0604010.

[537] J. Liu, R. D. McKeown, and M. J. Ramsey-Musolf, "Global Analysis of Nucleon Strange Form Factors at Low Q**2," *Phys. Rev. C* **76** (2007) 025202, arXiv:0706.0226 [nucl-ex].

[538] R. Gonzalez-Jimenez, J. Caballero, and T. Donnelly, "Parity Violation in Elastic Electron-Nucleon Scattering: Strangeness Content in the Nucleon," *Phys. Rept.* **524** (2013) 1–35, arXiv:1111.6918 [nucl-th].

[539] R. D. Young, R. D. Carlini, A. W. Thomas, and J. Roche, "Testing the standard model by precision measurement of the weak charges of quarks," *Phys. Rev. Lett.* **99** (2007) 122003, arXiv:0704.2618 [hep-ph].

[540] **OPAL** Collaboration, G. Abbiendi *et al.*, "Tests of the standard model and constraints on new physics from measurements of fermion pair production at 189-GeV to 209-GeV at LEP," *Eur. Phys. J. C* **33** (2004) 173–212, arXiv:hep-ex/0309053.

[541] **ZEUS** Collaboration, J. Breitweg *et al.*, "Search for contact interactions in deep inelastic $e^+p \to e^+X$ scattering at HERA," *Eur. Phys. J. C* **14** (2000) 239–254, arXiv:hep-ex/9905039.

[542] **H1** Collaboration, C. Adloff *et al.*, "Search for compositeness, leptoquarks and large extra dimensions in *eq* contact interactions at HERA," *Phys. Lett. B* **479** (2000) 358–370, arXiv:hep-ex/0003002.

[543] A. Friedland, M. L. Graesser, I. M. Shoemaker, and L. Vecchi, "Probing Nonstandard Standard Model Backgrounds with LHC Monojets," *Phys. Lett. B* **714** (2012) 267–275, arXiv:1111.5331 [hep-ph].

[544] D. Choudhury, K. Ghosh, and S. Niyogi, "Probing nonstandard neutrino interactions at the LHC Run II," *Phys. Lett. B* **784** (2018) 248–254.

[545] A. Aleksejevs, S. Barkanova, A. Ilyichev, Y. Kolomensky, and V. Zykunov, "One-loop electroweak corrections for polarized Moller scattering at different renormalization schemes and conditions," *Phys. Part. Nucl.* **44** (2013) 161–174, arXiv:1010.4185 [hep-ph].

[546] A. Aleksejevs, S. Barkanova, Y. Kolomensky, E. Kuraev, and V. Zykunov, "High precision calculations of electroweak radiative corrections for polarized Moller scattering at one loop and beyond," *Nuovo Cim.* **C035** no. 4, (2012) 192–197, arXiv:1110.6637 [hep-ph].

[547] A. Aleksejevs, S. Barkanova, Y. Kolomensky, E. Kuraev, and V. Zykunov, "Quadratic electroweak corrections for polarized Moller scattering," *Phys. Rev.* **D85** (2012) 013007, arXiv:1110.1750 [hep-ph].

[548] A. G. Aleksejevs, S. G. Barkanova, Yu. M. Bystritskiy, E. A. Kuraev, and V. A. Zykunov, "NNLO Electroweak corrections for polarized Møller scattering: One-loop insertions to boxes," *Phys. Part. Nucl. Lett.* **12** no. 5, (2015) 645–656, arXiv:1504.03560 [hep-ph].

[549] A. G. Aleksejevs, S. G. Barkanova, Yu. M. Bystritskiy, E. A. Kuraev, and V. A. Zykunov, "Two-loop electroweak vertex corrections for polarized Møller scattering," *Phys. Part. Nucl. Lett.* **13** no. 3, (2016) 310–317, arXiv:1508.07853 [hep-ph].

[550] A. G. Aleksejevs, S. G. Barkanova, Yu. M. Bystritskiy, E. A. Kuraev, A. N. Ilyichev, and V. A. Zykunov, "Parity violating Moller scattering asymmetry up to the two-loop level," arXiv:1202.0378 [hep-ph].

[551] J. Valle, "ASPECTS OF SUPERSTRING MODELS OF QUARKS AND LEPTONS," in *International Symposium on Nuclear Beta Decays and Neutrino: Neutrino Mass and V+A Interaction in Particle and Nuclear Physics*. 6, 1986.

[552] W. Chao, M. Gonderinger, and M. J. Ramsey-Musolf, "Higgs Vacuum Stability, Neutrino Mass, and Dark Matter," *Phys. Rev.* **D86** (2012) 113017, arXiv:1210.0491 [hep-ph].

[553] N. Haba, H. Ishida, N. Okada, and Y. Yamaguchi, "Vacuum stability and naturalness in type-II seesaw," *Eur. Phys. J.* **C76** no. 6, (2016) 333, arXiv:1601.05217 [hep-ph].

[554] E. J. Chun, H. M. Lee, and P. Sharma, "Vacuum Stability, Perturbativity, EWPD and Higgs-to-diphoton rate in Type II Seesaw Models," *JHEP* **11** (2012) 106, arXiv:1209.1303 [hep-ph].

[555] C. Bonilla, R. M. Fonseca, and J. W. F. Valle, "Consistency of the triplet seesaw model revisited," *Phys. Rev.* **D92** no. 7, (2015) 075028, arXiv:1508.02323 [hep-ph].

[556] N. Quintero, "Lepton-number-violating decays of heavy flavors induced by doubly-charged Higgs boson," *Phys. Rev.* **D87** no. 5, (2013) 056005, arXiv:1212.3016 [hep-ph].

[557] S. Kanemura, K. Yagyu, and H. Yokoya, "First constraint on the mass of doubly-charged Higgs bosons in the same-sign diboson decay scenario at the LHC," *Phys. Lett.* **B726** (2013) 316–319, arXiv:1305.2383 [hep-ph].

[558] E. J. Chun and P. Sharma, "Search for a doubly-charged boson in four lepton final states in type II seesaw," *Phys. Lett.* **B728** (2014) 256–261, arXiv:1309.6888 [hep-ph].

[559] K. Yagyu, "Doubly-charged Higgs bosons in the diboson decay scenario at the ILC," in *International Workshop on Future Linear Colliders (LCWS13) Tokyo, Japan, November 11-15, 2013*. 2014. arXiv:1405.5149 [hep-ph].

[560] S. Kanemura, M. Kikuchi, K. Yagyu, and H. Yokoya, "Bounds on the mass of doubly-charged Higgs bosons in the same-sign diboson decay scenario," *Phys. Rev.* **D90** no. 11, (2014) 115018, arXiv:1407.6547 [hep-ph].

[561] M. Muhlleitner and M. Spira, "A Note on doubly charged Higgs pair production at hadron colliders," *Phys. Rev.* **D68** (2003) 117701, arXiv:hep-ph/0305288 [hep-ph].

[562] E. J. Chun and P. Sharma, "Same-Sign Tetra-Leptons from Type II Seesaw," *JHEP* **08** (2012) 162, arXiv:1206.6278 [hep-ph].

[563] S. Kanemura, M. Kikuchi, H. Yokoya, and K. Yagyu, "LHC Run-I constraint on the mass of doubly charged Higgs bosons in the same-sign diboson decay scenario," *PTEP* **2015** (2015) 051B02, arXiv:1412.7603 [hep-ph].

[564] E. J. Chun and P. Sharma, "Same-sign tetra-leptons in type II seesaw at the LHC," in *Proceedings, 1st Toyama International Workshop on Higgs as a Probe of New Physics 2013 (HPNP2013): Toyama, Japan, February 13-16, 2013*. 2013. arXiv:1304.5059 [hep-ph].

[565] C.-W. Chiang, T. Nomura, and K. Tsumura, "Search for doubly charged Higgs bosons using the same-sign diboson mode at the LHC," *Phys. Rev.* **D85** (2012) 095023, arXiv:1202.2014 [hep-ph].

[566] D. K. Ghosh, N. Ghosh, I. Saha, and A. Shaw, "Revisiting the high-scale validity of Type-II seesaw model with novel LHC signature," arXiv:1711.06062 [hep-ph].

[567] M. Mitra, S. Niyogi, and M. Spannowsky, "Type-II Seesaw Model and Multilepton Signatures at Hadron Colliders," *Phys. Rev.* **D95** no. 3, (2017) 035042, arXiv:1611.09594 [hep-ph].

[568] C.-S. Chen, C.-Q. Geng, D. Huang, and L.-H. Tsai, "$h \to Z\gamma$ in Type-II seesaw neutrino model," *Phys. Lett.* **B723** (2013) 156–160, arXiv:1302.0502 [hep-ph].

[569] P. S. Bhupal Dev, D. K. Ghosh, N. Okada, and I. Saha, "125 GeV Higgs Boson and the Type-II Seesaw Model," *JHEP* **03** (2013) 150, arXiv:1301.3453 [hep-ph]. [Erratum: JHEP05,049(2013)].

[570] A. G. Akeroyd and H. Sugiyama, "Production of doubly charged scalars from the decay of singly charged scalars in the Higgs Triplet Model," *Phys. Rev.* **D84** (2011) 035010, arXiv:1105.2209 [hep-ph].

[571] C.-X. Yue, X.-S. Su, J. Zhang, and J. Wang, "Single production of the doubly charged Higgs boson via $e\gamma$ collision in the Higgs triplet model," *Commun. Theor. Phys.* **56** (2011) 709–717, arXiv:1010.4633 [hep-ph].

[572] A. G. Akeroyd and M. Aoki, "Single and pair production of doubly charged Higgs bosons at hadron colliders," *Phys. Rev.* **D72** (2005) 035011, arXiv:hep-ph/0506176 [hep-ph].

[573] A. G. Akeroyd and S. Moretti, "Enhancement of H to gamma gamma from doubly charged scalars in the Higgs Triplet Model," *Phys. Rev.* **D86** (2012) 035015, arXiv:1206.0535 [hep-ph].

[574] A. G. Akeroyd and S. Moretti, "Production of doubly charged scalars from the decay of a heavy SM-like Higgs boson in the Higgs Triplet Model," *Phys. Rev.* **D84** (2011) 035028, arXiv:1106.3427 [hep-ph].

[575] J. F. Ong, I. A. Jalil, and W. A. Tajuddin Wan Abdullah, "Charged Higgs boson contribution to $\bar{\nu}_e - e$ scattering from low to ultrahigh energy in Higgs triplet model," *Int. J. Theor. Phys.* **52** (2013) 679–688, arXiv:1103.5273 [hep-ph].

[576] A. G. Akeroyd and C.-W. Chiang, "Doubly charged Higgs bosons and three-lepton signatures in the Higgs Triplet Model," *Phys. Rev.* **D80** (2009) 113010, arXiv:0909.4419 [hep-ph].

[577] K. Huitu, T. J. Kärkkäinen, J. Maalampi, and S. Vihonen, "The effects of triplet Higgs bosons in long baseline neutrino experiments," arXiv:1711.02971 [hep-ph].

[578] A. Biswas, "All about $H^{\pm\pm}$ in Higgs Triplet Model," arXiv:1702.03847 [hep-ph].

[579] D. Das and A. Santamaria, "Updated scalar sector constraints in the Higgs triplet model," *Phys. Rev.* **D94** no. 1, (2016) 015015, arXiv:1604.08099 [hep-ph].

[580] M. Kikuchi, "Radiative corrections to the Higgs boson couplings in the Higgs triplet model," in *Proceedings, 1st Toyama International Workshop on Higgs as a Probe of New Physics 2013 (HPNP2013): Toyama, Japan, February 13-16, 2013*. 2013. arXiv:1305.0109 [hep-ph]. http://www.slac.stanford.edu/econf/C130213.1/pdfs/kikuchi.pdf.

[581] M. Aoki, S. Kanemura, M. Kikuchi, and K. Yagyu, "Radiative corrections to the Higgs boson couplings in the triplet model," *Phys. Rev.* **D87** no. 1, (2013) 015012, arXiv:1211.6029 [hep-ph].

[582] M. Aoki, S. Kanemura, M. Kikuchi, and K. Yagyu, "Renormalization of the Higgs Sector in the Triplet Model," *Phys. Lett.* **B714** (2012) 279–285, arXiv:1204.1951 [hep-ph].

[583] A. Arhrib, R. Benbrik, M. Chabab, G. Moultaka, and L. Rahili, "$h\gamma\gamma$ Coupling in Higgs Triplet Model," in *International Workshop on Future Linear Colliders (LCWS11) Granada, Spain, September 26-30, 2011*. 2012. arXiv:1202.6621 [hep-ph].

[584] S. Kanemura and K. Yagyu, "Radiative corrections to electroweak parameters in the Higgs triplet model and implication with the recent Higgs boson searches," *Phys. Rev.* **D85** (2012) 115009, arXiv:1201.6287 [hep-ph].

[585] M. Aoki, S. Kanemura, and K. Yagyu, "Testing the Higgs triplet model with the mass difference at the LHC," *Phys. Rev.* **D85** (2012) 055007, arXiv:1110.4625 [hep-ph].

[586] W. Rodejohann and H. Zhang, "Higgs triplets at like-sign linear colliders and neutrino mixing," *Phys. Rev.* **D83** (2011) 073005, arXiv:1011.3606 [hep-ph].

[587] C.-S. Chen and C.-M. Lin, "Type II Seesaw Higgs Triplet as the inflaton for Chaotic Inflation and Leptogenesis," *Phys. Lett.* **B695** (2011) 9–12, arXiv:1009.5727 [hep-ph].

[588] T. Fukuyama, H. Sugiyama, and K. Tsumura, "Constraints from muon g-2 and LFV processes in the Higgs Triplet Model," *JHEP* **03** (2010) 044, arXiv:0909.4943 [hep-ph].

[589] H. Nishiura and T. Fukuyama, "Determination of the unknown absolute neutrino mass and MNS parameters at the LHC in the Higgs triplet model," arXiv:0909.0595 [hep-ph].

[590] H. Nishiura and T. Fukuyama, "Measuring the lower bound of neutrino mass at LHC in Higgs Triplet Model," *Phys. Rev.* **D80** (2009) 017302, arXiv:0905.3963 [hep-ph].

[591] A. G. Akeroyd, M. Aoki, and H. Sugiyama, "Lepton Flavour Violating Decays tau —¿ anti-l ll and mu —¿ e gamma in the Higgs Triplet Model," *Phys. Rev.* **D79** (2009) 113010, arXiv:0904.3640 [hep-ph].

[592] S. T. Petcov, H. Sugiyama, and Y. Takanishi, "Neutrinoless Double Beta Decay and H+- +- —¿ l-prime+- l+- Decays in the Higgs Triplet Model," *Phys. Rev.* **D80** (2009) 015005, arXiv:0904.0759 [hep-ph].

[593] R. Godbole, B. Mukhopadhyaya, and M. Nowakowski, "Triplet Higgs bosons at e+ e- colliders," *Phys. Lett.* **B352** (1995) 388–393, arXiv:hep-ph/9411324 [hep-ph].

[594] I. Gogoladze, N. Okada, and Q. Shafi, "Higgs boson mass bounds in a type II seesaw model with triplet scalars," *Phys. Rev.* **D78** (2008) 085005, arXiv:0802.3257 [hep-ph].

[595] A. G. Akeroyd, M. Aoki, and H. Sugiyama, "Probing Majorana Phases and Neutrino Mass Spectrum in the Higgs Triplet Model at the CERN LHC," *Phys. Rev.* **D77** (2008) 075010, arXiv:0712.4019 [hep-ph].

[596] J. Garayoa and T. Schwetz, "Neutrino mass hierarchy and Majorana CP phases within the Higgs triplet model at the LHC," *JHEP* **03** (2008) 009, arXiv:0712.1453 [hep-ph].

[597] E. Ma and U. Sarkar, "Connecting dark energy to neutrinos with an observable higgs triplet," *Phys. Lett.* **B638** (2006) 356–358, arXiv:hep-ph/0602116 [hep-ph].

[598] C. A. de S. Pires, "Explicitly broken lepton number at low energy in the Higgs triplet model," *Mod. Phys. Lett.* **A21** (2006) 971–978, arXiv:hep-ph/0509152 [hep-ph].

[599] M. Kakizaki, Y. Ogura, and F. Shima, "Lepton flavor violation in the triplet Higgs model," *Phys. Lett.* **B566** (2003) 210–216, arXiv:hep-ph/0304254 [hep-ph].

[600] R. A. Alanakian, "Triplet Higgs bosons production in e- e- collisions," *Phys. Lett.* **B436** (1998) 139–144, arXiv:hep-ph/9706383 [hep-ph].

[601] J. A. Coarasa Perez, A. Mendez, and J. Sola, "Higgs triplet effects in purely leptonic processes," *Phys. Lett.* **B374** (1996) 131–137, arXiv:hep-ph/9511297 [hep-ph].

[602] A. Arhrib, R. Benbrik, G. Moultaka, and L. Rahili, "Type II Seesaw Higgsology and LEP/LHC constraints," arXiv:1411.5645 [hep-ph].

[603] F. Arbabifar, S. Bahrami, and M. Frank, "Neutral Higgs Bosons in the Higgs Triplet Model with nontrivial mixing," *Phys. Rev.* **D87** no. 1, (2013) 015020, arXiv:1211.6797 [hep-ph].

[604] Z.-L. Han, R. Ding, and Y. Liao, "LHC Phenomenology of Type II Seesaw: Nondegenerate Case," *Phys. Rev.* **D91** (2015) 093006, arXiv:1502.05242 [hep-ph].

[605] A. G. Akeroyd and C.-W. Chiang, "Phenomenology of Large Mixing for the CP-even Neutral Scalars of the Higgs Triplet Model," *Phys. Rev.* **D81** (2010) 115007, arXiv:1003.3724 [hep-ph].

[606] A. G. Akeroyd, S. Moretti, and H. Sugiyama, "Five-lepton and six-lepton signatures from production of neutral triplet scalars in the Higgs Triplet Model," *Phys. Rev.* **D85** (2012) 055026, arXiv:1201.5047 [hep-ph].

[607] A. G. Akeroyd and S. Moretti, "Enhancement of $H \to \gamma\gamma$ from charged Higgs bosons in the Higgs Triplet Model," *PoS* **CHARGED2012** (2012) 035, arXiv:1210.6882 [hep-ph].

[608] F. del Águila and M. Chala, "LHC bounds on Lepton Number Violation mediated by doubly and singly-charged scalars," *JHEP* **03** (2014) 027, arXiv:1311.1510 [hep-ph].

[609] J. Cao and J.-F. Shen, "Pair production of doubly charged Higgs boson at photon linear collider in the Higgs triplet model," *Mod. Phys. Lett.* **A29** no. 10, (2014) 1450041.

[610] J. F. Shen and J. Cao, "Pair production of charged and doubly charged Higgs bosons at ILC in the Higgs triplet model," *J. Phys.* **G41** (2014) 105003.

[611] Z.-L. Han, R. Ding, and Y. Liao, "LHC phenomenology of the type II seesaw mechanism: Observability of neutral scalars in the nondegenerate case," *Phys. Rev.* **D92** no. 3, (2015) 033014, arXiv:1506.08996 [hep-ph].

[612] Y.-P. Bi and J.-F. Shen, "Production of singly and doubly charged Higgs bosons at the TeV energy $e^-\gamma$ colliders," *EPL* **110** no. 4, (2015) 41001.

[613] J.-F. Shen, Y.-P. Bi, Y. Yu, and Y.-J. Zhang, "Production of singly and doubly charged Higgs bosons from Higgs triplet model at future linear colliders," *Int. J. Mod. Phys.* **A30** no. 16, (2015) 1550096.

[614] J.-F. Shen and Z.-X. Li, "Doubly charged Higgs bosons pair production through WW fusion at high-energy e^+e^- linear colliders," *EPL* **111** no. 3, (2015) 31001.

[615] J.-F. Shen, Y.-P. Bi, and Z.-X. Li, "Pair production of scalars at the ILC in the Higgs triplet model under the non-degenerate case," *EPL* **112** no. 3, (2015) 31002.

[616] J. Cao and X.-Y. Tian, "Doubly and singly charged Higgs pair production at high-energy e^+e^- linear colliders," *Int. J. Mod. Phys.* **A31** no. 10, (2016) 1650056.

[617] A. Melfo, M. Nemevsek, F. Nesti, G. Senjanovic, and Y. Zhang, "Type II Seesaw at LHC: The Roadmap," *Phys. Rev.* **D85** (2012) 055018, arXiv:1108.4416 [hep-ph].

[618] Z.-z. Xing and J.-y. Zhu, "Leptonic Unitarity Triangles and Effective Mass Triangles of the Majorana Neutrinos," *Nucl. Phys.* **B908** (2016) 302–317, arXiv:1511.00450 [hep-ph].

[619] K. Yagyu, "Testing the Higgs Model with Triplet Fields at the ILC," in *International Workshop on Future Linear Colliders (LCWS11) Granada, Spain, September 26-30, 2011*. 2011. arXiv:1111.5832 [hep-ph]. http://inspirehep.net/record/955203/files/arXiv:1111.5832.pdf.

[620] Z. Kang, J. Li, T. Li, Y. Liu, and G.-Z. Ning, "Light Doubly Charged Higgs Boson via the WW^* Channel at LHC," *Eur. Phys. J.* **C75** no. 12, (2015) 574, arXiv:1404.5207 [hep-ph].

[621] C. Bonilla, J. C. Romão, and J. W. F. Valle, "Electroweak breaking and neutrino mass: 'invisible' Higgs decays at the LHC (type II seesaw)," *New J. Phys.* **18** no. 3, (2016) 033033, arXiv:1511.07351 [hep-ph].

[622] P. Fileviez Perez, T. Han, G.-y. Huang, T. Li, and K. Wang, "Neutrino Masses and the CERN LHC: Testing Type II Seesaw," *Phys. Rev.* **D78** (2008) 015018, arXiv:0805.3536 [hep-ph].

[623] V. D. Barger, H. Baer, W.-Y. Keung, and R. J. N. Phillips, "Decays of Weak Vector Bosons and T Quarks Into Doubly Charged Higgs Scalars," *Phys. Rev.* **D26** (1982) 218.

[624] J. F. Gunion, J. Grifols, A. Mendez, B. Kayser, and F. I. Olness, "Higgs Bosons in Left-Right Symmetric Models," *Phys. Rev.* **D40** (1989) 1546.

[625] T. Han, B. Mukhopadhyaya, Z. Si, and K. Wang, "Pair production of doubly-charged scalars: Neutrino mass constraints and signals at the LHC," *Phys. Rev.* **D76** (2007) 075013, arXiv:0706.0441 [hep-ph].

[626] K. Huitu, J. Maalampi, A. Pietila, and M. Raidal, "Doubly charged Higgs at LHC," *Nucl. Phys.* **B487** (1997) 27–42, arXiv:hep-ph/9606311 [hep-ph].

[627] B. Dion, T. Gregoire, D. London, L. Marleau, and H. Nadeau, "Bilepton production at hadron colliders," *Phys. Rev.* **D59** (1999) 075006, arXiv:hep-ph/9810534 [hep-ph].

[628] P. S. B. Dev, C. M. Vila, and W. Rodejohann, "Naturalness in testable type II seesaw scenarios," *Nucl. Phys.* **B921** (2017) 436–453, arXiv:1703.00828 [hep-ph].

[629] Y. Sui and Y. Zhang, "Prospects of type-II seesaw at future colliders in light of the DAMPE e^+e^- excess," arXiv:1712.03642 [hep-ph].

[630] P. Agrawal, M. Mitra, S. Niyogi, S. Shil, and M. Spannowsky, "Probing the Type-II Seesaw Mechanism through the Production of Higgs Bosons at a Lepton Collider," arXiv:1803.00677 [hep-ph].

[631] Y. Cai, T. Han, T. Li, and R. Ruiz, "Lepton-Number Violation: Seesaw Models and Their Collider Tests," arXiv:1711.02180 [hep-ph].

[632] T. Li, "Type II Seesaw and tau lepton at the HL-LHC, HE-LHC and FCC-hh," arXiv:1802.00945 [hep-ph].

[633] P.-H. Gu and H.-J. He, "TeV Scale Neutrino Mass Generation, Minimal Inelastic Dark Matter, and High Scale Leptogenesis," *Phys. Rev. D* **99** no. 1, (2019) 015025, arXiv:1808.09377 [hep-ph].

[634] K. Babu and S. Jana, "Probing Doubly Charged Higgs Bosons at the LHC through Photon Initiated Processes," *Phys. Rev. D* **95** no. 5, (2017) 055020, arXiv:1612.09224 [hep-ph].

[635] **ATLAS** Collaboration, G. Aad *et al.*, "Search for anomalous production of prompt like-sign muon pairs and constraints on physics beyond the Standard Model with the ATLAS detector," *Phys. Rev.* **D85** (2012) 032004, arXiv:1201.1091 [hep-ex].

[636] **CDF** Collaboration, T. Aaltonen *et al.*, "Search for new physics in high p_T like-sign dilepton events at CDF II," *Phys. Rev. Lett.* **107** (2011) 181801, arXiv:1108.0101 [hep-ex].

[637] **ATLAS** Collaboration, G. Aad *et al.*, "Search for anomalous production of prompt like-sign lepton pairs at $\sqrt{s} = 7$ TeV with the ATLAS detector," *JHEP* **12** (2012) 007, arXiv:1210.4538 [hep-ex].

[638] **ATLAS** Collaboration, G. Aad *et al.*, "Search for doubly-charged Higgs bosons in like-sign dilepton final states at $\sqrt{s} = 7$ TeV with the ATLAS detector," *Eur. Phys. J.* **C72** (2012) 2244, arXiv:1210.5070 [hep-ex].

[639] **ATLAS** Collaboration, G. Aad *et al.*, "Search for new phenomena in events with three or more charged leptons in pp collisions at $\sqrt{s} = 8$ TeV with the ATLAS detector," *JHEP* **08** (2015) 138, arXiv:1411.2921 [hep-ex].

[640] **ATLAS** Collaboration, G. Aad *et al.*, "Search for heavy long-lived multi-charged particles in pp collisions at $\sqrt{s} =$ 8 TeV using the ATLAS detector," *Eur. Phys. J.* **C75** (2015) 362, arXiv:1504.04188 [hep-ex].

[641] **CMS** Collaboration, A. M. Sirunyan *et al.*, "Observation of electroweak production of same-sign W boson pairs in the two jet and two same-sign lepton final state in proton-proton collisions at $\sqrt{s} = 13$ TeV," *Phys. Rev. Lett.* **120** no. 8, (2018) 081801, arXiv:1709.05822 [hep-ex].

[642] A. Arhrib, R. Benbrik, M. Chabab, G. Moultaka, M. C. Peyranere, L. Rahili, and J. Ramadan, "The Higgs Potential in the Type II Seesaw Model," *Phys. Rev.* **D84** (2011) 095005, arXiv:1105.1925 [hep-ph].

[643] P. Dey, A. Kundu, and B. Mukhopadhyaya, "Some consequences of a Higgs triplet," *J. Phys.* **G36** (2009) 025002, arXiv:0802.2510 [hep-ph].

[644] W. Chao and H. Zhang, "One-loop renormalization group equations of the neutrino mass matrix in the triplet seesaw model," *Phys. Rev.* **D75** (2007) 033003, arXiv:hep-ph/0611323 [hep-ph].

[645] M. A. Schmidt, "Renormalization group evolution in the type I+ II seesaw model," *Phys. Rev.* **D76** (2007) 073010, arXiv:0705.3841 [hep-ph]. [Erratum: Phys. Rev.D85,099903(2012)].

[646] M. E. Machacek and M. T. Vaughn, "Two Loop Renormalization Group Equations in a General Quantum Field Theory. 1. Wave Function Renormalization," *Nucl. Phys.* **B222** (1983) 83–103.

[647] M. E. Machacek and M. T. Vaughn, "Two Loop Renormalization Group Equations in a General Quantum Field Theory. 2. Yukawa Couplings," *Nucl. Phys.* **B236** (1984) 221–232.

[648] M. E. Machacek and M. T. Vaughn, "Two Loop Renormalization Group Equations in a General Quantum Field Theory. 3. Scalar Quartic Couplings," *Nucl. Phys.* **B249** (1985) 70–92.

[649] C. Ford, I. Jack, and D. R. T. Jones, "The Standard model effective potential at two loops," *Nucl. Phys.* **B387** (1992) 373–390, arXiv:hep-ph/0111190 [hep-ph]. [Erratum: Nucl. Phys.B504,551(1997)].

[650] H. Arason, D. J. Castano, B. Keszthelyi, S. Mikaelian, E. J. Piard, P. Ramond, and B. D. Wright, "Renormalization group study of the standard model and its extensions. 1. The Standard model," *Phys. Rev.* **D46** (1992) 3945–3965.

[651] V. D. Barger, M. S. Berger, and P. Ohmann, "Supersymmetric grand unified theories: Two loop evolution of gauge and Yukawa couplings," *Phys. Rev.* **D47** (1993) 1093–1113, arXiv:hep-ph/9209232 [hep-ph].

[652] M.-x. Luo and Y. Xiao, "Two loop renormalization group equations in the standard model," *Phys. Rev. Lett.* **90** (2003) 011601, arXiv:hep-ph/0207271 [hep-ph].

[653] M. Gonderinger, H. Lim, and M. J. Ramsey-Musolf, "Complex Scalar Singlet Dark Matter: Vacuum Stability and Phenomenology," *Phys. Rev.* **D86** (2012) 043511, arXiv:1202.1316 [hep-ph].

[654] K. Riesselmann and S. Willenbrock, "Ruling out a strongly interacting standard Higgs model," *Phys. Rev.* **D55** (1997) 311–321, arXiv:hep-ph/9608280 [hep-ph].

[655] T. Hambye and K. Riesselmann, "Matching conditions and Higgs mass upper bounds revisited," *Phys. Rev.* **D55** (1997) 7255–7262, arXiv:hep-ph/9610272 [hep-ph].

[656] A. Alloul, N. D. Christensen, C. Degrande, C. Duhr, and B. Fuks, "FeynRules 2.0 - A complete toolbox for tree-level phenomenology," *Comput. Phys. Commun.* **185** (2014) 2250–2300, arXiv:1310.1921 [hep-ph].

[657] N. D. Christensen and C. Duhr, "FeynRules - Feynman rules made easy," *Comput. Phys. Commun.* **180** (2009) 1614–1641, arXiv:0806.4194 [hep-ph].

[658] C. Degrande, C. Duhr, B. Fuks, D. Grellscheid, O. Mattelaer, and T. Reiter, "UFO - The Universal FeynRules Output," *Comput. Phys. Commun.* **183** (2012) 1201–1214, arXiv:1108.2040 [hep-ph].

[659] J. Alwall, R. Frederix, S. Frixione, V. Hirschi, F. Maltoni, O. Mattelaer, H. S. Shao, T. Stelzer, P. Torrielli, and M. Zaro, "The automated computation of tree-level and next-to-leading order differential cross sections, and their matching to parton shower simulations," *JHEP* **07** (2014) 079, arXiv:1405.0301 [hep-ph].

[660] **ATLAS** Collaboration, M. Aaboud *et al.*, "Search for charged Higgs bosons produced in association with a top quark and decaying via $H^{\pm} \to \tau\nu$ using pp collision data recorded at $\sqrt{s} = 13$ TeV by the ATLAS detector," *Phys. Lett.* **B759** (2016) 555–574, arXiv:1603.09203 [hep-ex].

[661] **CMS** Collaboration, A. M. Sirunyan *et al.*, "Search for Charged Higgs Bosons Produced via Vector Boson Fusion and Decaying into a Pair of W and Z Bosons Using pp Collisions at $\sqrt{s} = 13$ TeV," *Phys. Rev. Lett.* **119** no. 14, (2017) 141802, arXiv:1705.02942 [hep-ex].

[662] **CMS** Collaboration, V. Khachatryan *et al.*, "Search for neutral resonances decaying into a Z boson and a pair of b jets or τ leptons," *Phys. Lett.* **B759** (2016) 369–394, arXiv:1603.02991 [hep-ex].

[663] T. Sjostrand, S. Mrenna, and P. Z. Skands, "PYTHIA 6.4 Physics and Manual," *JHEP* **05** (2006) 026, arXiv:hep-ph/0603175 [hep-ph].

[664] **DELPHES 3** Collaboration, J. de Favereau, C. Delaere, P. Demin, A. Giammanco, V. Lemaître, A. Mertens, and M. Selvaggi, "DELPHES 3, A modular framework for fast simulation of a generic collider experiment," *JHEP* **02** (2014) 057, arXiv:1307.6346 [hep-ex].

[665] https://github.com/delphes/delphes/tree/master/cards/FCC.

[666] I. Antcheva *et al.*, "ROOT: A C++ framework for petabyte data storage, statistical analysis and visualization," *Comput. Phys. Commun.* **180** (2009) 2499–2512, arXiv:1508.07749 [physics.data-an].

[667] A. Hocker *et al.*, "TMVA - Toolkit for Multivariate Data Analysis," *PoS ACAT* **040** (2007) , arXiv:physics/0703039.

[668] B. P. Roe, H.-J. Yang, J. Zhu, Y. Liu, I. Stancu, and G. McGregor, "Boosted decision trees, an alternative to artificial neural networks," *Nucl. Instrum. Meth.* **A543** no. 2-3, (2005) 577–584, arXiv:physics/0408124 [physics].

[669] https://fcc.web.cern.ch/Pages/default.aspx, FCC official website.

[670] M. Benedikt and F. Zimmermann. http://cerncourier.com/cws/article/cern/56603, CERN Courier 2014.

[671] A. Arhrib, R. Benbrik, M. Chabab, G. Moultaka, and L. Rahili, "Higgs boson decay into 2 photons in the type II Seesaw Model," *JHEP* **04** (2012) 136, arXiv:1112.5453 [hep-ph].

[672] **ATLAS, CMS** Collaboration, G. Aad *et al.*, "Measurements of the Higgs boson production and decay rates and constraints on its couplings from a combined ATLAS and CMS analysis of the LHC pp collision data at $\sqrt{s} = 7$ and 8 TeV," *JHEP* **08** (2016) 045, arXiv:1606.02266 [hep-ex].

[673] R. Contino *et al.*, "Physics at a 100 TeV pp collider: Higgs and EW symmetry breaking studies," *CERN Yellow Rep.* no. 3, (2017) 255–440, arXiv:1606.09408 [hep-ph].

[674] M. Cirelli, N. Fornengo, and A. Strumia, "Minimal dark matter," *Nucl. Phys.* **B753** (2006) 178–194, arXiv:hep-ph/0512090 [hep-ph].

[675] P. B. Pal, "COLD DARK MATTER IN THE DOUBLET - TRIPLET MODEL," *Phys. Lett.* **B205** (1988) 65–68.

[676] T. Hambye, F. S. Ling, L. Lopez Honorez, and J. Rocher, "Scalar Multiplet Dark Matter," *JHEP* **07** (2009) 090, arXiv:0903.4010 [hep-ph]. [Erratum: JHEP05,066(2010)].

[677] O. Fischer and J. J. van der Bij, "The scalar Singlet-Triplet Dark Matter Model," *JCAP* **1401** (2014) 032, arXiv:1311.1077 [hep-ph].

[678] F.-X. Josse-Michaux and E. Molinaro, "Triplet scalar dark matter and leptogenesis in an inverse seesaw model of neutrino mass generation," *Phys. Rev.* **D87** no. 3, (2013) 036007, arXiv:1210.7202 [hep-ph].

[679] T. Basak and S. Mohanty, "Triplet-Singlet Extension of the MSSM with a 125 GeV Higgs and Dark Matter," *Phys. Rev.* **D86** (2012) 075031, arXiv:1204.6592 [hep-ph].

[680] T. Araki, C. Q. Geng, and K. I. Nagao, "Dark Matter in Inert Triplet Models," *Phys. Rev.* **D83** (2011) 075014, arXiv:1102.4906 [hep-ph].

[681] S. S. AbdusSalam and T. A. Chowdhury, "Scalar Representations in the Light of Electroweak Phase Transition and Cold Dark Matter Phenomenology," *JCAP* **1405** (2014) 026, arXiv:1310.8152 [hep-ph].

[682] W.-B. Lu and P.-H. Gu, "Mixed Inert Scalar Triplet Dark Matter, Radiative Neutrino Masses and Leptogenesis," *Nucl. Phys.* **B924** (2017) 279–311, arXiv:1611.02106 [hep-ph].

[683] W. Chao, G.-J. Ding, X.-G. He, and M. Ramsey-Musolf, "Scalar Electroweak Multiplet Dark Matter," *JHEP* **08** (2019) 058, arXiv:1812.07829 [hep-ph].

[684] T. Abe, R. Kitano, and R. Sato, "Discrimination of dark matter models in future experiments," *Phys. Rev.* **D91** no. 9, (2015) 095004, arXiv:1411.1335 [hep-ph]. [Erratum: Phys. Rev.D96,no.1,019902(2017)].

[685] M. Cirelli, F. Sala, and M. Taoso, "Wino-like Minimal Dark Matter and future colliders," *JHEP* **10** (2014) 033, arXiv:1407.7058 [hep-ph]. [Erratum: JHEP01,041(2015)].

[686] K. Harigaya, K. Ichikawa, A. Kundu, S. Matsumoto, and S. Shirai, "Indirect Probe of Electroweak-Interacting Particles at Future Lepton Colliders," *JHEP* **09** (2015) 105, arXiv:1504.03402 [hep-ph].

[687] S. Matsumoto, S. Shirai, and M. Takeuchi, "Indirect Probe of Electroweakly Interacting Particles at the High-Luminosity Large Hadron Collider," *JHEP* **06** (2018) 049, arXiv:1711.05449 [hep-ph].

[688] M. Cirelli and A. Strumia, "Minimal Dark Matter: Model and results," *New J. Phys.* **11** (2009) 105005, arXiv:0903.3381 [hep-ph].

[689] Q.-H. Cao, T. Gong, K.-P. Xie, and Z. Zhang, "Measuring Relic Abundance of Minimal Dark Matter at Hadron Colliders," *Sci. China Phys. Mech. Astron.* **62** no. 8, (2019) 981011, arXiv:1810.07658 [hep-ph].

[690] L. Di Luzio, R. Gröber, and G. Panico, "Probing new electroweak states via precision measurements at the LHC and future colliders," *JHEP* **01** (2019) 011, arXiv:1810.10993 [hep-ph].

[691] C.-K. Chua and R.-C. Hsieh, "Study of Dirac fermionic dark matter," *Phys. Rev.* **D88** no. 3, (2013) 036011, arXiv:1305.7008 [hep-ph].

[692] K. Kadota and A. Spray, "Electroweak Multiplet Dark Matter at Future Lepton Colliders," *JHEP* **02** (2019) 017, arXiv:1811.00560 [hep-ph].

[693] M. Cirelli, T. Hambye, P. Panci, F. Sala, and M. Taoso, "Gamma ray tests of Minimal Dark Matter," *JCAP* **1510** no. 10, (2015) 026, arXiv:1507.05519 [hep-ph].

[694] C. Cai, Z.-H. Yu, and H.-H. Zhang, "CEPC Precision of Electroweak Oblique Parameters and Weakly Interacting Dark Matter: the Scalar Case," *Nucl. Phys.* **B924** (2017) 128–152, arXiv:1705.07921 [hep-ph].

[695] C. Cai, Z.-M. Huang, Z. Kang, Z.-H. Yu, and H.-H. Zhang, "Perturbativity Limits for Scalar Minimal Dark Matter with Yukawa Interactions: Septuplet," *Phys. Rev.* **D92** no. 11, (2015) 115004, arXiv:1510.01559 [hep-ph].

[696] Q.-F. Xiang, X.-J. Bi, P.-F. Yin, and Z.-H. Yu, "Exploring Fermionic Dark Matter via Higgs Boson Precision Measurements at the Circular Electron Positron Collider," *Phys. Rev.* **D97** no. 5, (2018) 055004, arXiv:1707.03094 [hep-ph].

[697] S. Chigusa, Y. Ema, and T. Moroi, "Probing electroweakly interacting massive particles with Drell–Yan process at 100 TeV hadron colliders," *Phys. Lett.* **B789** (2019) 106–113, arXiv:1810.07349 [hep-ph].

[698] S. Matsumoto, S. Shirai, and M. Takeuchi, "Indirect Probe of Electroweak-Interacting Particles with Mono-Lepton Signatures at Hadron Colliders," *JHEP* **03** (2019) 076, arXiv:1810.12234 [hep-ph].

[699] W. Kuramoto, T. Kuwahara, and R. Nagai, "Renormalization Effects on Electric Dipole Moments in Electroweakly Interacting Massive Particle Models," *Phys. Rev.* **D99** no. 9, (2019) 095024, arXiv:1902.05360 [hep-ph].

[700] T. Abe, S. Chigusa, Y. Ema, and T. Moroi, "Indirect studies of electroweakly interacting particles at 100 TeV hadron colliders," *Phys. Rev.* **D100** no. 5, (2019) 055018, arXiv:1904.11162 [hep-ph].

[701] M. Ibe, S. Matsumoto, and R. Sato, "Mass Splitting between Charged and Neutral Winos at Two-Loop Level," *Phys. Lett. B* **721** (2013) 252–260, arXiv:1212.5989 [hep-ph].

[702] R. Mahbubani, P. Schwaller, and J. Zurita, "Closing the window for compressed Dark Sectors with disappearing charged tracks," *JHEP* **06** (2017) 119, arXiv:1703.05327 [hep-ph]. [Erratum: JHEP10,061(2017)].

[703] T. Han, S. Mukhopadhyay, and X. Wang, "Electroweak Dark Matter at Future Hadron Colliders," *Phys. Rev.* **D98** no. 3, (2018) 035026, arXiv:1805.00015 [hep-ph].

[704] M. Saito, R. Sawada, K. Terashi, and S. Asai, "Discovery reach for wino and higgsino dark matter with a disappearing track signature at a 100 TeV *pp* collider," *Eur. Phys. J.* **C79** no. 6, (2019) 469, arXiv:1901.02987 [hep-ph].

[705] H. Fukuda, N. Nagata, H. Otono, and S. Shirai, "Higgsino Dark Matter or Not: Role of Disappearing Track Searches at the LHC and Future Colliders," *Phys. Lett.* **B781** (2018) 306–311, arXiv:1703.09675 [hep-ph].

[706] **CMS** Collaboration, V. Khachatryan *et al.*, "Search for long-lived charged particles in proton-proton collisions at $\sqrt{s} = 13$ TeV," *Phys. Rev.* **D94** no. 11, (2016) 112004, arXiv:1609.08382 [hep-ex].

[707] J. Alimena *et al.*, "Searching for Long-Lived Particles beyond the Standard Model at the Large Hadron Collider," arXiv:1903.04497 [hep-ex].

[708] M. J. Ramsey-Musolf, "The Electroweak Phase Transition: A Collider Target," arXiv:1912.07189 [hep-ph].

[709] B. Fuks, M. Klasen, D. R. Lamprea, and M. Rothering, "Revisiting slepton pair production at the Large Hadron Collider," *JHEP* **01** (2014) 168, arXiv:1310.2621 [hep-ph].

[710] J. Fiaschi, M. Klasen, and M. Sunder, "Slepton pair production with aNNLO+NNLL precision," arXiv:1911.02419 [hep-ph].

[711] D. Egana-Ugrinovic, M. Low, and J. T. Ruderman, "Charged Fermions Below 100 GeV," *JHEP* **05** (2018) 012, arXiv:1801.05432 [hep-ph].

[712] LEPSUSYWG, "Combined lep chargino results, up to 208 gev for low dm." http://lepsusy.web.cern.ch/lepsusy/www/inoslowdmsummer02/charginolowdm_pub.html.

[713] M. J. Dolan, C. Englert, and M. Spannowsky, "New Physics in LHC Higgs boson pair production," *Phys. Rev.* **D87** no. 5, (2013) 055002, arXiv:1210.8166 [hep-ph].

[714] T. Sjöstrand, S. Ask, J. R. Christiansen, R. Corke, N. Desai, P. Ilten, S. Mrenna, S. Prestel, C. O. Rasmussen, and P. Z. Skands, "An Introduction to PYTHIA 8.2," *Comput. Phys. Commun.* **191** (2015) 159–177, arXiv:1410.3012 [hep-ph].

[715] M. Cacciari, G. P. Salam, and G. Soyez, "FastJet User Manual," *Eur. Phys. J.* **C72** (2012) 1896, arXiv:1111.6097 [hep-ph].

[716] M. L. Mangano, M. Moretti, F. Piccinini, and M. Treccani, "Matching matrix elements and shower evolution for top-quark production in hadronic collisions," *JHEP* **01** (2007) 013, arXiv:hep-ph/0611129 [hep-ph].

[717] G. Bélanger *et al.*, "LHC-friendly minimal freeze-in models," *JHEP* **02** (2019) 186, arXiv:1811.05478 [hep-ph].

[718] K. Griest and D. Seckel, "Three exceptions in the calculation of relic abundances," *Phys. Rev.* **D43** (1991) 3191–3203.

[719] S. Mizuta and M. Yamaguchi, "Coannihilation effects and relic abundance of Higgsino dominant LSP(s)," *Phys. Lett.* **B298** (1993) 120–126, arXiv:hep-ph/9208251 [hep-ph].

[720] J. Edsjo and P. Gondolo, "Neutralino relic density including coannihilations," *Phys. Rev.* **D56** (1997) 1879–1894, arXiv:hep-ph/9704361 [hep-ph].

[721] A. Semenov, "LanHEP — A package for automatic generation of Feynman rules from the Lagrangian. Version 3.2," *Comput. Phys. Commun.* **201** (2016) 167–170, arXiv:1412.5016 [physics.comp-ph].

[722] A. Belyaev, N. D. Christensen, and A. Pukhov, "CalcHEP 3.4 for collider physics within and beyond the Standard Model," *Comput. Phys. Commun.* **184** (2013) 1729–1769, arXiv:1207.6082 [hep-ph].

[723] J. Hisano, S. Matsumoto, M. Nagai, O. Saito, and M. Senami, "Non-perturbative effect on thermal relic abundance of dark matter," *Phys. Lett.* **B646** (2007) 34–38, arXiv:hep-ph/0610249 [hep-ph].

[724] B. von Harling and K. Petraki, "Bound-state formation for thermal relic dark matter and unitarity," *JCAP* **12** (2014) 033, arXiv:1407.7874 [hep-ph].

[725] H. An, M. B. Wise, and Y. Zhang, "Effects of Bound States on Dark Matter Annihilation," *Phys. Rev. D* **93** no. 11, (2016) 115020, arXiv:1604.01776 [hep-ph].

[726] M. Cirelli, P. Panci, K. Petraki, F. Sala, and M. Taoso, "Dark Matter's secret liaisons: phenomenology of a dark U(1) sector with bound states," *JCAP* **05** (2017) 036, arXiv:1612.07295 [hep-ph].

[727] A. Mitridate, M. Redi, J. Smirnov, and A. Strumia, "Cosmological Implications of Dark Matter Bound States," *JCAP* **05** (2017) 006, arXiv:1702.01141 [hep-ph].

[728] J. D. March-Russell and S. M. West, "WIMPonium and Boost Factors for Indirect Dark Matter Detection," *Phys. Lett. B* **676** (2009) 133–139, arXiv:0812.0559 [astro-ph].

[729] P. Asadi, M. Baumgart, P. J. Fitzpatrick, E. Krupczak, and T. R. Slatyer, "Capture and Decay of Electroweak WIMPonium," *JCAP* **02** (2017) 005, arXiv:1610.07617 [hep-ph].

[730] W. Shepherd, T. M. Tait, and G. Zaharijas, "Bound states of weakly interacting dark matter," *Phys. Rev. D* **79** (2009) 055022, arXiv:0901.2125 [hep-ph].

[731] E. Braaten, E. Johnson, and H. Zhang, "Zero-range effective field theory for resonant wino dark matter. Part I. Framework," *JHEP* **11** (2017) 108, arXiv:1706.02253 [hep-ph].

[732] E. Braaten, E. Johnson, and H. Zhang, "Zero-range effective field theory for resonant wino dark matter. Part II. Coulomb resummation," *JHEP* **02** (2018) 150, arXiv:1708.07155 [hep-ph].

[733] E. Braaten, E. Johnson, and H. Zhang, "Zero-range effective field theory for resonant wino dark matter. Part III. Annihilation effects," *JHEP* **05** (2018) 062, arXiv:1712.07142 [hep-ph].

[734] J. Smirnov and J. F. Beacom, "TeV-Scale Thermal WIMPs: Unitarity and its Consequences," *Phys. Rev. D* **100** no. 4, (2019) 043029, arXiv:1904.11503 [hep-ph].

[735] M. Drees and M. Nojiri, "Neutralino - nucleon scattering revisited," *Phys. Rev.* **D48** (1993) 3483–3501, arXiv:hep-ph/9307208 [hep-ph].

[736] J. Hisano, K. Ishiwata, and N. Nagata, "A complete calculation for direct detection of Wino dark matter," *Phys. Lett.* **B690** (2010) 311–315, arXiv:1004.4090 [hep-ph].

[737] J. Hisano, K. Ishiwata, N. Nagata, and T. Takesako, "Direct Detection of Electroweak-Interacting Dark Matter," *JHEP* **07** (2011) 005, arXiv:1104.0228 [hep-ph].

[738] J. Hisano, D. Kobayashi, N. Mori, and E. Senaha, "Effective Interaction of Electroweak-Interacting Dark Matter with Higgs Boson and Its Phenomenology," *Phys. Lett.* **B742** (2015) 80–85, arXiv:1410.3569 [hep-ph].

[739] R. J. Hill and M. P. Solon, "Standard Model anatomy of WIMP dark matter direct detection I: weak-scale matching," *Phys. Rev.* **D91** (2015) 043504, arXiv:1401.3339 [hep-ph].

[740] R. J. Hill and M. P. Solon, "Standard Model anatomy of WIMP dark matter direct detection II: QCD analysis and hadronic matrix elements," *Phys. Rev.* **D91** (2015) 043505, arXiv:1409.8290 [hep-ph].

[741] J. Hisano, K. Ishiwata, and N. Nagata, "QCD Effects on Direct Detection of Wino Dark Matter," *JHEP* **06** (2015) 097, arXiv:1504.00915 [hep-ph].

[742] N. Khan, "Exploring the hyperchargeless Higgs triplet model up to the Planck scale," *Eur. Phys. J.* **C78** no. 4, (2018) 341, arXiv:1610.03178 [hep-ph].

[743] M. Chabab, M. C. Peyranère, and L. Rahili, "Probing the Higgs sector of $Y = 0$ Higgs Triplet Model at LHC," *Eur. Phys. J.* **C78** no. 10, (2018) 873, arXiv:1805.00286 [hep-ph].

[744] **MOLLER** Collaboration, J. Mammei, "The MOLLER Experiment," *Nuovo Cim.* **C035N04** (2012) 203–208, arXiv:1208.1260 [hep-ex].

[745] A. Czarnecki and W. J. Marciano, "Parity violating asymmetries at future lepton colliders," *Int. J. Mod. Phys.* **A13** (1998) 2235–2244, arXiv:hep-ph/9801394 [hep-ph].

[746] P. S. B. Dev, M. J. Ramsey-Musolf, and Y. Zhang, "Doubly-Charged Scalars in the Type-II Seesaw Mechanism: Fundamental Symmetry Tests and High-Energy Searches," *Phys. Rev.* **D98** no. 5, (2018) 055013, arXiv:1806.08499 [hep-ph].

[747] H. Davoudiasl, H.-S. Lee, and W. J. Marciano, "Muon Anomaly and Dark Parity Violation," *Phys. Rev. Lett.* **109** (2012) 031802, arXiv:1205.2709 [hep-ph].

[748] H. Davoudiasl, H.-S. Lee, and W. J. Marciano, "Muon g?2, rare kaon decays, and parity violation from dark bosons," *Phys. Rev.* **D89** no. 9, (2014) 095006, arXiv:1402.3620 [hep-ph].

[749] H. Davoudiasl, H.-S. Lee, and W. J. Marciano, "Low Q^2 weak mixing angle measurements and rare Higgs decays," *Phys. Rev.* **D92** no. 5, (2015) 055005, arXiv:1507.00352 [hep-ph].

[750] A. Czarnecki and W. J. Marciano, "Electroweak radiative corrections to polarized Moller scattering asymmetries," *Phys. Rev.* **D53** (1996) 1066–1072, arXiv:hep-ph/9507420 [hep-ph].

[751] A. G. Aleksejevs, S. G. Barkanova, Y. M. Bystritskiy, A. N. Ilyichev, E. A. Kuraev, and V. A. Zykunov, "Double-box contributions to Moeller scattering in the standard model," *Eur. Phys. J.* **C72** (2012) 2249.

[752] R.-D. Bucoveanu and H. Spiesberger, "QED radiative corrections for Polarized Lepton-Proton Scattering," *PoS* **SPIN2018** (2019) 115, arXiv:1903.12229 [hep-ph].

[753] V. A. Smirnov, *Analytic tools for Feynman integrals*, vol. 250. 2012.

[754] V. A. Smirnov, "Evaluating Feynman integrals," *Springer Tracts Mod. Phys.* **211** (2004) 1–244.

[755] V. A. Smirnov, "Applied asymptotic expansions in momenta and masses," *Springer Tracts Mod. Phys.* **177** (2002) 1–262.

[756] A. V. Smirnov, "FIRE5: a C++ implementation of Feynman Integral REduction," *Comput. Phys. Commun.* **189** (2015) 182–191, arXiv:1408.2372 [hep-ph].

[757] R. N. Lee, "LiteRed 1.4: a powerful tool for reduction of multiloop integrals," *J. Phys. Conf. Ser.* **523** (2014) 012059, arXiv:1310.1145 [hep-ph].

[758] C. Anastasiou and A. Lazopoulos, "Automatic integral reduction for higher order perturbative calculations," *JHEP* **07** (2004) 046, arXiv:hep-ph/0404258.

[759] C. Studerus, "Reduze-Feynman Integral Reduction in C++," *Comput. Phys. Commun.* **181** (2010) 1293–1300, arXiv:0912.2546 [physics.comp-ph].

[760] R. Mertig and R. Scharf, "TARCER: A Mathematica program for the reduction of two loop propagator integrals," *Comput. Phys. Commun.* **111** (1998) 265–273, arXiv:hep-ph/9801383.

[761] R. Cutkosky, "Singularities and discontinuities of Feynman amplitudes," *J. Math. Phys.* **1** (1960) 429–433.

[762] B. A. Kniehl, "Dispersion relations in loop calculations," *Acta Phys. Polon. B* **27** (1996) 3631–3644, arXiv:hep-ph/9607255.

[763] S. Bauberger, F. A. Berends, M. Bohm, and M. Buza, "Analytical and numerical methods for massive two loop selfenergy diagrams," *Nucl. Phys.* **B434** (1995) 383–407, arXiv:hep-ph/9409388 [hep-ph].

[764] G. 't Hooft and M. J. G. Veltman, "Scalar One Loop Integrals," *Nucl. Phys.* **B153** (1979) 365–401.

[765] A. Denner, "Techniques for calculation of electroweak radiative corrections at the one loop level and results for W physics at LEP-200," *Fortsch. Phys.* **41** (1993) 307–420, arXiv:0709.1075 [hep-ph].

[766] A. Freitas, W. Hollik, W. Walter, and G. Weiglein, "Electroweak two loop corrections to the $M_W - M_Z$ mass correlation in the standard model," *Nucl. Phys.* **B632** (2002) 189–218, arXiv:hep-ph/0202131 [hep-ph]. [Erratum: Nucl. Phys.B666,305(2003)].

[767] A. Sirlin, "A Class of Useful Identities Involving Correlated Direct Products of γ Matrices," *Nucl. Phys.* **B192** (1981) 93–99.

[768] A. Denner, S. Dittmaier, M. Roth, and L. H. Wieders, "Electroweak corrections to charged-current e+ e- —¿ 4 fermion processes: Technical details and further results," *Nucl. Phys.* **B724** (2005) 247–294, arXiv:hep-ph/0505042 [hep-ph]. [Erratum: Nucl. Phys.B854,504(2012)].

[769] M. Beneke and V. A. Smirnov, "Asymptotic expansion of Feynman integrals near threshold," *Nucl. Phys.* **B522** (1998) 321–344, arXiv:hep-ph/9711391 [hep-ph].

[770] V. A. Smirnov, "Problems of the strategy of regions," *Phys. Lett.* **B465** (1999) 226–234, arXiv:hep-ph/9907471 [hep-ph].

[771] W. Beenakker and A. Denner, "Infrared Divergent Scalar Box Integrals With Applications in the Electroweak Standard Model," *Nucl. Phys.* **B338** (1990) 349–370.

[772] A. I. Davydychev and J. B. Tausk, "Two loop selfenergy diagrams with different masses and the momentum expansion," *Nucl. Phys.* **B397** (1993) 123–142.

[773] M. Awramik, M. Czakon, and A. Freitas, "Electroweak two-loop corrections to the effective weak mixing angle," *JHEP* **11** (2006) 048, arXiv:hep-ph/0608099 [hep-ph].

[774] A. Aleksejevs, "Dispersion Approach in Two-Loop Calculations," *Phys. Rev.* **D98** no. 3, (2018) 036021, arXiv:1804.08914 [hep-th].

[775] W. J. Marciano, "Spin and precision electroweak physics," in *Spin structure in high-energy processes: Proceedings, 21st SLAC Summer Institute on Particle Physics, 26 Jul - 6 Aug 1993, Stanford, CA*, L. DePorcel and C. Dunwoodie,

eds. 1995. http://www.slac.stanford.edu/spires/find/books/www?cl=QCD161:S76:1993.

[776] F. Jegerlehner, "Variations on Photon Vacuum Polarization," arXiv:1711.06089 [hep-ph].

[777] A. Freitas, W. Hollik, W. Walter, and G. Weiglein, "Complete fermionic two loop results for the M(W) - M(Z) interdependence," *Phys. Lett.* **B495** (2000) 338–346, arXiv:hep-ph/0007091 [hep-ph]. [Erratum: Phys. Lett.B570,no.3-4,265(2003)].

[778] M. Awramik and M. Czakon, "Complete two loop electroweak contributions to the muon lifetime in the standard model," *Phys. Lett.* **B568** (2003) 48–54, arXiv:hep-ph/0305248 [hep-ph].

[779] T. Hahn, "Generating Feynman diagrams and amplitudes with FeynArts 3," *Comput. Phys. Commun.* **140** (2001) 418–431, arXiv:hep-ph/0012260 [hep-ph].

[780] H. H. Patel, "Package-X: A Mathematica package for the analytic calculation of one-loop integrals," *Comput. Phys. Commun.* **197** (2015) 276–290, arXiv:1503.01469 [hep-ph].

[781] G. Weiglein, R. Scharf, and M. Bohm, "Reduction of general two loop selfenergies to standard scalar integrals," *Nucl. Phys.* **B416** (1994) 606–644, arXiv:hep-ph/9310358 [hep-ph].

[782] A. I. Davydychev and J. B. Tausk, "Tensor reduction of two loop vacuum diagrams and projectors for expanding three point functions," *Nucl. Phys.* **B465** (1996) 507–520, arXiv:hep-ph/9511261 [hep-ph].

[783] M. Davier, A. Hoecker, B. Malaescu, and Z. Zhang, "A new evaluation of the hadronic vacuum polarisation contributions to the muon anomalous magnetic moment and to $\boldsymbol{\alpha(m_Z^2)}$," arXiv:1908.00921 [hep-ph].

[784] A. Keshavarzi, D. Nomura, and T. Teubner, "The $g-2$ of charged leptons, $\alpha(M_Z^2)$ and the hyperfine splitting of muonium," arXiv:1911.00367 [hep-ph].

[785] M. Steinhauser, "Leptonic contribution to the effective electromagnetic coupling constant up to three loops," *Phys. Lett.* **B429** (1998) 158–161, arXiv:hep-ph/9803313 [hep-ph].

[786] W. Marciano and A. Sirlin, "On Some General Properties of the O(alpha) Corrections to Parity Violation in Atoms," *Phys. Rev. D* **29** (1984) 75. [Erratum: Phys.Rev.D 31, 213 (1985)].

[787] **LIGO Scientific, Virgo** Collaboration, B. Abbott *et al.*, "Observation of Gravitational Waves from a Binary Black Hole Merger," *Phys. Rev. Lett.* **116** no. 6, (2016) 061102, arXiv:1602.03837 [gr-qc].

[788] **LIGO Scientific, Virgo** Collaboration, B. Abbott *et al.*, "GW170817: Observation of Gravitational Waves from a Binary Neutron Star Inspiral," *Phys. Rev. Lett.* **119** no. 16, (2017) 161101, arXiv:1710.05832 [gr-qc].

[789] M. Carena, S. Heinemeyer, C. E. M. Wagner, and G. Weiglein, "Suggestions for benchmark scenarios for MSSM Higgs boson searches at hadron colliders," *Eur. Phys. J.* **C26** (2003) 601–607, arXiv:hep-ph/0202167 [hep-ph].

[790] **ATLAS** Collaboration, G. Aad *et al.*, "Search for charged Higgs bosons decaying via $H^+ \to \tau\nu$ in top quark pair events using pp collision data at $\sqrt{s} = 7$ TeV with the ATLAS detector," *JHEP* **06** (2012) 039, arXiv:1204.2760 [hep-ex].

[791] **ATLAS** Collaboration, G. Aad *et al.*, "Search for charged Higgs bosons through the violation of lepton universality in $t\bar{t}$ events using pp collision data at $\sqrt{s} = 7$ TeV with the ATLAS experiment," *JHEP* **03** (2013) 076, arXiv:1212.3572 [hep-ex].

[792] **ATLAS** Collaboration, G. Aad *et al.*, "Search for a light charged Higgs boson in the decay channel $H^+ \to c\bar{s}$ in $t\bar{t}$ events using pp collisions at $\sqrt{s} = 7$ TeV with the ATLAS detector," *Eur. Phys. J.* **C73** no. 6, (2013) 2465, arXiv:1302.3694 [hep-ex].

[793] **ATLAS** Collaboration, G. Aad *et al.*, "Search for charged Higgs bosons decaying via $H^\pm \to \tau^\pm\nu$ in fully hadronic final states using pp collision data at $\sqrt{s} = 8$ TeV with the ATLAS detector," *JHEP* **03** (2015) 088, arXiv:1412.6663 [hep-ex].

[794] **ATLAS** Collaboration, G. Aad *et al.*, "Search for a Charged Higgs Boson Produced in the Vector-Boson Fusion Mode with Decay $H^\pm \to W^\pm Z$ using pp Collisions at $\sqrt{s} = 8$ TeV with the ATLAS Experiment," *Phys. Rev. Lett.* **114** no. 23, (2015) 231801, arXiv:1503.04233 [hep-ex].

[795] J. C. Pati and A. Salam, "Lepton Number as the Fourth Color," *Phys. Rev.* **D10** (1974) 275–289. [Erratum: Phys. Rev.D11,703(1975)].

[796] R. N. Mohapatra and J. C. Pati, "Left-Right Gauge Symmetry and an Isoconjugate Model of CP Violation," *Phys. Rev.* **D11** (1975) 566–571.

[797] G. Senjanovic and R. N. Mohapatra, "Exact Left-Right Symmetry and Spontaneous Violation of Parity," *Phys. Rev.* **D12** (1975) 1502.

[798] T. G. Rizzo, "Doubly Charged Higgs Bosons and Lepton Number Violating Processes," *Phys. Rev.* **D25** (1982) 1355–1364. [Addendum: Phys. Rev.D27,657(1983)].

[799] **ATLAS** Collaboration, G. Aad *et al.*, "Search for neutral Higgs bosons of the minimal supersymmetric standard model in pp collisions at $\sqrt{s} = 8$ TeV with the ATLAS detector," *JHEP* **11** (2014) 056, arXiv:1409.6064 [hep-ex].

[800] **ATLAS** Collaboration, G. Aad *et al.*, "Search for a CP-odd Higgs boson decaying to Zh in pp collisions at $\sqrt{s} = 8$ TeV with the ATLAS detector," *Phys. Lett.* **B744** (2015) 163–183, arXiv:1502.04478 [hep-ex].

[801] **CMS** Collaboration, V. Khachatryan *et al.*, "Search for a pseudoscalar boson decaying into a Z boson and the 125 GeV Higgs boson in $\ell^+\ell^- b\bar{b}$ final states," *Phys. Lett.* **B748** (2015) 221–243, arXiv:1504.04710 [hep-ex].

[802] **ATLAS** Collaboration, G. Aad *et al.*, "Search for an additional, heavy Higgs boson in the $H \to ZZ$ decay channel at $\sqrt{s} = 8$ TeV in *pp* collision data with the ATLAS detector," *Eur. Phys. J.* **C76** no. 1, (2016) 45, arXiv:1507.05930 [hep-ex].

[803] **ATLAS** Collaboration, G. Aad *et al.*, "Search for a high-mass Higgs boson decaying to a W boson pair in *pp* collisions at $\sqrt{s} = 8$ TeV with the ATLAS detector," *JHEP* **01** (2016) 032, arXiv:1509.00389 [hep-ex].

[804] **ATLAS** Collaboration, G. Aad *et al.*, "Constraints on new phenomena via Higgs boson couplings and invisible decays with the ATLAS detector," *JHEP* **11** (2015) 206, arXiv:1509.00672 [hep-ex].

[805] **CMS** Collaboration, V. Khachatryan *et al.*, "Searches for a heavy scalar boson H decaying to a pair of 125 GeV Higgs bosons hh or for a heavy pseudoscalar boson A decaying to Zh, in the final states with $h \to \tau\tau$," *Phys. Lett.* **B755** (2016) 217–244, arXiv:1510.01181 [hep-ex].

[806] **ATLAS** Collaboration, M. Aaboud *et al.*, "Search for Heavy Higgs Bosons A/H Decaying to a Top Quark Pair in *pp* Collisions at $\sqrt{s} = 8$ TeV with the ATLAS Detector," *Phys. Rev. Lett.* **119** no. 19, (2017) 191803, arXiv:1707.06025 [hep-ex].

[807] **ATLAS** Collaboration, M. Aaboud *et al.*, "Search for heavy resonances decaying to a W or Z boson and a Higgs boson in the $q\bar{q}^{(\prime)}b\bar{b}$ final state in *pp* collisions at $\sqrt{s} = 13$ TeV with the ATLAS detector," *Phys. Lett.* **B774** (2017) 494–515, arXiv:1707.06958 [hep-ex].

[808] **ATLAS** Collaboration, M. Aaboud *et al.*, "Searches for heavy ZZ and ZW resonances in the $\ell\ell qq$ and $\nu\nu qq$ final states in *pp* collisions at $\sqrt{s} = 13$ TeV with the ATLAS detector," *JHEP* **03** (2018) 009, arXiv:1708.09638 [hep-ex].

[809] **ATLAS** Collaboration, M. Aaboud *et al.*, "Search for additional heavy neutral Higgs and gauge bosons in the ditau final state produced in 36 fb^{-1} of pp collisions at $\sqrt{s} = 13$ TeV with the ATLAS detector," *JHEP* **01** (2018) 055, arXiv:1709.07242 [hep-ex].

[810] **ATLAS** Collaboration, M. Aaboud *et al.*, "A search for resonances decaying into a Higgs boson and a new particle X in the $XH \to qqbb$ final state with the ATLAS detector," *Phys. Lett.* **B779** (2018) 24–45, arXiv:1709.06783 [hep-ex].

[811] **ATLAS** Collaboration, M. Aaboud *et al.*, "Search for heavy resonances decaying into a W or Z boson and a Higgs boson in final states with leptons and b-jets in 36 fb^{-1} of $\sqrt{s} = 13$ TeV pp collisions with the ATLAS detector," arXiv:1712.06518 [hep-ex].

[812] **ATLAS** Collaboration, M. Aaboud *et al.*, "Search for a heavy Higgs boson decaying into a Z boson and another heavy Higgs boson in the $\ell\ell bb$ final state in pp collisions at $\sqrt{s} = 13$ TeV with the ATLAS detector," arXiv:1804.01126 [hep-ex].

[813] **CMS** Collaboration, A. M. Sirunyan *et al.*, "Search for a new scalar resonance decaying to a pair of Z bosons in proton-proton collisions at $\sqrt{s} = 13$ TeV," arXiv:1804.01939 [hep-ex].

[814] **CMS** Collaboration, A. M. Sirunyan *et al.*, "Search for $t\bar{t}H$ production in the $Hb\bar{b}$ decay channel with leptonic $t\bar{t}$ decays in proton-proton collisions at $\sqrt{s} =$ 13 TeV," arXiv:1804.03682 [hep-ex].

[815] A. Djouadi, "The Anatomy of electro-weak symmetry breaking. II. The Higgs bosons in the minimal supersymmetric model," *Phys. Rept.* **459** (2008) 1–241, arXiv:hep-ph/0503173 [hep-ph].